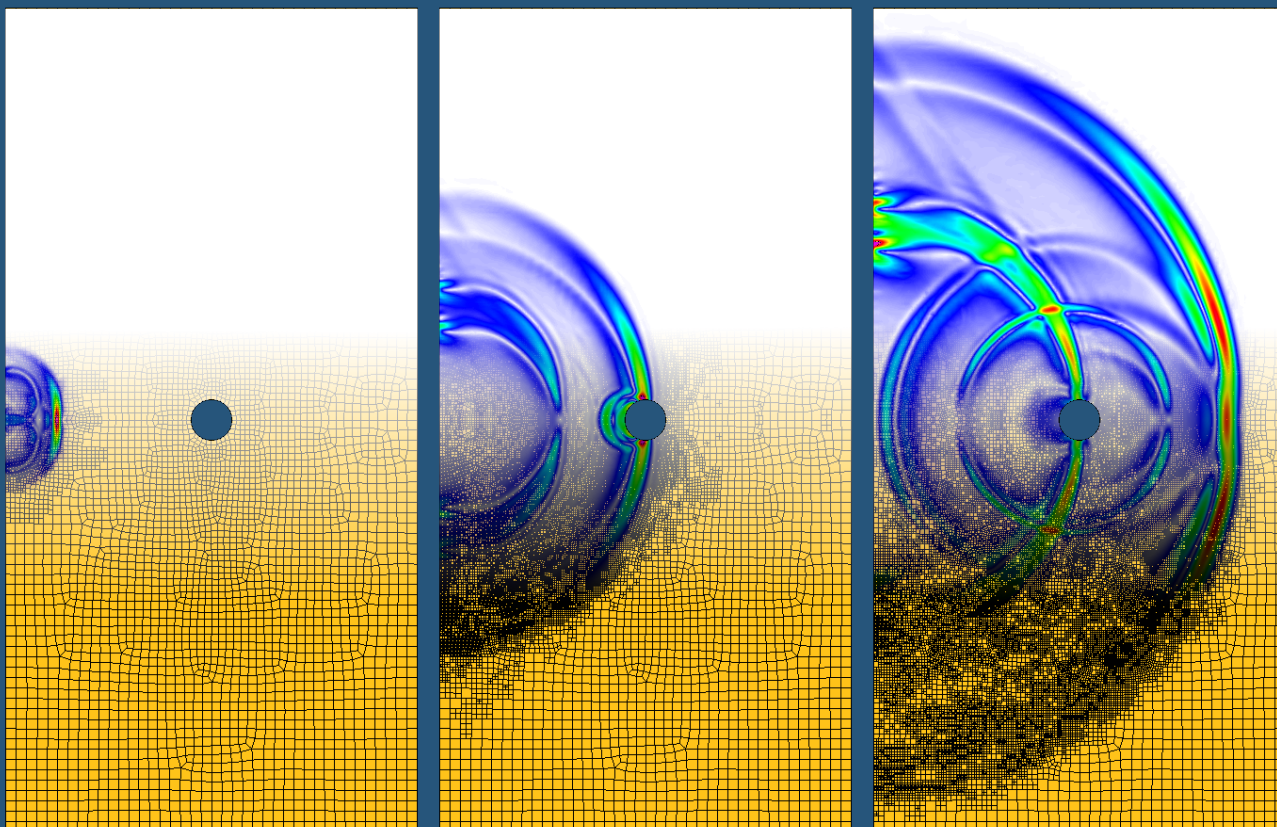


# ERROR ASSESSMENT AND ADAPTIVITY FOR STRUCTURAL TRANSIENT DYNAMICS

Francesc Verdugo



Doctoral Thesis  
Barcelona, October 2013



# ERROR ASSESSMENT AND ADAPTIVITY FOR STRUCTURAL TRANSIENT DYNAMICS

Francesc Verdugo

---



Doctoral Thesis

Advisors: Pedro Díez and Núria Parés

Barcelona, October 2013

Departament de Matemàtica Aplicada III  
Programa de Doctorat en Enginyeria Civil



## ABSTRACT

The finite element method is a valuable tool for simulating complex physical phenomena. However, any finite element based simulation has an intrinsic amount of error with respect to the exact solution of the selected physical model. Being aware of this error is of notorious importance if sensitive engineering decisions are taken on the basis of the numerical results. Assessing the error in elliptic problems (as structural statics) is a well known problem. However, assessing the error in structural transient dynamics is still ongoing research.

The present thesis aims at contributing on error assessment techniques for structural transient dynamics. First, a new approach is introduced to compute bounds of the error measured in some quantity of interest. The proposed methodology yields error bounds with better quality than the already available approaches. Second, an efficient methodology to compute approximations of the error in the quantity of interest is introduced. The proposed technique uses modal analysis to compute the solution of the adjoint problem associated with the selected quantity of interest. The resulting error estimate is very well suited for time-dependent problems, because the cost of computing the estimate at each time step is very low. Third, a space-time adaptive strategy is proposed. The local error indicators driving the adaptive process are computed using the previously mentioned modal-based error estimate. The resulting adapted approximations are more accurate than the ones obtained with a straightforward uniform mesh refinement. That is, the adapted computations lead to lower errors in the quantity of interest than the non-adapted ones for the same number of space-time elements. Fourth, a new type of quantities of interest are introduced for error assessment in time-dependent problems. These quantities (referred as timeline-dependent quantities of interest) are scalar time-dependent outputs of the transient solution and are better suited to time-dependent problems than the standard scalar ones. The error in timeline-dependent quantities is efficiently assessed using the modal-based description of the adjoint solution.

The thesis contributions are enclosed in five papers which are attached to the thesis document.

## KEYWORDS

Structural dynamics · finite element method · error assessment · error bounds  
space-time adaptivity · quantity of interest · adjoint problem · modal analysis



## ACKNOWLEDGMENTS

First, I would like to thank my advisors Pedro Díez and Núria Parés for their advice and support during these years. From Pedro, I have learned many things, including a very important one: it is possible to be an excellent specialist while having a wide knowledge and sensitiveness for other important aspects of life. I would also thank Pedro for his good advice, for his practical viewpoint of things and because finding an empty space in his busy agenda of Vice Rector has never been a problem. From Núria, I have also learned a lot, specially how to be rigorous with the little details. She has contributed very much to push the work forward these last two years. Many thanks to both of you. I have enjoyed very much working together.

I would also like to thank Folco Casadei for his collaboration in the topics related with adaptivity. It is impressive how fast he produces technical reports and replies emails! Thank you for being always open to answer questions and for the short stay in Ispra. I would also like to acknowledge the members of the jury for accepting our invitation. Counting with you is a honor.

I extend my gratitude to all members of the research group LaCàN, in particular to Antonio Huerta for providing the opportunity of joining the team. I am specially grateful to Sonia Fernández and Rubén Sevilla (now lecturer in Swansea) for introducing me into the group some years ago. I wish to acknowledge the support given by Antonio Rodríguez and the other colleagues of the module *Numerical Modelling* on the topics related with teaching. Thanks a lot to Josep Sarrate for solving particular doubts when required, and also to Marino Arroyo for accepting being in the jury.

My best wishes to all the office mates and friends I have meet in the group, specially those living in room 210! You have been the most effective way to forget for a moment about functional spaces and code bugs. I have enjoyed very much the lunch time together and other special moments. Thanks to Eloi for recalling me everyday that *poleo-menta* tea is exciting, to Esther for knowing everything and for solving many questions, to Elena for finding the optimistic viewpoint even when it is impossible, to Cristina for fighting constantly against injustice, to Raúl for his brilliant criticism and enthusiasm, to Alex for his wise opinions, to Abel for his sense of good and evil, to Miquel for explaining nice anecdotes, and to many others; David Modesto, Jordi, David Ortín, Omid, Raquel, Imma, Milan, Marco, Yongxing, Sergio, Giorgio, Eva, Richard, Lindaura, Alba, Xevi, Joan,... for nearly becoming part of my family.

I would also like to express my gratitude to the public education system for providing me the opportunity of growing as student and person, from the first day of the kindergarten to the last day of the PhD. I am particularly grateful to the maths teachers I meet at the high school *I.E.S. Damià Campeny* (Mataró) for being a crucial influence. I wanted also to acknowledge the funding provided by the *Universitat Politècnica de Catalunya* in the framework of the scholarship FPU-UPC.

Finally, I would like to express my very special thanks to the unconditional supports. Mama, thank you for convincing me again and again that “*todo saldrá bien*”. Papa, thank you for being so enthusiastic about the things I do. Many thanks also to my brother and sister. And the most special thanks is to you, Anna, for your support and patience during these two years and for making me aware of what is actually important.

Mataró, August 2013

# Contents

---

<b>Abstract</b>	<b>v</b>
<b>Acknowledgments</b>	<b>vii</b>
<b>Contents</b>	<b>ix</b>
<b>Thesis overview</b>	<b>1</b>
1 Introduction . . . . .	1
1.1 Motivation . . . . .	1
1.2 State-of-the-art . . . . .	3
1.3 Objectives and document layout . . . . .	8
2 Problem description . . . . .	10
2.1 Governing equations . . . . .	10
2.2 Numerical approximation . . . . .	11
2.3 Error to be assessed . . . . .	13
2.4 Adjoint problem . . . . .	14
3 Contributions . . . . .	16
3.1 Goal-oriented error bounds . . . . .	16
3.2 Modal-based goal-oriented error assessment . . . . .	21
3.3 Modal-based goal-oriented adaptivity . . . . .	26
3.4 Error assessment for timeline-quantities of interest . . . . .	34
4 Closure . . . . .	41
4.1 Summary . . . . .	41
4.2 Open research lines . . . . .	43
<b>Bibliography</b>	<b>47</b>
<b>Paper A Error assessment in structural transient dynamics</b>	<b>53</b>
<b>Paper B Computable bounds of functional outputs in linear visco-elastodynamics</b>	<b>113</b>

Paper C	Modal based goal-oriented error assessment for timeline-dependent quantities in transient dynamics	133
Paper D	Goal-oriented space-time adaptivity for transient dynamics using a modal description of the adjoint solution	171
Paper E	An algorithm for mesh refinement and un-refinement in fast transient dynamics	195

# Thesis overview

---

## 1 Introduction

### 1.1 Motivation

Finite element-based simulations have become a fundamental tool in engineering analysis. These techniques are valuable to simulate physical phenomena when experiments are too expensive or even impracticable. However, any finite element approximation has two inherent sources of error, the *modeling* error and the *discretization* error. Consequently, both errors have to be controlled to provide a reliable numerical solution. This is particularly important if sensitive decisions are taken on the basis of the numerical results.

The modeling error is the difference between *reality* and the selected mathematical model. The mathematical model is typically described by a set of partial differential equations (plus suitable initial and boundary conditions) which are approximated with numerical tools. The discretization error is the difference between the unknown *exact* solution of the mathematical model and the *computable* numerical approximation. The present work restricts to assessing the discretization error. Thus, the exact solution of the mathematical model is taken as the *truth* solution in the present error analysis. Assessing the modeling error is out of the scope of this work.

The numerical approximation is associated with a *discretization* of the computational domain based on a *computational mesh* or grid. Consequently, the choice of a *good enough* mesh is crucial to have a reliable solution. In practice, the quality of the computational mesh is bounded by the available computer resources, and therefore, a compromise between cost and quality has to be found.

*A posteriori* error assessment techniques allow the user of the finite element soft-

ware to be aware of which is the error associated with the selected discretization. This information is used to accept or reject the numerical approximation on the basis of the required accuracy for a specific application. Moreover, error assessment techniques provide local error information describing the distribution of the error over the computational domain. This information is used to build an *adapted* discretization. A fine mesh is employed only at the zones with large error contribution, making an efficient use of the computational resources.

This work focuses in structural transient dynamics. That is, structural problems under impulsive loads exiting a high frequency spectrum. In this situation, the solution of the problem is typically approximated using direct time-integration schemes instead of modal analysis, because the required number of vibration modes to characterize the solution is very high. The applications of structural transient dynamics include a high variety of elastic wave propagation problems. For instance, vulnerability of structures under explosions or impacts, or applications in geophysics as the propagation of earthquake waves.

Assessing the error in structural dynamics is particularly relevant because, as compared to the standard elliptic problems, the discretization errors are generated and propagated less intuitively or predictably. Moreover, the applications of structural transient dynamics include safety-related issues in buildings and large infrastructures. Consequently, a quality certification of the numerical solution is important in this context.

Nowadays, the error assessment and adaptive techniques are well established for elliptic problems as steady-state linear elasticity and heat transfer. However, these methodologies are still under development for structural transient dynamics (also referred as *elastodynamics*) and other second-order hyperbolic problems. Assessing the error in structural dynamics is a challenging topic. First, the available error estimates are expensive in terms of CPU time and memory requirements. Second, computing sharp error bounds is specially demanding using the available techniques. And third, the quantities of interest available for assessing the error are not particularly well suited for time-dependent problems. These difficulties compromise the application of the current error assessment techniques in practical engineering examples. Consequently, further research is required to overcome these difficulties.

## 1.2 State-of-the-art

Over the last three decades, numerous a posteriori error assessment techniques for finite element analysis have been proposed. Representative state-of-the-art reviews and books on this topic are introduced by Ainsworth and Oden (2000, 1997), Ladevèze and Pelle (2001), Rannacher (2001), Stein (2003), Gratsch and Bathe (2005), and Díez et al. (2010). These works focus mainly in elliptic problems and do not include the last advances particular to structural transient dynamics. A detailed review of the available error assessment techniques for structural transient dynamics is presented in the appended paper A. The state-of-the-art review presented in this introduction is a succinct version of the one found in paper A.

A posteriori error assessment techniques aim at assessing a particular error measure (i.e. a representative scalar value associated with the error) instead of approximating the error field at each point of the computational domain. Approximating the error field generally requires computing a reference solution using a much finer discretization, which is unaffordable in practice. Two different types of error measures are considered in the literature leading to two different types of error estimates: 1) energy-like error estimates and 2) goal-oriented error estimates.

### 1) Energy-like error estimates (also referred as *global* error estimates)

The error measure is defined as a *global* norm of the error (integrated over the whole computational domain). The standard norm considered for error assessment in elliptic problems is the norm induced by the bilinear form of the corresponding weak equations. This specific norm is referred as the *energy* norm because it is related with the energy of the underlying physical model. For instance, the energy norm in steady-state linear elasticity coincides with (the square root of) the potential elastic energy. Assessing the error energy norm is particularly straightforward in elliptic problems, because this particular error measure is closely related with the residual. Representative works assessing the error energy norm in elliptic problems are the pioneering references on error assessment by Babuška and Rheinboldt (1978), Ladevèze and Leguillon (1983), and Zienkiewicz and Zhu (1987).

The energy-like error measures for structural transient dynamics do not only include the potential elastic energy, but also the kinetic energy as well as the dissipated energy for problems containing a finite amount of damping. Refer-

ences by Li and Wiberg (1998), Wiberg and Li (1999), Schleupen and Ramm (2000), and Aubry et al. (1999) propose error estimates assessing the kinetic and elastic energy of the error. On the other hand, references by Ladevèze and Waeytens (2009), Waeytens (2010), Ladevèze (2008), and Waeytens et al. (2012) propose computable bounds of the dissipated energy associated with the error.

**2) Goal-oriented error estimates** (also referred as *local* error estimates)

In the context, the error measure is defined by means of a functional extracting a single representative scalar value of the solution of the problem. The end-user of the finite element software can define the functional such that the extracted value is a *quantity of interest* of the problem with a relevant physical meaning (e.g. the average of the solution in a specific *local* region of the domain). The error to be assessed is the error in the quantity of interest. That is, the difference between the quantity of interest associated with the exact solution and the quantity of interest associated with the finite element approximation. The techniques assessing the error in the quantity of interest are generally referred as *goal-oriented*.

Quantities of interest are error measures more meaningful than the standard energy-like global norms. However, assessing the error in an arbitrary quantity of interest requires approximating an auxiliary problem referred as the *adjoint* or *dual* problem. Thus, goal-oriented error estimates are usually more expensive than energy-like ones.

Goal-oriented error estimates are originally proposed for elliptic problems by Paraschivoiu et al. (1997), Cirak and Ramm (1998), and Prudhomme and Oden (1999). These techniques are extended to other problem types. For instance, estimates for the advection-diffusion-reaction equation are discussed by Parés et al. (2009). Similar approaches for the Stokes problem are presented by Larson et al. (2010). An extension to parabolic time-dependent problems is introduced by Parés et al. (2008a,b), and Díez and Calderón (2007). Moreover, the same type of tools are discussed for coupled problems by Larson and Bengzon (2008), Larson et al. (2008), Fick et al. (2010), Van Der Zee et al. (2011), and Asner et al. (2012). Finally, goal-oriented error estimates are also proposed for structural transient dynamics by Waeytens et al. (2012), Bangerth et al. (2010),

Schleupen and Ramm (2000), and Fuentes et al. (2006).

The specific techniques for assessing the error in structural transient dynamics are briefly presented in the following. The interested reader can find the specific details in the appended paper A. For the sake of presentation, the error assessment techniques are grouped here in three types: 1) recovery-based estimates, 2) the dual weighted residual method and 3) the constitutive relation error method. This classification is based on the different methodologies used to derive the error estimates.

### 1) Recovery-based error estimates

In the context of steady-state elasticity and other elliptic problems, recovery-based error estimates provide approximations of the error energy norm and local error indicators used for mesh adaptivity. The error estimate is derived as follows. First, the error energy norm is written in terms of the error in stresses using the complementary energy. The error in stresses is defined as the difference between the (unknown) exact stresses and the stresses associated with the finite element solution. Hence, the error estimate is obtained replacing the unknown exact stress by an enhanced version of the available finite element stress. The local error contributions are obtained by restricting the integrals involved in the definition of the complementary energy to the elements of the computational mesh.

The technique providing the enhanced stress field consists in computing (or *recovering*) a *continuous* stress as a post-process of the *discontinuous* finite element stress. There are two main approaches to compute the continuous stress. Either solving a global problem involving all the degrees of freedom of the mesh [Zienkiewicz and Zhu (1987)], or solving local problems involving a small subset of degrees of freedom [Zienkiewicz and Zhu (1992a,b)].

Recovery-based estimates are applied to structural dynamics to provide local error information driving mesh adaptivity, see references by Li and Wiberg (1998), Wiberg and Li (1999), Schleupen and Ramm (2000), and Erhart et al. (2006). The local error indicators are obtained performing at each time step the standard recovery techniques designed for steady-state problems. The elastic energy of the error is assessed using the previously presented stress recovery. However, the same approach do not holds for assessing the kinetic energy of the error, because it requires computing an enhanced version of the velocities.

Note that the finite element velocity is already continuous at the inter-element boundaries. Consequently, a specific recovery procedure is introduced for the velocities, see references by Wiberg and Li (1994) and Wiberg et al. (1999) for details.

The recovery techniques applied to time-dependent problems give approximations of the space discretization error, but they are not sufficient to assess the time discretization error. Hence, the recovery techniques allow to adapt only the space discretization. The time-discretization is adapted by introducing alternative error estimates for the time discretization, see reference by Schleupen and Ramm (2000) for details.

A complete review on recovery estimates for different problem types is introduced by Wiberg et al. (1997).

## 2) The dual weighted residual method

The dual residual method provides approximations of the error in the quantity of interest as well as local error indicators used for mesh adaptivity. The error estimate is derived in two stages. First, the error in the quantity of interest is expressed in terms of the exact solution of the adjoint problem and of the weak residual associated with the numerical approximation. Then, the error estimate is obtained by replacing the exact solution of the adjoint problem by a suitable numerical approximation, see the work by Rannacher and Stutzmeier (1997) for details. The local error indicators are obtained by restricting the integrals involved in the weak residual to the elements of the computational mesh.

The key ingredient of the dual weighted residual method is computing a suitable approximation of the adjoint solution. Here, the word “suitable” means that the adjoint approximation has to belong to a richer interpolation space than the one used for approximating the solution of original problem. This is required to avoid the cancellation of the assessed error by Galerkin orthogonality. The adjoint approximation is obtained either applying recovery techniques to a coarse-mesh approximation of the adjoint solution or solving the adjoint problem using higher order elements. Note that, this latter approach might be unaffordable in large examples.

The weighted residual method is applied to a high variety of problem types, even non-linear problems, as is shown in the review papers by Rannacher (2001), and

Becker and Rannacher (2001). This methodology is originally introduced for elliptic problems by Rannacher and Stuttmeier (1997). The extension to linear structural transient dynamics is proposed by Bangerth et al. (2010), Schleupen and Ramm (2000), Bangerth (1998), Rannacher (2001), Bangerth and Rannacher (1999), and Bangerth and Rannacher (2001). The non-linear dynamic case is considered by Fuentes et al. (2006). In the context of structural dynamics and other time-dependent problems, the dual weighted residual method is expensive in terms of CPU time and memory requirements. This is because the space-time adjoint solution has to be computed and stored as a whole (i.e. at each mesh vertex and time step) before computing the error estimate.

The rationale of the dual weighted residual method is used to assess the error in global norms as well. In the context of second order hyperbolic problems, Eriksson et al. (1996) propose an estimate for the  $L^2$  norm of the error at the final time of the computation. Following a similar approach, Aubry et al. (1999) propose an estimate of the total error energy (kinetic plus elastic). The resulting error estimate is completely *explicit* in the sense that it is computable as a direct post-process of the residual, without solving any auxiliary problem. For these particular error measures, the adjoint problem is only an auxiliary mathematical artifact used to derive the estimate. Consequently, the adjoint problem is not approximated.

### 3) Constitutive relation error method

The constitutive relation method furnishes bounds of the error energy norm as well as the error in the quantity of interest. Computing error bounds with this methodology requires building a stress-based approximation of the problem (fulfilling the equilibrium/momentum equations and the Neumann boundary conditions). The difference between the equilibrated stress and the stress associated with the finite element approximation is a computable error in stresses corresponding to the non-verification of the constitutive relation.

In the context of elliptic problems, the bound of the error energy norm is derived using the result by Prager and Synge (1947) which states that the complementary energy of the error in the constitutive relation is an upper bound of the error energy norm. The error in the quantity of interest is assessed by combining error bounds for the original and adjoint problems. Hence, a finite element

approximation as well as an equilibrated stress field are required for the adjoint problem.

The error bounds are computable once the equilibrated stresses are available. Stress equilibration techniques are proposed by Ladevèze and Leguillon (1983), Ainsworth and Oden (1997, 2000), and Parés et al. (2006). A comparison of different stress equilibration procedures is presented by Pled et al. (2011). Constitutive relation error estimates are *implicit* in the sense that the underlying stress equilibration technique is based on solving auxiliary local problems. In many contexts, constitutive relation error are equivalent to other implicit residual type error estimates, for instance the ones proposed by Ainsworth and Oden (1997), Ainsworth and Oden (2000), and Parés et al. (2006).

The constitutive relation error method is introduced in the literature originally for linear elliptic problems by Ladevèze and Leguillon (1983). The method is extended later to deal with a wide range of problem types. For instance, parabolic problems are considered by Chamoin and Ladevèze (2008). Non-linear problems are considered by Ladevèze and Moës (1999), Ladevèze et al. (2000), Ladevèze and Moës (1997), and Gallimard et al. (2000). The constitutive relation error method is applied to structural dynamics by Ladevèze (2008), Ladevèze and Waeytens (2009), Waeytens (2010), and Waeytens et al. (2012).

Computing error bounds in structural transient dynamics using the constitutive relation method has two main difficulties. First, the standard stress equilibration techniques designed for steady-state problems have to be repeated at each time step which is computationally demanding. Second, deriving the error bounds requires that the formulation of the problem includes some non-zero amount of damping. That is, the bounding properties are lost in the case of pure elasticity. In practice, the computed error bounds are very pessimistic for small values of the viscosity.

### 1.3 Objectives and document layout

The present thesis aims at contributing in the research field of a posteriori error assessment for structural dynamics by proposing new error estimates addressing the following difficulties: 1) the poor quality of the computable error bounds, 2) the

cost of computing goal-oriented error estimates, and 3) the limitation of standard quantities of interest when dealing with time-dependent problems.

**1) Enhancing the quality of goal-oriented error bounds.**

Further research is required to improve the quality of the available error bounds in structural transient dynamics. In the context of elliptic problems, the error bounds are derived using the result by Prager and Synge (1947) which holds because the bilinear form of the weak problem is an inner product. In structural dynamics, the associated bilinear form is not symmetric (hence, not an inner product), which makes computing error bounds challenging.

References by Parés et al. (2008a,b) derive error bounds for the time-dependent convection-diffusion-reaction equation. These references propose a methodology to deal with a non-symmetric bilinear form. Consequently, an analogous approach is investigated here for structural dynamics. The alternative error bounds are presented in section 3.1 and discussed in detail in paper B.

**2) Enhancing the efficiency of goal-oriented error estimates**

The available goal-oriented error estimates for structural dynamics consider direct time-integration methods for approximating the solution of the adjoint problem. The resulting error estimates are expensive in terms of memory requirements because the adjoint solution has to be computed and stored at each mesh node and time step. Moreover, error estimates generally require performing post-process operations (i.e stress recovery or equilibration) at each time step which might be unaffordable in large problems. Modal analysis is investigated as an alternative way to efficiently compute and store the adjoint solution. The modal-based error estimate is presented in section 3.2 and discussed in details in paper C. Moreover, the proposed error estimate is used for space-time adaptivity in section 3.3 and in paper D.

**3) Going beyond standard quantities of interest for time-dependent problems**

As previously announced, the quantities of interest available in the literature for error assessment are expressed in terms of a functional extracting a single representative scalar value of the solution. A quantity of interest for steady-state problems is usually the average of the unknown solution in a sub-region of the

computational domain. However, in time dependent problems, the definition of the quantity of interest must involve not only a spatial sub-domain but also a time interval of interest. The choice of this time frame is not always obvious for the end-user. This is because a single scalar value does not provide enough pieces of information about the whole time-space solution.

The preferred quantities of interest in time-dependent problems are time-dependent scalar functions instead of scalar values. For instance, the history of the average of the solution in a space sub-region of the computational domain. These type of quantities are referred in the following as *timeline*-dependent quantities of interest in contrast to the standard *scalar* quantities. Timeline-dependent quantities of interest are better suited to time-dependent problems because they preclude selecting the time frame. The error assessment strategy for timeline-dependent quantities is to be investigated. The resulting error estimates are presented in section 3.4 and in paper C.

The remainder of this document is structured in two parts. The first one is an overview of the thesis work. This includes the formal definition of the equations of structural dynamics and the error to be assessed, an overview of the main contributions, and the conclusions and further research. The second part consist of five appended papers where the contributions are discussed in detail. Paper A presents a comprehensive state-of-the-art review on error assessment for structural transient dynamics. Paper B discusses alternative error bounds. Paper C presents the modal-based approximation of the adjoint solution and the error assessment strategy for timeline-dependent quantities of interest. Paper D introduces an space-time adaptive strategy based on the modal description of the adjoint solution. Finally, paper E details the mesh refinement and un-refinement procedure considered in the adaptive strategy presented in paper D.

## 2 Problem description

### 2.1 Governing equations

A visco-elastic body occupies an open bounded domain  $\Omega \subset \mathbb{R}^d$ ,  $d \leq 3$ , with boundary  $\partial\Omega$ . The boundary is divided in two disjoint parts,  $\Gamma_N$  and  $\Gamma_D$  such that  $\partial\Omega = \bar{\Gamma}_N \cup \bar{\Gamma}_D$  and the considered time interval is  $I := (0, T]$ . Under the assumption of small

perturbations, the evolution of displacements  $\mathbf{u}(\mathbf{x}, t)$  and stresses  $\boldsymbol{\sigma}(\mathbf{x}, t)$ , for  $\mathbf{x} \in \Omega$  and  $t \in I$ , is described by the visco-elastodynamic equations

$$\rho(\ddot{\mathbf{u}} + a_1 \dot{\mathbf{u}}) - \nabla \cdot \boldsymbol{\sigma} = \mathbf{f} \quad \text{in } \Omega \times I, \quad (1a)$$

$$\mathbf{u} = \mathbf{0} \quad \text{on } \Gamma_D \times I, \quad (1b)$$

$$\boldsymbol{\sigma} \cdot \mathbf{n} = \mathbf{g} \quad \text{on } \Gamma_N \times I, \quad (1c)$$

$$\mathbf{u} = \mathbf{u}_0 \quad \text{at } \Omega \times \{0\}, \quad (1d)$$

$$\dot{\mathbf{u}} = \mathbf{v}_0 \quad \text{at } \Omega \times \{0\}, \quad (1e)$$

where an upper dot indicates derivation with respect to time, that is  $(\dot{\bullet}) := \frac{d}{dt}(\bullet)$ , and  $\mathbf{n}$  denotes the outward unit normal to  $\partial\Omega$ . The input data includes the mass density  $\rho = \rho(\mathbf{x}) > 0$ , the first Rayleigh coefficient  $a_1 \geq 0$ , the body force  $\mathbf{f} = \mathbf{f}(\mathbf{x}, t)$  and the traction  $\mathbf{g} = \mathbf{g}(\mathbf{x}, t)$  acting on the Neumann boundary  $\Gamma_N \times I$ . The initial conditions for displacements and velocities are  $\mathbf{u}_0 = \mathbf{u}_0(\mathbf{x})$  and  $\mathbf{v}_0 = \mathbf{v}_0(\mathbf{x})$  respectively. For the sake of simplicity and without any loss of generality, Dirichlet conditions (1b) are taken as homogeneous.

The set of equations (1) is closed with the constitutive law,

$$\boldsymbol{\sigma} := \mathcal{C} : \boldsymbol{\varepsilon}(\mathbf{u} + a_2 \dot{\mathbf{u}}), \quad (2)$$

where the parameter  $a_2 \geq 0$  is the second Rayleigh coefficient, the tensor  $\mathcal{C}$  is the standard 4th-order elastic Hooke tensor. The strains are given by the kinematic relation corresponding to small perturbations,  $\boldsymbol{\varepsilon}(\mathbf{w}) := \frac{1}{2} (\nabla \mathbf{w} + (\nabla \mathbf{w})^T)$ .

**Remark 1.** *The displacement field  $\mathbf{u}$  defined in equations (1) is the unknown exact solution which is taken as the truth in the following error assessment analysis.*

## 2.2 Numerical approximation

The input data of any a posteriori error assessment technique is an approximation of the exact solution of the underlying mathematical problem. In the following, the numerical approximation of problem (1) is referred as  $\tilde{\mathbf{u}} \approx \mathbf{u}$ . There are two main alternatives to compute this approximation. Either using finite elements for the space discretization and finite differences for the time discretization (e.g. the well known method proposed by Newmark (1959)) or using finite elements for both the space and time discretizations, see the work by Hughes and Hulbert (1988). Note however, these

are not the only available approximation techniques. Other approximation methods are based on finite volumes (Lee et al. (2013)), spectral elements (Komatitsch et al. (1999)) and boundary elements (Bouchona and Sánchez-Sesma (2007)). A detailed presentation of the available approximation methods in structural dynamics is out of the scope of this thesis overview. The reader is referred to the paper A or to references by Bangerth et al. (2010), and Bathe (1996) for specific details.

Most of the approximation methods are based on separated discretizations for the space and time domains (i.e. discretizing the whole space-time domain  $\Omega \times I$  with an unstructured mesh is non-standard). The time domain  $I$  is discretized using a time grid  $\mathcal{T} := \{t_0, t_1, \dots, t_N\}$ , where  $0 = t_0 < t_1 < \dots < t_N = T$  are the grid points. These points define the time intervals  $I_n := (t_{n-1}, t_n]$  with time step length  $\Delta t_n := t_n - t_{n-1}$ ,  $n = 1, \dots, N$ . On the other hand, the space domain  $\Omega$  is discretized using a finite element mesh. The set of all mesh elements is denoted by  $\mathcal{P}$ .

**Remark 2.** *In the context of mesh adaptivity for transient problems, the space finite element mesh  $\mathcal{P}$  is allowed to be different at each time point  $t_n \in \mathcal{T}$ . In that case, the finite element mesh associated with the time point  $t_n$  is denoted as  $\mathcal{P}_n$ . Consequently, the approximation method has to be able to properly transfer the numerical solution from one mesh to the other without lose of information. A detailed methodology to deal with changing meshes is found in the paper D.*

Problem (1) is typically discretized in space using standard finite elements. The finite element mesh  $\mathcal{P}$  is associated with a functional space, namely  $\mathbf{V}_0^{H,p}$ , containing continuous piecewise polynomial functions of degree  $p$ . The upper-script  $H$  stands for the characteristic mesh element size of the elements in  $\mathcal{P}$ . The discretization of (the weak version of) problem (1) in the space  $\mathbf{V}_0^{H,p}$  leads to a system of Ordinary Differential Equations (ODE). Solving this system yields the numerical approximation  $\tilde{\mathbf{u}}$ . The system of ODE is solved either with finite differences, as proposed by Newmark (1959), or using finite elements, see works by Eriksson et al. (1996), Johnson (1993), and Hughes and Hulbert (1988).

The approximation  $\tilde{\mathbf{u}}$  has to fulfill particular properties to be a valid input for the error analysis. Some error estimates (e.g. the ones proposed in the papers B and C) require only that the approximation  $\tilde{\mathbf{u}}$  is regular enough. This allows computing the numerical approximation with many different approximation methods. On the other hand, other error assessment strategies, e.g. the one proposed in appended paper D, require that the approximation  $\tilde{\mathbf{u}}$  is solved with a specific method. This

is because the error estimate requires the Galerkin orthogonality property associated with a particular discrete solution.

### 2.3 Error to be assessed

The discretization error associated with the approximation  $\tilde{\mathbf{u}}$  is defined as  $\mathbf{e} := \mathbf{u} - \tilde{\mathbf{u}}$ . A brute-force approach to approximate the unknown error  $\mathbf{e}$  is computing an *overkill* or *reference* solution of problem (1), namely  $\mathbf{u}^{\text{ovk}}$ . This overkill solution is computed using a much finer discretization than the one for  $\tilde{\mathbf{u}}$ . The overkill discretization is built by an  $H$ - or  $p$ -refinement of the finite element mesh  $\mathcal{P}$  and by adding more time points into the time partition  $\mathcal{T}$ . Then, the error is approximated replacing the exact solution  $\mathbf{u}$  by the overkill approximation  $\mathbf{u}^{\text{ovk}}$ , namely  $\mathbf{e} \approx \mathbf{u}^{\text{ovk}} - \tilde{\mathbf{u}}$ . Note that computing the overkill solution is unaffordable in large examples. Thus, a posteriori error assessment techniques aim at assessing the error in a more affordable way.

As previously announced, the error to be assessed is a specific error measure (an scalar value) instead of the error field  $\mathbf{e}(\mathbf{x}, t)$ . The error measure considered here is a quantity of interest associated with a functional  $L^\mathcal{O}(\cdot)$ . A commonly used quantity of interest in elastodynamics is represented by the linear functional

$$\begin{aligned} L^\mathcal{O}(\mathbf{w}) := & \int_0^T (\mathbf{f}^\mathcal{O}(t), \dot{\mathbf{w}}(t)) \, dt + \int_0^T (\mathbf{g}^\mathcal{O}(t), \dot{\mathbf{w}}(t))_{\Gamma_N} \, dt \\ & + m(\mathbf{v}^\mathcal{O}, \dot{\mathbf{w}}(T)) + a(\mathbf{u}^\mathcal{O}, \mathbf{w}(T)), \end{aligned} \quad (3)$$

where  $\mathbf{f}^\mathcal{O}$ ,  $\mathbf{g}^\mathcal{O}$ ,  $\mathbf{v}^\mathcal{O}$  and  $\mathbf{u}^\mathcal{O}$  are the data characterizing the quantity of interest. The weighting functions  $\mathbf{f}^\mathcal{O}$  and  $\mathbf{g}^\mathcal{O}$  allow to define weighted averages of velocities integrated in  $\Omega \times I$  and  $\Gamma_N \times I$  respectively. The fields  $\mathbf{v}^\mathcal{O}$  and  $\mathbf{u}^\mathcal{O}$  play the role of weighting functions defining averages of velocities and strains at the final simulation time  $T$ . In the definition of the quantity of interest (3), the following notations are used

$$\begin{aligned} (\mathbf{v}, \mathbf{w}) := & \int_\Omega \mathbf{v} \cdot \mathbf{w} \, d\Omega, \quad (\mathbf{v}, \mathbf{w})_{\Gamma_N} := \int_{\Gamma_N} \mathbf{v} \cdot \mathbf{w} \, d\Gamma, \quad m(\mathbf{v}, \mathbf{w}) := \int_\Omega \rho \mathbf{v} \cdot \mathbf{w} \, d\Omega, \quad \text{and} \\ a(\mathbf{v}, \mathbf{w}) := & \int_\Omega \boldsymbol{\varepsilon}(\mathbf{v}) : \boldsymbol{\mathcal{C}} : \boldsymbol{\varepsilon}(\mathbf{w}) \, d\Omega. \end{aligned}$$

The error to be assessed is the error in the quantity of interest,  $s^\text{e} := s - \tilde{s}$ , defined as the difference between the exact quantity of interest  $s := L^\mathcal{O}(\mathbf{u})$  and the computed one  $\tilde{s} := L^\mathcal{O}(\tilde{\mathbf{u}})$ . In the following, it is assumed that the functional  $L^\mathcal{O}(\cdot)$  is

linear. Thus,  $s^e = L^{\mathcal{O}}(\mathbf{e})$ . However, non-linear functionals can also be handled after a linearization, see references by Bangerth et al. (2010), and Fuentes et al. (2006) for details.

## 2.4 Adjoint problem

Assessing the error in the quantity of interest requires introducing an auxiliary problem associated with functional  $L^{\mathcal{O}}(\cdot)$ , referred as *adjoint* or *dual* problem. The adjoint problem allows rewriting the error in the quantity of interest in a more convenient way for error assessment. The problem defining the exact adjoint solution  $\mathbf{u}^d$  reads:

$$\rho(\ddot{\mathbf{u}}^d - a_1 \dot{\mathbf{u}}^d) - \nabla \cdot \boldsymbol{\sigma}^d(\mathbf{u}^d) = -\mathbf{f}^{\mathcal{O}} \quad \text{in } \Omega \times I, \quad (4a)$$

$$\mathbf{u}^d = \mathbf{0} \quad \text{on } \Gamma_D \times I, \quad (4b)$$

$$\boldsymbol{\sigma}^d(\mathbf{u}^d) \cdot \mathbf{n} = -\mathbf{g}^{\mathcal{O}} \quad \text{on } \Gamma_N \times I, \quad (4c)$$

$$\mathbf{u}^d = \mathbf{u}^{\mathcal{O}} \quad \text{at } \Omega \times \{T\}, \quad (4d)$$

$$\dot{\mathbf{u}}^d = \mathbf{v}^{\mathcal{O}} \quad \text{at } \Omega \times \{T\}, \quad (4e)$$

with the constitutive law

$$\boldsymbol{\sigma}^d(\mathbf{u}^d) := \mathbf{C} : \boldsymbol{\varepsilon}(\mathbf{u}^d - a_2 \dot{\mathbf{u}}^d). \quad (5)$$

Note that the definition of the adjoint problem (4) depends on the selected quantity of interest. That is, the external loads and *final* conditions of the adjoint problem are determined by the definition of quantity of interest in equation (3).

The adjoint problem (4) has exactly the same structure as the original (1) if integrated backwards in time starting from the final conditions (4d) and (4e). Thus, any of the available approximation techniques for elastodynamics can be considered for approximating the adjoint.

**Remark 3** (Illustrative example). *The following example illustrates the adjoint problem given in (4) in a one dimensional example. The spatial computational domain is  $\Omega = (0, 1)$  m, the boundaries are  $\Gamma_N = \{0 \text{ m}\}$  and  $\Gamma_D = \{1 \text{ m}\}$ , and the time interval is  $I = (0, 2]$  s. The material properties are  $E = 1 \text{ Pa}$ ,  $\nu = 0$ ,  $\rho = 1, \text{ kg/m}^3$  and  $a_1 = a_2 = 0 \text{ s}$ .*

*The adjoint problem illustrated in this remark is associated with the quantity of interest*

$$L^{\mathcal{O}}(w) = \int_I \int_{\Omega} \alpha(t) \beta(x) \dot{w}(x, t) \, dx \, dt, \quad (6)$$

where  $\alpha(t)$  and  $\beta(x)$  are the functions defined in figure 1. Note that the quantity

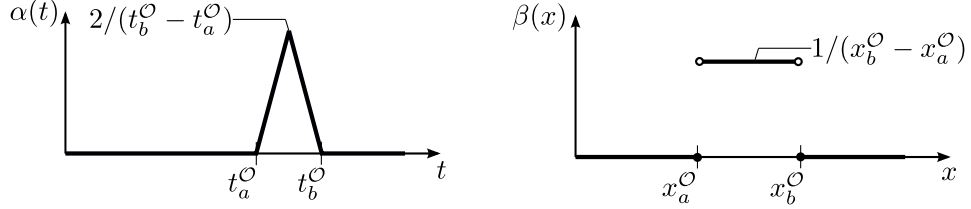


Figure 1: Definition of  $\alpha(t)$  and  $\beta(x)$ , (left) and (right) respectively.

of interest (6) corresponds to take  $\mathbf{g}^O = \mathbf{v}^O = \mathbf{u}^O = \mathbf{0}$  and  $\mathbf{f}^O = \alpha(t)\beta(x)$  in equation (3) and provides a weighted average of velocities in the space-time region  $S^O = (x_a^O, x_b^O) \times (t_a^O, t_b^O)$ , see figure 2. In this example, the region  $S^O$  is characterized by  $x_a^O = 0.2$  m  $x_b^O = 0.3$  m,  $t_a^O = 1.8$  s and  $t_b^O = 1.9$  s.

The adjoint problem associated with quantity (6) is plotted in figure 2. Note that the quantity of interest acts as the external loading of the adjoint problem. The quantity of interest generates a perturbation in the space-time region of interest  $S^O$  which propagates along the characteristic lines backwards in time. The adjoint solution is indeed the region of influence of the quantity of interest. That is, any perturbation taking place where the adjoint solution is zero has no influence in the quantity of interest.

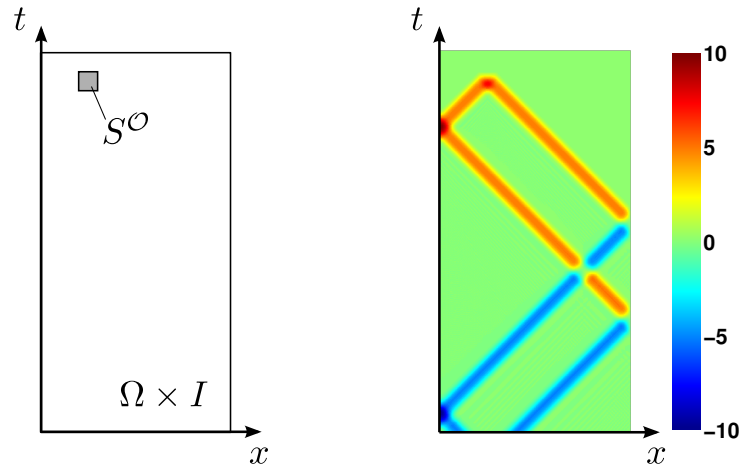


Figure 2: Illustration of the adjoint problem for the quantity of interest given in equation (6) (average of velocities in the region  $S^O$ ). Definition of the space-time domain  $\Omega \times I$  and region of interest  $S^O$  (left). Adjoint velocities [m/s] (right).

### 3 Contributions

This section is an overview of the major thesis contributions. The contributions are presented stressing out which are the main novelties, the key ideas of the proposed methods, and numerical examples.

#### 3.1 Goal-oriented error bounds

This section presents computable error bounds for structural dynamics. First, the strategy proposed by Waeytens (2010) is extended to deal with a linear Kelvin-Voigt visco-elastic model instead of a Maxwell model. This allows a simpler derivation of the error bounds allowing to concentrate in the mathematical difficulties. Note that the proposed approach is general enough to deal with more sophisticated visco-elastic models. Second, alternative error bounds are proposed improving the estimates introduced by Waeytens (2010). These contributions are enclosed in the appended papers A and B. The main rationale is summarized here.

The goal is to compute two scalar values  $\eta_L$  and  $\eta_U$  such that

$$\eta_L \leq L^O(\mathbf{e}) \leq \eta_U. \quad (7)$$

Computing the error bounds  $\eta_L$  and  $\eta_U$  with the constitutive relation method requires that the problem contains a finite amount of damping. In the following, it is assumed that  $a_1 = 0$  and  $a_2 > 0$  in order to meet this hypothesis. With this choice, all the damping introduced in the formulation comes from the constitutive relation (2) which is seen as a particular type of Kelvin-Voigt visco-elastic model.

The key ingredient allowing to compute the error bounds is building admissible pairs  $(\tilde{\mathbf{u}}, \tilde{\boldsymbol{\sigma}})$  and  $(\tilde{\mathbf{u}}^d, \tilde{\boldsymbol{\sigma}}^d)$  for the original and the adjoint problems. The admissible pair  $(\tilde{\mathbf{u}}, \tilde{\boldsymbol{\sigma}})$  for the original problem consists of a *Kinematically admissible* (K-admissible) displacement  $\tilde{\mathbf{u}}$  and a *Dynamically admissible* (D-admissible) stress tensor  $\tilde{\boldsymbol{\sigma}}$ .

The K-admissible displacement  $\tilde{\mathbf{u}}$  fulfills the initial and Dirichlet boundary conditions of the original problem (1). Typically, the K-admissible displacement is the computed numerical approximation  $\tilde{\mathbf{u}}$ . For that reason, the notation is the same for both for the K-admissible displacement and the numerical approximation. On the other hand, the D-admissible stress  $\tilde{\boldsymbol{\sigma}}$  is computed such that it is in dynamic equilibrium with the inertia force associated with the K-admissible displacement, namely  $-\rho\ddot{\tilde{\mathbf{u}}}$ , the body force  $\mathbf{f}$ , and boundary traction  $\mathbf{g}$  appearing in (1).

The adjoint admissible pair  $(\tilde{\mathbf{u}}^d, \tilde{\boldsymbol{\sigma}}^d)$  fulfills analogous properties but referred to the adjoint problem. Computing a D-admissible stress requires performing standard equilibration techniques designed for steady-state elasticity at each time point in the time grid  $\mathcal{T}$ . A more detailed definition of the admissible pairs  $(\tilde{\mathbf{u}}, \tilde{\boldsymbol{\sigma}})$  and  $(\tilde{\mathbf{u}}^d, \tilde{\boldsymbol{\sigma}}^d)$  and the methodology to compute them is found in the appended paper B.

The admissible pairs define the following errors in stresses

$$\tilde{\boldsymbol{\sigma}}^e := \tilde{\boldsymbol{\sigma}} - \boldsymbol{\sigma}(\tilde{\mathbf{u}}) \quad \text{and} \quad \tilde{\boldsymbol{\sigma}}^{d,e} := \tilde{\boldsymbol{\sigma}}^d - \boldsymbol{\sigma}(\tilde{\mathbf{u}}^d), \quad (8)$$

which are a measure of the non-verification of the constitutive relations (2) and (5) respectively. Note that the stress errors  $\tilde{\boldsymbol{\sigma}}^e$  and  $\tilde{\boldsymbol{\sigma}}^{d,e}$  are computable once the admissible pairs  $(\tilde{\mathbf{u}}, \tilde{\boldsymbol{\sigma}})$  and  $(\tilde{\mathbf{u}}^d, \tilde{\boldsymbol{\sigma}}^d)$  are available. The norms  $\|\tilde{\boldsymbol{\sigma}}^e\|_\sigma$  and  $\|\tilde{\boldsymbol{\sigma}}^{d,e}\|_\sigma$  are referred as the *constitutive relation error* for the original and adjoint problems following the terminology by Ladevèze and Pelle (2001). The space-time stress norm used to measure the error is

$$\|\boldsymbol{\tau}\|_\sigma := \left( \frac{1}{a_2} \int_I \int_\Omega \boldsymbol{\tau} : \mathbf{C}^{-1} : \boldsymbol{\tau} \, d\Omega \, dt \right)^{1/2}. \quad (9)$$

Note that the norm  $\|\cdot\|_\sigma$  is related with the dissipated energy due to the damping coefficient  $a_2$ . For this reason, the non-zero viscosity hypothesis has to be fulfilled in order to compute error bounds with this technique.

The error in the quantity of interest is bounded following two stages. First, the value  $L^\mathcal{O}(\mathbf{e})$  is bounded in terms of the energy norm of non-computable errors. Second, the non-computable errors are bounded using the constitutive relation errors  $\|\tilde{\boldsymbol{\sigma}}^e\|_\sigma$  and  $\|\tilde{\boldsymbol{\sigma}}^{d,e}\|_\sigma$ .

The first approach to bound the error  $L^\mathcal{O}(\mathbf{e})$  is already introduced by Waeytens (2010). The value  $L^\mathcal{O}(\mathbf{e})$  is bounded in terms of the unknown error  $\mathbf{e}$  as follows

$$|L^\mathcal{O}(\mathbf{e}) - \tilde{k}_1| \leq \|\tilde{\boldsymbol{\sigma}}^{d,e}\|_\sigma \|\mathbf{e}\|, \quad (10)$$

where  $\tilde{k}_1$  is a computable value, see paper B for a detailed proof. The norm  $\|\cdot\|$  is related with the stress norm  $\|\cdot\|_\sigma$  but taking displacements as argument, namely

$$\|\mathbf{w}\| := \left( a_2 \int_I \int_\Omega \boldsymbol{\varepsilon}(\dot{\mathbf{w}}) : \mathbf{C} : \boldsymbol{\varepsilon}(\dot{\mathbf{w}}) \, d\Omega \, dt \right)^{1/2}. \quad (11)$$

Then, the unknown error energy  $\|\mathbf{e}\|$  is bounded using the upper bound property of the constitutive relation error  $\|\tilde{\boldsymbol{\sigma}}^e\|_\sigma$

$$\|\mathbf{e}\| \leq \|\tilde{\boldsymbol{\sigma}}^e\|_\sigma, \quad (12)$$

see appended paper B. Hence, the computable bounds  $\eta_L$  and  $\eta_U$  are readily obtained by combining expressions (12) and (10), namely

$$\zeta_U := \|\tilde{\boldsymbol{\sigma}}^{d,e}\|_\sigma \|\tilde{\boldsymbol{\sigma}}^e\|_\sigma + \tilde{k}_1, \quad (13a)$$

$$\zeta_L := -\|\tilde{\boldsymbol{\sigma}}^{d,e}\|_\sigma \|\tilde{\boldsymbol{\sigma}}^e\|_\sigma + \tilde{k}_1. \quad (13b)$$

The error representation (10) is obtained using the Cauchy-Schwarz inequality which typically induces a large overestimation of the assessed error. This makes the error bounds given in (13) not sharp, with an unrealistic and impractical bound gap.

Alternative error bounds are proposed leading to a sharper bound gap than the one associated with the bounds (13). There are two equivalent ways to derive the alternative bounds. Either introducing auxiliary symmetric error equations, see paper B, or using an auxiliary error in stresses, see paper A. For the sake of brevity, only the latter approach is presented in this overview.

The alternative approach requires introducing an auxiliary stress field that stands for the error with respect to the averaged viscous stress, namely

$$\boldsymbol{\sigma}_{\text{ave}}^{e,\nu} := \boldsymbol{\sigma}^\nu - \frac{1}{2} (\tilde{\boldsymbol{\sigma}}^\nu + a_2 \mathbf{C} : \boldsymbol{\varepsilon}(\dot{\tilde{\mathbf{u}}})) , \quad (14)$$

where  $\boldsymbol{\sigma}^\nu := a_2 \mathbf{C} : \boldsymbol{\varepsilon}(\dot{\mathbf{u}})$  is the viscous stress associated with the exact solution,  $\tilde{\boldsymbol{\sigma}}^\nu := \tilde{\boldsymbol{\sigma}} - \mathbf{C} : \boldsymbol{\varepsilon}(\dot{\tilde{\mathbf{u}}})$  is the viscous stress associated with the D-admissible field, and  $a_2 \mathbf{C} : \boldsymbol{\varepsilon}(\dot{\tilde{\mathbf{u}}})$  is the viscous stress associated with the K-admissible field. Note that  $\boldsymbol{\sigma}_{\text{ave}}^{e,\nu}$  is not computable because it includes the exact solution  $\mathbf{u}$  in the term  $\boldsymbol{\sigma}^\nu$ . The stress  $\boldsymbol{\sigma}_{\text{ave}}^{e,\nu}$  is introduced as a mathematical artefact allowing to rewrite the error in the quantity of interest as

$$|L^\mathcal{O}(\mathbf{e}) - \tilde{k}_2| \leq \|\tilde{\boldsymbol{\sigma}}^{d,e}\|_\sigma \|\boldsymbol{\sigma}_{\text{ave}}^{e,\nu}\|_\sigma, \quad (15)$$

where  $\tilde{k}_2$  is a computable value. The computable bounds for the error in the quantity of interest are obtained introducing the following upper bound for the unknown value  $\|\boldsymbol{\sigma}_{\text{ave}}^{e,\nu}\|_\sigma$ ,

$$\|\boldsymbol{\sigma}_{\text{ave}}^{e,\nu}\|_\sigma \leq \frac{1}{2} \|\tilde{\boldsymbol{\sigma}}^e\|_\sigma. \quad (16)$$

The detailed proofs of equations (15) and (16) are given in paper A. Using expressions (15) and (16), the alternative bounds are readily obtained:

$$\zeta_U := \frac{1}{2} \|\tilde{\boldsymbol{\sigma}}^{d,e}\|_\sigma \|\tilde{\boldsymbol{\sigma}}^e\|_\sigma + \tilde{k}_2, \quad (17a)$$

$$\zeta_L := -\frac{1}{2} \|\tilde{\boldsymbol{\sigma}}^{d,e}\|_\sigma \|\tilde{\boldsymbol{\sigma}}^e\|_\sigma + \tilde{k}_2. \quad (17b)$$

The bound corresponding to (17) is  $\zeta_U - \zeta_L = \|\tilde{\boldsymbol{\sigma}}^{\text{d,e}}\|_\sigma \|\tilde{\boldsymbol{\sigma}}^{\text{e}}\|_\sigma$  whereas the bound gap in (13) is  $\zeta_U - \zeta_L = 2\|\tilde{\boldsymbol{\sigma}}^{\text{d,e}}\|_\sigma \|\tilde{\boldsymbol{\sigma}}^{\text{e}}\|_\sigma$ . Note that the bound gap in equation (17) is the half of the bound gap corresponding to equation (13). Consequently, the proposed error bounds (17) provides a sharper error assessment.

The numerical results included in paper B show that the proposed bounds (17) are indeed sharper than previously available ones (13). The computed bounds are very pessimistic for materials with a small amount of viscosity even for the new bounds (17). The numerical tests also reveal that the bound gap is reduced as the mesh is refined and, consequently, the strategy provides sharp bounds for fine enough meshes. Nevertheless, in practice, for low viscosity, the meshes providing accurate bounds are not computationally affordable. Therefore, further research is needed to explore alternative pertinent bounds for nearly elastic problems.

**Remark 4** (Illustrative example). *This example illustrates the performance of the proposed computable bounds in a 2D wave propagation problem. This is a reduced version of the second numerical example found in paper B. The problem geometry, see figure 3, is a rectangular plate  $\Omega := (-0.5, 0.5) \times (0, 0.5)$  m<sup>2</sup> clamped at the bottom side, initially at rest ( $\mathbf{u}_0 = \mathbf{v}_0 = \mathbf{0}$ ), which is loaded with the impulsive traction*

$$\mathbf{g}(t) = \begin{cases} -g(t)\mathbf{e}_2 & \text{on } \Gamma_g, \\ 0 & \text{elsewhere,} \end{cases} \quad (18)$$

with  $\Gamma_g := [(0.075, 0.125) \cup (-0.075, -0.125)] \times \{0.5\}$  m,  $\mathbf{e}_2 := (0, 1)$  and  $g(t)$  is the impulsive time-dependent function defined in figure 3 with parameters  $g_{\max} = 30$  Pa and  $t_g = 0.005$  s. No body force is acting in this example ( $\mathbf{f} = \mathbf{0}$ ). The material properties of the plate are Young's modulus  $E = 8/3$  Pa, Poisson's ratio  $\nu = 1/3$ , the density  $\rho = 1$  kg/m<sup>3</sup> and the damping coefficients  $a_1 = 0$  s<sup>-1</sup>,  $a_2 = 10^{-4}, 10^{-2}$  s. Note that two different values of the parameter  $a_2$  are considered. The final simulation time is  $T = 0.25$  s. The plain stress hypothesis is considered.

The external loading generates elastic waves propagating along the plate and reaching to the region of interest  $\Omega^\circ$ . The quantity of interest is an average of the vertical component of the velocity in this region during a time interval selected such that the wave is noticeable in  $\Omega^\circ$ , see figure 4. This quantity is defined as

$$L^\circ(\mathbf{w}) = \int_0^T \alpha(t)(\boldsymbol{\lambda}^\circ, \dot{\mathbf{w}}(t)) dt, \quad \text{where } \boldsymbol{\lambda}^\circ(\mathbf{x}) := \begin{cases} \frac{-\mathbf{e}_2}{\text{meas}(\Omega^\circ)} & \mathbf{x} \in \Omega^\circ \\ \mathbf{0} & \text{elsewhere} \end{cases}$$

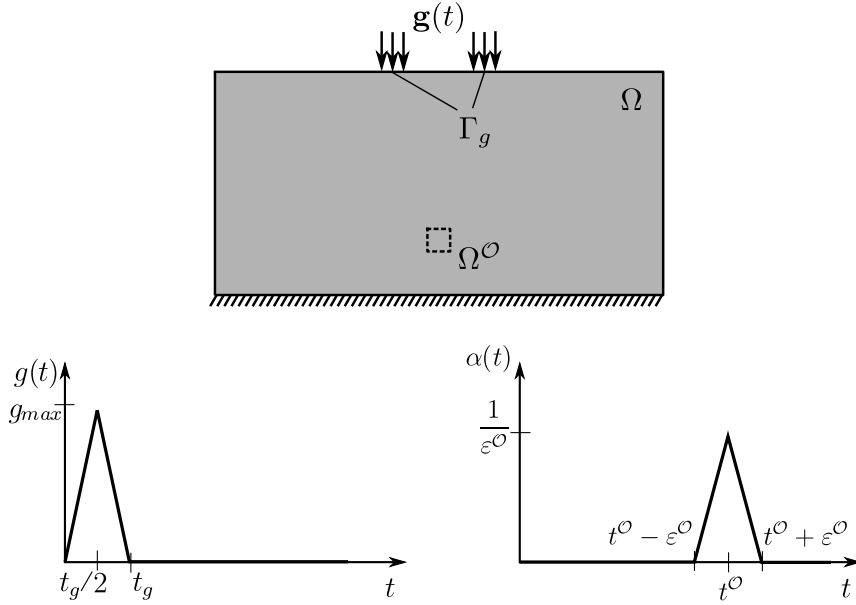


Figure 3: Problem geometry (top), time dependence of external load (left) and time dependence of the auxiliary function introduced to define the quantity of interest (right).

and the time dependent function  $\alpha(t)$  is defined in figure 3 with parameters  $\varepsilon^\circ = 0.01$  s and  $t^\circ = 0.217$  s. Note that the definition of the quantity of interest corresponds to take  $\mathbf{f}^\circ(\mathbf{x}, t) = \alpha(t)\boldsymbol{\lambda}^\circ(\mathbf{x})$  and  $\mathbf{g}^\circ = \mathbf{u}^\circ = \mathbf{v}^\circ = \mathbf{0}$  in equation (3).

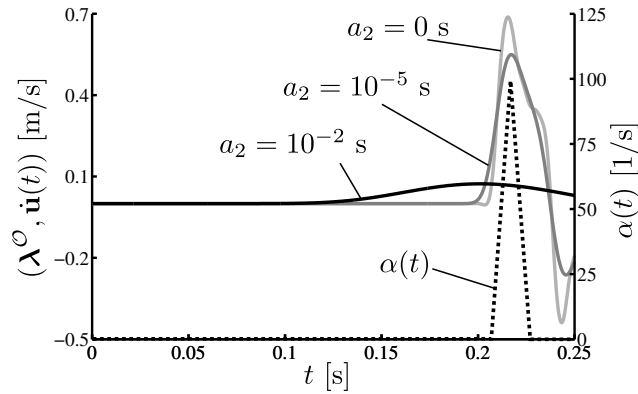


Figure 4: Time evolution of the average of the vertical velocity in the region  $\Omega^\circ$ , namely  $(\boldsymbol{\lambda}^\circ, \dot{\mathbf{u}}(t))$ , for three values of the viscosity (left y-axis). Time evolution of the weighting function  $\alpha(t)$  used to define the quantity of interest (right y-axis).

In this example, the computed error bounds,  $\eta_L$  and  $\eta_U$  are used to compute bounds of the exact quantity of interest  $L^\circ(\mathbf{u})$ , namely  $\tilde{\eta}_L \leq L^\circ(\mathbf{u}) \leq \tilde{\eta}_U$  with  $\tilde{\eta}_L := \eta_L +$

$L^{\mathcal{O}}(\tilde{\mathbf{u}})$  and  $\tilde{\eta}_{\mathcal{U}} := \eta_{\mathcal{U}} + L^{\mathcal{O}}(\tilde{\mathbf{u}})$ . Figure 5 shows the effectivity of the computed bounds  $\tilde{\eta}_{\mathcal{L}}$  and  $\tilde{\eta}_{\mathcal{U}}$  with respect the exact quantity of interest  $s = L^{\mathcal{O}}(\mathbf{u})$  which is computed using an overkill solution. Note that the bounds are sharper as the value of the viscosity increases or as the element size decreases. In particular, the quality of the bounds is very poor for small values of the viscosity. On the other hand, the proposed new bounds reduce in 50% the bound gap with respect to the previous approach. Note however that for the smallest values of the viscosity, this reduction is not sufficient to have bounds applicable in practical engineering examples.

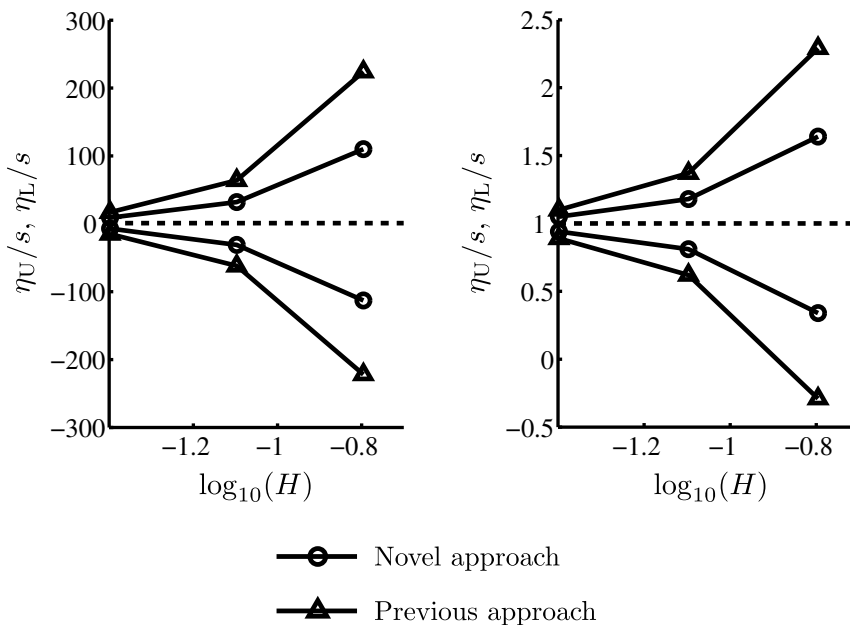


Figure 5: Convergence of the computed bounds for different values of element size and for two values of the viscosity-related parameter  $a_2 = 10^{-4}$  s (left) and  $a_2 = 10^{-2}$  s (right).

### 3.2 Modal-based goal-oriented error assessment

This section presents a novel approach to compute the adjoint problem arising in goal-oriented error assessment. The proposed approximation technique is based on the well-known modal analysis which is considered to approximate the time-dependence of the structural dynamic equations in many contexts, see for instance the book by Bathe (1996).

The modal-based strategy is particularly well suited for computing the adjoint problem associated with some particular quantities of interest. Following this approach, the adjoint solution is computed and stored for each vibration mode instead of for each time step. Moreover, the use of post-processing techniques in the space domain can be readily applied to the (space) description of the modes. This is performed just once for every relevant mode, with no need of carrying out the post-processing at each time step. Thus, the cost per time step is low.

The modal-based adjoint approximation aims at providing an efficient goal-oriented error assessment. The poor quality of the error bounds introduced in section 3.1 and the cost of computing the D-admissible fields suggest using the modal-based strategy to compute error approximations instead of error bounds. Note however, the proposed methodology is general enough to compute also error bounds.

The dual weighted residual method is considered here in order to compute approximations of the error in the quantity of interest. Following this approach, the error in the quantity of interest is expressed in terms of the exact solution of the adjoint problem as

$$L^{\mathcal{O}}(\mathbf{e}) = R(\mathbf{u}^{\text{d}}), \quad (19)$$

where  $R(\cdot)$  is the weak residual (integrated in space and time) associated with the approximation  $\tilde{\mathbf{u}}$ , namely

$$\begin{aligned} R(\mathbf{w}) &:= \int_0^T [l(\dot{\mathbf{w}}(t); t) - m(\ddot{\tilde{\mathbf{u}}}(t) + a_1 \dot{\tilde{\mathbf{u}}}(t), \dot{\mathbf{w}}(t)) - a(\tilde{\mathbf{u}}(t) + a_2 \dot{\tilde{\mathbf{u}}}(t), \dot{\mathbf{w}}(t))] dt \\ &\quad + m(\mathbf{v}_0 - \dot{\tilde{\mathbf{u}}}(0^+), \dot{\mathbf{w}}(0^+)) + a(\mathbf{u}_0 - \tilde{\mathbf{u}}(0^+), \mathbf{w}(0^+)), \quad \text{with} \\ l(\mathbf{w}; t) &:= (\mathbf{f}(t), \mathbf{w}) + (\mathbf{g}(t), \mathbf{w})_{\Gamma_N}. \end{aligned}$$

The error representation (19) allows obtaining the error in the quantity of interest provided that the exact solution of the adjoint problem is available. Conversely, if an accurate approximation of the adjoint solution is available, say  $\tilde{\mathbf{u}}^{\text{d}}$ , the error in the quantity of interest is estimated as

$$L^{\mathcal{O}}(\mathbf{e}) \approx R(\tilde{\mathbf{u}}^{\text{d}}) =: \tilde{s}^{\text{e}}. \quad (20)$$

The quality of the approximation  $\tilde{\mathbf{u}}^{\text{d}}$  is critical to obtain accurate estimates of the error in the scalar quantity of interest. The major novelty of the present approach is using modal analysis to compute the approximation  $\tilde{\mathbf{u}}^{\text{d}}$ .

Approximating function  $\tilde{\mathbf{u}}^{\text{d}}$  with modal analysis requires introducing a semidiscrete version (discrete in space and exact in time) of the adjoint problem (4). The

semidiscrete problem reads: find  $\mathbf{u}^{\text{d},H,p+1}(t) \in \mathcal{V}_0^{H,p+1}$  verifying the final conditions  $\mathbf{u}^{\text{d},H,p+1}(T) = \mathbf{u}^\mathcal{O}$  and  $\dot{\mathbf{u}}^{\text{d},H,p+1}(T) = \mathbf{v}^\mathcal{O}$  and such that for all  $t \in I$

$$\begin{aligned} m(\ddot{\mathbf{u}}^{\text{d},H,p+1}(t) - a_1 \dot{\mathbf{u}}^{\text{d},H,p+1}(t), \mathbf{w}) + a(\mathbf{u}^{\text{d},H,p+1}(t) - a_2 \dot{\mathbf{u}}^{\text{d},H,p+1}(t), \mathbf{w}) \\ = -l^\mathcal{O}(\mathbf{w}; t), \end{aligned} \quad (21)$$

for all test functions  $\mathbf{w} \in \mathcal{V}_0^{H,p+1}$ , where  $l^\mathcal{O}(\mathbf{w}; t) := (\mathbf{f}^\mathcal{O}(t), \mathbf{w}) + (\mathbf{g}^\mathcal{O}(t), \mathbf{w})_{\Gamma_N}$ . The finite element space  $\mathcal{V}_0^{H,p+1}$ , introduced in the definition of the semidiscrete problem (21) is obtained by increasing the polynomial degree of the space  $\mathcal{V}_0^{H,p}$  used to compute the numerical solution  $\tilde{\mathbf{u}}$ .

**Remark 5.** *The spacial resolution of the adjoint approximation  $\tilde{\mathbf{u}}^{\text{d}}$  has to be richer than the one of the numerical approximation  $\tilde{\mathbf{u}}$ . Otherwise, the error is underestimated when plugging the approximation  $\tilde{\mathbf{u}}^{\text{d}}$  into the residual  $R(\cdot)$  by an effect analogous to the Galerkin orthogonality. For this reason, the functional space used to define the semidiscrete problem (21) is  $\mathcal{V}_0^{H,p+1}$  instead of  $\mathcal{V}_0^{H,p}$ .*

A modal-based approximation of problem (21) requires introducing the generalized eigenvalue problem: find  $(\tilde{\omega}, \tilde{\mathbf{q}}) \in \mathbb{R} \times \mathcal{V}_0^{H,p+1}$  such that

$$a(\tilde{\mathbf{q}}, \mathbf{w}) = (\tilde{\omega})^2 m(\tilde{\mathbf{q}}, \mathbf{w}) \quad \forall \mathbf{w} \in \mathcal{V}_0^{H,p+1}. \quad (22)$$

The  $i$ -th eigenpair solution of this problem is referred as  $(\tilde{\omega}_i, \tilde{\mathbf{q}}_i)$ . Note that the number of eigenpairs is the number of degrees of freedom in the functional space  $\mathcal{V}_0^{H,p+1}$ , denoted by  $N_{\text{dof}}$ . Typically, the eigenpairs are sorted from low to high frequencies, namely  $\tilde{\omega}_1 \leq \tilde{\omega}_2 \leq \dots \leq \tilde{\omega}_{N_{\text{dof}}}$ , and eigenvectors are normalized to be orthonormal with respect the product  $m(\cdot, \cdot)$ , i.e.

$$m(\tilde{\mathbf{q}}_i, \tilde{\mathbf{q}}_j) = \delta_{ij}, \quad 1 \leq i, j \leq N_{\text{dof}}. \quad (23)$$

The complexity of the system of ODEs resulting from (21) is considerably reduced by expressing the semidiscrete adjoint solution  $\mathbf{u}^{\text{d},H,p+1}(\mathbf{x}, t)$  as a combination of the eigenvectors  $\tilde{\mathbf{q}}_i, i = 1, \dots, N_{\text{dof}}$ , namely

$$\mathbf{u}^{\text{d},H,p+1}(\mathbf{x}, t) = \sum_{i=1}^{N_{\text{dof}}} \tilde{\mathbf{q}}_i(\mathbf{x}) \tilde{y}_i(t). \quad (24)$$

Thus, the system of ODEs (21) is transformed into the uncoupled set of scalar ordinary differential equations (which can be solved analytically in many practical cases)

$$\ddot{\tilde{y}}_i - [a_1 + a_2(\tilde{\omega}_i)^2]\dot{\tilde{y}}_i + (\tilde{\omega}_i)^2\tilde{y}_i = -\tilde{l}_i, \quad (25a)$$

$$\tilde{y}_i(T) = \tilde{u}_i, \quad (25b)$$

$$\dot{\tilde{y}}_i(T) = \tilde{v}_i, \quad (25c)$$

where the r.h.s. terms  $\tilde{l}_i$ ,  $\tilde{u}_i$  and  $\tilde{v}_i$  are computed using the data characterizing the quantity of interest (35) and the eigenvector  $\tilde{\mathbf{q}}_i$ ,

$$\tilde{l}_i(t) := (\mathbf{f}^\mathcal{O}(t), \tilde{\mathbf{q}}_i) + (\mathbf{g}^\mathcal{O}(t), \tilde{\mathbf{q}}_i)_{\Gamma_N}, \quad u_i := m(\mathbf{u}^\mathcal{O}, \tilde{\mathbf{q}}_i) \quad \text{and} \quad v_i := m(\mathbf{v}^\mathcal{O}, \tilde{\mathbf{q}}_i). \quad (26)$$

The cost of computing  $M$  vibration modes scales as, see reference by Bathe (1996),

$$\mathcal{O}(N_{\text{dof}} \cdot N_{\text{bw}}^2) + \mathcal{O}(N_{\text{dof}} \cdot N_{\text{bw}} \cdot M) + \mathcal{O}(N_{\text{dof}} \cdot M^2),$$

where  $N_{\text{bw}}$  denotes the half-bandwidth of the finite element matrices associated with the functional space  $\mathcal{V}_0^{H,p+1}$ . Thus, the modal-based approach is not computationally affordable unless the modal description (24) is truncated up to the first  $M$  terms, being  $M \ll N_{\text{dof}}$ . Consequently, the adjoint approximation  $\tilde{\mathbf{u}}^d$  is defined as the truncated expansion

$$\tilde{\mathbf{u}}^d(\mathbf{x}, t) := \sum_{i=1}^M \tilde{\mathbf{q}}_i(\mathbf{x}) \tilde{y}_i(t). \quad (27)$$

Note that the number of required vibration modes  $M$  has to be selected such that the truncated high frequency modes (for  $i > M$ ) are negligible in (24). This is equivalent to assume that for  $i > M$  the values of  $\tilde{l}_i$ ,  $\tilde{u}_i$  and  $\tilde{v}_i$ , as defined in (26), are close to zero, and consequently  $\tilde{y}_i(t) \approx 0$ . This is guaranteed if the data  $\mathbf{f}^\mathcal{O}$ ,  $\mathbf{g}^\mathcal{O}$ ,  $\mathbf{u}^\mathcal{O}$  and  $\mathbf{v}^\mathcal{O}$  are well captured by the expansion of the first  $M$  eigenvectors.

The optimal choice to get an efficient response with the modal-based approach is selecting a quantity of interest defined using only the first vibration mode. For instance,

$$L^\mathcal{O}(\mathbf{w}) := m(\alpha_v \tilde{\mathbf{q}}_1, \dot{\mathbf{w}}(T)) + a(\alpha_u \tilde{\mathbf{q}}_1, \mathbf{w}(T)), \quad (28)$$

corresponding to take  $\mathbf{f}^\mathcal{O} = \mathbf{g}^\mathcal{O} = \mathbf{0}$ ,  $\mathbf{v}^\mathcal{O} = \alpha_v \tilde{\mathbf{q}}_1$  and  $\mathbf{u}^\mathcal{O} = \alpha_u \tilde{\mathbf{q}}_1$  in equation (3). The constants  $\alpha_v$  and  $\alpha_u$  are introduced in order to obtain consistent dimensions in (28). This quantity is a sum of averages of velocities and strains (or stresses) at time  $T$ . It can be interpreted as the projection of function  $\mathbf{w}$  to the first vibration mode at time  $T$ . This quantity of interest is computationally inexpensive because requires computing only one vibration mode ( $M = 1$ ).

A second choice is defining a quantity using the first  $M$  vibration modes, namely

$$L^{\mathcal{O}}(\mathbf{w}) = \sum_{i=1}^M (m(\alpha_{v,i}\mathbf{q}_i, \dot{\mathbf{w}}(T)) + a(\alpha_{u,i}\mathbf{q}_i, \mathbf{w}(T))),$$

corresponding to take  $\mathbf{f}^{\mathcal{O}} = \mathbf{g}^{\mathcal{O}} = \mathbf{0}$ ,  $\mathbf{v}^{\mathcal{O}} = \sum_{i=1}^M \alpha_{v,i}\tilde{\mathbf{q}}_i$  and  $\mathbf{u}^{\mathcal{O}} = \sum_{i=1}^M \alpha_{u,i}\tilde{\mathbf{q}}_i$  in equation (3). This quantity of interest represents more meaningful averages of velocities and strains at the final time  $T$ . For instance, a pseudo average of the velocities at time  $t = T$  in a subregion of the computational domain  $\Omega$  can be defined by properly selecting the coefficients  $\alpha_{v,i}$  and  $\alpha_{u,i}$ , see the first numerical example in paper D.

A third suitable quantity of interest is the average of displacements at the final time of the computation

$$L^{\mathcal{O}}(\mathbf{w}) := (\boldsymbol{\lambda}^{\mathcal{O}}, \mathbf{w}(T)) + (\boldsymbol{\lambda}_{\Gamma_N}^{\mathcal{O}}, \mathbf{w}(T))_{\Gamma_N}, \quad (29)$$

where the data  $\boldsymbol{\lambda}^{\mathcal{O}}$  and  $\boldsymbol{\lambda}_{\Gamma_N}^{\mathcal{O}}$  are weighting functions allowing to localize the average of displacements in some subdomains in  $\Omega$  and  $\Gamma_N$  respectively. The quantity (29) has to be rewritten in the same form as the generic quantity (3) in order to compute its associated enhanced approximation  $\tilde{\mathbf{u}}^{\mathcal{d}}$  using the rationale presented above. Thus, the quantity (29) is rewritten as

$$L^{\mathcal{O}}(\mathbf{w}) = a(\tilde{\mathbf{u}}^{\mathcal{O}}, \mathbf{u}(T)),$$

taking  $\mathbf{f}^{\mathcal{O}} = \mathbf{0}$ ,  $\mathbf{g}^{\mathcal{O}} = \mathbf{0}$ ,  $\mathbf{v}^{\mathcal{O}} = \mathbf{0}$  and  $\mathbf{u}^{\mathcal{O}} = \tilde{\mathbf{u}}^{\mathcal{O}}$  in equation (3), being  $\tilde{\mathbf{u}}^{\mathcal{O}}$  the solution of the static problem: find  $\tilde{\mathbf{u}}^{\mathcal{O}} \in \mathcal{V}_0^{H,p+1}$  such that

$$a(\tilde{\mathbf{u}}^{\mathcal{O}}, \mathbf{w}) = (\boldsymbol{\lambda}^{\mathcal{O}}, \mathbf{w}) + (\boldsymbol{\lambda}_{\Gamma_N}^{\mathcal{O}}, \mathbf{w})_{\Gamma_N} \quad \forall \mathbf{w} \in \mathcal{V}_0^{H,p+1}. \quad (30)$$

This quantity is more meaningful than the previous ones, but it requires computing several vibration modes ( $M > 1$ ) in order to properly capture  $\tilde{\mathbf{u}}^{\mathcal{O}}$  by the expansion of  $\tilde{\mathbf{q}}_i$ ,  $i = 1, \dots, M$ .

The numerical examples in paper C show that the proposed modal-based error estimate is accurate and accounts for both the space and time discretization errors. As previously announced, assessing the error in the quantity of interest (29) requires computing  $M > 1$  vibration modes. The results in paper C show that  $M = 60$  vibration modes provide an accurate error assessment in the examples considered therein.

The modal-based error estimate is the basis of the contributions presented in the following sections 3.3 and 3.4.

### 3.3 Modal-based goal-oriented adaptivity

The proposed adaptive technique is similar to the one discussed by Bangerth and Rannacher (1999), and Bangerth et al. (2010). The major novelty of the present approach is using modal analysis to approximate the adjoint solution instead of direct time-integration methods. The specific details of the technique are found in paper D.

The proposed space-time adaptive strategy aims at finding an optimal time discretization  $\mathcal{T}$  and an optimal space discretization  $\mathcal{P}_n$  at each time point  $t_n \in \mathcal{T}$  such that the assessed error  $\tilde{s}^e$  is under a user-defined tolerance  $s_{\text{tol}}^e$ , namely

$$|\tilde{s}^e| \leq s_{\text{tol}}^e. \quad (31)$$

Two main ingredients are required to achieve the optimal space-time discretization: 1) a procedure allowing to locally refine and un-refine the space and time discretizations, and 2) local error information allowing to identify which regions of the space-time domain have larger (or smaller) error contributions and therefore which regions have to be refined (or unrefined).

Adding and removing points form the time grid  $\mathcal{T}$  is trivial because the time interval  $I$  is a one dimensional domain. However, the strategy to refine and un-refine the space meshes  $\mathcal{P}_n$  is more involved. Here, a hierarchical tree-based mesh refinement strategy similar to the ones proposed by Demkowicz et al. (1989), and Yerry and Shephard (1983) is considered. In this context, the computational meshes  $\mathcal{P}_n$ ,  $n = 0, \dots, N$  are obtained recursively splitting the elements of an initial background mesh denoted as  $\mathcal{P}_{\text{bg}}$ , see figure 6. The particular refinement and un-refinement technique adopted here is detailed in paper E.

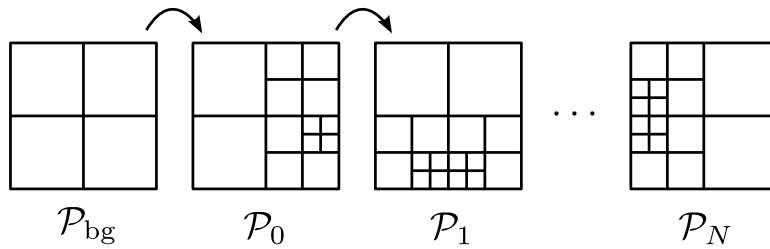


Figure 6: A hierarchical tree-based technique is used to build the space meshes  $\mathcal{P}_n$ ,  $n = 0, \dots, N$  starting from the background mesh  $\mathcal{P}_{\text{bg}}$ .

The tree-based data structure enormously facilitates the mesh refinement and un-refinement operations and also transferring information between different meshes.

However, this approach introduces *hanging* or *irregular* nodes. A constrained finite element approximation (i.e. Lagrange multipliers) is used to enforce the continuity of the finite element solution at the hanging nodes, see paper D.

The local information driving the adaptive procedure is given by the modal-based error estimate  $\tilde{s}^e$ . Note that the value  $\tilde{s}^e$  accounts for both the space and time discretization errors. Therefore, this single value does not give enough information allowing to decide whether the space or time discretizations (or both) have to be refined to reduce error.

In order to properly split the space and time error components, the adaptive strategy requires that the numerical solution fulfills the discrete version of a space-time variational problem. With this choice, a weak residual (integrated both in space and time) associated with the numerical solution is readily introduced. The splitting procedure uses the fact that the residual vanishes for the functions in the test space, that is Galerkin orthogonality holds.

Among the possible space-time variational formulations available for transient elastodynamics, the double field *time-continuous Galerkin method* considered by Eriksson et al. (1996), and Bangerth et al. (2010) is the selected numerical solver. Note, however, that the following rationale can be easily extended to other space-time variational formulations, for instance, the one proposed by Johnson (1993) or the one proposed by Hughes and Hulbert (1988), and Hulbert and Hughes (1990).

The selected double-field method introduces the velocity  $\dot{\mathbf{u}}$  as a new unknown of the problem. The numerical approximation is a pair  $\tilde{\mathbf{U}} := [\tilde{\mathbf{u}}_u, \tilde{\mathbf{u}}_v]$  consisting of independent approximations for displacements  $\tilde{\mathbf{u}}_u \approx \mathbf{u}$  and velocities. That is, the velocity  $\mathbf{u}_v$  is not strongly enforced to coincide with  $\dot{\mathbf{u}}_u$ . The relation between the approximated displacements and velocities is imposed weakly and therefore it yields  $\tilde{\mathbf{u}}_v \approx \dot{\mathbf{u}}$  instead of  $\tilde{\mathbf{u}}_v = \dot{\mathbf{u}}$ . The discretization error is defined as a double field function as well,

$$\mathbf{E} := [\mathbf{e}_u, \mathbf{e}_v] := [\mathbf{u} - \tilde{\mathbf{u}}_u, \dot{\mathbf{u}} - \tilde{\mathbf{u}}_v],$$

where  $\mathbf{e}_u$  and  $\mathbf{e}_v$  are the errors in displacements and velocities respectively.

The methodology used to assess the double field error  $\mathbf{E}$  is completely analogous to the one used for the single field error  $\mathbf{e}$ . The only difference is a technical modification in the definition of the quantity of interest  $L^{\mathcal{O}}(\cdot)$  and the residual  $R(\cdot)$  in order to

take as input a generic double field function  $\mathbf{W} = [\mathbf{w}_u, \mathbf{w}_v]$ . That is

$$\begin{aligned}
 L_{\text{DF}}^{\mathcal{O}}(\mathbf{W}) &:= \int_0^T l^{\mathcal{O}}(\mathbf{w}_v(t); t) dt \\
 &\quad + m(\mathbf{v}^{\mathcal{O}}, \mathbf{w}_v(T)) + a(\mathbf{u}^{\mathcal{O}}, \mathbf{w}_u(T)), \\
 R_{\text{DF}}(\mathbf{W}) &:= \int_0^T l(\mathbf{w}_v(t); t) dt + \\
 &\quad - \int_0^T m(\dot{\tilde{\mathbf{u}}}_v(t) + a_1 \tilde{\mathbf{u}}_v(t), \mathbf{w}_v(t)) dt \\
 &\quad - \int_0^T a(\tilde{\mathbf{u}}_u(t) + a_2 \tilde{\mathbf{u}}_v(t), \mathbf{w}_v(t)) dt \\
 &\quad - \int_0^T a(\dot{\tilde{\mathbf{u}}}_u(t) - \tilde{\mathbf{u}}_v(t), \mathbf{w}_u(t)) dt \\
 &\quad + m(\mathbf{v}_0 - \tilde{\mathbf{u}}_v(0^+), \mathbf{w}_v(0^+)) + a(\mathbf{u}_0 - \tilde{\mathbf{u}}_u(0^+), \mathbf{w}_u(0^+)).
 \end{aligned}$$

Note that the definition of the double-field quantity of interest  $L_{\text{DF}}^{\mathcal{O}}(\cdot)$  is consistent with the single-field quantity  $L^{\mathcal{O}}(\cdot)$  in the sense that, for a generic function  $\mathbf{w}$ ,  $L^{\mathcal{O}}(\mathbf{w}) = L_{\text{DF}}^{\mathcal{O}}([\mathbf{w}, \dot{\mathbf{w}}])$ . Note also that the residual  $R_{\text{DF}}(\cdot)$  has an extra term accounting for the non-verification of the relation between displacements and velocities.

The error in the quantity of interest  $s_{\text{DF}}^e := L_{\text{DF}}^{\mathcal{O}}(\mathbf{E})$  is assessed using an error representation analogous to equation (20), namely

$$L_{\text{DF}}^{\mathcal{O}}(\mathbf{E}) \approx R_{\text{DF}}(\tilde{\mathbf{U}}^d) =: \tilde{s}_{\text{DF}}^e, \quad (32)$$

where  $\tilde{\mathbf{U}}^d := [\tilde{\mathbf{u}}^d, \dot{\tilde{\mathbf{u}}}^d]$ . The adjoint solution  $\tilde{\mathbf{U}}^d$  is computed with the modal-based approach using the background mesh  $\mathcal{P}_{\text{bg}}$  (with element of order  $p + 1$ ). That is,  $\tilde{\mathbf{u}}^d(t), \dot{\tilde{\mathbf{u}}}^d(t) \in \mathcal{V}_0^{\text{bg}, p+1}$ , for  $t \in I$ , where  $\mathcal{V}_0^{\text{bg}, p+1}$  denotes the finite element space associated with the  $p + 1$  version of the background mesh. The background mesh  $\mathcal{P}_{\text{bg}}$  is selected for approximating the adjoint in order to simplify the representation of  $\tilde{\mathbf{U}}^d$  in the adapted meshes  $\mathcal{P}_n$ ,  $n = 0, \dots, N$ . As previously announced, having a  $p + 1$  approximation degree for the adjoint solution  $\tilde{\mathbf{U}}^d$  precludes the Galerkin orthogonality effect and the corresponding underestimation of the error. For the sake of a simpler notation, the subscript DF is omitted in the following.

Separating the space and time error contributions to  $\tilde{s}^e$  requires introducing the projection operators  $\mathbf{\Pi}^H$  and  $\mathbf{\Pi}^{\Delta t}$  associated with the space and time discretizations. The space projection  $\mathbf{\Pi}^H$  applied to a generic double field function  $\mathbf{W}$  returns a function  $\mathbf{\Pi}^H \mathbf{W}$  which is discrete in space (i.e. a continuous piecewise polynomial)

but not discrete in time. On the other hand, the time projection  $\mathbf{\Pi}^{\Delta t}$  returns a function which is discrete in time (a piecewise constant function) but not discrete in space, see figure 7. A formal definition of the operators  $\mathbf{\Pi}^H$  and  $\mathbf{\Pi}^{\Delta t}$  is given in paper D.

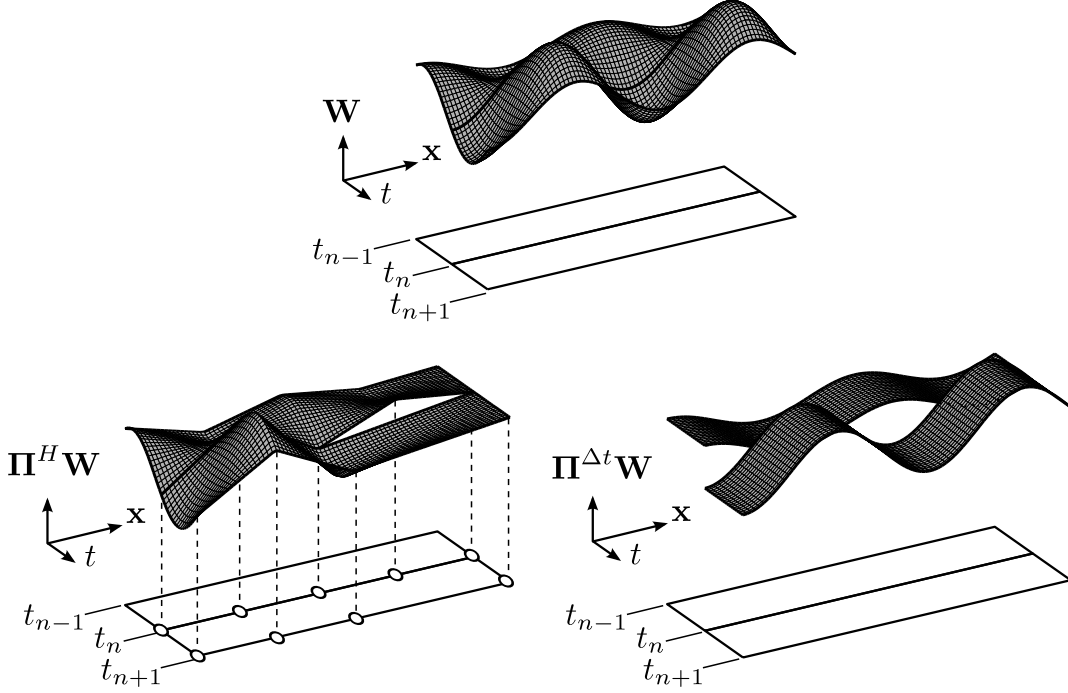


Figure 7: Illustration of the projection operators  $\mathbf{\Pi}^H$  and  $\mathbf{\Pi}^{\Delta t}$ . The figure displays (one field of) the original function  $\mathbf{W}$  inside the time intervals  $I_n = (t_{n-1}, t_n]$  and  $I_{n+1} = (t_n, t_{n+1}]$  (top) along with its projections in space and time  $\mathbf{\Pi}^H \mathbf{W}$  (left) and  $\mathbf{\Pi}^{\Delta t} \mathbf{W}$  (right).

The space and time errors are separated rewriting the value  $\tilde{s}^e$  as

$$\begin{aligned} \tilde{s}^e &= R(\tilde{\mathbf{U}}^d) \\ &= R(\tilde{\mathbf{U}}^d) - R(\mathbf{\Pi}^H \mathbf{\Pi}^{\Delta t} \tilde{\mathbf{U}}^d) \quad (\text{Galerkin orthogonality}) \\ &= R(\tilde{\mathbf{U}}^d) - R(\mathbf{\Pi}^H \tilde{\mathbf{U}}^d) + R(\mathbf{\Pi}^H \tilde{\mathbf{U}}^d) - R(\mathbf{\Pi}^H \mathbf{\Pi}^{\Delta t} \tilde{\mathbf{U}}^d). \end{aligned}$$

Hence, using the linearity of the residual  $R(\cdot)$  one has

$$\tilde{s}^e = \tilde{s}_s^e + \tilde{s}_t^e, \quad (33)$$

where  $\tilde{s}_s^e := R(\tilde{\mathbf{U}}^d - \mathbf{\Pi}^H \tilde{\mathbf{U}}^d)$  and  $\tilde{s}_t^e := R(\mathbf{\Pi}^H \tilde{\mathbf{U}}^d - \mathbf{\Pi}^H \mathbf{\Pi}^{\Delta t} \tilde{\mathbf{U}}^d)$ . The terms  $s_s^e$  and  $s_t^e$  are associated with the space and time discretization errors respectively. Note

that  $s_s^e$  tends to zero as the space discretization is refined because  $\mathbf{\Pi}^H \mathbf{U}^d$  tends to  $\mathbf{U}^d$ . Similarly,  $s_t^e$  tends to zero as the time discretization is refined because  $\mathbf{\Pi}^{\Delta t} \mathbf{U}^d$  tends to  $\mathbf{U}^d$ . The space and time error components  $s_s^e$  and  $s_t^e$  are used as refinement indicators because they can be reduced independently by respectively enriching the space and time discretizations. Note that the Galerkin orthogonality property is used to separate the space and time error contributions.

The sub-regions of the space-time domain  $\Omega \times I$  having a larger error contribution are identified by restricting the integrals involved in the values  $\tilde{s}_s^e$  and  $\tilde{s}_t^e$  to the mesh elements and time steps. This allows to adaptively refine the time grid  $\mathcal{T}$  and the finite element meshes  $\mathcal{P}_n$ ,  $n = 0, \dots, N$  to meet the desired error in the quantity of interest  $s_{\text{tol}}^e$ .

Note that changing the space discretization at each time step  $t_n \in \mathcal{T}$  is not computationally affordable. This is because remeshing operations, matrix assembly and data transfer between different meshes are costly operations and cannot, in general, be performed at each time step. Here, an adaptive strategy organized in time-blocks, similar to the one proposed by Carey et al. (2010), is adopted in order to reduce the number of mesh changes.

The blockwise adaptive strategy requires splitting the time interval  $I$  into  $N^{\text{bk}}$  time intervals (or time blocks), namely

$$I_m^{\text{bk}} := \left( \frac{T}{N^{\text{bk}}}(m-1), \frac{T}{N^{\text{bk}}}m \right], \quad m = 1, \dots, N^{\text{bk}}.$$

The blockwise adaptive strategy consists in taking the same space mesh inside each time interval  $I_m^{\text{bk}}$ , this mesh is denoted as  $\mathcal{P}_m^{\text{bk}}$  for  $m = 1, \dots, N^{\text{bk}}$ , see figure 8. Note that with this definition the computational meshes  $\mathcal{P}_n$  associated with the time points  $t_n \in I_m^{\text{bk}}$  are such that  $\mathcal{P}_n = \mathcal{P}_m^{\text{bk}}$ .

Additionally, the time step length is assumed to be constant inside the intervals  $I_m^{\text{bk}}$  and denoted by  $\Delta t_m^{\text{bk}}$ . Consequently, the time step length  $\Delta t_n$  associated with times  $t_n \in I_m^{\text{bk}}$  are such that  $\Delta t_n = \Delta t_m^{\text{bk}}$ , see figure 8.

Following this approach and notation, the adaptive strategy is reformulated as computing the optimal space meshes  $\mathcal{P}_m^{\text{bk}}$  and time step lengths  $\Delta t_m^{\text{bk}}$ , for all the time intervals  $I_m^{\text{bk}}$ ,  $m = 1, \dots, N^{\text{bk}}$  such that the associated numerical solution fulfills (31).

Once the adjoint solution is computed and stored, the main stages of the adaptive procedure are summarized as follows. The numerical solution is computed sequentially starting from the first time block  $I_1^{\text{bk}}$  until the last one  $I_{N^{\text{bk}}}^{\text{bk}}$ . In each time slab

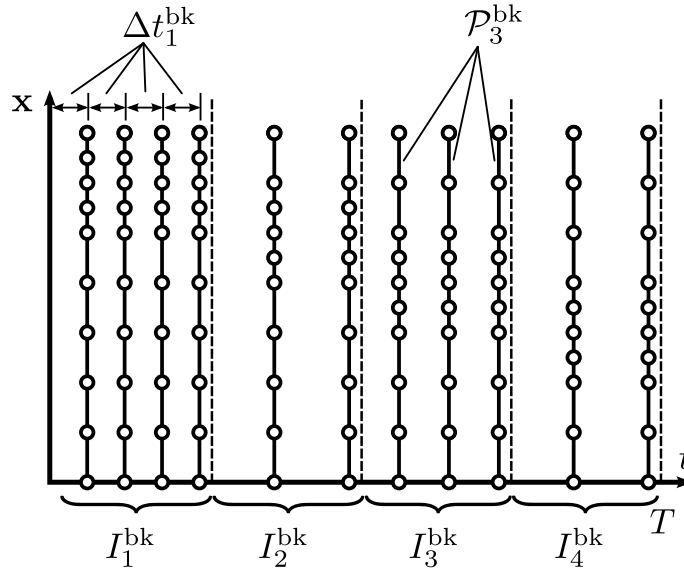


Figure 8: The space mesh is assumed to be constant inside the time intervals  $I_m^{\text{bk}}$ . In the same way, the time step length is also assumed to be constant inside each interval  $I_m^{\text{bk}}$ .

$I_m^{\text{bk}}$ , the numerical solution is computed and the corresponding local error contributions are estimated. The computed solution in  $I_m^{\text{bk}}$  is *accepted* or *rejected* using the information given by the local error contributions. The specific acceptability criterion is detailed in paper D. If the solution is accepted, the loop goes to the following time interval  $I_{m+1}^{\text{bk}}$ . Else, the space or time discretization (or both) associated with the interval  $I_m^{\text{bk}}$  are adapted using the local error information and the solution is re-computed in  $I_m^{\text{bk}}$ . The process of adapting the discretization and computing the numerical solution is repeated in the interval  $I_m^{\text{bk}}$  until the solution is accepted, see algorithm 1.

The numerical examples in paper D show that the proposed strategy furnishes adapted solutions fulfilling the user-defined error tolerance. That is, both the assessed and computed errors are below the user-defined error value. Moreover, the discretizations obtained with the proposed adaptive strategy are more efficient than the ones obtained with a uniform refinement of all mesh elements and time steps. The adapted discretizations give more accurate results than the non-adaptive ones for the same number of space-time elements.

**Remark 6** (Illustrative example). *This example illustrates the performance of the*

**Data:**

*Problem statement:* Problem geometry  $(\Omega, \Gamma_N, \Gamma_D)$ , final time  $(T)$ , material data  $(E, \nu, \rho)$ , loads and initial conditions  $(\mathbf{f}, \mathbf{g}, \mathbf{u}_0, \mathbf{v}_0)$ .

*Problem discretization:* background computational mesh  $(\mathcal{P}_{\text{bg}})$ .

*Error control:* data defining the quantity of interest  $(\mathbf{f}^\mathcal{O}, \mathbf{g}^\mathcal{O}, \mathbf{u}^\mathcal{O}, \mathbf{v}^\mathcal{O})$  and number of vibration modes  $M$ .

*Adaptivity parameters:* Number of time blocks  $(N^{\text{bk}})$ , prescribed error  $(s_{\text{tol}}^e)$  and other tuning parameters.

**Result:** Numerical approximation  $\tilde{\mathbf{U}}$ ; adapted space meshes  $\mathcal{P}_m^{\text{bk}}$  and time steps  $\Delta t_m^{\text{bk}}, m = 1, \dots, N^{\text{bk}}$ ; and error estimate  $\tilde{s}^e$  fulfilling  $|\tilde{s}^e| \leq s_{\text{tol}}^e$ .

// Modal analysis

Generate higher order space  $\mathcal{V}_0^{\text{bg}, p+1}$ ;

Compute the eigenpairs  $(\tilde{\omega}_i, \tilde{\mathbf{q}}_i), i = 1, \dots, M$  in the space  $\mathcal{V}_0^{\text{bg}, p+1}$ ;

// Adjoint problem (modal solution)

Compute the values  $\tilde{l}_i, \tilde{u}_i, \tilde{v}_i$  (using  $\mathbf{f}^\mathcal{O}, \mathbf{g}^\mathcal{O}, \mathbf{u}^\mathcal{O}, \mathbf{v}^\mathcal{O}$  and  $\tilde{\mathbf{q}}_i, i = 1, \dots, M$ );

Compute the time dependent functions  $\tilde{y}_i(t)$  (using  $\tilde{l}_i, \tilde{u}_i, \tilde{v}_i$  and  $\tilde{\omega}_i, i = 1, \dots, M$ );

// Problem computation, error assessment and adaptivity

Initialize discretization:  $\mathcal{P}_1^{\text{bk}} = \mathcal{P}_{\text{bg}}, \Delta t_1^{\text{bk}} = T/N^{\text{bk}}$ ;

**for**  $m = 1 \dots N^{\text{bk}}$  **do**

**repeat**

        // Compute solution and error estimate

        Compute solution  $\tilde{\mathbf{U}}$  in the time interval  $I_m^{\text{bk}}$  and estimate error contributions;

        // Mesh adaptivity

**if** *The solution is not accepted in  $I_m^{\text{bk}}$*  **then**

            Refine/unrefine the spatial mesh  $\mathcal{P}_m^{\text{bk}}$  and/or the time step  $\Delta t_m^{\text{bk}}$ ;

**end**

**until** *The solution is accepted in  $I_m^{\text{bk}}$* ;

    Set initial discretization for the next time interval:  $\mathcal{P}_{m+1}^{\text{bk}} = \mathcal{P}_m^{\text{bk}}$ ,

$\Delta t_{m+1}^{\text{bk}} = \Delta t_m^{\text{bk}}$ ;

**end**

Algorithm 1: Algorithm for problem approximation with error control and space-time mesh adaptivity.

*proposed space-time adaptive strategy in a 2D wave propagation problem. This example is a shorter version than the first numerical example in the appended paper D. The computational domain  $\Omega$  is a perforated rectangular plate,  $\Omega := (-0.5, 0.5) \times (0, 0.5) \setminus \Omega_0$  m<sup>2</sup>, with  $\Omega_0 := \{(x, y) \in \mathbb{R}^2 : x^2 + (y - 0.25)^2 \leq 0.025^2\}$  m<sup>2</sup>, see figure 9.*

The plate is clamped at the bottom side and the horizontal displacement is blocked at both vertical sides. The plate is initially at rest,  $\mathbf{u}_0 = \mathbf{v}_0 = \mathbf{0}$ , and loaded with the time dependent traction

$$\mathbf{g}(t) = \begin{cases} -g(t)\mathbf{e}_2 & \text{on } \Gamma_g, \\ 0 & \text{elsewhere,} \end{cases} \quad (34)$$

with  $\Gamma_g := (-0.025, 0.025) \times \{0.5\}$  m,  $\mathbf{e}_2 := (0, 1)$  and  $g(t)$  is the impulsive time-dependent function defined in figure 9 with parameters  $g_{\max} = 30$  Pa and  $t_g = 0.005$  s. No body force is acting in this example,  $\mathbf{f} = \mathbf{0}$ . The material properties of the plate are Young's modulus  $E = 8/3$  Pa, Poisson's ratio  $\rho = 1/3$ , the density  $\rho = 1$  kg/m<sup>3</sup> and the damping coefficients  $a_1 = 0$  d<sup>-1</sup>,  $a_2 = 10^{-4}$  s. The final simulation time is  $T = 0.25$  s. The plain stress hypothesis is considered.

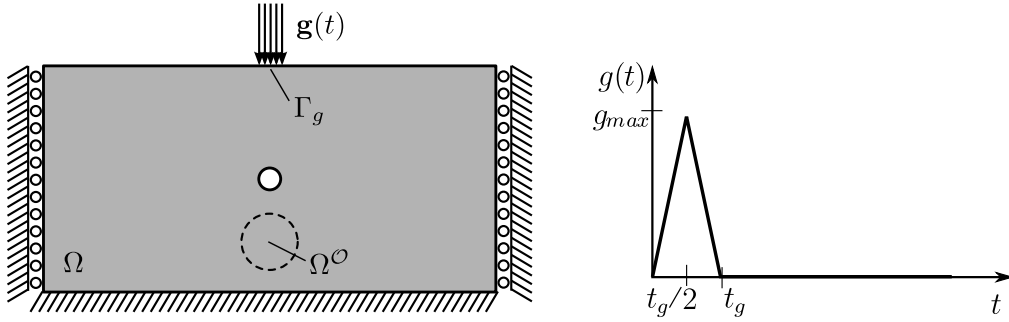


Figure 9: Definition of the problem geometry (left) and time-dependence of the external load (right).

The quantity of interest considered in this example is a weighted average of the velocities, namely

$$L^\circ(\mathbf{W}) := m(\mathbf{v}^\circ, \mathbf{w}_v(T)).$$

The weighting function  $\mathbf{v}^\circ$  considered here is plotted in figure 10 and defines a pseudo average of the vertical component of the final velocity near the region of interest  $\Omega^\circ := \{(x, y \in \mathbb{R}^2 : x^2 + (y - 0.1)^2 < 0.075^2)\}$  m<sup>2</sup>, see figure 9. Note that the  $x$ -component of  $\mathbf{v}^\circ$  is small compared to its  $y$ -component and, moreover, function  $\mathbf{v}^\circ$  takes larger values near  $\Omega^\circ$ . The weighting function  $\mathbf{v}^\circ$  is exactly represented using the expansion of the first  $M = 60$  vibration modes of the problem. Thus, the quantity of interest is well suited for the modal-based error estimate, because only  $M = 60$  vibration modes have to be computed to approximate the adjoint solution.

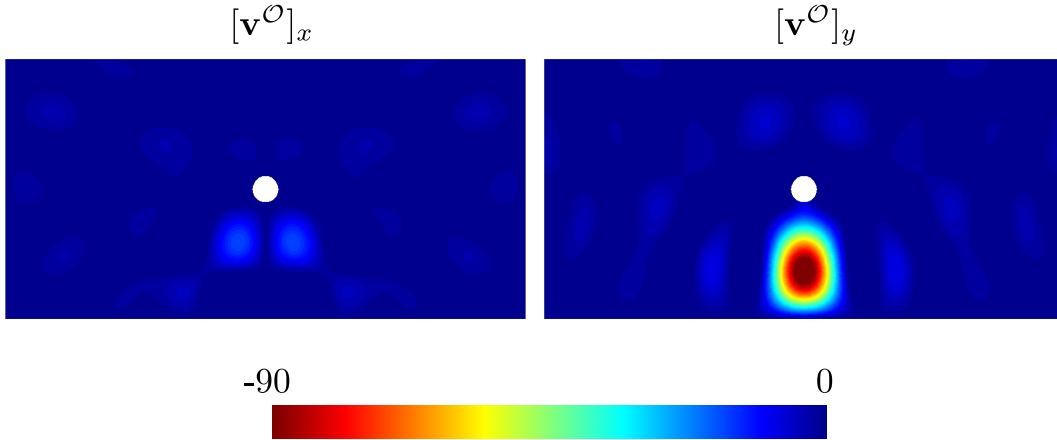


Figure 10: Weighting function  $\mathbf{v}^{\mathcal{O}}$  ( $x$ - and  $y$ -components) defining the quantity of interest  $L^{\mathcal{O}}(\cdot)$ .

Figure 11 shows several snapshots of an adapted numerical solution obtained with the proposed methodology imposing a target error  $s_{\text{tol}}^e = 5 \cdot 10^{-5}$  m/s corresponding to a 2.1% of the computed quantity  $\tilde{s} := L^{\mathcal{O}}(\tilde{\mathbf{U}}) = 2.4242 \cdot 10^{-2}$  m/s. The particular description of all the parameters used in this computation are found in paper D. The prescribed target error is fulfilled quite sharply with respect to the assessed error. That is, the assessed error  $\tilde{s}^e = -1.5756 \cdot 10^{-5}$  m/s fulfills  $|\tilde{s}^e| \leq s_{\text{tol}}^e$ , but  $|\tilde{s}^e|$  and  $s_{\text{tol}}^e$  are of the same order of magnitude. Moreover, the error with respect to an overkill solution, namely  $s_{\text{ovk}}^e := -1.5125 \cdot 10^{-5}$  m/s, is also below (in absolute value) the user-defined value  $s_{\text{tol}}^e$ . Note that the assessed error is a good approximation of the overkill error. That is, the effectivity of the error estimate,  $\tilde{s}^e/s_{\text{ovk}}^e = 1.041$ , is near one. The methodology to compute the overkill solution is also detailed in paper D.

Figure 12 shows the convergence of the estimates. As expected, the use of an adaptive refinement strategy leads to better approximations for the quantity of interest with less computational cost. The adapted solutions have a lower error than the uniform approximations for the same number of space-time cells.

### 3.4 Error assessment for timeline-quantities of interest

Selecting a scalar quantity of interest in time-dependent problems it is not always obvious. This is because, in many cases, a single scalar value does not give enough

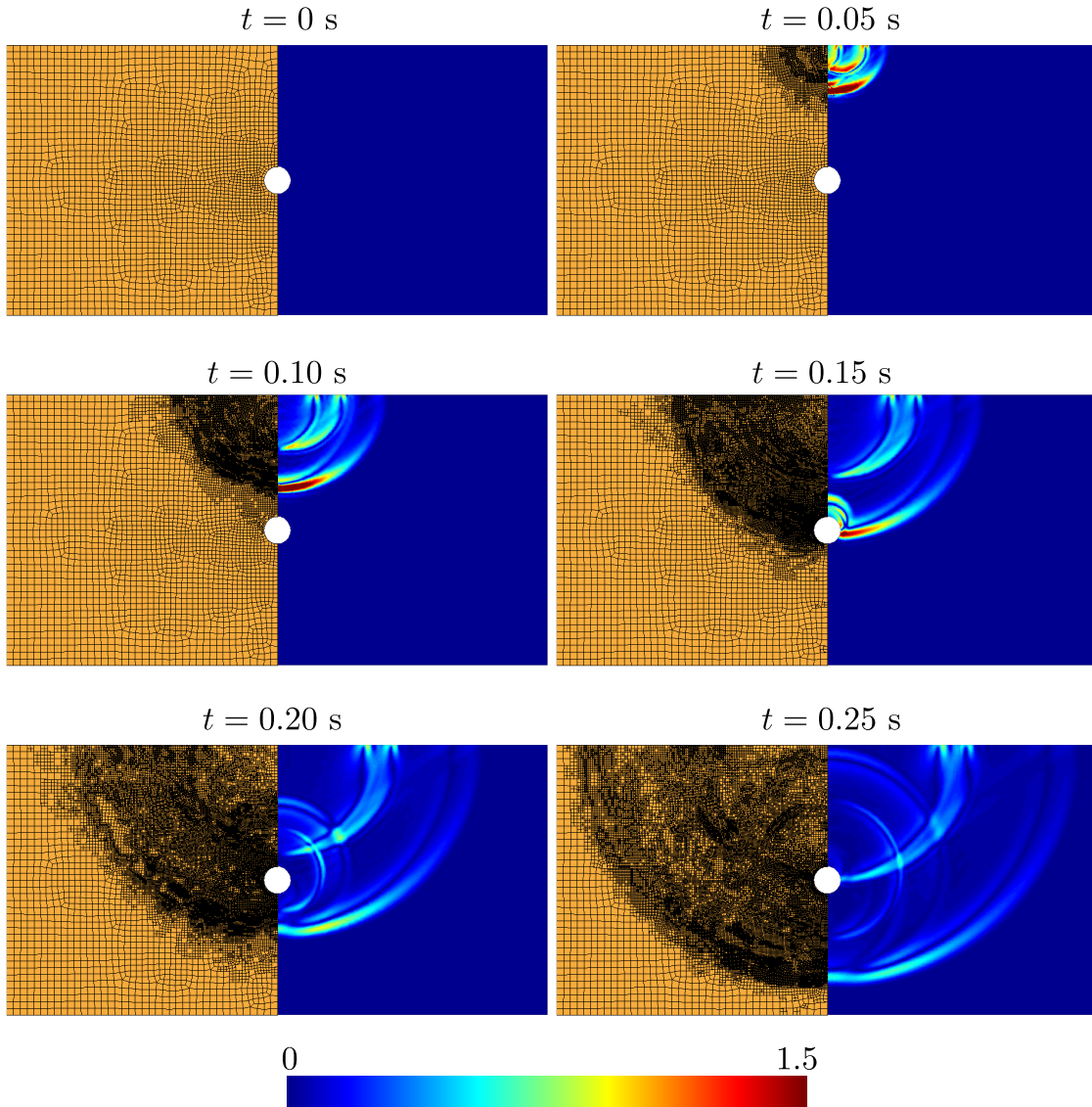


Figure 11: Snapshots of the computed solution (magnitude of velocities in m/s) and the computational mesh at several time points for the adapted solution verifying the prescribed target error  $s_{\text{tol}}^e = 5 \cdot 10^{-5}$  m/s.

pieces of information about a space-time solution. The preferred quantities of interest in time-dependent problems are typically the history (or evolution) of the space-average of the solution in a subregion of the domain. These quantities are time-dependent functions instead of single scalar values. This suggests introducing the so called timeline-dependent quantities of interest for error assessment in transient

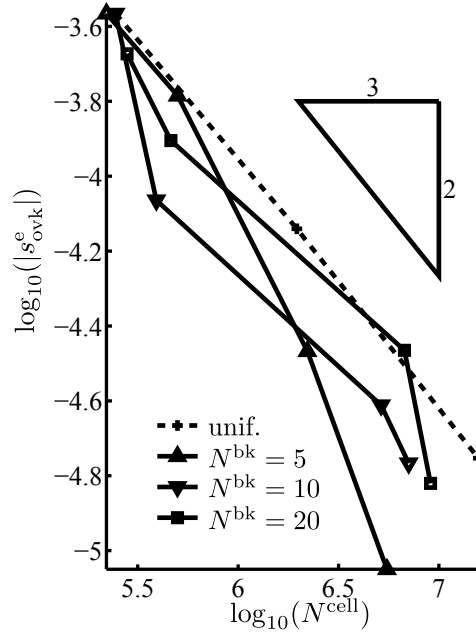


Figure 12: Error convergence for the adapted and uniform computations vs the number of used space-time cells ( $N^{\text{cells}}$ ). The adaptive solutions are obtained using three different number of time blocks  $N^{\text{bk}}$ .

problems.

Timeline-dependent quantities are associated with a bounded mapping  $L_{\text{TL}}^{\mathcal{O}}(\cdot)$  taking the space-time solution  $\mathbf{u}(\mathbf{x}, t)$  and returning a time-dependent scalar function  $s(t)$ , see figure 13. Note that the functional  $L_{\text{TL}}^{\mathcal{O}}(\cdot)$  is a different mathematical object than the functional  $L^{\mathcal{O}}(\cdot)$  associated with the standard quantities of interest, because  $L^{\mathcal{O}}(\cdot)$  returns a single scalar value (and not a time-dependent function). A convenient expression for  $L_{\text{TL}}^{\mathcal{O}}(\cdot)$  is defined as an extension of the functional  $L^{\mathcal{O}}(\cdot)$  defined in (3), namely

$$[L_{\text{TL}}^{\mathcal{O}}(\mathbf{w})](t) := \int_0^t (\mathbf{f}^{\mathcal{O}}(\tau), \dot{\mathbf{w}}(\tau)) \, d\tau + \int_0^t (\mathbf{g}^{\mathcal{O}}(\tau), \dot{\mathbf{w}}(\tau))_{\Gamma_N} \, d\tau + (\rho \mathbf{v}^{\mathcal{O}}, \dot{\mathbf{w}}(t)) + a(\mathbf{u}^{\mathcal{O}}, \mathbf{w}(t)), \quad (35)$$

where the functions  $\mathbf{f}^{\mathcal{O}}$  and  $\mathbf{g}^{\mathcal{O}}$  define weighted space-time averages of the solution in the interior domain  $\Omega$  or the Neumann boundary  $\Gamma_N$ , respectively, in the time interval  $[0, t]$  for a generic time  $t \in I$ . On the other hand, functions  $\mathbf{v}^{\mathcal{O}}$  and  $\mathbf{u}^{\mathcal{O}}$  define weighted space-averages of the velocities and displacements, respectively, at a generic time point  $t \in I$ . For the sake of simplicity, the notation  $L_{\text{TL}}^{\mathcal{O}}(\mathbf{w}; t) := [L_{\text{TL}}^{\mathcal{O}}(\mathbf{w})](t)$  is

introduced.

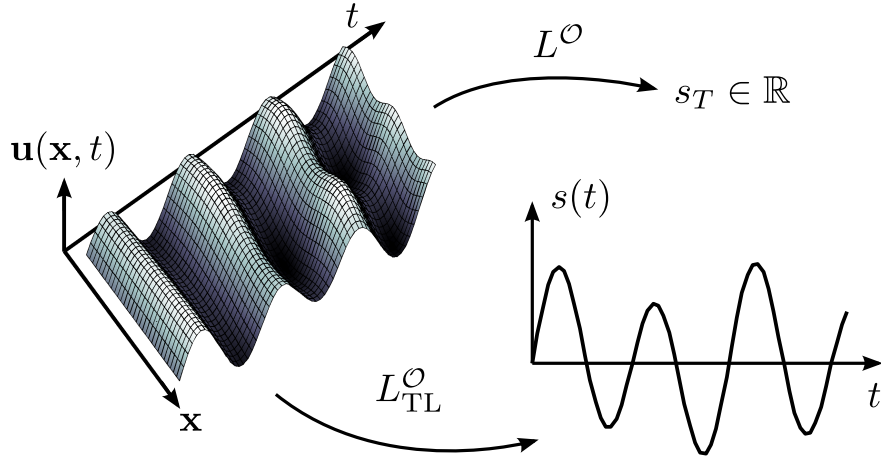


Figure 13: Illustration of scalar and timeline-dependent quantities of interest. The functional  $L^O(\cdot)$  maps the time-space solution  $\mathbf{u}(\mathbf{x}, t)$  into a scalar value  $s_T \in \mathbb{R}$ . The operator  $L^O_{TL}(\cdot)$  transforms  $\mathbf{u}(\mathbf{x}, t)$  into a time-dependent function  $s(t)$ .

The error to be assessed is the error in the timeline-dependent quantity of interest, namely

$$s^e(t) := s(t) - \tilde{s}(t),$$

where  $s(t) := L^O_{TL}(\mathbf{u}; t)$  is the exact timeline quantity and  $\tilde{s}(t) := L^O_{TL}(\tilde{\mathbf{u}}; t)$  is the computed one. Assessing the time-dependent function  $s^e(t)$  requires introducing an error representation similar to the one presented in equation (19) for the scalar quantity of interest. Thus, an auxiliary problem, analogous to the adjoint problem (4), has to be introduced for the timeline quantity  $L^O_{TL}(\cdot)$ .

Note that for a given time  $t \in I$ , the functional  $L^O_{TL}(\cdot)$  restricted to this time instance, namely  $L^O(\cdot) = L^O_{TL}(\cdot; t)$ , is a standard quantity of interest taking  $t$  as the *final* time. The associated adjoint problem is analogous to the one presented in (4) but replacing the final time  $T$  for the particular time instance  $t \in I$ . That is, the

adjoint solution  $\mathbf{u}_t^d$  associated with  $L_{\text{TL}}^{\mathcal{O}}(\cdot; t)$  is the solution of

$$\rho(\ddot{\mathbf{u}}_t^d - a_1 \dot{\mathbf{u}}_t^d) - \nabla \cdot \boldsymbol{\sigma}_t^d = -\mathbf{f}^{\mathcal{O}} \quad \text{in } \Omega \times [0, t], \quad (36a)$$

$$\mathbf{u}_t^d = \mathbf{0} \quad \text{on } \Gamma_D \times [0, t], \quad (36b)$$

$$\boldsymbol{\sigma}_t^d \cdot \mathbf{n} = -\mathbf{g}^{\mathcal{O}} \quad \text{on } \Gamma_N \times [0, t], \quad (36c)$$

$$\mathbf{u}_t^d = \mathbf{u}^{\mathcal{O}} \quad \text{at } \Omega \times \{t\}, \quad (36d)$$

$$\dot{\mathbf{u}}_t^d = \mathbf{v}^{\mathcal{O}} \quad \text{at } \Omega \times \{t\}, \quad (36e)$$

with the constitutive law

$$\boldsymbol{\sigma}_t^d := \mathbf{C} : \boldsymbol{\varepsilon}(\mathbf{u}_t^d - a_2 \dot{\mathbf{u}}_t^d). \quad (37)$$

The solution of equation (36) is denoted by  $\mathbf{u}_t^d$  emphasizing that there is a different adjoint solution for each time  $t$ . Consequently, equation (36) describes a family of adjoint problems, one for each time  $t \in I$ .

For a particular instance of time  $t \in I$ , the error representation of the value  $s^e(t)$  is similar to the standard scalar case (20) but taking the adjoint solution  $\mathbf{u}_t^d$  and restricting the residual  $R(\cdot)$  to the time interval  $[0, t]$ . That is

$$s^e(t) = R_t(\mathbf{u}_t^d), \quad (38)$$

where

$$\begin{aligned} R_t(\mathbf{w}) := & \int_0^t [l(\dot{\mathbf{w}}(\tau); \tau) - m(\ddot{\mathbf{u}}(\tau) + a_1 \dot{\mathbf{u}}(\tau), \dot{\mathbf{w}}(\tau)) - a(\tilde{\mathbf{u}}(\tau) + a_2 \dot{\mathbf{u}}(\tau), \dot{\mathbf{w}}(\tau))] \, d\tau \\ & + m(\mathbf{v}_0 - \dot{\mathbf{u}}(0^+), \dot{\mathbf{w}}(0^+)) + a(\mathbf{u}_0 - \tilde{\mathbf{u}}(0^+), \mathbf{w}(0^+)). \end{aligned}$$

Hence, an estimate for  $s^e(t)$  is obtained injecting an adjoint approximation  $\tilde{\mathbf{u}}_t^d \approx \mathbf{u}_t^d$  in equation (38), namely

$$s^e(t) \approx R_t(\tilde{\mathbf{u}}_t^d) =: \tilde{s}^e(t). \quad (39)$$

In practice, it is computationally unaffordable to independently compute the all the infinite approximations of the solutions  $\mathbf{u}_t^d$ , one for each time  $t \in I$ , and then using them in equation (38) to assess  $s^e(t)$ . However, for the particular case of  $\mathbf{f}^{\mathcal{O}}$  and  $\mathbf{g}^{\mathcal{O}}$  constant in time (which accounts for a number of interesting cases), the different functions  $\mathbf{u}_t^d$  corresponding to different time instances  $t \in I$  are all equivalent after a time translation. Thus, if  $\mathbf{u}_t^d$  is properly computed for a particular value of  $t$ , e.g.  $t = T$ , the general functions  $\mathbf{u}_t^d$  for  $t \neq T$  are easily recovered as a direct post-process of  $\mathbf{u}_T^d$ ,

$$\mathbf{u}_t^d(\tau) = \mathbf{u}_T^d(\tau + T - t). \quad (40)$$

This fundamental result, proved in paper C, is the crucial observation that allows assessing the error in the timeline-dependent quantity with an affordable cost.

The adjoint approximations  $\tilde{\mathbf{u}}_t^d$  used in the error estimate (39) are computed applying the time shift (40) to the adjoint approximation  $\tilde{\mathbf{u}}_T^d$  associated with the final time  $T$ ,

$$\tilde{\mathbf{u}}_t^d(\tau) := \tilde{\mathbf{u}}_T^d(\tau + T - t). \quad (41)$$

Thus, only one adjoint approximation  $\tilde{\mathbf{u}}_T^d$  has to be computed and the others are simply recovered with a time shift. The approximation  $\tilde{\mathbf{u}}_T^d$  is computed with the modal based-approach described in section 3.2. This choice is specially convenient for assessing the error in the timeline-dependent quantity of interest because it enormously simplifies the implementation of the time shift (41).

The performance of the error estimate for timeline-dependent quantities is studied in the paper C in three numerical examples. The results show that the error estimate is a good approximation of the error in the timeline-dependent quantity of interest. The quality of the error estimate depends on the number of vibration modes used to solve the auxiliary adjoint problems.

**Remark 7** (Illustrative example). *This example illustrates the performance of the error estimate  $\tilde{s}^e(t)$ . The computational domain is the three dimensional structure plotted in figure 14 which is clamped at the supports and it is loaded with the time-dependent traction*

$$\mathbf{g}(t) = \begin{cases} -g(t)\mathbf{e}_1 & \text{on } \Gamma_g, \\ \mathbf{0} & \text{elsewhere,} \end{cases}$$

where function  $g(t)$  is defined in figure 14 and the values  $g_{\max} = 1 \cdot 10^3$  Pa and  $t_g = 1 \cdot 10^{-3}$  s are considered. The set  $\Gamma_g$  is the boundary where the load is applied, see figure 14. The structure is initially at rest ( $\mathbf{u}_0 = \mathbf{v}_0 = \mathbf{0}$ ) and the body force is zero ( $\mathbf{f} = \mathbf{0}$ ). The material properties are Young's modulus  $E = 2 \cdot 10^{10}$  Pa, Poisson's ratio  $\nu = 0.2$ , density  $\rho = 2.4 \cdot 10^3$  kg/m<sup>3</sup> and viscosity  $a_1 = a_2 = 0$ . The final time is  $T = 0.02$  s .

*This example focuses in the timeline-dependent quantity of interest*

$$s(t) := \frac{1}{\text{meas}(\Gamma_g)} (\mathbf{e}_1, \mathbf{u}(t))_{\Gamma_g},$$

which is the average of the  $x$ -component of the displacement in the boundary  $\Gamma_g$  at every time  $t \in I$ .

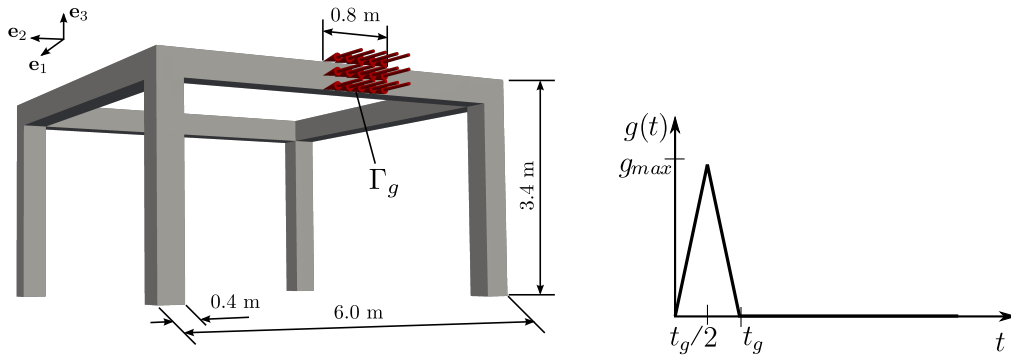


Figure 14: Problem geometry (left) and time description of the external load (right).

The problem is discretized with trilinear hexahedra in space and with the Newmark method in time with parameters  $\beta = 1/4$  and  $\gamma = 1/2$ . The approximated quantity of interest  $\tilde{s}(t) = L^O(\tilde{\mathbf{u}}; t)$  is computed from the approximate solution  $\tilde{\mathbf{u}}$  obtained with the coarse finite element mesh plotted in figure 15 and with  $N = 400$  time steps. The reference quantity of interest  $s(t) = L^O(\mathbf{u}; t)$  is obtained by assuming that the exact solution  $\mathbf{u}$  is fairly replaced by an overkill solution obtained using the reference mesh in figure 15 and  $N = 1600$  time steps. The error in the quantity of interest is evaluated using the reference solution, namely  $s^e(t) = s(t) - \tilde{s}(t)$ . Finally, the error estimate  $\tilde{s}^e(t)$  is computed using up to  $M = 60$  vibration modes for approximating the adjoints.

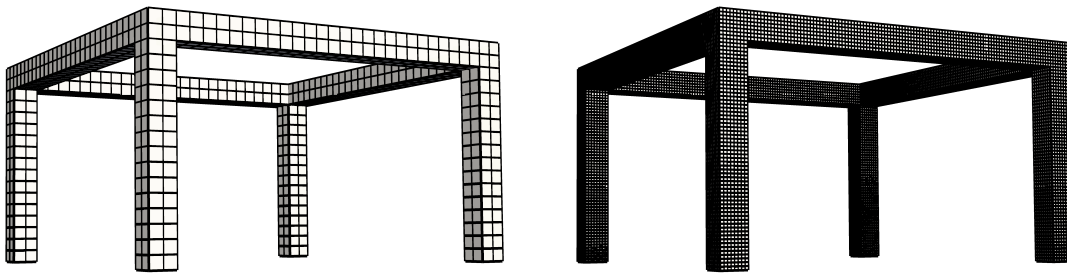


Figure 15: Coarse (left) and reference (right) meshes used in this example with 334 and 22016 elements respectively.

Figure 16 shows the computed and reference timeline-dependent quantities,  $\tilde{s}(t)$  and  $s(t)$ , along with the assessed and reference errors,  $\tilde{s}^e(t)$  and  $s^e(t)$ . Note that the quality of the error estimate  $\tilde{s}^e(t)$  increases with the number of vibration modes. For

$M = 60$  modes, the error estimate  $\tilde{s}^e(t)$  and the reference error  $s^e(t)$  are in very good agreement.

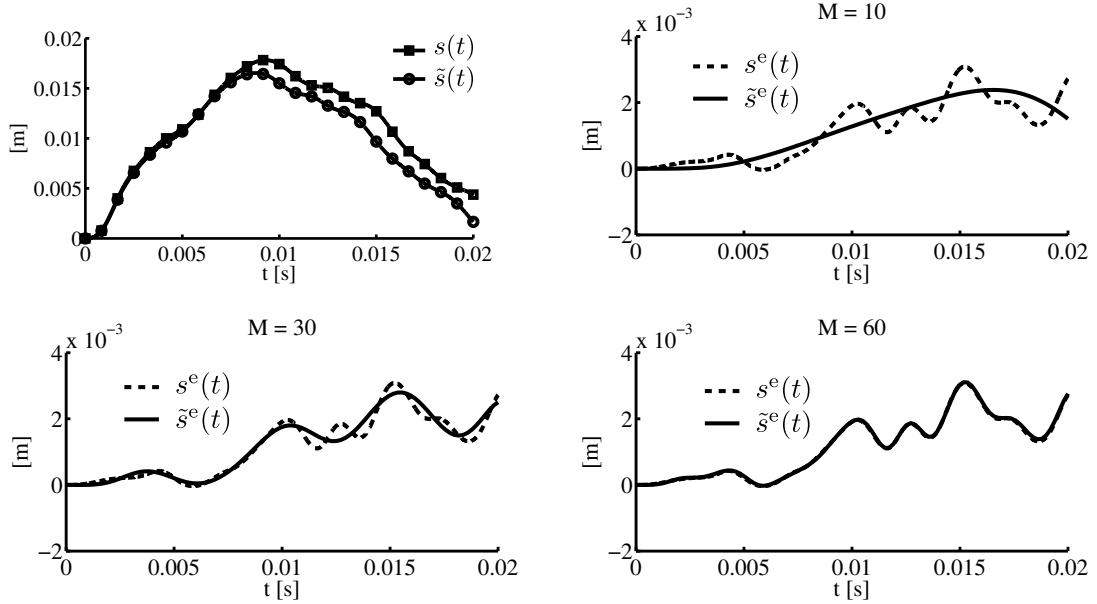


Figure 16: Approximated quantity of interest  $\tilde{s}(t)$  and reference quantity  $s(t)$  (top, left). Reference and assessed errors,  $s^e(t)$  and  $\tilde{s}^e(t)$ , for three different number of vibration modes for approximating the adjoints,  $M = 10$  (top, right),  $M = 30$  (bottom, left) and  $M = 60$  (bottom, right).

## 4 Closure

The main contributions as well as the open research lines are summarized in the following subsections.

### 4.1 Summary

- **Goal-oriented error bounds**

A new technique providing goal-oriented error bounds in the framework of linear structural dynamics is proposed. The novel error bounds are derived in two alternative and equivalent ways: 1) using symmetrized error equations, or 2) using an auxiliary error associated with the viscous stress. The first approach resembles to the one considered for the convection-diffusion-reaction equation,

and the second approach is analogous to the one considered in steady-state linear elasticity.

The proposed methodology yields estimates with better quality than the already available approaches. The bound gap of the novel approach is 50% sharper. The techniques providing error bounds in structural dynamics (including the proposed methodology) require that the formulation has a finite amount of damping. Consequently, the computed bounds are very pessimistic for materials with a small amount of damping. Further research is needed to explore alternative pertinent bounds for nearly elastic problems.

- **Modal-based goal-oriented error assessment**

An efficient goal-oriented error estimate for structural transient dynamics is introduced. The proposed methodology uses modal analysis to compute the adjoint problem instead of direct time-integration methods. The modal-based approach is particularly well suited for some quantities of interest and allows effectively computing and storing the adjoint solution. This is because the adjoint solution is computed and stored for each vibration mode instead of for each time step. Moreover, the modal-based description of the adjoint approximation facilitates the post-processing techniques applied to enhance its space accuracy. The post-processing is performed just once for every relevant mode instead of for each time step. The resulting estimate is well-suited for time-dependent problems because its cost per time step is very low.

The quality of the modal-based error estimate depends on the number of computed vibration modes. The required number of modes strongly depends on the definition of the quantity of interest. Consequently, some practical quantities of interest are proposed requiring only few low-frequency modes.

- **Modal-based goal-oriented adaptivity**

The proposed adaptive strategy aims at computing an optimal space-time discretization such that the computed solution has an error in the quantity of interest below a user-defined tolerance. The major novelty with respect previous approaches is that the local error information driving the adaptive process is computed using the modal-based error estimate.

The numerical examples show that the proposed technique provides adapted solutions fulfilling the user-defined error tolerance. That is, both the assessed and computed errors are below the user-defined error value. Moreover, the discretizations obtained with the proposed adaptive strategy are more efficient than the ones obtained with an uniform refinement of all mesh elements and time steps. The adapted discretizations give more accurate results than the non-adapted ones for the same number of space-time elements.

- **Error assessment for timeline-dependent quantities of interest**

A new type of quantities of interest for error assessment in structural transient dynamics are proposed. These quantities (referred as timeline-dependent quantities of interest) are scalar time-dependent outputs of the transient solution which are better suited to time-dependent problems than the standard scalar ones.

Assessing the error in the timeline-dependent quantity of interest requires approximating infinite standard adjoint problems. However, all these problems are similar and they can be recovered from a common parent problem (associated with the a scalar quantity of interest) by means of a simple translation of the time variable. The time shift is very efficiently performed if the adjoint solution is approximated with modal analysis, because the time-dependence of the adjoint solution is known analytically.

The proposed error estimate for timeline-dependent quantities provides accurate approximations of the error accounting for both the space and time discretization errors. The quality of the error estimate depends on the number of vibration modes used to solve the auxiliary adjoint problems.

## 4.2 Open research lines

- **Space-time adaptivity for explicit time-integration schemes**

The proposed space-time adaptive technique restricts to numerical approximations obtained with space-time variational methods as the time-continuous Galerkin method. Therefore, the adaptive technique cannot directly deal with explicit time-integration schemes using a lumped mass matrix. Explicit schemes are widely used in structural dynamics and, therefore, the corresponding extension of the proposed space-time adaptive technique is worth considering. The

main challenge of this extension is how to separate the effect of lumping the mass matrix from other error sources.

Note that another difficulty arises in mesh adaptivity for explicit schemes. At first sight, the use of local mesh refinement in combination of explicit schemes compromises the efficiency of the overall approximation process. Note that, in this context, the time step length is determined by the smallest element size of the computational mesh. Consequently, a local mesh refinement leads to a fine time step length for the whole computational mesh. However, this difficulty can be overcome using time-step partitioning techniques allowing to use different time step lengths in different regions of the domain, see for instance the work by Casadei and Halleux (2009).

- **Modal-based bounds of the error in the quantity of interest**

The modal-based description of the adjoint solution is used here to compute approximations of the error in the quantity of interest. However, modal analysis can be considered also to compute goal-oriented error bounds. One of the main advantages of this approach is that the modal description of the adjoint solution allows to efficiently compute the adjoint D-admissible stress. This is because the standard stress equilibration techniques are performed for few relevant modes instead for each time step. Thus, the cost per time step is reduced.

- **Error bounds in the timeline-quantity of interest.**

Bounds of the error in the timeline-dependent quantity are still to be explored. The error bounds presented in section 3.1 for standard quantities of interest can be extended to deal with timeline-dependent quantities. Using the time translation presented in section 3.4 and using a modal description for the adjoint solution, the error bounds in the timeline-dependent quantity of interest can be efficiently computed.

- **Enhanced goal-oriented error bounds**

The quality of the proposed error bounds is not enough for practical applications, specially in nearly elastic cases. The proposed bounds can be enhanced following the rationale presented by Parés (2005) designed for a generic non-symmetric problem. This approach introduces a continuous approximation of the error which is used to compute a correction factor improving the quality

of the error bounds. Consequently, the particularization of this methodology might lead to improved error bounds in structural transient dynamics.

- **Modal-based error assessment and timeline-dependent quantities of interest for other linear time-dependent problems**

The proposed modal-based error estimate as well as the proposed timeline-dependent quantities of interest can be extended to deal with other linear time-dependent problems (e.g. parabolic problems as the time-dependent heat equation).

- **Approximating the adjoint solution with other reduced order models**

Modal analysis can be seen as a particular reduced order model. More sophisticated reduced order models can be considered to describe the solution of the adjoint problem, for instance, the Proper Generalized Decomposition (PGD) introduced by Chinesta et al. (2011). This approach can be applied to deal with quantities of interest with a parametric definition. That is, the quantity of interest is defined introducing some free parameters, e.g., the position or shape of the zone of interest, the time instant of interest, etc. Note that the proposed timeline-dependent quantity of interest is indeed a particular parametric quantity where the selected parameter is the time instant of interest.

The PGD approach might allow to efficiently pre-compute and store the solution of the adjoint problem associated with the parametric quantity of interest for any value of the selected parameters in a given domain.



# Bibliography

---

- Ainsworth, M. and J. T. Oden (1997). A posteriori error estimation in finite element analysis. *Comput. Methods Appl. Mech. Engrg.* 142, 1–88.
- Ainsworth, M. and J. T. Oden (2000). *A posteriori error estimation in finite element analysis*. John Wiley & Sons Ltd.
- Asner, L., S. Tavener, and D. Kay (2012). Adjoint-based a posteriori error estimation for coupled time-dependent systems. *SIAM J. Sci. Comput.* 34, 2394–2419.
- Aubry, D., D. Lucas, and B. Tie (1999). Adaptive strategy for transient/coupled problems. Applications to thermoelasticity and elastodynamics. *Comput. Methods Appl. Mech. Engrg.* 176, 41–50.
- Babuška, I. and W. C. Rheinboldt (1978). Error estimates for adaptive finite element computations. *SIAM J. Numer. Anal.* 18, 736–754.
- Bangerth, W. (1998). *Adaptive Finite-Elemente-Methoden zur Lösung der Wellengleichung mit Anwendung in der Physik der Sonne*. Ph. D. thesis, Ruprecht-Karls-Universität Heidelberg.
- Bangerth, W., M. Geiger, and R. Rannacher (2010). Adaptive Galerkin finite element methods for the wave equation. *Computational Methods in Applied Mathematics* 1, 3–48.
- Bangerth, W. and R. Rannacher (1999). Finite element approximation of the acoustic wave equation: error control and mesh adaptation. *East-West Journal of Numerical Mathematics* 7, 263–282.
- Bangerth, W. and R. Rannacher (2001). Adaptive finite element techniques for the acoustic wave equation. *Journal of Computational Acoustics* 9, 575–591.
- Bathe, K. J. (1996). *Finite Element Procedures*. Prentice Hall.
- Becker, R. and R. Rannacher (2001). An optimal control approach to a posteriori error estimation in finite element methods. *Acta Numer.* 10, 1–102.

- Bouchona, M. and F. J. Sánchez-Sesma (2007). Boundary integral equations and boundary elements methods in elastodynamics. *Advances in Geophysics* 48, 157–189.
- Carey, V., D. Estep, A. Johansson, M. Larson, and S. Tavener (2010). Blockwise adaptivity for time dependent problems based on coarse scale adjoint solutions. *SIAM J. Sci. Comput.* 32, 2121–2145.
- Casadei, F. and J. P. Halleux (2009). Binary spatial partitioning of the central-difference time integration scheme for explicit fast transient dynamics. *Int. J. Numer. Meth. Engng.* 78, 1436–1473.
- Chamoin, L. and P. Ladevèze (2008). A non-intrusive method for the calculation of strict and efficient bounds of calculated outputs of interest in linear viscoelasticity problems. *Comput. Methods Appl. Mech. Engrg.* 197, 994–1014.
- Chinesta, F., P. Ladevèze, and E. Cueto (2011). A short review on model order reduction based on proper generalized decomposition. *Archives of Computational Methods in Engineering* 18, 395–404.
- Cirak, F. and E. Ramm (1998). A posteriori error estimation and adaptivity for linear elasticity using the reciprocal theorem. *Comput. Methods Appl. Mech. Engrg.* 156, 351–362.
- Demkowicz, L., J. T. Oden, W. Rachowicz, and O. Hardy (1989). Toward a universal h-p adaptive finite element strategy, Part 1. Constrained approximation and data structure. *Comput. Methods Appl. Mech. Engrg.* 77, 79–112.
- Díez, P. and G. Calderón (2007). Goal-oriented error estimation for transient parabolic problems. *Comput. Mech.* 39, 631–646.
- Díez, P., N. Parés, and A. Huerta (2010). *Encyclopedia of Aerospace Engineering*, Chapter Error estimation and quality control. John Wiley & Sons Ltd.
- Erhart, T., W. Wall, and E. Ramm (2006). Robust adaptive remeshing strategy for large deformations, transient impact simulations. *Int. J. Numer. Meth. Engrg.* 65, 2139–2166.
- Eriksson, K., D. Estep, P. Hansbo, and C. Johnson (1996). *Computational Differential Equations*. Studentlitteratur.
- Fick, P. W., E. H. van Brummelen, and K. G. van der Zee (2010). On the adjoint-consistent formulation of interface conditions in goal-oriented error estimation and adaptivity for fluid-structure interaction. *Comput. Methods Appl. Mech. Engrg.* 199, 3369–3385.

- Fuentes, D., D. Littlefield, J. T. Oden, and S. Prudhomme (2006). Extensions of goal-oriented error estimation methods to simulation of highly-nonlinear response of shock-loaded elastomer-reinforced structures. *Comput. Methods Appl. Mech. Engrg.* 195, 4659–4680.
- Gallimard, L., P. Ladeveze, and J. P. Pelle (2000). An enhanced error estimator on the constitutive relation for plasticity problems. *Computers and Structures* 78, 801–810.
- Gratsch, T. and K. J. Bathe (2005). A posteriori error estimation techniques in practical finite element analysis. *Computers and Structures* 83, 235–265.
- Hughes, T. J. R. and G. M. Hulbert (1988). Space-time finite element methods for elastodynamics: Formulations and error estimates. *Comput. Methods Appl. Mech. Engrg.* 66, 339–363.
- Hulbert, G. M. and T. J. R. Hughes (1990). Space-time finite element methods for second-order hyperbolic equations. *Comput. Methods Appl. Mech. Engrg.* 84, 327–348.
- Johnson, C. (1993). Discontinuous galerkin finite element methods for second order hyperbolic problems. *Comput. Methods Appl. Mech. Engrg.* 107, 117–129.
- Komatitsch, D., J. P. Vilotte, R. Vai, J. M. Castillo-Covarrubias, and F. J. Sánchez-Sesma (1999). The spectral element method for elastic wave equations—application to 2-D and 3-D seismic problems. *Int. J. Numer. Meth. Engrg.* 45, 1139–1164.
- Ladevèze, P. (2008). Strict upper error bounds for computed outputs of interest in computational structural mechanics. *Computational Mechanics* 42, 271–286.
- Ladevèze, P. and D. Leguillon (1983). Error estimate procedure in the finite element method. *SIAM J. on Numerical Analysis* 20, 485–509.
- Ladevèze, P. and N. Moës (1997). A new a posteriori error estimation for nonlinear time-depending finite element analysis. *Comput. Methods Appl. Mech. Engrg.* 157, 45–68.
- Ladevèze, P. and N. Moës (1999). Adaptive control for finite element analysis in plasticity. *Computers and Structures* 73, 45–60.
- Ladevèze, P., N. Moës, and B. Douchin (2000). Constitutive relation error estimators for (visco)plastic finite element analysis with softening. *Comput. Methods Appl. Mech. Engrg.* 176, 247–264.
- Ladevèze, P. and J. P. Pelle (2001). *La maîtrise du calcul en mécanique linéaire et non linéaire*. Lavoisier.

- Ladevèze, P. and J. Waeytens (2009). Model verification in dynamics through strict upper bounds. *Comput. Methods Appl. Mech. Engrg.* 198, 1775–1784.
- Larson, M. G. and F. Bengzon (2008). Adaptive finite element approximation of multiphysics problems. *Commun. Numer. Methods Engrg.* 24, 505–521.
- Larson, M. G., R. Soderlund, and F. Bengzon (2008). Adaptive finite element approximation of coupled flow and transport problems with applications in heat transfer. *Int. J. Numer. Meth. Fluids* 57, 1397–1420.
- Larsson, F., P. Díez, and A. Huerta (2010). A flux-free a posteriori error estimator for the incompressible Stokes problem using a mixed FE formulation. *Comput. Methods Appl. Mech. Engrg.* 199, 2383–2402.
- Lee, C. H., J. A. Gil, and J. Bonet (2013). Development of a cell centred upwind finite volume algorithm for a new conservation law formulation in structural dynamics. *Computers and Structures* 118, 13–38.
- Li, X. D. and N. E. Wiberg (1998). Implementation and adaptivity of a space-time finite element method for structural dynamics. *Comput. Methods Appl. Mech. Engrg.* 156, 211–229.
- Newmark, N. M. (1959). A method of computation for structural dynamics. *J. of Engineering Mechanics* 85, 67–94.
- Paraschivoiu, M., J. Peraire, and A. T. Patera (1997). A posteriori finite element bounds for linear-functional outputs of elliptic partial differential equations. *Comput. Methods Appl. Mech. Engrg.* 150, 289–321.
- Parés, N. (2005). *Error assessment for functional outputs of PDE's: bounds and goal-oriented adaptivity*. Ph. D. thesis, Universitat Politècnica de Catalunya.
- Parés, N., J. Bonet, A. Huerta, and J. Peraire (2006). The computation of bounds for linear-functional outputs of weak solutions to the two-dimensional elasticity equations. *Comput. Methods Appl. Mech. Engrg.* 195, 406–429.
- Parés, N., P. Díez, and A. Huerta (2008a). Bounds of functional outputs for parabolic problems. Part I: Exact bounds of the discontinuous galerkin time discretization. *Comput. Methods Appl. Mech. Engrg.* 197, 1641–1660.
- Parés, N., P. Díez, and A. Huerta (2008b). Bounds of functional outputs for parabolic problems. Part II: Bounds of the exact solution. *Comput. Methods Appl. Mech. Engrg.* 197, 1661–1679.
- Parés, N., P. Díez, and A. Huerta (2009). Exact bounds of the advection-diffusion-reaction equation using flux-free error estimates. *SIAM J. Sci. Comput.* 31, 3064–3089.

- Pled, F., L. Chamoin, and P. Ladevèze (2011). On the techniques for constructing admissible stress fields in model verification: Performances on engineering examples. *Int. J. Numer. Meth. Engng.* 88, 409–441.
- Prager, W. and J. Synge (1947). Approximations in elasticity based on the concept of function space. *Quart. Appl. Math.* 5, 241–269.
- Prudhomme, S. and J. T. Oden (1999). On goal-oriented error estimation for elliptic problems: application to the control of pointwise errors. *Comput. Methods Appl. Mech. Engrg.* 176, 313–331.
- Rannacher, R. (2001). Adaptive Galerkin finite element methods for partial differential equations. *Journal of Computational and Applied Mathematics* 128, 205–233.
- Rannacher, R. and F. T. Stuttmeier (1997). A feed-back approach to error control in finite element methods: application to linear elasticity. *Comput. Mech.* 19, 434–446.
- Schleupen, A. and E. Ramm (2000). Local and global error estimations in linear structural dynamics. *Computers and structures* 76, 741–756.
- Stein, E. (2003). *Error-controlled adaptive finite elements in solid mechanics*. John Wiley & Sons Ltd.
- Van Der Zee, K. G., E. H. Van Brummelen, I. Akkerman, and R. de Borst (2011). Goal-oriented error estimation and adaptivity for fluid-structure interaction using exact linearized adjoints. *Comput. Methods Appl. Mech. Engrg.* 200, 2738–2757.
- Waeytens, J. (2010). *Contrôle des calculs en dynamique: bornes strictes et pertinents sur une quantité d'intérêt*. Ph. D. thesis, LMT-Cachan.
- Waeytens, J., L. Chamoin, and P. Ladevèze (2012). Guaranteed error bounds on pointwise quantities of interest for transient viscodynamics problems. *Computational Mechanics* 49, 291–307.
- Wiberg, N. E., F. Abdulwahab, and X. D. Li (1997). Error estimation and adaptive procedures based on superconvergent patch recovery. *Archives of Comput. Meth. in Engrg.* 4, 203–242.
- Wiberg, N. E., R. Bausys, and P. Hager (1999). Adaptive h-version eigenfrequency analysis. *Computers and structures* 71, 565–584.
- Wiberg, N. E. and X. D. Li (1994). Superconvergent patch recovery of finite-element solution and a posteriori  $L_2$  norm error estimate. *Com. Num. Meth. Engrg.* 10, 313–320.
- Wiberg, N. E. and X. D. Li (1999). Adaptive finite element procedures for linear and non-linear dynamics. *Int. J. Numer. Meth. Engrg.* 46, 178–1802.

Yerry, M. A. and M. S. Shephard (1983). A modified quadtree approach to finite element mesh generation. *IEEE Computer graphics and Applications* 3, 34–46.

Zienkiewicz, O. C. and J. Z. Zhu (1987). A simple error estimator and adaptative procedure for practical engineering analysis. *Int. J. Numer. Meth. Engrg.* 24, 337–357.

Zienkiewicz, O. C. and J. Z. Zhu (1992a). The superconvergent patch recovery and a posteriori error estimates. Part 1: The recovery technique. *Int. J. Numer. Meth. Engrg.* 33, 1331–1364.

Zienkiewicz, O. C. and J. Z. Zhu (1992b). The superconvergent patch recovery and a posteriori error estimates. Part 2: Error estimates and adaptivity. *Int. J. Numer. Meth. Engrg.* 33, 1365–1382.

Paper A

# Error assessment in structural transient dynamics

F. Verdugo, N. Parés and P. Díez

---

Manuscript accepted for publication in  
the *Archives of Computational Methods  
in Engineering* (June 2013)



# Error assessment in structural transient dynamics \*

F. Verdugo<sup>1</sup>, N. Parés<sup>1,2</sup> and P. Díez<sup>1,3</sup>

<sup>1</sup>Laboratori de Càlcul Numèric (LaCàN),  
 Universitat Politècnica de Catalunya (UPC),  
 Jordi Girona 1-3 E-08034 Barcelona, Spain.

<sup>2</sup> Laboratori de Càlcul Numèric (LaCàN),  
 Escola Universitària d'Enginyeria Tècnica Industrial de Barcelona (EUETIB),  
 Compte d'Urgell, 187, E-08036, Barcelona, Spain.

<sup>3</sup>Centre Internacional de Mètodes Numèrics en Enginyeria (CIMNE),  
 Gran Capitán s/n, E-08034 Barcelona, Spain.  
 Email: {francesc.verdugo,nuria.pares,pedro.diez}@upc.edu

## Abstract

This paper presents in a unified framework the most representative state-of-the-art techniques on a posteriori error assessment for second order hyperbolic problems, i.e., structural transient dynamics. For the sake of presentation, the error estimates are grouped in four types: recovery-based estimates, the dual weighted residual method, the constitutive relation error method and error estimates for timeline-dependent quantities of interest. All these methodologies give a comprehensive overview on the available error assessment techniques in structural dynamics, both for energy-like and goal-oriented estimates.

**Keywords:** elastodynamics, transient dynamics, goal-oriented error assessment, adjoint problem, quantity of interest, recovery estimates, dual weighted residuals, constitutive relation error, timeline-dependent quantity of interest.

## Contents

<b>1</b>	<b>Introduction</b>	<b>2</b>
<b>2</b>	<b>Problem statement</b>	<b>4</b>
2.1	Strong equations . . . . .	4
2.2	Weak and discrete formulations . . . . .	4
2.2.1	Newmark-like methods . . . . .	4
2.2.2	Space-time variational formulations . . . . .	7

\*Manuscript accepted for publication in the *Archives of Computational Methods in Engineering*.

<b>3</b>	<b>Error measures and error representation</b>	<b>11</b>
3.1	Errors and error equations . . . . .	11
3.2	Energy measures . . . . .	12
3.3	Quantities of interest and adjoint problem . . . . .	13
3.4	Error representation with adjoint problem . . . . .	17
<b>4</b>	<b>Recovery estimates</b>	<b>18</b>
4.1	Space-time error splitting . . . . .	19
4.2	Assessing time discretization errors . . . . .	20
4.3	Assessing space discretization errors . . . . .	20
<b>5</b>	<b>Dual weighted residual &amp; explicit residual estimates</b>	<b>24</b>
5.1	Dual weighted residual method . . . . .	24
5.2	An $L^2$ -norm explicit estimate . . . . .	28
<b>6</b>	<b>Constitutive relation error and implicit estimates</b>	<b>31</b>
6.1	Computable upper bounds for the dissipation norm . . . . .	32
6.2	Error bounds in the quantity of interest . . . . .	33
6.2.1	Error bounds based on the Cauchy-Schwarz inequality . . . . .	34
6.2.2	Bounds using symmetric error equations . . . . .	35
6.2.3	Equivalent alternative approach . . . . .	36
6.3	Construction of D-admissible fields . . . . .	38
6.3.1	The hybrid fluxes method . . . . .	39
6.3.2	The flux-free method . . . . .	44
<b>7</b>	<b>Error assessment for timeline-dependent quantities of interest</b>	<b>45</b>
7.1	Timeline-dependent quantities of interest . . . . .	45
7.2	Error representation with family of adjoint problems . . . . .	46
7.3	Modal-based adjoint approximation . . . . .	48
<b>8</b>	<b>Closure</b>	<b>51</b>

## 1 Introduction

Discretization errors are intrinsic to any Finite Element (FE) solution. Consequently, the tools assessing and controlling the error or, conversely, the accuracy of the numerical approximation have deserved the attention of the FE community. These tools are especially

important if sensitive decisions are taken on the basis of the numerical results. Many *a posteriori* error estimators have been developed with application to different problem types. The application of these techniques to second-order hyperbolic problems (e.g. structural dynamics or elastodynamics) is particularly relevant because, as compared to the standard elliptic problems, the discretization errors are generated and propagated less intuitively or predictively.

The pioneering works on FE error assessment date back to the late 70's and provide estimates of the energy norm of the error in steady-state (elliptic) problems (e.g. linear elasticity or thermal problems), see [1, 2, 3]. Goal-oriented estimates aim at assessing the error of functional outputs of the solution, that is at measuring the error in some *Quantity of Interest* (QoI). They were introduced much later [4, 5, 6, 7]. In the context of elliptic problems, error estimates are currently pretty well established, both for energy (also denoted as global) and goal-oriented (often referred as local, because the QoI are localized in a particular zone), see [8, 9, 10, 11, 12, 13, 14] as state-of-the-art reviews and books.

The techniques developed for elliptic problems have been extended to other problem types. For instance, quasi-steady-state non-linear problems are addressed in references [15, 16, 17, 18], estimates for advection-diffusion-reaction equation are discussed in [19], similar approaches for the Stokes problem are presented in [20], and extension to parabolic time-dependent problems is introduced in [21, 22, 23]. Moreover, the same type of tools for coupled problems have been recently discussed in [24, 25, 26, 27, 28].

In the present paper, attention is devoted to the techniques allowing to assess the error in structural transient dynamics. In this context, different estimates provide also indicators driving mesh adaptive procedures, either using energy-like measures [29, 30, 31, 32, 33, 34] or QoI [35, 36, 37, 38]. Estimates providing error bounds are also available both for energy-like error measures [39, 40, 41] and goal-oriented ones [42, 43, 44, 45, 46, 47, 31].

The strategies assessing the error in structural transient dynamics are based on extending the standard estimates designed for steady state linear elasticity. This is still an open problem. The difficulties arise when freezing the time dependence into a series of static problems, in particular in the treatment of the inertia terms.

This review paper aims at presenting the state-of-the-art techniques on a posteriori error assessment for second order hyperbolic problems. Four types of error estimates are analyzed, offering an comprehensive overview: 1) recovery-based estimates, 2) dual weighted residual method, 3) constitutive relation error and 4) error assessment for timeline-dependent quantities of interest. The main rationale of each technique is presented following the most representative references. Note that the methodologies presented here are introduced using diverse notations by different authors. Here, the different estimates are described within a unified framework for the sake of an easier reading.

The remainder of the text is organized as follows. Section 2 presents the equations of structural dynamics (both strong and weak versions) and their corresponding approximations. Section 3 introduces the error to be assessed, the error equations and the error representations needed for successive sections. Section 4 is devoted to the recovery-based estimates while section 5 deals with the dual weighted residual method and other ex-

PLICIT residual estimates. Section 6 presents the constitutive relation error method and the corresponding error bounds. Finally, section 7 presents an error estimate for special quantities of interest called timeline-dependent quantities of interest. The article is closed with some concluding remarks.

## 2 Problem statement

### 2.1 Strong equations

A visco-elastic body occupies an open bounded domain  $\Omega \subset \mathbb{R}^d$ ,  $d \leq 3$ , with boundary  $\partial\Omega$ . The boundary is divided in two disjoint parts,  $\Gamma_N$  and  $\Gamma_D$  such that  $\partial\Omega = \bar{\Gamma}_N \cup \bar{\Gamma}_D$  and the considered time interval is  $I := (0, T]$ . Under the assumption of small perturbations, the evolution of displacements  $\mathbf{u}(\mathbf{x}, t)$  and stresses  $\boldsymbol{\sigma}(\mathbf{x}, t)$ ,  $\mathbf{x} \in \Omega$  and  $t \in I$ , is described by the visco-elastodynamic equations,

$$\rho(\ddot{\mathbf{u}} + a_1 \dot{\mathbf{u}}) - \nabla \cdot \boldsymbol{\sigma} = \mathbf{f} \quad \text{in } \Omega \times I, \quad (1a)$$

$$\mathbf{u} = \mathbf{0} \quad \text{on } \Gamma_D \times I, \quad (1b)$$

$$\boldsymbol{\sigma} \cdot \mathbf{n} = \mathbf{g} \quad \text{on } \Gamma_N \times I, \quad (1c)$$

$$\mathbf{u} = \mathbf{u}_0 \quad \text{at } \Omega \times \{0\}, \quad (1d)$$

$$\dot{\mathbf{u}} = \mathbf{v}_0 \quad \text{at } \Omega \times \{0\}, \quad (1e)$$

where an upper dot indicates derivation with respect to time, that is  $(\dot{\bullet}) := \frac{d}{dt}(\bullet)$ , and  $\mathbf{n}$  denotes the outward unit normal to  $\partial\Omega$ . The input data includes the mass density  $\rho = \rho(\mathbf{x}) > 0$ , the first Rayleigh coefficient  $a_1 \geq 0$ , the body force  $\mathbf{f} = \mathbf{f}(\mathbf{x}, t)$  and the traction  $\mathbf{g} = \mathbf{g}(\mathbf{x}, t)$  acting on the Neumann boundary  $\Gamma_N \times I$ . The initial conditions for displacements and velocities are  $\mathbf{u}_0 = \mathbf{u}_0(\mathbf{x})$  and  $\mathbf{v}_0 = \mathbf{v}_0(\mathbf{x})$  respectively. For the sake of simplicity and without any loss of generality, Dirichlet conditions (1b) are taken as homogeneous.

The set of equations (1) is closed with the constitutive law,

$$\boldsymbol{\sigma} := \mathbf{C} : \boldsymbol{\varepsilon}(\mathbf{u} + a_2 \dot{\mathbf{u}}), \quad (2)$$

where the parameter  $a_2 \geq 0$  is the second Rayleigh coefficient, the tensor  $\mathbf{C}$  is the standard 4th-order elastic Hooke tensor. The strains are given by the kinematic relation corresponding to small perturbations, that is  $\boldsymbol{\varepsilon}(\mathbf{w}) := \frac{1}{2}(\nabla \mathbf{w} + \nabla^T \mathbf{w})$ .

### 2.2 Weak and discrete formulations

#### 2.2.1 Newmark-like methods

The definition of the weak form of the problem requires introducing the following functional spaces: the standard Sobolev space associated with static displacement fields

$$\mathcal{V}_0 := \{ \mathbf{w} \in [H^1(\Omega)]^d : \mathbf{w} = \mathbf{0} \text{ on } \Gamma_D \},$$

equipped with the usual functional norm which is denoted by  $\|\cdot\|_{\mathbf{V}_0}$ . The Bochner space  $L^2(I; \mathbf{V}_0)$  associated with  $\mathbf{V}_0$  of square-integrable functions from  $I$  into  $\mathbf{V}_0$  is also introduced

$$L^2(I; \mathbf{V}_0) := \left\{ \mathbf{v} : I \rightarrow \mathbf{V}_0, \text{ such that } \int_0^T \|\mathbf{v}(t)\|_{\mathbf{V}_0}^2 dt < +\infty \right\}.$$

The solution of the problem,  $\mathbf{u}(\mathbf{x}, t)$ , belongs to the space  $\mathcal{W}$  defined as

$$\mathcal{W} := \left\{ \mathbf{w} \in L^2(I; \mathbf{V}_0) \text{ with } \dot{\mathbf{w}} \in L^2(I; [L^2(\Omega)]^d) \text{ and } \ddot{\mathbf{w}} \in L^2(I; \mathbf{V}'_0) \right\},$$

where  $\mathbf{V}'_0$  denotes the dual space of  $\mathbf{V}_0$ . Note that in particular this implies that any  $\mathbf{w} \in \mathcal{W}$  is such that  $\mathbf{w} \in C^0(\bar{I}; [L^2(\Omega)]^d)$  and  $\dot{\mathbf{w}} \in C^0(\bar{I}; \mathbf{V}'_0)$ , see [48]. That is, functions in  $\mathcal{W}$  and their time derivatives are continuous in time.

**Remark 1.** *Function  $\mathbf{u}$  is a transformation between  $\Omega \times I$  and  $\mathbb{R}^d$ , i.e.*

$$\begin{aligned} \mathbf{u} : \Omega \times I &\longrightarrow \mathbb{R}^d \\ (\mathbf{x}, t) &\longmapsto \mathbf{u}(\mathbf{x}, t). \end{aligned}$$

*It can also be seen as a transformation between  $I$  and  $\mathbf{V}_0$ , i.e.*

$$\begin{aligned} \mathbf{u} : I &\longrightarrow \mathbf{V}_0 \\ t &\longmapsto \mathbf{u}(t). \end{aligned}$$

*In the remainder of the paper, both notations are used, for  $\mathbf{u}$  and other functions, to denote the same mathematical objects depending on the context.*

Thus, the weak form (integrated in space) of problem (1) reads: find  $\mathbf{u} \in \mathcal{W}$  verifying the initial conditions  $\mathbf{u}(0) = \mathbf{u}_0$  and  $\dot{\mathbf{u}}(0) = \mathbf{v}_0$  and such that for all  $t \in I$

$$m(\ddot{\mathbf{u}}(t) + a_1 \dot{\mathbf{u}}(t), \mathbf{w}) + a(\mathbf{u}(t) + a_2 \dot{\mathbf{u}}(t), \mathbf{w}) = l(t; \mathbf{w}) \quad \forall \mathbf{w} \in \mathbf{V}_0, \quad (3)$$

where the standard linear and bilinear forms are introduced

$$\begin{aligned} a(\mathbf{v}, \mathbf{w}) &:= \int_{\Omega} \boldsymbol{\varepsilon}(\mathbf{v}) : \boldsymbol{\mathcal{C}} : \boldsymbol{\varepsilon}(\mathbf{w}) \, d\Omega \quad , \quad m(\mathbf{v}, \mathbf{w}) := \int_{\Omega} \rho \mathbf{v} \cdot \mathbf{w} \, d\Omega, \\ l(t; \mathbf{w}) &:= (\mathbf{f}(t), \mathbf{w}) + (\mathbf{g}(t), \mathbf{w})_{\Gamma_N}, \end{aligned}$$

along with the scalar products

$$(\mathbf{v}, \mathbf{w}) := \int_{\Omega} \mathbf{v} \cdot \mathbf{w} \, d\Omega \quad \text{and} \quad (\mathbf{v}, \mathbf{w})_{\Gamma_N} := \int_{\Gamma_N} \mathbf{v} \cdot \mathbf{w} \, d\Gamma.$$

A mesh of characteristic element size  $H$  discretizing the spatial domain  $\Omega$  is introduced together with its associated finite element space  $\mathbf{V}_0^H \subset \mathbf{V}_0$ . The degree of the complete polynomial basis in  $\mathbf{V}_0^H$  is denoted by  $p$ . This allows introducing the spatially-discrete and time-continuous version of equation (3) (semidiscrete problem), namely: find  $\mathbf{u}^H(t) \in \mathbf{V}_0^H$  such that for all  $t \in I$

$$m(\ddot{\mathbf{u}}^H(t) + a_1 \dot{\mathbf{u}}^H(t), \mathbf{w}) + a(\mathbf{u}^H(t) + a_2 \dot{\mathbf{u}}^H(t), \mathbf{w}) = l(t; \mathbf{w}) \quad \forall \mathbf{w} \in \mathbf{V}_0^H, \quad (4)$$

with initial conditions (1d) and (1e). In the case  $\mathbf{u}_0$  and  $\mathbf{v}_0$  are not in  $\mathcal{V}_0^H$ , (1d) and (1e) have to be replaced by  $\mathbf{u}^H(0) = \mathbf{\Pi}^H(\mathbf{u}_0)$  and  $\dot{\mathbf{u}}^H(0) = \mathbf{\Pi}^H(\mathbf{v}_0)$ , being  $\mathbf{\Pi}^H$  the interpolation operator mapping functions from the continuous space  $\mathcal{V}_0$  into the discrete space  $\mathcal{V}_0^H$ .

The Newmark method is a numerical time-marching scheme providing an approximation of the standard system of second order ODEs (4) arising in structural dynamics. A time-grid discretizing the time interval  $I$  is introduced,  $\mathcal{T} := \{t_0, t_1, \dots, t_N\}$ , where  $0 = t_0 < t_1 < \dots < t_N = T$ . The time points in  $\mathcal{T}$  define the time intervals  $I_n := (t_{n-1}, t_n]$ ,  $n = 1, \dots, N$ . The length of the time interval  $I_n$  is denoted by  $\Delta t_n := t_n - t_{n-1}$ , for  $n = 1, \dots, N$  and the characteristic time step for the time grid is

$$\Delta t := \max_{1 \leq n \leq N} (\Delta t_n).$$

The Newmark solution consists in displacements, velocities and accelerations at each time  $t_n$ ,  $\mathbf{u}_n^{H,\Delta t} \approx \mathbf{u}^H(t_n)$ ,  $\mathbf{v}_n^{H,\Delta t} \approx \dot{\mathbf{u}}^H(t_n)$  and  $\mathbf{a}_n^{H,\Delta t} \approx \ddot{\mathbf{u}}^H(t_n)$ , respectively, for  $n = 1, \dots, N$ , such that equation (4) is fulfilled at each time  $t_n \in \mathcal{T}$ , that is

$$m(\mathbf{a}_n^{H,\Delta t} + a_1 \mathbf{v}_n^{H,\Delta t}, \mathbf{w}) + a(\mathbf{u}_n^{H,\Delta t} + a_2 \mathbf{v}_n^{H,\Delta t}, \mathbf{w}) = l_n(\mathbf{w}) \quad \forall \mathbf{w} \in \mathcal{V}_0^H. \quad (5)$$

where  $l_n(\mathbf{w}) := l(t_n; \mathbf{w})$ .

At each time interval, it is assumed that  $\mathbf{u}_{n-1}^{H,\Delta t}, \mathbf{v}_{n-1}^{H,\Delta t}, \mathbf{a}_{n-1}^{H,\Delta t}$  are known and that the following discrete integral expressions hold

$$\begin{aligned} \mathbf{u}_n^{H,\Delta t} &= \mathbf{u}_{n-1}^{H,\Delta t} + \Delta t_n \mathbf{v}_{n-1}^{H,\Delta t} + \frac{1}{2} \Delta t_n^2 \left[ (1 - 2\beta) \mathbf{a}_{n-1}^{H,\Delta t} + 2\beta \mathbf{a}_n^{H,\Delta t} \right], \\ \mathbf{v}_n^{H,\Delta t} &= \mathbf{v}_{n-1}^{H,\Delta t} + \Delta t_n \left[ (1 - \gamma) \mathbf{a}_{n-1}^{H,\Delta t} + \gamma \mathbf{a}_n^{H,\Delta t} \right]. \end{aligned}$$

Thus, the only remaining unknown in equation (5) is  $\mathbf{a}_n^{H,\Delta t}$ , which is obtained solving a linear system of algebraic equations. Similarly, at time  $t_0$ , the displacements and velocities are determined by the initial conditions and the acceleration  $\mathbf{a}_0^{H,\Delta t}$  is computed by considering that

$$m(\mathbf{a}_0^{H,\Delta t} + a_1 \mathbf{\Pi}^H(\mathbf{v}_0), \mathbf{w}) + a(\mathbf{\Pi}^H(\mathbf{u}_0) + a_2 \mathbf{\Pi}^H(\mathbf{v}_0), \mathbf{w}) = l_0(\mathbf{w}) \quad \forall \mathbf{w} \in \mathcal{V}_0^H.$$

The scalars  $\beta$  and  $\gamma$  are the parameters of the Newmark method taking values in  $[0, 1]$ . For  $\gamma = 1/2$  the method is second order accurate and there is no numerical damping, whereas for  $\gamma > 1/2$  numerical damping is introduced. Moreover, the method is conditionally stable for  $\beta \geq \gamma/2 \geq 1/4$ . See [49] for specific details.

In the framework of using finite difference based time marching schemes, it is quite common that error estimation strategies require obtaining a numerical approximation of problem (1) more regular than the direct numerical solution, with stronger continuity requirements. This post-processed version of the numerical solution is denoted hereafter as  $\tilde{\mathbf{u}}$ , see for instance section 6. Note that the Newmark method does not directly provide a numerical approximation  $\tilde{\mathbf{u}} \in \mathcal{W}$ , since it is not even defined in the whole time interval  $I$  (it is only given at times  $t_n$  of the time grid).

The first step in order to recover an smooth numerical approximation is to extend the Newmark approximation into the whole time domain using a simple piecewise linear interpolation:

$$\mathbf{u}^{H,\Delta t}(\mathbf{x}, t) := \sum_{n=0}^N \mathbf{u}_n^{H,\Delta t}(\mathbf{x}) \theta_n(t), \quad (6a)$$

$$\mathbf{v}^{H,\Delta t}(\mathbf{x}, t) := \sum_{n=0}^N \mathbf{v}_n^{H,\Delta t}(\mathbf{x}) \theta_n(t), \quad (6b)$$

$$\mathbf{a}^{H,\Delta t}(\mathbf{x}, t) := \sum_{n=0}^N \mathbf{a}_n^{H,\Delta t}(\mathbf{x}) \theta_n(t), \quad (6c)$$

where the functions  $\theta_n(t)$ , for  $n = 0, \dots, N$ , are the one-dimensional piecewise linear shape functions related with the time partition  $\mathcal{T}$ . Note that, however, one cannot take  $\tilde{\mathbf{u}} = \mathbf{u}^{H,\Delta t}(\mathbf{x}, t)$  since this approximation does not meet the regularity requirements of the functional space  $\mathcal{W}$ ,  $\mathbf{u}^{H,\Delta t}(\mathbf{x}, t) \notin \mathcal{W}$ , because its time derivative is not continuous. Following [9], an admissible approximation  $\tilde{\mathbf{u}} \in \mathcal{W}$  is easily recovered from the Newmark solution using the information provided by the numerical accelerations, namely

$$\dot{\tilde{\mathbf{u}}}(\mathbf{x}, t) := \int_0^t \mathbf{a}^{H,\Delta t}(\mathbf{x}, \tau) d\tau + \mathbf{v}_0(\mathbf{x}), \quad (7a)$$

$$\tilde{\mathbf{u}}(\mathbf{x}, t) := \int_0^t \dot{\tilde{\mathbf{u}}}(\mathbf{x}, \tau) d\tau + \mathbf{u}_0(\mathbf{x}). \quad (7b)$$

Note that the recovered function  $\tilde{\mathbf{u}}$  belongs to the following discrete space

$$\mathcal{W}^{H,\Delta t} := \{ \mathbf{w} \in C^1(\bar{I}; \mathcal{V}_0^H) \text{ with } \mathbf{w}|_{I_n} \in \mathbb{P}^q(I_n; \mathcal{V}_0^H), n = 1, \dots, N \},$$

where  $\mathbb{P}^q(\cdot)$  represent the space of polynomials of order  $q$  in time (where for the particular expression (7b), the polynomial order is  $q = 3$ ). Note that by construction the approximation  $\tilde{\mathbf{u}}$  exactly verifies the initial conditions and that the admissible acceleration coincides with the Newmark solution,  $\ddot{\tilde{\mathbf{u}}} = \mathbf{a}^{H,\Delta t}$ . Note that the displacements  $\mathbf{u}^{H,\Delta t}$  and  $\tilde{\mathbf{u}}$  do not coincide but they converge to the same function as  $\Delta t$  tends to zero.

### 2.2.2 Space-time variational formulations

The main objective of a posteriori error estimation techniques is to evaluate the error in some specific scalar measure (energy-type norms or quantities of interest). The error is related with the non-verification of the equation to be solved, that is with the residual. In order to properly define the residual associated with some numerical approximation, a space-time variational form of the problem is required. Note that the variational format is employed to derive the error estimate, not necessarily to solve the problem. For instance, the Newmark method is not using any time variational form. However, there are some a posteriori error estimation techniques using the full variational formulation both for the problem approximation and for the error assessment strategy, see [35, 50, 29, 30].

Among the possible space-time variational formulations available for transient elastodynamics, four options are considered in the remainder of the paper. They correspond to the choices made by the authors that designed the error estimation strategies presented here. The first option is a Single Field (SF) Galerkin method based on the approach introduced by Hughes and Hulbert [51, 52]. The other three options follow a Double Field (DF) formulation. The second option, based on [35], is a time-Continuous Galerkin approach using the *mass* product  $m(\cdot, \cdot)$  to enforce the displacement-velocity consistency, and it will be referred as CGM. The third option, denoted by CGA, very similar to the previous one, differs in the fact that displacement-velocity consistency is enforced using the bilinear form  $a(\cdot, \cdot)$ , see [50]. The fourth case is a double field discontinuous Galerkin method introduced by Johnson [53] and it is denoted by DG.

The SF approach uses the following weak form of problem (1) (the SF reference is omitted in the notation): find  $\mathbf{u} \in \mathcal{W}$  such that

$$B(\mathbf{u}, \mathbf{w}) = L(\mathbf{w}) \quad \forall \mathbf{w} \in \mathcal{W}, \quad (8)$$

where

$$B(\mathbf{v}, \mathbf{w}) := \int_I m(\ddot{\mathbf{v}} + a_1 \dot{\mathbf{v}}, \dot{\mathbf{w}}) dt + \int_I a(\mathbf{v} + a_2 \dot{\mathbf{v}}, \dot{\mathbf{w}}) dt + m(\dot{\mathbf{v}}(0^+), \dot{\mathbf{w}}(0^+)) + a(\mathbf{v}(0^+), \mathbf{w}(0^+)),$$

and

$$L(\mathbf{w}) := \int_I l(t; \dot{\mathbf{w}}(t)) dt + m(\mathbf{v}_0, \dot{\mathbf{w}}(0^+)) + a(\mathbf{u}_0, \mathbf{w}(0^+)).$$

The value  $B(\mathbf{u}, \mathbf{u})$  is the total energy associated with the displacement  $\mathbf{u}$ , which plays a role in obtaining error bounds, see section 6. This formulation is used to derive error estimation strategies but does not provide a practical methodology to compute the numerical approximation of the problem. This is because the weak equation (8) leads to a fully coupled space-time problem with a prohibitive computational cost.

An usual alternative in transient elastodynamics is using Double field (or mixed) formulations, which introduce the velocity  $\dot{\mathbf{u}}$  as new unknown. Thus, the unknown is the double field function  $\mathbf{U} := [\mathbf{u}_u, \mathbf{u}_v] := [\mathbf{u}, \dot{\mathbf{u}}]$ . The main advantage of mixed formulations is that they allow alleviating the continuity requirements on the solution. Instead of  $\mathbf{u} \in \mathcal{W}$ , the solution is  $\mathbf{U} \in \mathcal{W}_0 \times \mathcal{W}_0$  where

$$\mathcal{W}_0 := \{\mathbf{w} \in L^2(I; \mathcal{V}_0) \text{ with } \dot{\mathbf{w}} \in L^2(I; \mathcal{V}'_0)\}.$$

Note that, in particular, this implies that  $\mathbf{u}_u$  and  $\mathbf{u}_v \in C^0(\bar{I}; [L^2(\Omega)]^d)$  but their derivatives are not necessarily continuous.

The trial space for the double field time-continuous and time-discontinuous Galerkin formulations is defined as

$$\widehat{\mathcal{W}} := \{\mathbf{w} \in L^2(I; \mathcal{V}_0) \text{ with } \mathbf{w}|_{I_n} \in H^1(I_n; \mathcal{V}_0), n = 1, \dots, N\}.$$

Note that functions in  $\widehat{\mathcal{W}}$  may be time-discontinuous. This property is necessary to decouple the solution in successive time intervals  $I_n$ .

With these notations, the double field time continuous Galerkin weak form of problem (1) presented in [35] reads: find  $\mathbf{U} \in \mathcal{W}_0 \times \mathcal{W}_0$  such that for all

$$B_{\text{CGM}}(\mathbf{U}, \mathbf{W}) = L_{\text{CGM}}(\mathbf{W}) \quad \forall \mathbf{W} \in \widehat{\mathcal{W}} \times \widehat{\mathcal{W}}, \quad (9)$$

where  $B_{\text{CGM}}(\cdot, \cdot)$  and  $L_{\text{CGM}}(\cdot)$  are defined as

$$\begin{aligned} B_{\text{CGM}}(\mathbf{U}, \mathbf{W}) := & \int_I m(\dot{\mathbf{u}}_v + a_1 \mathbf{u}_v, \mathbf{w}_v) dt + \int_I a(\mathbf{u}_u + a_2 \mathbf{u}_v, \mathbf{w}_v) dt + m(\mathbf{u}_v(0^+), \mathbf{w}_v(0^+)) \\ & + \int_I m(\dot{\mathbf{u}}_u - \mathbf{u}_v, \mathbf{w}_u) dt + m(\mathbf{u}_u(0^+), \mathbf{w}_u(0^+)), \end{aligned} \quad (10a)$$

$$L_{\text{CGM}}(\mathbf{W}) := \int_I l(t; \mathbf{w}_v) dt + m(\mathbf{u}_0, \mathbf{w}_u(0^+)) + m(\mathbf{v}_0, \mathbf{w}_v(0^+)), \quad (10b)$$

and the general notation  $\mathbf{W} := [\mathbf{w}_u, \mathbf{w}_v]$  is used. Note that the constrain  $\dot{\mathbf{v}}_u = \mathbf{v}_v$  is weakly enforced using the mass product defined by  $m(\cdot, \cdot)$  and this is the reason of using  $\mathbf{M}$  in the notation for this approach.

A fully discrete solution is obtained replacing the infinite dimensional spaces involved in the weak form (9) by the discrete spaces

$$\mathcal{W}_0^{H, \Delta t} := \{\mathbf{v} \in C^0(\bar{I}; \mathcal{V}_0^H) \text{ with } \mathbf{v}|_{I_n} \in \mathbb{P}^q(I_n; \mathcal{V}_0^H), n = 1, \dots, N\}, \quad (11a)$$

$$\widehat{\mathcal{W}}^{H, \Delta t} := \{\mathbf{v} \in L^2(I; \mathcal{V}_0^H) \text{ with } \mathbf{v}|_{I_n} \in \mathbb{P}^{q-1}(I_n; \mathcal{V}_0^H), n = 1, \dots, N\}. \quad (11b)$$

Functions in  $\mathcal{W}_0^{H, \Delta t}$  are continuous, piecewise polynomial both in space and time, whereas functions in  $\widehat{\mathcal{W}}^{H, \Delta t}$  are also piecewise polynomials in space and time, continuous in space but not necessarily continuous in time. It is worth noting that the polynomials for the time discretization in  $\mathcal{W}_0^{H, \Delta t}$  are one degree higher than the ones in  $\widehat{\mathcal{W}}^{H, \Delta t}$ . However, properly accounting for the initial conditions, the dimensions of  $\mathcal{W}_0^{H, \Delta t}$  and  $\widehat{\mathcal{W}}^{H, \Delta t}$  coincide due to the continuity requirements of  $\mathcal{W}_0^{H, \Delta t}$ .

The fully discrete equation reads: find  $\tilde{\mathbf{U}} := [\tilde{\mathbf{u}}_u, \tilde{\mathbf{u}}_v] \in \mathcal{W}_0^{H, \Delta t} \times \mathcal{W}_0^{H, \Delta t}$  such that

$$B_{\text{CGM}}(\tilde{\mathbf{U}}, \mathbf{W}) = L_{\text{CGM}}(\mathbf{W}) \quad \forall \mathbf{W} \in \widehat{\mathcal{W}}^{H, \Delta t} \times \widehat{\mathcal{W}}^{H, \Delta t}. \quad (12)$$

As mentioned before, although problem (12) is integrated over the whole space-time domain  $\Omega \times I$ , the discontinuities of the test functions allow decoupling the problem into  $N$  problems posed over the time slabs  $\Omega \times I_n$ ,  $n = 1, \dots, N$ . To be more precise,  $\tilde{\mathbf{U}}$  is computed recursively starting from  $I_1$  and going forward in time (from  $n = 1$  to  $N$ ). In each time slab,  $\tilde{\mathbf{U}}|_{I_n} \in \mathbb{P}^q(I_n; \mathcal{V}_0^H) \times \mathbb{P}^q(I_n; \mathcal{V}_0^H)$  is the solution of (12) where the function  $\mathbf{W}$  is restricted to  $I_n$  (with a zero value outside the time slab). The unknown  $\tilde{\mathbf{U}}|_{I_n}$  accounts for the *initial* conditions given by the solution at the end point of the previous time-slab,  $\tilde{\mathbf{U}}|_{I_n}(t_n^+) = \tilde{\mathbf{U}}|_{I_{n-1}}(t_{n-1}^-) = [\tilde{\mathbf{u}}_u(t_{n-1}^-), \tilde{\mathbf{u}}_v(t_{n-1}^-)]$  (or  $[\mathbf{u}_0, \mathbf{v}_0]$  for the first slab). In general, this method requires solving for each time step  $2q$  coupled spatial problems in  $\mathcal{V}_0^H$ . Recall that the Newmark method requires a single problem in  $\mathcal{V}_0^H$  at each time step. However, for  $q = 1$  the block system of algebraic linear equations of

double size can be pre-processed to make it equivalent to the Newmark method with parameters  $\beta = 1/4$  and  $\gamma = 1/2$ , see [35] for a detailed proof.

Eriksson *et al.* [50] consider an alternative energy consistent weak form analogous to (9), where the velocity-displacement compatibility and initial conditions for the displacements are enforced using the energy product  $a(\cdot, \cdot)$ . The weak formulation reads: find  $\mathbf{U} \in \mathcal{W}_0 \times \mathcal{W}_0$  such that

$$B_{\text{CGA}}(\mathbf{U}, \mathbf{W}) = L_{\text{CGA}}(\mathbf{W}) \quad \forall \mathbf{W} \in \widehat{\mathcal{W}} \times \widehat{\mathcal{W}}. \quad (13)$$

where

$$\begin{aligned} B_{\text{CGA}}(\mathbf{U}, \mathbf{W}) &:= \int_I m(\dot{\mathbf{u}}_v + a_1 \mathbf{u}_v, \mathbf{w}_v) dt + \int_I a(\mathbf{u}_u + a_2 \mathbf{u}_v, \mathbf{w}_v) dt + m(\mathbf{u}_v(0^+), \mathbf{w}_v(0^+)) \\ &\quad + \int_I a(\dot{\mathbf{u}}_u - \mathbf{u}_v, \mathbf{w}_u) dt + a(\mathbf{u}_u(0^+), \mathbf{w}_u(0^+)), \\ L_{\text{CGA}}(\mathbf{W}) &:= \int_I l(t; \mathbf{w}_v) dt + a(\mathbf{u}_0, \mathbf{w}_u(0^+)) + m(\mathbf{v}_0, \mathbf{w}_v(0^+)). \end{aligned}$$

It is easily seen that the bilinear form  $B_{\text{CGA}}(\cdot, \cdot)$  is energy consistent, namely  $B_{\text{CGA}}(\mathbf{U}, \mathbf{U}) = B(\mathbf{u}, \mathbf{u})$ . Note that the previous CGM variational formulation does not fulfill this property, that is  $B_{\text{CGM}}(\mathbf{U}, \mathbf{U}) \neq B(\mathbf{u}, \mathbf{u})$ . This is due to the fact that for CGM both the initial conditions for the displacements  $\mathbf{u}_u(0^+) = \mathbf{u}_0$  and the compatibility condition between velocities and displacements  $\mathbf{u}_v = \dot{\mathbf{u}}_u$  are enforced in weak form using the mass product  $m(\cdot, \cdot)$ .

The discrete version of problem (13) reads: find  $\tilde{\mathbf{U}} \in \mathcal{W}_0^{H, \Delta t} \times \mathcal{W}_0^{H, \Delta t}$  such that

$$B_{\text{CGA}}(\tilde{\mathbf{U}}, \mathbf{W}) = L_{\text{CGA}}(\mathbf{W}) \quad \forall \mathbf{W} \in \widehat{\mathcal{W}}^{H, \Delta t} \times \widehat{\mathcal{W}}^{H, \Delta t}. \quad (14)$$

Finally, the double field discontinuous Galerkin method introduced by Johnson [53] is presented. This approach is a variant of the weak problem (13) in which both the trial and test functions are allowed to be discontinuous at time points in  $\mathcal{T}$ .

The continuity of the solution is weakly imposed by adding extra terms to the variational formulation, penalizing the time jumps of the solution at  $\mathcal{T}$ . The time discontinuous Galerkin weak form reads: find  $\mathbf{U} \in \widehat{\mathcal{W}} \times \widehat{\mathcal{W}}$  such that

$$B_{\text{DG}}(\mathbf{U}, \mathbf{W}) = L_{\text{CGA}}(\mathbf{W}) \quad \forall \mathbf{W} \in \widehat{\mathcal{W}} \times \widehat{\mathcal{W}}, \quad (15)$$

where

$$\begin{aligned} B_{\text{DG}}(\mathbf{U}, \mathbf{W}) &:= \sum_{n=1}^N \int_{I_n} (m(\dot{\mathbf{u}}_v + a_1 \mathbf{u}_v, \mathbf{w}_v) + a(\mathbf{u}_u + a_2 \mathbf{u}_v, \mathbf{w}_v)) dt + m(\mathbf{u}_v(0^+), \mathbf{w}_v(0^+)) \\ &\quad + \sum_{n=1}^N \int_{I_n} a(\dot{\mathbf{u}}_u - \mathbf{u}_v, \mathbf{w}_u) dt + a(\mathbf{u}_u(0^+), \mathbf{w}_u(0^+)) \\ &\quad + \sum_{n=1}^{N-1} m(\mathbf{u}_v(t_n^+) - \mathbf{u}_v(t_n^-), \mathbf{w}_v(t_n^+)) + \sum_{n=1}^{N-1} a(\mathbf{u}_v(t_n^+) - \mathbf{u}_u(t_n^-), \mathbf{w}_u(t_n^+)). \end{aligned}$$

Note that, in order to obtain an energy consistent bilinear form, the jumps of the velocities and displacements at time  $t_n$ ,  $\mathbf{u}_v(t_n^+) - \mathbf{u}_v(t_n^-)$  and  $\mathbf{u}_u(t_n^+) - \mathbf{u}_u(t_n^-)$  respectively, are introduced differently in the formulation. The mass bilinear form  $m(\cdot, \cdot)$  is used for velocities whereas the energy product  $a(\cdot, \cdot)$  is used for displacements, in such a way that  $B_{\text{DG}}(\mathbf{U}, \mathbf{U}) = B(\mathbf{u}, \mathbf{u})$ .

The discrete version of problem (15) is obtained replacing the space  $\widehat{\mathcal{W}}$  by the discrete space  $\widehat{\mathcal{W}}^{H,\Delta t}$  defined in equation (11b), namely: find  $\widehat{\mathbf{U}} := [\widehat{\mathbf{u}}_u, \widehat{\mathbf{u}}_v] \in \widehat{\mathcal{W}}^{H,\Delta t} \times \widehat{\mathcal{W}}^{H,\Delta t}$  such that

$$B_{\text{DG}}(\widehat{\mathbf{U}}, \mathbf{W}) = L_{\text{CGA}}(\mathbf{W}) \quad \forall \mathbf{W} \in \widehat{\mathcal{W}}^{H,\Delta t} \times \widehat{\mathcal{W}}^{H,\Delta t}. \quad (16)$$

The discrete problem (16) leads to  $N$  uncoupled local problems posed over the time slabs  $\Omega \times I_n$ ,  $n = 1, \dots, N$ . As in the previous double field formulations, the solution is computed recursively starting from  $I_1$  and going forward in time. This approach requires solving, in each time slab,  $2(q+1)$  coupled spatial problems in  $\mathcal{V}_0^H$ . Thus, for  $q = 1$  the dimension of the linear system to be solved in each time slab is four times larger than the system to be solved with the Newmark method. An efficient resolution strategy for this problem is presented in [29].

The error estimation techniques described in the forthcoming sections are presented using the previous variational formulations. Specifically, the recovery estimates described in section 4 consider the double field discontinuous Galerkin formulation (15), the explicit estimates and dual weighted residual technique described in section 5 are based on the double field time-continuous formulations (9) and (13) and finally, the implicit error estimates presented in section 6 require deriving error representations based on the standard single-field time-continuous Galerkin method (8).

### 3 Error measures and error representation

#### 3.1 Errors and error equations

The error associated with a single field numerical approximation  $\tilde{\mathbf{u}} \approx \mathbf{u}$ , for instance the one introduced in (7), is defined as

$$\mathbf{e} := \mathbf{u} - \tilde{\mathbf{u}} \in \mathcal{W}. \quad (17)$$

Function  $\mathbf{e}$  fulfills the following residual equation: find  $\mathbf{e} \in \mathcal{W}$

$$B(\mathbf{e}, \mathbf{w}) = L(\mathbf{w}) - B(\tilde{\mathbf{u}}, \mathbf{w}) =: R(\mathbf{w}). \quad (18)$$

Equation (18) is derived replacing the exact solution  $\mathbf{u}$  by  $\tilde{\mathbf{u}} + \mathbf{e}$  into (8) and using the linearity of forms  $B(\cdot, \cdot)$  and  $L(\cdot)$ . Note that, the residual  $R(\cdot)$  is well defined only if the numerical approximation  $\tilde{\mathbf{u}}$  is regular enough, that is  $\tilde{\mathbf{u}} \in \mathcal{W}$ . Thus, error techniques making use of the residual equation (18), in particular those presented in section 6, require that  $\tilde{\mathbf{u}} \in \mathcal{W}$ .

In the case of using a double field formulation as (12) or (14), the numerical solution has the form  $\tilde{\mathbf{U}} = [\tilde{\mathbf{u}}_u, \tilde{\mathbf{u}}_v] \in \mathcal{W}_0^{H,\Delta t} \times \mathcal{W}_0^{H,\Delta t}$  and the error is defined by

$$\mathbf{E} := [\mathbf{e}_u, \mathbf{e}_v] := [\mathbf{u} - \tilde{\mathbf{u}}_u, \dot{\mathbf{u}} - \tilde{\mathbf{u}}_v] \in \mathcal{W}_0 \times \mathcal{W}_0,$$

where  $\mathbf{e}_u$  and  $\mathbf{e}_v$  are the errors in displacements and velocities respectively. Here, two different residual equations for the double field error  $\mathbf{E}$  are derived replacing the exact solution  $\mathbf{U}$  by  $\tilde{\mathbf{U}} + \mathbf{E}$  either into equation (9) or (13). That is, the error  $\mathbf{E} \in \mathcal{W}_0 \times \mathcal{W}_0$  is the solution of both

$$B_{\text{CGM}}(\mathbf{E}, \mathbf{W}) = L_{\text{CGM}}(\mathbf{W}) - B_{\text{CGM}}(\tilde{\mathbf{U}}, \mathbf{W}) =: R_{\text{CGM}}(\mathbf{W}) \quad \forall \mathbf{W} \in \mathcal{W}_0 \times \mathcal{W}_0. \quad (19)$$

and

$$B_{\text{CGA}}(\mathbf{E}, \mathbf{W}) = L_{\text{CGA}}(\mathbf{W}) - B_{\text{CGA}}(\tilde{\mathbf{U}}, \mathbf{W}) =: R_{\text{CGA}}(\mathbf{W}) \quad \forall \mathbf{W} \in \mathcal{W}_0 \times \mathcal{W}_0. \quad (20)$$

Note that the previous two equations have the same solution, which is precisely  $\mathbf{E}$ . In practice, the criterion for selecting either equation (19) or (20) depends on whether the Galerkin orthogonality property holds or not. This is because in the error estimation procedures presented in section 5, Galerkin orthogonality is required to properly split the time and space error contributions.

Thus, if the numerical approximation  $\tilde{\mathbf{U}}$  is the solution of the discrete problem (12), the error estimation strategy utilizes equation (19) since, in this case, the following Galerkin orthogonality property holds,

$$R_{\text{CGM}}(\mathbf{W}) = 0 \quad \text{for all } \mathbf{W} \in \widehat{\mathcal{W}}^{H,\Delta t} \times \widehat{\mathcal{W}}^{H,\Delta t}. \quad (21)$$

Analogously, if the numerical approximation  $\tilde{\mathbf{U}}$  is solution of the discrete problem (14), then the error estimation strategy takes equation (20) because

$$R_{\text{CGA}}(\mathbf{W}) = 0 \quad \text{for all } \mathbf{W} \in \widehat{\mathcal{W}}^{H,\Delta t} \times \widehat{\mathcal{W}}^{H,\Delta t}.$$

If the numerical approximation is computed using other techniques, like the Newmark method, both residual equations could be used for error estimation, but the error estimation technique could not rely on Galerkin orthogonality.

The double field formulation (15) could also be used to derive a residual equation for the double field error  $\mathbf{E}$ . However, in the remainder of the paper this formulation is only used for recovery type estimates (which do not utilize a residual equation).

### 3.2 Energy measures

As previously mentioned, the bilinear form  $B(\cdot, \cdot)$  induces an energy measure in elastodynamics. For the sake of providing a physical interpretation, the energy norm  $B(\mathbf{u}, \mathbf{u})$  reads as follows:

$$B(\mathbf{u}, \mathbf{u}) = \|\mathbf{u}\|^2 + \frac{1}{2}\|\dot{\mathbf{u}}(T)\|_m^2 + \frac{1}{2}\|\mathbf{u}(T)\|_a^2 + \frac{1}{2}\|\mathbf{v}_0\|_m^2 + \frac{1}{2}\|\mathbf{u}_0\|_a^2, \quad (22)$$

where  $\|\mathbf{v}\|_m^2 := m(\mathbf{v}, \mathbf{v})$  and  $\|\mathbf{v}\|_a^2 := a(\mathbf{v}, \mathbf{v})$  are the squared norms induced by the bilinear forms  $m(\cdot, \cdot)$  and  $a(\cdot, \cdot)$ , respectively, and the space-time norm  $\|\cdot\|$  is defined as

$$\|\mathbf{v}\| := \left( \int_I a_1 \|\dot{\mathbf{v}}\|_m^2 dt + \int_I a_2 \|\dot{\mathbf{v}}\|_a^2 dt \right)^{1/2}. \quad (23)$$

The terms  $\frac{1}{2}\|\dot{\mathbf{u}}(T)\|_m^2$  and  $\frac{1}{2}\|\mathbf{u}(T)\|_a^2$  are the kinetic and elastic energy of  $\mathbf{u}$  at time  $t = T$ , while the term  $\|\mathbf{u}\|^2$  stands for the dissipated energy between times  $t = 0$  and  $t = T$  due to the presence of damping in the equations, introduced by  $a_1$  and  $a_2$ .

The different terms in (22) are used in the following to measure the error. For instance, the recovery estimates presented in section 4 make use of the squared norm  $\|\cdot\|_m^2 + \|\cdot\|_a^2$ . Note that this is the only relevant energy measure of the error in the case of elastodynamics (for  $a_1 = a_2 = 0$  the dissipated error is zero,  $\|\mathbf{e}\| = 0$ ). On the contrary, dissipation is crucial to derive error bounds, as it is shown in section 6. Actually, the techniques computing upper bounds yield estimates  $\eta_{\text{ener}}$  such that  $\|\mathbf{e}\| \leq \eta_{\text{ener}}$ .

However, there are norms different than those appearing in (22) which are also used in the literature. As an example, reference [54] measures the error with an  $L^2$  norm of the displacements at the final simulation time  $T$ .

### 3.3 Quantities of interest and adjoint problem

Information provided by global error estimates (based on global norms) is not sufficient to make engineering decisions. Alternatively, the end-user often prefers measuring the error using some specific Quantity of Interest (QoI), which are particular functional outputs of the solution.

The quantity of interest is defined by a functional  $L^\mathcal{O} : \mathcal{W} \rightarrow \mathbb{R}$  which extracts a single representative scalar value of the whole space-time solution. The value  $L^\mathcal{O}(\mathbf{u})$  is the quantity of interest, which is approximated by  $L^\mathcal{O}(\tilde{\mathbf{u}})$  given a numerical approximation of the solution  $\tilde{\mathbf{u}} \approx \mathbf{u}$ . Goal-oriented error estimation strategies aim at assessing the quality of  $L^\mathcal{O}(\tilde{\mathbf{u}})$ , that is, the difference between the exact quantity of interest  $L^\mathcal{O}(\mathbf{u})$  and the approximated one  $L^\mathcal{O}(\tilde{\mathbf{u}})$ ,  $L^\mathcal{O}(\mathbf{u}) - L^\mathcal{O}(\tilde{\mathbf{u}})$ . In the remainder of the paper it is assumed that the functional  $L^\mathcal{O}$  is linear. Thus,  $L^\mathcal{O}(\mathbf{u}) - L^\mathcal{O}(\tilde{\mathbf{u}})$  coincides with  $L^\mathcal{O}(\mathbf{e})$ . However, non-linear functionals can also be handled using the same strategies after a simple linearization, see [35, 47] for details.

The estimation of value  $L^\mathcal{O}(\mathbf{e})$  requires introducing an auxiliary problem associated with functional  $L^\mathcal{O}(\cdot)$ , usually denoted by *adjoint* or *dual* problem [31, 47, 42, 43, 44, 45, 46]. The variational form of the adjoint problem consists in finding  $\mathbf{u}^d \in \mathcal{W}$  such that

$$B(\mathbf{w}, \mathbf{u}^d) = L^\mathcal{O}(\mathbf{w}) \quad \forall \mathbf{w} \in \mathcal{W}. \quad (24)$$

The adjoint solution  $\mathbf{u}^d$  characterizes the quantity of interest defined by  $L^\mathcal{O}(\cdot)$ . Note that if  $\mathbf{u}^d$  is available, the computable quantity  $L(\mathbf{u}^d)$  is equal to the quantity of interest  $L^\mathcal{O}(\mathbf{u})$ . In that sense,  $\mathbf{u}^d$  can be seen as the Riesz representation of functional  $L^\mathcal{O}(\cdot)$ .

In practice,  $L^\mathcal{O}(\cdot)$  is selected with the same structure as the functional  $L(\cdot)$ , namely

$$L^\mathcal{O}(\mathbf{w}) := \int_0^T (\mathbf{f}^\mathcal{O}(t), \dot{\mathbf{w}}(t)) dt + \int_0^T (\mathbf{g}^\mathcal{O}(t), \dot{\mathbf{w}}(t))_{\Gamma_N} dt + m(\mathbf{v}^\mathcal{O}, \dot{\mathbf{w}}(T)) + a(\mathbf{u}^\mathcal{O}, \mathbf{w}(T)), \quad (25)$$

where  $\mathbf{f}^\mathcal{O}$ ,  $\mathbf{g}^\mathcal{O}$ ,  $\mathbf{v}^\mathcal{O}$  and  $\mathbf{u}^\mathcal{O}$  are the data characterizing the quantity of interest. The functions  $\mathbf{f}^\mathcal{O}$  and  $\mathbf{g}^\mathcal{O}$  extract global or localized averages of velocities in  $\Omega$  and  $\Gamma_N$ , respectively, over the whole time interval  $[0, T]$ . The fields  $\mathbf{v}^\mathcal{O}$  and  $\mathbf{u}^\mathcal{O}$  play the role of weighting functions to compute averages of velocities and strains at the final simulation time  $T$ .

In this case, the associated strong form of the adjoint problem is

$$\rho(\ddot{\mathbf{u}}^d - a_1 \dot{\mathbf{u}}^d) - \nabla \cdot \boldsymbol{\sigma}^d = -\mathbf{f}^\mathcal{O} \quad \text{in } \Omega \times I, \quad (26a)$$

$$\mathbf{u}^d = \mathbf{0} \quad \text{on } \Gamma_D \times I, \quad (26b)$$

$$\boldsymbol{\sigma}^d \cdot \mathbf{n} = -\mathbf{g}^\mathcal{O} \quad \text{on } \Gamma_N \times I, \quad (26c)$$

$$\mathbf{u}^d = \mathbf{u}^\mathcal{O} \quad \text{at } \Omega \times \{T\}, \quad (26d)$$

$$\dot{\mathbf{u}}^d = \mathbf{v}^\mathcal{O} \quad \text{at } \Omega \times \{T\}, \quad (26e)$$

with the constitutive law

$$\boldsymbol{\sigma}^d(\mathbf{u}^d) := \mathcal{C} : \boldsymbol{\varepsilon}(\mathbf{u}^d - a_2 \dot{\mathbf{u}}^d). \quad (27)$$

Note that the terms affected by  $a_1$  and  $a_2$  have opposite sign that the ones in the original problem (1). Consequently, the adjoint problem has exactly the same structure as the original (1) if integrated backwards in time starting from the *final conditions* (26d) and (26e).

Having selected the format of the quantity of interest given in (25) yields the adjoint problem (24) analogous to the original one (1). Thus, the same computer code available for solving the original problem (1) can be reused to solve the adjoint problem (26).

**Remark 2.** Note that the functional  $L^\mathcal{O}(\cdot)$  as defined in (25) does not directly allow to compute averages of the displacements of  $\mathbf{u}$  over the time interval  $I = (0, T]$ , namely

$$\int_I (\boldsymbol{\lambda}(t), \mathbf{u}(t)) dt. \quad (28)$$

However, it is easy to see that it is possible to express this quantity as

$$\int_I (\boldsymbol{\lambda}(t), \mathbf{u}(t)) dt = \int_0^T (\mathbf{f}^\mathcal{O}(t), \dot{\mathbf{u}}(t)) dt - (\mathbf{f}^\mathcal{O}(0), \mathbf{u}_0),$$

for

$$\mathbf{f}^\mathcal{O}(t) = \int_t^T \boldsymbol{\lambda}(\xi) d\xi. \quad (29)$$

Since the term  $(\mathbf{f}^\mathcal{O}(0), \mathbf{u}_0)$  is constant, assessing the error in the quantity of interest (28) is equivalent to assess  $L^\mathcal{O}(\mathbf{e})$  where the data characterizing  $L^\mathcal{O}(\cdot)$  are  $\mathbf{g}^\mathcal{O} = \mathbf{v}^\mathcal{O} = \mathbf{u}^\mathcal{O} = \mathbf{0}$  and  $\mathbf{f}^\mathcal{O}$  defined in equation (29).

Similarly, the average of displacements at the final time of the computation

$$(\boldsymbol{\lambda}^\circ, \mathbf{u}(T)) + (\boldsymbol{\lambda}_N^\circ, \mathbf{u}(T))_{\Gamma_N}, \quad (30)$$

where the data  $\boldsymbol{\lambda}^\circ$  and  $\boldsymbol{\lambda}_N^\circ$  are weighting functions allowing to localize the average of displacements in some sub-domains in  $\Omega$  and  $\Gamma_N$  respectively, is neither directly included in (25). In this case, an auxiliary problem is introduced: find  $\mathbf{u}^\circ \in \mathcal{V}_0$  solution of the static problem

$$a(\mathbf{u}^\circ, \mathbf{w}) = (\boldsymbol{\lambda}^\circ, \mathbf{w}) + (\boldsymbol{\lambda}_N^\circ, \mathbf{w})_{\Gamma_N} \quad \forall \mathbf{w} \in \mathcal{V}_0. \quad (31)$$

Note that here  $\mathbf{u}^\circ$  is not given as part of the data  $\boldsymbol{\lambda}^\circ$  and  $\boldsymbol{\lambda}_N^\circ$  characterizing (30). The function  $\mathbf{u}^\circ$  has to be computed as the solution of (31). Taking  $\mathbf{w} = \mathbf{e}(T)$  in (31) it is easily seen that assessing the error in the quantity of interest (30) is equivalent to assess  $L^\circ(\mathbf{e})$  where in this case the data characterizing  $L^\circ(\cdot)$  are  $\mathbf{f}^\circ = \mathbf{g}^\circ = \mathbf{v}^\circ = \mathbf{0}$  and  $\mathbf{u}^\circ$  defined in equation (31).

**Remark 3** (Illustrative example). *The following example illustrates the adjoint problem given in (26) for a one dimensional example. The spatial computational domain is  $\Omega = (0, 1)$  m, the boundaries are  $\Gamma_N = \{0 \text{ m}\}$  and  $\Gamma_D = \{1 \text{ m}\}$ , and the time interval is  $I = (0, 2]$  s. The material properties are  $E = 1$  Pa,  $\nu = 0$ ,  $\rho = 1$ , kg/m<sup>3</sup> and  $a_1 = a_2 = 0$  s. Two different adjoint problems are illustrated in this remark, associated with the quantities of interest*

$$L_1^\circ(w) = \int_I \int_\Omega \alpha(t)\beta(x)\dot{w}(x,t) \, dx \, dt \quad \text{and} \quad L_2^\circ(w) = \int_I \int_\Omega \alpha(t)\beta(x)w(x,t) \, dx \, dt,$$

where  $\alpha(t)$  and  $\beta(x)$  are the time dependent functions defined in figure 1. Note that

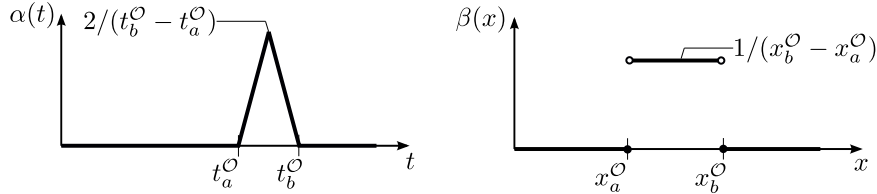


Figure 1: Definition of  $\alpha(t)$  and  $\beta(x)$ , (left) and (right) respectively.

$L_1^\circ(\cdot)$  corresponds to take  $\mathbf{g}^\circ = \mathbf{v}^\circ = \mathbf{u}^\circ = \mathbf{0}$  and  $\mathbf{f}^\circ = \alpha(t)\beta(x)$  in equation (25) and provides a weighted average of velocities in the space-time region  $S^\circ = (x_a^\circ, x_b^\circ) \times (t_a^\circ, t_b^\circ)$ . On the other hand,  $L_2^\circ(\cdot)$  corresponds to take  $\boldsymbol{\lambda} = \alpha(t)\beta(x)$  in (28) and provides a weighted average of displacement in  $S^\circ$ . In this example, the region  $S^\circ$  is characterized by  $x_a^\circ = 0.2$  m  $x_b^\circ = 0.3$  m,  $t_a^\circ = 1.8$  s and  $t_b^\circ = 1.9$  s.

The adjoint problems associated with quantities  $L_1^\circ$  and  $L_2^\circ$  are plotted in figure 2. Note that, the adjoint solutions are indeed the region of influence of each quantity of interest. That is, any perturbation taking place where the adjoint solution is zero has no influence in the quantity of interest. Note also that, the influence regions are different for quantities  $L_1^\circ$  and  $L_2^\circ$  even though they provide information of the solution  $\mathbf{u}$  in the same space-time region  $S^\circ$ .

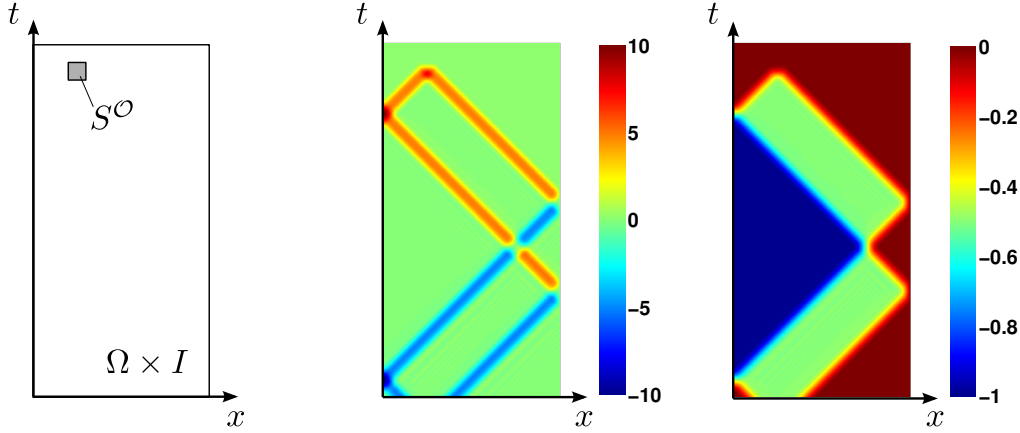


Figure 2: Illustration of the adjoint problem for two quantities of interest  $L_1^\mathcal{O}$  and  $L_2^\mathcal{O}$  (average of velocities and displacements in the region  $S^\mathcal{O}$ , respectively). Definition of the space-time domain  $\Omega \times I$  and region of interest  $S^\mathcal{O}$  (left). Adjoint velocities [m/s] for quantity  $L_1^\mathcal{O}$  (center). Adjoint velocities [m/s] for quantity  $L_2^\mathcal{O}$  (right).

The definition of the adjoint problem given in (24) depends on the weak form selected for the direct problem. Thus, the adjoint problems associated with the double field formulations CGM and CGA presented in (9) and (13) are introduced in the following. Note that the regularity restrictions for these problems are weaker than those of the previous adjoint problem. The adjoint problem associated with the formulation denoted as DG is not presented because, as previously said, this formulation is only used in the context of recovery type estimates for energy error measures.

The quantity of interest of a double field function  $\mathbf{W} = [\mathbf{w}_u, \mathbf{w}_v] \in \mathcal{W}_0 \times \mathcal{W}_0$  is defined as

$$L_D^\mathcal{O}(\mathbf{W}) := L_u^\mathcal{O}(\mathbf{w}_u) + L_v^\mathcal{O}(\mathbf{w}_v), \quad (32)$$

where  $L_v^\mathcal{O} : \mathcal{W}_0 \rightarrow \mathbb{R}$  and  $L_u^\mathcal{O} : \mathcal{W}_0 \rightarrow \mathbb{R}$  are linear functionals extracting quantities of interest from velocities and displacements respectively. The variational form of the adjoint problem associated with a double field quantity  $L_D^\mathcal{O}(\cdot)$  is introduced for both formulations CGM and CGA given in section 2.2.2. Specifically, if the variational formulation CGM presented in (9) is considered, then, the adjoint problem reads: find  $\mathbf{U}^d := [\mathbf{u}_u^d, \mathbf{u}_v^d] \in \mathcal{W}_0 \times \mathcal{W}_0$  such that

$$B_{\text{CGM}}(\mathbf{W}, \mathbf{U}^d) = L_D^\mathcal{O}(\mathbf{W}) \quad \forall \mathbf{W} \in \mathcal{W}_0 \times \mathcal{W}_0, \quad (33)$$

while considering the variational formulation CGA of (13) yields: find  $\mathbf{U}^d \in \mathcal{W}_0 \times \mathcal{W}_0$  such that

$$B_{\text{CGA}}(\mathbf{W}, \mathbf{U}^d) = L_D^\mathcal{O}(\mathbf{W}) \quad \forall \mathbf{W} \in \mathcal{W}_0 \times \mathcal{W}_0. \quad (34)$$

As discussed for the single field quantities of interest, in many practical applications it is important that the adjoint variational problem admits a strong form representation like the one given in (26). This introduces restrictions to the form of the linear functionals describing the quantities of interest as given in (32).

Equation (33) leads to the strong equations (26) for functionals  $L_u^\mathcal{O}(\cdot)$  and  $L_v^\mathcal{O}(\cdot)$  defined as

$$L_u^\mathcal{O}(\mathbf{w}_u) := m(\mathbf{u}^\mathcal{O}, \mathbf{w}_u(T)) \text{ and} \quad (35a)$$

$$L_v^\mathcal{O}(\mathbf{w}_v) := \int_0^T (\mathbf{f}^\mathcal{O}(t), \mathbf{w}_v(t)) \, dt + \int_0^T (\mathbf{g}^\mathcal{O}(t), \mathbf{w}_v(t))_{\Gamma_N} \, dt + m(\mathbf{v}^\mathcal{O}, \mathbf{w}_v(T)), \quad (35b)$$

while equation (33) leads to the strong problem (26) for

$$L_u^\mathcal{O}(\mathbf{w}_u) := a(\mathbf{u}^\mathcal{O}, \mathbf{w}_u(T)) \text{ and} \quad (36a)$$

$$L_v^\mathcal{O}(\mathbf{w}_v) := \int_0^T (\mathbf{f}^\mathcal{O}(t), \mathbf{w}_v(t)) \, dt + \int_0^T (\mathbf{g}^\mathcal{O}(t), \mathbf{w}_v(t))_{\Gamma_N} \, dt + m(\mathbf{v}^\mathcal{O}, \mathbf{w}_v(T)). \quad (36b)$$

It is worth noting that the quantity of interest associated to the energy consistent double field formulation CGA is the equivalent to the single field quantity of interest defined in (25). This is because the definition of  $L_D^\mathcal{O}$  in (36) is such that  $L_D^\mathcal{O}([\mathbf{w}, \dot{\mathbf{w}}]) = L^\mathcal{O}(\mathbf{w})$ .

### 3.4 Error representation with adjoint problem

The adjoint problem allows rewriting the error in the quantity of interest in terms of residuals, combining the original and adjoint problems. Thus, the error assessment for the quantity of interest is performed using standard error estimation techniques designed for global error measures. Different error representations for  $L^\mathcal{O}(\mathbf{e})$ , or similarly for  $L_D^\mathcal{O}(\mathbf{E})$  in the case of a double field formulation, are used for the error assessment strategies presented here.

Techniques aiming at furnishing bounds for the error in the quantity of interest, like the ones presented in section 6, consider an error representation based on the adjoint weak residual,  $R^d(\cdot)$ , associated with the numerical approximation of the adjoint problem  $\tilde{\mathbf{u}}^d \approx \mathbf{u}^d$ . This error representation reads

$$L^\mathcal{O}(\mathbf{e}) = R^d(\mathbf{e}) + B(\mathbf{e}, \tilde{\mathbf{u}}^d) = R^d(\mathbf{e}) + R(\tilde{\mathbf{u}}^d), \quad (37)$$

where

$$R^d(\mathbf{w}) := L^\mathcal{O}(\mathbf{w}) - B(\mathbf{w}, \tilde{\mathbf{u}}^d). \quad (38)$$

Equation (37) is derived taking  $\mathbf{w} = \mathbf{e}$  into (38) along with the definition of the primal residual. In equation (37), the error in the quantity of interest is expressed as the non-computable term  $R^d(\mathbf{e})$  plus the computable term  $R(\tilde{\mathbf{u}}^d)$ . Thus, bounds for  $L^\mathcal{O}(\mathbf{e})$  are obtained finding bounds for  $R^d(\mathbf{e})$ . Note that,  $R(\tilde{\mathbf{u}}^d)$  is a computable quantity, not necessarily equal to zero. Therefore, numerical approximations  $\tilde{\mathbf{u}}$  and  $\tilde{\mathbf{u}}^d$  are not assumed to fulfill any Galerkin orthogonality property. That allows using many different computational methodologies to obtain  $\tilde{\mathbf{u}}$  and  $\tilde{\mathbf{u}}^d$ . The only requirement is that the numerical solutions are regular enough, that is  $\tilde{\mathbf{u}}, \tilde{\mathbf{u}}^d \in \mathbf{W}$  and that the bounds for  $R^d(\mathbf{e})$  are available.

On the other hand, the error estimates presented in section 5 utilize a different error representation. In this case, the error in the quantity of interest is expressed using the

primal residual and the exact adjoint solution. The following development is analogous for the CGM and the CGA formulations. For the sake of simplicity, the presentation is done for CGM but equivalent expressions stand replacing CGM by CGA. One of the simpler versions of the error representation reads

$$L_D^{\mathcal{O}}(\mathbf{E}) = R_{\text{CGM}}(\mathbf{U}^d). \quad (39)$$

The previous equation is a direct consequence of the definition of both the residuals and the adjoint solution.

In the error estimation setup, replacing  $\mathbf{U}^d$  by an approximated value  $\tilde{\mathbf{U}}^d$ , the error representation (39) gives an accurate approximation of the error in the quantity of interest. However, the local error contributions provided by the local restrictions of this residual expression are often too pessimistic due to the cancellation effect of the contributions of opposite sign with large absolute values, see [55]. Thus, equation (39) is not used directly to compute error maps for space-time mesh adaptivity. The error representation (39) is modified adding and subtracting an arbitrary function  $\mathbf{W}^{H,\Delta t} \in \mathcal{W}_0^{H,\Delta t} \times \mathcal{W}_0^{H,\Delta t}$  in the argument of the residual,

$$L_D^{\mathcal{O}}(\mathbf{E}) = R_{\text{CGM}}(\mathbf{U}^d - \mathbf{W}^{H,\Delta t}) + R_{\text{CGM}}(\mathbf{W}^{H,\Delta t}). \quad (40)$$

Then, using Galerkin orthogonality of the residuals it follows

$$L_D^{\mathcal{O}}(\mathbf{E}) = R_{\text{CGM}}(\mathbf{U}^d - \mathbf{W}^{H,\Delta t}). \quad (41)$$

Globally, the error representation (41) is identical to (39). However, their local restrictions are different and, if  $\mathbf{W}^{H,\Delta t}$  is properly selected, (41) provides a map of local error contributions better suited for adaptive purposes. In practice, the function  $\mathbf{W}^{H,\Delta t}$  is taken as the projection onto the test space  $\mathcal{W}_0^{H,\Delta t} \times \mathcal{W}_0^{H,\Delta t}$  of the computed adjoint approximation  $\tilde{\mathbf{U}}^d$ , see section 5 for details.

Note that the estimated error distribution given by representation (41) is valid only if Galerkin orthogonality holds. In practice it means that, if equation (41) is used, then  $\tilde{\mathbf{U}}$  must be the solution of the discrete problem (12).

## 4 Recovery estimates

In the following, recovery type error estimates in the framework of elastodynamics, see [29, 30, 31], are applied to the DG formulations. That is, they assess the error with respect to the solution  $\hat{\mathbf{U}}$  of the discrete problem (16). Recovery type error estimates provide error indicators for the space and time components of the error, namely  $\eta_n^s$  and  $\eta_n^t$ , associated with a point  $t_n$  of the time discretization  $\mathcal{T}$ . These indicators are input data for an adaptive procedure, allowing to select the mesh size and time step and to design adapted discretizations.

## 4.1 Space-time error splitting

For a given time  $t_n \in \mathcal{T}$ , the error associated with the DG approximation  $\widehat{\mathbf{U}} = [\widehat{\mathbf{u}}_u, \widehat{\mathbf{u}}_v]$  is defined as

$$\mathbf{E}(t_n) := \mathbf{U}(t_n) - \widehat{\mathbf{U}}(t_n^-) = [\mathbf{u}(t_n) - \widehat{\mathbf{u}}_u(t_n^-), \dot{\mathbf{u}}(t_n) - \widehat{\mathbf{u}}_v(t_n^-)].$$

Note that the error  $\mathbf{E}(t_n)$  measures both the space and time discretization errors at time  $t_n$ . In order to separate the contribution of the space and time errors, the error  $\mathbf{E}(t_n)$  is decomposed into

$$\mathbf{E}(t_n) = \mathbf{E}^s(t_n) + \mathbf{E}^t(t_n),$$

where  $\mathbf{E}^s(t_n)$  and  $\mathbf{E}^t(t_n)$  are defined as

$$\mathbf{E}^s(t_n) := \mathbf{U}(t_n) - \mathbf{U}^H(t_n) \quad \text{and} \quad \mathbf{E}^t(t_n) := \mathbf{U}^H(t_n) - \widehat{\mathbf{U}}(t_n^-). \quad (42)$$

Note that  $\mathbf{E}^s(t_n)$  and  $\mathbf{E}^t(t_n)$  are defined introducing function  $\mathbf{U}^H = [\mathbf{u}^H, \dot{\mathbf{u}}^H]$ , being  $\mathbf{u}^H$  the exact (in time) solution of the semidiscrete problem (4), which is unknown. Function  $\mathbf{U}^H$  tends to the exact solution  $\mathbf{U}$  as  $H$  tends to zero. Consequently, also  $\mathbf{E}^s(t_n)$  tends to zero with  $H$  and therefore it is referred as the space discretization error. Similarly, the term  $\mathbf{E}^t(t_n)$  tends to zero as the time step, used in the discretization of equation (4), tends to zero. Thus,  $\mathbf{E}^t(t_n)$  is associated with the error produced by the time discretization.

In order to derive local error indicators, the space and time discretization errors are measured using the kinetic and elastic energy. Note that the error measure used here corresponds to the total energy if the viscosity vanishes ( $a_1 = a_2 = 0$ ):

$$\|\mathbf{E}^s(t_n)\|_{m+a}^2 := \|\mathbf{e}_v^s(t_n)\|_m^2 + \|\mathbf{e}_u^s(t_n)\|_a^2 \quad \text{and} \quad \|\mathbf{E}^t(t_n)\|_{m+a}^2 := \|\mathbf{e}_v^t(t_n)\|_m^2 + \|\mathbf{e}_u^t(t_n)\|_a^2.$$

The goal of recovery error estimates is to furnish error indicators  $\eta_n^s$  and  $\eta_n^t$  such that

$$\eta_n^s \approx \|\mathbf{E}^s(t_n)\|_{m+a}^2 \quad \text{and} \quad \eta_n^t \approx \|\mathbf{E}^t(t_n)\|_{m+a}^2.$$

The time error indicators  $\eta_n^t$ ,  $n = 1, \dots, N$  are directly used to define the desired size of the time step at each time  $t_n$ . On the other hand, the space error indicator  $\eta_n^s$  is decomposed into element contributions

$$\eta_n^s = \sum_{k=1}^{N_{\text{el}}} \eta_{n,k}^s, \quad (43)$$

where  $\eta_{n,k}^s$  is an estimate of the contribution of element  $\Omega_k$  to the norm  $\|\mathbf{E}^s(t_n)\|_{m+a}^2$ . The space error indicators  $\eta_{n,k}^s$  allow defining a desired element size in the zone of element  $\Omega_k$  at time  $t_n$ . Thus, combining the information provided by  $\eta_n^t$  and  $\eta_{n,k}^s$ , the adapted space and time discretizations are designed to meet the precision required.

The remainder of this section is devoted to the actual computation of the error indicators  $\eta_{k,n}^s$  and  $\eta_n^t$ .

## 4.2 Assessing time discretization errors

The local error indicators  $\eta_n^t \approx \|\mathbf{E}^t(t_n)\|_{m+a}^2$  are computed in references [29, 30] using the time-discontinuities of the DG approximation  $\widehat{\mathbf{U}}$ , namely

$$\eta_n^t := \|\widehat{\mathbf{U}}(t_n^+) - \widehat{\mathbf{U}}(t_n^-)\|_{m+a} = \|\hat{\mathbf{u}}_v(t_n^+) - \hat{\mathbf{u}}_v(t_n^-)\|_m^2 + \|\hat{\mathbf{u}}_u(t_n^+) - \hat{\mathbf{u}}_u(t_n^-)\|_a^2.$$

This definition is suggested by the super-convergent properties of the time-DG formulations, stating that the solution at  $t_n^-$  is much more accurate than the solution at  $t_n^+$ .

References [56, 57, 31] introduce alternative indicators  $\eta_n^t$  if the numerical approximation is a time-continuous function  $\widetilde{\mathbf{U}}$  instead of the DG approximation  $\widehat{\mathbf{U}}$ . In that case the indicators cannot be computed using the time jumps and, therefore, the following alternative definition is introduced

$$\eta_n^t := \|\mathbf{U}^*(t_n) - \widetilde{\mathbf{U}}(t_n)\|_{m+a}^2 = \|\mathbf{u}_v^*(t_n) - \tilde{\mathbf{u}}_v(t_n^-)\|_m^2 + \|\mathbf{u}_u^*(t_n) - \tilde{\mathbf{u}}_u(t_n^-)\|_a^2.$$

where  $\mathbf{U}^*(t_n)$  is an enhanced (in time) function computed using the numerical approximation  $\widetilde{\mathbf{U}}$  at previous time steps, see reference [31] for specific details. The post-processed solution  $\mathbf{U}^*(t_n)$  replaces the exact (in time) approximation  $\mathbf{U}^H(t_n)$  in order to obtain an error estimate.

## 4.3 Assessing space discretization errors

The natural post-process of the numerical solution for the recovery type error estimators, is performed for stress fields rather than for the displacements, see [3]. In this context, energy is measured in terms of stresses using the complementary energy norm  $\|\cdot\|_{\bar{a}}$  defined as

$$\|\boldsymbol{\sigma}\|_{\bar{a}}^2 := \bar{a}(\boldsymbol{\sigma}, \boldsymbol{\sigma}) \quad \text{where} \quad \bar{a}(\boldsymbol{\sigma}, \boldsymbol{\tau}) := \int_{\Omega} \boldsymbol{\sigma} : \mathbf{C}^{-1} : \boldsymbol{\tau} \, d\Omega.$$

Thus, value  $\|\mathbf{E}^s(t_n)\|_{m+a}^2$  is rewritten using  $\|\cdot\|_{\bar{a}}$  as

$$\|\mathbf{E}^s(t_n)\|_{m+a}^2 = \|\dot{\mathbf{u}}(t_n) - \dot{\mathbf{u}}^H(t_n)\|_m^2 + \|\boldsymbol{\sigma}(\mathbf{u}(t_n)) - \boldsymbol{\sigma}(\mathbf{u}^H(t_n))\|_{\bar{a}}^2. \quad (44)$$

In the framework of space error indicators, the semi-discrete (exact in time) functions  $\dot{\mathbf{u}}^H(t_n)$  and  $\boldsymbol{\sigma}(\mathbf{u}^H(t_n))$  are assumed to fairly approximate  $\hat{\mathbf{u}}_v(t_n)$  and  $\boldsymbol{\sigma}(\hat{\mathbf{u}}_u(t_n))$ . This is equivalent to assume that the time integration error of the numerical approximation  $\widehat{\mathbf{U}}(t_n) = [\hat{\mathbf{u}}_u(t_n), \hat{\mathbf{u}}_v(t_n)]$  is small. This requires reducing the time discretization error before assessing the space discretization error. Thus, the adaptive strategy aims at reaching the prescribed time accuracy at each time  $t_n$  before starting with the space adaptive procedure.

A computable value for  $\|\mathbf{E}^s(t_n)\|_{m+a}^2$  using equation (44) is obtained recovering approximations of the exact velocities  $\mathbf{v}_n^* \approx \dot{\mathbf{u}}(t_n)$  and stresses  $\boldsymbol{\sigma}_n^* \approx \boldsymbol{\sigma}(\mathbf{u}(t_n))$  with some post-process of  $\widehat{\mathbf{U}}(t_n)$ . Introducing these approximations, the space error contributions  $\eta_n^s \approx \|\mathbf{E}^s(t_n)\|_{m+a}^2$ ,  $n = 1, \dots, N$ , are computed as

$$\eta_n^s := \|\mathbf{v}_n^* - \hat{\mathbf{u}}_v(t_n^-)\|_m^2 + \|\boldsymbol{\sigma}_n^* - \boldsymbol{\sigma}(\hat{\mathbf{u}}_u(t_n^-))\|_{\bar{a}}^2. \quad (45)$$

The error indicator  $\eta_n^s$  corresponding to time  $t_n$  is decomposed into elementary contributions  $\eta_{n,k}^s$  associated with element  $\Omega_k$  of the mesh. The elementary contributions  $\eta_{n,k}^s$  are computed restricting the integrals in equation (45) to the elements  $\Omega_k$ . The numerical methodology providing  $\mathbf{v}_n^*$  and  $\boldsymbol{\sigma}_n^*$  is detailed below.

The post-processed stress  $\boldsymbol{\sigma}_n^*$  is usually computed using standard stress recovery techniques originally presented for static problems, see [3, 58, 59]. These techniques allow recovering an enhanced continuous stress field  $\boldsymbol{\sigma}_n^*$ , which is obtained projecting each component of the space-discontinuous stress field  $\boldsymbol{\sigma}(\hat{\mathbf{u}}_u(t_n^-))$  into the continuous finite element functional space used to approximate displacements and velocities, see figure 3. That is, the enhanced stress  $\boldsymbol{\sigma}_n^*$  is recovered in the space

$$\mathcal{S}^H := \{\boldsymbol{\tau} \in [C^0(\bar{\Omega})]^{d(d+1)/2} : \boldsymbol{\tau}|_{\Omega_k} \in [\mathbb{P}^p(\Omega_k)]^{d(d+1)/2}, k = 1, \dots, N_{\text{el}}\},$$

where  $\mathbb{P}^p(\Omega_k)$  is the space of polynomials of degree  $p$  on the element  $\Omega_k$ . In particular, the stress field  $\boldsymbol{\sigma}_n^* \in \mathcal{S}^H$  is sought as a linear combination of nodal shape functions, namely

$$\boldsymbol{\sigma}_n^* = \sum_{j=1}^{N_{\text{nod}}} \boldsymbol{\sigma}_n^*(\mathbf{x}_j) N_j(\mathbf{x}),$$

where  $N_j(\mathbf{x})$  is the finite element shape function of degree  $p$  associated to the node  $\mathbf{x}_j$ , being  $N_{\text{nod}}$  the total number of nodes. The output of the recovery procedure are the nodal values of the recovered stress field  $\boldsymbol{\sigma}_n^*(\mathbf{x}_j), j = 1, \dots, N_{\text{nod}}$ , describing the stress  $\boldsymbol{\sigma}_n^* \in \mathcal{S}^H$ .

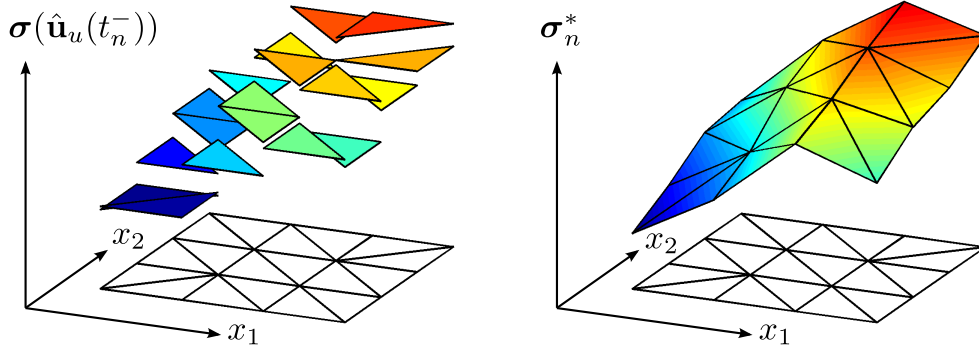


Figure 3: The the discontinuous stress field  $\boldsymbol{\sigma}(\hat{\mathbf{u}}_u(t_n^-))$  (left) is projected into the continuous space generated by the shape functions furnishing the stress field  $\boldsymbol{\sigma}_n^*$  (right) for all time steps  $n = 1, \dots, N$  (illustrated for  $p = 1$ ).

Several strategies are studied in the literature for the stress recovery. Two of the most common techniques are summarized hereafter. First, the pioneering reference by Zienkiewicz and Zhu [3] proposes to recover the stress field  $\boldsymbol{\sigma}_n^*$  using a global  $L^2$ -projection. Specifically, the recovered stress  $\boldsymbol{\sigma}_n^*$  is found solving the global discrete problem: find  $\boldsymbol{\sigma}_n^* \in \mathcal{S}^H$  such that

$$(\boldsymbol{\sigma}_n^*, \boldsymbol{\tau}) = (\boldsymbol{\sigma}(\hat{\mathbf{u}}_u(t_n^-)), \boldsymbol{\tau}) \quad \forall \boldsymbol{\tau} \in \mathcal{S}^H, \quad (46)$$

where  $(\cdot, \cdot)$  denotes the  $L^2$ -product in  $\mathcal{S}^H$ . Problem (46) is equivalent to a linear system of equations with a global mass matrix, for each component of the stress tensor, and at each time step  $t_n$ . If the space mesh changes, then the mass matrix has to be reassembled and *inverted* at each time step. Hence, this technique is not very well suited in dynamic problems. In that case, stress recovery techniques involving only local problems are preferred, as the well known SPR technique also introduced by Zienkiewicz and Zhu [58, 59].

The SPR technique allows recovering the nodal values of the recovered stress field  $\sigma_n^*(\mathbf{x}_j)$  solving local small problems associated to the mesh nodes (nodal patches). The values  $\sigma_n^*(\mathbf{x}_j)$  are found using the information provided by the set of Gauss points  $\mathcal{X}^{\omega_j}$  inside the patch  $\omega_j := \text{supp}(N_j) \subset \Omega$  surrounding the  $j$ -th node, see figure 4. A local stress field

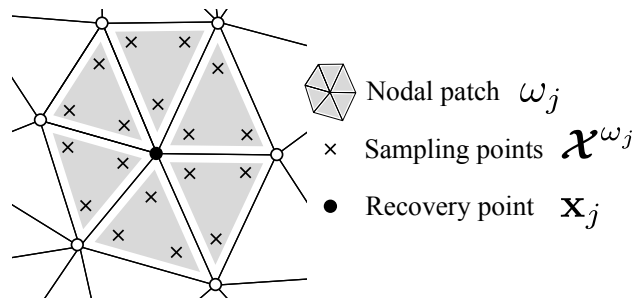


Figure 4: Definition of nodal patches and sampling points for stress recovery.

of polynomial degree  $\tilde{p}$ ,  $\sigma_n^{\omega_j} \in [\mathbb{P}^{\tilde{p}}(\omega_j)]^{d(d+1)/2}$ , is defined on the patch  $\omega_j$ . The recovered stresses  $\sigma_n^{\omega_j}$  are computed as the least squares fitting of the values of the stress  $\sigma(\hat{\mathbf{u}}_u(t_n^-))$  at the sampling points  $\mathcal{X}^{\omega_j}$ . Specifically, the stress  $\sigma_n^{\omega_j}$  is defined as

$$\sigma_n^{\omega_j} := \arg \min_{\mathbf{w} \in [\mathbb{P}^{\tilde{p}}(\omega_j)]^{d(d+1)/2}} \sum_{\mathbf{x} \in \mathcal{X}^{\omega_j}} (\mathbf{w}(\mathbf{x}) - \sigma(\hat{\mathbf{u}}_u(t_n^-))(\mathbf{x}))^2. \quad (47)$$

The recovered value  $\sigma_n^*(\mathbf{x}_j)$  is then taken to be the value of the local stress field  $\sigma_n^{\omega_j}$  at point  $\mathbf{x}_j$ , that is  $\sigma_n^*(\mathbf{x}_j) := \sigma_n^{\omega_j}(\mathbf{x}_j)$ . In practice, for linear elements,  $\tilde{p}$  is taken equal to 2. In any case,  $\tilde{p}$  must be such that the dimension of  $\mathbb{P}^{\tilde{p}}(\omega_j)$  is lower than the cardinal of  $\mathcal{X}^{\omega_j}$  to guarantee that the least squares projection is well posed.

On the other hand, the technique furnishing the enhanced velocities  $\mathbf{v}_n^*$  consists, basically, in increasing the interpolation degree of the computed velocity  $\hat{\mathbf{u}}_v(t_n^-)$ , see figure 5. This type of post-process is used in other contexts, for instance, in assessing the error  $L^2$ -norm in static problems [60, 61] or, in building enhanced vibration modes and eigenfrequencies [62]. In the following, the post-process strategy introduced in [62] is presented.

Let  $\Omega_k^{\text{patch}}$  denote the patch of elements around  $\Omega_k$ , consisting of all the elements sharing at least one node with  $\Omega_k$ , and let  $\mathcal{X}_k$  and  $\mathcal{X}_k^{\text{patch}}$  denote the set of nodes of element  $\Omega_k$  and patch  $\Omega_k^{\text{patch}}$  respectively, see figure 6.

The post-processed velocity field  $\mathbf{v}_n^*$  is found using the information provided by the restriction of  $\hat{\mathbf{u}}_v(t_n^-)$  to  $\Omega_k^{\text{patch}}$ . Specifically, a velocity field  $\mathbf{v}_n^{\mathcal{X}_k} \in [\mathbb{P}^{p+1}(\Omega_k^{\text{patch}})]^d$  is found

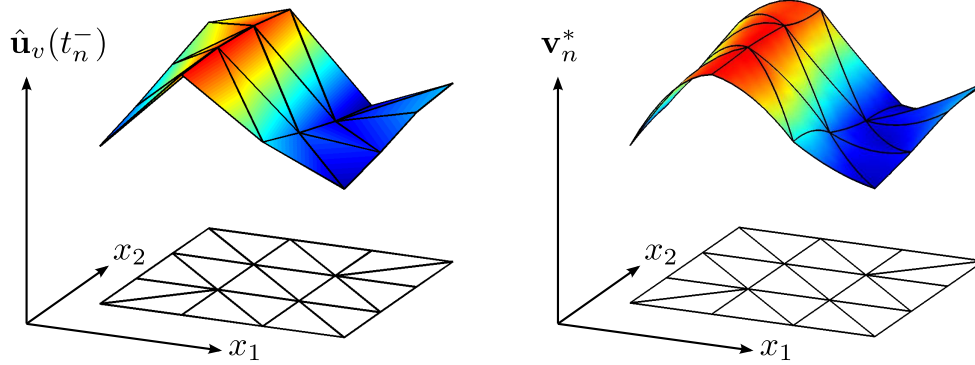


Figure 5: The recovery techniques for the velocities consist in increasing the interpolation order of  $\hat{\mathbf{u}}_v(t_n^-)$  (left) furnishing the recovered velocities  $\mathbf{v}_n^*$  (right).

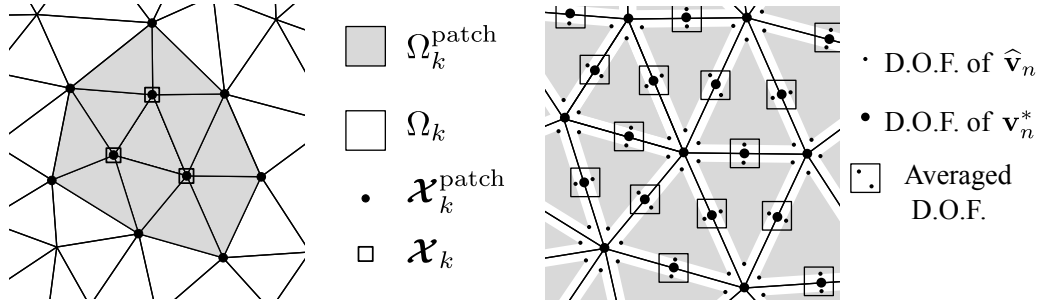


Figure 6: Definition of element patches (left) and illustration of the averaging of discontinuous function  $\hat{\mathbf{v}}_n$  into the continuous function  $\mathbf{v}_n^*$  (right).

such that it fits the values of  $\hat{\mathbf{u}}_v(t_n^-)$  at  $\mathcal{X}_k^{\text{patch}}$  in a least squares sense and coincides with  $\hat{\mathbf{u}}_v(t_n^-)$  at  $\mathcal{X}_k$ . That is,

$$\mathbf{v}_n^{\mathcal{X}_k} = \arg \min_{\mathbf{w} \in [\mathbb{P}^{p+1}(\Omega_k^{\text{patch}})]^d} \sum_{\mathbf{x} \in \mathcal{X}_k^{\text{patch}}} (\mathbf{w}(\mathbf{x}) - \hat{\mathbf{u}}_v(\mathbf{x}, t_n^-))^2 \quad (48)$$

constrained to  $\mathbf{w}(\mathbf{x}) = \hat{\mathbf{u}}_v(\mathbf{x}, t_n^-)$  for  $\mathbf{x} \in \mathcal{X}_k$ .

Problem (48) results in  $d$  (one for each component of the velocity, all with the same *mass* matrix) linear system of equations of size equal to the dimension of  $\mathbb{P}^{p+1}$  for each element of the computational mesh.

In order to obtain the post-processed velocity field  $\mathbf{v}_n^*$ , first the contributions of the restriction of the local recovered functions  $\mathbf{v}_n^{\mathcal{X}_k}$  to the corresponding element  $\Omega_k$  are summed,  $\hat{\mathbf{v}}_n := \sum_k \mathbf{v}_n^{\mathcal{X}_k}|_{\Omega_k}$ . Note that  $\hat{\mathbf{v}}_n$  is discontinuous because, for two neighboring elements  $\Omega_k$  and  $\Omega_{k'}$  with a common side  $\Gamma_{kk'} := \bar{\Omega}_k \cap \bar{\Omega}_{k'}$ , functions  $\mathbf{v}_n^{\mathcal{X}_k}|_{\Omega_k}$  and  $\mathbf{v}_n^{\mathcal{X}_{k'}}|_{\Omega_{k'}}$  coincide at the endpoints of  $\Gamma_{kk'}$  but, in general, not in the other points of  $\Gamma_{kk'}$ . In order to build up a continuous approximation  $\mathbf{v}_n^*$ , the local contributions are averaged on the

element sides. Typically  $\mathbf{v}_n^{\mathcal{X}^k}|_{\Omega_k}$  is represented with the nodal values of a finite element of degree  $p + 1$ . Therefore, computing  $\mathbf{v}_n^*$  is simply performed by just averaging the values of the degrees of freedom associated with the element edges (not vertices), as illustrated in figure 6.

## 5 Dual weighted residual & explicit residual estimates

### 5.1 Dual weighted residual method

This section presents the so-called Dual Weighted Residual (DWR) technique providing estimates for the error in the quantity of interest. This technique is introduced by Rannacher and Stuttmeier in the context of steady state linear elasticity problems [63], but it is also applied to linear elastodynamics [35, 31, 36, 14, 37, 38]. In particular, the dual weighted residual technique is presented here in the context of elastodynamics following [35].

The dual weighted residual methodology provides a scalar estimate  $\eta^{\text{dwr}}$  for the error in the quantity of interest

$$\eta^{\text{dwr}} \approx L_{\text{D}}^{\mathcal{O}}(\mathbf{E}),$$

where, here, the error  $\mathbf{E}$  is defined with respect the solution  $\tilde{\mathbf{U}}$  of the discrete double-field problem (12). Following [35] the developments are restricted to linear time descriptions, that is  $q = 1$ .

The error estimate  $\eta^{\text{dwr}}$  is obtained replacing the exact adjoint solution  $\mathbf{U}^{\text{d}}$  by an appropriate approximation  $\tilde{\mathbf{U}}^{\text{d}}$  in the error representation (39), namely

$$\eta^{\text{dwr}} := R_{\text{CGM}}(\tilde{\mathbf{U}}^{\text{d}}). \quad (49)$$

The scalar estimate  $\eta^{\text{dwr}}$  provides a single scalar quantity, which may be used in the framework of an adaptive procedure as a stopping criterion. That is, to check whether the computed numerical approximation has reached the desired accuracy. Additionally, the dual weighted residual method provides local error indicators (typically element by element) to drive goal-oriented adaptive procedures. This information is used to improve the space-time discretization in order to reduce the error  $\eta^{\text{dwr}}$ .

Deriving the local error indicators requires rewriting the error representation (41) in such a way that the contributions of the space and time discretization errors are separated. This allows to decide whether the space or the time discretizations (or both) have to be refined. First, in order to separate the space and time errors in the error representation (41), the projection  $\Pi^{\Delta t} \Pi^H \mathbf{U}^{\text{d}}$  of  $\mathbf{U}^{\text{d}}$  in the space  $\widehat{\mathcal{W}}^{H, \Delta t} \times \widehat{\mathcal{W}}^{H, \Delta t}$  is introduced, where  $\Pi^{\Delta t}$  is a projection of a time dependent function into the space of time piecewise constant functions and  $\Pi^H$  is the classical nodal interpolation projecting space-dependent functions into  $\mathcal{V}_0^H$ . In practice,  $\Pi^{\Delta t}$  is defined for a time-dependent

function  $\mathbf{w}$  taking the average of  $\mathbf{w}$  inside each time interval  $I_n$

$$\Pi^{\Delta t} \mathbf{w}|_{I_n} := \frac{1}{\text{meas}(I_n)} \int_{I_n} \mathbf{w} \, dt.$$

Note that the error in the projection  $\mathbf{w} - \Pi^{\Delta t} \mathbf{w}$  is orthogonal to piecewise constant functions in time

$$\int_{I_n} (\mathbf{w} - \Pi^{\Delta t} \mathbf{w}) \cdot \mathbf{v} \, dt = 0 \quad \forall \mathbf{v} \in [\mathbb{P}^0(I_n)]^d. \quad (50)$$

Thus, taking  $\mathbf{W}^{H,\Delta t} = \Pi^{\Delta t} \Pi^H \mathbf{U}^d$  in (41) yields

$$L_D^{\mathcal{O}}(\mathbf{E}) = R_{\text{CGM}}(\mathbf{U}^d - \Pi^{\Delta t} \Pi^H \mathbf{U}^d). \quad (51)$$

**Remark 4.** Figure 7 illustrates the projection operators  $\Pi^H$  and  $\Pi^{\Delta t}$  using the adjoint velocity  $\mathbf{u}_v^d$  shown in figure 2 associated to the quantity of interest  $L_1^{\mathcal{O}}(\cdot)$ . The exact adjoint velocity  $\mathbf{u}_v^d \in \mathcal{W}$  is continuous both in space and time. Function  $\Pi^{\Delta t} \mathbf{u}_v^d \in \widehat{\mathcal{W}}^{\Delta t}$ , with

$$\widehat{\mathcal{W}}^{\Delta t} := \{\mathbf{v} \in [L^2(I; \mathcal{V}_0)]^d : \mathbf{v}|_{I_n} \in [\mathbb{P}^{q-1}(I_n; \mathcal{V}_0)]^d, n = 1, \dots, N\},$$

is piecewise polynomial (constant for  $q = 1$ ) in time. However, the spacial description of functions in  $\widehat{\mathcal{W}}^{\Delta t}$  is infinite dimensional. Finally, the fully discrete projection  $\Pi^{\Delta t} \Pi^H \mathbf{u}_v^d \in \widehat{\mathcal{W}}^{H,\Delta t}$  is continuous and piecewise polynomial in space, see figure 7.

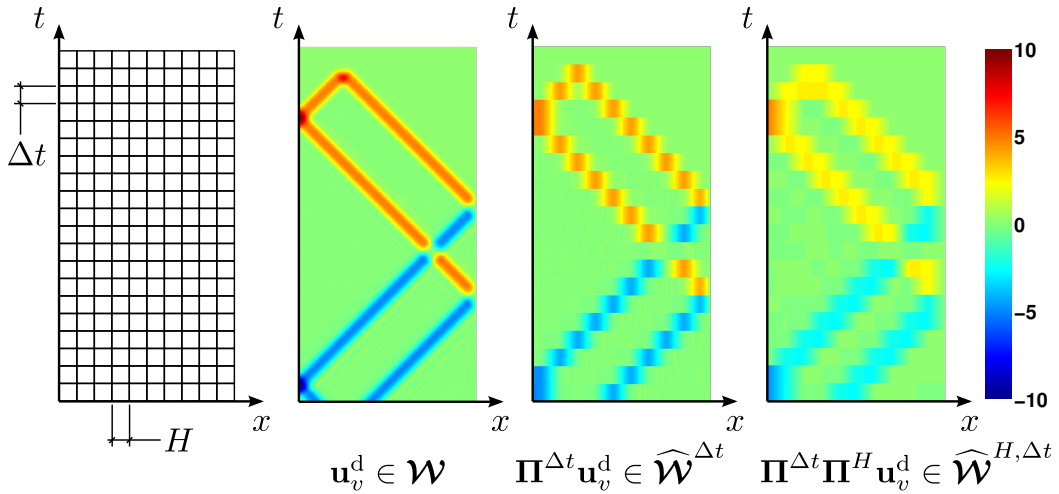


Figure 7: Space-time discretization defining the spaces  $\widehat{\mathcal{W}}^{\Delta t}$  and  $\widehat{\mathcal{W}}^{H,\Delta t}$  (outer left). Adjoint velocity field  $\mathbf{u}_v^d$  associated to the quantity of interest  $L_1^{\mathcal{O}}(\cdot)$  (see figure 2) and its projections  $\Pi^{\Delta t} \mathbf{u}_v^d \in \widehat{\mathcal{W}}^{\Delta t}$  and  $\Pi^{\Delta t} \Pi^H \mathbf{u}_v^d \in \widehat{\mathcal{W}}^{H,\Delta t}$  (right).

The space and time errors are separated adding and subtracting  $\Pi^{\Delta t} \mathbf{U}^d$  in equation (51)

$$L_D^{\mathcal{O}}(\mathbf{E}) = R_{\text{CGM}}(\mathbf{U}^d - \Pi^{\Delta t} \mathbf{U}^d) + R_{\text{CGM}}(\Pi^{\Delta t} (\mathbf{U}^d - \Pi^H \mathbf{U}^d)). \quad (52)$$

The terms  $R_{\text{CGM}}(\mathbf{U}^d - \mathbf{\Pi}^{\Delta t} \mathbf{U}^d)$  and  $R_{\text{CGM}}(\mathbf{\Pi}^{\Delta t}(\mathbf{U}^d - \mathbf{\Pi}^H \mathbf{U}^d))$  are associated with the time and space discretization errors respectively. Indeed,  $R_{\text{CGM}}(\mathbf{U}^d - \mathbf{\Pi}^{\Delta t} \mathbf{U}^d)$  tends to zero as the time discretization is refined whereas  $R_{\text{CGM}}(\mathbf{\Pi}^{\Delta t}(\mathbf{U}^d - \mathbf{\Pi}^H \mathbf{U}^d))$  tends to zero as the space discretization is refined.

Once the space and time errors are separated, the next step to obtain the local error contributions is splitting the integrals in  $R_{\text{CGM}}(\cdot)$  using the space-time cells  $\Omega_k \times I_n$  associated with the elements  $\Omega_k$  and time intervals  $I_n$ . That is

$$\begin{aligned} R_{\text{CGM}}(\mathbf{W}) &= \sum_{n=1}^N \sum_{k=1}^{N_{\text{el}}} \int_{I_n} [(\mathbf{f}, \mathbf{w}_v)_{\Omega_k} + (\mathbf{g}, \mathbf{w})_{\Gamma_N \cap \partial \Omega_k} - m(\dot{\tilde{\mathbf{u}}}_v, \mathbf{w}_v)_{\Omega_k} - a(\tilde{\mathbf{u}}_u, \mathbf{w}_v)] dt \\ &\quad \sum_{n=1}^N \sum_{k=1}^{N_{\text{el}}} \int_{I_n} (\mathbf{r}_u, \mathbf{w}_u)_{\Omega_k} dt + \sum_{k=1}^{N_{\text{el}}} [(\mathbf{r}_u^0, \mathbf{w}_u(0))_{\Omega_k} + (\mathbf{r}_v^0, \mathbf{w}_v(0))_{\Omega_k}], \end{aligned} \quad (53)$$

where

$$\mathbf{r}_u := \rho(\dot{\tilde{\mathbf{u}}}_u - \tilde{\mathbf{u}}_v), \quad \mathbf{r}_u^0 := \rho(\mathbf{u}_0 - \tilde{\mathbf{u}}_u(0)), \quad \mathbf{r}_v^0 := \rho(\mathbf{v}_0 - \tilde{\mathbf{u}}_v(0)).$$

The residual  $R_{\text{CGM}}(\cdot)$  is written in equation (53) for the particular case of pure elasticity ( $a_1 = a_2 = 0$ ) following reference [35].

An alternative format of the residual is derived integrating by parts the term  $a(\tilde{\mathbf{u}}_u, \mathbf{w}_v)$  in (53). Thus, the strong residuals associated with the interior of the elements and the element boundaries (edges or faces) are introduced

$$\mathbf{r}_v^{\text{el}} := \mathbf{f} - \rho \dot{\tilde{\mathbf{u}}}_v + \nabla \cdot \boldsymbol{\sigma}(\tilde{\mathbf{u}}_u), \quad \text{in } \Omega_k, k = 1, \dots, N_{\text{el}}, \quad \text{and} \quad \mathbf{r}_v^{\text{fa}} := \begin{cases} -\frac{1}{2} \llbracket \boldsymbol{\sigma}(\tilde{\mathbf{u}}_u) \cdot \mathbf{n} \rrbracket & \text{on } \Gamma^{\text{int}}, \\ \mathbf{g} - \boldsymbol{\sigma}(\tilde{\mathbf{u}}_u) \cdot \mathbf{n} & \text{on } \Gamma_N, \end{cases}$$

being  $\Gamma^{\text{int}}$  the set of interelement boundaries (mesh edges or faces). The jump  $\llbracket \boldsymbol{\sigma} \cdot \mathbf{n} \rrbracket$  is defined on a generic element interface  $\Gamma_l = \partial \Omega_k \cap \partial \Omega_{k'} \in \Gamma^{\text{int}}$  as  $\llbracket \boldsymbol{\sigma} \cdot \mathbf{n} \rrbracket := \boldsymbol{\sigma}|_{\Omega_k} \cdot \mathbf{n}_k + \boldsymbol{\sigma}|_{\Omega_{k'}} \cdot \mathbf{n}_{k'}$  where  $\mathbf{n}_k$  and  $\mathbf{n}_{k'}$  are the outward unit normals to  $\partial \Omega_k$  and  $\partial \Omega_{k'}$  respectively. Equation (53) is therefore rewritten as

$$\begin{aligned} R_{\text{CGM}}(\mathbf{W}) &= \sum_{n=1}^N \sum_{k=1}^{N_{\text{el}}} \int_{I_n} [(\mathbf{r}_u, \mathbf{w}_u)_{\Omega_k} + (\mathbf{r}_v^{\text{el}}, \mathbf{w}_v)_{\Omega_k} + (\mathbf{r}_v^{\text{fa}}, \mathbf{w}_v)_{\partial \Omega_k}] \\ &\quad + \sum_{k=1}^{N_{\text{el}}} [(\mathbf{r}_u^0, \mathbf{w}_u(0))_{\Omega_k} + (\mathbf{r}_v^0, \mathbf{w}_v(0))_{\Omega_k}], \end{aligned} \quad (54)$$

where functions  $\mathbf{r}_u$ ,  $\mathbf{r}_v^{\text{el}}$ ,  $\mathbf{r}_v^{\text{fa}}$ ,  $\mathbf{r}_u^0$  and  $\mathbf{r}_v^0$  are the computable strong residuals contributing to  $R_{\text{CGM}}(\cdot)$ . This new format of the residual is interesting because, when restricted to elements and time slabs, it provides better space-time local indicators than the original one (53).

The local (element by element) error contributions associated with the space and time discretization errors are obtained using the residual decomposition (54) in the error

representation (52):

$$\begin{aligned}
 L_D^{\mathcal{O}}(\mathbf{E}) &= \sum_{k=1}^{N_{\text{el}}} [(\mathbf{r}_u^0, \mathbf{u}_u^{\text{d}}(0) - \mathbf{\Pi}^{\Delta t} \mathbf{\Pi}^H \mathbf{u}_u^{\text{d}}(0))_{\Omega_k} + (\mathbf{r}_v^0, \mathbf{u}_v^{\text{d}}(0) - \mathbf{\Pi}^{\Delta t} \mathbf{\Pi}^H \mathbf{u}_v^{\text{d}}(0))] \\
 &+ \sum_{n=1}^N \sum_{k=1}^{N_{\text{el}}} \int_{I_n} [(\mathbf{r}_u - \mathbf{\Pi}^{\Delta t} \mathbf{r}_u, \mathbf{u}_u^{\text{d}} - \mathbf{\Pi}^{\Delta t} \mathbf{u}_u^{\text{d}})_{\Omega_k} + (\mathbf{r}_u, \mathbf{\Pi}^{\Delta t} \mathbf{u}_u^{\text{d}} - \mathbf{\Pi}^{\Delta t} \mathbf{\Pi}^H \mathbf{u}_u^{\text{d}})_{\Omega_k}] \\
 &+ \sum_{n=1}^N \sum_{k=1}^{N_{\text{el}}} \int_{I_n} [(\mathbf{r}_v^{\text{el}} - \mathbf{\Pi}^{\Delta t} \mathbf{r}_v^{\text{el}}, \mathbf{u}_v^{\text{d}} - \mathbf{\Pi}^{\Delta t} \mathbf{u}_v^{\text{d}})_{\Omega_k} + (\mathbf{r}_v^{\text{el}}, \mathbf{\Pi}^{\Delta t} \mathbf{u}_v^{\text{d}} - \mathbf{\Pi}^{\Delta t} \mathbf{\Pi}^H \mathbf{u}_v^{\text{d}})_{\Omega_k}] \\
 &+ \sum_{n=1}^N \sum_{k=1}^{N_{\text{el}}} \int_{I_n} [(\mathbf{r}_v^{\text{fa}} - \mathbf{\Pi}^{\Delta t} \mathbf{r}_v^{\text{fa}}, \mathbf{u}_v^{\text{d}} - \mathbf{\Pi}^{\Delta t} \mathbf{u}_v^{\text{d}})_{\partial\Omega_k} + (\mathbf{r}_v^{\text{fa}}, \mathbf{\Pi}^{\Delta t} \mathbf{u}_v^{\text{d}} - \mathbf{\Pi}^{\Delta t} \mathbf{\Pi}^H \mathbf{u}_v^{\text{d}})_{\partial\Omega_k}], \tag{55}
 \end{aligned}$$

where functions  $\mathbf{\Pi}^{\Delta t} \mathbf{r}_u$ ,  $\mathbf{\Pi}^{\Delta t} \mathbf{r}_v^{\text{el}}$  and  $\mathbf{\Pi}^{\Delta t} \mathbf{r}_v^{\text{fa}}$  are introduced into equation (55) using the orthogonality property (50).

Equation (55) leads to local error contributions which might have opposite signs from element to element. In practice, the remeshing criteria, which translate the local error contributions into a desired element size, require that the input local indicators are positive. The positive error contributions are obtained using the Cauchy–Schwartz inequality in equation (55), namely

$$|L_D^{\mathcal{O}}(\mathbf{E})| \leq \sum_{k=1}^{N_{\text{el}}} \eta_k^{\text{dwr,i}} + \sum_{n=0}^N \sum_{k=1}^{N_{\text{el}}} [\eta_{n,k}^{\text{dwr,s}} + \eta_{n,k}^{\text{dwr,t}}], \tag{56}$$

with

$$\eta_k^{\text{dwr,i}} := \|\mathbf{r}_u^0\|_{\Omega_k} \|\mathbf{u}_u^{\text{d}}(0) - \mathbf{\Pi}^{\Delta t} \mathbf{\Pi}^H \mathbf{u}_u^{\text{d}}(0)\|_{\Omega_k} + \|\mathbf{r}_v^0\|_{\Omega_k} \|\mathbf{u}_v^{\text{d}}(0) - \mathbf{\Pi}^{\Delta t} \mathbf{\Pi}^H \mathbf{u}_v^{\text{d}}(0)\|_{\Omega_k}, \tag{57a}$$

$$\eta_{n,k}^{\text{dwr,t}} := \|\mathbf{r}_u - \mathbf{\Pi}^{\Delta t} \mathbf{r}_u\|_{\Omega_k \times I_n} \|\mathbf{u}_u^{\text{d}} - \mathbf{\Pi}^{\Delta t} \mathbf{u}_u^{\text{d}}\|_{\Omega_k \times I_n} + \|\mathbf{r}_v^{\text{el}} - \mathbf{\Pi}^{\Delta t} \mathbf{r}_v^{\text{el}}\|_{\Omega_k \times I_n} \|\mathbf{u}_v^{\text{d}} - \mathbf{\Pi}^{\Delta t} \mathbf{u}_v^{\text{d}}\|_{\Omega_k \times I_n} \tag{57b}$$

$$+ \|\mathbf{r}_v^{\text{fa}} - \mathbf{\Pi}^{\Delta t} \mathbf{r}_v^{\text{fa}}\|_{\partial\Omega_k \times I_n} \|\mathbf{u}_v^{\text{d}} - \mathbf{\Pi}^{\Delta t} \mathbf{u}_v^{\text{d}}\|_{\partial\Omega_k \times I_n}, \tag{57c}$$

$$\eta_{n,k}^{\text{dwr,s}} := \|\mathbf{r}_u\|_{\Omega_k} \|\mathbf{\Pi}^{\Delta t} \mathbf{u}_u^{\text{d}} - \mathbf{\Pi}^{\Delta t} \mathbf{\Pi}^H \mathbf{u}_u^{\text{d}}\|_{\Omega_k \times I_n} + \|\mathbf{r}_v^{\text{el}}\|_{\Omega_k \times I_n} \|\mathbf{\Pi}^{\Delta t} \mathbf{u}_v^{\text{d}} - \mathbf{\Pi}^{\Delta t} \mathbf{\Pi}^H \mathbf{u}_v^{\text{d}}\|_{\Omega_k \times I_n} \tag{57d}$$

$$+ \|\mathbf{r}_v^{\text{fa}}\|_{\partial\Omega_k \times I_n} \|\mathbf{\Pi}^{\Delta t} \mathbf{u}_v^{\text{d}} - \mathbf{\Pi}^{\Delta t} \mathbf{\Pi}^H \mathbf{u}_v^{\text{d}}\|_{\partial\Omega_k \times I_n}, \tag{57e}$$

where the notation  $\|\cdot\|_{\Omega_k}$ ,  $\|\cdot\|_{\Omega_k \times I_n}$  and  $\|\cdot\|_{\partial\Omega_k \times I_n}$  is used to denote the  $L^2$  norms in  $\Omega_k$ ,  $\Omega_k \times I_n$  and  $\partial\Omega_k \times I_n$  respectively. Note that 1)  $\eta_k^{\text{dwr,i}}$  is the contribution of element  $\Omega_k$  to the interpolation error due to the initial conditions, 2)  $\eta_{n,k}^{\text{dwr,t}}$  is the contribution of the space-time slab  $\Omega_k \times I_n$  to the time discretization error and 3)  $\eta_{n,k}^{\text{dwr,s}}$  is the contribution of the space-time slab  $\Omega_k \times I_n$  to the space discretization error.

The inequality in equation (56) guarantees that the error in the quantity of interest is controlled if the local errors  $\eta_k^{\text{dwr,i}}$ ,  $\eta_{n,k}^{\text{dwr,s}}$ ,  $\eta_{n,k}^{\text{dwr,t}}$  are small enough. Thus, the local error indicators  $\eta_k^{\text{dwr,i}}$ ,  $\eta_{n,k}^{\text{dwr,s}}$ ,  $\eta_{n,k}^{\text{dwr,t}}$  are useful to drive goal-oriented adaptive procedures aiming

at efficiently controlling  $|L^\mathcal{O}(\mathbf{e})|$ . However, these local error indicators cannot be used to obtain a reliable assessment of  $L^\mathcal{O}(\mathbf{e})$ , which is better estimated directly with equation (49).

Note that the local error contributions in equation (57) are not fully computable. They involve the norms of the strong residuals which are computable, but they also involve the unknown *exact* solution of the adjoint problem,  $\mathbf{U}^d$ . Computable local error indicators from equation (57) are obtained following two alternative approaches.

On the one hand, the exact adjoint solution  $\mathbf{U}^d$  is replaced in (57) by a suitable approximation  $\tilde{\mathbf{U}}^d$  as previously done in equation (49). The approximation  $\tilde{\mathbf{U}}^d$  must belong to a richer space than  $\widehat{\mathcal{W}}^{H,\Delta t} \times \widehat{\mathcal{W}}^{H,\Delta t}$  in order to preclude Galerkin cancellation. Function  $\tilde{\mathbf{U}}^d$  is computed in [64, 35] as post-process of the numerical adjoint approximation using recovery techniques. Alternatively, references [35, 47] compute  $\tilde{\mathbf{U}}^d$  solving a global problem in a richer space obtained with  $H$ - or  $p$ -refinement. This second approach might be computationally unaffordable in three-dimensional demanding problems.

On the other hand, computable local indicators are obtained introducing a priori error estimates for the adjoint interpolation errors  $\mathbf{U}^d - \mathbf{\Pi}^{\Delta t} \mathbf{\Pi}^H \mathbf{U}^d$  and  $\mathbf{U}^d - \mathbf{\Pi}^{\Delta t} \mathbf{U}^d$  appearing in equation (57). This allows to write the adjoint interpolation error in terms of higher order derivatives (both in space and time) of  $\mathbf{U}^d$ . Then, the unknown high order derivatives of  $\mathbf{U}^d$  are replaced by a post-process of the computed adjoint approximation, see [31, 35] for details. The use of *a priori* interpolation estimates introduces unknown constants in the final expression of the estimate. However, the local information given by the computable part of the estimate is used to perform space-time mesh adaptivity.

## 5.2 An $L^2$ -norm explicit estimate

This section briefly summarizes reference [50] deriving explicit estimates for the  $L^2$ -norm of the final displacement error,  $\|\mathbf{e}_u(T)\| = (\mathbf{e}_u(T), \mathbf{e}_u(T))^{1/2}$ . An analogous rationale holds for assessing the total energy of the error,  $\|\mathbf{e}_v(T)\|_m^2 + \|\mathbf{e}_u(T)\|_a^2$ , see references [34, 53].

Here, the  $L^2$ -norm of the error is seen as a particular quantity of interest to be estimated using the DWR approach presented in section 5.1. The non-linear character of this quantity of interest induces a corresponding functional output  $L_D^\mathcal{O}(\cdot)$  involving the unknown error  $\mathbf{e}_u(T)$ . This functional output induces an adjoint problem that plays a role in the derivation of the estimate. However, it is worth mentioning that the estimate is explicit and it does not require solving any adjoint problem.

The presentation in reference [50] considers the wave equation as model problem (with a scalar unknown). The equations of structural dynamics (1) are a general framework (with vectorial unknown) for a second order hyperbolic problem, that are seen as a generalization of the wave equation. Thus, the concepts introduced in [50] are presented here in the framework of problem (1) for the sake of a unified exposition.

Following [50], the Dirichlet boundary conditions are defined on the whole boundary,  $\Gamma_D = \partial\Omega$ , the density is taken  $\rho = 1$  and the initial conditions are assumed to be exactly represented by the numerical approximation, that is  $\mathbf{u}_0 - \tilde{\mathbf{u}}_u(0) = \mathbf{0}$  and  $\mathbf{v}_0 - \tilde{\mathbf{u}}_v(0) = \mathbf{0}$ .

The global  $L^2$ -norm of the final displacement error,  $\|\mathbf{e}_u(T)\|$ , is assessed introducing the auxiliary quantity of interest

$$L_D^{\mathcal{O}}(\mathbf{W}) := (\mathbf{e}_u(T), \mathbf{w}_u(T)). \quad (58)$$

Note that, with this definition, the error in the quantity of interest is indeed the  $L^2$ -norm of the final displacement error,

$$L_D^{\mathcal{O}}(\mathbf{E}) = (\mathbf{e}_u(T), \mathbf{e}_u(T)) = \|\mathbf{e}_u(T)\|^2.$$

Assuming that  $\mathbf{U}^d$  is the solution of the adjoint problem (34) associated with the quantity of interest (58), the value  $\|\mathbf{e}_u(T)\|$  can be expressed using the error representation (41). That is

$$\|\mathbf{e}_u(T)\|^2 = L_D^{\mathcal{O}}(\mathbf{E}) = R_{\text{CGA}}(\mathbf{U}^d - \mathbf{\Pi}^{\Delta t} \mathbf{\Pi}^H \mathbf{U}^d), \quad (59)$$

where  $\mathbf{W}^{H, \Delta t}$  is replaced in (41) by the projection of the adjoint solution  $\mathbf{\Pi}^{\Delta t} \mathbf{\Pi}^H \mathbf{U}^d$ . The error representation (59) involves the residual  $R_{\text{CGA}}(\cdot)$  instead of  $R_{\text{CGM}}(\cdot)$  because the numerical approximation  $\tilde{\mathbf{U}}$  is computed in reference [50] with the discrete CGA problem (14), and consequently, the orthogonality property holds only for  $R_{\text{CGA}}(\cdot)$ .

The space and time errors are separated adding and subtracting the projection  $\mathbf{\Pi}^H \mathbf{U}^d$  into equation (59),

$$L_D^{\mathcal{O}}(\mathbf{E}) = R_{\text{CGA}}(\mathbf{U}^d - \mathbf{\Pi}^H \mathbf{U}^d) + R_{\text{CGA}}(\mathbf{\Pi}^H (\mathbf{U}^d - \mathbf{\Pi}^{\Delta t} \mathbf{U}^d)), \quad (60)$$

where the terms  $R_{\text{CGA}}(\mathbf{U}^d - \mathbf{\Pi}^H \mathbf{U}^d)$  and  $R_{\text{CGA}}(\mathbf{\Pi}^H (\mathbf{U}^d - \mathbf{\Pi}^{\Delta t} \mathbf{U}^d))$  are related with the space and time discretization errors respectively. The space projection operator  $\mathbf{\Pi}^H$  is defined here as the  $L^2$ -projection in the space  $\mathcal{V}_0^H$  instead of the usual nodal interpolation, see reference [50]. This technicality is required to ensure some orthogonality properties. That is,  $\mathbf{\Pi}^H \mathbf{w}$  is defined for a generic function  $\mathbf{w} \in \mathcal{V}_0$  as the solution of the problem: find  $\mathbf{\Pi}^H \mathbf{w} \in \mathcal{V}_0^H$  such that

$$(\mathbf{\Pi}^H \mathbf{w}, \mathbf{v}) = (\mathbf{w}, \mathbf{v}), \quad \forall \mathbf{v} \in \mathcal{V}_0^H.$$

The derivation of the explicit error estimate is split into three conceptual steps: 1) equation (60) is rewritten using the orthogonality properties of the operators  $\mathbf{\Pi}^H$  and  $\mathbf{\Pi}^{\Delta t}$  and integrating by parts in time, 2) the adjoint interpolation errors are expressed in terms of high order derivatives of the adjoint solution using *a priori* error estimates and 3) the resulting high order derivatives are bounded using a stability property of the adjoint solution. These steps are detailed below.

First, using the orthogonality properties of the operators  $\mathbf{\Pi}^H$  and  $\mathbf{\Pi}^{\Delta t}$ , equation (60) is rewritten as

$$\begin{aligned} L_D^{\mathcal{O}}(\mathbf{E}) &= \int_I (\mathbf{f} - \mathbf{\Pi}^H \mathbf{f}, \dot{\mathbf{u}}^d - \mathbf{\Pi}^H \dot{\mathbf{u}}^d) dt + \int_I (\mathbf{f} - \mathbf{\Pi}^{\Delta t} \mathbf{f}, \mathbf{\Pi}^H (\dot{\mathbf{u}}^d - \mathbf{\Pi}^{\Delta t} \dot{\mathbf{u}}^d)) dt \\ &\quad - \int_I a(\tilde{\mathbf{u}}_u, \dot{\mathbf{u}}^d - \mathbf{\Pi}^H \dot{\mathbf{u}}^d) dt - \int_I a(\tilde{\mathbf{u}}_u - \mathbf{\Pi}^{\Delta t} \tilde{\mathbf{u}}_u, \mathbf{\Pi}^H (\dot{\mathbf{u}}^d - \mathbf{\Pi}^{\Delta t} \dot{\mathbf{u}}^d)) dt \\ &\quad - \int_I a(\dot{\tilde{\mathbf{u}}}_u - \tilde{\mathbf{u}}_v, \mathbf{u}^d - \mathbf{\Pi}^H \mathbf{u}^d) dt + \int_I a(\tilde{\mathbf{u}}_v - \mathbf{\Pi}^{\Delta t} \tilde{\mathbf{u}}_v, \mathbf{\Pi}^H (\mathbf{u}^d - \mathbf{\Pi}^{\Delta t} \mathbf{u}^d)) dt. \end{aligned} \quad (61)$$

Then, integrating by parts the time integrals in the term

$$\int_I a(\tilde{\mathbf{u}}_u, \dot{\mathbf{u}}^d - \Pi^H \dot{\mathbf{u}}^d) dt,$$

equation (61) yields

$$\begin{aligned} L_D^{\mathcal{O}}(\mathbf{E}) &= \int_I (\mathbf{f} - \Pi^H \mathbf{f}, \dot{\mathbf{u}}^d - \Pi^H \dot{\mathbf{u}}^d) dt + \int_I (\mathbf{f} - \Pi^{\Delta t} \mathbf{f}, \Pi^H (\dot{\mathbf{u}}^d - \Pi^{\Delta t} \dot{\mathbf{u}}^d)) dt \\ &\quad - \int_I a(\tilde{\mathbf{u}}_u - \Pi^{\Delta t} \tilde{\mathbf{u}}_u, \Pi^H (\dot{\mathbf{u}}^d - \Pi^{\Delta t} \dot{\mathbf{u}}^d)) dt \\ &\quad + \int_I a(\tilde{\mathbf{u}}_v, \mathbf{u}^d - \Pi^H \mathbf{u}^d) dt + \int_I a(\tilde{\mathbf{u}}_v - \Pi^{\Delta t} \tilde{\mathbf{u}}_v, \Pi^H (\mathbf{u}^d - \Pi^{\Delta t} \mathbf{u}^d)) dt \\ &\quad - a(\tilde{\mathbf{u}}_u(T), \mathbf{u}^d(T) - \Pi^H \mathbf{u}^d(T)) + a(\tilde{\mathbf{u}}_u(0), \mathbf{u}^d(0) - \Pi^H \mathbf{u}^d(0)). \end{aligned} \quad (62)$$

Second, previous equation is rewritten using a priori error estimates for the interpolation errors  $\mathbf{u}^d - \Pi^H \mathbf{u}^d$  and  $\mathbf{u}^d - \Pi^{\Delta t} \mathbf{u}^d$ , see reference [50] for details:

$$\begin{aligned} |L_D^{\mathcal{O}}(\mathbf{E})| &\leq C_1 \left( \max_{t \in I} \|\ddot{\mathbf{u}}^d(t)\| \right) \left( \int_I \Delta t \|\mathbf{f} - \Pi^{\Delta t} \mathbf{f}\| dt + \int_I \Delta t \|\Delta_H (\tilde{\mathbf{u}}_u - \Pi^{\Delta t} \tilde{\mathbf{u}}_u)\| dt \right) \\ &\quad + C_2 \left( \max_{t \in I} \|\dot{\mathbf{u}}^d(t)\|_a \right) \left( \int_I \|H(\mathbf{f} - \Pi^H \mathbf{f})\| dt + \int_I \Delta t \|\tilde{\mathbf{u}}_v - \Pi^{\Delta t} \tilde{\mathbf{u}}_v\|_a dt \right) \\ &\quad + C_3 \left( \max_{t \in I} \|\nabla \cdot \boldsymbol{\sigma}^d(\mathbf{u}^d(t))\| \right) \left( \int_I \|H^2 R_2(\tilde{\mathbf{u}}_v)\| dt + \|H^2 R_2(\tilde{\mathbf{u}}_v(T))\| + \|H^2 R_2(\tilde{\mathbf{u}}_v(0))\| \right) \end{aligned} \quad (63)$$

where the discrete laplacian operator  $\Delta_H$  is defined for a generic function  $\mathbf{w} \in \mathcal{V}_0$  as : find  $\Delta_H \mathbf{w} \in \mathcal{V}_0^H$  such that

$$(\Delta_H \mathbf{w}, \mathbf{v}) = a(\mathbf{w}, \mathbf{v}), \quad \forall \mathbf{w} \in \mathcal{V}_0^H,$$

and the operator  $R_2(\cdot)$  is defined for a generic function  $\mathbf{w} \in \mathcal{V}_0^H$  as

$$R_2(\mathbf{w})|_{\Omega_k} := \frac{1}{2H_k} \max_{\mathbf{x} \in \partial\Omega_k} \left| \llbracket \mathbf{s}^E(\mathbf{w}(\mathbf{x})) \cdot \mathbf{n}(\mathbf{x}) \rrbracket \right|.$$

Third, the factors in (63) involving the adjoint solution are bounded in terms of the error  $\|\mathbf{e}_u(T)\|$  using the following stability property of the adjoint solution  $\mathbf{u}^d$  associated with the quantity of interest (58).

**Theorem 1.** *The solution  $\mathbf{u}^d$  of the adjoint problem (34) for quantity defined in (58), which strong form is*

$$\rho \ddot{\mathbf{u}}^d - \nabla \cdot \boldsymbol{\sigma}^d(\mathbf{u}^d) = \mathbf{0} \quad \text{in } \Omega \times I, \quad (64a)$$

$$\mathbf{u}^d = \mathbf{0} \quad \text{on } \Gamma_D \times I, \quad (64b)$$

$$\boldsymbol{\sigma}^d \cdot \mathbf{n} = \mathbf{0} \quad \text{on } \Gamma_N \times I, \quad (64c)$$

$$-\nabla \cdot \boldsymbol{\sigma}(\mathbf{u}^d) = \mathbf{e}_u \quad \text{at } \Omega \times \{T\}, \quad (64d)$$

$$\dot{\mathbf{u}}^d = \mathbf{0} \quad \text{at } \Omega \times \{T\}, \quad (64e)$$

fulfills

$$\max_{t \in I} (\|\ddot{\mathbf{u}}^d(t)\|^2 + \|\dot{\mathbf{u}}^d(t)\|_a^2 + \|\nabla \cdot \boldsymbol{\sigma}(\mathbf{u}^d(t))\|^2) \leq C \|\mathbf{e}_u(T)\|^2. \quad (65)$$

The proof can be found in [50, Lemma 17.3].

Using the stability property (65) and recalling that  $L_D^{\mathcal{O}}(\mathbf{E}) = \|\mathbf{e}_u(T)\|^2$ , equation (63) yields

$$\begin{aligned} \|\mathbf{e}_u(T)\| \leq C & \left( \int_I \Delta t \|\mathbf{f} - \mathbf{\Pi}^{\Delta t} \mathbf{f}\| \, dt + \int_I \Delta t \|\Delta_H(\tilde{\mathbf{u}}_u - \mathbf{\Pi}^{\Delta t} \tilde{\mathbf{u}}_u)\| \, dt \right. \\ & + \int_I \Delta t \|\tilde{\mathbf{u}}_v - \mathbf{\Pi}^{\Delta t} \tilde{\mathbf{u}}_v\|_a \, dt + \int_I \|H(\mathbf{f} - \mathbf{\Pi}^H \mathbf{f})\| \, dt \\ & \left. + \int_I \|H^2 R_2(\tilde{\mathbf{u}}_v)\| \, dt + \|H^2 R_2(\tilde{\mathbf{u}}_u(T))\| + \|H^2 R_2(\tilde{\mathbf{u}}_u(0))\| \right). \quad (66) \end{aligned}$$

Constant  $C$  in the previous expression is unknown. Nevertheless the computable part of the error estimate is split into space-time local contributions providing information on the relative magnitude of the error generated at each region of the computational domain. This information can be used for adaptive purposes. The three first terms in the right hand side of equation (66) are associated with the time discretization error while the four last terms are associated with the space discretization. The local contributions associated with these terms are used to adapt the corresponding space or time discretization.

## 6 Constitutive relation error and implicit estimates

This section aims at computing bounds for the error in the dissipation norm  $\|\mathbf{e}\|$  and in the quantity of interest  $L^{\mathcal{O}}(\mathbf{e})$  using the so-called constitutive relation error estimates [9]. These estimates require an underlying stress equilibration technique based on solving local problems. The residual is playing the role of the loading of the local problems, and therefore the solution is not an explicit post-process of the residual. Thus, these strategies are also denoted as implicit residual type estimates. In many contexts, constitutive relation error estimates and implicit residual type estimates are fully equivalent.

The goal is to compute scalar values  $\eta_{\text{ener}}$ ,  $\eta_L$  and  $\eta_U$  such that

$$\|\mathbf{e}\| \leq \eta_{\text{ener}} \quad \text{and} \quad \eta_L \leq L^{\mathcal{O}}(\mathbf{e}) \leq \eta_U. \quad (67)$$

Deriving the error bounds  $\eta_{\text{ener}}$ ,  $\eta_L$  and  $\eta_U$  using constitutive relation estimates requires that problem (1) contains some damping (i.e. either  $a_1$  or  $a_2$  is different from zero). This means that the bounding properties of the estimate are lost in the limit case of pure elasticity ( $a_1 = a_2 = 0$ ). Non-zero damping allows computing the error bounds (67) following a rationale analogous to the one used in steady-state problems [9].

The technique providing  $\eta_{\text{ener}}$ ,  $\eta_L$  and  $\eta_U$  is presented here following reference [46], where the model problem under consideration corresponds to taking  $a_1 = 0$  and  $a_2 > 0$  in equations (1). Thus, in the remaining of this section, the coefficient  $a_1$  is assumed to be

zero and  $a_2$  is assumed to be strictly positive. The same rationale holds for other damped versions of problem (1). For instance, references [44, 42, 45] introduce damping in the constitutive relation (2) using the linear Maxwell viscous model.

## 6.1 Computable upper bounds for the dissipation norm

The key ingredient to compute error bounds is building a pair  $(\tilde{\boldsymbol{\sigma}}, \tilde{\mathbf{u}})$  of a *dynamically admissible* (D-admissible) stress and a *kinematically admissible* (K-admissible) displacement.

On the one hand, the set of K-admissible displacements is defined as

$$\mathcal{U} := \{\mathbf{w} \in \mathcal{W} : \mathbf{w} = \mathbf{u}_0 \text{ at } \Omega \times \{0\} \text{ and } \dot{\mathbf{w}} = \mathbf{v}_0 \text{ at } \Omega \times \{0\}\}.$$

Functions in  $\mathcal{U}$  are continuous with continuous time derivative and exactly fulfilling both the homogeneous Dirichlet condition (1b) and the initial conditions (1d) and (1e). On the other hand, the space of D-admissible stresses is defined for a given K-admissible displacement  $\tilde{\mathbf{u}} \in \mathcal{U}$  as

$$\mathcal{S}(\tilde{\mathbf{u}}) := \left\{ \boldsymbol{\tau} \in \mathcal{Z} : \int_I (\boldsymbol{\tau}, \boldsymbol{\varepsilon}(\dot{\mathbf{w}})) dt = \int_I (l(t; \dot{\mathbf{w}}) - (\rho \ddot{\tilde{\mathbf{u}}}, \dot{\mathbf{w}})) dt \quad \forall \mathbf{w} \in \mathcal{W} \right\}, \quad (68)$$

where

$$\mathcal{Z} := \{\boldsymbol{\tau} : [\boldsymbol{\tau}]_{ij} \in L^2(\Omega \times I) \quad i, j \leq d\}, \quad (69)$$

and for  $\boldsymbol{\tau}, \boldsymbol{\varepsilon} \in \mathcal{Z}$ , the standard  $L^2$  product in  $\Omega$  reads

$$(\boldsymbol{\tau}, \boldsymbol{\varepsilon}) := \int_{\Omega} \boldsymbol{\tau} : \boldsymbol{\varepsilon} d\Omega.$$

The stress tensors in  $\mathcal{S}(\tilde{\mathbf{u}})$  are in dynamic equilibrium with respect the external loads plus the inertia forces associated with  $\ddot{\tilde{\mathbf{u}}}$ . For that reason, the definition of (and the notation for) the set  $\mathcal{S}(\tilde{\mathbf{u}})$  depends on the K-admissible displacement  $\tilde{\mathbf{u}}$ . A stress tensor  $\tilde{\boldsymbol{\sigma}} \in \mathcal{S}(\tilde{\mathbf{u}})$  is generally discontinuous between mesh elements, while the traction vector  $\tilde{\boldsymbol{\sigma}} \cdot \mathbf{n}$  is continuous across element edges (or faces in 3D). The weak form of the dynamic equilibrium is implicitly stated in the definition of  $\mathcal{S}(\tilde{\mathbf{u}})$  given in (68). The equivalent strong formulation for D-admissibility enforces point wise equilibrium in the interior of the elements and traction continuity across the element interfaces. Thus, for a given finite element mesh, a D-admissible stress  $\tilde{\boldsymbol{\sigma}}$  fulfills

$$\begin{aligned} -\nabla \cdot \tilde{\boldsymbol{\sigma}} &= \mathbf{f} - \rho \ddot{\tilde{\mathbf{u}}} \quad \text{on } \Omega^{\text{int}} \times I, \\ \tilde{\boldsymbol{\sigma}} \cdot \mathbf{n} &= \mathbf{g} \quad \text{on } \Gamma_{\text{N}} \times I, \\ \llbracket \tilde{\boldsymbol{\sigma}} \cdot \mathbf{n} \rrbracket &= \mathbf{0} \quad \text{on } \Gamma^{\text{int}} \times I, \end{aligned}$$

where  $\Omega^{\text{int}}$  is the interior of the elements of the mesh and  $\Gamma^{\text{int}}$  is the set of interelement faces (or edges in 2D).

The admissible pair  $(\tilde{\boldsymbol{\sigma}}, \tilde{\mathbf{u}}) \in \mathcal{S}(\tilde{\mathbf{u}}) \times \mathcal{U}$  defines the following stress error

$$\tilde{\boldsymbol{\sigma}}^e := \tilde{\boldsymbol{\sigma}} - \boldsymbol{\sigma}(\tilde{\mathbf{u}}), \quad (70)$$

which corresponds to the non verification of the constitutive relation (2). The so-called *constitutive relation error* (following the terminology by Ladevèze and co-workers) is then computed as  $\|\tilde{\boldsymbol{\sigma}}^e\|_\sigma$  where  $\|\cdot\|_\sigma$  is the stress version of the space-time norm  $\|\cdot\|$  defined in (23), namely

$$\|\boldsymbol{\tau}\|_\sigma^2 := \frac{1}{a_2} \int_I \|\boldsymbol{\tau}\|_a^2 dt.$$

For the particular case  $a_1 = 0$ , the displacement and stress norms are related by  $\|\mathbf{w}\| = \|a_2 \mathbf{C} : \boldsymbol{\varepsilon}(\dot{\mathbf{w}})\|_\sigma$ .

The constitutive relation error  $\|\tilde{\boldsymbol{\sigma}}^e\|_\sigma$  is computable once the fields  $\tilde{\boldsymbol{\sigma}}$  and  $\tilde{\mathbf{u}}$  are available. Note that,  $\|\tilde{\boldsymbol{\sigma}}^e\|_\sigma = 0$  if and only if  $\tilde{\boldsymbol{\sigma}} = \boldsymbol{\sigma}$  and  $\tilde{\mathbf{u}} = \mathbf{u}$ . Consequently,  $\|\tilde{\boldsymbol{\sigma}}^e\|_\sigma$  is adopted as a pertinent error measure. Moreover, the value  $\|\tilde{\boldsymbol{\sigma}}^e\|_\sigma$  provides information about the unknown error  $\mathbf{e}$ , as shown by the following theorem. For the sake of simplifying, the operators identifying the elastic and viscous contributions of the constitutive law are introduced as  $\mathbf{s}^E(\mathbf{u}) := \mathbf{C} : \boldsymbol{\varepsilon}(\mathbf{u})$  and  $\mathbf{s}^\nu(\mathbf{u}) := a_2 \mathbf{C} : \boldsymbol{\varepsilon}(\dot{\mathbf{u}})$ .

**Theorem 2.** *Given an admissible pair  $(\tilde{\boldsymbol{\sigma}}, \tilde{\mathbf{u}}) \in \mathcal{S}(\tilde{\mathbf{u}}) \times \mathcal{U}$ , the errors  $\mathbf{e}$  and  $\tilde{\boldsymbol{\sigma}}^e$  defined in equations (17) and (70), respectively, fulfill*

$$\|\tilde{\boldsymbol{\sigma}}^e\|_\sigma^2 = \|\dot{\mathbf{e}}(T)\|_m^2 + \|\mathbf{e}(T)\|_a^2 + \|\mathbf{e}\|^2 + \|\boldsymbol{\sigma}^\nu - \tilde{\boldsymbol{\sigma}}^\nu\|_\sigma^2, \quad (71)$$

where  $\boldsymbol{\sigma}^\nu := \mathbf{s}^\nu(\mathbf{u})$  and  $\tilde{\boldsymbol{\sigma}}^\nu := \tilde{\boldsymbol{\sigma}} - \mathbf{s}^E(\tilde{\mathbf{u}})$ .

For the proof, the reader is referred to [46, Theorem 1].

A direct consequence of theorem 2 is the relation  $\|\tilde{\boldsymbol{\sigma}}^e\|_\sigma^2 \geq \|\dot{\mathbf{e}}(T)\|_m^2 + \|\mathbf{e}(T)\|_a^2 + \|\mathbf{e}\|^2$  and, in particular, the following upper bound

$$\eta_{\text{ener}} := \|\tilde{\boldsymbol{\sigma}}^e\|_\sigma \geq \|\mathbf{e}\|. \quad (72)$$

Moreover, expression (72) is particularly important because it is used to bound the quantity of interest.

## 6.2 Error bounds in the quantity of interest

Bounds of the error in the quantity of interest  $L^{\mathcal{O}}(\mathbf{e})$  are obtained combining admissible pairs for both the original and the adjoint problems,  $(\tilde{\mathbf{u}}, \tilde{\boldsymbol{\sigma}})$  and  $(\tilde{\mathbf{u}}^d, \tilde{\boldsymbol{\sigma}}^d)$ . The space of *adjoint kinematically admissible* displacements is defined as

$$\mathcal{U}^d := \{\mathbf{w} \in \mathcal{W} : \mathbf{w} = \mathbf{u}^{\mathcal{O}} \text{ at } \Omega \times \{T\} \text{ and } \dot{\mathbf{w}} = \mathbf{v}^{\mathcal{O}} \text{ at } \Omega \times \{T\}\}.$$

The space of *adjoint dynamically admissible* stress fields is defined for a given  $\tilde{\mathbf{u}}^d \in \mathcal{U}^d$  as

$$\mathcal{S}^d(\tilde{\mathbf{u}}^d) := \left\{ \boldsymbol{\tau} \in \mathcal{Z} : \int_I (\boldsymbol{\tau}, \boldsymbol{\varepsilon}(\dot{\mathbf{w}})) dt = \int_I (l^{\mathcal{O}}(t; \dot{\mathbf{w}}) - (\rho \ddot{\mathbf{u}}^d, \dot{\mathbf{w}})) dt \quad \forall \mathbf{w} \in \mathcal{W} \right\},$$

where  $l^\mathcal{O}(t; \mathbf{w}) := (\mathbf{f}^\mathcal{O}(t), \mathbf{w}) + (\mathbf{g}^\mathcal{O}(t), \mathbf{w})_{\Gamma_N}$ .

The admissible pair  $(\tilde{\mathbf{u}}^d, \tilde{\boldsymbol{\sigma}}^d) \in \mathcal{U}^d \times \mathcal{S}^d(\tilde{\mathbf{u}}^d)$  provides the error in stresses associated with the non verification of the adjoint constitutive relation (27),

$$\tilde{\boldsymbol{\sigma}}^{d,e} := \tilde{\boldsymbol{\sigma}}^d - \boldsymbol{\sigma}^d(\tilde{\mathbf{u}}^d). \quad (73)$$

The bounds for  $L^\mathcal{O}(\mathbf{e})$  are computed using the constitutive relation errors  $\tilde{\boldsymbol{\sigma}}^e$  and  $\tilde{\boldsymbol{\sigma}}^{d,e}$ , as defined in (70) and (73). Actually,  $\tilde{\boldsymbol{\sigma}}^e$  and  $\tilde{\boldsymbol{\sigma}}^{d,e}$  are used to obtain bounds for  $R^d(\mathbf{e})$ , which is the non-computable part of the error representation (37). There are three different approaches to derive upper bounds on the basis of the constitutive relation errors, which are described in the following.

### 6.2.1 Error bounds based on the Cauchy-Schwarz inequality

References [42, 43, 44, 45] derive computable bounds using the Cauchy-Schwarz inequality. The bounds for  $R^d(\mathbf{e})$  are obtained noting that if  $(\tilde{\mathbf{u}}^d, \tilde{\boldsymbol{\sigma}}^d)$  is an adjoint admissible pair, then its associated error  $\tilde{\boldsymbol{\sigma}}^{d,e}$  verifies

$$\bar{B}^\nu(\tilde{\boldsymbol{\sigma}}^{d,e}, \mathbf{s}^\nu(\mathbf{w})) = R^d(\mathbf{w}) \quad \forall \mathbf{w} \in \mathcal{W}, \quad (74)$$

where  $\bar{B}^\nu(\cdot, \cdot)$  is the bilinear form

$$\bar{B}^\nu(\boldsymbol{\tau}_1, \boldsymbol{\tau}_2) := \frac{1}{a_2} \int_I \bar{a}(\boldsymbol{\tau}_1, \boldsymbol{\tau}_2) dt. \quad (75)$$

Note that the bilinear form  $\bar{B}^\nu(\cdot, \cdot)$  induces the stress energy norm  $\|\cdot\|_\sigma$ , that is  $\|\boldsymbol{\tau}\|_\sigma^2 := \bar{B}^\nu(\boldsymbol{\tau}, \boldsymbol{\tau})$ .

Taking  $\mathbf{w} = \mathbf{e}$ , equation (74) yields

$$R^d(\mathbf{e}) = \bar{B}^\nu(\tilde{\boldsymbol{\sigma}}^{d,e}, \mathbf{s}^\nu(\mathbf{e})).$$

Being  $\bar{B}^\nu$  symmetric-positive-definite, the Cauchy-Schwarz inequality holds and yields

$$|R^d(\mathbf{e})| \leq \|\tilde{\boldsymbol{\sigma}}^{d,e}\|_\sigma \|\mathbf{s}^\nu(\mathbf{e})\|_\sigma = \|\tilde{\boldsymbol{\sigma}}^{d,e}\|_\sigma \|\mathbf{e}\|.$$

The factor involving the unknown error  $\mathbf{e}$  is bounded using the equation (72) leading to the following computable bound for  $|R^d(\mathbf{e})|$ ,

$$|R^d(\mathbf{e})| \leq \|\tilde{\boldsymbol{\sigma}}^{d,e}\|_\sigma \|\tilde{\boldsymbol{\sigma}}^e\|_\sigma.$$

The computable bounds for the error in the quantity of interest are readily obtained using the previous result together with the computable part of the error representation (37). That is,

$$\zeta_L^{\text{C-S}} \leq L^\mathcal{O}(\mathbf{e}) \leq \zeta_U^{\text{C-S}},$$

where

$$\zeta_U^{\text{C-S}} := \|\tilde{\boldsymbol{\sigma}}^{d,e}\|_\sigma \|\tilde{\boldsymbol{\sigma}}^e\|_\sigma + R(\tilde{\mathbf{u}}^d), \quad (76a)$$

$$\zeta_L^{\text{C-S}} := -\|\tilde{\boldsymbol{\sigma}}^{d,e}\|_\sigma \|\tilde{\boldsymbol{\sigma}}^e\|_\sigma + R(\tilde{\mathbf{u}}^d). \quad (76b)$$

The use of the Cauchy-Schwarz inequality is typically inducing a large overestimation of the quantities assessed. This is because the two *vectors*  $\tilde{\boldsymbol{\sigma}}^{d,e}$  and  $\mathbf{s}^\nu(\mathbf{e})$  are, in general, far of being *parallel*. This makes the error bounds given in (76) not sharp, with an unrealistic and impractical bound gap.

### 6.2.2 Bounds using symmetric error equations

Alternative error bounds, based on different algebraic identities, are often used in the literature to derive sharper bounds than the ones obtained with the Cauchy-Schwarz approach. For instance, the parallelogram identity is used in [7, 65, 66] in the context of linear elasticity and in [21, 22] for transient convection-diffusion-reaction equations. In the framework of structural dynamics reference [46] proposes a bounding expression, alternative to the one in equation (76) originally proposed in reference [45].

The derivation of the alternative bounds requires introducing symmetrized equations for the original and adjoint errors. However, it is worth noting that this is only a mathematical artifact and, in practice, the error bounds are computed using only the admissible pairs  $(\tilde{\mathbf{u}}, \tilde{\boldsymbol{\sigma}})$  and  $(\tilde{\mathbf{u}}^d, \tilde{\boldsymbol{\sigma}}^d)$  without solving any auxiliary symmetrized error equations.

The symmetrized error equations read: find  $\mathbf{e}^\nu \in \mathbf{U}_0$  and  $\mathbf{e}^{d,\nu} \in \mathbf{U}_0^d$  such that

$$B^\nu(\mathbf{e}^\nu, \mathbf{w}) = R(\mathbf{w}) \quad \forall \mathbf{w} \in \mathcal{W}, \quad (77a)$$

$$B^\nu(\mathbf{e}^{d,\nu}, \mathbf{w}) = R^d(\mathbf{w}) \quad \forall \mathbf{w} \in \mathcal{W}, \quad (77b)$$

where the spaces  $\mathbf{U}_0$  and  $\mathbf{U}_0^d$  are defined respectively as

$$\mathbf{U}_0 := \{\mathbf{w} \in \mathcal{W} : \mathbf{w} = 0 \text{ at } \Omega \times \{0\} \text{ and } \dot{\mathbf{w}} = 0 \text{ at } \Omega \times \{0\}\},$$

and

$$\mathbf{U}_0^d := \{\mathbf{w} \in \mathcal{W} : \mathbf{w} = 0 \text{ at } \Omega \times \{T\} \text{ and } \dot{\mathbf{w}} = 0 \text{ at } \Omega \times \{T\}\}.$$

Equations (77) resemble the residual equation (18) for the primal error  $\mathbf{e}$ . Note that the difference is that the non symmetric bilinear form  $B(\cdot, \cdot)$  is replaced by the symmetric one  $B^\nu(\cdot, \cdot)$  defined as

$$B^\nu(\mathbf{v}, \mathbf{w}) := a_2 \int_I a(\dot{\mathbf{v}}, \dot{\mathbf{w}}) dt.$$

It is easily shown that for any scalar value  $\kappa \neq 0$ , see [46], the following algebraic identity holds:

$$-\frac{1}{4} \|\kappa \mathbf{e}^\nu - \frac{1}{\kappa} \mathbf{e}^{d,\nu}\|^2 \leq R^d(\mathbf{e}) \leq \frac{1}{4} \|\kappa \mathbf{e}^\nu + \frac{1}{\kappa} \mathbf{e}^{d,\nu}\|^2. \quad (78)$$

Functions  $\kappa \mathbf{e}^\nu \pm \frac{1}{\kappa} \mathbf{e}^{d,\nu}$  are solutions of the infinite dimensional problems (77). Therefore, the error bounds proposed in (78) are not computable. However, introducing the constitutive relation errors of the original and adjoint problem, the computable bounds for  $\|\kappa \mathbf{e}^\nu \pm \frac{1}{\kappa} \mathbf{e}^{d,\nu}\|$  are

$$\|\kappa \mathbf{e}^\nu \pm \frac{1}{\kappa} \mathbf{e}^{d,\nu}\| \leq \|\kappa \tilde{\boldsymbol{\sigma}}^e \pm \frac{1}{\kappa} \tilde{\boldsymbol{\sigma}}^{d,e}\|_\sigma. \quad (79)$$

The final bounds for  $L^{\mathcal{O}}(\mathbf{e})$  are derived substituting expression (79) in equation (78) and adding the correction term  $R(\tilde{\mathbf{u}}^d)$

$$\zeta_U := \frac{1}{4} \|\kappa \tilde{\boldsymbol{\sigma}}^e + \frac{1}{\kappa} \tilde{\boldsymbol{\sigma}}^{d,e}\|_\sigma^2 + R(\tilde{\mathbf{u}}^d), \quad (80a)$$

$$\zeta_L := -\frac{1}{4} \|\kappa \tilde{\boldsymbol{\sigma}}^e - \frac{1}{\kappa} \tilde{\boldsymbol{\sigma}}^{d,e}\|_\sigma^2 + R(\tilde{\mathbf{u}}^d), \quad (80b)$$

where  $\zeta_L$  and  $\zeta_U$  are such that

$$\zeta_L \leq L^{\mathcal{O}}(\mathbf{e}) \leq \zeta_U.$$

The error bounds (80) have a similar (but not identical) structure as the ones obtained using the parallelogram rule in linear elasticity. In both cases, the error in the quantity of interest is expressed in terms of energy measures of linear combinations of the original and adjoint errors. The main difference with respect to the parallelogram approach is that, here, energy-like lower bounds of the error are not used to obtain sharper bounds for the quantity of interest.

Note that the bounds (80) hold for any non-zero scalar parameter  $\kappa$ . In practice, the parameter  $\kappa$  is determined such that it minimizes the bound gap, yielding the optimal value

$$\kappa = \left( \frac{\|\tilde{\boldsymbol{\sigma}}^{\text{d,e}}\|_{\sigma}}{\|\tilde{\boldsymbol{\sigma}}^{\text{e}}\|_{\sigma}} \right)^{1/2}. \quad (81)$$

The error bounds  $\zeta_U, \zeta_L$  proposed in (80) are sharper than  $\zeta_U^{\text{C-S}}, \zeta_L^{\text{C-S}}$  in (76) obtained using the Cauchy-Schwartz inequality. Indeed, introducing the optimal value of  $\kappa$  given by (81) into the bound expression (80) yields

$$\zeta_U = \frac{1}{2} \|\tilde{\boldsymbol{\sigma}}^{\text{d,e}}\|_{\sigma} \|\tilde{\boldsymbol{\sigma}}^{\text{e}}\|_{\sigma} + R(\tilde{\mathbf{u}}^{\text{d}}) + \frac{1}{2} \bar{B}^{\nu}(\tilde{\boldsymbol{\sigma}}^{\text{d,e}}, \tilde{\boldsymbol{\sigma}}^{\text{e}}), \quad (82\text{a})$$

$$\zeta_L = -\frac{1}{2} \|\tilde{\boldsymbol{\sigma}}^{\text{d,e}}\|_{\sigma} \|\tilde{\boldsymbol{\sigma}}^{\text{e}}\|_{\sigma} + R(\tilde{\mathbf{u}}^{\text{d}}) + \frac{1}{2} \bar{B}^{\nu}(\tilde{\boldsymbol{\sigma}}^{\text{d,e}}, \tilde{\boldsymbol{\sigma}}^{\text{e}}). \quad (82\text{b})$$

The bound gap, that is the difference between the upper and lower bound, is therefore  $\zeta_U - \zeta_L = \|\tilde{\boldsymbol{\sigma}}^{\text{d,e}}\|_{\sigma} \|\tilde{\boldsymbol{\sigma}}^{\text{e}}\|_{\sigma}$  whereas the bound gap of the bounds in equation (76) is  $\zeta_U^{\text{C-S}} - \zeta_L^{\text{C-S}} = 2\|\tilde{\boldsymbol{\sigma}}^{\text{d,e}}\|_{\sigma} \|\tilde{\boldsymbol{\sigma}}^{\text{e}}\|_{\sigma}$ . Hence, the bound gap in equation (80) is half of the bound gap corresponding to equation (76), that is  $\zeta_U - \zeta_L = \frac{1}{2}(\zeta_U^{\text{C-S}} - \zeta_L^{\text{C-S}})$ , and provides a sharper error assessment.

### 6.2.3 Equivalent alternative approach

The error bounds (82) are derived here using an alternative presentation, without introducing the symmetrized error equations and following a rationale similar to the one presented in references [67, 68] for steady-state linear elasticity. This alternative approach requires introducing an auxiliary stress field that stands for the error with respect to the averaged viscous stress, namely

$$\boldsymbol{\sigma}_{\text{ave}}^{\text{e},\nu} := \boldsymbol{\sigma}^{\nu} - \frac{1}{2} (\tilde{\boldsymbol{\sigma}}^{\nu} + \mathbf{s}^{\nu}(\tilde{\mathbf{u}})). \quad (83)$$

Note that  $\boldsymbol{\sigma}_{\text{ave}}^{\text{e},\nu}$  is introduced as a mathematical artifact (it is not computable because it involves the exact solution  $\mathbf{u}$ ) allowing to rewrite the residual  $R^{\text{d}}(\mathbf{e})$  as

$$R^{\text{d}}(\mathbf{e}) = \bar{B}^{\nu}(\tilde{\boldsymbol{\sigma}}^{\text{d,e}}, \mathbf{s}^{\nu}(\mathbf{e})) = \bar{B}^{\nu}(\tilde{\boldsymbol{\sigma}}^{\text{d,e}}, \boldsymbol{\sigma}_{\text{ave}}^{\text{e},\nu}) + \frac{1}{2} \bar{B}^{\nu}(\tilde{\boldsymbol{\sigma}}^{\text{d,e}}, \tilde{\boldsymbol{\sigma}}^{\text{e}}). \quad (84)$$

Hence, the bounds for  $R^d(\mathbf{e})$  are obtained bounding the value  $\bar{B}^\nu(\tilde{\boldsymbol{\sigma}}^{d,e}, \boldsymbol{\sigma}_{\text{ave}}^{e,\nu})$  which is the only non-computable term in the right hand side of equation (84). The computable bound for  $\bar{B}^\nu(\tilde{\boldsymbol{\sigma}}^{d,e}, \boldsymbol{\sigma}_{\text{ave}}^{e,\nu})$  is derived by applying the Cauchy-Schwartz inequality

$$|\bar{B}^\nu(\tilde{\boldsymbol{\sigma}}^{d,e}, \tilde{\boldsymbol{\sigma}}_{\text{ave}}^e)| \leq \|\tilde{\boldsymbol{\sigma}}^{d,e}\|_\sigma \|\tilde{\boldsymbol{\sigma}}_{\text{ave}}^{e,\nu}\|_\sigma, \quad (85)$$

and then bounding  $\|\tilde{\boldsymbol{\sigma}}_{\text{ave}}^{e,\nu}\|_\sigma$ . The following theorem proves that the constitutive relation error  $\tilde{\boldsymbol{\sigma}}^e$  provides a bound for  $\|\tilde{\boldsymbol{\sigma}}_{\text{ave}}^{e,\nu}\|_\sigma$ .

**Theorem 3.** *The constitutive relation error  $\tilde{\boldsymbol{\sigma}}^e$  defined in equation (70) leads to the following upper bound of the averaged stress error  $\boldsymbol{\sigma}_{\text{ave}}^{e,\nu}$  defined in equation (83),*

$$\frac{1}{2} \|\tilde{\boldsymbol{\sigma}}^e\|_\sigma \geq \|\boldsymbol{\sigma}_{\text{ave}}^{e,\nu}\|_\sigma. \quad (86)$$

*Proof.* Using the relation  $\boldsymbol{\sigma}_{\text{ave}}^{e,\nu} = \mathbf{s}^\nu(\mathbf{e}) - \frac{1}{2}\tilde{\boldsymbol{\sigma}}^e$ , the value  $\|\boldsymbol{\sigma}_{\text{ave}}^{e,\nu}\|_\sigma^2$  is rewritten as

$$\begin{aligned} \|\boldsymbol{\sigma}_{\text{ave}}^{e,\nu}\|_\sigma^2 &= \frac{1}{4} \|\tilde{\boldsymbol{\sigma}}^e\|_\sigma^2 + \|\mathbf{s}^\nu(\mathbf{e})\|_\sigma^2 - \bar{B}^\nu(\mathbf{s}^\nu(\mathbf{e}), \tilde{\boldsymbol{\sigma}}^e), \\ &= \frac{1}{4} \|\tilde{\boldsymbol{\sigma}}^e\|_\sigma^2 + \bar{B}^\nu(\mathbf{s}^\nu(\mathbf{e}), \mathbf{s}^\nu(\mathbf{e}) - \tilde{\boldsymbol{\sigma}}^e), \\ &= \frac{1}{4} \|\tilde{\boldsymbol{\sigma}}^e\|_\sigma^2 + \bar{B}^\nu(\mathbf{s}^\nu(\mathbf{e}), \boldsymbol{\sigma}^\nu - \tilde{\boldsymbol{\sigma}}^\nu). \end{aligned}$$

The proof is concluded noting that  $\bar{B}^\nu(\mathbf{s}^\nu(\mathbf{e}), \boldsymbol{\sigma}^\nu - \tilde{\boldsymbol{\sigma}}^\nu) \leq 0$ , which directly proves that (86) holds.

The statement  $\bar{B}^\nu(\mathbf{s}^\nu(\mathbf{e}), \boldsymbol{\sigma}^\nu - \tilde{\boldsymbol{\sigma}}^\nu) \leq 0$  is proved noting that, for an admissible pair  $(\tilde{\mathbf{u}}, \tilde{\boldsymbol{\sigma}}) \in \mathcal{U} \times \mathcal{S}(\tilde{\mathbf{u}})$ , the following relation holds

$$0 = \int_I (\rho(\ddot{\mathbf{u}} - \ddot{\tilde{\mathbf{u}}}, \dot{\mathbf{e}}) dt + \int_I (\boldsymbol{\sigma} - \tilde{\boldsymbol{\sigma}}, \boldsymbol{\varepsilon}(\dot{\mathbf{e}})) dt. \quad (87)$$

Then, injecting the expression

$$\boldsymbol{\sigma} - \tilde{\boldsymbol{\sigma}} = \mathbf{s}^E(\mathbf{u} - \tilde{\mathbf{u}}) + \boldsymbol{\sigma}^\nu - \tilde{\boldsymbol{\sigma}}^\nu,$$

into equation (87) one has

$$\begin{aligned} 0 &= \int_I (\rho\ddot{\mathbf{e}}, \dot{\mathbf{e}}) dt + \int_I a(\mathbf{e}, \dot{\mathbf{e}}) dt + \bar{B}^\nu(\mathbf{s}^\nu(\mathbf{e}), \boldsymbol{\sigma}^\nu - \tilde{\boldsymbol{\sigma}}^\nu) \\ &= \frac{1}{2} \int_I \frac{d}{dt} (\rho\dot{\mathbf{e}}, \dot{\mathbf{e}}) dt + \frac{1}{2} \int_I \frac{d}{dt} a(\mathbf{e}, \mathbf{e}) dt + \bar{B}^\nu(\mathbf{s}^\nu(\mathbf{e}), \boldsymbol{\sigma}^\nu - \tilde{\boldsymbol{\sigma}}^\nu) \\ &= \frac{1}{2} [\|\dot{\mathbf{e}}\|_m^2 + \|\mathbf{e}\|_a^2]_{t=0}^{t=T} + \bar{B}^\nu(\mathbf{s}^\nu(\mathbf{e}), \boldsymbol{\sigma}^\nu - \tilde{\boldsymbol{\sigma}}^\nu). \end{aligned}$$

Taking into account that  $\mathbf{e}(0) = \dot{\mathbf{e}}(0) = \mathbf{0}$ , one has

$$\bar{B}^\nu(\mathbf{s}^\nu(\mathbf{e}), \boldsymbol{\sigma}^\nu - \tilde{\boldsymbol{\sigma}}^\nu) = -\frac{1}{2} \|\dot{\mathbf{e}}(T)\|_m^2 - \frac{1}{2} \|\mathbf{e}(T)\|_a^2,$$

which proves that  $\bar{B}^\nu(\mathbf{s}^\nu(\mathbf{e}), \boldsymbol{\sigma}^\nu - \tilde{\boldsymbol{\sigma}}^\nu) \leq 0$ .  $\square$

Using equations (85) and (86), the computable bound for  $|\bar{B}^\nu(\tilde{\boldsymbol{\sigma}}^{\text{d,e}}, \tilde{\boldsymbol{\sigma}}_{\text{ave}}^{\text{e}})|$  is readily obtained as

$$|\bar{B}^\nu(\tilde{\boldsymbol{\sigma}}^{\text{d,e}}, \tilde{\boldsymbol{\sigma}}_{\text{ave}}^{\text{e}})| \leq \frac{1}{2} \|\tilde{\boldsymbol{\sigma}}^{\text{d,e}}\|_\sigma \|\tilde{\boldsymbol{\sigma}}^{\text{e}}\|_\sigma. \quad (88)$$

Using equation (88) together with equations (84) and (37), the result given in equation (82) is derived in an alternative way, without using the symmetrized error equations.

### 6.3 Construction of D-admissible fields

This section describes in detail the computation of a D-admissible stress  $\tilde{\boldsymbol{\sigma}} \in \mathcal{S}(\tilde{\mathbf{u}})$ , given a K-admissible field  $\tilde{\mathbf{u}} \in \mathcal{U}$ . The presentation focuses in the original problem because the same methodology is used also for the adjoint problem.

The stress  $\tilde{\boldsymbol{\sigma}} \in \mathcal{S}(\tilde{\mathbf{u}})$  is characterized by a series of stresses  $\tilde{\boldsymbol{\sigma}}_n$ ,  $n = 0, \dots, N$  at the time points in  $\mathcal{T}$ . Each  $\tilde{\boldsymbol{\sigma}}_n$  is seen as a statically equilibrated stress field for some loading. Thus, the D-admissible stress  $\tilde{\boldsymbol{\sigma}}$  is eventually computed solving a series of static equilibration problems following the standard procedures described in [9, 8, 66].

The following theorem demonstrates how the the D-admissible stress  $\tilde{\boldsymbol{\sigma}} \in \mathcal{S}(\tilde{\mathbf{u}})$  can be computed in terms of the statically equilibrated stresses  $\tilde{\boldsymbol{\sigma}}_n$ ,  $n = 0, \dots, N$ .

**Theorem 4.** *Given the external loads  $\mathbf{f}, \mathbf{g}$  and a K-admissible field  $\tilde{\mathbf{u}} \in \mathcal{U}$ , then a D-admissible stress  $\tilde{\boldsymbol{\sigma}} \in \mathcal{S}(\tilde{\mathbf{u}})$  is straightforwardly defined through piecewise linear interpolation in time*

$$\tilde{\boldsymbol{\sigma}}(\mathbf{x}, t) := \sum_{n=0}^N \tilde{\boldsymbol{\sigma}}_n(\mathbf{x}) \theta_n(t), \quad (89)$$

provided that: 1) the stress fields  $\tilde{\boldsymbol{\sigma}}_n$ ,  $n = 0, \dots, N$  fulfill the static equilibrium condition

$$(\tilde{\boldsymbol{\sigma}}_n, \boldsymbol{\varepsilon}(\mathbf{w})) = l_n(\mathbf{w}) - (\rho \ddot{\mathbf{u}}_n, \mathbf{w}) \quad \forall \mathbf{w} \in \mathcal{V}_0, \quad (90)$$

or equivalently

$$\nabla \cdot \tilde{\boldsymbol{\sigma}}_n = \mathbf{f}_n - \rho \ddot{\mathbf{u}}_n \quad \text{in } \Omega^{\text{int}}, \quad (91a)$$

$$[[\tilde{\boldsymbol{\sigma}}_n \cdot \mathbf{n}]] = \mathbf{0} \quad \text{on } \Gamma^{\text{int}}, \quad (91b)$$

$$\tilde{\boldsymbol{\sigma}}_n \cdot \mathbf{n} = \mathbf{g}_n \quad \text{on } \Gamma_N, \quad (91c)$$

and 2) the external loads  $\mathbf{f}, \mathbf{g}$  and the acceleration  $\ddot{\mathbf{u}}$  are piecewise linear in time, i.e.

$$\mathbf{f}(\mathbf{x}, t) = \sum_{n=0}^N \mathbf{f}_n(\mathbf{x}) \theta_n(t), \quad (92a)$$

$$\mathbf{g}(\mathbf{x}, t) = \sum_{n=0}^N \mathbf{g}_n(\mathbf{x}) \theta_n(t), \quad (92b)$$

$$\ddot{\mathbf{u}}(\mathbf{x}, t) = \sum_{n=0}^N \ddot{\mathbf{u}}_n(\mathbf{x}) \theta_n(t). \quad (92c)$$

Most of the techniques providing D-admissible stresses, see [9, 8, 66], require as input an approximation of the stresses, say  $\boldsymbol{\sigma}_n^{H,\Delta t} \approx \boldsymbol{\sigma}(t_n)$ , fulfilling a discrete form of (90), namely

$$(\rho \ddot{\mathbf{u}}_n, \mathbf{w}) + (\boldsymbol{\sigma}_n^{H,\Delta t}, \boldsymbol{\varepsilon}(\mathbf{w})) = l_n(\mathbf{w}) \quad \forall \mathbf{w} \in \mathcal{V}_0^H, \quad (93)$$

being  $\mathcal{V}_0^H$  the usual functional space associated with the computational mesh. This relation guarantees that the local problems are solvable.

Note that equation (93) holds defining the admissible solution  $\tilde{\mathbf{u}}$  as in (7), that is  $\ddot{\mathbf{u}}_n = \mathbf{a}_n^{H,\Delta t}$ , and taking discrete stress as  $\boldsymbol{\sigma}_n^{H,\Delta t} := \mathcal{C} : \boldsymbol{\varepsilon}(\mathbf{u}_n^{H,\Delta t} + a_2 \mathbf{v}_n^{H,\Delta t})$  (being  $\mathbf{u}_n^{H,\Delta t}$  and  $\mathbf{v}_n^{H,\Delta t}$  the Newmark displacements and velocities).

### 6.3.1 The hybrid fluxes method

The hybrid fluxes method introduced by Ladevèze in [2] is a classical stress equilibration technique. It is also denoted in more recent works by EET (Element Equilibration Technique). This methodology provides stress fields  $\tilde{\boldsymbol{\sigma}}_n$ ,  $n = 0, \dots, N$ , fulfilling equations (90) and (91). The construction of the equilibrated stress field  $\tilde{\boldsymbol{\sigma}}_n$  is based on some approximate stress  $\boldsymbol{\sigma}_n^{H,\Delta t}$  that is taken as the input of the procedure. This section is devoted to present this methodology, stressing the technical details of its application to compute D-admissible stresses.

Some additional notations are needed to introduce the hybrid fluxes method. The location of a generic node of the computational mesh is denoted by  $\mathbf{x}_i$ ,  $i = 1, \dots, N_{\text{no}}$ , being  $N_{\text{no}}$  the total number of nodes. As introduced before, elements in the mesh are denoted by  $\Omega_k \subset \Omega$ ,  $k = 1, \dots, N_{\text{el}}$ , where  $N_{\text{el}}$  is the total number of elements. Element sides (or faces in 3D) are denoted by  $\Gamma_l \subset \bar{\Omega}$ ,  $l = 1, \dots, N_{\text{fa}}$ , being  $N_{\text{fa}}$  their total number (note that  $\Gamma_l$  is either an inter-element boundary, that is  $\Gamma_l = \partial\Omega_k \cap \partial\Omega_{k'}$  for some  $k$  and  $k'$  or a boundary element side, that is  $\Gamma_l = \partial\Omega_k \cap \partial\Omega$  for some  $k$ ). Also, some sets of indices are introduced describing the connectivity of every node  $\mathbf{x}_i$ , element  $\Omega_k$  and face  $\Gamma_l$ . The set  $\mathcal{N}(\Omega_k)$  is the standard connectivity information containing the indices of the nodes of element  $\Omega_k$ . The set  $\mathcal{E}(\mathbf{x}_i)$  contains the indices of the elements to which node  $\mathbf{x}_i$  belongs. The set  $\mathcal{F}(\mathbf{x}_i)$  contains the indices of the sides/faces to which node  $\mathbf{x}_i$  belongs. The set  $\mathcal{F}(\Omega_k)$  contains the indices of the faces of element  $\Omega_k$ . Finally, the set  $\mathcal{N}(\Gamma_l)$  contains the indices of the nodes of face  $\Gamma_l$ . Figure 8 illustrates the definitions of these sets.

The equilibrated stresses  $\tilde{\boldsymbol{\sigma}}_n$  at time  $t_n$ ,  $n = 0, \dots, N$ , is computed solving local equilibrium problems element-by-element. Each local problem consists in finding the restriction of  $\tilde{\boldsymbol{\sigma}}_n$  to element  $\Omega_k$  of the mesh,  $k = 1, \dots, N_{\text{el}}$ , such that

$$\nabla \cdot \tilde{\boldsymbol{\sigma}}_n = \mathbf{f}_n - \rho \ddot{\mathbf{u}}_n \quad \text{in } \Omega_k, \quad (94a)$$

$$\tilde{\boldsymbol{\sigma}}_n \cdot \mathbf{n}_k = \eta_{kl} \mathbf{t}_n \quad \text{on } \partial\Gamma_l \subset \Omega_k. \quad (94b)$$

It is worth noting that the boundary conditions (94b) for the local problem (94) are not known and they require obtaining the inter-element tractions  $\mathbf{t}_n$ , defined on every  $\Gamma_l$ , for  $l = 1, \dots, N_{\text{fa}}$ . The coefficient  $\eta_{kl}$  takes the values 1 or -1, depending on the orientation of the face  $\Gamma_l$  with respect to  $\Omega_k$ . It is assumed that the orientation of  $\Gamma_l$  is given by a

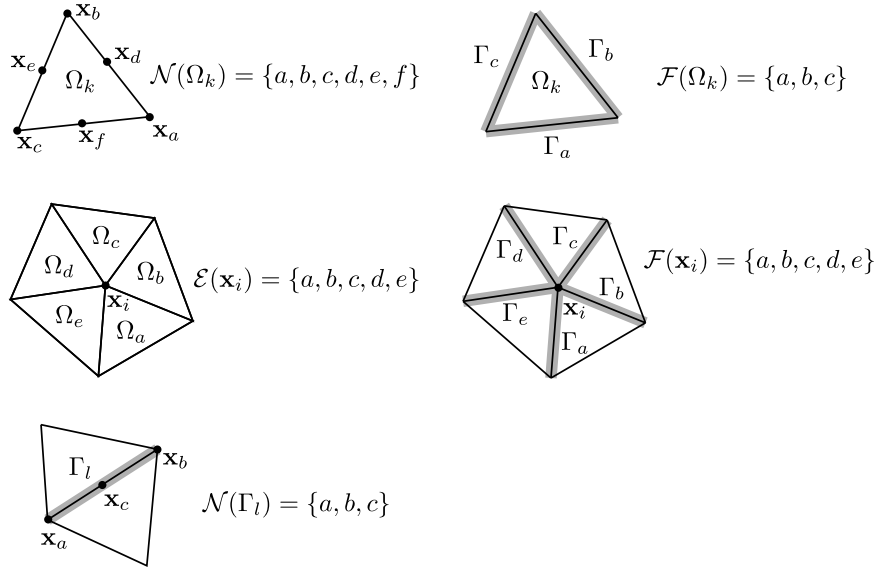


Figure 8: Illustration of sets  $\mathcal{N}(\Omega_k)$ ,  $\mathcal{F}(\Omega_k)$ ,  $\mathcal{E}(\mathbf{x}_i)$ ,  $\mathcal{F}(\mathbf{x}_i)$  and  $\mathcal{N}(\Gamma_l)$ .

normal unit vector  $\tilde{\mathbf{n}}_l$  and then  $\eta_{kl} = \tilde{\mathbf{n}}_l \cdot \mathbf{n}_k$ . Moreover, equation(94) is a pure Neumann problem and therefore is only well posed if the prescribed loads, the body forces and the tractions in the right-hand-sides of (94a) and (94b), are in equilibrium.

Thus, the inter-element tractions  $\mathbf{t}_n$  must be computed previous to solving the local problems (94) and they must fulfill local equilibrium, namely

$$\sum_{l \in \mathcal{F}(\Omega_k)} \int_{\Gamma_l} \eta_{kl} \mathbf{t}_n \cdot \mathbf{w} \, d\Gamma + \int_{\Omega_k} (\mathbf{f}_n - \rho \ddot{\mathbf{u}}_n) \cdot \mathbf{w} \, d\Omega = 0, \quad (95)$$

for all  $\mathbf{w}$  in the space of rigid body motions. This space is defined as (in 3D)  $\text{span}\{(1, 0, 0)^T, (0, 1, 0)^T, (0, 0, 1)^T, (-y, x, 0)^T, (-z, 0, x)^T, (0, -z, y)^T\}$ .

On the faces on the Neumann boundary, that is for  $\Gamma_l \subset \Gamma_N$ , the tractions have to match the actual boundary conditions (91c), that is  $\eta_{kl} \mathbf{t}_n = \mathbf{g}_n$ .

At the first sight, obtaining the inter-element tractions  $\mathbf{t}_n$  fulfilling (95) leads to a global problem and requires solving the unknowns for all the faces  $\Gamma_l$ , for  $l = 1, \dots, N_{\text{fa}}$ , resulting in a large system of linear equations. In practice, this problem is decoupled into local computations thanks to the idea introduced in [2], which is based on enforcing locally (for each element  $\Omega_k$ ) the so-called *prolongation condition*

$$\int_{\Omega_k} (\tilde{\boldsymbol{\sigma}}_n - \boldsymbol{\sigma}_n^{H, \Delta t}) \cdot \nabla \varphi_i \, d\Omega = \mathbf{0} \quad \forall i \in \mathcal{N}(\Omega_k), \quad (96)$$

where  $\varphi_i$  is the shape function associated with node  $\mathbf{x}_i$ . Note that this additional restriction is selecting a particular solution for  $\mathbf{t}_n$  and hence of  $\tilde{\boldsymbol{\sigma}}_n$ . The problem (95) is decoupled into local computations precisely for this particular solution.

Assuming that  $\boldsymbol{\sigma}^{H,\Delta t}$  is such that (93) holds, enforcing the prolongation condition (96) is equivalent to find  $\mathbf{t}_n$  such that

$$\sum_{l \in \mathcal{F}(\Omega_k)} \int_{\Gamma_l} \eta_{kl} \mathbf{t}_n \varphi_i \, d\Gamma = \int_{\Omega_k} (\boldsymbol{\sigma}_n^{H,\Delta t} \cdot \nabla \varphi_i - (\mathbf{f}_n - \rho \ddot{\mathbf{u}}_n) \varphi_i) \, d\Omega, \quad (97)$$

for all mesh elements  $\Omega_k$ ,  $k = 1, \dots, N_{\text{el}}$  and for all nodes  $i \in \mathcal{N}(\Omega_k)$ , pertaining to element  $\Omega_k$ .

If  $\mathbf{t}_n$  fulfills (97) and (93) holds, then the equilibrium condition (95) is satisfied and  $\tilde{\boldsymbol{\sigma}}_n$  can be computed solving the local problems (94). Thus, the tractions  $\mathbf{t}_n$  are obtained such that they fulfill equation (97).

The following definitions are introduced:

$$\mathbf{b}_{il} := \int_{\Gamma_l} \mathbf{t}_n \varphi_i \, d\Gamma \quad \text{and} \quad \mathbf{j}_{ki} := \int_{\Omega_k} (\boldsymbol{\sigma}_n^{H,\Delta t} \cdot \nabla \varphi_i - (\mathbf{f}_n - \rho \ddot{\mathbf{u}}_n) \varphi_i) \, d\Omega. \quad (98)$$

Note that  $\mathbf{b}_{il}$  is nonzero only if  $l \in \mathcal{F}(\mathbf{x}_i)$  or, conversely, if  $i \in \mathcal{N}(\Gamma_l)$ . Thus, equation (97) yields

$$\sum_{l \in (\mathcal{F}(\Omega_k) \cap \mathcal{F}(\mathbf{x}_i))} \eta_{kl} \mathbf{b}_{il} = \mathbf{j}_{ki}, \quad (99)$$

for all mesh elements  $\Omega_k$ ,  $k = 1, \dots, N_{\text{el}}$  and for all nodes  $i \in \mathcal{N}(\Omega_k)$ .

Expression (99) is a linear system of vectorial equations (vectorial, in the sense that  $\mathbf{b}_{il}$  and  $\mathbf{j}_{ki}$  are vectors). The number of vectorial equations is equal to the number of elements  $N_{\text{el}}$  times the number of element nodes (i.e. three for linear triangles). The unknowns are the values  $\mathbf{b}_{il}$ , for  $l = 1, \dots, N_{\text{fa}}$  and  $i \in \mathcal{N}(\Gamma_l)$ , which are the projections of the traction  $\mathbf{t}_n$  in the FE functional space (restricted to the faces). The number of unknowns is  $N_{\text{fa}}$  times the number of edge/face nodes (i.e. two for linear triangles). The number of unknowns is typically larger than the number of equations, and therefore, additional criteria are required to select one of the solutions.

**Remark 5.** *For the sake of illustration, the equations and unknowns accounting is performed for linear 2D triangles in the case of a Dirichlet problem. The number of equations in (99) is  $N_{\text{eq}} = 3N_{\text{el}}$  and the number of unknowns is  $N_{\text{unk}} = 2N_{\text{fa}}$ . The number of mesh faces is expressed in terms of the number of mesh elements as  $N_{\text{fa}} = \frac{3}{2}N_{\text{el}} + \frac{1}{2}N_{\partial\Omega}$ , where  $N_{\partial\Omega}$  is the number of faces on the boundary. Thus, the number of unknowns and equations are such that  $N_{\text{unk}} = N_{\text{eq}} + N_{\partial\Omega} > N_{\text{eq}}$ .*

At first sight, expression (99) leads to a global system of equations, involving the complete computational domain. However, the global system is decoupled into  $N_{\text{no}}$  local systems, associated with each node of the mesh,  $\mathbf{x}_i$ , and involving only the unknowns  $\mathbf{b}_{il}$  for  $l \in \mathcal{F}(\mathbf{x}_i)$ . In other words, the range for  $i$  and  $k$  in the system of equations (99) is rewritten as: for  $i = 1, \dots, N_{\text{no}}$  and then for all  $k \in \mathcal{E}(\mathbf{x}_i)$ . In that sense, for a given value of  $i$ , stating (99) for all  $k \in \mathcal{E}(\mathbf{x}_i)$  leads to a system of equations involving only the unknowns  $\mathbf{b}_{il}$  for  $l \in \mathcal{F}(\mathbf{x}_i)$  which do not participate in any other local system associated

with a different node. For a given  $\mathbf{x}_i$ ,  $i = 1, \dots, N_{\text{no}}$ , the local problem is a reformulation of (99) reading

$$\sum_{l \in (\mathcal{F}(\Omega_k) \cap \mathcal{F}(\mathbf{x}_i))} \eta_{kl} \mathbf{b}_{il} = \mathbf{j}_{ki}, \quad \forall k \in \mathcal{E}(\mathbf{x}_i). \quad (100)$$

All the unknown values  $\mathbf{b}_{il}$ , for  $l = 1, \dots, N_{\text{fa}}$  and  $i \in \mathcal{N}(\Gamma_l)$ , are determined once the local problems are solved for all mesh nodes  $\mathbf{x}_i$ ,  $i = 1, \dots, N_{\text{no}}$ .

The actual resolution of the system (100) depends whether the current node is interior or on the boundary, and (for higher order elements) if the node coincides with a mesh vertex or not. See reference [9] for a detailed discussion of all these cases.

For the sake of simplicity, the presentation in detail of one of these local systems is restricted to the particular case of an interior (not on the boundary) node  $\mathbf{x}_i$ , being also an element vertex. In this case, the number of equations in system (100) is  $\#\mathcal{E}(\mathbf{x}_i)$  (one for each element in  $\mathcal{E}(\mathbf{x}_i)$ ,  $\#$  denotes the cardinal) and the number of unknowns is  $\#\mathcal{F}(\mathbf{x}_i)$  (one for each face in  $\mathcal{F}(\mathbf{x}_i)$ ). Note that the number of elements in  $\mathcal{E}(\mathbf{x}_i)$  coincides with the number of faces in  $\mathcal{F}(\mathbf{x}_i)$  because the node  $\mathbf{x}_i$  is interior. Thus, the local system (100) has the same number of equations and unknowns. The square matrix associated with the local system of equations (100) has entries  $\eta_{kl}$  (thus, equal to  $\pm 1$  or equal to 0 if  $k \notin \mathcal{E}(\Gamma_l)$ ) and does not have full rank. The rank deficiency is readily shown by summing up all the equations of system (100) (summing up in  $k$ ). Note that for a given face  $\Gamma_l$  there are only two adjacent elements, say  $\tilde{k}$  and  $\tilde{k}'$ . Consequently, the resulting equation is

$$\sum_{l \in \mathcal{F}(\mathbf{x}_i)} (\eta_{\tilde{k}l} + \eta_{\tilde{k}'l}) \mathbf{b}_{il} = \sum_{k \in \mathcal{E}(\mathbf{x}_i)} \mathbf{j}_{ki},$$

Note that  $\eta_{\tilde{k}l} + \eta_{\tilde{k}'l} = 0$  and therefore problem (100) is solvable only if the right hand side data fulfills

$$\sum_{k \in \mathcal{E}(\mathbf{x}_i)} \mathbf{j}_{ki} = \mathbf{0}.$$

The previous requirement is fulfilled if equation (93) holds. In fact, this is a version of the Galerkin orthogonality property. Under this assumption, system (100) is compatible but, due to the rank deficiency, it has infinite solutions. A particular solution is found such that it minimizes the functional

$$\Phi_i(\mathbf{b}_{il}) := \frac{1}{2} \sum_{l \in \mathcal{F}(\mathbf{x}_i)} (\mathbf{b}_{il} - \bar{\mathbf{b}}_{il})^2,$$

with

$$\bar{\mathbf{b}}_{il} := \frac{1}{2} \int_{\Gamma_l} (\boldsymbol{\sigma}_n^{H,\Delta t}|_{\Omega_{\tilde{k}}} + \boldsymbol{\sigma}_n^{H,\Delta t}|_{\Omega_{\tilde{k}'}}) \cdot \tilde{\mathbf{n}}_l \varphi_i \, d\Gamma.$$

Once the quantities  $\mathbf{b}_{il}$ , for  $l = 1, \dots, N_{\text{fa}}$  and  $i \in \mathcal{N}(\Gamma_l)$ , are available, the tractions  $\mathbf{t}_n$  are completely determined. In some cases, is it useful to parametrize tractions  $\mathbf{t}_n$  using nodal values instead of quantities  $\mathbf{b}_{il}$ . Specifically, the nodal values parametrizing the

restriction of  $\mathbf{t}_n$  to the face  $\Gamma_l$  are obtained solving a linear system of equations with the *mass* matrix with entries

$$\int_{\Gamma_l} \varphi_i \varphi_j \, d\Gamma, \quad i, j \in \mathcal{N}(\Gamma_l),$$

and the right hand side vector containing the values  $\mathbf{b}_{il}$ ,  $i \in \mathcal{N}(\Gamma_l)$ . For 2D linear elements, the system to be solved at each element side has two unknowns and two equations.

Once the tractions  $\mathbf{t}_n$  are available, the stress field  $\tilde{\boldsymbol{\sigma}}_n$  is obtained solving the local problems (94) in each element  $\Omega_k$ . The local Neumann problems (94) can be solved taking as unknowns either displacements (standard FE approach) or stresses (the so-called dual formulations). The standard displacement-based approach uses a finite element solver locally, selecting a reference mesh (created with  $H$  or  $p$  refinement) discretizing each element. The local approximate solution undervaluates the energy of the exact solution and therefore the global upper bound property is not strictly guaranteed. The resulting estimates are referred as *asymptotic* [69] because the upper bound property holds only asymptotically, as the element size of the reference mesh tends to zero (or the degree of the polynomial tends to infinity). Alternatively, the dual approach (taking stresses as unknowns) provides directly D-admissible piecewise polynomial solutions for  $\tilde{\boldsymbol{\sigma}}_n$ . In this case, the upper bound property is guaranteed and therefore the estimates are denoted as *strict*.

The general procedure to compute the stress  $\tilde{\boldsymbol{\sigma}}_n$  is summarized in algorithm 1.

**Data:**

- Approximate stress field  $\boldsymbol{\sigma}_n^{H, \Delta t}$ ,
- K-admissible displacement  $\tilde{\mathbf{u}}_n$  and
- geometrical information of the finite element mesh (nodes, elements and faces)

**Result:**

- Equilibrated stress  $\tilde{\boldsymbol{\sigma}}_n$

```

// Compute equilibrated interelement tractions
for  $i = 1, \dots, N_{\text{no}}$  (loop in nodes  $\mathbf{x}_i$ ) do
    | compute  $\mathbf{b}_{il}$ ,  $l = 1, \dots, \mathcal{F}(\mathbf{x}_i)$  solving local system (100);
end
(Traction  $\mathbf{t}_n$  at  $\Gamma_l$ ,  $l = 1, \dots, N_{\text{fa}}$  is characterized from the values  $\mathbf{b}_{il}$ )
// Compute equilibrated stress
for  $k = 1, \dots, N_{\text{el}}$  (loop in elements  $\Omega_k$ ) do
    | compute the equilibrated stress  $\tilde{\boldsymbol{\sigma}}_n$  solving the local problems (94);
end
    
```

**Algorithm 1:** Computation of equilibrated stresses  $\tilde{\boldsymbol{\sigma}}_n$  with the hybrid fluxes method.

### 6.3.2 The flux-free method

The flux free method furnishes equilibrated stresses  $\tilde{\boldsymbol{\sigma}}_n$ ,  $n = 0, \dots, N$ , fulfilling equations (90) and (91) without requiring any equilibrated tractions to set the boundary conditions of the local problems. That is, the local Neumann problems do not require enforcing any flux on the boundary. This reduces considerably the implementation complexity of the method.

The equilibrated stresses  $\tilde{\boldsymbol{\sigma}}_n$ ,  $n = 0, \dots, N$ , are generated as a correction of the computed stress  $\boldsymbol{\sigma}_n^{H,\Delta t}$ ,

$$\tilde{\boldsymbol{\sigma}}_n^{\text{ff}} := \mathbf{C} : \boldsymbol{\varepsilon}(\tilde{\mathbf{e}}_n) + \boldsymbol{\sigma}_n^{H,\Delta t}, \quad (101)$$

where  $\tilde{\mathbf{e}}_n$  is an estimate of the error in displacements, computed solving local flux free problems [66]. As for the hybrid fluxes method, the computed stress  $\boldsymbol{\sigma}_n^{H,\Delta t}$  has to fulfill equation (93) to ensure solvability of the local problems.

For the sake of simplicity, the presentation is restricted to linear elements. In this case, all the nodes  $\mathbf{x}_i$ ,  $i = 1, \dots, N_{\text{no}}$ , are also mesh vertices. The main rationale of the flux free method is to define function  $\tilde{\mathbf{e}}_n$  as the addition of local estimates  $\tilde{\mathbf{e}}_n^i$  associated with the mesh vertices, namely

$$\tilde{\mathbf{e}}_n := \sum_{i=1}^{N_{\text{no}}} \tilde{\mathbf{e}}_n^i. \quad (102)$$

Each local estimate  $\tilde{\mathbf{e}}_n^i$  is computed solving a problem defined in the patch  $\omega^i := \text{supp}(\varphi_i)$  centered at node  $\mathbf{x}_i$ . The local problem is solved with a refined finite element mesh in the patch  $\omega^i$ . The characteristic element size of this refined mesh is  $h \ll H$  and the corresponding functional space is denoted by  $\mathcal{V}_{\omega^i}^h$ .

The local estimate  $\tilde{\mathbf{e}}_n^i$  is one solution of the problem: find  $\tilde{\mathbf{e}}_n^i \in \mathcal{V}_{\omega^i}^h$  such that

$$a(\tilde{\mathbf{e}}_n^i, \mathbf{w}) = R_n(\varphi_i(\mathbf{w} - \boldsymbol{\Pi}^H \mathbf{w})) \quad \forall \mathbf{w} \in \mathcal{V}_{\omega^i}^h, \quad (103)$$

where the weak residual  $R_n$  stands for

$$R_n(\mathbf{w}) := l_n(\mathbf{w}) - (\rho \ddot{\mathbf{u}}_n, \mathbf{w}) - (\boldsymbol{\sigma}_n^{H,\Delta t}, \boldsymbol{\varepsilon}(\mathbf{w})). \quad (104)$$

Here, the operator  $\boldsymbol{\Pi}^H : \mathcal{V}_0 \rightarrow \mathcal{V}_0^H$  is the interpolation operator in  $\mathcal{V}_0^H$ . Once  $\tilde{\mathbf{e}}_n^i$  are computed for  $i = 1, \dots, N_{\text{no}}$  solving (103),  $\tilde{\mathbf{e}}_n$  is recovered using (102) and the stress field  $\tilde{\boldsymbol{\sigma}}_n$  follows from (101).

It is worth noting that the flux-free method requires that the residual  $R_n$  fulfills Galerkin orthogonality. It allows introducing the projection  $\boldsymbol{\Pi}^H \mathbf{w}$  into the residual  $R_n(\cdot)$  which guarantees the well-posedness (solvability) of the local problems. Note that, if equation (93) holds, then the residual  $R_n$  introduced in (104) fulfills

$$R_n(\mathbf{w}) = 0 \quad \forall \mathbf{w} \in \mathcal{V}_0^H.$$

The flux-free recovered stresses  $\tilde{\boldsymbol{\sigma}}_n$  are equilibrated in the asymptotic sense, that is fulfilling equilibrium equations (91) but referred to a discrete space associated with the

reference  $h$ -mesh. Thus, the estimate provided by  $\tilde{\boldsymbol{\sigma}}_n$  does not yield a strict upper bound with respect to the exact error, as indicated in theorem 2. Even though, the flux-free estimate furnishes an asymptotic upper bound, that is the bounding properties hold when the element size  $h$  of the reference mesh tends to zero. The flux free method leads to strict bounds if the local problems are solved in stresses with a dual formulation, see [70] for details.

The procedure to compute the stress field  $\tilde{\boldsymbol{\sigma}}_n$  with the flux free approach is detailed in algorithm 2.

**Data:**

- Approximate stress field  $\boldsymbol{\sigma}_n^{H,\Delta t}$ ,
- K-admissible displacement  $\tilde{\mathbf{u}}_n$  and
- geometrical information of the finite element mesh (nodes and elements).

**Result:**

- Equilibrated stress  $\tilde{\boldsymbol{\sigma}}_n$ .

```

// Compute flux-free error estimate
initialize error estimate:  $\tilde{\mathbf{e}}_n = \mathbf{0}$ ;
for  $i = 1, \dots, N_{\text{no}}$  (loop in nodes  $\mathbf{x}_i$ ) do
    | compute the local estimates  $\tilde{\mathbf{e}}_n^i$  solving local systems (103);
    | add the contribution of  $\tilde{\mathbf{e}}_n^i$  to the global flux free estimate:  $\tilde{\mathbf{e}}_n \leftarrow \tilde{\mathbf{e}}_n + \tilde{\mathbf{e}}_n^i$ ;
end
// Compute equilibrated stress
Post-process  $\tilde{\mathbf{e}}_n$  into  $\tilde{\boldsymbol{\sigma}}_n = \mathcal{C} : \boldsymbol{\varepsilon}(\tilde{\mathbf{e}}_n) + \boldsymbol{\sigma}_n^{H,\Delta t}$ ;
    
```

**Algorithm 2:** Computation of the equilibrated stresses  $\tilde{\boldsymbol{\sigma}}_n$  with the flux-free method.

## 7 Error assessment for timeline-dependent quantities of interest

### 7.1 Timeline-dependent quantities of interest

Reference [71] introduces a new type of goal-oriented estimates assessing the error in so-called *timeline-dependent quantities of interest*. These new quantities are scalar time-dependent outputs of the solution instead of single scalar values and are specially well suited to transient problems. Timeline-dependent quantities are associated with a bounded mapping  $L_{\text{TL}}^{\mathcal{O}}(\cdot)$  taking a function  $\mathbf{w}$  in the solution space  $\mathcal{W}$  and returning a time-dependent scalar function, that is

$$L_{\text{TL}}^{\mathcal{O}} : \mathcal{W} \longrightarrow \mathcal{L}^2(I)$$

$$\mathbf{w} \longmapsto L_{\text{TL}}^{\mathcal{O}}(\mathbf{w}).$$

Note that the functional  $L_{\text{TL}}^{\mathcal{O}}(\cdot)$  is a different mathematical object than the functional  $L^{\mathcal{O}}(\cdot)$  associated with the standard quantities of interest because  $L_{\text{TL}}^{\mathcal{O}}(\cdot)$  returns a time-dependent scalar function and  $L^{\mathcal{O}}(\cdot)$  returns a single scalar value, see figure 9.

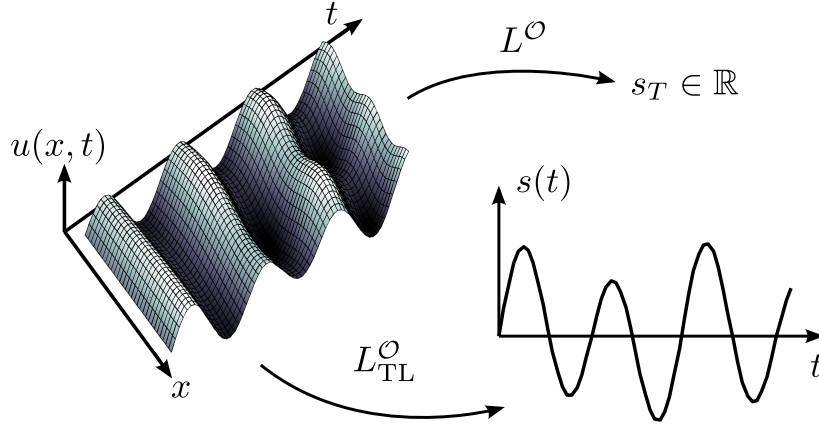


Figure 9: Illustration of scalar and timeline-dependent quantities of interest. The functional  $L^{\mathcal{O}}$  maps the time-space solution  $\mathbf{u}$  into a scalar value  $s_T \in \mathbb{R}$ . The operator  $L_{\text{TL}}^{\mathcal{O}}$  transforms  $\mathbf{u}$  into a time-dependent function  $s(t)$ .

A convenient expression for  $L_{\text{TL}}^{\mathcal{O}}(\cdot)$  is defined as an extension of the functional  $L^{\mathcal{O}}(\cdot)$  defined in (25),

$$[L_{\text{TL}}^{\mathcal{O}}(\mathbf{w})](t) := \int_0^t (\mathbf{f}^{\mathcal{O}}(\tau), \dot{\mathbf{w}}(\tau)) \, d\tau + \int_0^t (\mathbf{g}^{\mathcal{O}}(\tau), \dot{\mathbf{w}}(\tau))_{\Gamma_N} \, d\tau + (\rho \mathbf{v}^{\mathcal{O}}, \dot{\mathbf{w}}(t)) + a(\mathbf{u}^{\mathcal{O}}, \mathbf{w}(t)), \quad (105)$$

where the functions  $\mathbf{f}^{\mathcal{O}}$  and  $\mathbf{g}^{\mathcal{O}}$  define weighted averages of the solution in the interior domain  $\Omega$  or the Neumann boundary  $\Gamma_N$ , respectively, in the time interval  $[0, t]$  for a generic time  $t \in I$ . On the other hand, functions  $\mathbf{v}^{\mathcal{O}}$  and  $\mathbf{u}^{\mathcal{O}}$  define weighted averages of the velocities and displacements, respectively, at a generic time point  $t \in I$ . For the sake of simplicity, the notation  $L_{\text{TL}}^{\mathcal{O}}(\mathbf{w}; t) := [L_{\text{TL}}^{\mathcal{O}}(\mathbf{w})](t)$  is introduced.

The aim of reference [71] is assessing the quality of the computed timeline-dependent quantity,  $\tilde{s}(t) := L_{\text{TL}}^{\mathcal{O}}(\tilde{\mathbf{u}}; t)$ , with respect to the exact quantity of interest,  $s(t) := L_{\text{TL}}^{\mathcal{O}}(\mathbf{u}; t)$ . That is, the goal is to assess the error in the quantity of interest which is now a function of time

$$s^e(t) := s(t) - \tilde{s}(t).$$

## 7.2 Error representation with family of adjoint problems

Assessing the error in the timeline-quantity  $s^e(t)$  requires introducing an error representation similar to the one presented in section 3.4 for the scalar quantity of interest. Thus, an auxiliary problem, analogous to the adjoint problem (24), has to be introduced for the timeline quantity  $L_{\text{TL}}^{\mathcal{O}}(\cdot)$ .

This auxiliary problem is defined noting that, for a given time  $t \in I$ , the value  $s(t) = L_{\text{TL}}^{\mathcal{O}}(\mathbf{u}; t)$  is seen as a scalar quantity of interest taking  $t$  as the *final* time. This scalar quantity of interest is characterized as  $L^{\mathcal{O}}(\cdot) = L_{\text{TL}}^{\mathcal{O}}(\cdot; t)$ . Thus, the adjoint problem associated with  $L_{\text{TL}}^{\mathcal{O}}(\cdot; t)$ , for a given  $t \in I$ , is analogous to the one presented in 3.3 and reads: find  $\mathbf{u}_t^{\text{d}} \in \mathcal{W}|_{[0,t]}$  such that

$$B_t(\mathbf{w}, \mathbf{u}_t^{\text{d}}) = L_{\text{TL}}^{\mathcal{O}}(\mathbf{w}; t) \quad \forall \mathbf{w} \in \mathcal{W}|_{[0,t]}, \quad (106)$$

where the bilinear form  $B_t(\cdot, \cdot)$  is defined as

$$\begin{aligned} B_t(\mathbf{v}, \mathbf{w}) := & \int_0^t (\rho(\ddot{\mathbf{v}}(\tau) + a_1\dot{\mathbf{v}}(\tau)), \dot{\mathbf{w}}(\tau)) \, d\tau + \int_0^t a(\mathbf{v}(\tau) + a_2\dot{\mathbf{v}}(\tau), \dot{\mathbf{w}}(\tau)) \, d\tau \\ & + (\rho\dot{\mathbf{v}}(0^+), \dot{\mathbf{w}}(0^+)) + a(\mathbf{v}(0^+), \mathbf{w}(0^+)), \end{aligned}$$

and the space  $\mathcal{W}|_{[0,t]}$  denotes the restriction of  $\mathcal{W}$  to the time interval  $[0, t]$ .

Note that the solution of equation (106) is denoted by  $\mathbf{u}_t^{\text{d}}$  emphasizing that there is a different solution for each time  $t$ . Consequently, equation (106) describes a family of problems, one for each time  $t$ .

Analogously as for the derivation of the adjoint problem for the scalar quantity of interest (26), the associated strong form of problem (106), for the functional  $L_{\text{TL}}^{\mathcal{O}}(\cdot)$  defined in (105), is readily derived as

$$\rho(\ddot{\mathbf{u}}_t^{\text{d}} - a_1\dot{\mathbf{u}}_t^{\text{d}}) - \nabla \cdot \boldsymbol{\sigma}_t^{\text{d}} = -\mathbf{f}^{\mathcal{O}} \quad \text{in } \Omega \times [0, t], \quad (107a)$$

$$\mathbf{u}_t^{\text{d}} = \mathbf{0} \quad \text{on } \Gamma_{\text{D}} \times [0, t], \quad (107b)$$

$$\boldsymbol{\sigma}_t^{\text{d}} \cdot \mathbf{n} = -\mathbf{g}^{\mathcal{O}} \quad \text{on } \Gamma_{\text{N}} \times [0, t], \quad (107c)$$

$$\mathbf{u}_t^{\text{d}} = \mathbf{u}^{\mathcal{O}} \quad \text{at } \Omega \times \{t\}, \quad (107d)$$

$$\dot{\mathbf{u}}_t^{\text{d}} = \mathbf{v}^{\mathcal{O}} \quad \text{at } \Omega \times \{t\}, \quad (107e)$$

with the constitutive law

$$\boldsymbol{\sigma}_t^{\text{d}} := \mathbf{C} : \boldsymbol{\varepsilon}(\mathbf{u}_t^{\text{d}} - a_2\dot{\mathbf{u}}_t^{\text{d}}). \quad (108)$$

Recall that the data  $\mathbf{f}^{\mathcal{O}}$ ,  $\mathbf{g}^{\mathcal{O}}$ ,  $\mathbf{u}^{\mathcal{O}}$  and  $\mathbf{v}^{\mathcal{O}}$  enters in the definition of  $L_{\text{TL}}^{\mathcal{O}}(\cdot; t)$  as indicated in (105). Note that for each time  $t$ , problem (107) is of the same type as (26) and therefore has to be integrated backwards in time. Thus, the family of adjoint problems associated with the timeline-dependent quantity  $L_{\text{TL}}^{\mathcal{O}}$  is a family of standard problems in elastodynamics.

For a particular instance of time  $t$ , the error representation of the timeline-dependent quantity of interest  $s^e(t)$  is similar to the standard scalar case but taking the adjoint solution  $\mathbf{u}_t^{\text{d}}$  related with the particular value  $t \in I$ , namely

$$s^e(t) = R_t(\mathbf{u}_t^{\text{d}}), \quad (109)$$

where

$$R_t(\mathbf{w}) := L_t(\mathbf{w}; t) - B_t(\tilde{\mathbf{u}}, \mathbf{w}) \quad \text{and}$$

$$L_t(\mathbf{w}) := \int_0^t l(\tau; \dot{\mathbf{w}}(\tau)) \, d\tau + (\rho\mathbf{v}_0, \dot{\mathbf{w}}(0^+)) + a(\mathbf{u}_0, \mathbf{w}(0^+)).$$

Hence, an estimate for  $s^e(t)$  is obtained injecting an enhanced adjoint approximation  $\tilde{\mathbf{u}}_t^d$  in equation (109)

$$s^e(t) \approx R_t(\tilde{\mathbf{u}}_t^d) =: \tilde{s}^e. \quad (110)$$

Obviously, it is not possible, in practice, to independently compute the infinite solutions  $\tilde{\mathbf{u}}_t^d$  (one for each time  $t \in I$ ) and then using them in equation (109) to assess  $s^e(t)$ . However, taking  $\mathbf{f}^\mathcal{O}$  and  $\mathbf{g}^\mathcal{O}$  constant in time (which accounts for a number of interesting cases), the different functions  $\mathbf{u}_t^d$  corresponding to different time instances are all equivalent after a time translation. Thus, if  $\mathbf{u}_t^d$  is properly computed for a particular value of  $t$ , for instance  $t = T$ , the general functions  $\mathbf{u}_t^d$  for  $t \neq T$  are easily recovered as a direct post-process of  $\mathbf{u}_T^d$ . This fundamental result, shown in the following theorem, is the crucial observation that allows the error estimation technique to be brought to fruition.

**Theorem 5.** *For a given  $t$ , let  $\mathbf{u}_t^d$  be the solution of the adjoint problem defined by equations (107). Assume that data  $\mathbf{f}^\mathcal{O}$  and  $\mathbf{g}^\mathcal{O}$  in (105) are constant in time, i.e.  $\mathbf{f}^\mathcal{O}(\mathbf{x}, t) = \mathbf{f}^\mathcal{O}(\mathbf{x})$  and  $\mathbf{g}^\mathcal{O}(\mathbf{x}, t) = \mathbf{g}^\mathcal{O}(\mathbf{x})$ .*

*Then,  $\mathbf{u}_t^d$  is related with the adjoint solution associated with the final time  $T$ ,  $\mathbf{u}_T^d$ , via the time translation*

$$\mathbf{u}_t^d(\tau) = \mathbf{u}_T^d(\tau + T - t). \quad (111)$$

A proof of this theorem may be found in [71].

Consequently, The adjoint approximations  $\tilde{\mathbf{u}}_t^d$  used in the error estimate (110) are computed applying the time shift (111) to the adjoint approximation  $\tilde{\mathbf{u}}_T^d$  associated with the final time  $T$

$$\tilde{\mathbf{u}}_t^d(\tau) := \tilde{\mathbf{u}}_T^d(\tau + T - t). \quad (112)$$

Thus, only one adjoint approximation  $\tilde{\mathbf{u}}_T^d$  has to be computed and the others are simply recovered by a time shift.

### 7.3 Modal-based adjoint approximation

The error estimate  $\tilde{s}^e(t)$  is computed once the approximation  $\tilde{\mathbf{u}}_T^d \approx \mathbf{u}_T^d$  is available. This section is devoted to the actual computation of  $\tilde{\mathbf{u}}_T^d$ . Note that  $\mathbf{u}_T^d$  coincides with the adjoint solution  $\mathbf{u}^d$  associated with the scalar quantity of interest  $L^\mathcal{O}(\cdot)$ . Consequently, computing  $\tilde{\mathbf{u}}_T^d$  is equivalent to compute an approximation  $\tilde{\mathbf{u}}^d \approx \mathbf{u}^d$ .

Function  $\tilde{\mathbf{u}}^d$  (or equivalently  $\tilde{\mathbf{u}}_T^d$ ) is obtained using the standard approximation techniques for elastodynamics. However, if  $\tilde{\mathbf{u}}^d$  has to be used for a timeline estimate  $\tilde{s}^e(t)$ , then, a better option is using *modal analysis*, see reference [71]. The modal based description of  $\tilde{\mathbf{u}}^d$  simplifies the time shift (111) required to assess the error in the timeline quantity and makes the actual computation of  $\tilde{s}^e(t)$  more efficient.

Approximating function  $\tilde{\mathbf{u}}^d$  with modal analysis requires introducing a semidiscrete version (discrete in space and exact in time) of the adjoint problem (26). The semidiscrete

problem reads: find  $\mathbf{u}^{\text{d},H,p+1}(t) \in \mathcal{V}_0^{H,p+1}$  verifying the final conditions  $\mathbf{u}^{\text{d},H,p+1}(T) = \mathbf{u}^\mathcal{O}$  and  $\dot{\mathbf{u}}^{\text{d},H,p+1}(T) = \mathbf{v}^\mathcal{O}$  and such that for all  $t \in I$

$$m(\ddot{\mathbf{u}}^{\text{d},H,p+1}(t) - a_1 \dot{\mathbf{u}}^{\text{d},H,p+1}(t), \mathbf{w}) + a(\mathbf{u}^{\text{d},H,p+1}(t) - a_2 \dot{\mathbf{u}}^{\text{d},H,p+1}(t), \mathbf{w}) = -l^\mathcal{O}(t; \mathbf{w}), \quad (113)$$

for all test function  $\mathbf{w} \in \mathcal{V}_0^{H,p+1}$ , where  $l^\mathcal{O}(t; \mathbf{w}) := (\mathbf{f}^\mathcal{O}(t), \mathbf{w}) + (\mathbf{g}^\mathcal{O}(t), \mathbf{w})_{\Gamma_N}$  and  $\mathcal{V}_0^{H,p+1}$  is the functional space obtained with  $p$ -refinement of the original functional space  $\mathcal{V}_0^H$ .

**Remark 6.** *The spacial resolution of the adjoint approximation  $\tilde{\mathbf{u}}^{\text{d}}$  has to be richer than the one of the numerical approximation  $\tilde{\mathbf{u}}$ . Otherwise, the error is underestimated when plugging the approximation  $\tilde{\mathbf{u}}^{\text{d}}$  into the residual  $R(\cdot)$  by an effect analogous to Galerkin orthogonality. For that reason the functional space used to define the semidiscrete problem (113) is  $\mathcal{V}_0^{H,p+1}$  instead of  $\mathcal{V}_0^H$ .*

A modal-based approximation of the problem (113) is obtained introducing the generalized eigenvalue problem: find  $(\tilde{\omega}, \tilde{\mathbf{q}}) \in \mathbb{R} \times \mathcal{V}_0^{H,p+1}$  such that

$$a(\tilde{\mathbf{q}}, \mathbf{w}) = (\tilde{\omega})^2 m(\tilde{\mathbf{q}}, \mathbf{w}) \quad \forall \mathbf{w} \in \mathcal{V}_0^{H,p+1}. \quad (114)$$

The  $i$ -th eigenpair solution of this problem is referred as  $(\tilde{\omega}_i, \tilde{\mathbf{q}}_i)$ . Note that the number of eigenpairs is the number of degrees of freedom in the functional space  $\mathcal{V}_0^{H,p+1}$ , denoted by  $N_{\text{dof}}$ . Typically, the eigenpairs are sorted from low to high frequencies, namely  $\tilde{\omega}_1 \leq \tilde{\omega}_2 \leq \dots \leq \tilde{\omega}_{N_{\text{dof}}}$ , and eigenvectors are normalized to be orthonormal with respect the product  $m(\cdot, \cdot)$ , i.e.

$$m(\tilde{\mathbf{q}}_i, \tilde{\mathbf{q}}_j) = \delta_{ij}, \quad 1 \leq i, j \leq N_{\text{dof}}. \quad (115)$$

The complexity of the system of ODEs resulting from (113) is considerably reduced by expressing the adjoint solution  $\mathbf{u}^{\text{d},H,p+1}(\mathbf{x}, t)$  as a combination of the eigenvectors  $\tilde{\mathbf{q}}_i, i = 1, \dots, N_{\text{dof}}$ , that is

$$\mathbf{u}^{\text{d},H,p+1}(\mathbf{x}, t) = \sum_{i=1}^{N_{\text{dof}}} \tilde{\mathbf{q}}_i(\mathbf{x}) \tilde{y}_i(t). \quad (116)$$

Thus, the system of ODEs (113) is transformed into the uncoupled set of scalar ordinary differential equations

$$\ddot{\tilde{y}}_i - [a_1 + a_2(\tilde{\omega}_i)^2] \dot{\tilde{y}}_i + (\tilde{\omega}_i)^2 \tilde{y}_i = \tilde{l}_i, \quad (117a)$$

$$\tilde{y}_i(T) = \tilde{u}_i, \quad (117b)$$

$$\dot{\tilde{y}}_i(T) = \tilde{v}_i, \quad (117c)$$

where the r.h.s. terms  $\tilde{l}_i$ ,  $\tilde{u}_i$  and  $\tilde{v}_i$  are computed using the data characterizing the quantity of interest (105) and the eigenvector  $\tilde{\mathbf{q}}_i$ ,

$$\tilde{l}_i(t) := (\mathbf{f}^\mathcal{O}(t), \tilde{\mathbf{q}}_i) + (\mathbf{g}^\mathcal{O}(t), \tilde{\mathbf{q}}_i)_{\Gamma_N}, \quad u_i := m(\mathbf{u}^\mathcal{O}, \tilde{\mathbf{q}}_i) \quad \text{and} \quad v_i := m(\mathbf{v}^\mathcal{O}, \tilde{\mathbf{q}}_i). \quad (118)$$

The cost of modal analysis scales as, see references [72, 73, 74],

$$\mathcal{O}(N_{\text{dof}} \cdot N_{\text{bw}}^2) + \mathcal{O}(N_{\text{dof}}^2 \cdot N_{\text{bw}}) + \mathcal{O}(N_{\text{dof}}^3),$$

where  $N_{\text{bw}}$  denotes the half-bandwidth of the finite element matrices associated with the functional space  $\mathcal{V}_0^{H,p+1}$ . Thus, the modal-based approach is not computationally affordable unless the modal description (116) is truncated up to the first  $M$  terms, being  $M \ll N_{\text{dof}}$ . Consequently, the adjoint approximation  $\tilde{\mathbf{u}}^{\text{d}}$  is defined as the truncated expansion

$$\tilde{\mathbf{u}}^{\text{d}}(\mathbf{x}, t) := \sum_{i=1}^M \tilde{\mathbf{q}}_i(\mathbf{x}) \tilde{y}_i(t). \quad (119)$$

Note that the number of required vibration modes  $M$  has to be selected such that the truncated high frequency modes (for  $i > M$ ) are negligible in (116). That is, such that  $\tilde{\mathbf{u}}^{\text{d}}$  is a good approximation to  $\mathbf{u}^{\text{d},H}$ . This is equivalent to assume that for  $i > M$  the values of  $\tilde{l}_i$ ,  $\tilde{u}_i$  and  $\tilde{v}_i$ , as defined in (118), are close to zero, and consequently  $\tilde{y}_i(t) \approx 0$ . This is guaranteed if the data  $\mathbf{f}^{\mathcal{O}}$ ,  $\mathbf{g}^{\mathcal{O}}$ ,  $\mathbf{u}^{\mathcal{O}}$  and  $\mathbf{v}^{\mathcal{O}}$  are well captured by the expansion of the first  $M$  eigenvectors.

Once  $\tilde{\mathbf{u}}^{\text{d}}$  (or equivalently  $\tilde{\mathbf{u}}_T^{\text{d}}$ ) is available, the adjoint family  $\tilde{\mathbf{u}}_t^{\text{d}}$  is recovered using the time shift (111). Then,  $\tilde{\mathbf{u}}_t^{\text{d}}$  is plugged in equation (110) furnishing the timeline error estimate  $\tilde{s}^e(t)$ .

**Remark 7.** (*Illustrative example*) This example illustrates the performance of the error estimate  $\tilde{s}^e(t)$ . The computational domain is the three dimensional structure plotted in figure 10 which is clamped at the supports and it is loaded with the time-dependent traction

$$\mathbf{g}(t) = \begin{cases} -g(t)\mathbf{e}_1 & \text{on } \Gamma_g, \\ \mathbf{0} & \text{elsewhere,} \end{cases}$$

where function  $g(t)$  is defined in figure 10 and the values  $g_{\text{max}} = 1 \cdot 10^3$  Pa and  $t_g = 1 \cdot 10^{-3}$  s are considered. The set  $\Gamma_g$  is the boundary where the load is applied, see figure 10. The structure is initially at rest ( $\mathbf{u}_0 = \mathbf{v}_0 = \mathbf{0}$ ) and the body force is zero ( $\mathbf{f} = \mathbf{0}$ ). The material properties are Young's modulus  $E = 2 \cdot 10^{10}$  Pa, Poisson's ratio  $\nu = 0.2$ , density  $\rho = 2.4 \cdot 10^3$  kg/m<sup>3</sup> and viscosity  $a_1 = a_2 = 0$ . The final time is  $T = 0.02$  s .

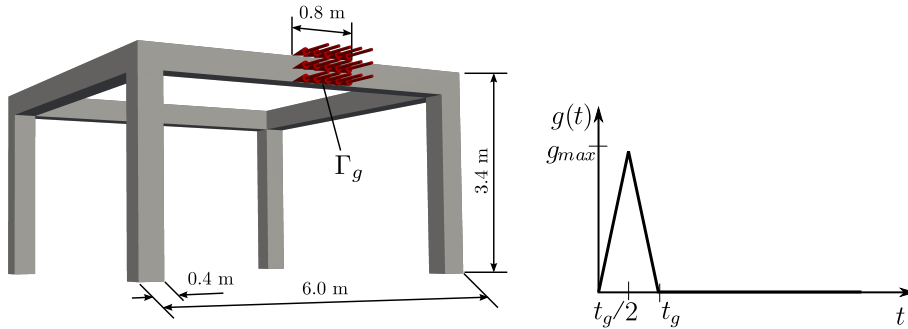


Figure 10: Problem geometry (left) and time description of the external load (right).

This example focuses in the timeline-dependent quantity of interest

$$s(t) := \frac{1}{\text{meas}(\Gamma_g)} (\mathbf{e}_1, \mathbf{u}(t))_{\Gamma_g},$$

which is the average of the  $x$ -component of the displacement in the boundary  $\Gamma_g$  at every time  $t \in I$ .

The problem is discretized with trilinear hexahedra in space and with the Newmark method in time with parameters  $\beta = 1/4$  and  $\gamma = 1/2$ . The approximated quantity of interest  $\tilde{s}(t) = L^{\mathcal{O}}(\tilde{\mathbf{u}}; t)$  is computed from the approximate solution  $\tilde{\mathbf{u}}$  obtained with the coarse finite element mesh plotted in figure 11 and with  $N = 400$  time steps. The reference quantity of interest  $s(t) = L^{\mathcal{O}}(\mathbf{u}; t)$  is obtained by assuming that the exact solution  $\mathbf{u}$  is fairly replaced by a reference solution obtained using the reference mesh in figure 11 and  $N = 1600$  time steps. The error in the quantity of interest is evaluated using the reference solution, namely  $s^e(t) = s(t) - \tilde{s}(t)$ . Finally, the error estimate  $\tilde{s}^e(t)$  is computed using up to  $M = 60$  vibration modes for approximating the adjoints.

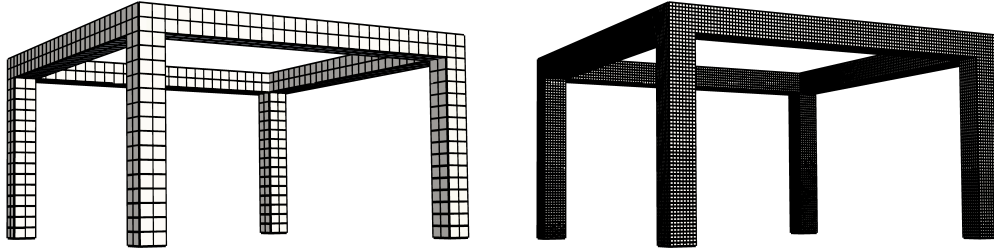


Figure 11: Coarse (left) and reference (right) meshes used in this example with 334 and 22016 elements respectively.

Figure 12 shows the computed and reference timeline-dependent quantities,  $\tilde{s}(t)$  and  $s(t)$ , along with the assessed and reference errors,  $\tilde{s}^e(t)$  and  $s^e(t)$ . Note that the quality of the error estimate  $\tilde{s}^e(t)$  increases with the number of vibration modes. For  $M = 60$  modes, the error estimate  $\tilde{s}^e(t)$  and the reference error  $s^e(t)$  are in very good agreement.

## 8 Closure

The most significant error assessment techniques for structural transient dynamics are reviewed, namely: recovery-based estimates, dual weighted residuals, constitutive relation error and error assessment for timeline-dependent quantities of interest.

The recovery-based estimates for transient dynamics are an extension of the recovery procedures available for steady state linear elasticity. The classical space recovery allows assessing only the space discretization error. Thus, to carry out adaptive procedures, the time discretization errors have to be accounted independently. Moreover, the standard stress recovery techniques are not sufficient to assess the kinetic energy of the error. Thus, a specific recovery procedure is also introduced for the velocities.

The dual weighted residuals approach produces accurate approximations to the error in the quantity of interest and also provides local error indicators for mesh adaptivity. The error estimate is obtained by plugging an enhanced approximation of the adjoint

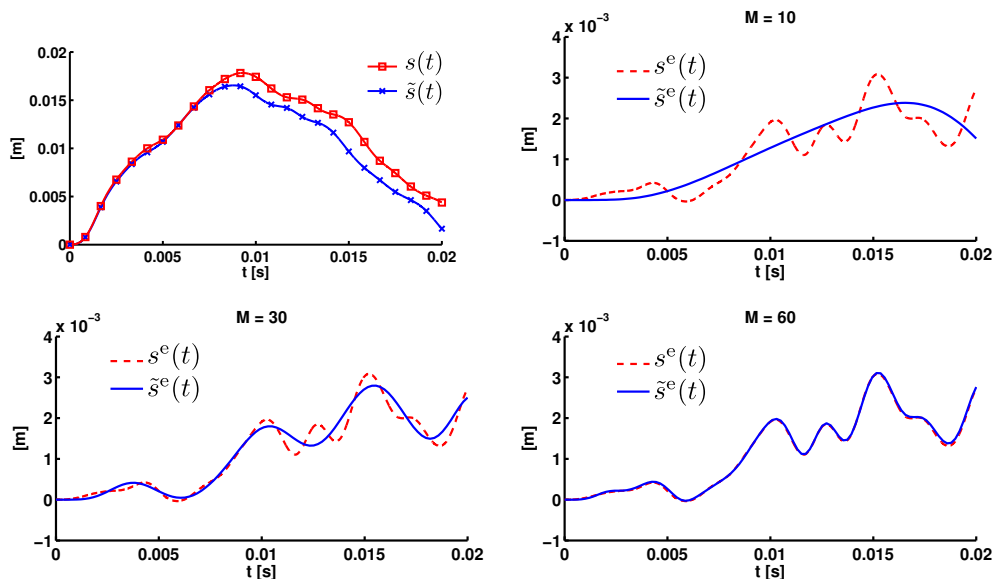


Figure 12: Approximated quantity of interest  $\tilde{s}(t)$  and reference quantity  $s(t)$  (top, left). Reference and assessed errors,  $s^e(t)$  and  $\tilde{s}^e(t)$ , for three different number of vibration modes for approximating the adjoints,  $M = 10$  (top, right),  $M = 30$  (bottom, left) and  $M = 60$  (bottom, right).

problem into the space-time weak residual associated with the numerical solution. This technique accounts for both the space and time discretization errors and it is used to adapt both space and time grids.

The constitutive relation error estimates furnish bounds of the error both in an energy measure and in the quantity of interest. The extension of this technique to elastodynamics is based in a key hypothesis: the formulation contains a certain amount of damping. Thus, the computed bounds degenerate as the value of the damping tends to zero. Computing the error bounds requires obtaining admissible stress fields for both the original and the adjoint problems.

Finally, an error estimate for the so-called timeline-dependent quantities of interest is described. This kind of quantities are scalar time-dependent functions and are specially well suited to analyze the outcome of transient problems. Although at the first sight this type of quantities require characterizing a family of adjoint problems, approximating the adjoint solution with a modal approach constitutes an efficient and affordable tool to assess them.

## Acknowledgment

Partially supported by Ministerio de Educación y Ciencia, Grant DPI2011-27778-C02-02 and Universitat Politècnica de Catalunya (UPC-BarcelonaTech), grant UPC-FPU.

## References

- [1] I. Babuška and W. C. Rheinboldt. Error estimates for adaptive finite element computations. *SIAM J. Numer. Anal.*, 18:736–754, 1978.
- [2] P. Ladevèze and D. Leguillon. Error estimate procedure in the finite element method. *SIAM J. on Numerical Analysis*, 20:485–509, 1983.
- [3] O. C. Zienkiewicz and J. Z. Zhu. A simple error estimator and adaptative procedure for practical engineering analysis. *Int. J. Numer. Meth. Engrg.*, 24:337–357, 1987.
- [4] M. Paraschivoiu, J. Peraire, and A. T. Patera. A posteriori finite element bounds for linear-functional outputs of elliptic partial differential equations. *Comput. Methods Appl. Mech. Engrg.*, 150:289–321, 1997.
- [5] N. Parés, J. Bonet, A. Huerta, and J. Peraire. The computation of bounds for linear-functional outputs of weak solutions to the two-dimensional elasticity equations. *Comput. Methods Appl. Mech. Engrg.*, 195:406–429, 2006.
- [6] F. Cirak and E. Ramm. A posteriori error estimation and adaptivity for linear elasticity using the reciprocal theorem. *Comput. Methods Appl. Mech. Engrg.*, 156:351–362, 1998.
- [7] S. Prudhomme and J. T. Oden. On goal-oriented error estimation for elliptic problems: application to the control of pointwise errors. *Comput. Methods Appl. Mech. Engrg.*, 176:313–331, 1999.
- [8] M. Ainsworth and J. T. Oden. *A posteriori error estimation in Finite element analysis*. John Wiley & Sons Ltd., 2000.
- [9] P. Ladevèze and J. P. Pelle. *La maîtrise du calcul en mécanique linéaire et non linéaire*. Lavoisier, 2001.
- [10] E. Stein. *Error-controlled adaptive finite elements in solid mechanics*. John Wiley & Sons Ltd., 2003.
- [11] M. Ainsworth and J. T. Oden. A posteriori error estimation in finite element analysis. *Comput. Methods Appl. Mech. Engrg.*, 142:1–88, 1997.
- [12] T. Gratsch and K. J. Bathe. A posteriori error estimation techniques in practical finite element analysis. *Computers and Structures*, 83:235–265, 2005.
- [13] P. Díez, N. Parés, and A. Huerta. *Encyclopedia of Aerospace Engineering*, chapter Error estimation and quality control. John Wiley & Sons Ltd., 2010.
- [14] R. Rannacher. Adaptive Galerkin finite element methods for partial differential equations. *Journal of Computational and Applied Mathematics*, 128:205–233, 2001.

- [15] L. Gallimard, P. Ladeveze, and J. P. Pelle. An enhanced error estimator on the constitutive relation for plasticity problems. *Computers and Structures*, 78:801–810, 2000.
- [16] P. Ladevèze. Constitutive relation errors for fe analysis considering (visco-)plasticity and damage. *Int. J. Numer. Meth. Engrg.*, 52:527–542, 2001.
- [17] P. Ladevèze and N. Moës. Adaptive control for finite element analysis in plasticity. *Computers and Structures*, 73:45–60, 1999.
- [18] P. Ladevèze, N. Moës, and B. Douchin. Constitutive relation error estimators for (visco)plastic finite element analysis with softening. *Comput. Methods Appl. Mech. Engrg.*, 176:247–264, 2000.
- [19] N. Parés, P. Díez, and A. Huerta. Exact bounds of the advection-diffusion-reaction equation using flux-free error estimates. *SIAM J. Sci. Comput.*, 31:3064–3089, 2009.
- [20] F. Larsson, P. Díez, and A. Huerta. A flux-free a posteriori error estimator for the incompressible Stokes problem using a mixed FE formulation. *Comput. Methods Appl. Mech. Engrg.*, 199:2383–2402, 2010.
- [21] N. Parés, P. Díez, and A. Huerta. Bounds of functional outputs for parabolic problems. Part I: Exact bounds of the discontinuous galerkin time discretization. *Comput. Methods Appl. Mech. Engrg.*, 197:1641–1660, 2008.
- [22] N. Parés, P. Díez, and A. Huerta. Bounds of functional outputs for parabolic problems. Part II: Bounds of the exact solution. *Comput. Methods Appl. Mech. Engrg.*, 197:1661–1679, 2008.
- [23] P. Díez and G. Calderón. Goal-oriented error estimation for transient parabolic problems. *Comput. Mech.*, 39:631–646, 2007.
- [24] M. G. Larson and F. Bengzon. Adaptive finite element approximation of multiphysics problems. *Commun. Numer. Methods Engrg.*, 24:505–521, 2008.
- [25] M. G. Larson, R. Soderlund, and F. Bengzon. Adaptive finite element approximation of coupled flow and transport problems with applications in heat transfer. *Int. J. Numer. Meth. Fluids*, 57:1397–1420, 2008.
- [26] P. W. Fick, E. H. van Brummelen, and K. G. van der Zee. On the adjoint-consistent formulation of interface conditions in goal-oriented error estimation and adaptivity for fluid-structure interaction. *Comput. Methods Appl. Mech. Engrg.*, 199:3369–3385, 2010.
- [27] K. G. van der Zee, E. H. van Brummelen, I. Akkerman, and R. de Borst. Goal-oriented error estimation and adaptivity for fluid-structure interaction using exact linearized adjoints. *Comput. Methods Appl. Mech. Engrg.*, 200:2738–2757, 2011.
- [28] L. Asner, S. Tavener, and D. Kay. Adjoint-based a posteriori error estimation for coupled time-dependent systems. *SIAM J. Sci. Comput.*, 34:2394–2419, 2012.

- [29] X. D. Li and N. E. Wiberg. Implementation and adaptivity of a space-time finite element method for structural dynamics. *Comput. Methods Appl. Mech. Engrg.*, 156:211–229, 1998.
- [30] N. E. Wiberg and X. D. Li. Adaptive finite element procedures for linear and non-linear dynamics. *Int. J. Numer. Meth. Engrg.*, 46:178–1802, 1999.
- [31] A. Schleupen and E. Ramm. Local and global error estimations in linear structural dynamics. *Computers and structures*, 76:741–756, 2000.
- [32] L. L. Thompson and D. He. Adaptive space-time finite element methods for the wave equation on unbounded domains. *Comput. Methods Appl. Mech. Engrg.*, 194:1947–2000, 2005.
- [33] S. Lahiri, J. Bonet, and J. Peraire. A variationally consistent mesh adaptation method for triangular elements in explicit lagrangian dynamics. *Int. J. Numer. Meth. Engrg.*, 82:1073–1113, 2010.
- [34] D. Aubry, D. Lucas, and B. Tie. Adaptive strategy for transient/coupled problems. Applications to thermoelasticity and elastodynamics. *Comput. Methods Appl. Mech. Engrg.*, 176:41–50, 1999.
- [35] W. Bangerth, M. Geiger, and R. Rannacher. Adaptive Galerkin finite element methods for the wave equation. *Computational Methods in Applied Mathematics*, 1:3–48, 2010.
- [36] W. Bangerth. *Adaptive Finite-Elemente-Methoden zur Lösung der Wellengleichung mit Anwendung in der Physik der Sonne*. PhD thesis, Ruprecht-Karls-Universität Heidelberg, 1998.
- [37] W. Bangerth and R. Rannacher. Finite element approximation of the acoustic wave equation: error control and mesh adaptation. *East-West Journal of Numerical Mathematics*, 7:263–282, 1999.
- [38] W. Bangerth and R. Rannacher. Adaptive finite element techniques for the acoustic wave equation. *Journal of Computational Acoustics*, 9:575–591, 2001.
- [39] J. P. Combe, P. Ladevèze, and J. P. Pelle. Discretization error estimator for transient dynamic simulations. *Advances in Engrg. Software*, 33:553–563, 2002.
- [40] J. P. Combe, P. Ladevèze, and J. P. Pelle. Constitutive relation error estimator for transient finite element analysis. *Comput. Methods Appl. Mech. Engrg.*, 176:165–185, 1999.
- [41] P. Ladevèze and J. P. Pelle. Estimation of discretization errors in dynamics. *Computers and Structures*, 81:1133–1148, 2003.
- [42] P. Ladevèze and J. Waeytens. Model verification in dynamics through strict upper bounds. *Comput. Methods Appl. Mech. Engrg.*, 198:1775–1784, 2009.

- [43] J. Waeytens. *Contrôle des calculs en dynamique: bornes strictes et pertinents sur une quantité d'intérêt*. PhD thesis, LMT-Cachan, 2010.
- [44] P. Ladevèze. Strict upper error bounds for computed outputs of interest in computational structural mechanics. *Computational Mechanics*, 42:271–286, 2008.
- [45] J. Waeytens, L. Chamoin, and P. Ladevèze. Guaranteed error bounds on point-wise quantities of interest for transient viscodynamics problems. *Computational Mechanics*, 49:291–307, 2012.
- [46] F. Verdugo and P. Díez. Computable bounds of functional outputs in linear visco-elastodynamics. *Comput. Methods Appl. Mech. Engrg.*, 245–246:313–330, 2012.
- [47] D. Fuentes, D. Littlefield, J. T. Oden, and S. Prudhomme. Extensions of goal-oriented error estimation methods to simulation of highly-nonlinear response of shock-loaded elastomer-reinforced structures. *Comput. Methods Appl. Mech. Engrg.*, 195:4659–4680, 2006.
- [48] L. C. Evans. *Partial Differential Equations*. American Mathematical Society, 1998.
- [49] N. M. Newmark. A method of computation for structural dynamics. *J. of Engineering Mechanics*, 85:67–94, 1959.
- [50] K. Eriksson, D. Estep, P. Hansbo, and C. Johnson. *Computational Differential Equations*. Studentlitteratur, 1996.
- [51] T. J. R. Hughes and G. M. Hulbert. Space-time finite element methods for elastodynamics: Formulations and error estimates. *Comput. Methods Appl. Mech. Engrg.*, 66:339–363, 1988.
- [52] G. M. Hulbert and T. J. R. Hughes. Space-time finite element methods for second-order hyperbolic equations. *Comput. Methods Appl. Mech. Engrg.*, 84:327–348, 1990.
- [53] C. Johnson. Discontinuous galerkin finite element methods for second order hyperbolic problems. *Comput. Methods Appl. Mech. Engrg.*, 107:117–129, 1993.
- [54] C. Johnson. *Numerical solution of partial differential equations by the finite element method*. Cambridge University Press, 1990.
- [55] P. Díez and G. Calderón. Remeshing criteria and proper error representations for goal oriented h-adaptivity. *Comput. Methods Appl. Mech. Engrg.*, 196:719–733, 2007.
- [56] O. C. Zienkiewicz and Y. M. Xie. A simple error estimator and adaptive time stepping procedure for dynamic analysis. *Earthquake Engineering & Structural Dynamics*, 20:871–887, 1991.
- [57] X. D. Li, L. F. Zeng, and N. E. Wiberg. A simple error estimator and adaptive time stepping procedure for dynamic analysis. *Com. Num. Meth. Engrg.*, 9:273–292, 1993.

- [58] O. C. Zienkiewicz and J. Z. Zhu. The superconvergent patch recovery and a posteriori error estimates. part 1: The recovery technique. *Int. J. Numer. Meth. Engrg.*, 33:1331–1364, 1992.
- [59] O. C. Zienkiewicz and J. Z. Zhu. The superconvergent patch recovery and a posteriori error estimates. Part 2: Error estimates and adaptivity. *Int. J. Numer. Meth. Engrg.*, 33:1365–1382, 1992.
- [60] N. E. Wiberg and X. D. Li. Superconvergent patch recovery of finite–element solution and a posteriori  $L_2$  norm error estimate. *Com. Num. Meth. Engrg.*, 10:313–320, 1994.
- [61] X. D. Li and N. E. Wiberg. A posteriori error estimate by element patch post-processing, adaptive analysis in energy and  $L_2$  norms. *Computers and Structures*, 53:907–919, 1994.
- [62] N. E. Wiberg, R. Bausys, and P. Hager. Adaptive h-version eigenfrequency analysis. *Computers and structures*, 71:565–584, 1999.
- [63] R. Rannacher and F. T. Stüttmeier. A feed-back approach to error control in finite element methods: application to linear elasticity. *Comput. Mech.*, 19:434–446, 1997.
- [64] W. Bangerth and R. Rannacher. *Adaptive Finite Element Methods for Differential Equations*. Birkhäuser, 2003.
- [65] J. T. Oden and S. Prudhomme. Goal-oriented error estimation and adaptivity for the finite element method. *Computers and Math. with Appl.*, 41:735–765, 2001.
- [66] N. Parés, P. Díez, and A. Huerta. A subdomain-based flux-free a posteriori error estimators. *Comput. Methods Appl. Mech. Engrg.*, 195:297–323, 2006.
- [67] J. P. Moitinho de Almeida and O. J. B. Almeida Pereira. Upper bounds of the error in local quantities using equilibrated and compatible finite element solutions for linear elastic problems. *Comput. Methods Appl. Mech. Engrg.*, 195:279–296, 2006.
- [68] O. J. B. Almeida Pereira and J. P. Moitinho de Almeida. Dual adaptive finite element refinement for multiple local quantities in linear elastostatics. *Int. J. Numer. Meth. Engrg.*, 83:347–365, 2010.
- [69] F. Pled, L. Chamoin, and P. Ladevèze. On the techniques for constructing admissible stress fields in model verification: Performances on engineering examples. *Int. J. Numer. Meth. Engrg.*, 88:409–441, 2011.
- [70] R. Cottereau, P. Díez, and A. Huerta. Strict error bounds for linear solid mechanics problems using a subdomain-based flux-free method. *Comput. Mech.*, 44:533–547, 2009.
- [71] F. Verdugo, N. Parés, and P. Díez. Modal based goal-oriented error assessment for timeline-dependent quantities in transient dynamics. *Int. J. Numer. Meth. Engrg.* In print.

- [72] A. Rafique, N. Kapre, and G. A. Constantinides. A high throughput FPGA-based implementation of the lanczos method for the symmetric extremal eigenvalue problem. In *8th International Symposium on Applied Reconfigurable Computing*, January 2012.
- [73] K. J. Bathe. *Finite Element Procedures*. Prentice Hall, 1996.
- [74] L. N. Trefethen and D. Bau. *Numerical linear algebra*. Society for Industrial & Applied Mathematics, 1997.

## Paper B

# Computable bounds of functional outputs in linear visco-elastodynamics

F. Verdugo and P. Díez

---

*Computer Methods in Applied Mechanics  
and Engineering, Volumes 245-246,  
Pages 313-330, 2012*





Contents lists available at SciVerse ScienceDirect

Comput. Methods Appl. Mech. Engrg.

journal homepage: [www.elsevier.com/locate/cma](http://www.elsevier.com/locate/cma)



## Computable bounds of functional outputs in linear visco-elastodynamics

Francesc Verdugo<sup>a</sup>, Pedro Díez<sup>a,b,\*</sup>

<sup>a</sup> Universitat Politècnica de Catalunya (UPC), Laboratori de Càlcul Numèric (LaCàN), Jordi Girona 1-3, E-08034 Barcelona, Spain

<sup>b</sup> Centre Internacional de Mètodes Numèrics en Enginyeria (CIMNE), Gran Capitán s/n, E-08034 Barcelona, Spain

### ARTICLE INFO

#### Article history:

Received 5 January 2012

Received in revised form 6 June 2012

Accepted 20 June 2012

Available online 6 July 2012

#### Keywords:

Computable bounds

Quantity of interest

Adjoint problem

Goal-oriented error assessment

Visco-elastodynamics

### ABSTRACT

This work presents a new technique yielding computable bounds of quantities of interest in the framework of linear visco-elastodynamics. A novel expression for the error representation is introduced, alternative to the previous ones using the Cauchy–Schwarz inequality. The proposed formulation utilizes symmetrized forms of the error equations to derive error bounds in terms of energy error measures. The practical implementation of the method is based on constructing admissible fields for both the original problem and the adjoint problem associated with the quantity of interest. Here, the flux-free technique is considered to compute the admissible stress fields. The proposed methodology yields estimates with better quality than the ones based on the Cauchy–Schwarz inequality. In the studied examples the bound gaps obtained are approximately halved, that is the estimated intervals of confidence are reduced.

© 2012 Elsevier B.V. All rights reserved.

### 1. Introduction

The pioneering works discussing error estimators for elliptic problems [1–3] introduced techniques assessing the energy norm of the error in Finite Element Analysis. These tools are essential to assess the reliability of numerical simulations and they are also a key ingredient for subsequent strategies providing more meaningful error measures [4–7]. The latter, aiming at assessing arbitrary functional outputs of the solution describing some quantity of interest, are referred as goal-oriented error estimators.

Error estimates for elliptic (steady state) problems have reached an amazing degree of maturity, with different techniques providing excellent error estimates in an extensive collection of model problems. The error estimation tools dealing with transient problems are not so popular, especially in the case of structural dynamics. Some of the contributions on this last topic are, on the one hand, the energy error estimates presented by Aubry et al. [8], Li and Wiberg [9,10] and Ladevèze and co-workers [11–14] and, on the other hand, the goal-oriented estimates proposed by Schleupen and Ramm [15], Fuentes et al. [16] and Ladevèze and co-workers [17–20].

Interest has been paid also to the error assessment tools providing bounds, that is yielding one-sided estimates (both lower bounds guaranteeing that the error is underestimated and upper bounds guaranteeing that the error is overestimated). This topic

has been addressed recently in many references, see for instance [5] where Parés et al. propose bounds of linear outputs for the linear elastic case. The estimates providing bounds have also been extended to transient problems, see for instance [21] where the transient convection–diffusion–reaction equation is considered. To the best knowledge of the authors, the only references discussing bounds in a quantity of interest for linear visco-elastodynamics are due to Ladevèze and co-workers [17–20].

The present work aims at finding an alternative error representation improving the estimates introduced in [18]. The strategy presented in [18] is briefly revisited, using an algebraic rationale without the requirement of any thermodynamic framework. In order to simplify the developments, a linear Kelvin–Voigt constitutive relation is considered here, instead of the Maxwell model. This allows a simpler derivation, using only algebraic arguments, with no need of any mechanical consideration. Generalization to nonlinear models would require a general thermodynamical framework.

The proposed method describes how to compute lower and upper bounds of a linear output  $L^o(\mathbf{u})$  of the exact solution  $\mathbf{u}$ , namely  $\zeta_L$  and  $\zeta_U$  such that  $\zeta_L \leq L^o(\mathbf{u}) \leq \zeta_U$ . The novel contribution of this work is the introduction of an alternative expression for values  $\zeta_L$  and  $\zeta_U$ . This new expression reduces the bound gap: with respect to the existing technique based on the Cauchy–Schwarz inequality, the bound gap is approximately halved. The basic rationale is similar to the one considered for linear elasticity. Bounds for the quantity of interest are obtained as a proper combination of bounds for a global energy measure of both the original and the adjoint problems. The key ingredient is the computation of admissible fields for both problems. An other novelty with respect to [18] is the utilization of the flux-free technique [22] in order to build the admissible stress fields.

\* Corresponding author at: Universitat Politècnica de Catalunya (UPC), Laboratori de Càlcul Numèric (LaCàN), Jordi Girona 1-3, E-08034 Barcelona, Spain.

E-mail addresses: [francesc.verdugo@upc.edu](mailto:francesc.verdugo@upc.edu) (F. Verdugo), [pedro.diez@upc.edu](mailto:pedro.diez@upc.edu) (P. Díez).

The remainder of this article is organized as follows. Section 2 introduces the equations of visco-elastodynamics and its numerical approximation with the Newmark method. Section 3 is devoted to obtain upper bounds of energy error measures. Section 4 discusses how to obtain bounds in quantities of interest following the error representation presented in [18]. Section 5 introduces the new error representation leading to better bounded estimates. Section 6 contains the numerical examples. The paper is closed with some concluding remarks.

## 2. Problem statement

### 2.1. Governing equations

A visco-elastic body occupies the open bounded domain  $\Omega \subset \mathbb{R}^d$ ,  $d \leq 3$ , with boundary  $\partial\Omega$ . The boundary is divided in two disjoint parts,  $\Gamma_N$  and  $\Gamma_D$  such that  $\partial\Omega = \overline{\Gamma_N} \cup \overline{\Gamma_D}$ . The time interval under consideration is  $I := [0, T]$ . Under the assumption of small perturbations, the evolution of displacements  $\mathbf{u}(\mathbf{x}, t)$  and stresses  $\boldsymbol{\sigma}(\mathbf{x}, t)$ ,  $\mathbf{x} \in \Omega$  and  $t \in I$ , is described by the visco-elastodynamic equations,

$$\rho \ddot{\mathbf{u}} - \nabla \cdot \boldsymbol{\sigma} = \mathbf{f} \quad \text{in } \Omega \times I, \quad (1a)$$

$$\mathbf{u} = \mathbf{0} \quad \text{on } \Gamma_D \times I, \quad (1b)$$

$$\boldsymbol{\sigma} \cdot \mathbf{n} = \mathbf{g} \quad \text{on } \Gamma_N \times I, \quad (1c)$$

$$\mathbf{u} = \mathbf{u}_0 \quad \text{at } \Omega \times \{0\}, \quad (1d)$$

$$\dot{\mathbf{u}} = \mathbf{v}_0 \quad \text{at } \Omega \times \{0\}, \quad (1e)$$

where  $\rho = \rho(\mathbf{x}) > 0$  is the mass density and an upper dot indicates partial derivation with respect to time, that is  $(\dot{\bullet}) := \frac{d}{dt}(\bullet)$ . The body force is denoted by  $\mathbf{f}$ ,  $\mathbf{g}$  is the traction acting on the Neumann boundary  $\Gamma_N \times I$  and  $\mathbf{n}$  is the outward unit normal to  $\partial\Omega$ . Functions  $\mathbf{u}_0 = \mathbf{u}_0(\mathbf{x})$  and  $\mathbf{v}_0 = \mathbf{v}_0(\mathbf{x})$  are the initial conditions for displacements and velocities respectively. For the sake of simplicity and without any loss of generality, Dirichlet conditions (1b) are taken as homogeneous, see Appendix A for details. The set of Eqs. (1) is closed with the constitutive law,

$$\boldsymbol{\sigma} := \mathcal{C} : \boldsymbol{\varepsilon}(\mathbf{u} + \tau \dot{\mathbf{u}}), \quad (2)$$

corresponding to the Kelvin–Voigt linear visco-elastic model. The parameter  $\tau > 0$  is a characteristic time related with the amount of viscosity of the medium. The introduction of this parameter is fundamental in obtaining bounds. For  $\tau = 0$  the bounding properties are lost. The tensor  $\mathcal{C}$  is the standard 4th-order elastic Hooke tensor. The kinematic relation (corresponding to small perturbations)  $\boldsymbol{\varepsilon}(\mathbf{w}) := \frac{1}{2}(\nabla \mathbf{w} + \nabla^T \mathbf{w})$  is considered.

In the following it is useful to rewrite the constitutive relation (2) as

$$\boldsymbol{\sigma} := \mathbf{s}(\mathbf{u}) = \mathbf{s}^E(\mathbf{u}) + \mathbf{s}^V(\mathbf{u}),$$

where

$$\mathbf{s}^E(\mathbf{w}) := \mathcal{C} : \boldsymbol{\varepsilon}(\mathbf{w}), \quad (3a)$$

$$\mathbf{s}^V(\mathbf{w}) := \tau \mathcal{C} : \boldsymbol{\varepsilon}(\dot{\mathbf{w}}). \quad (3b)$$

The following notation is introduced for the elastic and viscous part of the stress  $\boldsymbol{\sigma}$  respectively:

$$\boldsymbol{\sigma}^E := \mathbf{s}^E(\mathbf{u}), \quad (4a)$$

$$\boldsymbol{\sigma}^V := \mathbf{s}^V(\mathbf{u}). \quad (4b)$$

**Remark 1.** The following analysis can be generalized for other more sophisticated linear Kelvin–Voigt models. These models can be introduced taking alternative expressions for  $\mathbf{s}^V$  in Eq. (3b). This would lead to a technical modification in the definition of the

bilinear forms  $B^V$  and  $\bar{B}^V$  introduced in Eqs. (13) and (14b) below. Note however that the main rationale of the methodology presented in the paper is straightforwardly generalized to deal with more complex visco-elastic models.

The subsequent analysis requires introducing a variational version of problem (1). To this end, the following spaces are introduced

$$\mathcal{W} := \left\{ \mathbf{w} : \begin{array}{l} \mathbf{w}(\mathbf{x}, \cdot) \in [H^2(I)]^d \quad \forall \mathbf{x} \in \Omega \\ \mathbf{w}(\cdot, t) \in [H^1(\Omega)]^d \quad \forall t \in I \\ \mathbf{w} = \mathbf{0} \quad \text{at } \Gamma_D \times I \end{array} \right\},$$

and

$$\mathcal{U} := \left\{ \mathbf{w} \in \mathcal{W} : \begin{array}{l} \mathbf{w} = \mathbf{u}_0 \quad \text{at } \Omega \times \{0\} \\ \dot{\mathbf{w}} = \mathbf{v}_0 \quad \text{at } \Omega \times \{0\} \end{array} \right\}.$$

Functions in  $\mathcal{U}$  are said to be *kinematically admissible* or *K-admissible*. They are continuous in space–time with continuous time derivative and they fulfill the initial and Dirichlet conditions. The variational version of (1) reads: find  $\mathbf{u} \in \mathcal{U}$  such that

$$B(\mathbf{u}, \mathbf{w}) = L(\mathbf{w}) \quad \forall \mathbf{w} \in \mathcal{W}, \quad (5)$$

where

$$B(\mathbf{v}, \dot{\mathbf{w}}) := \int_I (\rho \dot{\mathbf{v}} \cdot \dot{\mathbf{w}}) dt + \int_I a(\mathbf{v} + \tau \dot{\mathbf{v}}, \dot{\mathbf{w}}) dt, \quad (6a)$$

$$L(\mathbf{w}) := \int_I l(\dot{\mathbf{w}}) dt, \quad (6b)$$

$$l(\mathbf{w}) := (\mathbf{f}, \mathbf{w}) + (\mathbf{g}, \mathbf{w})_{\Gamma_N}, \quad (6c)$$

$$(\mathbf{v}, \mathbf{w}) := \int_{\Omega} \mathbf{v} \cdot \mathbf{w} d\Omega, \quad (6d)$$

$$(\mathbf{v}, \mathbf{w})_{\Gamma_N} := \int_{\Gamma_N} \mathbf{v} \cdot \mathbf{w} d\Gamma, \quad (6e)$$

$$a(\mathbf{v}, \mathbf{w}) := \int_{\Omega} \boldsymbol{\varepsilon}(\mathbf{v}) : \mathcal{C} : \boldsymbol{\varepsilon}(\mathbf{w}) d\Omega. \quad (6f)$$

A numerical solution of the original problem (1) may be found without using this time–space variational setting. Nevertheless, the variational formulation is useful in the following to assess the error and, in particular, in order to obtain error bounds.

### 2.2. Numerical approximation

The well known Newmark method [23] is considered for the numerical approximation of problem (1). The Newmark method is chosen because it is commonly used in practical applications and commercial codes. Note however that the present study is applicable to other semidiscrete methods and straightforwardly generalizable to space–time formulations, for instance those introduced by Hughes and Hulbert [24,25]. In fact, taking as reference methodology the Newmark or other semidiscrete methods is actually more involved than the space–time ones. This is because they combine finite elements and finite differences and therefore the discrete solution cannot take advantage of variational properties. However, this drawback can be easily overcome as it is shown later.

As previously noted, The Newmark and other semidiscrete methods are based on a FE discretization in space and finite differences in time. Thus, a variational setting in space for each  $t \in I$  is required. The following space has to be introduced:

$$\mathcal{V}_0 := \left\{ \mathbf{w} \in [H^1(\Omega)]^d : \mathbf{w} = \mathbf{0} \quad \text{on } \Gamma_D \right\}.$$

Eqs. (1) are rewritten as: for all  $t \in I$  find  $\mathbf{u}(\cdot, t) \in \mathcal{V}_0$  such that

$$(\rho \ddot{\mathbf{u}}(\cdot, t), \mathbf{w}) + a(\mathbf{u}(\cdot, t) + \tau \dot{\mathbf{u}}(\cdot, t), \mathbf{w}) = l(\mathbf{w}) \quad \forall \mathbf{w} \in \mathcal{V}_0, \quad (7)$$

with initial conditions  $\mathbf{u}(\cdot, t) = \mathbf{u}_0$  and  $\dot{\mathbf{u}}(\cdot, t) = \mathbf{v}_0$ . After discretization in  $\mathcal{V}_0^H \subset \mathcal{V}_0$  ( $H$  stands for the characteristic mesh element size) Eq. (7) leads to a system of second order ODEs, which is discretized in time introducing the following partition of the time interval  $I$ ,

$$\mathcal{T} := \{t_0 = 0, t_1, \dots, t_N = T\}.$$

Each interval of the partition  $\mathcal{T}$  is characterized by the time step  $\Delta t_n := t_n - t_{n-1}$ . The characteristic time step for the partition is taken as the maximum:  $\Delta t := \max_n(\Delta t_n)$ .

The proposed methodology is applicable to any method producing fields  $\mathbf{u}_n^{H,\Delta t}, \mathbf{v}_n^{H,\Delta t}, \mathbf{a}_n^{H,\Delta t} \in \mathcal{V}_0^H$  for  $n = 0, \dots, N$  such that they fulfill the following condition

$$(\rho \mathbf{a}_n^{H,\Delta t}, \mathbf{w}) + a(\mathbf{u}_n^{H,\Delta t} + \tau \mathbf{v}_n^{H,\Delta t}, \mathbf{w}) = l_n(\mathbf{w}) \quad \forall \mathbf{w} \in \mathcal{V}_0^H, \quad (8)$$

where

$$l_n(\mathbf{w}) := (\mathbf{f}_n, \mathbf{w}) + (\mathbf{g}_n, \mathbf{w})_{\Gamma_N},$$

$$\mathbf{f}_n(\mathbf{x}) := \mathbf{f}(\mathbf{x}, t_n),$$

$$\mathbf{g}_n(\mathbf{x}) := \mathbf{g}(\mathbf{x}, t_n),$$

and the initial conditions  $\mathbf{u}_0^{H,\Delta t} = \mathbf{u}_0$  and  $\mathbf{v}_0^{H,\Delta t} = \mathbf{v}_0$ .

Note that the solution provided by the Newmark method complies with this requirement. In fact, the Newmark solution at time  $t_n$  is computed injecting the Taylor expansions

$$\mathbf{u}_n^{H,\Delta t} = \mathbf{u}_{n-1}^{H,\Delta t} + \Delta t_n \mathbf{v}_{n-1}^{H,\Delta t} + \frac{1}{2} \Delta t_n^2 [(1 - 2\beta) \mathbf{a}_{n-1}^{H,\Delta t} + 2\beta \mathbf{a}_n^{H,\Delta t}],$$

$$\mathbf{v}_n^{H,\Delta t} = \mathbf{v}_{n-1}^{H,\Delta t} + \Delta t_n [(1 - \gamma) \mathbf{a}_{n-1}^{H,\Delta t} + \gamma \mathbf{a}_n^{H,\Delta t}],$$

in Eq. (8) and assuming that the values  $\mathbf{u}_{n-1}^{H,\Delta t}, \mathbf{v}_{n-1}^{H,\Delta t}, \mathbf{a}_{n-1}^{H,\Delta t}$  are known. The displacements and velocities at time  $t_0$  are determined by the initial conditions  $\mathbf{u}_0$  and  $\mathbf{v}_0$ , and the acceleration  $\mathbf{a}_0^{H,\Delta t}$  is build such that

$$(\rho \mathbf{a}_0^{H,\Delta t}, \mathbf{w}) + a(\mathbf{u}_0 + \tau \mathbf{v}_0, \mathbf{w}) = l_0(\mathbf{w}) \quad \forall \mathbf{w} \in \mathcal{V}_0^H.$$

The scalars  $\beta$  and  $\gamma$  are the parameters of the Newmark method taking values in  $[0, 1]$ .

Note that the fields  $\mathbf{u}_n^{H,\Delta t}, \mathbf{v}_n^{H,\Delta t}, \mathbf{a}_n^{H,\Delta t}$  do not define functions in the whole time interval  $I$ , but only in the time partition. However, they can be extended to the interior of the time steps using a simple linear interpolation:

$$\mathbf{u}^{H,\Delta t}(\mathbf{x}, t) := \sum_{n=0}^N \mathbf{u}_n^{H,\Delta t}(\mathbf{x}) \theta_n(t), \quad (9a)$$

$$\mathbf{v}^{H,\Delta t}(\mathbf{x}, t) := \sum_{n=0}^N \mathbf{v}_n^{H,\Delta t}(\mathbf{x}) \theta_n(t), \quad (9b)$$

$$\mathbf{a}^{H,\Delta t}(\mathbf{x}, t) := \sum_{n=0}^N \mathbf{a}_n^{H,\Delta t}(\mathbf{x}) \theta_n(t), \quad (9c)$$

where functions  $\theta_n(t)$ ,  $n = 0, \dots, N$  are piecewise linear shape functions related with the time partition  $\mathcal{T}$ .

### 2.3. Interpretation of the damping factor

Before going further, it is worth analyzing the physical meaning of the parameter  $\tau$ . This parameter is fundamental in the obtention of the bounds. The amount of damping associated with  $\tau$  is characterized by the so-called dimensionless damping factor denoted by  $\xi$ . For the Kelvin–Voigt model presented in Eq. (2),  $\xi$  has the following expression (see [18] for details):

$$\xi := \frac{1}{2} \tau \omega_0,$$

where  $\omega_0 := \sqrt{\lambda_0}$ , being  $\lambda_0$  the lowest eigenvalue of the following generalized eigenvalue problem: find  $\lambda \in \mathbb{R}$  and  $\mathbf{q} \in \mathcal{V}_0$  such that

$$a(\mathbf{q}, \mathbf{w}) = \lambda(\rho \mathbf{q}, \mathbf{w}), \quad \forall \mathbf{w} \in \mathcal{V}_0. \quad (10)$$

The value  $\xi = 0\%$  corresponds to pure elasticity whereas  $\xi = 100\%$  means that all vibration modes of the problem are dumped out. In the latter case, the corresponding solution is a pure decaying exponential. In practice, the eigenvalue  $\lambda_0$  is approximated using the discrete space  $\mathcal{V}_0^H \subset \mathcal{V}_0$  which results in the generalized eigenvalue problem

$$\mathbf{K} \mathbf{q} = \lambda \mathbf{M} \mathbf{q},$$

where  $\mathbf{K}, \mathbf{M}$  are the stiffness and mass matrices corresponding with the forms in (10).

## 3. Constitutive relation error: upper bound of energy error measures

### 3.1. Discretization error

Note that the numerical solution provided by the Newmark method, namely  $\mathbf{u}^{H,\Delta t}, \mathbf{v}^{H,\Delta t}$  and  $\mathbf{a}^{H,\Delta t}$ , is such that the velocities are not the time derivatives of the displacements and accelerations are not the time derivatives of the velocities. Moreover, their time dependence is not regular enough to fit in the variational setup described in Eq. (5), that is  $\mathbf{u}^{H,\Delta t} \notin \mathcal{U}$ . A new displacement field  $\hat{\mathbf{u}} \in \mathcal{U}$  is introduced as a postprocess of the Newmark solution in order to analyze the corresponding error using the variational setup. The detailed construction of  $\hat{\mathbf{u}}$  is described in Section 3.5. In the remainder of the paper, the error analysis is referred to the approximate solution  $\hat{\mathbf{u}}$ .

The error associated with  $\hat{\mathbf{u}}$ , namely

$$\hat{\mathbf{e}} := \mathbf{u} - \hat{\mathbf{u}}, \quad (11)$$

lives in the space

$$\mathcal{U}_0 := \left\{ \mathbf{w} \in \mathcal{W} : \begin{array}{l} \mathbf{w} = 0 \quad \text{at } \Omega \times \{0\} \\ \dot{\mathbf{w}} = 0 \quad \text{at } \Omega \times \{0\} \end{array} \right\},$$

and fulfills the variational residual equation: find  $\hat{\mathbf{e}} \in \mathcal{U}_0$  such that

$$B(\hat{\mathbf{e}}, \mathbf{w}) = \hat{R}(\mathbf{w}) \quad \forall \mathbf{w} \in \mathcal{W}, \quad (12)$$

where

$$\hat{R}(\mathbf{w}) := L(\mathbf{w}) - B(\hat{\mathbf{u}}, \mathbf{w}).$$

Note that the residual  $\hat{R}$  does not verify the Galerkin orthogonality property because in general for arbitrary  $\hat{\mathbf{u}} \in \mathcal{U}$  and  $\mathbf{w} \in \mathcal{W}$ ,  $B(\hat{\mathbf{u}}, \mathbf{w}) \neq L(\mathbf{w})$ .

### 3.2. Energy measures

The first step to achieve bounds of the error  $\hat{\mathbf{e}}$  in a quantity of interest is obtaining bounds of this error in a suitable energy measure. The measure to be used is associated with the following symmetric bilinear form

$$B^v(\mathbf{v}, \mathbf{w}) := \tau \int_I a(\dot{\mathbf{v}}, \dot{\mathbf{w}}) dt. \quad (13)$$

**Remark 2.** The form  $B^v$  is related with the symmetric part of the form  $B$ , i.e.

$$\frac{1}{2} [B(\mathbf{v}, \mathbf{w}) + B(\mathbf{w}, \mathbf{v})] = \frac{1}{2} [(\rho \dot{\mathbf{v}}, \dot{\mathbf{w}}) + a(\mathbf{v}, \mathbf{w})]_{t=0}^{t=T} + B^v(\mathbf{v}, \mathbf{w}).$$

Note that  $B^v$  coincides with the dissipative term of the symmetric part of  $B$ , hence the superscript “v” is used in  $B^v$  marking its relation with the viscosity. The difference between  $B^v$  and the symmetric part of  $B$  are the terms defined at times  $t = 0$  and  $t = T$  which are not related with the viscosity. Note that the higher is the value  $\tau$ , the closer  $B^v$  and the symmetric part of  $B$  are.

It is useful defining equivalent versions of forms  $a$  and  $B^v$  taking stresses as arguments:

$$\bar{a}(\boldsymbol{\tau}_1, \boldsymbol{\tau}_2) := (\boldsymbol{\tau}_1, \mathcal{C}^{-1} : \boldsymbol{\tau}_2), \quad (14a)$$

$$\bar{B}^v(\boldsymbol{\tau}_1, \boldsymbol{\tau}_2) := \frac{1}{\tau} \int_I \bar{a}(\boldsymbol{\tau}_1, \boldsymbol{\tau}_2) dt. \quad (14b)$$

The relations  $a(\mathbf{v}, \mathbf{w}) = \bar{a}(\mathbf{s}^E(\mathbf{v}), \mathbf{s}^E(\mathbf{w}))$  and  $B^v(\mathbf{v}, \mathbf{w}) = \bar{B}^v(\mathbf{s}^v(\mathbf{v}), \mathbf{s}^v(\mathbf{w}))$  hold for all  $\mathbf{v}$  and  $\mathbf{w}$ . The bilinear forms  $B^v$  and  $\bar{B}^v$  lead to the energy measures:

$$\|\mathbf{w}\|^2 := B^v(\mathbf{w}, \mathbf{w}) = \tau \int_I \|\dot{\mathbf{w}}\|^2 dt,$$

$$\|\boldsymbol{\tau}\|_\sigma^2 := \bar{B}^v(\boldsymbol{\tau}, \boldsymbol{\tau}) = \frac{1}{\tau} \int_I \|\boldsymbol{\tau}\|_\sigma^2 dt,$$

where  $\|\mathbf{w}\|^2 := a(\mathbf{w}, \mathbf{w})$  and  $\|\boldsymbol{\tau}\|_\sigma^2 := \bar{a}(\boldsymbol{\tau}, \boldsymbol{\tau})$ . Note that the notation introduced above is such that norms with subscript “ $\sigma$ ” and bilinear forms with upper bar take stresses as arguments.

**Remark 3.** The bilinear form  $B$  is not symmetric but it is related with the following energy measure

$$B(\mathbf{v}, \mathbf{v}) = \frac{1}{2} \left[ \|\dot{\mathbf{v}}\|^2 + \|\mathbf{v}\|^2 \right]_{t=0}^{t=T} + \|\mathbf{v}\|^2, \quad (15)$$

which corresponds to the increment of the free energy (kinetic and elastic) plus the dissipated energy due to the viscosity. Note that the dissipated energy coincides with the energy related to the bilinear form  $B^v$ . In particular for  $\mathbf{v} = \dot{\mathbf{e}}$  one has

$$B(\dot{\mathbf{e}}, \dot{\mathbf{e}}) \geq \|\dot{\mathbf{e}}\|^2. \quad (16)$$

This relation is derived from (15) noting that  $\dot{\mathbf{e}}(0) = \dot{\mathbf{e}}(T) = 0$  and  $\|\dot{\mathbf{e}}\|_{t=0}^2 + \|\dot{\mathbf{e}}\|_{t=T}^2 \geq 0$ . The relation (16) is important because it is used later to derive bounds in the quantity of interest.

### 3.3. Admissible fields

The construction of an admissible pair  $(\hat{\boldsymbol{\sigma}}, \hat{\mathbf{u}}) \in \mathcal{S}(\hat{\mathbf{u}}) \times \mathcal{U}$  is the key ingredient in order to obtain upper bounds of the energy of  $\hat{\mathbf{e}}$ . The space of admissible stresses  $\mathcal{S}(\hat{\mathbf{u}})$  is defined for a given  $\hat{\mathbf{u}} \in \mathcal{U}$  as follows

$$\mathcal{S}(\hat{\mathbf{u}}) := \left\{ \boldsymbol{\tau} \in \mathcal{Z} : \int_I (\boldsymbol{\tau}, \boldsymbol{\varepsilon}(\dot{\mathbf{w}})) dt = L(\mathbf{w}) - \int_I (\rho \ddot{\mathbf{u}}, \dot{\mathbf{w}}) dt \quad \forall \mathbf{w} \in \mathcal{W} \right\}, \quad (17)$$

where

$$\mathcal{Z} := \left\{ \boldsymbol{\tau} : [\boldsymbol{\tau}]_j \in L^2(\Omega \times I) \quad i, j \leq d \right\}, \quad (18)$$

and for  $\boldsymbol{\tau}, \boldsymbol{\varepsilon} \in \mathcal{Z}$

$$(\boldsymbol{\tau}, \boldsymbol{\varepsilon}) := \int_\Omega \boldsymbol{\tau} : \boldsymbol{\varepsilon} d\Omega.$$

The space  $\mathcal{S}(\hat{\mathbf{u}})$  contains the *dynamically admissible* or *D-admissible* stresses. These stress tensors are in dynamic equilibrium with respect the external loads and with the inertia forces related to the admissible acceleration  $\hat{\mathbf{u}}$ . They can be discontinuous between mesh elements but the vector  $\hat{\boldsymbol{\sigma}} \cdot \mathbf{n}$  has to be continuous across element edges. The equivalent strong condition for a function  $\hat{\boldsymbol{\sigma}} \in \mathcal{S}(\hat{\mathbf{u}})$  associated with a domain decomposition given by a finite element mesh is

$$-\nabla \cdot \hat{\boldsymbol{\sigma}} = \mathbf{f} - \rho \hat{\mathbf{u}} \quad \text{on } \Omega_{\text{int}} \times I,$$

$$\hat{\boldsymbol{\sigma}} \cdot \mathbf{n} = \mathbf{g} \quad \text{on } \Gamma_N \times I,$$

$$[[\hat{\boldsymbol{\sigma}} \cdot \mathbf{n}]] = 0 \quad \text{on } \Gamma_{\text{int}} \times I,$$

where  $\Omega_{\text{int}}$  is the interior of the elements of the mesh and  $\Gamma_{\text{int}}$  is the set of all interior element edges. Note that the definition of  $\mathcal{S}(\hat{\mathbf{u}})$

requires the previous selection of a field  $\hat{\mathbf{u}} \in \mathcal{U}$ . This is a particularity of the dynamic case. A method to build a D-admissible field  $\hat{\boldsymbol{\sigma}}$  from the numerical solution  $\hat{\mathbf{u}}$  is shown in Section 3.6.

In the following, it is useful to introduce the notations

$$\hat{\boldsymbol{\sigma}}^E := \mathbf{s}^E(\hat{\mathbf{u}}), \quad (19a)$$

$$\hat{\boldsymbol{\sigma}}^v := \hat{\boldsymbol{\sigma}} - \hat{\boldsymbol{\sigma}}^E, \quad (19b)$$

which are a decomposition of the admissible stress  $\hat{\boldsymbol{\sigma}}$  into elastic and viscous parts, i.e.  $\hat{\boldsymbol{\sigma}} = \hat{\boldsymbol{\sigma}}^E + \hat{\boldsymbol{\sigma}}^v$ .

### 3.4. Global error representation and computable error bounds

The admissible pair  $(\hat{\boldsymbol{\sigma}}, \hat{\mathbf{u}}) \in \mathcal{S}(\hat{\mathbf{u}}) \times \mathcal{U}$  defines the following error in stresses

$$\hat{\boldsymbol{\sigma}}^e := \hat{\boldsymbol{\sigma}} - \mathbf{s}(\hat{\mathbf{u}}). \quad (20)$$

This error corresponds to the non verification of the constitutive relation (2) associated with the admissible pair. The value  $\|\hat{\boldsymbol{\sigma}}^e\|_\sigma$  is the so called *constitutive relation error* (following the terminology by Ladevèze and co-workers) and it is computable once the fields  $\hat{\boldsymbol{\sigma}}$  and  $\hat{\mathbf{u}}$  are available. Note that,  $\|\hat{\boldsymbol{\sigma}}^e\|_\sigma = 0$  if and only if  $\hat{\boldsymbol{\sigma}} = \mathbf{s}$  and  $\hat{\mathbf{u}} = \mathbf{u}$ . Consequently,  $\|\hat{\boldsymbol{\sigma}}^e\|_\sigma$  is adopted as a pertinent error measure. Moreover, the value  $\|\hat{\boldsymbol{\sigma}}^e\|_\sigma$  is also meaningful because it is related with the unknown error  $\hat{\mathbf{e}}$ .

**Theorem 1.** Given an admissible pair  $(\hat{\boldsymbol{\sigma}}, \hat{\mathbf{u}}) \in \mathcal{S}(\hat{\mathbf{u}}) \times \mathcal{U}$ , the errors defined in Eqs. (20) and (11),  $\hat{\boldsymbol{\sigma}}^e$  and  $\hat{\mathbf{e}}$ , fulfill

$$\|\hat{\boldsymbol{\sigma}}^e\|_\sigma^2 = |\dot{\hat{\mathbf{e}}}|_{t=T}^2 + \|\hat{\mathbf{e}}\|_{t=T}^2 + \|\hat{\mathbf{e}}\|^2 + \|\boldsymbol{\sigma}^v - \hat{\boldsymbol{\sigma}}^v\|_\sigma^2. \quad (21)$$

being  $\boldsymbol{\sigma}^v$  and  $\hat{\boldsymbol{\sigma}}^v$  defined in (4b) and (19b).

**Proof.** First, note that  $\|\hat{\boldsymbol{\sigma}}^e\|_\sigma^2$  can be rewritten as

$$\|\hat{\boldsymbol{\sigma}}^e\|_\sigma^2 = \|\hat{\boldsymbol{\sigma}} - \mathbf{s}(\hat{\mathbf{u}})\|_\sigma^2 = \|\hat{\boldsymbol{\sigma}}^v - \mathbf{s}^v(\hat{\mathbf{u}})\|_\sigma^2.$$

Adding and subtracting  $\boldsymbol{\sigma}^v$  in the last term yields

$$\begin{aligned} \|\hat{\boldsymbol{\sigma}}^e\|_\sigma^2 &= \|\hat{\boldsymbol{\sigma}}^v - \boldsymbol{\sigma}^v + \boldsymbol{\sigma}^v - \mathbf{s}^v(\hat{\mathbf{u}})\|_\sigma^2 \\ &= \|\hat{\boldsymbol{\sigma}}^v - \boldsymbol{\sigma}^v\|_\sigma^2 + \|\hat{\mathbf{e}}\|^2 - 2\bar{B}^v(\boldsymbol{\sigma}^v - \hat{\boldsymbol{\sigma}}^v, \boldsymbol{\sigma}^v - \mathbf{s}^v(\hat{\mathbf{u}})). \end{aligned}$$

Hence, it remains to prove that

$$\bar{B}^v(\boldsymbol{\sigma}^v - \hat{\boldsymbol{\sigma}}^v, \boldsymbol{\sigma}^v - \mathbf{s}^v(\hat{\mathbf{u}})) = -\frac{1}{2} |\dot{\hat{\mathbf{e}}}|_{t=T}^2 - \frac{1}{2} \|\hat{\mathbf{e}}\|_{t=T}^2. \quad (22)$$

By admissibility of  $\hat{\mathbf{u}} \in \mathcal{U}$  and  $\hat{\boldsymbol{\sigma}} \in \mathcal{S}(\hat{\mathbf{u}})$  it follows that

$$0 = \int_I (\rho(\hat{\mathbf{u}} - \ddot{\hat{\mathbf{u}}}, \dot{\hat{\mathbf{e}}}) dt + \int_I (\boldsymbol{\sigma} - \hat{\boldsymbol{\sigma}}, \boldsymbol{\varepsilon}(\dot{\hat{\mathbf{e}}})) dt. \quad (23)$$

Then, injecting the expression

$$\boldsymbol{\sigma} - \hat{\boldsymbol{\sigma}} = \mathbf{s}^E(\mathbf{u} - \hat{\mathbf{u}}) + \boldsymbol{\sigma}^v - \hat{\boldsymbol{\sigma}}^v,$$

into Eq. (23) one has

$$\begin{aligned} 0 &= \int_I (\rho \ddot{\hat{\mathbf{e}}}, \dot{\hat{\mathbf{e}}}) dt + \int_I a(\hat{\mathbf{e}}, \dot{\hat{\mathbf{e}}}) dt + \bar{B}^v(\boldsymbol{\sigma}^v - \hat{\boldsymbol{\sigma}}^v, \boldsymbol{\sigma}^v - \mathbf{s}^v(\hat{\mathbf{u}})) \\ &= \frac{1}{2} \int_I \frac{d}{dt} (\rho \dot{\hat{\mathbf{e}}}, \dot{\hat{\mathbf{e}}}) dt + \frac{1}{2} \int_I \frac{d}{dt} a(\hat{\mathbf{e}}, \dot{\hat{\mathbf{e}}}) dt + \bar{B}^v(\boldsymbol{\sigma}^v - \hat{\boldsymbol{\sigma}}^v, \boldsymbol{\sigma}^v - \mathbf{s}^v(\hat{\mathbf{u}})) \\ &= \frac{1}{2} \left[ |\dot{\hat{\mathbf{e}}}|^2 + \|\hat{\mathbf{e}}\|^2 \right]_{t=0}^{t=T} + \bar{B}^v(\boldsymbol{\sigma}^v - \hat{\boldsymbol{\sigma}}^v, \boldsymbol{\sigma}^v - \mathbf{s}^v(\hat{\mathbf{u}})). \end{aligned}$$

The proof is concluded by taking into account that  $\dot{\hat{\mathbf{e}}}(0) = \dot{\hat{\mathbf{e}}}(T) = 0$ .  $\square$

**Theorem 1** furnishes the relation  $\|\hat{\boldsymbol{\sigma}}^e\|_\sigma^2 \geq |\dot{\hat{\mathbf{e}}}|_{t=T}^2 + \|\hat{\mathbf{e}}\|_{t=T}^2 + \|\hat{\mathbf{e}}\|^2$  and, in particular, the following upper bound

$$\|\hat{\boldsymbol{\sigma}}^e\|_\sigma \geq \|\hat{\mathbf{e}}\|. \quad (24)$$

Expression (24) is particularly important because it is used to bound the quantity of interest.

### 3.5. Construction of K-admissible fields

The first step to build an admissible pair  $(\hat{\sigma}, \hat{\mathbf{u}}) \in \mathcal{S}(\hat{\mathbf{u}}) \times \mathcal{U}$  is to define the K-admissible field  $\hat{\mathbf{u}} \in \mathcal{U}$ . The method of the linear accelerations [26, Chapter 7] is considered in the present case. This method is preferred because it simplifies the subsequent construction of the D-admissible field.

The basic idea is to take the admissible acceleration equal to  $\mathbf{a}^{H,\Delta t}$  as defined in (9c) and then integrate in time to obtain the admissible velocity and the admissible displacement:

$$\ddot{\hat{\mathbf{u}}}(\mathbf{x}, t) := \mathbf{a}^{H,\Delta t}(\mathbf{x}, t), \quad (25a)$$

$$\dot{\hat{\mathbf{u}}}(\mathbf{x}, t) := \int_0^t \ddot{\hat{\mathbf{u}}}(\mathbf{x}, \xi) d\xi + \mathbf{v}_0^{H,\Delta t}(\mathbf{x}), \quad (25b)$$

$$\hat{\mathbf{u}}(\mathbf{x}, t) := \int_0^t \dot{\hat{\mathbf{u}}}(\mathbf{x}, \xi) d\xi + \mathbf{u}_0^{H,\Delta t}(\mathbf{x}). \quad (25c)$$

**Remark 4.** The error representation presented in Section 3.4 (and also its counterpart for error in quantities of interest presented in Section 4.3) holds for any admissible solution  $\hat{\mathbf{u}} \in \mathcal{U}$ . Note however that the stress equilibration procedures required to obtain computable bounds, see Section 3.6, may require additional constraints on  $\hat{\mathbf{u}} \in \mathcal{U}$ . Note that the choice for  $\hat{\mathbf{u}}$  defined in Eq. (25) fulfills the requirements of the stress equilibration technique used in Section 3.7.

### 3.6. Construction of D-admissible fields

Once the field  $\hat{\mathbf{u}} \in \mathcal{U}$  is available, the D-admissible field is built such that  $\hat{\sigma} \in \mathcal{S}(\hat{\mathbf{u}})$ . The construction of  $\hat{\sigma}$  is more involved than the one for  $\hat{\mathbf{u}}$ . The reason is that the admissible stress has to be equilibrated in a dynamic sense. The dynamic equilibration reduces to static equilibration at each time  $t \in \mathcal{T}$  if certain conditions are satisfied. This property allows using the standard equilibration techniques for the static problem that are well studied in the literature [26,27,22]. These conditions are not a strong restriction but they are worth to be stressed out. They read:

- The external loads  $\mathbf{f}$  and  $\mathbf{g}$  have to be continuous in time and with linear time-dependence in the time slabs of the time partition  $\mathcal{T}$ .
- The acceleration  $\ddot{\hat{\mathbf{u}}}$  associated with the K-admissible field has to be continuous in time and with linear time-dependence in the time slabs of the timepartition  $\mathcal{T}$ .

Moreover, if local stress equilibration techniques [26,27,22] are used to compute the D-admissible field  $\hat{\sigma}$  (as in this article) further considerations should be regarded:

- The input of the local stress equilibration is not only the admissible field  $\hat{\mathbf{u}}$ , but also the fields  $\mathbf{u}_n^{H,\Delta t}, \mathbf{v}_n^{H,\Delta t}, \mathbf{a}_n^{H,\Delta t} \in \mathcal{V}_0^H$  fulfilling Eq. (8). Moreover,  $\hat{\mathbf{u}}$  has to be such that  $\hat{\mathbf{u}}(t_n) = \mathbf{a}_n^{H,\Delta t}$  for  $n = 0, \dots, N$ , in order to build a stress field  $\hat{\sigma}$  fulfilling Eq. (18). In a practical point of view, it means that the fields  $\mathbf{u}_n^{H,\Delta t}, \mathbf{v}_n^{H,\Delta t}, \mathbf{a}_n^{H,\Delta t}$  cannot be cleared out once the field  $\hat{\mathbf{u}}$  is available.

The following theorem demonstrates how the dynamic equilibration reduces to a bunch of static equilibrations.

**Theorem 2.** *Given the external loads  $\mathbf{f}, \mathbf{g}$  and a K-admissible field  $\hat{\mathbf{u}} \in \mathcal{U}$ , then a D-admissible stress  $\hat{\sigma} \in \mathcal{S}(\hat{\mathbf{u}})$  is straightforwardly defined through linear interpolation in time*

$$\hat{\sigma}(\mathbf{x}, t) := \sum_{n=0}^N \hat{\sigma}_n(\mathbf{x}) \theta_n(t), \quad (26)$$

provided that: 1) the stress fields  $\hat{\sigma}_n$ ,  $n = 0, \dots, N$  fulfill the static equilibrium condition

$$(\hat{\sigma}_n, \boldsymbol{\varepsilon}(\mathbf{w})) = l_n(\mathbf{w}) - (\rho \ddot{\hat{\mathbf{u}}}_n, \mathbf{w}) \quad \forall \mathbf{w} \in \mathcal{V}_0, \quad (27)$$

and 2) the external loads  $\mathbf{f}, \mathbf{g}$  and the acceleration  $\ddot{\hat{\mathbf{u}}}$  are piecewise linear in time, i.e.

$$\mathbf{f}(\mathbf{x}, t) = \sum_{n=0}^N \mathbf{f}_n(\mathbf{x}) \theta_n(t), \quad (28a)$$

$$\mathbf{g}(\mathbf{x}, t) = \sum_{n=0}^N \mathbf{g}_n(\mathbf{x}) \theta_n(t), \quad (28b)$$

$$\ddot{\hat{\mathbf{u}}}(\mathbf{x}, t) = \sum_{n=0}^N \ddot{\hat{\mathbf{u}}}_n(\mathbf{x}) \theta_n(t). \quad (28c)$$

**Proof.** The proof is obtained introducing expressions (28) and (26) in the definition (17).  $\square$

Theorem 2 allows building the admissible field  $\hat{\sigma}$  from the stresses  $\hat{\sigma}_n$ ,  $n = 0, \dots, N$  fulfilling Eq. (27). The stress fields  $\hat{\sigma}_n$  are not unique and they can be computed with different techniques, e.g. [26,28].

Refs. [26,28] deal with strict estimates. That is, they provide stress fields  $\hat{\sigma}_n$  fulfilling exactly Eq. (27). This work focuses in asymptotic estimates, i.e. Eq. (27) is solved using a reference mesh. The resulting approximations to stresses  $\hat{\sigma}_n$  fulfill Eq. (27) only asymptotically, that is the equilibrium condition is fulfilled if the element size of the reference mesh tends to zero. The asymptotic approach is adopted for its ease of implementation. However, it is worth noting that all the developments (except the remainder of this section) are general and also valid for strict estimates.

A direct version (but prohibitive) of an asymptotic estimate is to approximate  $\hat{\sigma}_n$  with a displacement-based problem using a global reference mesh with element size  $h \ll H$ . This mesh can be generated as a nested subdivision of the existing one, generating the space  $\mathcal{V}_0^h$  such that  $\mathcal{V}_0^h \subset \mathcal{V}_0 \subset \mathcal{V}_0$ . The reference problem providing this solution reads: find  $\mathbf{u}^h \in \mathcal{V}_0^h$  such that

$$a(\mathbf{u}_n^h, \mathbf{w}) = l_n(\mathbf{w}) - (\rho \ddot{\hat{\mathbf{u}}}_n, \mathbf{w}) \quad \forall \mathbf{w} \in \mathcal{V}_0^h.$$

The displacement field  $\mathbf{u}_n^h$  is associated with the stress field  $\hat{\sigma}_n^{\text{ref}} := \boldsymbol{\varepsilon}(\mathbf{u}_n^h)$ . The time dependent stress  $\hat{\sigma}_n^{\text{ref}}$  is defined from all the  $\hat{\sigma}_n^{\text{ref}}$  in the same fashion as for Eq. (26):

$$\hat{\sigma}^{\text{ref}}(\mathbf{x}, t) := \sum_{n=0}^N \theta_n(t) \hat{\sigma}_n^{\text{ref}}(\mathbf{x}). \quad (29)$$

In the remainder of the paper, for all practical purposes,  $\hat{\sigma}^{\text{ref}}$  is assumed to fairly replace  $\hat{\sigma}$  as for the results concerning the error in the constitutive relation introduced in Section 3.4.

### 3.7. Flux-free error estimates

The methods allowing to compute a D-admissible stress field with an affordable computational cost require using domain decomposition. That is, solving local counterparts of Eq. (27). The two main approaches for domain decomposition are the hybrid-flux [26] and the flux-free methodologies [22], using respectively as local subdomains the elements and patches of elements centered in one node (stars). Other approaches furnish D-admissible fields solving global dual problems (having stresses as unknowns) on the original finite element mesh, see for instance [29,30]. Here, the flux-free approach is selected.

This section is devoted to briefly review this technique and its specific application in the context of this paper. The objective is generating a collection of stress fields  $\hat{\sigma}_n^h$  fulfilling an asymptotic version of Eq. (27). Thus, an asymptotically D-admissible stress  $\hat{\sigma}^{\text{ff}}$  is computed from  $\hat{\sigma}_n^{\text{ff}}$  similarly to (29).

The stress fields  $\hat{\sigma}_n^{\text{ff}}$ ,  $n = 0, \dots, N$ , are generated using approximations to the error in displacements at time  $t_n$ ,  $\tilde{\mathbf{e}}_n$ , namely

$$\hat{\sigma}_n^{\text{ff}} := \mathcal{C} : \boldsymbol{\varepsilon}(\tilde{\mathbf{e}}_n + \mathbf{u}_n^{H,\Delta t} + \tau \mathbf{v}_n^{H,\Delta t}). \quad (30)$$

As previously said, the estimates  $\tilde{\mathbf{e}}_n$  are obtained with the flux free method, see [22] for details, as a sum of local contributions associated with patches of elements. The main rationale of this method is to compute function  $\tilde{\mathbf{e}}_n$  as the addition of local estimates  $\tilde{\mathbf{e}}_n^i$ , i.e.

$$\tilde{\mathbf{e}}_n := \sum_{i \in \mathcal{N}} \tilde{\mathbf{e}}_n^i, \quad (31)$$

where  $\mathcal{N}$  is the set of the indices of the vertex nodes in the mesh. In fact, each local estimate  $\tilde{\mathbf{e}}_n^i$  is computed in the element patch centered at the  $i$ -th node,  $i \in \mathcal{N}$ . This element patch is defined as the support of the shape function  $\phi^i$  of the  $i$ -th node, that is  $\omega^i := \text{supp}(\phi^i)$ .

The local estimate  $\tilde{\mathbf{e}}_n^i$  lives in the space  $\mathcal{V}_{\omega^i}^h$  which is the restriction of  $\mathcal{V}_0^h$  to  $\omega^i$ , namely

$$\mathcal{V}_{\omega^i}^h := \mathcal{V}_0^h \cap [H^1(\omega^i)]^d.$$

The sum of all these local spaces generates the broken space  $\hat{\mathcal{V}}_0^h$  which is the space where  $\tilde{\mathbf{e}}_n$  lives. Functions in  $\hat{\mathcal{V}}_0^h$  are of the same type as in  $\mathcal{V}_0^h$  but they are allowed to be discontinuous between the elements of the mesh.

Each local estimate  $\tilde{\mathbf{e}}_n^i$  is one solution of the problem: find  $\tilde{\mathbf{e}}_n^i \in \mathcal{V}_{\omega^i}^h$  such that

$$a(\tilde{\mathbf{e}}_n^i, \mathbf{w}) = R_n(\phi^i(\mathbf{w} - \Pi^H \mathbf{w})) \quad \forall \mathbf{w} \in \mathcal{V}_{\omega^i}^h, \quad (32)$$

where

$$R_n(\mathbf{w}) := I_n(\mathbf{w}) - (\rho \mathbf{a}_n^{H,\Delta t}, \mathbf{w}) - a(\mathbf{u}_n^{H,\Delta t} + \tau \mathbf{v}_n^{H,\Delta t}, \mathbf{w}), \quad (33)$$

is the residual of the Newmark solution at time  $t_n \in \mathcal{T}$ . The operator  $\Pi^H : \mathcal{V}_0 \rightarrow \mathcal{V}_0^h$  is the interpolation operator in  $\mathcal{V}_0^h$ .

It is worth noting that the flux-free method (or other alternative local stress equilibration technique) requires that the residual  $R_n$  fulfills Galerkin orthogonality. It is crucial in the well-posedness (solvability) of the local problems. In fact, for the residual  $R_n$  introduced in (33), the following expression holds

$$R_n(\mathbf{w}) = 0 \quad \forall \mathbf{w} \in \mathcal{V}_0^h.$$

Recall that the definition of the D-admissible space  $\mathcal{S}(\hat{\mathbf{u}})$  depends on  $\hat{\mathbf{u}}$ . Note however that  $\hat{\mathbf{u}}$  is not explicitly involved in Eq. (32), which is the seed problem to provide  $\hat{\sigma}^{\text{ff}}$ . This is not contradictory because the K-admissible field  $\hat{\mathbf{u}}$  is build such that  $\hat{\mathbf{u}} = \mathbf{a}^{H,\Delta t}$ .

Once  $\tilde{\mathbf{e}}_n^i$  are computed for  $i \in \mathcal{N}$  solving (32),  $\tilde{\mathbf{e}}_n$  is recovered using (31) and the stress field  $\hat{\sigma}_n^{\text{ff}}$  follows from (30). The D-admissible estimate  $\hat{\sigma}^{\text{ff}}$  is completed using the time interpolation analogous to (29).

The flux-free recovered stresses  $\hat{\sigma}^{\text{ff}}$  is D-admissible in the asymptotic sense, that is fulfilling equilibrium as stated is Eq. (17) but referred to a discrete space associated with the reference  $h$ -mesh (replacing  $\mathcal{W}$  by the discrete  $h$ -version). Thus, the estimate provided by  $\hat{\sigma}^{\text{ff}}$  does not yield a strict upper bound with respect to the exact error, as indicated in Theorem 1. Nevertheless, the flux-free estimate furnishes an asymptotic upper bound, that is a true upper bound with respect to the reference quantity associated with  $\hat{\sigma}^{\text{ref}}$ . This is stated in the following theorem.

**Theorem 3.** *Given the K-admissible field  $\hat{\mathbf{u}} \in \mathcal{U}$  defined in (25), the following relation holds for the two asymptotic D-admissible fields  $\hat{\sigma}^{\text{ref}}$  and  $\hat{\sigma}^{\text{ff}}$*

$$\|\hat{\sigma}^{\text{ff}} - \mathbf{s}(\hat{\mathbf{u}})\|_{\sigma} \geq \|\hat{\sigma}^{\text{ref}} - \mathbf{s}(\hat{\mathbf{u}})\|_{\sigma}. \quad (34)$$

**Proof.** Note that  $\hat{\sigma}^{\text{ff}}$  and  $\hat{\sigma}^{\text{ref}}$  can be expressed as

$$\hat{\sigma}^{\text{ref}} = \mathcal{C} : \boldsymbol{\varepsilon}(\mathbf{u}^{H,\Delta t} + \tau \mathbf{v}^{H,\Delta t} + \mathbf{e}^h),$$

$$\hat{\sigma}^{\text{ff}} = \mathcal{C} : \boldsymbol{\varepsilon}(\mathbf{u}^{H,\Delta t} + \tau \mathbf{v}^{H,\Delta t} + \tilde{\mathbf{e}}).$$

by considering

$$\mathbf{u}^h(\mathbf{x}, t) := \sum_{n=0}^N \mathbf{u}_n^h(\mathbf{x}) \theta_n(t), \quad \tilde{\mathbf{e}}(\mathbf{x}, t) := \sum_{n=0}^N \tilde{\mathbf{e}}_n(\mathbf{x}) \theta_n(t) \quad \text{and}$$

$$\mathbf{e}^h := \mathbf{u}^h - \mathbf{u}^{H,\Delta t} - \tau \mathbf{v}^{H,\Delta t}.$$

Thus,

$$\begin{aligned} \|\hat{\sigma}^{\text{ref}} - \mathbf{s}(\hat{\mathbf{u}})\|_{\sigma}^2 &= \frac{1}{\tau} \int_I \|\mathbf{e}^h + (\mathbf{u}^{H,\Delta t} - \hat{\mathbf{u}}) + \tau(\mathbf{v}^{H,\Delta t} - \dot{\hat{\mathbf{u}}})\|^2 dt \\ &= \frac{1}{\tau} \int_I \left\{ \|\mathbf{e}^h\|^2 + \|\mathbf{d}\|^2 + 2a(\mathbf{e}^h, \mathbf{d}) \right\} dt, \end{aligned}$$

and

$$\begin{aligned} \|\hat{\sigma}^{\text{ff}} - \mathbf{s}(\hat{\mathbf{u}})\|_{\sigma}^2 &= \frac{1}{\tau} \int_I \|\tilde{\mathbf{e}} + (\mathbf{u}^{H,\Delta t} - \hat{\mathbf{u}}) + \tau(\mathbf{v}^{H,\Delta t} - \dot{\hat{\mathbf{u}}})\|^2 dt \\ &= \frac{1}{\tau} \int_I \left\{ \|\tilde{\mathbf{e}}\|^2 + \|\mathbf{d}\|^2 + 2a(\tilde{\mathbf{e}}, \mathbf{d}) \right\} dt, \end{aligned} \quad (35)$$

where

$$\mathbf{d} := (\mathbf{u}^{H,\Delta t} - \hat{\mathbf{u}}) + \tau(\mathbf{v}^{H,\Delta t} - \dot{\hat{\mathbf{u}}}).$$

Then, the proof of the theorem reduces to

$$\|\tilde{\mathbf{e}}\|^2 + 2a(\tilde{\mathbf{e}}, \mathbf{d}) \geq \|\mathbf{e}^h\|^2 + 2a(\mathbf{e}^h, \mathbf{d}).$$

Note that fields  $\mathbf{e}^h$  and  $\tilde{\mathbf{e}}$  have been defined such that

$$R(\mathbf{d}) = a(\tilde{\mathbf{e}}, \mathbf{d}) = a(\mathbf{e}^h, \mathbf{d}),$$

where

$$R(\mathbf{w}(\mathbf{x}, t)) := \sum_{n=0}^N R_n(\mathbf{w}(\mathbf{x}, t_n)) \theta_n(t).$$

The proof is concluded by observing that

$$\|\tilde{\mathbf{e}}\|^2 \geq \|\mathbf{e}^h\|^2,$$

which is a consequence of the construction of the flux-free estimates, see [22] for details.  $\square$

## 4. Bounds of linear functional outputs

### 4.1. Quantity of interest

The present study aims at obtaining bounds for some given quantity of interest of the solution, denoted by  $L^{\circ}(\mathbf{u})$ , being  $L^{\circ}$  a linear form such that

$$L^{\circ} : \mathcal{U} \rightarrow \mathbb{R}$$

$$\mathbf{w} \mapsto L^{\circ}(\mathbf{w}).$$

The structure of  $L^{\circ}$  is restricted to be as follows:

$$\begin{aligned} L^{\circ}(\mathbf{w}) &:= \int_I (\mathbf{f}^{\circ}, \dot{\mathbf{w}}) dt \quad (\text{average of velocities in } \Omega \times I) \\ &+ \int_I (\mathbf{g}^{\circ}, \dot{\mathbf{w}})_{\Gamma_N} dt \quad (\text{average of velocities on } \Gamma_N \times I) \\ &+ (\rho \mathbf{v}^{\circ}, \dot{\mathbf{w}}(T)) \quad (\text{average of velocities at } \Omega \times \{T\}) \\ &+ a(\mathbf{u}^{\circ}, \mathbf{w}(T)) \quad (\text{average of strains at } \Omega \times \{T\}), \end{aligned} \quad (36)$$

where  $\mathbf{f}^\circ$ ,  $\mathbf{g}^\circ$ ,  $\mathbf{v}^\circ$  and  $\mathbf{u}^\circ$  are the data characterizing the quantity of interest. The interpretation of each term of the previous equation is indicated inline, being  $\mathbf{w}$  a displacement. This functional is rewritten in a more compact form:

$$L^\circ(\mathbf{w}) = L^d(\mathbf{w}) + (\rho \mathbf{v}^\circ, \dot{\mathbf{w}}(T)) + a(\mathbf{u}^\circ, \mathbf{w}(T)), \quad (37)$$

where

$$L^d(\mathbf{w}) := \int_I l^d(\dot{\mathbf{w}}) dt,$$

$$l^d(\mathbf{v}) := (\mathbf{f}^\circ, \mathbf{w}) + (\mathbf{g}^\circ, \mathbf{w})_{\Gamma_N}.$$

#### 4.2. Adjoint problem

The *adjoint* or *dual* problem of Eqs. (1) associated with the quantity of interest given in (36) consists in finding  $\mathbf{u}^d$  such that

$$\rho \ddot{\mathbf{u}}^d - \nabla \cdot \boldsymbol{\sigma}^d = \mathbf{f}^\circ \quad \text{in } \Omega \times I, \quad (38a)$$

$$\mathbf{u}^d = 0 \quad \text{on } \Gamma_D \times I, \quad (38b)$$

$$\boldsymbol{\sigma}^d \cdot \mathbf{n} = \mathbf{g}^\circ \quad \text{on } \Gamma_N \times I, \quad (38c)$$

$$\mathbf{u}^d = -\mathbf{u}^\circ \quad \text{at } \Omega \times \{T\}, \quad (38d)$$

$$\dot{\mathbf{u}}^d = -\mathbf{v}^\circ \quad \text{at } \Omega \times \{T\}, \quad (38e)$$

with the constitutive law

$$\boldsymbol{\sigma}^d := \mathcal{C} : \boldsymbol{\varepsilon}(\mathbf{u}^d - \boldsymbol{\tau} \dot{\mathbf{u}}^d). \quad (39)$$

The external loads and final conditions of the adjoint problem are determined by the definition of quantity of interest in Eq. (36). The adjoint problem has not the same form as the original one because it has final conditions instead of initial ones and negative damping.

**Remark 5.** The adjoint problem (38) has the same form as the original (1) if integrated backwards in time. Note that introducing the change of variables  $t^* := T - t$ , the associated new unknown is  $\mathbf{u}^*(t^*) := \mathbf{u}^d(T - t^*)$ ,

which is solution of the following equations

$$\rho \ddot{\mathbf{u}}^* - \nabla \cdot \boldsymbol{\sigma}^* = \mathbf{f}^\circ \quad \text{in } \Omega \times I, \quad (40a)$$

$$\mathbf{u}^* = 0 \quad \text{on } \Gamma_D \times I, \quad (40b)$$

$$\boldsymbol{\sigma}^* \cdot \mathbf{n} = \mathbf{g}^\circ \quad \text{on } \Gamma_N \times I, \quad (40c)$$

$$\mathbf{u}^* = -\mathbf{u}^\circ \quad \text{at } \Omega \times \{t^* = 0\}, \quad (40d)$$

$$\dot{\mathbf{u}}^* = \mathbf{v}^\circ \quad \text{at } \Omega \times \{t^* = 0\}, \quad (40e)$$

with

$$\boldsymbol{\sigma}^* := \mathcal{C} : \boldsymbol{\varepsilon}(\mathbf{u}^* + \boldsymbol{\tau} \dot{\mathbf{u}}^*).$$

Note that problem (40) has exactly the same form (including stability properties associated with the sign of the damping term) as (1).

A variational setting for the adjoint problem (38) is required in the following. To this end, the adjoint trial space is defined as

$$\mathcal{U}^d := \left\{ \mathbf{w} \in \mathcal{W} : \begin{array}{l} \mathbf{w} = -\mathbf{u}^\circ \quad \text{at } \Omega \times \{T\}, \\ \dot{\mathbf{w}} = -\mathbf{v}^\circ \quad \text{at } \Omega \times \{T\} \end{array} \right\}.$$

The set  $\mathcal{U}^d$  contains the *adjoint kinematically admissible* or *adjoint K-admissible* displacements. These functions have the same regularity constrains and boundary conditions as the ones in  $\mathcal{U}$  and the final conditions of the adjoint problem (38).

With this notation, the weak form of the adjoint problem (38) reads: find  $\mathbf{u}^d \in \mathcal{U}^d$  such that

$$B^d(\mathbf{u}^d, \mathbf{w}) = L^d(\mathbf{w}) \quad \forall \mathbf{w} \in \mathcal{W}, \quad (41)$$

where for  $\mathbf{v}, \mathbf{w} \in \mathcal{W}$

$$B^d(\mathbf{v}, \mathbf{w}) := \int_I (\rho \dot{\mathbf{v}}, \dot{\mathbf{w}}) dt + \int_I a(\mathbf{v} - \boldsymbol{\tau} \dot{\mathbf{v}}, \dot{\mathbf{w}}) dt.$$

Note that  $B^d$  is similar to the bilinear form of the original problem defined in Eq. (6a) but with opposite sign of the damping term. The following relation holds between forms  $B$  and  $B^d$ :

$$B(\mathbf{v}, \mathbf{w}) = -B^d(\mathbf{w}, \mathbf{v}) + [(\rho \dot{\mathbf{w}}, \dot{\mathbf{v}}) + a(\mathbf{w}, \mathbf{v})]_{t=0}^{t=T}. \quad (42)$$

This relation is easily derived noting that

$$\begin{aligned} B(\mathbf{v}, \mathbf{w}) &= \int_I (\rho \dot{\mathbf{v}}, \dot{\mathbf{w}}) dt + \int_I a(\mathbf{v} + \boldsymbol{\tau} \dot{\mathbf{v}}, \dot{\mathbf{w}}) dt \\ &= - \int_I (\rho \dot{\mathbf{w}}, \dot{\mathbf{v}}) dt - \int_I a(\mathbf{w} - \boldsymbol{\tau} \dot{\mathbf{w}}, \dot{\mathbf{v}}) dt \\ &\quad + [(\rho \dot{\mathbf{w}}, \dot{\mathbf{v}}) + a(\mathbf{w}, \mathbf{v})]_{t=0}^{t=T}. \end{aligned}$$

#### 4.3. Error representation in the quantity of interest

Bounds of the quantity of interest  $L^\circ(\mathbf{u})$  are obtained combining admissible pairs for both the original and the adjoint problem,  $(\boldsymbol{\sigma}, \dot{\mathbf{u}})$  and  $(\boldsymbol{\sigma}^d, \dot{\mathbf{u}}^d)$ . These admissible pairs allow to express the error in the quantity of interest  $L^\circ(\hat{\mathbf{e}})$  in terms of energy products, see Theorem 4 below. Moreover, bounds for the quantity of interest are obtained from energy estimates, using Eq. (24) or similar variations.

The admissible pair for the adjoint problem (38) is obtained such that  $(\boldsymbol{\sigma}^d, \dot{\mathbf{u}}^d) \in \mathcal{S}^d(\dot{\mathbf{u}}^d) \times \mathcal{U}^d$ . The space of *adjoint dynamically admissible* or *adjoint D-admissible* fields is defined for a given  $\dot{\mathbf{u}}^d \in \mathcal{U}^d$  as follows

$$\mathcal{S}^d(\dot{\mathbf{u}}^d) := \left\{ \boldsymbol{\tau} \in \mathcal{Z} : \int_I (\boldsymbol{\tau}, \boldsymbol{\varepsilon}(\dot{\mathbf{w}})) dt = L^d(\mathbf{w}) - \int_I (\rho \ddot{\mathbf{u}}^d, \dot{\mathbf{w}}) dt \quad \forall \mathbf{w} \in \mathcal{W} \right\}.$$

The space  $\mathcal{S}^d(\dot{\mathbf{u}}^d)$  contains stress tensors in dynamic equilibrium respect to the loads of the adjoint problem and the inertia related to the acceleration  $\ddot{\mathbf{u}}^d$ .

The admissible pair  $(\boldsymbol{\sigma}^d, \dot{\mathbf{u}}^d) \in \mathcal{S}(\dot{\mathbf{u}}^d) \times \mathcal{U}^d$  determines the error in stresses for the adjoint problem:

$$\boldsymbol{\sigma}^{d,e} := \boldsymbol{\sigma}^d - \mathcal{S}^E(\dot{\mathbf{u}}^d) + \mathcal{S}^V(\dot{\mathbf{u}}^d),$$

which corresponds to the non verification of the constitutive relation of the adjoint problem (39). The constitutive relation error of the adjoint problem is the value  $\|\boldsymbol{\sigma}^{d,e}\|_\sigma$ .

The errors  $\boldsymbol{\sigma}^e$  and  $\boldsymbol{\sigma}^{d,e}$  are seen as the solutions of the residual error equations

$$\bar{B}^V(\boldsymbol{\sigma}^e, \mathcal{S}^V(\mathbf{w})) = \hat{R}(\mathbf{w}) \quad \forall \mathbf{w} \in \mathcal{W}, \quad (43a)$$

$$\bar{B}^V(\boldsymbol{\sigma}^{d,e}, \mathcal{S}^V(\mathbf{w})) = \hat{R}^d(\mathbf{w}) \quad \forall \mathbf{w} \in \mathcal{W}, \quad (43b)$$

where the residual for the adjoint problem is defined by

$$\hat{R}^d(\mathbf{w}) := L^d(\mathbf{w}) - B^d(\dot{\mathbf{u}}^d, \mathbf{w}).$$

The previous relations are easily derived from the definition of D-admissibility. For instance, Eq. (43a) follows from the property included in the definition of  $\mathcal{S}(\dot{\mathbf{u}})$  in Eq. (17) by simply subtracting  $\int_I a(\dot{\mathbf{u}} + \boldsymbol{\tau} \dot{\mathbf{u}}, \dot{\mathbf{w}}) dt$  at each hand side. The proof for (43b) is analogous.

**Theorem 4.** If  $(\boldsymbol{\sigma}, \dot{\mathbf{u}}) \in \mathcal{S}(\dot{\mathbf{u}}) \times \mathcal{U}$  and  $(\boldsymbol{\sigma}^d, \dot{\mathbf{u}}^d) \in \mathcal{S}^d(\dot{\mathbf{u}}^d) \times \mathcal{U}^d$  are two admissible pairs for the original and adjoint problems, then the following error representation holds

$$L^\circ(\hat{\mathbf{e}}) + \hat{\alpha} = \hat{R}^d(\hat{\mathbf{e}}), \quad (44)$$

or alternatively

$$L^\circ(\hat{\mathbf{e}}) + \hat{\alpha} = \bar{B}^V(\boldsymbol{\sigma}^{d,e}, \mathcal{S}^V(\hat{\mathbf{e}})), \quad (45)$$

where  $\hat{\alpha}$  is the following correcting term

$$\hat{\alpha} := \hat{R}(\hat{\mathbf{u}}^d) = \bar{B}^v(\hat{\boldsymbol{\sigma}}^e, \mathbf{s}^v(\hat{\mathbf{u}}^d)).$$

**Proof.** Introducing  $\hat{\mathbf{e}}$  in the definition of  $L^O$  in Eq. (37) and using the statement of the adjoint problem (41), it yields

$$L^O(\hat{\mathbf{e}}) = B^d(\mathbf{u}^d, \hat{\mathbf{e}}) + (\rho \mathbf{v}^o, \hat{\mathbf{e}}(T)) + a(\mathbf{u}^o, \hat{\mathbf{e}}(T)).$$

Adding and subtracting  $\hat{\mathbf{u}}^d$  in the first argument of  $B^d$ , it yields

$$L^O(\hat{\mathbf{e}}) = B^d(\mathbf{u}^d - \hat{\mathbf{u}}^d, \hat{\mathbf{e}}) + B^d(\hat{\mathbf{u}}^d, \hat{\mathbf{e}}) + (\rho \mathbf{v}^o, \hat{\mathbf{e}}(T)) + a(\mathbf{u}^o, \hat{\mathbf{e}}(T))$$

This expression is rewritten using the relation in Eq. (42), taking  $\mathbf{w} = \hat{\mathbf{u}}^d$  and  $\mathbf{v} = \hat{\mathbf{e}}$ ,

$$L^O(\hat{\mathbf{e}}) = B^d(\mathbf{u}^d - \hat{\mathbf{u}}^d, \hat{\mathbf{e}}) - B(\hat{\mathbf{e}}, \hat{\mathbf{u}}^d) + (\rho \mathbf{v}^o, \hat{\mathbf{e}}(T)) + a(\mathbf{u}^o, \hat{\mathbf{e}}(T)) + [(\rho \hat{\mathbf{u}}^d, \hat{\mathbf{e}}) + a(\hat{\mathbf{u}}^d, \hat{\mathbf{e}})]_{t=0}^{t=T}.$$

Taking into account the definition of the residuals  $\hat{R}$  and  $\hat{R}^d$  and the initial conditions for the original error,  $\hat{\mathbf{e}}(0) = \hat{\mathbf{e}}(0) = 0$  and the final conditions for the adjoint problem,  $\hat{\mathbf{u}}^d(T) = -\mathbf{u}^o$  and  $\hat{\mathbf{u}}^d(T) = -\mathbf{v}^o$ , the previous expression results in

$$L^O(\hat{\mathbf{e}}) = \hat{R}^d(\hat{\mathbf{e}}) - \hat{R}(\hat{\mathbf{u}}^d).$$

This proves expression (44). Expression (45) is derived using the residual representation of Eqs. (43).  $\square$

As previously said, this result relates  $L^O(\hat{\mathbf{e}})$  with the energy-like quantities  $\hat{R}^d(\hat{\mathbf{e}})$  and  $B^v(\hat{\boldsymbol{\sigma}}^{d,e}, \mathbf{s}^v(\hat{\mathbf{e}}))$ . Note that  $\hat{\alpha}$  accounts for the lack of Galerkin orthogonality of residual  $\hat{R}$  and it is computable once the admissible fields are available.

#### 4.4. Bounds based on the Cauchy–Schwarz inequality

Bounds based on the Cauchy–Schwarz inequality are already introduced for visco-elastodynamics in Ref. [18]. These bounds are derived from the error representation in Eq. (45) along with the Cauchy–Schwarz inequality:

$$|L^O(\hat{\mathbf{e}}) + \hat{\alpha}| \leq \| \hat{\boldsymbol{\sigma}}^{d,e} \|_{\sigma} \| \mathbf{s}^v(\hat{\mathbf{e}}) \|_{\sigma} = \| \hat{\boldsymbol{\sigma}}^{d,e} \|_{\sigma} \| \hat{\mathbf{e}} \|_{\sigma}. \quad (46)$$

Note that the last factor in the latter expression is not computable because involves the unknown error  $\hat{\mathbf{e}}$ . An upper bound estimate for this factor is the error in the constitutive relation of the original problem, see Eq. (24). Introducing this estimate in the previous equation a computable bound for the error in the quantity of interest is readily recovered:

$$|L^O(\hat{\mathbf{e}}) + \hat{\alpha}| \leq \| \hat{\boldsymbol{\sigma}}^{d,e} \|_{\sigma} \| \hat{\boldsymbol{\sigma}}^e \|_{\sigma}.$$

The quantities defined as

$$\zeta_U^{C-S} := L^O(\hat{\mathbf{u}}) + \| \hat{\boldsymbol{\sigma}}^{d,e} \|_{\sigma} \| \hat{\boldsymbol{\sigma}}^e \|_{\sigma} - \hat{\alpha},$$

$$\zeta_L^{C-S} := L^O(\hat{\mathbf{u}}) - \| \hat{\boldsymbol{\sigma}}^{d,e} \|_{\sigma} \| \hat{\boldsymbol{\sigma}}^e \|_{\sigma} - \hat{\alpha},$$

are indeed upper and lower bounds of  $L^O(\mathbf{u})$ , that is

$$\zeta_L^{C-S} \leq L^O(\mathbf{u}) \leq \zeta_U^{C-S}. \quad (47)$$

## 5. Alternative error bounds

### 5.1. Alternative error representation and (non-computable) bounds

Alternative error bounds are often used in the literature to improve the poor quality of the bounds based on the Cauchy–Schwarz inequality. For instance, the parallelogram rule is applied in works [7,31,22] in the context of linear elasticity. Similar strategies based on algebraic identities are also applied to problems with non-symmetric bilinear forms as the case of the steady and transient

convection–diffusion–reaction equations, see Ref. [21]. However, to the best knowledge of the authors, these kind of approaches have not been used in the framework of linear visco-elastodynamics.

In the following, an alternative error representation is used to derive error bounds for quantities of interest in the context of visco-elastodynamics. The derivation of the basic rationale requires introducing symmetrized equations for the original and adjoint errors. Note, however, that the actual implementation of these strategies does not require solving the auxiliary symmetrized problems because the upper bound estimates are computed using only the admissible fields introduced above. These ideas are similar to those used in [21].

Consider the following symmetrized error equations: find  $\hat{\mathbf{e}}^v \in \mathcal{U}_0$  and  $\hat{\mathbf{e}}^{d,v} \in \mathcal{U}_0^d$  such that

$$B^v(\hat{\mathbf{e}}^v, \mathbf{w}) = \hat{R}(\mathbf{w}) \quad \forall \mathbf{w} \in \mathcal{W}, \quad (48a)$$

$$B^v(\hat{\mathbf{e}}^{d,v}, \mathbf{w}) = \hat{R}^d(\mathbf{w}) \quad \forall \mathbf{w} \in \mathcal{W}, \quad (48b)$$

and

$$\mathcal{U}_0^d := \left\{ \mathbf{w} \in \mathcal{W} : \begin{array}{l} \mathbf{w} = \mathbf{0} \quad \text{at } \Omega \times \{T\} \\ \dot{\mathbf{w}} = \mathbf{0} \quad \text{at } \Omega \times \{T\} \end{array} \right\}.$$

Eqs. (48) resemble the residual Eq. (12) for the error  $\hat{\mathbf{e}}$ . Note that the difference is that the bilinear form  $B$  is replaced by the symmetric one  $B^v$ .

**Theorem 5.** *If  $\hat{\mathbf{e}}^v$  and  $\hat{\mathbf{e}}^{d,v}$  are solution of Eqs. (48a) and (48b) then, for any  $\kappa \in \mathbb{R}$ ,  $\kappa \neq 0$ ,*

$$-\frac{1}{4} \| \kappa \hat{\mathbf{e}}^v - \frac{1}{\kappa} \hat{\mathbf{e}}^{d,v} \|^2 \leq L^O(\hat{\mathbf{e}}) + \hat{\alpha} \leq \frac{1}{4} \| \kappa \hat{\mathbf{e}}^v + \frac{1}{\kappa} \hat{\mathbf{e}}^{d,v} \|^2. \quad (49)$$

**Proof.** Taking  $\mathbf{w} = \kappa \hat{\mathbf{e}}$  in Eqs. (48a) and (48b), a linear combination of them (with weights  $\kappa$  and  $\pm 1/\kappa$ ) results in

$$B^v \left( \kappa \hat{\mathbf{e}}^v \pm \frac{1}{\kappa} \hat{\mathbf{e}}^{d,v}, \kappa \hat{\mathbf{e}} \right) = \kappa^2 \hat{R}(\hat{\mathbf{e}}) \pm \hat{R}^d(\hat{\mathbf{e}}).$$

Taking  $\mathbf{w} = \hat{\mathbf{e}}$  in Eq. (12) and using Eq. (16) it is obtained that

$$\hat{R}(\hat{\mathbf{e}}) \geq \| \hat{\mathbf{e}} \|^2.$$

Hence,

$$B^v \left( \kappa \hat{\mathbf{e}}^v \pm \frac{1}{\kappa} \hat{\mathbf{e}}^{d,v}, \kappa \hat{\mathbf{e}} \right) \geq \kappa^2 \| \hat{\mathbf{e}} \|^2 \pm L^O(\hat{\mathbf{e}}) \pm \hat{\alpha}, \quad (50)$$

where the term involving the adjoint residual,  $\hat{R}^d(\hat{\mathbf{e}})$  has been replaced by  $L^O(\hat{\mathbf{e}}) + \hat{\alpha}$  using Eq. (44) of Theorem 4.

On the other hand, one has that

$$B^v \left( \kappa \hat{\mathbf{e}}^v \pm \frac{1}{\kappa} \hat{\mathbf{e}}^{d,v}, \kappa \hat{\mathbf{e}} \right) - \kappa^2 \| \hat{\mathbf{e}} \|^2 \leq \frac{1}{4} \| \kappa \hat{\mathbf{e}}^v \pm \frac{1}{\kappa} \hat{\mathbf{e}}^{d,v} \|^2. \quad (51)$$

This is a direct consequence of considering the following expansion

$$\begin{aligned} 0 &\leq \| \frac{1}{2} \left( \kappa \hat{\mathbf{e}}^v \pm \frac{1}{\kappa} \hat{\mathbf{e}}^{d,v} \right) - \kappa \hat{\mathbf{e}} \|^2 \\ &= \frac{1}{4} \| \kappa \hat{\mathbf{e}}^v \pm \frac{1}{\kappa} \hat{\mathbf{e}}^{d,v} \|^2 + \kappa^2 \| \hat{\mathbf{e}} \|^2 - B^v \left( \kappa \hat{\mathbf{e}}^v \pm \frac{1}{\kappa} \hat{\mathbf{e}}^{d,v}, \kappa \hat{\mathbf{e}} \right). \end{aligned}$$

Thus, the proof is completed using Eq. (51) in Eq. (50)

$$\begin{aligned} \pm L^O(\hat{\mathbf{e}}) \pm \hat{\alpha} &\leq B^v \left( \kappa \hat{\mathbf{e}}^v \pm \frac{1}{\kappa} \hat{\mathbf{e}}^{d,v}, \kappa \hat{\mathbf{e}} \right) - \kappa^2 \| \hat{\mathbf{e}} \|^2 \\ &\leq \frac{1}{4} \| \kappa \hat{\mathbf{e}}^v \pm \frac{1}{\kappa} \hat{\mathbf{e}}^{d,v} \|^2. \quad \square \end{aligned}$$

**Remark 6.** Theorem 5 gives an alternative error representation in the quantity of interest. The structure of bounds in expression (49) is similar (but not the same) to those obtained using the

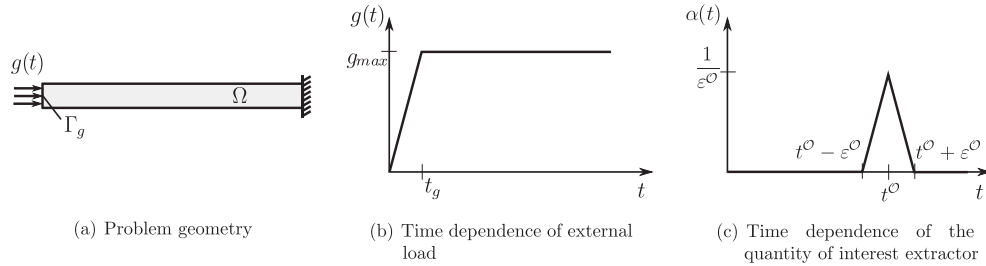


Fig. 1. Example 1: Problem statement and quantity of interest.

parallelogram rule in linear elasticity, where the error in the quantity of interest is also expressed in terms of energy measures of linear combinations of the original and adjoint errors. The main difference with respect the parallelogram rule is that, here lower bounds of the error are not computed.

Eq. (49) allows bounding  $L^O(\hat{\mathbf{e}})$  by computing  $\|\mathbf{z}^\pm\|^2$ , where  $\mathbf{z}^\pm := \kappa \hat{\mathbf{e}}^v \pm \frac{1}{\kappa} \hat{\mathbf{e}}^{d,v}$ . These two functions are solutions of

$$B^v(\mathbf{z}^\pm, \mathbf{w}) = \hat{R}^\pm(\mathbf{w}) \quad \forall \mathbf{w} \in \mathcal{W}, \quad (52)$$

where

$$\hat{R}^\pm(\mathbf{w}) := \kappa \hat{R}(\mathbf{w}) \pm \frac{1}{\kappa} \hat{R}^d(\mathbf{w}).$$

Functions  $\mathbf{z}^\pm$  are solutions of the infinite dimensional problems (52). Therefore, the error bounds proposed in (49), corresponding to the values of  $\|\mathbf{z}^\pm\|^2$ , are not computable. In the following, computable bounds are obtained from an auxiliary field  $\sigma_{z^\pm}$ , in the same fashion as the energy-like bounds described in Section 3.

### 5.2. Computable error bounds

As shown in Sections 3 and 4, the standard approach to obtain a computable error bound is to find a D-admissible stress. The admissible stress associated with  $\mathbf{z}^\pm$  is denoted by  $\sigma_{z^\pm}$  which fulfills the stress-version of Eq. (52), i.e.

$$\bar{B}^v(\sigma_{z^\pm}, \mathbf{s}^v(\mathbf{w})) = \hat{R}^\pm(\mathbf{w}) \quad \forall \mathbf{w} \in \mathcal{W}. \quad (53)$$

Comparing Eq. (53) and the residual representation of Eqs. (43), one concludes that the following linear combination of  $\hat{\sigma}^e$  and  $\hat{\sigma}^{d,e}$

$$\sigma_{z^\pm} := \kappa \hat{\sigma}^e \pm \frac{1}{\kappa} \hat{\sigma}^{d,e}, \quad (54)$$

is solution of (53). The value  $\|\sigma_{z^\pm}\|_\sigma$  is indeed an upper bound of  $\|\mathbf{z}^\pm\|$  as the following theorem shows.

**Theorem 6.** *Being  $\mathbf{z}^\pm$  and  $\sigma_{z^\pm}$  solutions of Eqs. (52) and (53) respectively, the following inequality holds*

$$\|\mathbf{z}^\pm\| \leq \|\sigma_{z^\pm}\|_\sigma.$$

**Proof.** On the one hand, one has that

$$\begin{aligned} 0 &\leq \|\sigma_{z^\pm} - \mathbf{s}^v(\mathbf{z}^\pm)\|_\sigma^2 = \|\sigma_{z^\pm}\|_\sigma^2 + \|\mathbf{z}^\pm\|^2 - 2\bar{B}^v(\sigma_{z^\pm}, \mathbf{s}^v(\mathbf{z}^\pm)) \\ &= \|\sigma_{z^\pm}\|_\sigma^2 + \|\mathbf{z}^\pm\|^2 - 2\hat{R}^\pm(\mathbf{z}^\pm). \end{aligned} \quad (55)$$

On the other hand, taking  $\mathbf{w} = \mathbf{z}^\pm$  in Eq. (52) one gets

$$\hat{R}^\pm(\mathbf{z}^\pm) = \|\mathbf{z}^\pm\|^2.$$

The proof is completed by substituting the latter expression into the last term of Eq. (55), namely

$$0 \leq \|\sigma_{z^\pm}\|_\sigma^2 - \|\mathbf{z}^\pm\|^2. \quad \square$$

Thus, using expression (54) for  $\sigma_{z^\pm}$ , an upper bound of  $\|\mathbf{z}^\pm\|^2$  is computed as

$$\|\kappa \hat{\sigma}^e \pm \frac{1}{\kappa} \hat{\sigma}^{d,e}\|_\sigma \geq \|\mathbf{z}^\pm\|. \quad (56)$$

As previously announced, expression (56) allows computing bounds for  $L^O(\hat{\mathbf{e}})$  without any use of the symmetrized error Eqs. (48). In fact, the introduction of the symmetrized error equations is only a mathematical artifact that allows deriving an alternative bounding expression. The final bounds for  $L^O(\mathbf{u})$  are derived substituting expression (56) in Eq. (49):

$$\begin{aligned} \zeta_U &:= L^O(\hat{\mathbf{u}}) + \frac{1}{4} \|\kappa \hat{\sigma}^e + \frac{1}{\kappa} \hat{\sigma}^{d,e}\|_\sigma^2 - \hat{\alpha}, \\ \zeta_L &:= L^O(\hat{\mathbf{u}}) - \frac{1}{4} \|\kappa \hat{\sigma}^e - \frac{1}{\kappa} \hat{\sigma}^{d,e}\|_\sigma^2 - \hat{\alpha}, \end{aligned}$$

where  $\zeta_U$  and  $\zeta_L$  are such that

$$\zeta_L \leq L^O(\mathbf{u}) \leq \zeta_U. \quad (57)$$

Note that  $\hat{\sigma}^e$  and  $\hat{\sigma}^{d,e}$  are eventually computed using asymptotic techniques, for instance the flux-free strategies. In this case, the upper bound properties (57) hold only asymptotically, that is if the size of the reference mesh is *small enough*. In practice, due to the overestimation introduced in the subsequent approximations, the estimates obtained are upper bound of the error in all the exam-

**Table 1**  
Example 1: Parameterization.

Geometry		
$\Omega$	$(0, 1) \times (0, 0.1)$	m <sup>2</sup>
$\Gamma_g$	$\{0\} \times (0, 1)$	m
$T$	$10^{-3}$	s
Material properties		
$E$	$2 \times 10^{11}$	Pa
$\nu$	0	
$\rho$	$8 \times 10^3$	kg/m <sup>3</sup>
$\tau$	$\{10^{-6}, 10^{-5}, 10^{-4}\}$	s
$\xi$	$\{0.393, 3.93, 39.3\}$	%
External load		
$\hat{g}_{\max}$	$10^8$	Pa
$t_g$	$0.05 \times 10^{-3}$	s
Quantity of interest		
$\epsilon^O$	$0.05 \times 10^{-3}$	s
$t^O$	$0.65 \times 10^{-3}$	s

ples. The parameter  $\kappa$  is determined such that it minimizes  $\|\kappa \hat{\sigma}^e \pm \frac{1}{\kappa} \hat{\sigma}^{d,e}\|_\sigma^2$ . This is achieved by enforcing

$$\frac{\partial}{\partial \kappa} \|\kappa \hat{\sigma}^e \pm \frac{1}{\kappa} \hat{\sigma}^{d,e}\|_\sigma^2 = 0 \Rightarrow \kappa \|\hat{\sigma}^e\|_\sigma^2 - \frac{1}{\kappa^3} \|\hat{\sigma}^{d,e}\|_\sigma^2 = 0$$

that is to say

$$\kappa = \left( \frac{\|\hat{\sigma}^{d,e}\|_\sigma}{\|\hat{\sigma}^e\|_\sigma} \right)^{1/2}$$

**Table 2**  
Example 1: Space and time discretizations.

	D.O.F.	H (m)	# Elements	N
Mesh 1	246	0.0190	160	330
Mesh 2	810	0.0095	640	660
Mesh 3	2898	0.0047	2560	1320
Mesh 4	10,914	0.0023	10,240	2640

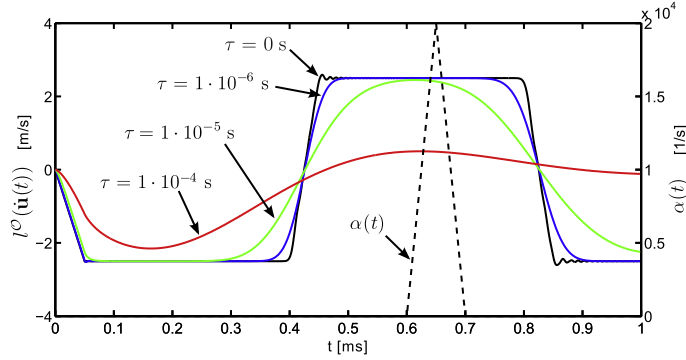


Fig. 2. Example 1: Time evolution of the of the average  $F^O(\hat{\mathbf{u}}(t))$  for three values of the viscosity (left y-axis) and time evolution of the weighting function  $\alpha(t)$  (right y-axis).

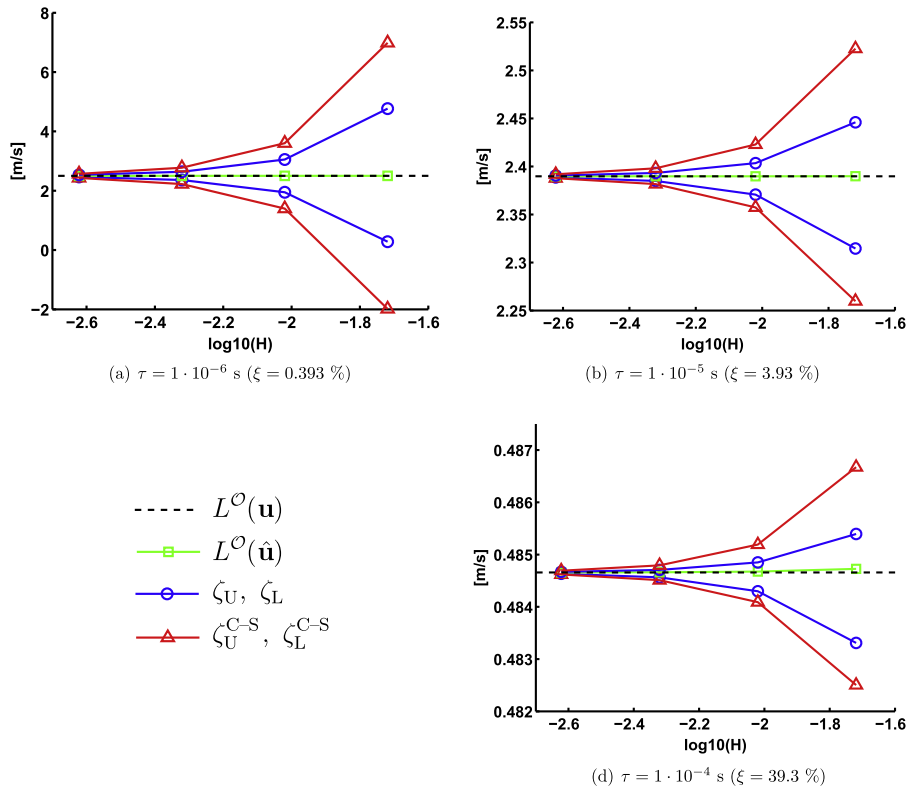


Fig. 3. Example 1: Convergence of the computed bounds for different values of element size and viscosity.

# COMPUTABLE BOUNDS OF FUNCTIONAL OUTPUTS IN LINEAR VISCO-ELASTODYNAMICS

F. Verdugo, P. Díez / *Comput. Methods Appl. Mech. Engrg.* 245–246 (2012) 313–330

323

## 6. Numerical examples

The error bounds corresponding to the Cauchy–Schwarz formulation, see expressions (47), and the error bounds proposed here, see (57), are compared in two academic examples. The first is a 1D bar and the second a 2D plate.

### 6.1. Example 1: 1D bar

The visco-elastic bar of Fig. 1(a) is considered. It is clamped at the right end and loaded on the left end with the time dependent traction described in Fig. 1(b). The material properties are displayed in Table 1, note that three different values of the viscosity are considered and that the Poisson ratio  $\nu$  is taken as zero in order to have a pure 1D problem. The damping factors  $\xi$  associated

with the values of the viscosities,  $10^{-6}$ ,  $10^{-5}$  and  $10^{-4}$  s, are 0.393%, 3.93% and 39.3% respectively. In this example, homogeneous initial conditions are considered. The geometry description of the bar and other parameters of the problem are also reported in Table 1.

This example focuses in the following quantity of interest:

$$L^\circ(\mathbf{w}) := \int_I \alpha(t) l^\circ(\dot{\mathbf{w}}(t)) dt,$$

where

$$l^\circ(\mathbf{w}) = (\mathbf{g}^\circ, \mathbf{w})_{\Gamma_g},$$

and

$$\mathbf{g}^\circ(\mathbf{x}) := \frac{-\mathbf{e}_1}{\text{meas}(\Gamma_g)},$$

**Table 3**  
Example 1: Convergence of the computed quantity of interest and the computed bounds. Results in (m/s).

$\tau$ (s)	D.O.F.	$L^\circ(\hat{\mathbf{u}})$	$L^\circ(\mathbf{u})$	$\zeta_U/L^\circ(\mathbf{u})$	$\zeta_L/L^\circ(\mathbf{u})$	$\zeta_U^{C-S}/L^\circ(\mathbf{u})$	$\zeta_L^{C-S}/L^\circ(\mathbf{u})$
$1 \times 10^{-6}$	246	2.499898	2.499999	1.906818	0.112661	2.794118	-0.794196
	810	2.500008	2.499999	1.220276	0.779112	1.441168	0.558840
	2898	2.499999	2.499999	1.055171	0.944885	1.110285	0.889714
	10,914	2.499999	2.499999	1.013780	0.986224	1.027555	0.972444
$1 \times 10^{-5}$	246	2.389878	2.389779	1.023540	0.968521	1.055623	0.945586
	810	2.389811	2.389779	1.005730	0.992021	1.013863	0.986444
	2898	2.389786	2.389779	1.001439	0.997990	1.003486	0.996589
	10,914	2.389779	2.389779	1.000359	0.999496	1.000872	0.999145
$1 \times 10^{-4}$	246	0.484727	0.484657	1.001518	0.997216	1.004156	0.995553
	810	0.484674	0.484657	1.000397	0.999259	1.001101	0.998825
	2898	0.484661	0.484657	1.000099	0.999808	1.000280	0.999697
	10,914	0.484657	0.484657	1.000023	0.999949	1.000068	0.999922

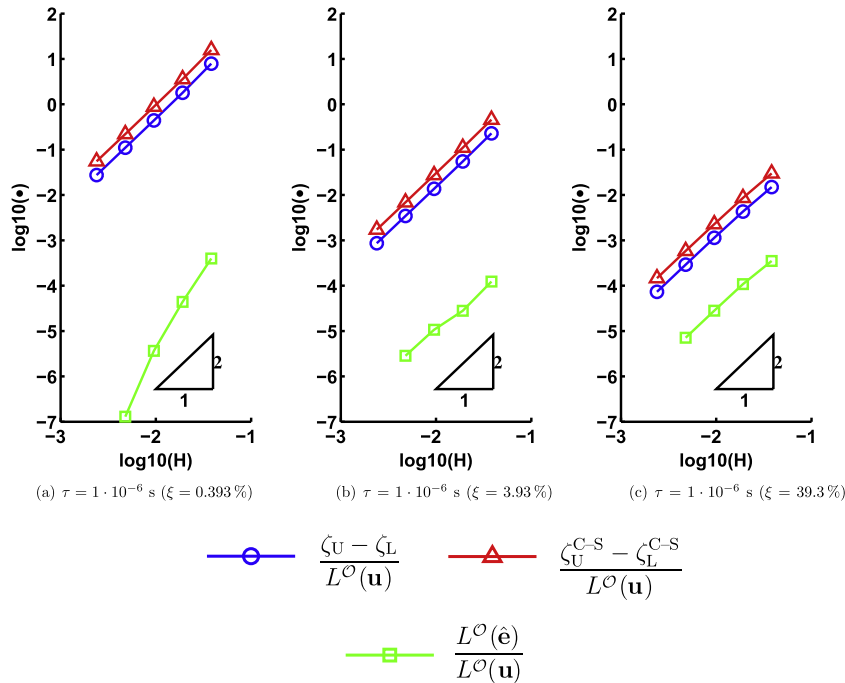


**Fig. 4.** Example 1: Convergence of the computed bound gap and the reference error for different values of element size and viscosity.

being  $\mathbf{e}_1$  the unit vector in the  $x$ -axis. Given the definition of the weighting function  $\alpha(t)$  in Fig. 1(c), the functional  $L^O$  represents an average of the velocities at the region of the Neumann boundary  $\Gamma_g$  in the time interval  $[t^o - \varepsilon^o, t^o + \varepsilon^o]$ .

The numerical simulation is carried out for four different meshes with decreasing element size. The ratio  $H/\Delta t$  is kept constant in the refinement processes in order to obtain proper convergence curves (note that if the time step is constant along the refinement, the error reduction is limited by a threshold given by the time discretization). The quantity kept constant is the ratio  $H/\Delta t$  (both  $H$  and  $\Delta t$  with the same exponent) because the method used has the same order of convergence both in space and time (linear elements are used in the spatial discretization), see [32,33] for the a priori estimates in space and time respectively.

In all computations the time step is taken as  $\Delta t = 0.8H/c$ , where the scalar  $c = \sqrt{E/\rho}$  is the sound speed of the medium. The Newmark parameters are taken as  $\beta = 1, \gamma = 0.5$ . The number of degrees of freedom, time steps and other parameters related with the discretization are given in Table 2. In all the examples, linear triangular meshes are used for computations. The flux-free strategy is used with a reference mesh of element size  $h := H/4$ . The value of the exact solution  $\mathbf{u}$  displayed in some figures and tables correspond to the reference solution obtained with the finer mesh (mesh 4).

Fig. 2 shows the time evolution of the average  $L^O(\hat{\mathbf{u}})$  and the weighting function  $\alpha(t)$ . Note that  $L^O(\mathbf{u})$  is directly obtained integrating in time the product of  $L^O(\hat{\mathbf{u}})$  and  $\alpha(t)$ . Note that, Fig. 2 contains an extra curve corresponding to a pure alastic solution ( $\tau = 0$  s). This is a way to illustrate the amount of damping introduced in the computations.

In a first phase, the behavior of the two bounds with respect to 1) the mesh element size and 2) the viscosity of the medium is analyzed. These two parameters are considered because they have a strong influence in the quality of the bounds. Fig. 3 and Table 3 show the convergence of the bounds for all the values of the viscosity considered in this example. It is observed that the bound gap decreases in the refinement process. This is as expected because

the bound gap is directly related with the residual of the numerical solution. On the other hand, the bounds are sharper for the higher values of the viscosity. In fact, the derivation of the bounding properties requires having the viscosity-related parameter  $\tau$  and therefore the quality of the bounds is degraded if  $\tau$  tends to zero.

Fig. 4 displays the convergence rate of the bound gap and the error  $L^O(\hat{\mathbf{e}})$ . Note that the obtained rate for the bound gap (slope 2 with respect to the element size) is consistent with the expected value, that corresponds to twice the expected convergence rate for the energy of the error (1 for linear elements). Note that the quality of the bounds increases as long as the mesh is refined or the viscosity increases. The bounds are also improved when the proposed bounding expression (57) is considered instead of the one based on the Cauchy–Schwarz inequality (47).

Note that, the bound gap is theoretically an upper bound of the error  $L^O(\hat{\mathbf{e}})$ . It is observed in Fig. 4 that the computed bound gap is indeed a true upper bound, but it strongly overestimates the error. The smaller is the parameter  $\tau$ , the less accurate is this upper bound.

As it is previously stated, the bounds  $\zeta_{\text{U}}$  and  $\zeta_{\text{L}}$  are computed using asymptotic estimates which are based on a reference mesh. Table 4 shows the influence of considering two different element sizes for the reference mesh. These sizes are, on the one hand,  $h := H/4$  which is the reference mesh size considered as the standard choice in this example and, on the other hand,  $h := H/8$ . The results for both element sizes agree in one significant digit for the coarsest mesh and in three significant digits for the finest mesh. The smaller is the reference size  $h$  the larger is the bound gap. This

**Table 4**  
Example 1: Influence of the reference mesh element size in the computed bounds for  $\tau = 1 \cdot 10^{-5}$  s. Results in (m/s).

D.O.F.	$\zeta_{\text{L}}$ for $h := H/4$	$\zeta_{\text{L}}$ for $h := H/8$	$\zeta_{\text{U}}$ for $h := H/4$	$\zeta_{\text{U}}$ for $h := H/8$
246	2.314553383	2.275610548	2.446035694	2.474136312
810	2.370712445	2.360881927	2.403474732	2.410236611
2898	2.384977566	2.382535545	2.393218595	2.394892692
10,914	2.388575410	2.387970113	2.390638593	2.391053021

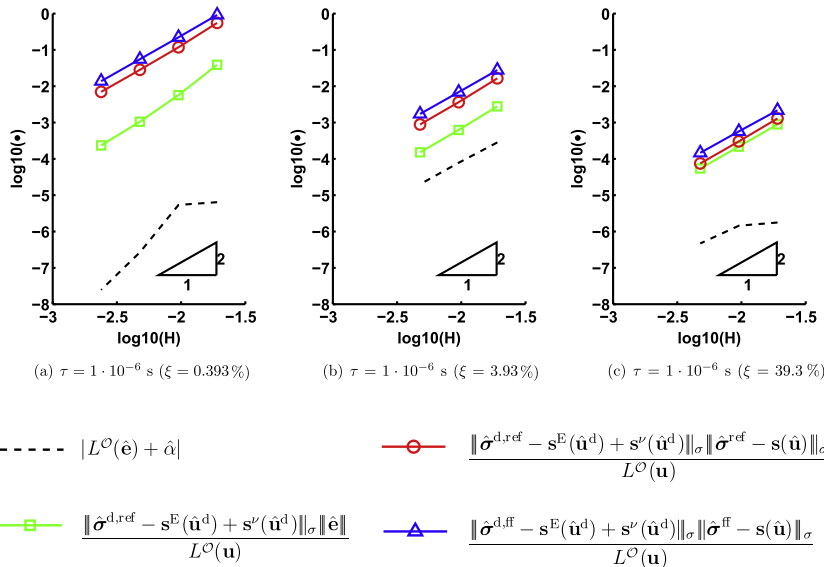


**Fig. 5.** Example 1: Analysis of the loss of effectivity for the bounds based on the Cauchy–Schwarz inequality. The plotted curves are associated with the error measures appearing in Eq. (58).

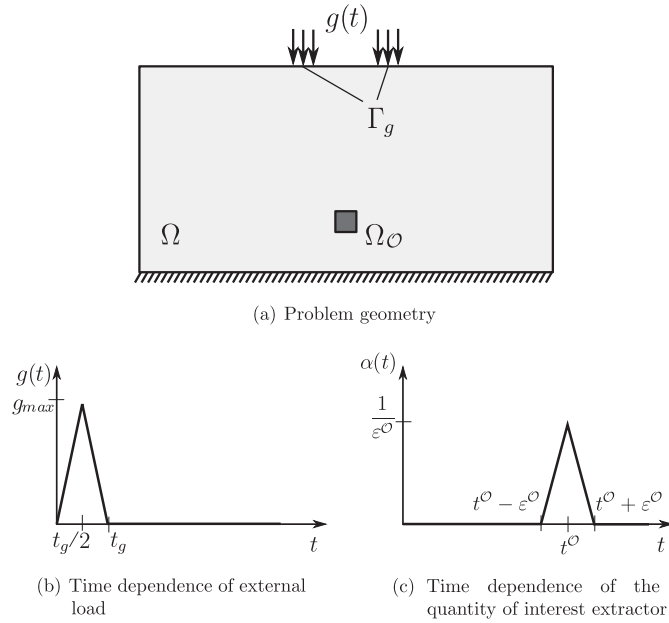


Fig. 6. Example 2: Problem statement and quantity of interest.

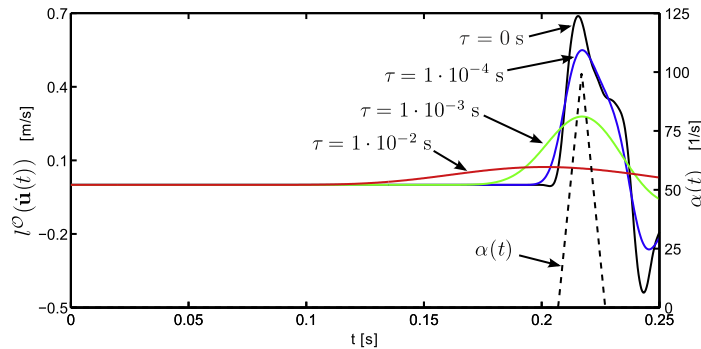


Fig. 7. Example 2: Time evolution of the of the average  $l^O(\dot{\mathbf{u}}(t))$  for three values of the viscosity (left y-axis) and time evolution of the weighting function  $\alpha(t)$  (right y-axis).

is a standard for asymptotic estimates. Note that in all cases the computed values are true bounds with respect the reference value  $L^O(\mathbf{u}) = 2.389779 \text{ m/s}$  independently of the considered reference mesh size.

In a second phase, the origin of the poor quality of the bounds based on the Cauchy–Schwarz inequality is investigated. The goal is to analyze the loss of effectivity introduced by each mathematical manipulation involved in the derivation of the bounds. Three steps are identified in the process of obtaining the bounds that correspond to the successive relations between the four terms below:

$$\begin{aligned}
 |L^O(\hat{\mathbf{e}}) + \hat{\alpha}| &\lesssim \| \hat{\boldsymbol{\sigma}}^{\text{d,ref}} - \mathbf{s}^E(\hat{\mathbf{u}}^{\text{d}}) + \mathbf{s}^v(\hat{\mathbf{u}}^{\text{d}}) \|_{\sigma} \| \hat{\mathbf{e}} \| \\
 &\lesssim \| \hat{\boldsymbol{\sigma}}^{\text{d,ref}} - \mathbf{s}^E(\hat{\mathbf{u}}^{\text{d}}) + \mathbf{s}^v(\hat{\mathbf{u}}^{\text{d}}) \|_{\sigma} \| \hat{\boldsymbol{\sigma}}^{\text{ref}} - \mathbf{s}(\hat{\mathbf{u}}) \|_{\sigma} \\
 &\leq \| \hat{\boldsymbol{\sigma}}^{\text{d,ff}} - \mathbf{s}^E(\hat{\mathbf{u}}^{\text{d}}) + \mathbf{s}^v(\hat{\mathbf{u}}^{\text{d}}) \|_{\sigma} \| \hat{\boldsymbol{\sigma}}^{\text{ff}} - \mathbf{s}(\hat{\mathbf{u}}) \|_{\sigma} \quad (58)
 \end{aligned}$$

The first step corresponds to Eq. (46) and is related with the use of the Cauchy–Schwarz inequality. The second step corresponds to use

Table 5  
Example 2: Parameterization.

Geometry		
$\Omega$	$(-0.5, 0.5) \times (0, 0.5)$	$\text{m}^2$
$\Omega_O$	$(-0.025, 0.025) \times (0.1, 0.15)$	$\text{m}^2$
$\Gamma_g$	$[(0.075, 0.125) \cup (-0.075, -0.125)] \times (0, 0.5)$	$\text{m}$
$T$	0.25	$\text{s}$
Material properties		
$E$	8/3	$\text{Pa}$
$\nu$	1/3	
$\rho$	1	$\text{kg/m}^3$
$\tau$	$\{10^{-4}, 10^{-3}, 10^{-2}\}$	$\text{s}$
$\xi$	$\{0.0247, 0.247, 2.47\}$	$\%$
External load		
$g_{\text{max}}$	30	$\text{Pa}$
$t_g$	0.005	$\text{s}$
Quantity of interest		
$\varepsilon^O$	0.01	$\text{s}$
$t^O$	0.2170	$\text{s}$

the upper bound property of the constitutive relation error, see Eq. (24). The third step is associated with the overestimation introduced by the flux-free estimate, see (34). The symbol  $\lesssim$  indicates that upper bound is not strict but asymptotic. Note that only the last term is actually computable in a practical case. Nevertheless, in this academic example, the reference stresses  $\hat{\sigma}^{\text{ref}}$  and  $\hat{\sigma}^{\text{d.ref}}$  and the reference version of the error  $\hat{e}$  can also be computed, taking a reference mesh size and time step as  $h := H/4$  and  $\delta t = \Delta t/4$ .

Fig. 5 displays the convergence curves of the values in expression (58) for all values of the viscosity considered in this example. Note that most of the effectivity is lost after the application of Cauchy–Schwarz. The introduction of the constitutive relation error also strongly deteriorates the effectivity for the lowest value of the viscosity. The flux-free technique does not seriously deteriorate the effectivity compared to the other steps.

**Table 6**  
Example 2: Space and time discretizations.

	D.O.F.	$H$ (mm)	# Elements	$N$
Mesh 1	24,000	0.16	23,596	325
Mesh 2	95,190	0.08	94,384	650
Mesh 3	379,146	0.04	377,536	1300

6.2. Example 2: 2D plate

The second numerical example illustrates the performance of the bounds in a full 2D problem. This example is inspired in one from [34]. It consists of a rectangular plate initially at rest which is loaded with two impulsive tractions, see Fig. 6. This action generates elastic waves propagating along the plate and reaching to

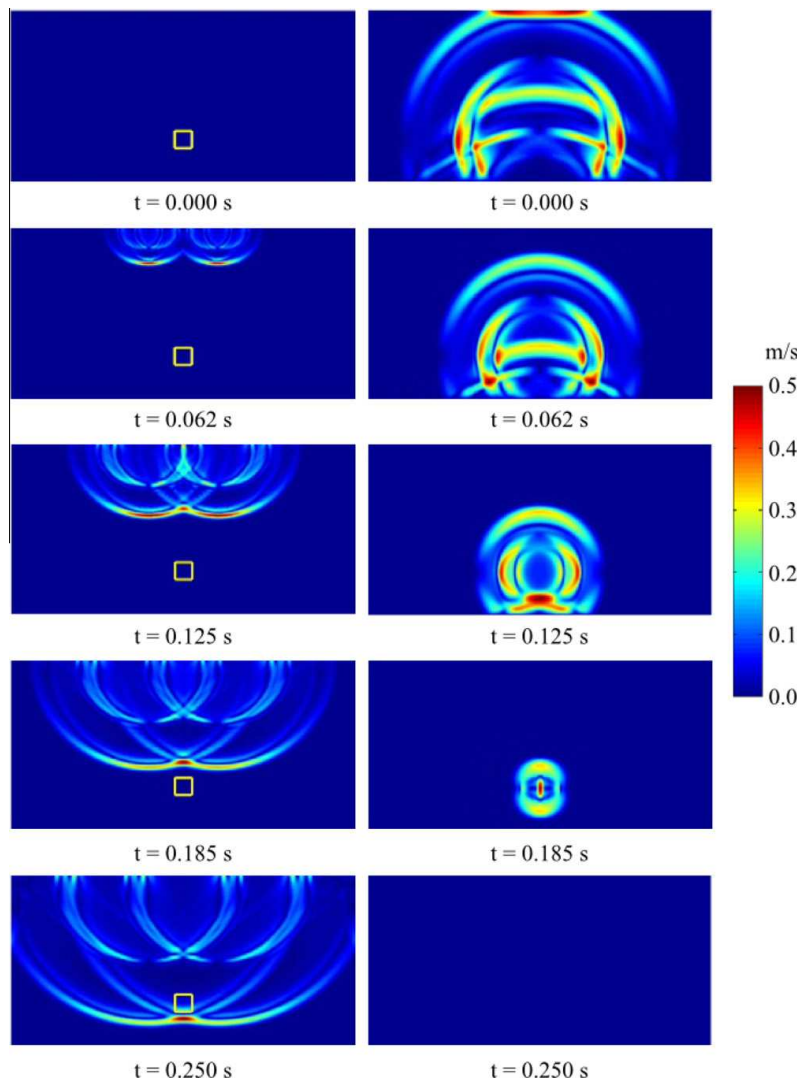


Fig. 8. Example 2: Magnitude of the original (left) and adjoint (right) velocities for  $\tau = 10^{-4}$  s ( $\xi = 0.0247\%$ ).

the region of interest  $\Omega^o$ . The quantity of interest is an average of velocities in this region during a time interval (selected such that the wave is noticeable in this region, see Fig. 7). This quantity is defined as

$$L^o(\mathbf{w}) := \int_I \alpha(t) l^o(\dot{\mathbf{w}}(t)) dt,$$

where

$$l^o(\mathbf{w}) := (\mathbf{f}^o, \mathbf{w}),$$

and

$$\mathbf{f}^o(\mathbf{x}) := \begin{cases} \frac{-\mathbf{e}_2}{\text{meas}(\Omega^o)} & \mathbf{x} \in \Omega^o \\ \mathbf{0} & \text{else} \end{cases}$$

Vector  $\mathbf{e}_2$  is the unit vector in the  $y$ -axis and  $\alpha(t)$  is defined in Fig. 6c. All the parameters involved in the problem are specified in Table 5.

The problem is solved with three different meshes with decreasing element size, see Table 6. In all cases linear triangles are considered. The time step is chosen such that  $\Delta t = 0.8H/c$ . The reference mesh for the flux-free method is taken as  $h := H/4$ . The value of the exact solution  $\mathbf{u}$  displayed in some figures and tables correspond to the reference solution obtained with the finer mesh (mesh 3) Other parameters related with the discretization are given in Table 6.

Several snap shots of the numerical solution of the original and adjoint problems are shown in Figs. 8–10 for the three values of the viscosity under consideration. The damping factors  $\xi$  associated with the values of the viscosity parameter,  $10^{-4}$ ,  $10^{-3}$  and  $10^{-2}$  s, are 0.0247%, 0.247% and 2.47% respectively. Note that for the origi-

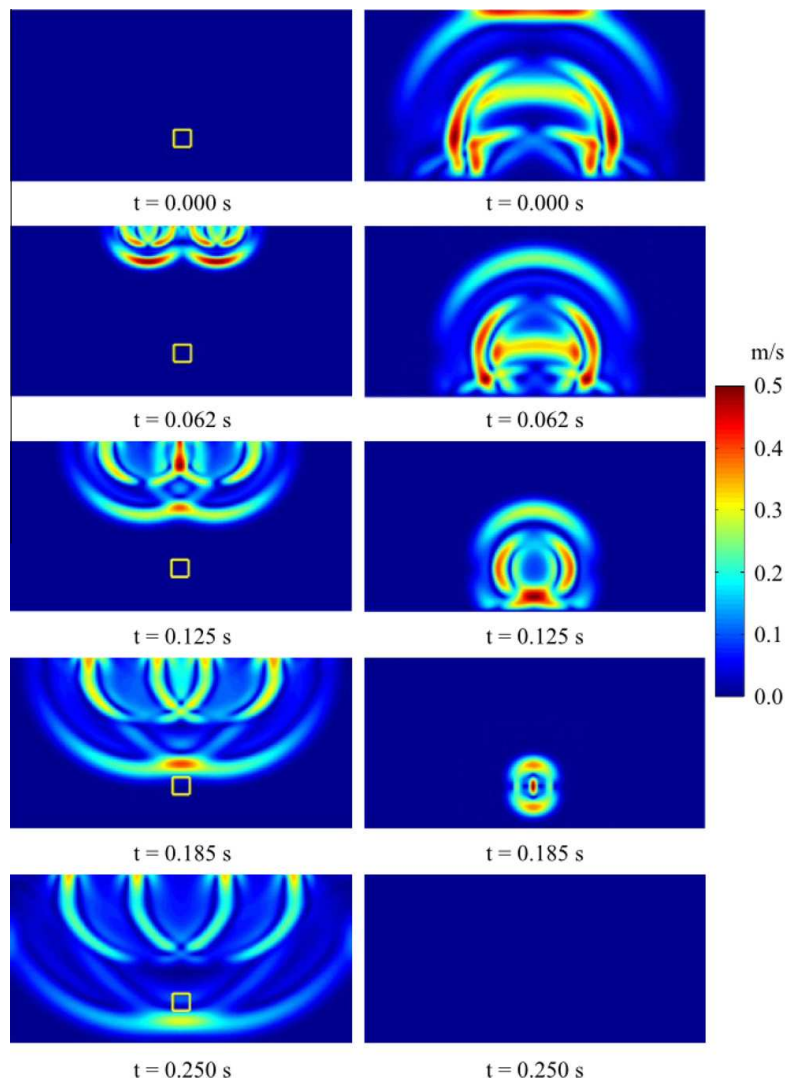


Fig. 9. Example 2: Magnitude of the original (left) and adjoint (right) velocities for  $\tau = 10^{-3}$  s ( $\xi = 0.247\%$ ).

nal problem the elastic waves propagate forward in time, and backward in time for the adjoint.

Fig. 11 shows the computed value  $L^0(\hat{\mathbf{u}})$  and the bounds obtained for the three values of the viscosity and decreasing element size. In addition, Table 7 shows the effectivity of the computed bounds. Note that in this case the bounds are also sharper for higher values of  $\tau$  and for smaller element sizes. In particular, for  $\tau = 10^{-4}$  s and  $\tau = 10^{-3}$  s the bounds are not sharp at all, even for mesh number 3, which can be considered an overkill mesh. Note that, in these two cases, the bounds do not allow identifying which is the sign of the quantity of interest. For  $\tau = 10^{-2}$  s the bounds are much sharper. The proposed bounds reduce in approximately 50% the bound gap with respect to the ones based on the Cauchy–Schwarz inequality, in all cases. Note however that for the small values of the viscosity,  $\tau = 10^{-4}$  s and  $\tau = 10^{-3}$  s, this

reduction is not sufficient to have bounds applicable in practical engineering examples.

**7. Conclusion**

Bounds for linear functional outputs are derived for linear visco-elastodynamics. A new bounding expression is presented which improves the quality with respect to the previous approaches based on the Cauchy–Schwarz inequality. The proposed new approach is based on an alternative error representation, involving symmetrized error equations, which is derived precluding the use of the Cauchy–Schwarz inequality.

The key ingredient for the practical application of the method is the construction of admissible fields for both the original and adjoint problems. The proposed formulation is valid for any numeri-

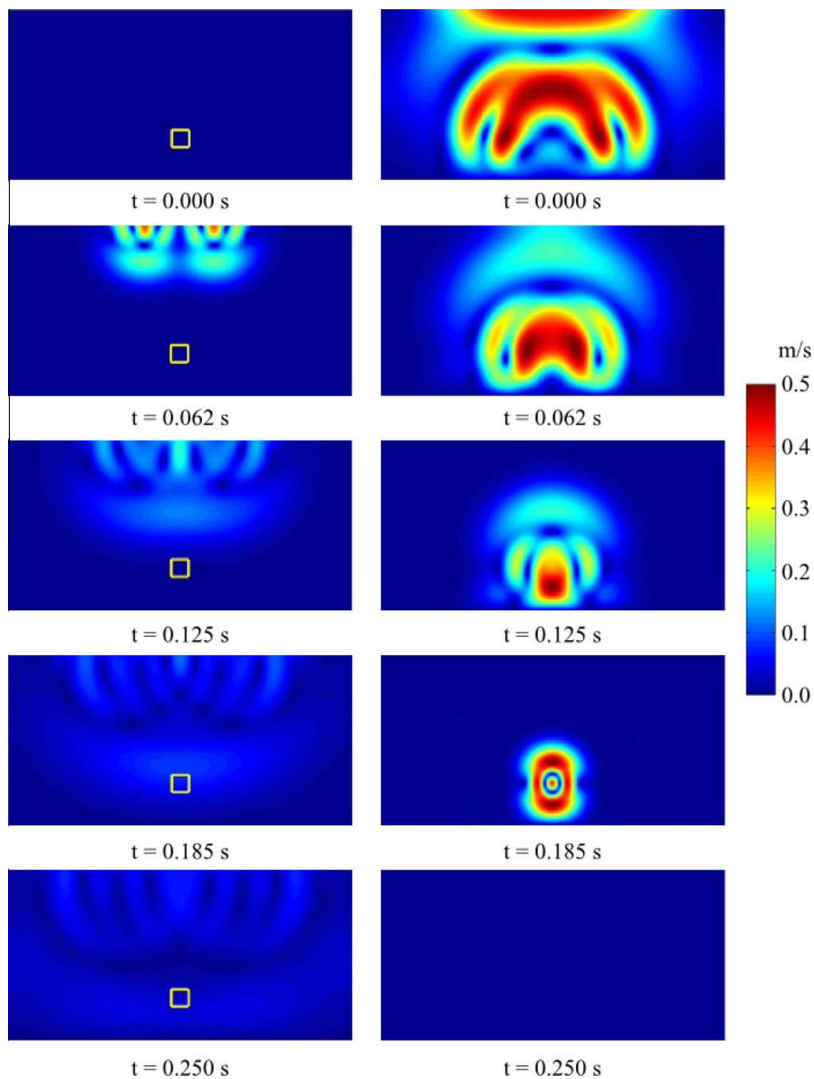


Fig. 10. Example 2: Magnitude of the original (left) and adjoint (right) velocities for  $\tau = 10^{-2}$  s  $\zeta = (2.47\%)$ .

# COMPUTABLE BOUNDS OF FUNCTIONAL OUTPUTS IN LINEAR VISCO-ELASTODYNAMICS

F. Verdugo, P. Díez / Comput. Methods Appl. Mech. Engrg. 245–246 (2012) 313–330

329

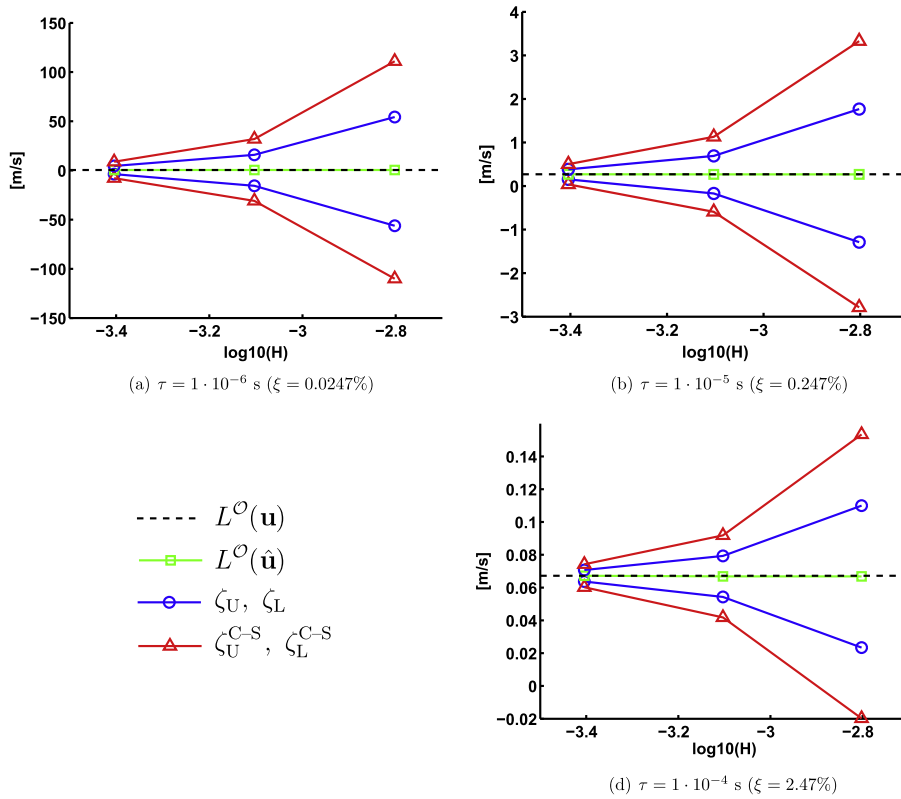


Fig. 11. Example 2: Convergence of the computed bounds for different values of element size and viscosity.

**Table 7**  
Example 2: Convergence of the computed bounds. Results in (m/s).

$\tau$ (s)	D.O.F.	$L^O(\dot{\mathbf{u}})$	$L^O(\mathbf{u})$	$\zeta_U/L^O(\mathbf{u})$	$\zeta_L/L^O(\mathbf{u})$	$\zeta_U^{C-S}/L^O(\mathbf{u})$	$\zeta_L^{C-S}/L^O(\mathbf{u})$
$1 \times 10^{-4}$	24,000	0.4937	0.4960	110.0524	-113.8099	224.8397	-222.8850
	95,190	0.4932	0.4960	32.1210	-31.5976	64.7088	-62.7284
	379,146	0.4960	0.4960	9.2333	-7.6063	17.8371	-15.8420
$1 \times 10^{-3}$	24,000	0.2681	0.2697	6.5943	-4.8098	12.4183	-10.3898
	95,190	0.2681	0.2697	2.5800	-0.6352	4.2187	-2.2117
	379,146	0.2697	0.2697	1.4224	0.5637	1.8595	0.1422
$1 \times 10^{-2}$	24,000	0.0668	0.0672	1.6457	0.3498	2.2953	-0.2967
	95,190	0.0668	0.0672	1.1867	0.8121	1.3745	0.6252
	379,146	0.0672	0.0672	1.0520	0.9477	1.1043	0.8956

cal method, provided that the numerical solution furnishes admissible fields (possibly after some post processing). Here, the K-admissible field is computed as a post process of the Newmark solution. On the other hand, the D-admissible field is computed with the asymptotic flux-free strategy. This method is based on a reference mesh and therefore, the proposed bounds hold when the element size of the reference mesh is fine enough. In practice, the numerical examples show that the computed values are indeed true bounds of the quantity of interest.

All the developments in the paper require that the formulation includes a certain amount of viscosity. In the present case, the linear Kelvin–Voigt model is considered. The quality of the results obtained degenerate in the limit case of elasticity (zero or very small

viscosity). In materials with small amounts of viscosity, the bounds obtained are pessimistic. The numerical tests reveal that when the meshes are refined the bound gap tends to be reduced and, correspondingly, the strategy provides sharp bounds for fine enough meshes. Nevertheless, in practice, for low viscosity, the meshes providing accurate bounds are not computationally affordable. Therefore, further research is needed to explore alternative pertinent bounds for nearly elastic problems.

### Acknowledgement

Partially supported by Ministerio de Educación y Ciencia, Grant DPI2011-27778-C02-02 and Univeritat Politècnica de Catalunya

(UPC-BarcelonaTech), Grant UPC-FPU. The support of the Col·legi d'Enginyers de Camins, Canals i Ports (Catalunya) is also gratefully acknowledged.

**Appendix A. Non-homogeneous Dirichlet conditions**

It is well known that non-homogeneous Dirichlet conditions does not introduce any extra conceptual difficulty. In the case of non homogeneous Dirichlet conditions it suffices to define an arbitrary (and easy to produce) function  $\psi$  fulfilling them, that is such that  $\psi = \mathbf{u}_D$  on  $\Gamma_D \times I$ . Once  $\psi$  is available, the analysis is done for function  $\mathbf{u}^* := \mathbf{u} - \psi$  fulfilling homogeneous conditions,  $\mathbf{u}^* = \mathbf{0}$  on  $\Gamma_D \times I$ . Note that, function  $\mathbf{u}^* \in \mathcal{U}$  fulfills the weak form

$$B(\mathbf{u}^*, \mathbf{w}) = L^*(\mathbf{w}) \quad \forall \mathbf{w} \in \mathcal{W},$$

where  $L^*(\mathbf{w}) := L(\mathbf{w}) - B(\psi, \mathbf{w})$  and equivalently, the strong form

$$\rho \ddot{\mathbf{u}}^* - \nabla \cdot \boldsymbol{\sigma}(\mathbf{u}^*) = \mathbf{f} - \rho \ddot{\psi} - \nabla \cdot \boldsymbol{\sigma}(\psi) \quad \text{in } \Omega \times I,$$

$$\mathbf{u}^* = \mathbf{0} \quad \text{on } \Gamma_D \times I,$$

$$\boldsymbol{\sigma}(\mathbf{u}^*) \cdot \mathbf{n} = \mathbf{g} - \boldsymbol{\sigma}(\psi) \cdot \mathbf{n} \quad \text{on } \Gamma_N \times I,$$

$$\mathbf{u}^* = \mathbf{u}_0 - \psi \quad \text{at } \Omega \times \{0\},$$

$$\dot{\mathbf{u}}^* = \mathbf{v}_0 - \dot{\psi} \quad \text{at } \Omega \times \{0\}.$$

Thus, the non-homogeneous conditions are easily reduced to homogeneous adding some correction terms to the forcing data of the original problem.

Function  $\psi$  can be builded using the shape functions of the computational mesh

$$\psi(\mathbf{x}, t) := \sum_{i \in \mathcal{N}_D} N_i(\mathbf{x}) \mathbf{u}_D(\mathbf{x}_i, t), \tag{A.1}$$

where  $\mathcal{N}_D$  is the set of indices of nodes lying on the Dirichlet boundary  $\Gamma_D$  and  $\mathbf{x}_i$  is the position of the  $i$ -th node. Note that  $\psi$  has to be such that  $\psi \in \mathcal{U}$  ( $H^1$  in space and  $H^2$  in time) in order to properly define  $L^*$ . The regularity in space is guaranteed by the shape functions. The regularity in time should be provided by the Dirichlet condition  $\mathbf{u}_D$ . That is,  $\mathbf{u}_D$  has to be such that  $\mathbf{u}_D(\mathbf{x}, \cdot) \in [H^2(I)]^d$  for all  $\mathbf{x} \in \Gamma_D$ .

**References**

[1] I. Babuška, W. Rheinboldt, Error estimates for adaptive finite element computations, *SIAM J. Numer. Anal.* 18 (1978) 736–754.  
 [2] P. Ladevèze, D. Leguillon, Error estimate procedure in the finite element method, *SIAM J. Numer. Anal.* 20 (1983) 485–509.  
 [3] O. Zienkiewicz, J. Zhu, A simple error estimator and adaptative procedure for practical engineering analysis, *Int. J. Numer. Meth. Engrg.* 24 (1987) 337–357.  
 [4] M. Paraschivou, J. Peraire, A. Patera, A posteriori finite element bounds for linear-functional outputs of elliptic partial differential equations, *Comput. Meth. Appl. Mech. Engrg.* 150 (1997) 289–321.  
 [5] N. Parés, J. Bonet, A. Huerta, J. Peraire, The computation of bounds for linear-functional outputs of weak solutions to the two-dimensional elasticity equations, *Comput. Meth. Appl. Mech. Engrg.* 195 (2006) 406–429.  
 [6] F. Cirak, E. Ramm, A posteriori error estimation and adaptivity for linear elasticity using the reciprocal theorem, *Comput. Meth. Appl. Mech. Engrg.* 156 (1998) 351–362.  
 [7] S. Prudhomme, J. Oden, On goal-oriented error estimation for elliptic problems: application to the control of pointwise errors, *Comput. Meth. Appl. Mech. Engrg.* 176 (1999) 313–331.

[8] D. Aubry, D. Lucas, B. Tie, Adaptive strategy for transient/coupled problems Applications to thermoelasticity and elastodynamics, *Comput. Meth. Appl. Mech. Engrg.* 176 (1999) 41–50.  
 [9] X. Li, N. Wiberg, Implementation and adaptivity of a space-time finite element method for structural dynamics, *Comput. Meth. Appl. Mech. Engrg.* 156 (1998) 211–229.  
 [10] N. Wiberg, X. Li, Adaptive finite element procedures for linear and non-linear dynamics, *Int. J. Numer. Meth. Engrg.* 46 (1999) 178–1802.  
 [11] L. Chamoin, P. Ladevèze, A non-intrusive method for the calculation of strict and efficient bounds of calculated outputs of interest in linear viscoelasticity problems, *Comput. Meth. Appl. Mech. Engrg.* 197 (2008) 994–1014.  
 [12] J. Combe, P. Ladevèze, J. Pelle, Discretization error estimator for transient dynamic simulations, *Adv. Eng. Softw.* 33 (2002) 553–563.  
 [13] J. Combe, P. Ladevèze, J. Pelle, Constitutive relation error estimator for transient finite element analysis, *Comput. Meth. Appl. Mech. Engrg.* 176 (1999) 165–185.  
 [14] P. Ladevèze, J. Pelle, Estimation of discretization errors in dynamics, *Comput. Struct.* 81 (2003) 1133–1148.  
 [15] A. Schleupen, E. Ramm, Local and global error estimations in linear structural dynamics, *Comput. Struct.* 76 (2000) 741–756.  
 [16] D. Fuentes, D. Littlefield, J. dOden, S. Prudhomme, Extensions of goal-oriented error estimation methods to simulation of highly-nonlinear response of shock-loaded elastomer-reinforced structures, *Comput. Meth. Appl. Mech. Engrg.* 195 (2006) 4659–4680.  
 [17] P. Ladevèze, J. Waeytens, Model verification in dynamics trough strict upper bounds, *Comput. Meth. Appl. Mech. Engrg.* 198 (2009) 1775–1784.  
 [18] J. Waeytens, Contrôle des calculs en dynamique: bornes strictes et pertinentes sur une quantité d'intérêt, Ph.D. thesis, LMT-Cachan, 2010.  
 [19] P. Ladevèze, Strict upper error bounds for computed outputs of interest in computational structural mechanics, *Comput. Mech.* 42 (2008) 271–286.  
 [20] J. Waeytens, L. Chamoin, P. Ladevèze, Guaranteed error bounds on pointwise quantities of interest for transient viscodynamics problems, *Comput. Mech.* 49 (2012) 291–307.  
 [21] N. Parés, P. Diez, A. Huerta, Bounds of functional outputs for parabolic problems part I: exact bounds of the discontinuous galerkin time discretization, *Comput. Meth. Appl. Mech. Engrg.* 197 (2008) 1641–1660.  
 [22] N. Parés, P. Diez, A. Huerta, A subdomain-based flux-free a posteriori error estimators, *Comput. Meth. Appl. Mech. Engrg.* 195 (2006) 297–323.  
 [23] N. Newmark, A method of computation for structural dynamics, *J. Eng. Mech.* 85 (1959) 67–94.  
 [24] J. Hughes, M. Hulbert, Space-time finite element methods for elastodynamics: Formulations and error estimates, *Comput. Meth. Appl. Mech. Engrg.* 66 (1988) 327–348.  
 [25] M. Hulbert, J. Hughes, Space-time finite element methods for second-order hyperbolic equations, *Comput. Meth. Appl. Mech. Engrg.* 84 (1990) 327–348.  
 [26] P. Ladevèze, J. Pelle, La maîtrise du calcul en mécanique linéaire et non linéaire, Lavoisier, 2001.  
 [27] M. Ainsworth, J. Oden, A Posteriori Error Estimation in Finite Element Analysis, John Wiley & Sons, Ltd., 2000.  
 [28] R. Cottreau, P. Diez, A. Huerta, Strict error bounds for linear solid mechanics problems using a subdomain-based flux-free method, *Comput. Meth.* 44 (2009) 533–547.  
 [29] J.P. Moitinho de Almeida, O.J.B. Almeida Pereira, Upper bounds of the error in local quantities using equilibrated and compatible finite element solutions for linear elastic problems, *Comput. Meth. Appl. Mech. Engrg.* 195 (2006) 279–296.  
 [30] O.J.B. Almeida Pereira, J.P. Moitinho de Almeida, Dual adaptive finite element refinement for multiple local quantities in linear elastostatics, *Int. J. Numer. Meth. Engrg.* 83 (2010) 347–365.  
 [31] J. Oden, S. Prudhomme, Goal-oriented error estimation and adaptivity for the finite element method, *Comput. Meth. Appl.* 41 (2001) 735–765.  
 [32] C. Johnson, Numerical Solution of Partial Differential Equations by the Finite Element Method, Cambridge University Press, 1990.  
 [33] P. Raviart, J. Thomas, Introduction à l'analyse numérique des équations aux dérivées partielles, Masson, 1983.  
 [34] N. Nguyen, J. Peraire, B. Cockburn, High-order implicit hybridizable discontinuous Galerkin methods for acoustics and elastodynamics, *J. Comput. Phys.* 230 (2011) 3695–3718.

## Paper C

# Modal based goal-oriented error assessment for timeline-dependent quantities in transient dynamics

F. Verdugo, N. Parés and P. Díez

---

*International Journal for Numerical Methods in Engineering*, Volume 95, Issue 8, Pages 685–720, 2013



## Modal-based goal-oriented error assessment for timeline-dependent quantities in transient dynamics

F. Verdugo<sup>1</sup>, N. Parés<sup>1</sup> and P. Díez<sup>1,2,\*</sup>,<sup>†</sup>

<sup>1</sup>Laboratori de Càlcul Numèric (LaCàN), Universitat Politècnica de Catalunya (UPC), Jordi Girona 1-3 E-08034  
Barcelona, Spain

<sup>2</sup>Centre Internacional de Mètodes Numèrics en Enginyeria (CIMNE), Gran Capitán s/n, E-08034 Barcelona, Spain

### SUMMARY

This article presents a new approach to assess the error in specific quantities of interest in the framework of linear elastodynamics. In particular, a new type of quantities of interest (referred as timeline-dependent quantities) is proposed. These quantities are scalar time-dependent outputs of the transient solution, which are better suited to time-dependent problems than the standard scalar ones, frozen in time. The proposed methodology furnishes error estimates for both the standard scalar and the new timeline-dependent quantities of interest. The key ingredient is the modal-based approximation of the associated adjoint problems, which allows efficiently computing and storing the adjoint solution.

The approximated adjoint solution is readily post-processed to produce an enhanced solution, requiring only one spatial post-process for each vibration mode and using the time-harmonic hypothesis to recover the time dependence. Thus, the proposed goal-oriented error estimate consists in injecting this enhanced adjoint solution into the residual of the direct problem. The resulting estimate is very well suited for transient dynamic simulations because the enhanced adjoint solution is computed before starting the forward time integration of the direct problem. Thus, the cost of the error estimate at each time step is very low. Copyright © 2013 John Wiley & Sons, Ltd.

Received 6 December 2012; Revised 1 May 2013; Accepted 9 May 2013

KEY WORDS: goal-oriented error assessment; elastodynamics; transient dynamics; adjoint problem; quantity of interest; timeline-dependent quantity of interest; modal analysis

### 1. INTRODUCTION

Assessing the reliability and/or improving efficiency of the finite element based approximations has motivated the development of a huge variety of error assessment techniques [1–5]. The pioneering references on this topic focus in steady-state elliptic problems, for example, linear elasticity or steady heat transfer. In the context of elliptic problems, the early works consider the energy norm as an error measure [6–8]. Much later, functional outputs or *quantities of interest* are introduced to assess the error [9–12]. The estimates assessing the error in quantities of interest are usually referred in the literature as *goal-oriented* [12]. These techniques are extended to deal with other linear and non-linear problems, as well as with time-dependent problems. The following references illustrate the high variety of applications of the goal-oriented approach: for quasi-steady-state non-linear problems [13–16], for the advection–diffusion–reaction equation [17], for the Stokes problem [18], for parabolic time-dependent problems [19–21], and for coupled problems [22–26].

Different error estimation techniques are proposed also for second order hyperbolic problems (e.g. wave equation or elastodynamics). In this context, some are providing error indicators to

\*Correspondence to: Pedro Díez, Laboratori de Càlcul Numèric (LaCàN), Departament de Matemàtica Aplicada III, Universitat Politècnica de Catalunya (UPC), Building C2, Jordi Girona 1-3 E-08034 Barcelona, Spain.

<sup>†</sup>E-mail: pedro.diez@upc.edu

drive mesh adaptive procedures, either using energy-like measures [27–32] or quantities of interest [33–37]. Other references introduce error estimates as a quality certification for the numerical approximation, without direct application to adaptivity, see [38–40] for energy-like error measures and [29, 41–46] for goal-oriented estimates.

To the best knowledge of the authors, the few references cited earlier as goal-oriented error assessment techniques constitute the current state-of-the-art in elastodynamics. This is still an open research topic, with many challenging issues.

The first challenge is reducing the high computational cost of these estimates. Assessing the error in a quantity of interest (instead of the standard energy norm) requires approximating an auxiliary adjoint problem associated with the selected quantity. At the first sight, the numerical computation of this problem is as expensive as the original one. The cost of computing the adjoint problem is reduced by using ad hoc techniques (for instance enriching the adjoint interpolation with handbook functions [41, 42, 44]), but this reduction is not sufficient to make it affordable. Alternative computations of the adjoint solution in time-dependent problems are proposed by [47] using a coarse-scale discretization and [48] using the adjoint solution of an auxiliary steady-state problem.

Moreover, the need of combining the original and adjoint solutions drastically increases the memory requirements. This is because the original solution is solved forwards in time and the adjoint backwards. Thus, to combine them, at least one of the two solutions has to be stored in memory as a whole (i.e., for each mesh-DOF and for each time step). Another important overhead is introduced by the post-processing techniques (recovery, equilibration, computation of residuals...), which are required to assess the error. This overhead can be non-negligible because the post-processing operations have to be performed at every time step. This extra cost is also present in energy-like estimates, but in the goal-oriented context, it can be even higher if the same operations have to be performed for the adjoint problem as well.

Another important issue associated with goal-oriented estimates for elastodynamics (and also for other time-dependent problems) is the definition of the quantity of interest itself. Typically, the quantity is expressed in terms of a (linear) functional, which transforms the solution of the problem into a single representative scalar value. Standard quantities in steady-state problems are averages of the unknown variables in subregions of interest in the computational domain. In time-dependent problems, the definition of the quantity of interest must involve not only a spatial subdomain but also a time interval of interest. The choice of this time frame is not always obvious for the end user. This is because a single scalar value does not provide enough pieces of information about the whole time-space solution. This suggests introducing a new type of quantities of interest precluding the need of providing the time frame. The output of such a quantity of interest is not anymore a scalar quantity but a time-dependent function. The major novelty of this article is the introduction of this new type of quantities. They are referred as *timeline-dependent* quantities of interest in contrast with the standard *scalar* quantities.

The key ingredient of the proposed methodology is a modal-based approximation for the adjoint solution. This is a new approach, with respect to previous goal-oriented estimates for elastodynamics [45], which use direct time integration schemes (e.g., Newmark-like methods) to solve the adjoint problem. The modal-based strategy is particularly well suited for some particular quantities of interest and allows effectively computing and storing the adjoint problem. Moreover, the use of post-processing techniques in the space domain (flux recovery or equilibration) can be readily applied to the (spatial) description of the modes. Note that this is performed just once for every relevant mode, with no need of carrying out the post-processing at each time step. Dealing with timeline-dependent quantities is much simpler with this approach, because it simplifies the time-translation operation.

The modal-based approach is valid for linear problems and linear quantities of interest. Although a wide range of applications is devised, the modal assessment of the timeline-dependent quantities is valid for some particular cases inducing a time-translation invariance. Moreover, to be competitive with direct time integration methods, a modal approach requires that the quantity of interest is described with a reduced number of vibration modes. These factors could be seen as a limitation of the proposed technique. However, the examples presented here demonstrate that the approach is useful in many practical applications.

The error estimates proposed here are obtained injecting an enhanced adjoint approximation into the weak residual of the original problem. As previously noted, the treatment of the adjoint solution is very efficient, thanks to the modal-based approach. The recovery procedure employed for both eigenvectors and eigenfrequencies is similar to the one proposed by Wiberg *et al.* [49].

The remainder of the paper is structured as follows. Section 2 introduces the equations of elastodynamics, the numerical strategies to solve them, and the types of quantities of interest we aim at assessing, in particular, the so-called timeline-dependent quantities. Section 3 presents the modal-based error estimate for the standard scalar quantities of interest. Section 4 extends the rationale of previous section to the timeline-dependent quantities. Section 5 contains numerical examples demonstrating the suitability of the proposed estimates. Finally, we draw some concluding remarks.

## 2. PROBLEM STATEMENT

### 2.1. Governing equations

Consider a visco-elastic body occupying an open-bounded domain  $\Omega \subset \mathbb{R}^d$ ,  $d \leq 3$ , with boundary  $\partial\Omega$ . The boundary is divided in two disjoint parts,  $\Gamma_N$  and  $\Gamma_D$ , such that  $\partial\Omega = \bar{\Gamma}_N \cup \bar{\Gamma}_D$  and the time interval under consideration is  $I := [0, T]$ . Under the assumption of small perturbations, the evolution of displacements  $\mathbf{u}(\mathbf{x}, t)$  and stresses  $\boldsymbol{\sigma}(\mathbf{x}, t)$ ,  $\mathbf{x} \in \Omega$  and  $t \in I$ , is described by the visco-elastodynamic equations,

$$\rho (\ddot{\mathbf{u}} + a_1 \dot{\mathbf{u}}) - \nabla \cdot \boldsymbol{\sigma} = \mathbf{f} \quad \text{in } \Omega \times I, \tag{1a}$$

$$\mathbf{u} = \mathbf{0} \quad \text{on } \Gamma_D \times I, \tag{1b}$$

$$\boldsymbol{\sigma} \cdot \mathbf{n} = \mathbf{g} \quad \text{on } \Gamma_N \times I, \tag{1c}$$

$$\mathbf{u} = \mathbf{u}_0 \quad \text{at } \Omega \times \{0\}, \tag{1d}$$

$$\dot{\mathbf{u}} = \mathbf{v}_0 \quad \text{at } \Omega \times \{0\}, \tag{1e}$$

where an upper dot indicates partial derivation with respect to time, that is  $(\dot{\bullet}) := \frac{d}{dt}(\bullet)$ , and  $\mathbf{n}$  denotes the outward unit normal to  $\partial\Omega$ . The problem data are the mass density  $\rho = \rho(\mathbf{x}) > 0$ , the first Rayleigh coefficient  $a_1 \geq 0$ , the body force  $\mathbf{f} = \mathbf{f}(\mathbf{x}, t)$ , and the traction  $\mathbf{g} = \mathbf{g}(\mathbf{x}, t)$  acting on the Neumann boundary  $\Gamma_N \times I$ . The initial conditions for displacements and velocities are  $\mathbf{u}_0 = \mathbf{u}_0(\mathbf{x})$  and  $\mathbf{v}_0 = \mathbf{v}_0(\mathbf{x})$ , respectively. For the sake of simplicity and without any loss of generality, Dirichlet conditions (1b) are taken as homogeneous.

The set of equations (1) is closed with the constitutive law,

$$\boldsymbol{\sigma} = \mathcal{C} : \boldsymbol{\varepsilon}(\mathbf{u} + a_2 \dot{\mathbf{u}}), \tag{2}$$

where the parameter  $a_2 \geq 0$  is the second Rayleigh coefficient,  $\boldsymbol{\varepsilon}(\mathbf{w}) := \frac{1}{2}(\nabla \mathbf{w} + \nabla^T \mathbf{w})$  is the kinematic relation (corresponding to small perturbations) and  $\mathcal{C}$  is the standard fourth-order elastic Hooke tensor fulfilling

$$\left. \begin{aligned} \mathcal{C}_{ijkl} &= \mathcal{C}_{klij} && \text{(major symmetry),} \\ \mathcal{C}_{ijkl} &= \mathcal{C}_{jikl} \\ \mathcal{C}_{ijkl} &= \mathcal{C}_{ijlk} \end{aligned} \right\} \text{(minor symmetries).}$$

The major symmetry of the stress tensor is used later to derive the constitutive relation of the adjoint problem.

The definition of the weak form of the problem requires introducing the following functional spaces: the standard Sobolev space associated with static displacement fields

$$\mathcal{V}_0 := \left\{ \mathbf{w} \in [H^1(\Omega)]^d : \mathbf{w} = \mathbf{0} \text{ on } \Gamma_D \right\}$$

and the Bochner space  $\mathcal{L}^2(0, T; \mathcal{V}_0)$  associated with  $\mathcal{V}_0$  of square-integrable functions from  $I$  into  $\mathcal{V}_0$

$$\mathcal{L}^2(0, T; \mathcal{V}_0) := \left\{ \mathbf{v} : I \rightarrow \mathcal{V}_0, \mathbf{v}(t) \text{ is } \mathcal{V}_0\text{-measurable and } \int_0^T \|\mathbf{v}(t)\|_{\mathcal{V}_0}^2 dt < +\infty \right\}.$$

The solution of the problem,  $\mathbf{u}(\mathbf{x}, t)$ , belongs to the space  $\mathcal{W}$  defined as

$$\mathcal{W} := \left\{ \mathbf{w} \in \mathcal{L}^2(0, T; \mathcal{V}_0) \text{ with } \dot{\mathbf{w}} \in \mathcal{L}^2\left(0, T; [\mathcal{L}^2(\Omega)]^d\right) \text{ and } \ddot{\mathbf{w}} \in \mathcal{L}^2(0, T; \mathcal{V}'_0) \right\},$$

and  $\mathcal{V}'_0$  denotes the dual space of  $\mathcal{V}_0$ . Note that in particular, this implies that  $\mathbf{u} \in \mathcal{C}([0, T]; [\mathcal{L}^2(\Omega)]^d)$  and  $\dot{\mathbf{u}} \in \mathcal{C}([0, T]; \mathcal{V}'_0)$ , see [50]. That is, functions in  $\mathcal{W}$  are continuous functions both in space and time, with continuous time derivative.

*Remark 1*

Function  $\mathbf{u}$  is a transformation from  $\Omega \times I$  and  $\mathbb{R}^d$ , that is,

$$\begin{aligned} \mathbf{u} : \Omega \times I &\longrightarrow \mathbb{R}^d \\ (\mathbf{x}, t) &\longmapsto \mathbf{u}(\mathbf{x}, t). \end{aligned}$$

It can also be seen as a transformation from  $i$  and  $\mathcal{V}_0$ , that is,

$$\begin{aligned} \mathbf{u} : I &\longrightarrow \mathcal{V}_0 \\ t &\longmapsto \mathbf{u}(t). \end{aligned}$$

In the remainder of the paper, both notations are used, for  $\mathbf{u}$  and other functions, to denote the same mathematical objects depending on the context.

Thus, the weak form (integrated in space) of problem (1) reads as follows: find  $\mathbf{u} \in \mathcal{W}$  verifying the initial conditions  $\mathbf{u}(0) = \mathbf{u}_0$  and  $\dot{\mathbf{u}}(0) = \mathbf{v}_0$  and such that for all  $t \in I$

$$(\rho(\ddot{\mathbf{u}}(t) + a_1\dot{\mathbf{u}}(t)), \mathbf{w}) + a(\mathbf{u}(t) + a_2\dot{\mathbf{u}}(t), \mathbf{w}) = l(t; \mathbf{w}) \quad \forall \mathbf{w} \in \mathcal{V}_0, \tag{3}$$

where the standard linear and bilinear forms have been introduced

$$a(\mathbf{v}, \mathbf{w}) := \int_{\Omega} \boldsymbol{\varepsilon}(\mathbf{v}) : \mathcal{C} : \boldsymbol{\varepsilon}(\mathbf{w}) \, d\Omega \quad , \quad l(t; \mathbf{w}) := (\mathbf{f}(t), \mathbf{w}) + (\mathbf{g}(t), \mathbf{w})_{\Gamma_N},$$

along with the scalar products

$$(\mathbf{v}, \mathbf{w}) := \int_{\Omega} \mathbf{v} \cdot \mathbf{w} \, d\Omega \quad \text{and} \quad (\mathbf{v}, \mathbf{w})_{\Gamma_N} := \int_{\Gamma_N} \mathbf{v} \cdot \mathbf{w} \, d\Gamma.$$

The error estimation strategy presented in the succeeding text requires a space–time variational framework. The single field formulation introduced by Hughes and Hulbert [51, 52] is considered. Thus, the space–time integrated weak form of (3) reads as follows: find  $\mathbf{u} \in \mathcal{W}$  such that

$$B(\mathbf{u}, \mathbf{w}) = L(\mathbf{w}) \quad \forall \mathbf{w} \in \mathcal{W}, \tag{4}$$

where

$$B(\mathbf{v}, \mathbf{w}) := \int_I (\rho(\ddot{\mathbf{v}} + a_1\dot{\mathbf{v}}), \dot{\mathbf{w}}) dt + \int_I a(\mathbf{v} + a_2\dot{\mathbf{v}}, \dot{\mathbf{w}}) dt + (\rho\dot{\mathbf{v}}(0^+), \dot{\mathbf{w}}(0^+)) + a(\mathbf{v}(0^+), \mathbf{w}(0^+))$$

and

$$L(\mathbf{w}) := \int_I l(t; \dot{\mathbf{w}}(t)) dt + (\rho\mathbf{v}_0, \dot{\mathbf{w}}(0^+)) + a(\mathbf{u}_0, \mathbf{w}(0^+)).$$

2.2. Numerical approximation

In the following developments,  $\hat{\mathbf{u}} \in \mathcal{W}$  is assumed to be an approximation of the solution of the boundary value problem (1). Note that  $\hat{\mathbf{u}}$  must have  $C^0$ -continuity in space and  $C^1$ -continuity in time. Most typically, the approximation computed with a standard methodology, say  $\mathbf{u}^{H,\Delta t}$ , does not fulfill these continuity requirements and has to be post-processed to obtain a suitable  $\hat{\mathbf{u}}$ . Here,  $\mathbf{u}^{H,\Delta t}$  is computed by using the Newmark method [53], which is widely adopted in practical applications and commercial codes.

A mesh of characteristic element size  $H$  discretizing the spatial domain is introduced together with its associated finite element space  $\mathcal{V}_0^H \subset \mathcal{V}_0$ . The degree of the complete polynomial basis in  $\mathcal{V}_0^H$  is denoted by  $p$ . This allows introducing the spatially discrete and time-continuous version of Equation (3) (semidiscrete problem), namely: find  $\mathbf{u}^H(t) \in \mathcal{V}_0^H$  such that for all  $t \in I$

$$(\rho(\ddot{\mathbf{u}}^H(t) + a_1\dot{\mathbf{u}}^H(t)), \mathbf{w}) + a(\mathbf{u}^H(t) + a_2\dot{\mathbf{u}}^H(t), \mathbf{w}) = l(t; \mathbf{w}) \quad \forall \mathbf{w} \in \mathcal{V}_0^H, \quad (5)$$

with initial conditions  $\mathbf{u}^H(0) = \mathbf{\Pi}^H(\mathbf{u}_0)$  and  $\dot{\mathbf{u}}^H(0) = \mathbf{\Pi}^H(\mathbf{v}_0)$ , being  $\mathbf{\Pi}^H$  the interpolation operator mapping functions from the continuous space  $\mathcal{V}_0$  into the discrete space  $\mathcal{V}_0^H$ .

The Newmark method is a numerical time-marching scheme providing an approximation of the standard system of second order ODEs (5) arising in structural dynamics. A time grid discretizing the time interval  $I$  is introduced,  $\mathcal{T} := \{t_0, t_1, \dots, t_N\}$ , where  $0 = t_0 < t_1 < \dots < t_N = T$ . Time steps are denoted by  $\Delta t_n := t_n - t_{n-1}$ , for  $n = 1, \dots, N$ , and the characteristic time step for the time grid is

$$\Delta t := \max_{1 \leq n \leq N} (\Delta t_n).$$

The Newmark solution consists in displacements, velocities, and accelerations at each time  $t_n$ ,  $\mathbf{u}_n^{H,\Delta t} \approx \mathbf{u}^H(t_n)$ ,  $\mathbf{v}_n^{H,\Delta t} \approx \dot{\mathbf{u}}^H(t_n)$  and  $\mathbf{a}_n^{H,\Delta t} \approx \ddot{\mathbf{u}}^H(t_n)$ , for  $n = 1, \dots, N$ , such that Equation (5) is fulfilled at each time  $t_n \in \mathcal{T}$ , that is

$$(\rho(\mathbf{a}_n^{H,\Delta t} + a_1\mathbf{v}_n^{H,\Delta t}), \mathbf{w}) + a(\mathbf{u}_n^{H,\Delta t} + a_2\mathbf{v}_n^{H,\Delta t}, \mathbf{w}) = l(t_n; \mathbf{w}) \quad \forall \mathbf{w} \in \mathcal{V}_0^H. \quad (6)$$

Assuming that  $\mathbf{u}_{n-1}^{H,\Delta t}$ ,  $\mathbf{v}_{n-1}^{H,\Delta t}$ ,  $\mathbf{a}_{n-1}^{H,\Delta t}$  are known and that the following discrete integral expressions hold

$$\begin{aligned} \mathbf{u}_n^{H,\Delta t} &= \mathbf{u}_{n-1}^{H,\Delta t} + \Delta t_n \mathbf{v}_{n-1}^{H,\Delta t} + \frac{1}{2} \Delta t_n^2 \left[ (1 - 2\beta) \mathbf{a}_{n-1}^{H,\Delta t} + 2\beta \mathbf{a}_n^{H,\Delta t} \right], \\ \mathbf{v}_n^{H,\Delta t} &= \mathbf{v}_{n-1}^{H,\Delta t} + \Delta t_n \left[ (1 - \gamma) \mathbf{a}_{n-1}^{H,\Delta t} + \gamma \mathbf{a}_n^{H,\Delta t} \right], \end{aligned}$$

the only remaining unknown in Equation (6) is  $\mathbf{a}_n^{H,\Delta t}$ , which is obtained by solving a linear system of algebraic equations. Similarly, at time  $t_0$ , the displacements and velocities are determined by the initial conditions  $\mathbf{u}_0$  and  $\mathbf{v}_0$ , and the acceleration  $\mathbf{a}_0^{H,\Delta t}$  is computed by considering that

$$\left( \rho(\mathbf{a}_0^{H,\Delta t} + a_1\mathbf{v}_0), \mathbf{w} \right) + a(\mathbf{u}_0 + a_2\mathbf{v}_0, \mathbf{w}) = l_0(\mathbf{w}) \quad \forall \mathbf{w} \in \mathcal{V}_0^H.$$

The scalars  $\beta$  and  $\gamma$  are the parameters of the Newmark method taking values in  $[0, 1]$ . For  $\gamma = 1/2$ , the method is second order accurate and there is no numerical damping, whereas for  $\gamma > 1/2$ , numerical damping is introduced. Moreover, the method is conditionally stable for  $\beta \geq \gamma/2 \geq 1/4$ . See [53] for specific details.

Note that the Newmark method does not directly provide a numerical approximation  $\hat{\mathbf{u}} \in \mathcal{W}$ , because the approximation is not even defined in the whole time interval  $I$  (it is only given at times

$t_n$  of the time grid). The first step to recover the numerical approximation is to extend the Newmark approximation into the whole time domain by using a simple piecewise linear interpolation:

$$\mathbf{u}^{H,\Delta t}(\mathbf{x}, t) := \sum_{n=0}^N \mathbf{u}_n^{H,\Delta t}(\mathbf{x})\theta_n(t), \tag{7a}$$

$$\mathbf{v}^{H,\Delta t}(\mathbf{x}, t) := \sum_{n=0}^N \mathbf{v}_n^{H,\Delta t}(\mathbf{x})\theta_n(t), \tag{7b}$$

$$\mathbf{a}^{H,\Delta t}(\mathbf{x}, t) := \sum_{n=0}^N \mathbf{a}_n^{H,\Delta t}(\mathbf{x})\theta_n(t), \tag{7c}$$

where the functions  $\theta_n(t)$ , for  $n = 0, \dots, N$ , are the one-dimensional piecewise linear shape functions related with the time partition  $\mathcal{T}$ . Note that, however, one cannot take  $\hat{\mathbf{u}} = \mathbf{u}^{H,\Delta t}(\mathbf{x}, t)$  because this approximation does not meet the regularity requirements of the functional space  $\mathcal{W}$ ;  $\mathbf{u}^{H,\Delta t}(\mathbf{x}, t) \notin \mathcal{W}$  because its time derivative is not continuous.

Following [2], an admissible approximation  $\hat{\mathbf{u}} \in \mathcal{W}$  is easily recovered from the Newmark solution by using the information provided by the numerical accelerations, namely

$$\hat{\mathbf{v}}(\mathbf{x}, t) := \int_0^t \mathbf{a}^{H,\Delta t}(\mathbf{x}, \tau) \, d\tau + \mathbf{\Pi}^H(\mathbf{v}_0(\mathbf{x})), \tag{8a}$$

$$\hat{\mathbf{u}}(\mathbf{x}, t) := \int_0^t \hat{\mathbf{v}}(\mathbf{x}, \tau) \, d\tau + \mathbf{\Pi}^H(\mathbf{u}_0(\mathbf{x})). \tag{8b}$$

Note that by construction, the approximation  $\hat{\mathbf{u}}$  exactly verifies the initial conditions up to the resolution of the spatial finite element mesh (i.e.,  $\hat{\mathbf{u}}(0) = \mathbf{\Pi}^H(\mathbf{u}_0)$  and  $\hat{\mathbf{u}}'(0) = \mathbf{\Pi}^H(\mathbf{v}_0)$ ) and that the admissible acceleration coincides with the Newmark solution,  $\hat{\mathbf{u}}'' = \mathbf{a}^{H,\Delta t}$ . Note that the displacements  $\mathbf{u}^{H,\Delta t}$  and  $\hat{\mathbf{u}}$  do not coincide but that they both tend to the exact (in time) solution of the semi-discrete problem (5) as  $\Delta t$  tends to zero.

### 2.3. Scalar and timeline-dependent quantities of interest

A posteriori goal-oriented error estimation techniques aim at assessing the quality of the approximations of scalar outputs of the solution. These techniques are of utmost practical interest because engineering decisions are usually based on representative scalar values of the whole time-space solution  $\mathbf{u}$ . The scalar output of interest is  $s_T := L^\mathcal{O}(\mathbf{u})$ , and its corresponding approximation is  $\hat{s}_T := L^\mathcal{O}(\hat{\mathbf{u}})$ , where  $L^\mathcal{O}(\cdot)$  is a bounded linear functional

$$\begin{aligned} L^\mathcal{O} : \mathcal{W} &\longrightarrow \mathbb{R} \\ \mathbf{w} &\longmapsto L^\mathcal{O}(\mathbf{w}), \end{aligned}$$

extracting a single representative scalar value of the whole time-space solution  $\mathbf{u}$ . For instance, the quantity of interest can be described as

$$s_T = L^\mathcal{O}(\mathbf{u}) := \int_0^T (\mathbf{f}^\mathcal{O}(t), \dot{\mathbf{u}}(t)) \, dt + \int_0^T (\mathbf{g}^\mathcal{O}(t), \dot{\mathbf{u}}(t))_{\Gamma_N} \, dt + (\rho \mathbf{v}^\mathcal{O}, \dot{\mathbf{u}}(T)) + a(\mathbf{u}^\mathcal{O}, \mathbf{u}(T)), \tag{9}$$

where  $\mathbf{f}^\mathcal{O}$ ,  $\mathbf{g}^\mathcal{O}$ ,  $\mathbf{v}^\mathcal{O}$ , and  $\mathbf{u}^\mathcal{O}$  are the data characterizing the quantity of interest. The functions  $\mathbf{f}^\mathcal{O}$  and  $\mathbf{g}^\mathcal{O}$  extract global or localized averages of velocities in  $\Omega$  and  $\Gamma_N$ , respectively, over the whole time simulation  $[0, t]$ , whereas  $\mathbf{v}^\mathcal{O}$  and  $\mathbf{u}^\mathcal{O}$  assess averages of velocities and strains or displacements respectively at the final simulation time  $T$ .

Goal-oriented error estimation techniques are crucial in assessing the quality of numerical simulations because they provide meaningful information to both drive adaptive mesh refinements or to certify the accuracy of the computations, not only in global measures but also in representative

quantities of interest. The extension of standard techniques, developed for static problems, to transient dynamic simulations allows certifying the accuracy of the computations with respect to a single scalar output of the whole space–time solution but does not provide information of the evolution of the solution during the simulation process. One of the aims of this work is to extend the paradigm of classical goal-oriented error estimation by introducing the new concept of *timeline-dependent quantities of interest*.

Timeline-dependent quantities of interest are defined to be time-dependent functions providing information of the problem variables for all time  $t \in [0, T]$ . That is, the quantity of interest is no longer a scalar value but a function of time  $s(t)$ . In contrast with *scalar* quantities of interest which can only be computed by having at hand the complete simulation, the timeline-dependent quantity can be produced along the time-marching scheme.

To be specific, timeline-dependent quantities of interest are defined as an extension of (9) as

$$s(t) := \int_0^t (\mathbf{f}^\mathcal{O}(\tau), \dot{\mathbf{u}}(\tau)) \, d\tau + \int_0^t (\mathbf{g}^\mathcal{O}(\tau), \dot{\mathbf{u}}(\tau))_{\Gamma_N} \, d\tau + (\rho \mathbf{v}^\mathcal{O}, \dot{\mathbf{u}}(t)) + a(\mathbf{u}^\mathcal{O}, \mathbf{u}(t)), \quad (10)$$

where the scalar quantity of interest is recovered for the particular case  $s_T = s(T)$ . Note that timeline-dependent quantities of interest can be represented via a bounded mapping

$$\begin{aligned} L_{\text{TL}}^\mathcal{O} : \mathcal{W} &\longrightarrow \mathcal{L}^2(I) \\ \mathbf{w} &\longmapsto L_{\text{TL}}^\mathcal{O}(\mathbf{w}), \end{aligned}$$

where

$$L_{\text{TL}}^\mathcal{O}(\mathbf{w})(t) := \int_0^t (\mathbf{f}^\mathcal{O}(\tau), \dot{\mathbf{w}}(\tau)) \, d\tau + \int_0^t (\mathbf{g}^\mathcal{O}(\tau), \dot{\mathbf{w}}(\tau))_{\Gamma_N} \, d\tau + (\rho \mathbf{v}^\mathcal{O}, \dot{\mathbf{w}}(t)) + a(\mathbf{u}^\mathcal{O}, \mathbf{w}(t)). \quad (11)$$

Thus, the function  $L_{\text{TL}}^\mathcal{O}(\cdot)$ , instead of extracting a scalar value of the whole time–space solution, extracts a function of time, and in particular when applied to the exact solution of the problem  $\mathbf{u}$ ,  $L_{\text{TL}}^\mathcal{O}(\mathbf{u})(t) = s(t)$  provides a time-dependent function  $s \in \mathcal{L}^2(I)$ , see Figure 1. For the sake of simplicity, the following notation is adopted  $L_{\text{TL}}^\mathcal{O}(\mathbf{w}; t) := L_{\text{TL}}^\mathcal{O}(\mathbf{w})(t)$ .

*Remark 2*

Note that for a given  $t \in I$ , the timeline-dependent quantity of interest  $s(t)$  defined in (10) extracts a scalar value of the time–space solution by using information in the time interval  $[0, t]$ , namely,  $s(t) = L_{\text{TL}}^\mathcal{O}(\mathbf{u}_{[0,t]})(t)$  and thus can be computed along the time marching scheme. Moreover, the estimates for the quantity of interest  $s(t)$  at a given time provide local (in time) error indicators that can be used to adaptively refine the finite element mesh along time.

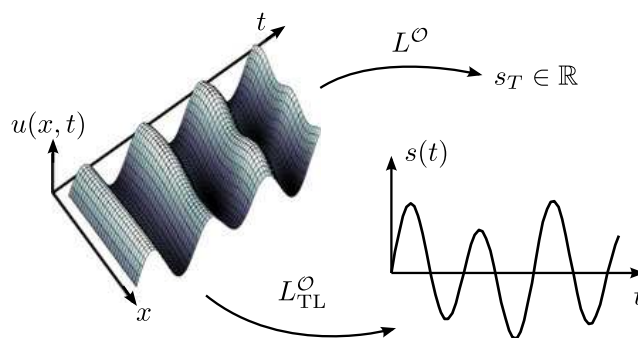


Figure 1. Illustration of scalar and timeline-dependent quantities of interest. The functional  $L^\mathcal{O}$  maps the time–space solution  $\mathbf{u}$  into a scalar value  $s_T \in \mathbb{R}$ . The operator  $L_{\text{TL}}^\mathcal{O}$  transforms  $\mathbf{u}$  into a time-dependent function  $s(t)$ .

The aim of timeline-dependent goal-oriented error estimation strategies is assessing the quality of  $\hat{s}(t) = L_{TL}^{\mathcal{O}}(\hat{\mathbf{u}}; t)$ , that is the difference between the exact quantity of interest  $s(t) = L_{TL}^{\mathcal{O}}(\mathbf{u}; t)$  and the approximation obtained with the numerical simulation  $\hat{s}(t)$ . Note that this has to be estimated for all  $t \in I$ .

Thus, the goal is to assess and control the error in the quantity of interest, which is now a function of time

$$s^e(t) := s(t) - \hat{s}(t).$$

Recall that the assessment of the error in a scalar quantity, for instance the value of  $s$  at  $t = T$ ,  $s_T^e := s_T - \hat{s}_T = s(T) - \hat{s}(T) = s^e(T)$ , requires introducing an adjoint problem. Thus,  $s_T^e$  is estimated in terms of *energy* products of the errors in the direct (or *primal*) and adjoint problems, which have to be integrated both in space and time.

The adjoint problem has the same structure of the direct one but reverted in time. Consequently, the adjoint solution has to be computed backwards in time and stored beforehand to use it to estimate the error during the forward time integration of the direct problem. An alternative approach is to solve and store both the direct and the dual problem independently and to compute the error estimate afterwards. However, the latter option does not allow adapting the spatial mesh along the time stepping procedure.

Moreover, the standard numerical integration of the adjoint solution and its storage are often computationally unaffordable. To overcome this difficulty, in Section 3, the adjoint problem is solved by using a modal analysis strategy. This reduces both the computational cost and the memory requirements for the adjoint problem. Moreover, the information provided by modal solution of the adjoint problem is straightforwardly used to adapt the finite element mesh along the computation of the direct problem.

The advantages of using the modal description of the solution of the adjoint problem are even more manifest if dealing with a timeline-dependent quantity of interest,  $s(t)$ . In this case, there is no longer a single adjoint problem but a family of them, each one associated with each time  $T$  in  $I$ . For some particular quantities of interest, the members of this family of functions can be generated as a translation in time of a representative member of the family. If this representative member is characterized by a modal description, both the translation and the combination with the solution of the direct problem are simply implemented and computationally efficient. This is described in detail in Section 4.

### 3. A MODAL-BASED ERROR REPRESENTATION FOR SCALAR QUANTITIES OF INTEREST

This section is devoted to present a novel approach to assess the error of  $\hat{\mathbf{u}}$  measured by a scalar quantity of interest  $L^{\mathcal{O}}$  using the modal analysis to obtain a proper approximation of the adjoint solution.

#### 3.1. Error representation and adjoint problem

An auxiliary problem associated with the functional  $L^{\mathcal{O}}(\cdot)$ , usually denoted by *adjoint* or *dual* problem [29, 41–44, 46], is introduced to derive an error representation. The variational form of the adjoint problem consists in finding  $\mathbf{u}^d \in \mathcal{W}$  such that

$$B(\mathbf{w}, \mathbf{u}^d) = L^{\mathcal{O}}(\mathbf{w}) \quad \forall \mathbf{w} \in \mathcal{W}. \tag{12}$$

The adjoint solution  $\mathbf{u}^d$  characterizes the quantity of interest defined by  $L^{\mathcal{O}}(\cdot)$ . Note that having  $\mathbf{u}^d$  at hand allows explicitly computing the quantity of interest associated with the loading described by  $L(\cdot)$ . This is because if  $\mathbf{u}^d$  is available, the quantity  $L(\mathbf{u}^d)$  is computable and coincides with  $L^{\mathcal{O}}(\mathbf{u})$ . The associated strong form of the adjoint problem is

$$\rho(\ddot{\mathbf{u}}^d - a_1 \dot{\mathbf{u}}^d) - \nabla \cdot \boldsymbol{\sigma}^d = -\mathbf{f}^{\mathcal{O}} \quad \text{in } \Omega \times I, \tag{13a}$$

$$\mathbf{u}^d = \mathbf{0} \quad \text{on } \Gamma_D \times I, \tag{13b}$$

$$\boldsymbol{\sigma}^d \cdot \mathbf{n} = -\mathbf{g}^O \quad \text{on } \Gamma_N \times I, \tag{13c}$$

$$\mathbf{u}^d = \mathbf{u}^O \quad \text{at } \Omega \times \{T\}, \tag{13d}$$

$$\dot{\mathbf{u}}^d = \mathbf{v}^O \quad \text{at } \Omega \times \{T\}, \tag{13e}$$

with the constitutive law

$$\boldsymbol{\sigma}^d := \mathbf{C} : \boldsymbol{\varepsilon}(\mathbf{u}^d - a_2 \dot{\mathbf{u}}^d). \tag{14}$$

Note that the terms affected by  $a_1$  and  $a_2$  have opposite sign that the ones in the original problem (1). Consequently, the adjoint problem has to be integrated backwards in time, starting from the *final conditions* (13d) and (13e).

The semidiscrete equation associated with the adjoint problem (13) reads as follows: find  $\mathbf{u}^{d,H}(t) \in \mathcal{V}_0^H$  verifying the final conditions  $\mathbf{u}^{d,H}(T) = \mathbf{u}^O$  and  $\dot{\mathbf{u}}^{d,H}(T) = \mathbf{v}^O$  and such that for all  $t \in I$

$$(\rho(\ddot{\mathbf{u}}^{d,H}(t) - a_1 \dot{\mathbf{u}}^{d,H}(t)), \mathbf{w}) + a(\mathbf{u}^{d,H}(t) - a_2 \dot{\mathbf{u}}^{d,H}(t), \mathbf{w}) = -l^O(t; \mathbf{w}) \quad \forall \mathbf{w} \in \mathcal{V}_0^H, \tag{15}$$

where  $l^O(t; \mathbf{w}) := (\mathbf{f}^O(t), \mathbf{w}) + (\mathbf{g}^O(t), \mathbf{w})_{\Gamma_N}$ .

The solution of the adjoint problem  $\mathbf{u}^d$  allows representing the error in the quantity of interest in terms of residuals. Indeed, taking  $\mathbf{w} = \hat{\mathbf{e}} := \mathbf{u} - \hat{\mathbf{u}}$  in equation (12) yields

$$L^O(\hat{\mathbf{e}}) = B(\hat{\mathbf{e}}, \mathbf{u}^d). \tag{16}$$

The residual error equation for  $\hat{\mathbf{e}}$  is readily derived from (4) as

$$B(\hat{\mathbf{e}}, \mathbf{w}) = \hat{R}(\mathbf{w}) := L(\mathbf{w}) - B(\hat{\mathbf{u}}, \mathbf{w}), \quad \text{for all } \mathbf{w} \in \mathcal{W}, \tag{17}$$

being  $\hat{R}(\cdot)$  the weak residual associated with the approximation  $\hat{\mathbf{u}}$ . Hence, the resulting error representation

$$L^O(\hat{\mathbf{e}}) = \hat{R}(\mathbf{u}^d) \tag{18}$$

allows obtaining the error in the quantity of interest, provided that the exact solution of the adjoint problem is available.

Conversely, if an accurate approximation of the adjoint solution is available, say  $\tilde{\mathbf{u}}^d$ , the error in the quantity of interest is estimated as [21, 46]

$$s_T^e = L^O(\hat{\mathbf{e}}) \approx \hat{R}(\tilde{\mathbf{u}}^d) =: \tilde{s}_T^e. \tag{19}$$

The quality of the functional approximation  $\tilde{\mathbf{u}}^d$  is critical to obtain accurate estimates of the error in the scalar quantity of interest.

### 3.2. Modal-based approximation for the adjoint problem

The *modal analysis* or *mode superposition*, see [54], provides information on the dynamical behavior of the structural system: its natural vibration modes and frequencies. This information is often used to obtain numerical solutions of the problem avoiding the time integration of the complete system of ODE resulting from (5). This technique can be used to solve both the primal and adjoint problems, corresponding both to the same structural system (the eigenvalue problem to be solved is the same). Here, this technique is applied to the adjoint problem to find a proper approximation  $\tilde{\mathbf{u}}^d$ .

The natural modes and frequencies of the problem are computed, solving the generalized eigenvalue problem associated with the homogeneous undamped version of the semidiscrete problem (either (5) for the primal or (15) for the adjoint). That is, taking  $l(t; \mathbf{w}) = 0$  or  $l^O(t; \mathbf{w}) = 0$  and

$a_1 = a_2 = 0$ . Thus, the natural frequencies and modes  $(\omega_i^H, \mathbf{q}_i^H) \in \mathbb{R} \times \mathcal{V}_0^H, i = 1, \dots, N_{\text{dof}}$  are the eigenvalues and eigenfunctions of

$$a(\mathbf{q}^H, \mathbf{w}) = (\omega^H)^2 (\rho \mathbf{q}^H, \mathbf{w}) \quad \forall \mathbf{w} \in \mathcal{V}_0^H. \tag{20}$$

Note that the number of eigenpair solutions of this problem is the number of DOFs in the computational  $H$ -mesh, denoted by  $N_{\text{dof}}$ . Eigenpairs are sorted from low to high frequencies, namely  $\omega_1^H \leq \omega_2^H \dots \leq \omega_{N_{\text{dof}}}^H$ , and eigenvectors are normalized to be orthonormal with respect to the product  $(\rho \cdot, \cdot)$ , that is,

$$(\rho \mathbf{q}_i^H, \mathbf{q}_j^H) = \delta_{ij}, \quad 1 \leq i, j \leq N_{\text{dof}}. \tag{21}$$

The modal analysis is applied to obtain the adjoint solution  $\mathbf{u}^{\text{d},H}(\mathbf{x}, t)$  by expressing it as a linear combination of the eigenvectors  $\mathbf{q}_i^H, i = 1, \dots, N_{\text{dof}}$ , that is

$$\mathbf{u}^{\text{d},H}(\mathbf{x}, t) = \sum_{i=1}^{N_{\text{dof}}} \mathbf{q}_i^H(\mathbf{x}) y_i^H(t). \tag{22}$$

Thus, for the new unknowns of the problem,  $y_i^H(t)$ , the system of ODEs resulting from (15) is transformed into the uncoupled set of scalar ordinary differential equations

$$\ddot{y}_i^H - [a_1 + a_2 (\omega_i^H)^2] \dot{y}_i^H + (\omega_i^H)^2 y_i^H = l_i, \tag{23a}$$

$$y_i^H(T) = u_i, \tag{23b}$$

$$\dot{y}_i^H(T) = v_i, \tag{23c}$$

where the r.h.s. terms  $l_i, u_i$ , and  $v_i$  are computed by using the data characterizing the quantity of interest (9) and the eigenvector  $\mathbf{q}_i^H$

$$l_i(t) := (\mathbf{f}^\mathcal{O}(t), \mathbf{q}_i^H) + (\mathbf{g}^\mathcal{O}(t), \mathbf{q}_i^H)_{\Gamma_N}, \quad u_i := (\rho \mathbf{u}^\mathcal{O}, \mathbf{q}_i^H) \quad \text{and} \quad v_i := (\rho \mathbf{v}^\mathcal{O}, \mathbf{q}_i^H). \tag{24}$$

*Remark 3*

The time-dependent coefficients of the decomposition (22),  $y_i^H(t)$ , may be computed in many cases by analytically solving (23). In particular, for constant-in-time data  $\mathbf{f}^\mathcal{O}$  and  $\mathbf{g}^\mathcal{O}$ , the term  $l_i$  is also constant in time, and it is easy to see that taking  $\alpha = a_1 + a_2 \omega_i^2$  then

$$y_i^H(t) = \frac{1}{2} e^{(\alpha + \sqrt{\alpha^2 - 4\omega_i^2})(t-T)/2} \left( \frac{2v_i \omega_i^2 - \alpha u_i \omega_i^2 + \alpha l_i}{\omega_i^2 \sqrt{\alpha^2 - 4\omega_i^2}} + u_i - \frac{l_i}{\omega_i^2} \right) + \frac{1}{2} e^{(\alpha - \sqrt{\alpha^2 - 4\omega_i^2})(t-T)/2} \left( \frac{-2v_i \omega_i^2 + \alpha u_i \omega_i^2 - \alpha l_i}{\omega_i^2 \sqrt{\alpha^2 - 4\omega_i^2}} + u_i - \frac{l_i}{\omega_i^2} \right) + \frac{l_i}{\omega_i^2},$$

if  $\alpha^2 - 4\omega_i^2 \neq 0$ . If not, for  $\alpha^2 - 4\omega_i^2 = 0$

$$y_i^H(t) = \left( \left( u_i - \frac{l_i}{\omega_i^2} \right) (1 + T - t) + (T - t)v_i \right) e^{-\alpha(T-t)/2} + \frac{l_i}{\omega_i^2}.$$

Note that if  $\alpha^2 - 4\omega_i^2 < 0$ , the arguments of the exponential functions are complex numbers, but  $y_i^H(t)$  remains a real function.

The cost of modal analysis scales as [54–56]

$$\mathcal{O}(N_{\text{dof}} \cdot N_{\text{bw}}^2) + \mathcal{O}(N_{\text{dof}}^2 \cdot N_{\text{bw}}) + \mathcal{O}(N_{\text{dof}}^3),$$

where  $N_{\text{bw}}$  denotes the half bandwidth of the finite element matrices associated with the computational  $H$ -mesh. This is computationally unaffordable unless the modal description (22) is truncated up to the first  $M$  terms, being  $M \ll N_{\text{dof}}$ , namely

$$\mathbf{u}^{\text{d},H,M}(\mathbf{x}, t) := \sum_{i=1}^M \mathbf{q}_i^H(\mathbf{x}) y_i^H(t). \quad (25)$$

The cost of the truncated modal analysis scales as

$$\mathcal{O}(N_{\text{dof}} \cdot N_{\text{bw}}^2) + \mathcal{O}(N_{\text{dof}} \cdot N_{\text{bw}} \cdot M) + \mathcal{O}(N_{\text{dof}} \cdot M^2).$$

Note that modal analysis is competitive with respect to the Newmark method only if the number of computed eigenvectors  $M$  is small when compared with the number of computed time steps  $N$ . The cost estimate for the Newmark method reads [54]

$$\mathcal{O}(N_{\text{dof}} \cdot N_{\text{bw}}^2) + \mathcal{O}(N_{\text{dof}} \cdot N_{\text{bw}} \cdot N).$$

Thus, modal analysis is competitive with respect to Newmark method if  $M$  is significantly lower than  $N$ .

Note that the number of required vibration modes  $M$  has to be selected such that the truncated high frequency modes (for  $i > M$ ) are negligible in (22). That is,  $\mathbf{u}^{\text{d},H,M}$  is a good approximation to  $\mathbf{u}^{\text{d},H}$ . This is equivalent to assume that for  $i > M$ , the values of  $l_i$ ,  $u_i$ , and  $v_i$ , as defined in (24), are close to zero, and consequently,  $y_i^H(t) \approx 0$ . This is guaranteed if the data  $\mathbf{f}^{\mathcal{O}}$ ,  $\mathbf{g}^{\mathcal{O}}$ ,  $\mathbf{u}^{\mathcal{O}}$ , and  $\mathbf{v}^{\mathcal{O}}$  are well captured by the expansion of the first  $M$  eigenvectors.

*Remark 4*

The eigenpairs  $(\omega_i^H, \mathbf{q}_i^H)$  are  $H$ -discrete approximations of the following infinite-dimensional generalized eigenvalue problem: find  $\omega \in \mathbb{R}$  and  $\mathbf{q} \in \mathcal{V}_0$  such that

$$a(\mathbf{q}, \mathbf{w}) = \omega^2(\rho \mathbf{q}, \mathbf{w}) \quad \forall \mathbf{w} \in \mathcal{V}_0. \quad (26)$$

The computed eigenfrequencies and eigenvectors  $(\omega_i^H, \mathbf{q}_i^H)$ , solutions of (20), are good approximations of (26),  $(\omega_i, \mathbf{q}_i)$ , only for the lower frequency modes [54]. This is supporting the choice of considering only the first  $M$  terms in the expansion (22).

3.3. Spatial enhancement of the adjoint approximation

Taking  $\tilde{\mathbf{u}}^{\text{d}} = \mathbf{u}^{\text{d},H,M}$  in (19) as an approximation to  $\mathbf{u}^{\text{d}}$  provides a raw estimate for the error in the quantity of interest. This requires injecting  $\mathbf{u}^{\text{d},H,M}$  as an argument of the residual. However, the resulting value  $\hat{R}(\mathbf{u}^{\text{d},H,M})$  is expected to be null if time integration is assumed to be exact or, in any case, very small. This is because  $\mathbf{u}^{\text{d},H,M}$  and  $\hat{\mathbf{u}}$  have the same spatial resolution, associated with  $\mathcal{V}_0^H$ , producing an effect analogous to Galerkin orthogonality.

Thus, it is advisory to use an *enhanced* approximation  $\tilde{\mathbf{u}}^{\text{d}}$  having a richer space resolution than  $\mathbf{u}^{\text{d},H,M}$ .

The proposed approach is to find  $\tilde{\mathbf{u}}^{\text{d}}$  as a higher order polynomial approximation (piecewise  $p + 1$  polynomials in the  $H$ -mesh), obtained from  $\mathbf{u}^{\text{d},H,M}$  by using *recovery techniques* [57, 58].

The computed eigenpairs  $(\omega_i^H, \mathbf{q}_i^H)$ ,  $i = 1, \dots, M$  are post-processed into enhanced eigenpairs  $(\tilde{\omega}_i, \tilde{\mathbf{q}}_i)$ , by using a technique similar to [49]. The core of the post-processing technique is computing  $\tilde{\mathbf{q}}_i$  from  $\mathbf{q}_i^H$  by using a space recovery technique described in detail in the succeeding text. Once  $\tilde{\mathbf{q}}_i$  is available,  $\tilde{\omega}_i$  is readily computed by using Rayleigh coefficients

$$\tilde{\omega}_i := \frac{a(\tilde{\mathbf{q}}_i, \tilde{\mathbf{q}}_i)}{(\rho \tilde{\mathbf{q}}_i, \tilde{\mathbf{q}}_i)}. \quad (27)$$

The enhanced time-dependent functions  $\tilde{y}_i(t)$  are computed by using the enhanced vibration modes  $(\tilde{\omega}_i, \tilde{\mathbf{q}}_i)$  solving the set of scalar ODEs

$$\ddot{\tilde{y}}_i - [a_1 + a_2(\tilde{\omega}_i)^2] \dot{\tilde{y}}_i + (\tilde{\omega}_i)^2 \tilde{y}_i = \tilde{l}_i, \quad (28a)$$

$$\tilde{y}_i(T) = \tilde{u}_i, \tag{28b}$$

$$\dot{\tilde{y}}_i(T) = \tilde{v}_i, \tag{28c}$$

where  $\tilde{l}_i(t) := (\mathbf{f}^\mathcal{O}(t), \tilde{\mathbf{q}}_i) + (\mathbf{g}^\mathcal{O}(t), \tilde{\mathbf{q}}_i)_{\Gamma_N}$ , and  $\tilde{u}_i$  and  $\tilde{v}_i$  are the coefficients best fitting  $\mathbf{u}^\mathcal{O}$  and  $\mathbf{v}^\mathcal{O}$  in the enhanced eigenvector basis, that is

$$\mathbf{u}^\mathcal{O} \approx \sum_{i=1}^{N_{\text{dof}}} \tilde{\mathbf{q}}_i(\mathbf{x}) \tilde{u}_i \quad \text{and} \quad \mathbf{v}^\mathcal{O} \approx \sum_{i=1}^{N_{\text{dof}}} \tilde{\mathbf{q}}_i(\mathbf{x}) \tilde{v}_i. \tag{29}$$

*Remark 5*

Note that the enhanced eigenvectors  $\{\tilde{\mathbf{q}}_i\}_{i=1,\dots,M}$  are no longer orthonormal. In limit cases, it may even occur that the enhanced eigenvectors are not linearly independent. Thus, the final conditions for the ODE's,  $\tilde{u}_i$  and  $\tilde{v}_i$ , cannot be computed by using simple scalar products, such as in (24). The values  $\tilde{u}_i$  and  $\tilde{v}_i$  are computed by solving a small least squares problems minimizing the squared error of equations (29). A simpler alternative used in the examples and providing fair results, similar to the least squares approach, is taking  $\tilde{u}_i = u_i$  and  $\tilde{v}_i = v_i$ .

Finally,  $\tilde{\mathbf{u}}^d$  is computed as the expansion of enhanced vibration modes, that is,

$$\tilde{\mathbf{u}}^d(\mathbf{x}, t) := \sum_{i=1}^M \tilde{\mathbf{q}}_i(\mathbf{x}) \tilde{y}_i(t). \tag{30}$$

The recovery procedure for the adjoint solution is performed only once, previous to the direct computation. The harmonic time description is highly efficient because it does not require any further post-process at every time step.

The post-processing technique to enhance the eigenvectors, from  $\mathbf{q}_i^H$  to  $\tilde{\mathbf{q}}_i$ , consists in a local (for each element of the  $H$ -mesh) least squares fitting of a  $p + 1$  degree polynomial.

Let  $\Omega_e \subset \Omega$ ,  $e = 1, \dots, N_{e1}$  be the elements of the  $H$ -mesh ( $N_{e1}$  is the total number of elements). Let  $\Omega_e^{\text{patch}}$  denote the patch of elements around  $\Omega_e$ , consisting of all the elements sharing nodes with  $\Omega_e$ , and let  $\mathcal{X}_e$  and  $\mathcal{X}_e^{\text{patch}}$  denote the set of nodes of element  $\Omega_e$  and patch  $\Omega_e^{\text{patch}}$ , respectively, see Figure 2.

The least squares problem stated in each patch  $\Omega_e^{\text{patch}}$  reads as follows: find  $\mathbf{q}_i^e \in [\mathbb{P}^{p+1}(\Omega_e^{\text{patch}})]^d$  such that  $\mathbf{q}_i^e(\mathbf{x}) = \mathbf{q}_i^H(\mathbf{x})$  for  $\mathbf{x} \in \mathcal{X}_e$  (it coincides with  $\mathbf{q}_i^H$  at the nodes of  $\Omega_e$ ) and

$$\mathbf{q}_i^e = \arg \min_{\mathbf{w} \in [\mathbb{P}^{p+1}(\Omega_e^{\text{patch}})]^d} \sum_{\mathbf{x} \in \mathcal{X}_e^{\text{patch}}} (\mathbf{w}(\mathbf{x}) - \mathbf{q}_i^H(\mathbf{x}))^2, \tag{31}$$

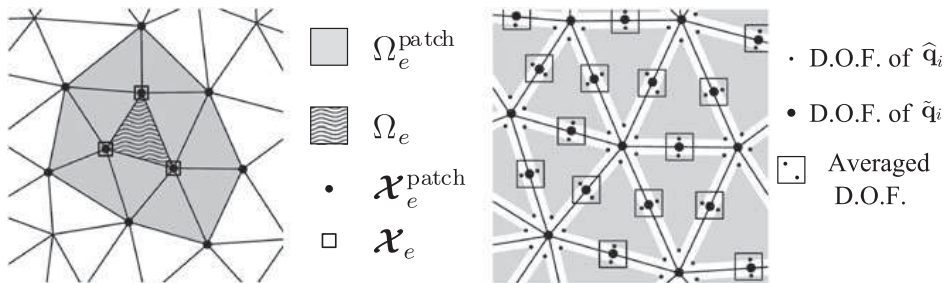


Figure 2. Definition of element patches (left) and illustration of the averaging of discontinuous function  $\hat{\mathbf{q}}_i$  into the continuous function  $\tilde{\mathbf{q}}_i$  (right).

where  $\mathbb{P}^{p+1}(\Omega_e^{\text{patch}})$  denotes the space of polynomials of degree  $p + 1$  in  $\Omega_e^{\text{patch}}$ . Problem (31) results in a small linear system of equations for each element of the computational  $H$ -mesh.

The post-processed eigenvector  $\tilde{\mathbf{q}}_i$  is obtained assembling the contributions of the restriction of the local recovered functions  $\mathbf{q}_i^e$  to the corresponding element  $\Omega_e$ ,  $\hat{\mathbf{q}}_i := \sum_e \mathbf{q}_i^e|_{\Omega_e}$ . Note that  $\hat{\mathbf{q}}_i$  is discontinuous because, for two neighboring elements  $\Omega_e$  and  $\Omega_{e'}$  with a common side  $\Gamma_{ee'} := \bar{\Omega}_e \cap \bar{\Omega}_{e'}$ , functions  $\mathbf{q}_i^e$  and  $\mathbf{q}_i^{e'}$  coincide at the endpoints of  $\Gamma_{ee'}$  but, in general, not in the other points of  $\Gamma_{ee'}$ . To build up a continuous approximation  $\tilde{\mathbf{q}}_i$ , the local contributions are averaged on the element sides. This is simply performed averaging the values of the DOFs associated with the element edges (not vertices), as illustrated in Figure 2.

### 3.4. Practical quantities of interest in modal-based error assessment

The suitability of the modal-based technique introduced earlier to approximate the solution of the dual problem depends on the particular choice for the quantity of interest. This section presents two types of quantities of interest such that the proposed modal-based estimate is computationally affordable. Note that the cost of building the error estimate is related with the number of eigenmodes  $M$  required to properly capture the data characterizing the quantity of interest  $\mathbf{f}^\circ$ ,  $\mathbf{g}^\circ$ ,  $\mathbf{u}^\circ$ , and  $\mathbf{v}^\circ$ . Thus, the quantities of interest presented in this section are selected such that they require a small number of eigenmodes  $M$ . Other quantities of interest such as the ones presented in [29, 41, 42, 44, 46] may require a higher number of eigenmodes, and consequently, the proposed technique is not competitive with respect to other alternatives.

The optimal choice to obtain an efficient response with this approach is selecting a quantity of interest defined by using only the first vibration mode

$$L_1^\circ(\mathbf{u}) := \int_I (\alpha_f \rho \mathbf{q}_1, \dot{\mathbf{u}}(t)) dt + (\rho \mathbf{q}_1, \dot{\mathbf{u}}(T)) + a(\alpha_u \mathbf{q}_1, \mathbf{u}(T)). \quad (32)$$

This corresponds to take  $\mathbf{f}^\circ = \alpha_f \rho \mathbf{q}_1$ ,  $\mathbf{g}^\circ = \mathbf{0}$ ,  $\mathbf{v}^\circ = \mathbf{q}_1$ , and  $\mathbf{u}^\circ = \alpha_u \mathbf{q}_1$  in Equation (9). The constants  $\alpha_f$  and  $\alpha_u$  are introduced to obtain consistent dimensions in (32). This quantity has not a direct physical interpretation other than being a sum of averages of velocities (both in time and space and in space for time  $T$ ) and an energy average of the strains (or stresses) at time  $T$ . Moreover, this quantity of interest is computationally inexpensive because it requires computing only one vibration mode ( $M = 1$ ).

Note that, following (30), computing the enhanced approximation  $\tilde{\mathbf{u}}^d$  associated with (32) and the estimate  $\hat{R}(\tilde{\mathbf{u}}^d)$  does not require having at hand the exact eigenvector  $\mathbf{q}_1$ , which is replaced by  $\tilde{\mathbf{q}}_1$ . Note that this requires taking  $\mathbf{f}^\circ = \alpha_f \rho \tilde{\mathbf{q}}_1$ ,  $\mathbf{g}^\circ = \mathbf{0}$ ,  $\mathbf{v}^\circ = \tilde{\mathbf{q}}_1$ , and  $\mathbf{u}^\circ = \alpha_u \tilde{\mathbf{q}}_1$  in Equations (28) and (29) but not in the definition of the quantity of interest  $L_1^\circ(\mathbf{w})$  in (32). It is worth noting that the numerical experiments (see the example in Section 5.2) demonstrate that the estimate  $\hat{R}(\tilde{\mathbf{u}}^d)$  is a fair approximation of the error measured with the *exact* quantity of interest (taking  $\mathbf{q}_1$  and not  $\tilde{\mathbf{q}}_1$  in (32)).

A second choice for a suitable quantity is considering the average of displacements at the final time of the computation

$$L_2^\circ(\mathbf{u}) := (\lambda^\circ, \mathbf{u}(T)) + (\lambda_N^\circ, \mathbf{u}(T))_{\Gamma_N}, \quad (33)$$

where the data  $\lambda^\circ$  and  $\lambda_N^\circ$  are weighting functions allowing to localize the average of displacements in some subdomains in  $\Omega$  and  $\Gamma_N$ , respectively. The quantity (33) has to be rewritten in the same form as the generic quantity (9) to compute its associated enhanced approximation  $\tilde{\mathbf{u}}^d$  by using the aforementioned rationale. Thus, the quantity (33) is rewritten as

$$L_2^\circ(\mathbf{u}) = a(\mathbf{u}^\circ, \mathbf{u}(T)),$$

taking  $\mathbf{f}^\circ = \mathbf{0}$ ,  $\mathbf{g}^\circ = \mathbf{0}$ ,  $\mathbf{v}^\circ = \mathbf{0}$  in equation (9) and being  $\mathbf{u}^\circ$  the solution of the static problem, find  $\mathbf{u}^\circ \in \mathcal{V}_0$  such that

$$a(\mathbf{u}^\circ, \mathbf{w}) = (\lambda^\circ, \mathbf{w}) + (\lambda_N^\circ, \mathbf{w})_{\Gamma_N} \quad \forall \mathbf{w} \in \mathcal{V}_0. \quad (34)$$

Note that here,  $\mathbf{u}^\mathcal{O}$  is not given as part of the data  $\boldsymbol{\lambda}^\mathcal{O}$  and  $\boldsymbol{\lambda}_N^\mathcal{O}$  characterizing  $L_2^\mathcal{O}$ . The function  $\mathbf{u}^\mathcal{O}$  has to be computed as the solution of (34) and therefore  $\mathbf{u}^\mathcal{O}$  has to be approximated by some  $\tilde{\mathbf{u}}^\mathcal{O}$ . This enhanced approximation is obtained by applying the post-processing technique presented in Section 3.3 to the discrete solution  $\mathbf{u}^{\mathcal{O},H} \in \mathcal{V}_0^H$  of problem (34). The error estimate  $\hat{R}(\tilde{\mathbf{u}}^d)$  is readily computed after obtaining an enhanced adjoint approximation  $\tilde{\mathbf{u}}^d$ , which is obtained by using the procedure described in Section 3.3 using  $\tilde{\mathbf{u}}^\mathcal{O}$  instead of  $\mathbf{u}^\mathcal{O}$ . This quantity is more meaningful than the previous one, but it requires, in general, computing several vibration modes ( $M > 1$ ) to properly capture  $\tilde{\mathbf{u}}^\mathcal{O}$  by the expansion of  $\tilde{\mathbf{q}}_i, i = 1, \dots, M$ .

4. ASSESSING TIMELINE-DEPENDENT QUANTITIES

The first part of this section extends concepts already introduced for scalar quantities, to timeline-dependent quantities. Second, an associated error estimate is introduced, based on the modal-based description of the adjoint solution.

4.1. Error representation and family of adjoint problems

Recall that, for a given time  $t \in I, s(t) = L_{TL}^\mathcal{O}(\mathbf{u}; t)$ . In that sense, for this particular value of  $t, s(t)$  is seen as a scalar quantity of interest, taking  $t$  as the *final* time. This scalar quantity of interest is characterized as  $L^\mathcal{O}(\cdot) = L_{TL}^\mathcal{O}(\cdot; t)$ . The associated adjoint problem is analogous to the one presented in 3.1 and reads as follows: find  $\mathbf{u}_t^d \in \mathcal{W}|_{[0,t]}$  such that

$$B_t(\mathbf{w}, \mathbf{u}_t^d) = L_{TL}^\mathcal{O}(\mathbf{w}; t) \quad \forall \mathbf{w} \in \mathcal{W}|_{[0,t]}. \tag{35}$$

Note that the solution of this problem is denoted by  $\mathbf{u}_t^d$  emphasizing that there is a different solution for each time  $T$ . Consequently, equation (35) describes a family of problems, one for each time  $T$ . The bilinear form in (35) is defined as

$$B_t(\mathbf{v}, \mathbf{w}) := \int_0^t (\rho(\ddot{\mathbf{v}}(\tau) + a_1 \dot{\mathbf{v}}(\tau)), \dot{\mathbf{w}}(\tau)) \, d\tau + \int_0^t a(\mathbf{v}(\tau) + a_2 \dot{\mathbf{v}}(\tau), \dot{\mathbf{w}}(\tau)) \, d\tau + (\rho \dot{\mathbf{v}}(0^+), \dot{\mathbf{w}}(0^+)) + a(\mathbf{v}(0^+), \mathbf{w}(0^+)),$$

and the space  $\mathcal{W}|_{[0,t]}$  denotes the restriction of  $\mathcal{W}$  to the time interval  $[0, t]$ . Analogously, as for the derivation of (13), the associated strong form of problem (35) is readily derived as

$$\rho(\ddot{\mathbf{u}}_t^d - a_1 \dot{\mathbf{u}}_t^d) - \nabla \cdot \boldsymbol{\sigma}_t^d = -\mathbf{f}^\mathcal{O} \quad \text{in } \Omega \times [0, t], \tag{36a}$$

$$\mathbf{u}_t^d = \mathbf{0} \quad \text{on } \Gamma_D \times [0, t], \tag{36b}$$

$$\boldsymbol{\sigma}_t^d \cdot \mathbf{n} = -\mathbf{g}^\mathcal{O} \quad \text{on } \Gamma_N \times [0, t], \tag{36c}$$

$$\mathbf{u}_t^d = \mathbf{u}^\mathcal{O} \quad \text{at } \Omega \times \{t\}, \tag{36d}$$

$$\dot{\mathbf{u}}_t^d = \mathbf{v}^\mathcal{O} \quad \text{at } \Omega \times \{t\}, \tag{36e}$$

with the constitutive law

$$\boldsymbol{\sigma}_t^d := \mathcal{C} : \boldsymbol{\varepsilon}(\mathbf{u}_t^d - a_2 \dot{\mathbf{u}}_t^d). \tag{37}$$

Recall that the data  $\mathbf{f}^\mathcal{O}, \mathbf{g}^\mathcal{O}, \mathbf{u}^\mathcal{O}$ , and  $\mathbf{v}^\mathcal{O}$  enters in the definition of  $L_{TL}^\mathcal{O}(\cdot; t)$  as indicated in (11). Note that for each time  $T$ , problem (36) is of the same type as (13) and therefore has to be integrated backwards in time. Thus, the family of adjoint problems associated with the timeline-dependent quantity  $L_{TL}^\mathcal{O}$  is a family of standard problems in elastodynamics.

For a particular instance of time  $t$ , the error representation of the timeline-dependent quantity of interest  $s^e(t)$  is similar to the standard scalar case but taking the adjoint solution  $\mathbf{u}_t^d$  related with the particular value  $t \in I$ , namely

$$s^e(t) = \hat{R}_t(\mathbf{u}_t^d), \tag{38}$$

where

$$\begin{aligned} \hat{R}_t(\mathbf{w}) &:= L_t(\mathbf{w}; t) - B_t(\hat{\mathbf{u}}, \mathbf{w}) \quad \text{and} \\ L_t(\mathbf{w}) &:= \int_0^t l(\tau; \dot{\mathbf{w}}(\tau)) \, d\tau + (\rho \mathbf{v}_0, \dot{\mathbf{w}}(0^+)) + a(\mathbf{u}_0, \mathbf{w}(0^+)). \end{aligned}$$

Hence, an estimate for  $s^e(t)$  is obtained by injecting an enhanced adjoint approximation  $\tilde{\mathbf{u}}_t^d$  in Equation (38)

$$s^e(t) \approx \hat{R}_t(\tilde{\mathbf{u}}_t^d). \tag{39}$$

Obviously, it is not possible in practice to independently compute the infinite solutions  $\tilde{\mathbf{u}}_t^d$  (one for each time  $t \in I$ ) and then using them in equation (38) to assess  $s^e(t)$ . However, taking  $\mathbf{f}^O$  and  $\mathbf{g}^O$  constant in time (which accounts for a number of interesting cases), the different functions  $\mathbf{u}_t^d$  corresponding to different time instances are all equivalent after a time translation. Thus, if  $\mathbf{u}_T^d$  is properly computed for a particular value of  $t$ , for instance  $t = T$ , the general functions  $\mathbf{u}_t^d$  for  $t \neq T$  are easily recovered as a direct post-process of  $\mathbf{u}_T^d$ . This fundamental result, shown in the following theorem, is the crucial observation that allows the error estimation technique to be brought to fruition.

*Theorem 1*

For a given  $T$ , let  $\mathbf{u}_T^d$  be the solution of the adjoint problem defined by equation (36). Assume that data  $\mathbf{f}^O$  and  $\mathbf{g}^O$  in (10) are constant in time, that is,  $\mathbf{f}^O(\mathbf{x}, t) = \mathbf{f}^O(\mathbf{x})$  and  $\mathbf{g}^O(\mathbf{x}, t) = \mathbf{g}^O(\mathbf{x})$ .

Then,  $\mathbf{u}_t^d$  is related with the adjoint solution associated with the final time  $T$ ,  $\mathbf{u}_T^d$ , via the time translation

$$\mathbf{u}_t^d(\tau) = \mathbf{u}_T^d(\tau + T - t). \tag{40}$$

*Proof*

Let  $\mathbf{u}_t^*(\tau) := \mathbf{u}_T^d(\tau + T - t)$ . Then, the proof of the theorem follows at once by showing that the solution  $\mathbf{u}_t^*(\tau)$  verifies (36).

Observe that the adjoint solution  $\mathbf{u}_T^d$  defined in (13) takes values in all the simulation period  $I = [0, T]$ . When restricting the time interval  $i$  to  $[T - t, T]$  for a particular  $t \in I$ , the restricted solution  $\mathbf{u}_T^d(s)$ ,  $s \in [T - t, T]$  verifies that

$$\begin{aligned} \rho(\ddot{\mathbf{u}}_T^d - a_1 \dot{\mathbf{u}}_T^d) - \nabla \cdot \boldsymbol{\sigma}_T^d &= -\mathbf{f}^O \quad \text{in } \Omega \times [T - t, T], \\ \mathbf{u}_T^d &= \mathbf{0} \quad \text{on } \Gamma_D \times [T - t, T], \\ \boldsymbol{\sigma}_T^d \cdot \mathbf{n} &= -\mathbf{g}^O \quad \text{on } \Gamma_N \times [T - t, T], \\ \mathbf{u}_T^d &= \mathbf{u}^O \quad \text{at } \Omega \times \{T\}, \\ \dot{\mathbf{u}}_T^d &= \mathbf{v}^O \quad \text{at } \Omega \times \{T\}, \end{aligned}$$

along with the constitutive law

$$\boldsymbol{\sigma}_T^d := \mathcal{C} : \boldsymbol{\varepsilon}(\mathbf{u}_T^d - a_2 \dot{\mathbf{u}}_T^d).$$

Applying the translation  $s = \tau + T - t$ , the restricted solution  $\mathbf{u}_T^d(s)$  defined in  $[T - t, T]$  transforms into  $\mathbf{u}_t^*(\tau) = \mathbf{u}_T^d(\tau + T - t)$  defined in  $[0, t]$  verifying

$$\rho(\ddot{\mathbf{u}}_t^* - a_1 \dot{\mathbf{u}}_t^*) - \nabla \cdot \boldsymbol{\sigma}_t^* = -\mathbf{f}^O(\tau - T + t) \quad \text{in } \Omega \times [0, t], \tag{41a}$$

$$\mathbf{u}_t^* = \mathbf{0} \quad \text{on } \Gamma_D \times [0, t], \tag{41b}$$

$$\boldsymbol{\sigma}_t^* \cdot \mathbf{n} = -\mathbf{g}^O(\tau - T + t) \quad \text{on } \Gamma_N \times [0, t], \tag{41c}$$

$$\mathbf{u}_t^* = \mathbf{u}^O \quad \text{at } \Omega \times \{t\}, \tag{41d}$$

$$\dot{\mathbf{u}}_t^* = \mathbf{v}^O \quad \text{at } \Omega \times \{t\}, \tag{41e}$$

with the constitutive law

$$\boldsymbol{\sigma}_t^* := \mathcal{C} : \boldsymbol{\varepsilon}(\mathbf{u}_t^* - a_2 \dot{\mathbf{u}}_t^*).$$

Note that, equations (36) and (41) are identical except for the external loads. Thus, the result follows from the assumption that the loads  $\mathbf{f}^O$  and  $\mathbf{g}^O$  are constant in time.  $\square$

Theorem (1) allows to efficiently recover the family of enhanced approximations  $\tilde{\mathbf{u}}_T^d$  from the enhanced approximation  $\tilde{\mathbf{u}}_T^d$  as

$$\tilde{\mathbf{u}}_t^d(\tau) = \tilde{\mathbf{u}}_T^d(\tau + T - t). \tag{42}$$

Consequently, the approximation  $\tilde{\mathbf{u}}_T^d$  is the base for assessing the error both in the scalar and timeline-dependent quantities, providing in the latter case more meaningful information. The translation (42) is performed very efficiently by means of the modal description of  $\tilde{\mathbf{u}}_T^d$ :

$$\tilde{\mathbf{u}}_t^d(\tau) = \sum_{i=1}^M \tilde{\mathbf{q}}_i \tilde{y}_i(\tau + T - t). \tag{43}$$

Recall that, functions  $\tilde{y}_i$  may be known analytically in many cases, and therefore, computing the translation  $\tilde{y}_i(\tau + T - t)$  is inexpensive in that case.

4.2. Error estimates for timeline-dependent quantities of interest: algorithmic details

The methodology proposed here aims at assessing the error in the timeline-dependent quantity  $s^e(t)$  at the computational times  $\mathcal{T} = \{t_0, \dots, t_N\}$  introduced earlier. Thus, the resulting estimates are  $\tilde{s}_j^e \approx s^e(t_j)$  for  $j = 0, \dots, N$ . This option could be generalized without any additional conceptual difficulty to use a different set of points  $\tilde{t}_0, \dots, \tilde{t}_{\tilde{N}}$ .

Once the recovered solution of the adjoint problem corresponding to  $t_j$ ,  $\tilde{\mathbf{u}}_{t_j}^d$ , is available, the estimate  $\tilde{s}_j^e$  is computed following equation (39)

$$\tilde{s}_j^e := \hat{R}_{t_j}(\tilde{\mathbf{u}}_{t_j}^d) \quad \text{for } j = 0, \dots, N.$$

The previous equation is rewritten by using the modal description (43) as

$$\tilde{s}_j^e = \sum_{i=1}^M \left[ \int_0^{t_j} \hat{r}(\tau; \tilde{\mathbf{q}}_i) \dot{\tilde{y}}_i(\tau + T - t_j) \, d\tau + \hat{r}_{0,v}(\tilde{\mathbf{q}}_i) \dot{\tilde{y}}_i(T - t_j) + \hat{r}_{0,u}(\tilde{\mathbf{q}}_i) \tilde{y}_i(T - t_j) \right], \tag{44}$$

where

$$\hat{r}(\tau; \tilde{\mathbf{q}}_i) := l(\tau; \tilde{\mathbf{q}}_i) - \left( \rho(\ddot{\tilde{\mathbf{u}}}(\tau) + a_1 \dot{\tilde{\mathbf{u}}}(\tau)), \tilde{\mathbf{q}}_i \right) - a \left( \hat{\mathbf{u}}(\tau) + a_2 \dot{\hat{\mathbf{u}}}(\tau), \tilde{\mathbf{q}}_i \right), \tag{45a}$$

$$\hat{r}_{0,u}(\tilde{\mathbf{q}}_i) := a \left( \mathbf{u}_0 - \Pi^H \mathbf{u}_0, \tilde{\mathbf{q}}_i \right), \tag{45b}$$

$$\hat{r}_{0,v}(\tilde{\mathbf{q}}_i) := \left( \rho(\mathbf{v}_0 - \Pi^H \mathbf{v}_0), \tilde{\mathbf{q}}_i \right). \tag{45c}$$

Expressions (44) and (45) describe the proposed error estimate. Note that the quantities  $\hat{r}_{0,u}$  and  $\hat{r}_{0,v}$  introduced in (45b) and (45c) are independent of the selected time  $t_j$  and also of  $\tau$ . Thus, these two quantities are computed just once for each mode  $\tilde{\mathbf{q}}_i$ , independently of the number of sampling points selected,  $N$ , and the number of time-integration points used to compute the expression in (44). The quantity  $\hat{r}$  in (45a) depends on  $\tau$  but not on  $t_j$  and therefore has to be evaluated once for each mode  $\tilde{\mathbf{q}}_i$  and for each integration point of the time quadrature to integrate the expression (44). This suggests taking the same time-integration points for each sampling time  $t_j$  (but using only those previous to  $t_j$ ). The option adopted here is to use a composed Gauss quadrature based on the Newmark time partition. With this choice, the estimate  $\tilde{s}_j^e$  is computed as the sum of contributions of the initial conditions and the time steps

$$\tilde{s}_j^e = \sum_{n=0}^N \tilde{s}_{j,n}^e \quad \text{for } j = 0, \dots, N,$$

where  $\tilde{s}_{j,0}^e$  is defined as

$$\tilde{s}_{j,0}^e := \sum_{i=1}^M \left[ \hat{r}_{0,v}(\tilde{\mathbf{q}}_i) \dot{y}_i(T - t_j) + \hat{r}_{0,u}(\tilde{\mathbf{q}}_i) \tilde{y}_i(T - t_j) \right],$$

and  $\tilde{s}_{j,n}^e$  is defined for  $n \neq 0$  as

$$\tilde{s}_{j,n}^e := \begin{cases} \sum_{i=1}^M \int_{t_{n-1}}^{t_n} \hat{r}(\tau; \tilde{\mathbf{q}}_i) \dot{y}_i(\tau + T - t_j) d\tau & \text{if } t_j > t_{n-1}, \\ 0 & \text{otherwise.} \end{cases}$$

The algorithm providing the admissible approximation  $\hat{\mathbf{u}}$  and the estimates  $\tilde{s}_j^e$ ,  $j = 0, \dots, N$ , is detailed in algorithm 1.

### 5. NUMERICAL EXAMPLES

This section presents the performance of the error estimates both for the scalar and timeline-dependent quantities of interest in three numerical examples.

All the examples are plane stress problems that are approximated in space by using linear ( $p = 1$ ) triangles and in time by using the Newmark method with parameters  $\beta = 1/4$  and  $\gamma = 1/2$ . The Newmark method is unconditionally stable for this particular choice of  $\beta$  and  $\gamma$ . Therefore, no stability restrictions have to be imposed to the time step length  $\Delta t$ .

#### 5.1. Example 1

This example illustrates the performance of the proposed error estimates in a 2D wave propagation problem. The problem definition is taken from [45] where it is used to test an error estimate providing error bounds in quantities of interest.

The problem geometry is the rectangular plate sketched in Figure 3(a). The plate is initially at rest ( $\mathbf{u}_0 = \mathbf{v}_0 = \mathbf{0}$ ) and loaded with the time dependent traction

$$\mathbf{g} = \begin{cases} -g(t)\mathbf{e}_2 & \text{on } \Gamma_g, \\ 0 & \text{elsewhere,} \end{cases} \quad (46)$$

where  $\mathbf{e}_2 := (0, 1)$  and  $g(t)$  is the impulsive time-dependent function defined in Figure 3(b) with parameters  $g_{\max} = 30$  Pa and  $t_g = 0.005$  s. No body force is acting in this example ( $\mathbf{f} = \mathbf{0}$ ).

Table I details the geometrical parameters and material data, where  $E$  and  $\nu$  are the Young's modulus and Poisson's ratio, respectively, and the parameter  $\xi$  is the dimensionless damping factor. In the examples included here, we take  $a_1 = 0$ , and its corresponding value is  $\xi := \frac{1}{2}\omega_1 a_2$ , see [42, 45]. Three different values of the viscosity parameter  $a_2$  are considered. The solution of the

```

Data: Problem geometry  $(\Omega, \Gamma_N, \Gamma_D)$ , final time  $(T)$ , material data  $(E, \nu, \rho)$ , loads and initial
        conditions  $(\mathbf{f}, \mathbf{g}, \mathbf{u}_0, \mathbf{v}_0)$ , computational mesh  $(\mathcal{V}_0^H)$ , time partition  $(\mathcal{T})$ , data defining
        the timeline quantity of interest  $(\mathbf{f}^\mathcal{O}, \mathbf{g}^\mathcal{O}, \mathbf{u}^\mathcal{O}, \mathbf{v}^\mathcal{O})$  and number of vibration modes  $M$ .
Result: Admissible solution  $\hat{\mathbf{u}}$  and timeline error estimates  $\tilde{s}_j^e, j = 0, \dots, N$ .
// Modal analysis
Compute the eigenpairs  $(\omega_i^H, \mathbf{q}_i^H)$  and post-process them into  $(\tilde{\omega}_i, \tilde{\mathbf{q}}_i), i = 1, \dots, M$ ;
// Adjoint problem
Compute the values  $\tilde{l}_i, \tilde{u}_i, \tilde{v}_i$  (using  $\mathbf{f}^\mathcal{O}, \mathbf{g}^\mathcal{O}, \mathbf{u}^\mathcal{O}, \mathbf{v}^\mathcal{O}$  and  $\tilde{\mathbf{q}}_i, i = 1, \dots, M$ );
Compute the time dependent functions  $\tilde{y}_i(t)$  (using  $\tilde{l}_i, \tilde{u}_i, \tilde{v}_i$  and  $\tilde{\omega}_i, i = 1, \dots, M$ );
// Initialize computation
Initialize Newmark solution  $\mathbf{u}_0^{H,\Delta t} = \mathbf{\Pi}^H \mathbf{u}_0, \mathbf{v}_0^{H,\Delta t} = \mathbf{\Pi}^H \mathbf{v}_0$ ;
Initialize admissible solution  $\hat{\mathbf{u}}(0) = \mathbf{u}_0^{H,\Delta t}, \dot{\hat{\mathbf{u}}}(0) = \mathbf{v}_0^{H,\Delta t}$ ;
Initialize estimate  $\tilde{s}_j^e = \tilde{s}_{j,0}^e, j = 0, \dots, N$ ;
// Time stepping
for  $n = 1 \dots N$  do
    // Compute solution
    Compute Newmark solution  $\mathbf{u}_n^{H,\Delta t}, \mathbf{v}_n^{H,\Delta t}, \mathbf{a}_n^{H,\Delta t}$ ;
    Compute the admissible solution  $\hat{\mathbf{u}}$  in the time interval  $[t_{n-1}, t_n]$ ;
    // Error assessment
    Compute contributions to the estimates  $\tilde{s}_j^e = \tilde{s}_j^e + \tilde{s}_{j,n}^e, j = n, \dots, N$ 
    (using the admissible solution  $\hat{\mathbf{u}}$  and the modal based description of the adjoint  $\tilde{\mathbf{q}}_i$  and  $\tilde{y}_i$ );
end
    
```

**Algorithm 1:** Algorithm for problem approximation and error assessment.

problem consists of elastic waves propagating along the plate, see [45] for a qualitative description of the solution.

In a first phase, the error estimate is analyzed for the scalar quantity of interest

$$s_T := (\rho \mathbf{q}_1, \dot{\mathbf{u}}(T)). \tag{47}$$

This quantity is a particular case of the quantities represented by the functional  $L_1^\mathcal{O}$  presented in Section 3.4. The quantity  $s_T$  is associated with the *exact* first eigenvector of the generalized eigenvalue problem (26), which is unknown. In the following, function  $\mathbf{q}_1$  is replaced by a reference eigenvector  $\mathbf{q}_1^{H,p+1}$  solution of the eigenvalue problem (26) in the discrete space  $\mathcal{V}_0^{H,p+1}$ . The space  $\mathcal{V}_0^{H,p+1}$

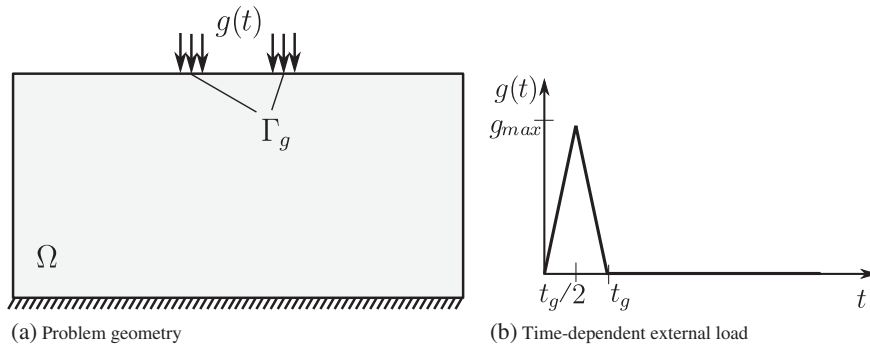


Figure 3. Example 1: Problem statement. (a) Problem geometry; (b) Time-dependent external load.

Table I. Example 1: Problem parameterization.

Geometry			Material properties		
$\Omega$	$(-0.5, 0.5) \times (0, 0.5)$	$\text{m}^2$	$E$	8/3	Pa
$\Gamma_g$	$[(0.075, 0.125) \cup (-0.075, -0.125)] \times (0.5)$	m	$\nu$	1/3	
$T$	0.25	s	$\rho$	1	$\text{kg/m}^3$
			$a_1$	0	s
			$a_2$	$\{0, 10^{-4}, 10^{-2}\}$	s
			$\xi$	$\{0, 0.0247, 2.47\}$	%

Table II. Example 1: Space and time discretizations.

Mesh id.	$N_{\text{nod}}$	# Elements	Type	$H$ [m]
1	3051	5899	Triangle	$3.2 \cdot 10^{-3}$
2	12000	23596	Triangle	$1.6 \cdot 10^{-3}$
3	47595	94384	Triangle	$7.9 \cdot 10^{-4}$

Time step id.	# steps	$\Delta t$ [s]
1	100	$2.5 \cdot 10^{-3}$
2	200	$1.3 \cdot 10^{-3}$
3	400	$6.2 \cdot 10^{-4}$
4	800	$3.1 \cdot 10^{-4}$

is obtained, increasing by one the interpolation order of  $\mathcal{V}_0^H$ . To have a reference error to assess the effectivity of the presented error estimation approach, the *exact* solution  $\mathbf{u}$  (which is also unknown) is replaced by an admissible reference solution computed by using the space  $\mathcal{V}_0^{H,p+1}$  and a time step length  $\Delta t/2$ . Note that the proposed approximations to  $\mathbf{u}$  and  $\mathbf{q}_1$  are discretization-dependent.

The numerical solution of the problem  $\hat{\mathbf{u}}$  is computed for three different meshes and four time step lengths. Table II contains detailed information on both the space and time discretizations. The element size  $H$  appearing in Table II is defined as the size of the smallest triangular element, where the size of a triangular element is taken as the diameter of its inscribed circle. The coarsest mesh (referred as mesh id. 1) is plotted in Figure 4. Note that only half of the computational domain  $\Omega$  is discretized by introducing suitable symmetry conditions.

Each computational mesh provides the approximation to the quantity of interest

$$\hat{s}_T = (\rho \mathbf{q}_1, \hat{\mathbf{u}}(T)). \tag{48}$$

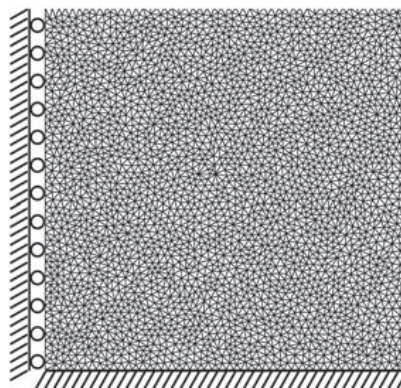


Figure 4. Example 1: Computational domain and coarsest computational mesh.

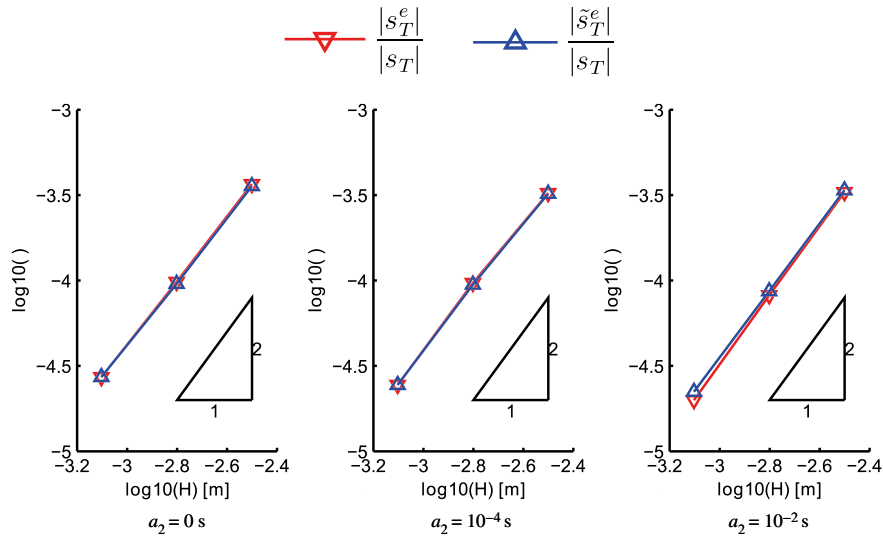


Figure 5. Example 1: Evolution of the relative error along a uniform  $H$  refinement process, for three values of the viscosity parameter  $a_2$ . Exact (reference) values described by the red triangles pointing downwards and estimated values described by the blue triangles pointing upwards. The results are computed with a constant time step length  $\Delta t = 6.2 \cdot 10^{-4}$  s.

The error  $s_T^e = s_T - \hat{s}_T$  is computed by using the reference value for  $s_T$  previously defined. On the other hand, the estimate  $\tilde{s}_T^e$  is computed following Section 3.4. Note that for the quantity of interest introduced in (47), only one vibration mode ( $M = 1$ ) is required to build the enhanced adjoint approximation  $\hat{\mathbf{u}}^d$ .

Figures 5 and 6 show the space and time convergence of the errors  $s_T^e$  and  $\tilde{s}_T^e$  for the three different values of the damping parameter  $a_2$  given in Table I. The space convergence curves are obtained, keeping constant the time step length,  $\Delta t = 6.2 \cdot 10^{-4}$  s, whereas the time convergence curves are obtained, keeping constant the space discretization, that is, using meshes id. 1 and 3, respectively.

Figure 5 shows that the estimate  $\tilde{s}_T^e$  is in very good agreement with the reference value  $s_T^e$ . The optimal convergence rate for quantities of interest is two times the rate for the energy norm. That is, the error in the quantity of interest converges as  $\mathcal{O}(H^2)$ , see [59]. Note that the optimal space convergence rate is achieved both for  $\tilde{s}_T^e$  and  $s_T^e$ .

Note in Figure 6 that the time convergence plots rapidly converge to a constant value, which is the committed space discretization error. Thus, the time discretization errors of  $\tilde{s}_T^e$  and  $s_T^e$  are very small when compared with the space discretization errors. Even for the coarser mesh, the reduction of the time step does not vary the accuracy of the approximations.

Figures 5 and 6 show that the effectivities of the estimate  $\tilde{s}_T^e$  is qualitatively the same for all the values of the damping parameter  $a_2$ , even in the limit case  $a_2 = 0$ . Thus, the presented technique is robust with respect to the damping parameter. Recall that the same behavior is not observed when dealing with error estimation techniques providing error bounds whose effectivities degenerate as the amount of damping tends to zero, see [41–45]. In fact, existing techniques providing error bounds in energy norms or in quantities of interest can not even deal with the case  $a_2 = 0$ .

A related timeline-dependent quantity is considered also for this example,

$$s(t) = (\rho \mathbf{q}_1, \dot{\mathbf{u}}(t)).$$

Figure 7 shows the reference and approximated timeline quantities  $s(t)$  and  $\hat{s}(t) := (\rho \mathbf{q}_1, \dot{\hat{\mathbf{u}}}(t))$  and the reference and estimated errors  $s^e(t)$  and  $\hat{s}^e(t)$  for mesh id. 1 and time step id. 3, see Table II. As in the scalar case, the proposed estimate  $\tilde{s}^e(t)$  is really close to the reference value  $s^e(t)$  in all cases, also for  $a_2 = 0$ . It can be observed that, in this example, the quantity of interest associated to the

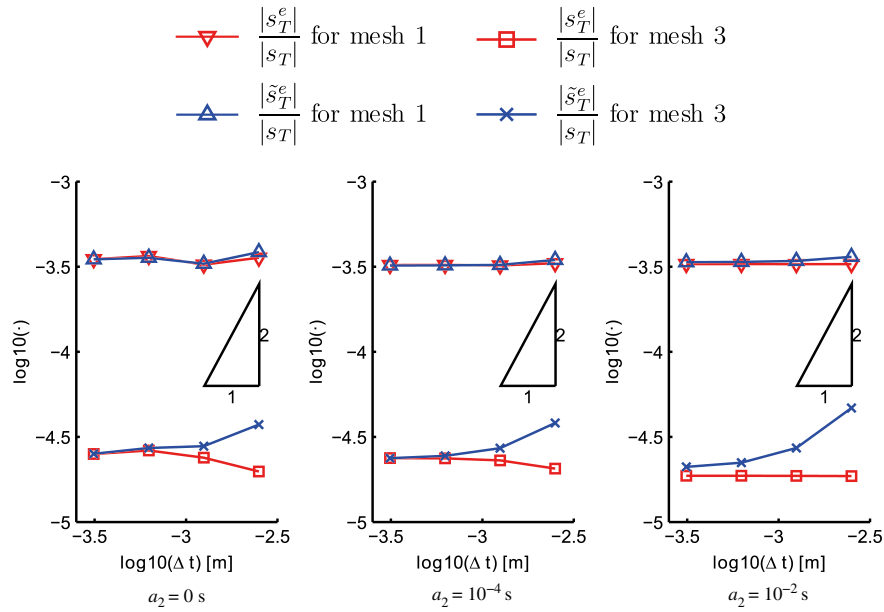


Figure 6. Example 1: Evolution of the relative error along a uniform  $\Delta t$  refinement process, for three values of the viscosity parameter  $a_2$ . Exact (reference) values described by the red triangles pointing downwards (mesh 1) and squares (mesh 3) and estimated values described by the blue triangles pointing upwards (mesh 1) and crosses (mesh 3).

lowest eigenvector  $\mathbf{q}_1$  is nearly unaffected by the change in the damping coefficient  $a_2$ . However, the time-dependent errors  $s^e(t)$  and its approximations  $\tilde{s}^e(t)$  are smoothed out as the coefficient  $a_2$  increases.

5.2. Example 2

Consider the structure given in Figure 8(a). The structure is initially at rest ( $\mathbf{u}_0 = \mathbf{v}_0 = \mathbf{0}$ ), clamped at the supports, and subjected to the time-dependent traction

$$\mathbf{g} = \begin{cases} g(t)\mathbf{e}_1 & \text{on } \Gamma_g, \\ 0 & \text{elsewhere.} \end{cases}$$

The set  $\Gamma_g$  is the region of the Neumann boundary where the load is applied,  $\mathbf{e}_1 := (1, 0)$  is the first cartesian unit vector, and function  $g(t)$  describes the time evolution of  $\mathbf{g}$  given in Figure 8(b). The traction  $\mathbf{g}$  is the only external loading in this example (that is  $\mathbf{f} = \mathbf{0}$ ). Other material and geometric parameters univocally defining the problem are reported in Table III.

Consider the scalar quantities of interest

$$s_{u,T} := (\boldsymbol{\lambda}_N^\mathcal{O}, \mathbf{u}(T))_{\Gamma_g} \text{ and } s_{v,T} := (\rho\mathbf{q}_1, \dot{\mathbf{u}}(T)),$$

where  $\boldsymbol{\lambda}_N^\mathcal{O} := \mathbf{e}_1/\text{meas}(\Gamma_g)$ . The quantity  $s_{u,T}$  is an average of the horizontal displacements at the Neumann boundary  $\Gamma_g$ . Note that  $s_{u,T}$  is a particular case of the quantities represented by the functional  $L_2^\mathcal{O}(\cdot)$  introduced in Section 3.4. On the other hand,  $s_{v,T}$  is a weighted average of the velocities, and it is a particular case of the quantities represented by  $L_1^\mathcal{O}(\cdot)$ , also introduced in Section 3.4. The unknown values  $s_{u,T}$  and  $s_{v,T}$  are approximated in this example with an *overkill* discretization

$$s_{u,T} = (\boldsymbol{\lambda}_N^\mathcal{O}, \mathbf{u}^{\text{ovk}}(T))_{\Gamma_g} \text{ and } s_{v,T} = (\rho\mathbf{q}_1^{\text{ovk}}, \dot{\mathbf{u}}^{\text{ovk}}(T)),$$

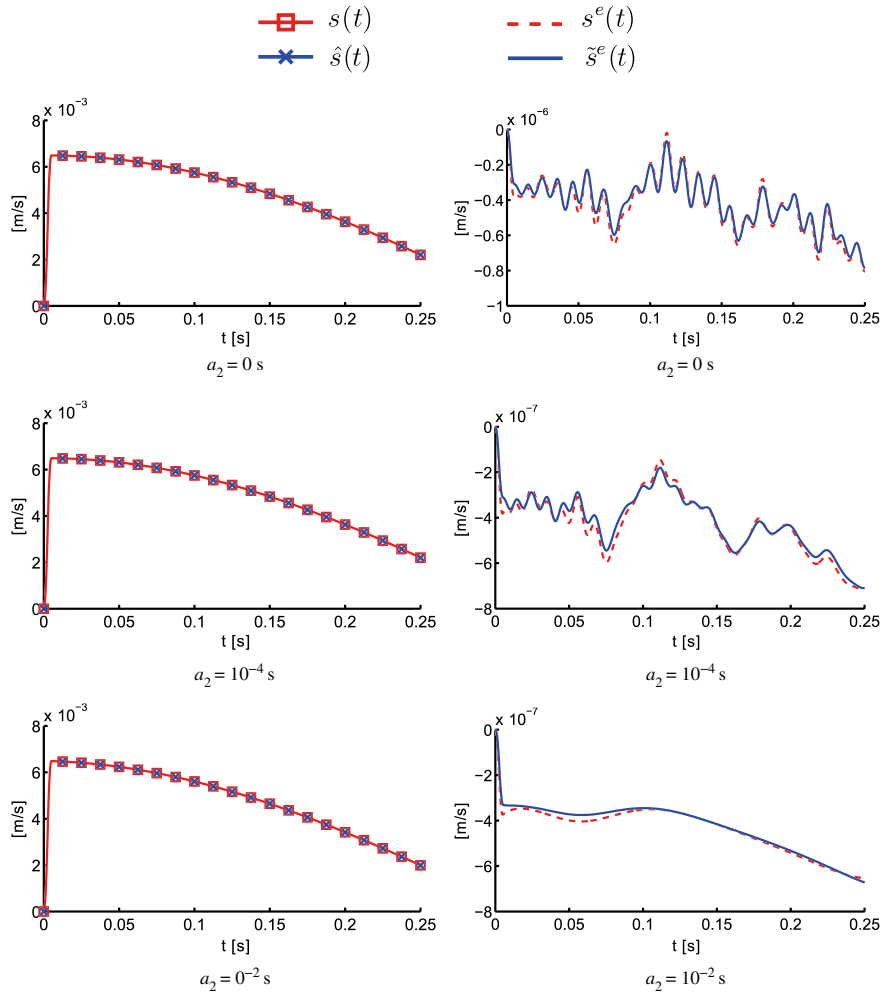


Figure 7. Example 1: Approximated and reference timeline-dependent quantity (left) and estimated and reference errors in the timeline-dependent quantity (right) for the three values of the damping parameter  $a_2$  ( $a_2 = 0$  s, top;  $a_2 = 10^{-2}$  s, center;  $a_2 = 10^{-4}$  s, bottom).

where the superscript  $()^{\text{ovk}}$  refers to functions computed with the overkill discretization. The parameters of the overkill discretization are given in Table IV. Note that only one overkill discretization is considered in this example, which does not depend on the selected  $H$ -mesh.

The space and time discretizations used in this example are shown in Table IV. The particular combinations of space–time discretizations that are actually taken into account are represented in Figure 9. The same figure shows the coarsest finite element mesh (mesh id. 1). The other meshes are obtained as nested subdivisions of the coarser one.

The space–time discretization of the problem provides the approximation  $\hat{s}_{u,T} = (\lambda_N^{\mathcal{O}}, \hat{\mathbf{u}}(T))_{\Gamma_g}$  and  $\hat{s}_{v,T} = (\rho \mathbf{q}_1^H, \hat{\mathbf{u}}(T))$  to the exact quantities of interest  $s_{u,T}$  and  $s_{v,T}$ , respectively. Note that the approximation  $\hat{s}_{v,T}$  is computed by using the discrete eigenvector  $\mathbf{q}_1^H$  instead of the exact one  $\mathbf{q}_1$  (approached by  $\mathbf{q}_1^{\text{ovk}}$ ). The reason is that  $(\rho \mathbf{q}_1^H, \hat{\mathbf{u}}(T))$  provides a very good approximation to  $(\rho \mathbf{q}_1^{\text{ovk}}, \hat{\mathbf{u}}(T))$  in this example.

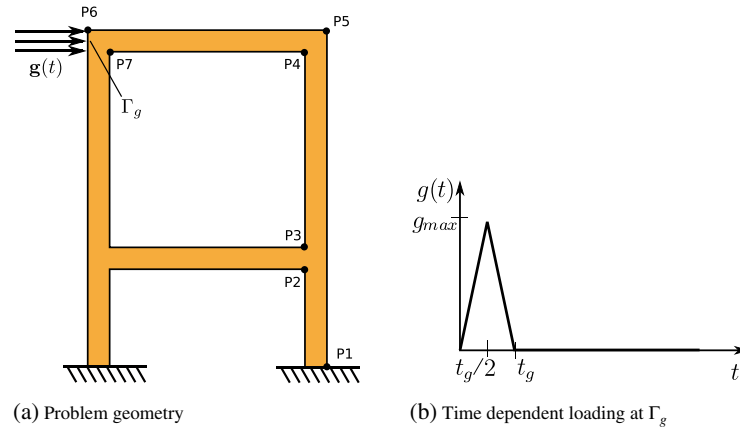


Figure 8. Example 2: Problem statement.

Table III. Example 2: Problem parameterization.

Geometry (data in m)	Physical properties
$P_1 := (0.55, 0.00)$	$E = 2 \cdot 10^{11}$ Pa
$P_2 := (0.45, 0.45)$	$\nu = 0.2$
$P_3 := (0.45, 0.55)$	$\rho = 8 \cdot 10^3$ kg/m <sup>3</sup>
$P_4 := (0.45, 1.45)$	$a_1 = 0$ s
$P_5 := (0.55, 1.55)$	$a_2 \in \{0, 1 \cdot 10^{-4}, 1 \cdot 10^{-3}\}$ s
$P_6 := (-0.55, 1.55)$	$\xi \in \{0, 1.75, 17.6\}$ %
$P_7 := (-0.45, 1.45)$	$T = 2 \cdot 10^{-3}$ s
$\Gamma_g := \{-0.55\} \times (1.45, 1.55)$	External load
	$g_{\max} = 10^8$ Pa
	$t_g = 2 \cdot 10^{-4}$ s

Table IV. Example 2: Space and time discretizations.

Mesh id.	$N_{\text{dof}}$	# Elements	Type	$p$	$H$ [m]
1	3394	2902	Triangle	1	$7.41 \cdot 10^{-3}$
2	12592	11608	Triangle	1	$3.71 \cdot 10^{-3}$
3	48400	46432	Triangle	1	$1.85 \cdot 10^{-3}$
ovk.	189664	185744	Triangle	1	$9.26 \cdot 10^{-4}$
Time step id.		# steps	$\Delta t$ [s]		
	1	100	$2.00 \cdot 10^{-5}$		
	2	200	$1.00 \cdot 10^{-5}$		
	3	400	$5.00 \cdot 10^{-6}$		
	4	800	$2.50 \cdot 10^{-6}$		
	ovk.	3200	$6.25 \cdot 10^{-7}$		

The estimates  $\tilde{s}_{u,T}^e \approx s_{u,T}^e := s_{u,T} - \hat{s}_{u,T}$  and  $\tilde{s}_{v,T}^e \approx s_{v,T}^e := s_{v,T} - \hat{s}_{v,T}$  are computed following the strategy of Section 3. As mentioned in Section 3.4, the computation of the displacement estimate  $\tilde{s}_{u,T}^e$ , requires introducing the auxiliary linear elasticity problem

$$a(\mathbf{u}^\circ, \mathbf{w}) = (\boldsymbol{\lambda}_N^\circ, \mathbf{w})_{\Gamma_g} \quad \forall \mathbf{v} \in \mathcal{V}_0, \quad (49)$$

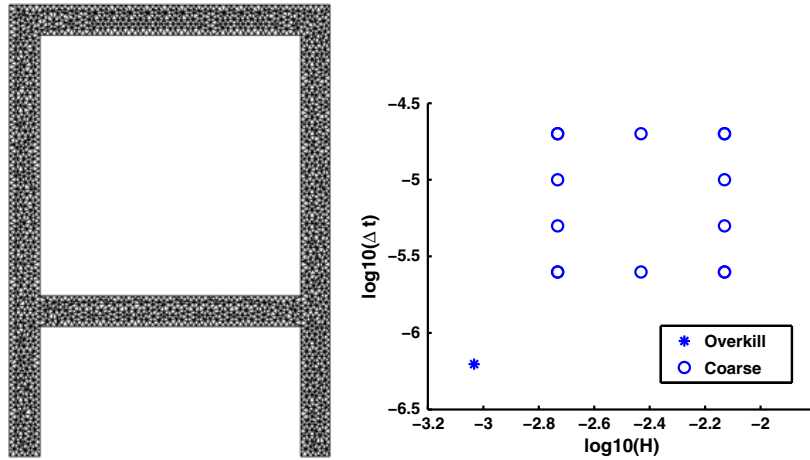


Figure 9. Example 2: Coarsest finite element mesh used in this example (left). Element sizes and time step lengths used in the example (right).

which allows rewriting the quantity  $s_{u,T}$  as

$$s_{u,T} = a(\mathbf{u}^{\mathcal{O}}, \hat{\mathbf{u}}(T)).$$

Recall that, computing the enhanced adjoint solution  $\tilde{\mathbf{u}}^d$  for this quantity requires finding the values  $\tilde{u}_i, i = 1, \dots, M$  such that

$$\mathbf{u}^{\mathcal{O}} \approx \sum_{i=1}^M \tilde{u}_i \tilde{\mathbf{q}}_i.$$

Because  $\mathbf{u}^{\mathcal{O}}$  is not available, it is replaced by an enhanced field  $\tilde{\mathbf{u}}^{\mathcal{O}}$  obtained by post-processing  $\mathbf{u}^{\mathcal{O},H}$ , the finite element approximation of the elasticity problem (49), by using the technique explained in Section 3.3. The values  $\tilde{u}_i$  are computed by using three different strategies. The first one is to recover the coefficients  $\tilde{u}_i^1$  by using the least squares technique described in remark 5. The second assumes that the recovered eigenvectors are orthonormal and recovers the coefficients as  $\tilde{u}_i^2 = (\rho \tilde{\mathbf{u}}^{\mathcal{O}}, \tilde{\mathbf{q}}_i)$ . Finally, the third strategy uses the original orthonormal eigenvectors  $\mathbf{q}_i^H$ ,  $\tilde{u}_i^3 = (\rho \mathbf{u}^{\mathcal{O},H}, \tilde{\mathbf{q}}_i^H)$ . Figure 10 shows that the least squares technique allows to properly recover the extractor  $\tilde{\mathbf{u}}^{\mathcal{O}}$  by increasing the number of modes  $M$  in the decomposition. The two cheaper alternatives (2 and 3) behave very differently. Assuming that the recovered eigenvectors behave like an orthonormal basis, provide non-converging approximations to the extractor  $\tilde{\mathbf{u}}^{\mathcal{O}}$ . Strategies 1 and 3 provide very close results. The third strategy is considered in this example to compute the values  $\tilde{u}_i$ . The default number of vibration modes used to compute the estimate  $\tilde{s}_{u,T}^e$  in this example is  $M = 60$ .

Figures 11 and 12 show the convergence of the computed estimates  $\tilde{s}_{u,T}^e$  and  $\tilde{s}_{v,T}^e$  and of the overkill errors  $s_{u,T}^e$  and  $s_{v,T}^e$  with respect to the space and time discretizations, respectively, for two different values of the damping parameter  $a_2$ . The space convergence curves are obtained, keeping the time discretization constant, whereas the time convergence plots are obtained, keeping the space discretization constant.

Figure 11 shows that the errors  $\tilde{s}_{v,T}^e$  and  $s_{v,T}^e$  converge at the optimal space convergence rate. On the other hand, the errors  $\tilde{s}_{u,T}^e$  and  $s_{u,T}^e$  converge at the optimal rate for all cases except one ( $a_2 = 0$  s and  $\Delta t = 2.00 \cdot 10^{-5}$  s). In this case, the time discretization error is dominant with respect to the spatial error, and thus refining the spatial mesh does not yield any gain in accuracy. In the other cases, the space integration error is dominant and therefore the optimal space convergence is achieved.

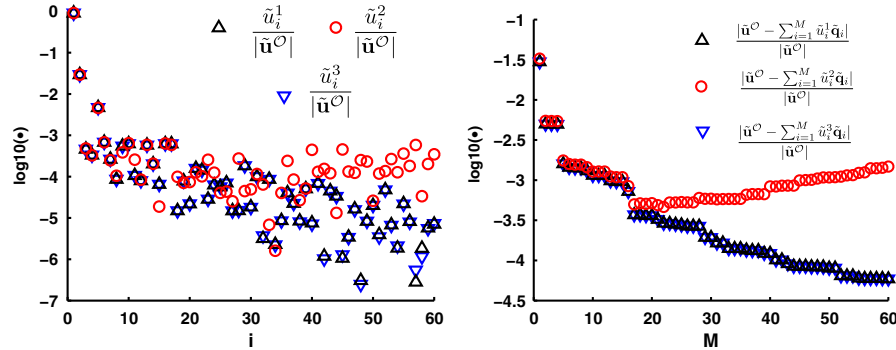


Figure 10. Example 2: Comparison of three different strategies providing the values  $\tilde{u}_i$ ,  $i = 1, \dots, M$  (left). Convergence of the three different representations of the extractor  $\tilde{\mathbf{u}}^O$  in the recovered eigenvector basis  $\{\tilde{\mathbf{q}}_i\}_{i=1, \dots, M}$  (right).

Figure 12 shows that the optimal time convergence rate is achieved for the values  $\tilde{s}_{u,T}^e$  and  $s_{u,T}^e$  computed with  $H = 7.4 \cdot 10^{-3}$  m and  $a_2 = 0$ . That is the only case where the time discretization errors are dominant. In the other cases, the space discretization error is dominant and therefore the time convergence stagnates to a constant value.

Consequently, Figures 11 and 12 show that the estimates  $\tilde{s}_{u,T}^e$  and  $\tilde{s}_{v,T}^e$  properly assess the error associated with both the spatial and time discretizations.

Table V shows the effectivities of the estimates shown in Figures 11 and 12. Note that the effectivities for the estimate  $\tilde{s}_{v,T}^e$  are better than for  $\tilde{s}_{u,T}^e$ . That is because  $\tilde{s}_{u,T}^e$  has a truncation error associated with the number of vibration modes  $M$ , whereas  $\tilde{s}_{v,T}^e$  only requires one vibration mode ( $M = 1$ ) and therefore has no truncation error. The effectivities for the estimate  $\tilde{s}_{u,T}^e$  are better for the high values of the viscosity parameter  $a_2$ . That is because when the viscosity is high, the high frequencies of the problem are damped, and therefore the truncation error associated with  $M$  becomes less relevant. However, the estimates  $\tilde{s}_{u,T}^e$  and  $\tilde{s}_{v,T}^e$  give accurate error approximations regardless of the amount of damping. This is a major difference with respect to the estimates [42, 45] furnishing bounds of the error that are only applicable for a non-zero amount of dissipation and that strongly degenerate as the dissipation vanishes.

To analyze the recovery procedure for the vibration modes, the effectivity of the post-processed pair  $(\tilde{\omega}_i, \tilde{\mathbf{q}}_i)$  is assessed comparing them with the pair  $(\omega_i^{H,p+1}, \mathbf{q}_i^{H,p+1})$  solution of the eigenvalue problem (20) in the space  $\mathcal{V}_0^{H,p+1}$ . The effectivity of the finite element and enhanced eigenmodes are quantified by the indicators

$$\eta_i = \frac{\omega_i^H}{\omega_i^{H,p+1}} \quad \text{and} \quad \tilde{\eta}_i = \frac{\tilde{\omega}_i}{\omega_i^{H,p+1}}.$$

Table VI shows the computed eigenvalues in the coarse mesh  $\omega_i^H$ , the recovered  $\tilde{\omega}_i$  and the reference ones  $\omega_i^{H,p+1}$ , along with the computed effectivities  $\eta_i$  and  $\tilde{\eta}_i$  for several eigemodes. Note that the recovered eigenpairs are in very good agreement with the reference values. Thus, the use of the simple and cheap recovery procedure allows considerably improving the accuracy of the discrete eigenvalues  $\omega_i^H$ .

Consider now the timeline-dependent quantities associated with  $s_{u,T}$  and  $s_{v,T}$ , namely

$$s_u(t) = (\boldsymbol{\lambda}_N^O, \mathbf{u}(t))_{\Gamma_g} \quad \text{and} \quad s_v(t) = (\rho \mathbf{q}_1, \dot{\mathbf{u}}(t)).$$

The problem discretization provides the approximations

$$\hat{s}_u(t) = (\boldsymbol{\lambda}_N^O, \hat{\mathbf{u}}(t))_{\Gamma_g} \quad \text{and} \quad \hat{s}_v(t) = (\rho \mathbf{q}_1^H, \hat{\dot{\mathbf{u}}}(t)).$$

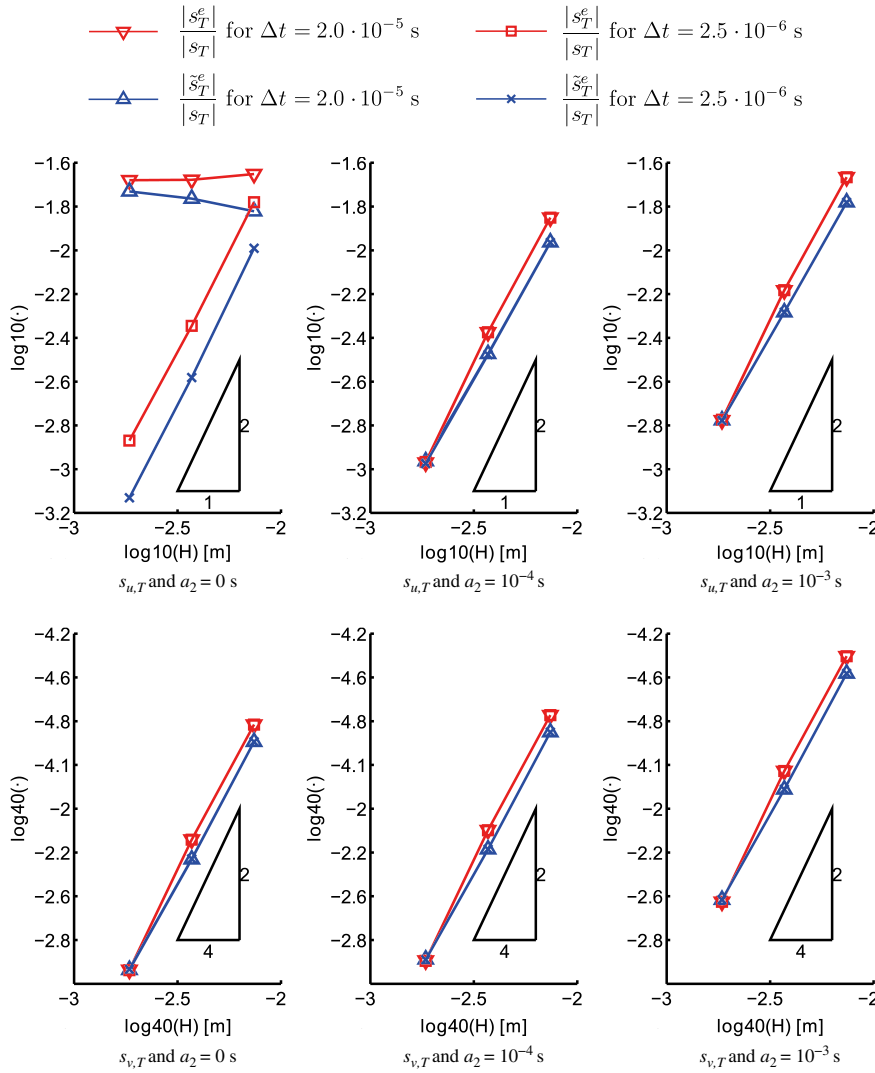


Figure 11. Example 2: Evolution of the relative error along a uniform  $H$  refinement process, for three values of the viscosity parameter  $a_2$ . Exact (overkill) values described by the red triangles pointing downwards ( $\Delta t = 2.0 \cdot 10^{-5}$  s) and red squares ( $\Delta t = 2.5 \cdot 10^{-6}$  s) and estimated values described by the blue triangles pointing upwards ( $\Delta t = 2.0 \cdot 10^{-5}$  s) and blue crosses ( $\Delta t = 2.5 \cdot 10^{-6}$  s).

Figure 13 plots the values of the *exact* quantities of interest  $s_u(t)$  and  $s_v(t)$  computed by using the overkill mesh and the approximations  $\hat{s}_u(t)$  and  $\hat{s}_v(t)$  for the three different values of the parameter  $a_2$ . Note that the approximations  $\hat{s}_u(t)$  and  $\hat{s}_v(t)$  are in very good agreement with the exact ones  $s_u(t)$  and  $s_v(t)$ .

Figure 14 shows the evolution of the errors  $s_u^e(t) = s_u(t) - \hat{s}_u(t)$  and  $s_v^e(t) = s_v(t) - \hat{s}_v(t)$  jointly with the assessed errors  $\tilde{s}_u^e(t)$  and  $\tilde{s}_v^e(t)$  for three meshes keeping constant  $\Delta t = 2.0 \cdot 10^{-5}$  s and  $a_2 = 0$  s. For both quantities of interest, the *exact* errors  $s_u^e(t)$  and  $s_v^e(t)$  are fairly well approximated with the estimates  $\tilde{s}_u^e(t)$  and  $\tilde{s}_v^e(t)$ . Note that the quality of the estimate  $\tilde{s}_v^e(t)$  improves as the element size is decreased. This is because the eigenpair  $(\omega_1^H, \mathbf{q}_1^H)$  is better captured by the fine mesh

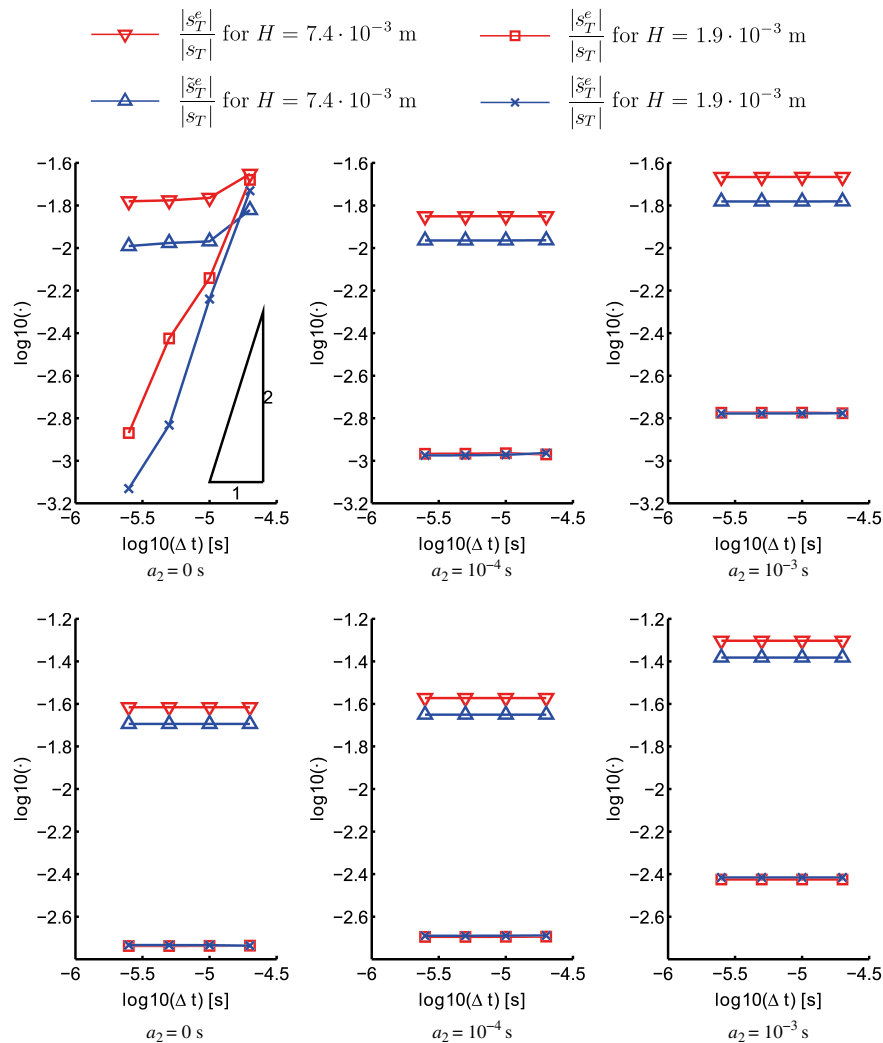


Figure 12. Example 2: Evolution of the relative error along a uniform  $\Delta t$  refinement process, for three values of the viscosity parameter  $a_2$ . Exact (overkill) values described by the red triangles pointing downwards ( $H = 7.4 \cdot 10^{-3}$  m) and red squares ( $H = 1.9 \cdot 10^{-3}$  m) and estimated values described by the blue triangles pointing upwards ( $H = 7.4 \cdot 10^{-3}$  m) and blue crosses ( $H = 1.9 \cdot 10^{-3}$  m).

than for the coarser ones. On the other hand, the estimate  $\tilde{s}_u^e(t)$  reproduces the average behavior of the error  $s_u^e(t)$ . However, more vibration modes should be considered in computing  $\tilde{s}_u^e(t)$  to capture all the features.

Figure 15 shows the dependence of the error estimates  $\tilde{s}_u^e(t)$  on the number of vibrations modes  $M$  using mesh id. 2 and time step id. 4. The higher is  $M$ , the better  $\tilde{s}_u^e(t)$  approximates  $s_u^e(t)$ . This is because the truncation error associated with  $M$  is reduced. On the other hand, the estimate is closer to the reference value as the damping parameter  $a_2$  increases. That is because the high frequencies of the problem are damped and the truncation error becomes less important. This is related to the parabolic character of the damping term. Note that in parabolic problems, errors tend to dissipate along the time evolution, see [60].

Table V. Example 2: Effectivities of the error estimates.

$H$ [m]	$\Delta t$ [s]	$a_2 = 0$ s		$a_2 = 1 \cdot 10^{-4}$ s		$a_2 = 1 \cdot 10^{-3}$ s	
		$\frac{\bar{s}_{u,T}^e}{s_{u,T}^e}$	$\frac{\bar{s}_{v,T}^e}{s_{v,T}^e}$	$\frac{\bar{s}_{u,T}^e}{s_{u,T}^e}$	$\frac{\bar{s}_{v,T}^e}{s_{v,T}^e}$	$\frac{\bar{s}_{u,T}^e}{s_{u,T}^e}$	$\frac{\bar{s}_{v,T}^e}{s_{v,T}^e}$
$7.41 \cdot 10^{-3}$	$2.0 \cdot 10^{-5}$	0.676	0.835	0.771	0.835	0.766	0.834
$7.41 \cdot 10^{-3}$	$1.0 \cdot 10^{-5}$	0.624	0.835	0.769	0.835	0.767	0.834
$7.41 \cdot 10^{-3}$	$5.0 \cdot 10^{-6}$	0.630	0.835	0.769	0.835	0.767	0.834
$7.41 \cdot 10^{-3}$	$2.5 \cdot 10^{-6}$	0.616	0.835	0.769	0.835	0.767	0.834
$1.85 \cdot 10^{-3}$	$2.0 \cdot 10^{-5}$	0.889	1.000	1.016	1.012	0.999	1.022
$1.85 \cdot 10^{-3}$	$1.0 \cdot 10^{-5}$	0.797	1.008	0.983	1.012	0.992	1.022
$1.85 \cdot 10^{-3}$	$5.0 \cdot 10^{-6}$	0.391	1.010	0.983	1.012	0.992	1.022
$1.85 \cdot 10^{-3}$	$2.5 \cdot 10^{-6}$	0.548	1.010	0.983	1.012	0.992	1.022
$7.41 \cdot 10^{-3}$	$2.0 \cdot 10^{-5}$	0.676	0.835	0.771	0.835	0.766	0.834
$3.70 \cdot 10^{-3}$	$2.0 \cdot 10^{-5}$	0.820	0.813	0.797	0.818	0.795	0.824
$1.85 \cdot 10^{-3}$	$2.0 \cdot 10^{-5}$	0.889	1.000	1.016	1.012	0.999	1.022
$7.41 \cdot 10^{-3}$	$2.5 \cdot 10^{-6}$	0.616	0.835	0.769	0.835	0.767	0.834
$3.70 \cdot 10^{-3}$	$2.5 \cdot 10^{-6}$	0.580	0.817	0.789	0.818	0.793	0.824
$1.85 \cdot 10^{-3}$	$2.5 \cdot 10^{-6}$	0.548	1.010	0.983	1.012	0.992	1.022

Table VI. Example 2: Effectivity of the recovered eigenfrequencies [rad/s]. The eigenvalues obtained using the overkill mesh are  $\omega_1^{\text{ovk}} = 3.3585 \cdot 10^2$ ,  $\omega_{20}^{\text{ovk}} = 1.4625 \cdot 10^4$ ,  $\omega_{40}^{\text{ovk}} = 3.8587 \cdot 10^4$ , and  $\omega_{60}^{\text{ovk}} = 6.3211 \cdot 10^4$ .

$H$ [m]	$i$	$\omega_i^H$	$\tilde{\omega}_i$	$\omega_i^{H,p+1}$	$\eta_i$	$\tilde{\eta}_i$
$7.41 \cdot 10^{-3}$	1	$3.5282 \cdot 10^2$	$3.3984 \cdot 10^2$	$3.3667 \cdot 10^2$	1.0480	1.0094
$7.41 \cdot 10^{-3}$	20	$1.5243 \cdot 10^4$	$1.4780 \cdot 10^4$	$1.4745 \cdot 10^4$	1.0338	1.0024
$7.41 \cdot 10^{-3}$	40	$4.0870 \cdot 10^4$	$3.9257 \cdot 10^4$	$3.9035 \cdot 10^4$	1.0470	1.0057
$7.41 \cdot 10^{-3}$	60	$6.7082 \cdot 10^4$	$6.5151 \cdot 10^4$	$6.4901 \cdot 10^4$	1.0336	1.0039
$3.71 \cdot 10^{-3}$	1	$3.4111 \cdot 10^2$	$3.3703 \cdot 10^2$	$3.3596 \cdot 10^2$	1.0153	1.0032
$3.71 \cdot 10^{-3}$	20	$1.4863 \cdot 10^4$	$1.4745 \cdot 10^4$	$1.4734 \cdot 10^4$	1.0088	1.0007
$3.71 \cdot 10^{-3}$	40	$3.9476 \cdot 10^4$	$3.9058 \cdot 10^4$	$3.9004 \cdot 10^4$	1.0121	1.0014
$3.71 \cdot 10^{-3}$	60	$6.5174 \cdot 10^4$	$6.4933 \cdot 10^4$	$6.4862 \cdot 10^4$	1.0048	1.0011
$1.85 \cdot 10^{-4}$	1	$3.3736 \cdot 10^2$	$3.3607 \cdot 10^2$	$3.3562 \cdot 10^2$	1.0052	1.0013
$1.85 \cdot 10^{-4}$	20	$1.4766 \cdot 10^4$	$1.4735 \cdot 10^4$	$1.4729 \cdot 10^4$	1.0025	1.0004
$1.85 \cdot 10^{-4}$	40	$3.9088 \cdot 10^4$	$3.9009 \cdot 10^4$	$3.8993 \cdot 10^4$	1.0024	1.0004
$1.85 \cdot 10^{-4}$	60	$6.4953 \cdot 10^4$	$6.4871 \cdot 10^4$	$6.4847 \cdot 10^4$	1.0016	1.0004

As previously noted, the quality of the estimates clearly depends on the number of modes: as expected, when  $M$  increases and only the recovery procedure for each vibration mode affects the quality of the estimator. It is also worth noting that even though a fairly large number of modes are required to properly detect all the features of the evolution of the error in the quantity of interest, the shape of the curve is captured for reasonable low values of  $M$ . Finally, observe that, for the same number of modes, the estimate is closer to the reference value as the damping parameter  $a_2$  increases.

5.3. Example 3

The example presented here is similar to the previous one but increasing the structural complexity. The aim is to demonstrate that the proposed methodology is not limited to simple academic

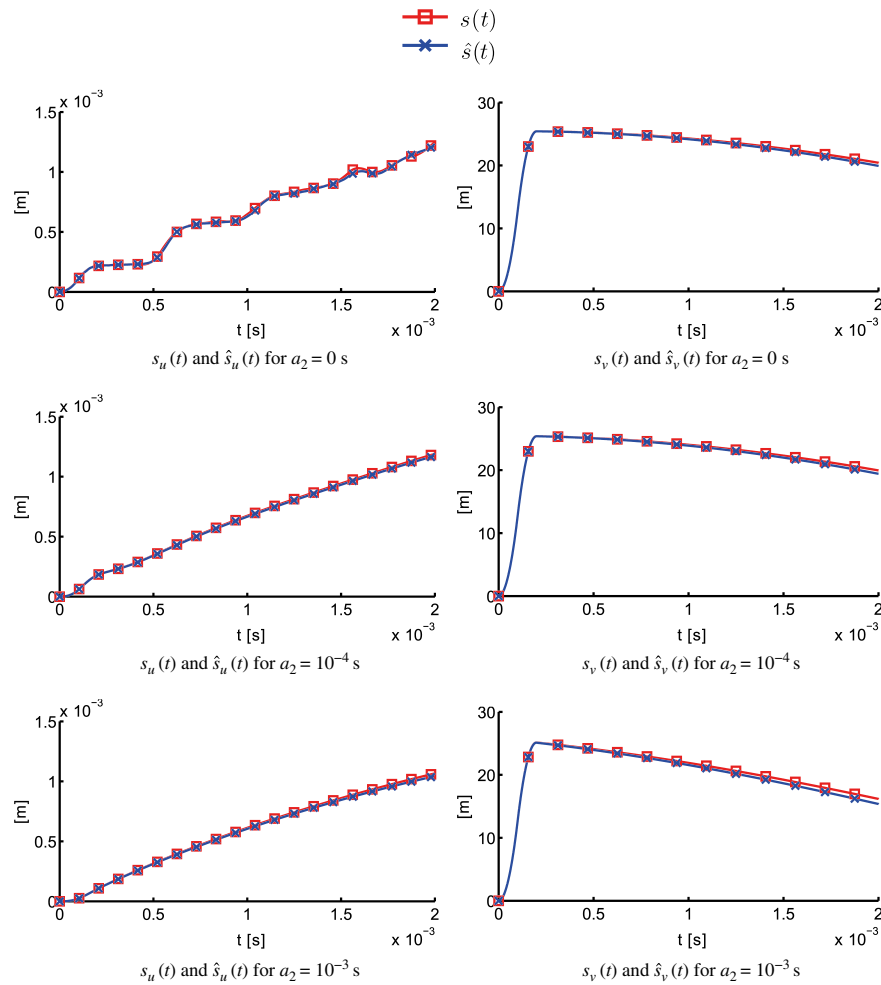


Figure 13. Example 2: Evolution of the timeline-dependent quantities  $s_u(t)$  (left) and  $s_v(t)$  (right) for three values of the parameter  $a_2$ . The approximate quantities  $\hat{s}_u(t)$  and  $\hat{s}_v(t)$  are computed with the discretization  $H = 7.41 \cdot 10^{-3}$  m and  $\Delta t = 2.0 \cdot 10^{-5}$  s.

cases. This example is efficiently tackled with an affordable number of modes and computational resources.

Consider the structure defined in Figure 16. The structure is initially at rest ( $\mathbf{u}_0 = \mathbf{v}_0 = \mathbf{0}$ ) and locally loaded with the time dependent traction

$$\mathbf{g}(\mathbf{x}, t) := \begin{cases} g(t)\mathbf{e}_2 & \mathbf{x} \in \Gamma_g, \\ 0 & \mathbf{x} \in \Gamma_N \setminus \Gamma_g. \end{cases}$$

The time weighting function  $g(t)$  is also a triangular-shaped function such as in Figure 8(b). Table VII contains all the parameters uniquely defining the problem. The response of the structure under the action of this load is shown in Figure 17 for several simulation times.

In this example, the quantity of interest is an average of the vertical component of the displacements in the region  $\Gamma_g$ . Both the value of the average at the final simulation time and its evolution are considered, thus the following two quantities of interest are examined

$$s_T = (\boldsymbol{\lambda}_N, \mathbf{u}(T))_{\Gamma_g} \quad \text{and} \quad s(t) = (\boldsymbol{\lambda}_N, \mathbf{u}(t))_{\Gamma_g},$$

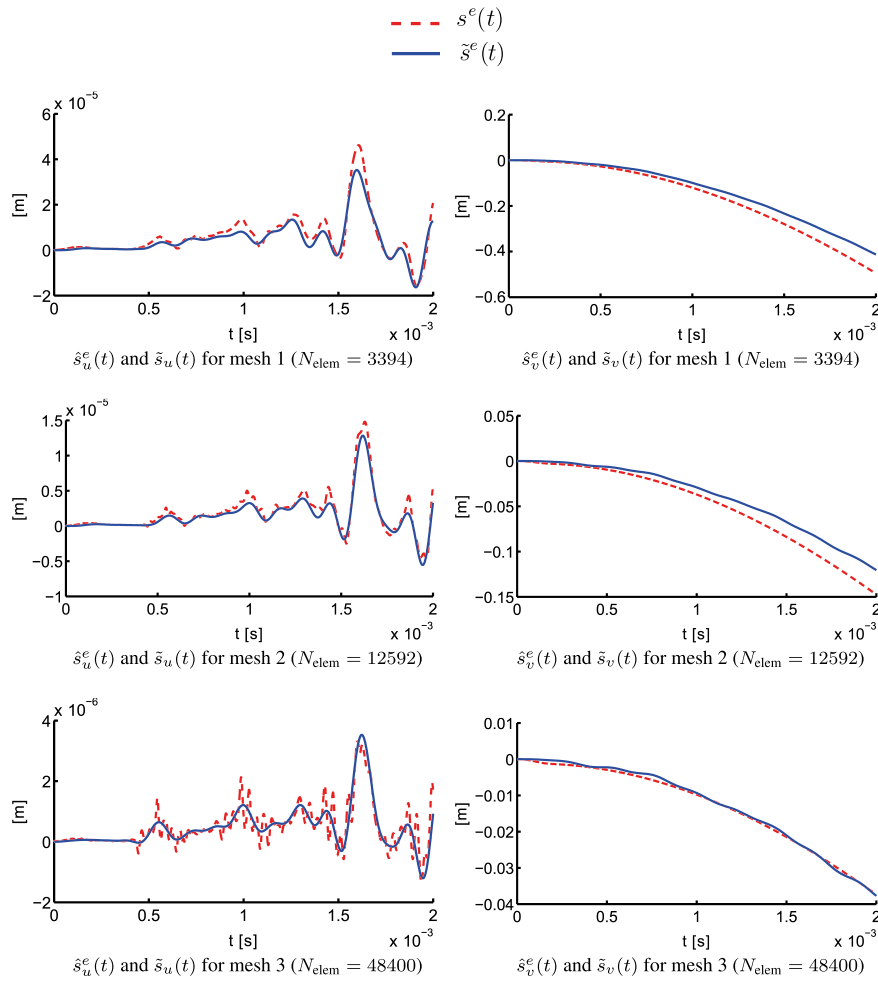


Figure 14. Example 2: Time evolution of the errors associated to  $s_u(t)$  (left) and  $s_v(t)$  (right) for the three computational meshes and keeping constant  $\Delta t = 2.50 \cdot 10^{-6}$  s.

where  $\lambda_N^O = \mathbf{e}_2 / \text{meas}(\Gamma_g)$ . Note that these quantities coincide with  $s_{u,T}$  and  $s_u(t)$  of the previous example, but here, the subscript  $u$  is omitted being the only quantities of interest under study. Recall that dealing with this quantity of interest requires introducing an auxiliary extractor  $\mathbf{u}^O$ .

Several meshes and time step lengths are considered to evaluate the performance of the proposed estimates, see Table VIII. Table VIII also shows the parameters of the *overkill* discretization used to approximate the exact quantities  $s_T$  and  $s(t)$ .

Using the same notation as in the previous examples,  $\hat{s}_T$  and  $\hat{s}(t)$  are the approximated quantities of interest and  $\tilde{s}_T^c$  and  $\tilde{s}^c(t)$  are the estimates of the *exact* errors  $s_T^c = s_T - \hat{s}_T$  and  $s^c(t) = s(t) - \hat{s}(t)$ .

Figure 18 shows the space and time convergence of the estimate  $\tilde{s}_T^c$  and the overkill error  $s_T^c$ . The space convergence curves are obtained for a constant time step length of  $\Delta t = 1.00 \cdot 10^{-4}$  s. The computed estimates are fairly close to the overkill values, and its accuracy improves as the number of eigenmodes increases. The results for  $M = 40$  and  $M = 60$  are quite close, and thus, there is no significant gain in increasing the number of modes in the decomposition far beyond  $M = 40$  because the performance of the error estimates is controlled by the recovery procedure. The time convergence plot is obtained by using different time steps for a constant element size

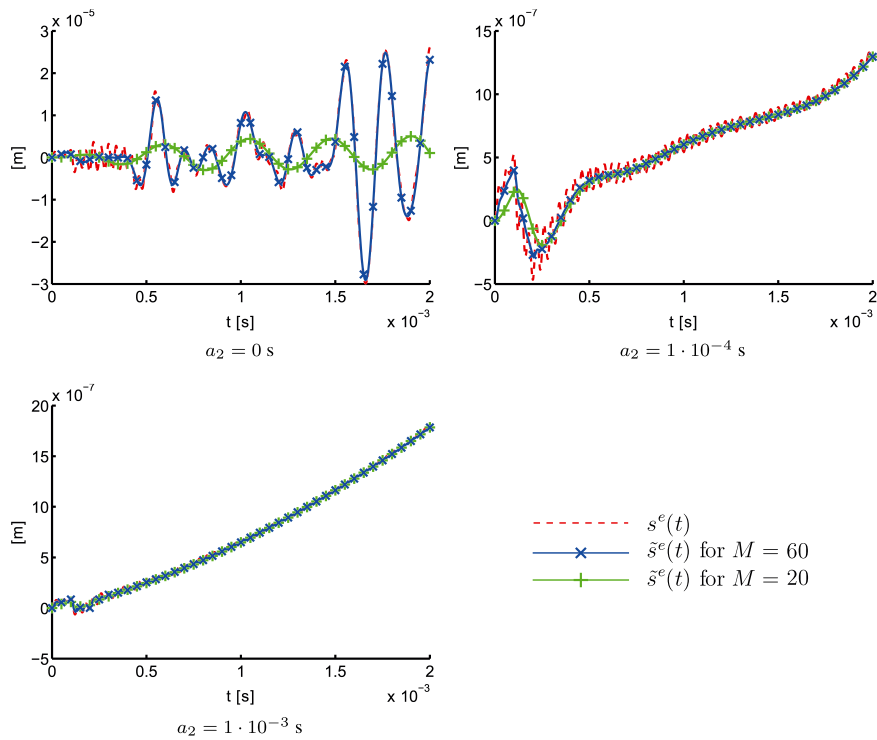


Figure 15. Example 2: Dependence of the assessed error  $\tilde{s}_u^e(t)$  on the number of vibration modes  $M$  for three values for the parameter  $a_2$ .

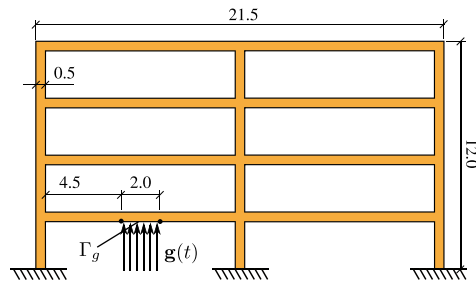


Figure 16. Example 3: Problem statement and geometry definition.

$H = 1.15 \cdot 10^{-1}$  m. In this case, the space discretization error is dominant with respect to the time discretization error, and therefore, reducing the time step length does not yield any gain in accuracy.

Table IX shows the effectivities of the estimate  $\tilde{s}_\Gamma^e$  for different spatial mesh and number of eigenmodes. The quality of the estimate improves as the number of eigenmodes increases. However, a rough approximation of the error, which might be sufficient in some applications, is already obtained with  $M = 20$  modes.

Figure 19 shows the evolution of the timeline-dependent quantity of interest  $s(t)$  along with the approximations  $\hat{s}(t)$  computed by using the three spatial meshes for a fixed time step  $\Delta t = 10^{-4}$  s.

Table VII. Example 3: Problem parameterization.

Physical properties	External load
$E = 2.7 \cdot 10^{10}$ Pa	$g_{\max} = 1 \cdot 10^8$ Pa
$\nu = 0.2$	$t_g = 1 \cdot 10^{-3}$ s
$\rho = 2.5 \cdot 10^3$ kg/m <sup>3</sup>	
$a_1 = 0$ s	
$a_2 = 0$ s	
$T = 2 \cdot 10^{-2}$ s	

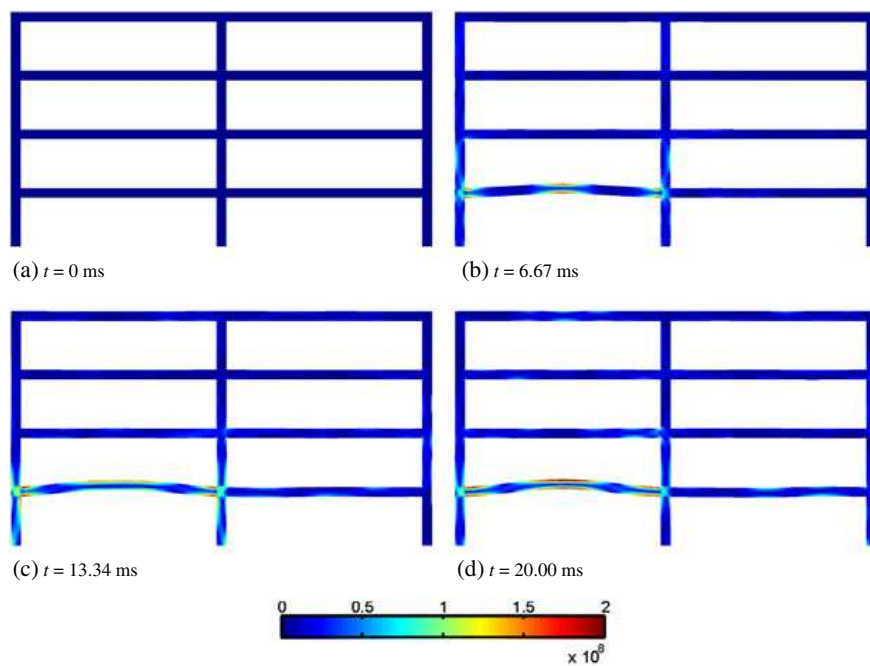


Figure 17. Example 3: Deformed geometry and von Mises criterion at several times. Solution computed using the mesh id. 3 and time step id. 4.

Table VIII. Example 3: Space and time discretizations.

Mesh id.	$N_{\text{dof}}$	# Elements	Type	$p$	$H$ [m]
1	2774	1876	Triangle	1	$1.15 \cdot 10^{-1}$
2	9310	7504	Triangle	1	$5.77 \cdot 10^{-2}$
3	33638	30016	Triangle	1	$2.89 \cdot 10^{-2}$
ovk.	127318	120064	Triangle	1	$1.44 \cdot 10^{-2}$
Time step id.	# steps	$\Delta t$ [s]			
1	100	$1.00 \cdot 10^{-4}$			
2	200	$5.00 \cdot 10^{-5}$			
3	400	$2.50 \cdot 10^{-5}$			
4	800	$1.25 \cdot 10^{-5}$			
ovk.	3200	$6.25 \cdot 10^{-6}$			

As can be seen, the approximations of the quantity of interest converge to the *overkill* value as the mesh is refined, because the errors due to the time integration are negligible.

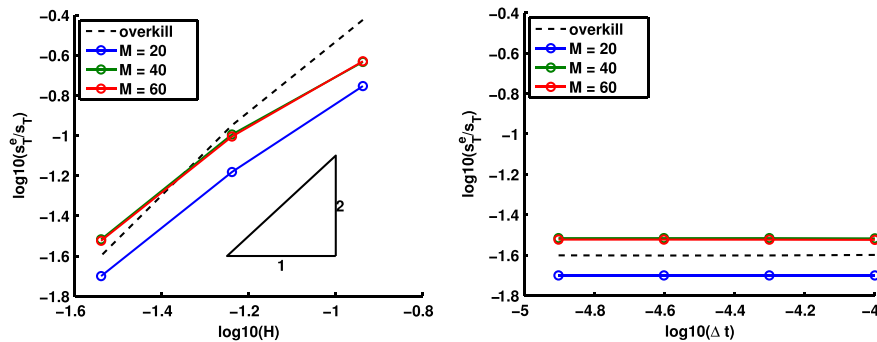


Figure 18. Example 3: Space (left) and time (right) convergence of estimate  $s_T^e$  and of the reference error  $\tilde{s}_T^e$  for different number of vibration modes  $M$ .

Table IX. Example 3: Computed effectivities.

$H$ [m]	$\Delta t$ [s]	$\tilde{s}_T^e / s_T^e$		
		$M = 20$	$M = 40$	$M = 60$
$1.15 \cdot 10^{-1}$	$1.00 \cdot 10^{-4}$	0.468	0.617	0.622
$5.77 \cdot 10^{-2}$	$1.00 \cdot 10^{-4}$	0.586	0.900	0.879
$2.89 \cdot 10^{-2}$	$1.00 \cdot 10^{-4}$	0.792	1.207	1.188

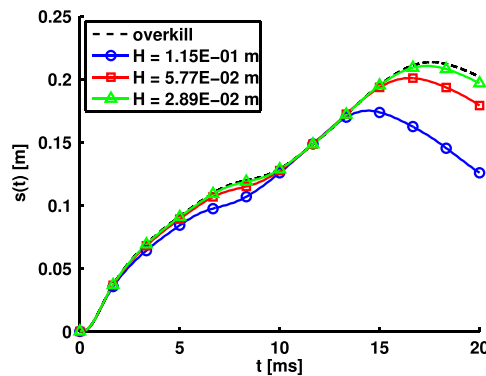


Figure 19. Example 3: Time evolution of the timeline-dependent quantity  $s(t)$  and its approximation  $\hat{s}(t)$  computed by using the three different computational meshes for a fixed time step  $\Delta t = 10^{-4}$  s.

Finally, Figure 20 shows the computed estimates  $\tilde{s}^e(t)$  obtained, varying the number of eigenmodes in the adjoint decomposition and for several meshes. As in the previous examples, the accuracy of the estimates increases with the number of considered eigenmodes. The estimate  $\tilde{s}^e(t)$ , computed by using  $M = 20$  modes, reproduces the average behavior of  $s^e(t)$ , whereas the estimate  $\tilde{s}^e(t)$ , computed by using  $M = 40$  or  $M = 60$  modes, is a reasonably good approximation to  $s^e(t)$ .

## 6. CONCLUSIONS

This article presents a new type of goal-oriented error estimates assessing the error in timeline-dependent quantities of interest. Timeline-dependent quantities are outputs of the solution describing the time evolution of some space-post-processed functional. Compared with the traditional scalar

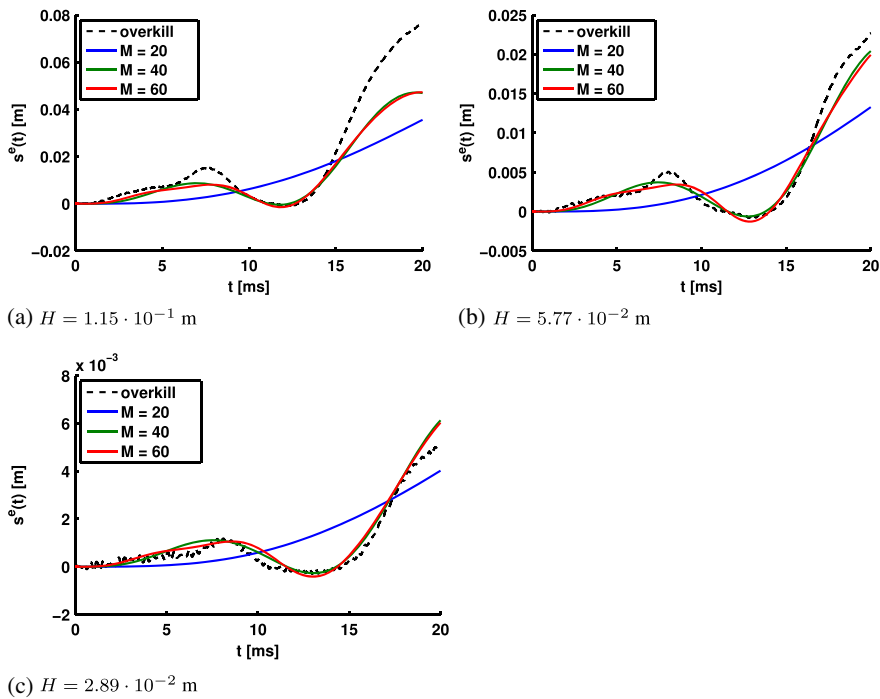


Figure 20. Example 3: Computed estimates  $\tilde{s}^e(t)$  using different number of eigenmodes and overkill error  $s^e(t)$  for the three computational meshes and a fixed time step  $\Delta t = 10^{-4}$  s.

quantities of interest, this approach fits better the requirements of end-users in dynamic problems. Assessing the error in timeline-dependent quantities involves a family of infinite adjoint problems (one for each time instant in the time interval under consideration). However, all these adjoint problems are similar, and they can be recovered from a common parent problem (associated with the a scalar quantity of interest) by means of a simple translation (shift) of the time variable.

The second novelty in this paper is the approximation of the adjoint problem using a decomposition into vibration modes. This allows efficiently precomputing and storing the adjoint solution. Thus, the error estimate is computed along the time integration of the original problem. This approach applies both for the scalar and timeline quantities, but it is specially indicated for the latter because it simplifies the implementation of the time shift.

The error estimation strategies proposed in this work are based on an explicit approach. The error estimate is computed, injecting an enhanced approximation of the adjoint solution into the residual of the direct problem. The enhancement is based on a local postprocess of the computed eigenvectors, performed only once and not at each time step. This approach is very efficient for some quantities of interest in which the adjoint solution is fairly represented in a modal description.

The numerical examples show that the proposed estimates have a good effectivity for both the scalar and timeline quantities of interest, accounting both for space and time discretization errors. Contrary to other error estimates for linear visco-elastodynamics, the proposed estimates do not degenerate in the limit case of pure elasticity (i.e., when no damping is introduced in the formulation).

In current ongoing work, the proposed error estimation techniques are used as driving indicators for mesh adaptivity.

ACKNOWLEDGEMENTS

This paper is partially supported by Ministerio de Educación y Ciencia (Grant DPI2011-27778-C02-02) and Universitat Politècnica de Catalunya (UPC-BarcelonaTech) (Grant UPC-FPU). The support of the Col·legi d'Enginyers de Camins, Canals i Ports (Catalunya) is also gratefully acknowledged.

REFERENCES

1. Ainsworth M, Oden J. *A Posteriori Error Estimation in Finite Element Analysis*. John Wiley & Sons Ltd.: New York, 2000.
2. Ladevèze P, Pelle J. *La maîtrise du Calcul en Mécanique Linéaire et Non linéaire*. Lavoisier: Paris, 2001.
3. Stein E. *Error-Controlled Adaptive Finite Elements in Solid Mechanics*. John Wiley & Sons Ltd.: Chichester, United Kingdom, 2003.
4. Ainsworth M, Oden J. A posteriori error estimation in finite element analysis. *Computer Methods in Applied Mechanics and Engineering* 1997; **142**:1–88.
5. Gratsch T, Bathe K. A posteriori error estimation techniques in practical finite element analysis. *Computers and Structures* 2005; **83**:235–265.
6. Babuška I, Rheinboldt W. Error estimates for adaptive finite element computations. *SIAM Journal on Numerical Analysis* 1978; **18**:736–754.
7. Ladevèze P, Leguillon D. Error estimate procedure in the finite element method. *SIAM Journal on Numerical Analysis* 1983; **20**:485–509.
8. Zienkiewicz O, Zhu J. A simple error estimator and adaptive procedure for practical engineering analysis. *International Journal for Numerical Methods in Engineering* 1987; **24**:337–357.
9. Paraschivoiu M, Peraire J, Patera A. A posteriori finite element bounds for linear-functional outputs of elliptic partial differential equations. *Computer Methods in Applied Mechanics and Engineering* 1997; **150**:289–321.
10. Parés N, Bonet J, Huerta A, Peraire J. The computation of bounds for linear-functional outputs of weak solutions to the two-dimensional elasticity equations. *Computer Methods in Applied Mechanics and Engineering* 2006; **195**:406–429.
11. Cirak F, Ramm E. A posteriori error estimation and adaptivity for linear elasticity using the reciprocal theorem. *Computer Methods in Applied Mechanics and Engineering* 1998; **156**:351–362.
12. Prudhomme S, Oden J. On goal-oriented error estimation for elliptic problems: application to the control of pointwise errors. *Computer Methods in Applied Mechanics and Engineering* 1999; **176**:313–331.
13. Gallimard L, Ladeveze P, Pelle J. An enhanced error estimator on the constitutive relation for plasticity problems. *Computers and Structures* 2000; **78**:801–810.
14. Ladevèze P. Constitutive relation errors for FE analysis considering (visco)plasticity and damage. *International Journal for Numerical Methods in Engineering* 2001; **52**:527–542.
15. Ladevèze P, Moës N. Adaptive control for finite element analysis in plasticity. *Computers and Structures* 1999; **73**:45–60.
16. Ladevèze P, Moës N, Douchin B. Constitutive relation error estimators for (visco)plastic finite element analysis with softening. *Computer Methods in Applied Mechanics and Engineering* 2000; **176**:247–264.
17. Parés N, Díez P, Huerta A. Exact bounds of the advection–diffusion–reaction equation using flux-free error estimates. *SIAM Journal on Scientific Computing* 2009; **31**:3064–3089.
18. Larsson F, Díez P, Huerta A. A flux-free a posteriori error estimator for the incompressible Stokes problem using a mixed FE formulation. *Computer Methods in Applied Mechanics and Engineering* 2010; **199**:2383–2402.
19. Parés N, Díez P, Huerta A. Bounds of functional outputs for parabolic problems. Part I: exact bounds of the discontinuous Galerkin time discretization. *Computer Methods in Applied Mechanics and Engineering* 2008; **197**:1641–1660.
20. Parés N, Díez P, Huerta A. Bounds of functional outputs for parabolic problems. Part II: Bounds of the exact solution. *Computer Methods in Applied Mechanics and Engineering* 2008; **197**:1661–1679.
21. Díez P, Calderón G. Goal-oriented error estimation for transient parabolic problems. *Computational Mechanics* 2007; **39**:631–646.
22. Larson M, Bengzon F. Adaptive finite element approximation of multiphysics problems. *Communications in Numerical Methods in Engineering* 2008; **24**:505–521.
23. Larson M, Soderlund R, Bengzon F. Adaptive finite element approximation of coupled flow and transport problems with applications in heat transfer. *International Journal for Numerical Methods in Fluids* 2008; **57**:1397–1420.
24. Fick P, van Brummelen E, van der Zee K. On the adjoint-consistent formulation of interface conditions in goal-oriented error estimation and adaptivity for fluid-structure interaction. *Computer Methods in Applied Mechanics and Engineering* 2010; **199**:3369–3385.
25. van der Zee K, van Brummelen E, Akkerman I, de Borst R. Goal-oriented error estimation and adaptivity for fluid-structure interaction using exact linearized adjoints. *Computer Methods in Applied Mechanics and Engineering* 2011; **200**:2738–2757.
26. Asner L, Tavener S, Kay D. Adjoint-based a posteriori error estimation for coupled time-dependent systems. *SIAM Journal on Scientific Computing* 2012; **34**:2394–2419.
27. Li X, Wiberg N. Implementation and adaptivity of a space–time finite element method for structural dynamics. *Computer Methods in Applied Mechanics and Engineering* 1998; **156**:211–229.

28. Wiberg N, Li X. Adaptive finite element procedures for linear and non-linear dynamics. *International Journal for Numerical Methods in Engineering* 1999; **46**:178–1802.
29. Schleupen A, Ramm E. Local and global error estimations in linear structural dynamics. *Computers and Structures* 2000; **76**:741–756.
30. Thompson L, He D. Adaptive space-time finite element methods for the wave equation on unbounded domains. *Computer Methods in Applied Mechanics and Engineering* 2005; **194**:1947–2000.
31. Lahiri S, Bonet J, Peraire J. A variationally consistent mesh adaptation method for triangular elements in explicit Lagrangian dynamics. *International Journal for Numerical Methods in Engineering* 2010; **82**:1073–1113.
32. Aubry D, Lucas D, Tie B. Adaptive strategy for transient/coupled problems. Applications to thermoelasticity and elastodynamics. *Computer Methods in Applied Mechanics and Engineering* 1999; **176**:41–50.
33. Bangert W, Geiger M, Rannacher R. Adaptive Galerkin finite element methods for the wave equation. *Computational Methods in Applied Mathematics* 2010; **1**:3–48.
34. Bangert W. Adaptive Finite-Elemente-Methoden zur Lösung der Wellengleichung mit Anwendung in der Physik der Sonne. *Ph.D. Thesis*, Ruprecht-Karls-Universität Heidelberg, 1998.
35. Rannacher R. Adaptive Galerkin finite element methods for partial differential equations. *Journal of Computational and Applied Mathematics* 2001; **128**:205–233.
36. Bangert W, Rannacher R. Finite element approximation of the acoustic wave equation: error control and mesh adaptation. *East-West Journal of Numerical Mathematics* 1999; **7**:263–282.
37. Bangert W, Rannacher R. Adaptive finite element techniques for the acoustic wave equation. *Journal of Computational Acoustics* 2001; **9**:575–591.
38. Combe J, Ladevèze P, Pelle J. Discretization error estimator for transient dynamic simulations. *Advances in Engineering Software* 2002; **33**:553–563.
39. Combe J, Ladevèze P, Pelle J. Constitutive relation error estimator for transient finite element analysis. *Computer Methods in Applied Mechanics and Engineering* 1999; **176**:165–185.
40. Ladevèze P, Pelle J. Estimation of discretization errors in dynamics. *Computers and Structures* 2003; **81**:1133–1148.
41. Ladevèze P, Waeytens J. Model verification in dynamics through strict upper bounds. *Computer Methods in Applied Mechanics and Engineering* 2009; **198**:1775–1784.
42. Waeytens J. Contrôle des calculs en dynamique: bornes strictes et pertinents sur une quantité d'intérêt. *Ph.D. Thesis*, LMT-Cachan, 2010.
43. Ladevèze P. Strict upper error bounds for computed outputs of interest in computational structural mechanics. *Computational Mechanics* 2008; **42**:271–286.
44. Waeytens J, Chamois L, Ladevèze P. Guaranteed error bounds on pointwise quantities of interest for transient viscodynamics problems. *Computational Mechanics* 2012; **49**:291–307.
45. Verdugo F, Díez P. Computable bounds of functional outputs in linear visco-elastodynamics. *Computer Methods in Applied Mechanics and Engineering* 2012; **245–246**:313–330.
46. Fuentes D, Littlefield D, Oden J, Prudhomme S. Extensions of goal-oriented error estimation methods to simulation of highly-nonlinear response of shock-loaded elastomer-reinforced structures. *Computer Methods in Applied Mechanics and Engineering* 2006; **195**:4659–4680.
47. Carey V, Estep D, Johansson A, Larson M, Tavener S. Blockwise adaptivity for time dependent problems based on coarse scale adjoint solutions. *SIAM Journal on Scientific Computing* 2010; **32**:2121–2145.
48. Braack M, Burman E, Taschenberger N. Duality based a posteriori error estimation for quasi-periodic solutions using time averages. *SIAM Journal on Scientific Computing* 2011; **33**:2199–2216.
49. Wiberg N, Bausys R, Hager P. Adaptive h-version eigenfrequency analysis. *Computers and Structures* 1999; **71**:565–584.
50. Evans L. *Partial Differential Equations*. American Mathematical Society, 1998.
51. Hughes T, Hulbert M. Space-time finite element methods for elastodynamics: formulations and error estimates. *Computer Methods in Applied Mechanics and Engineering* 1988; **66**:339–363.
52. Hulbert M, Hughes T. Space-time finite element methods for second-order hyperbolic equations. *Computer Methods in Applied Mechanics and Engineering* 1990; **84**:327–348.
53. Newmark N. A method of computation for structural dynamics. *Journal of Engineering Mechanics* 1959; **85**:67–94.
54. Bathe K. *Finite Element Procedures*. Prentice Hall, 1996.
55. Rafique A, Kapre N, Constantinides G. A high throughput FPGA-based implementation of the lanczos method for the symmetric extremal eigenvalue problem. *8th International Symposium on Applied Reconfigurable Computing*, Hong Kong, 2012; 239–250.
56. Trefethen L, Bau D. *Numerical Linear Algebra*. Society for Industrial & Applied Mathematics, 1997.
57. Zienkiewicz O, Zhu J. The superconvergent patch recovery and a posteriori error estimates. Part I: the recovery technique. *International Journal for Numerical Methods in Engineering* 1992; **33**:1331–1364.
58. Wiberg N, Abdulwahab F, Li X. Error estimation and adaptive procedures based on superconvergent patch recovery. *Archives of Computational Methods in Engineering* 1997; **4**:203–242.
59. Díez P, Calderón G. Remeshing criteria and proper error representations for goal oriented h-adaptivity. *Computer Methods in Applied Mechanics and Engineering* 2007; **196**:719–733.
60. Eriksson K, Johnson C, Logg A. Adaptive computational methods for parabolic problems. In *Encyclopedia of Computational Mechanics*, Vol. 1, Stein E, de Borst R, Hughes T (eds), chap. 24. John Wiley: Chichester, United Kingdom, 2004; 675–702.

# Paper D

Goal-oriented space-time  
adaptivity for transient dynamics  
using a modal description  
of the adjoint solution

F. Verdugo, N. Parés and P. Díez

---

Submitted manuscript



## Goal-oriented space-time adaptivity for transient dynamics using a modal description of the adjoint solution\*

F. Verdugo<sup>1</sup>, N. Parés<sup>1,2</sup> and P. Díez<sup>1,3</sup>

<sup>1</sup>Laboratori de Càlcul Numèric (LaCàN),  
Universitat Politècnica de Catalunya (UPC),  
Jordi Girona 1-3 E-08034 Barcelona, Spain.

<sup>2</sup> Laboratori de Càlcul Numèric (LaCàN),  
Escola Universitària d'Enginyeria Tècnica Industrial de Barcelona (EUETIB),  
Compte d'Urgell, 187, E-08036, Barcelona, Spain.

<sup>3</sup>Centre Internacional de Mètodes Numèrics en Enginyeria (CIMNE),  
Gran Capitán s/n, E-08034 Barcelona, Spain.

Email: {francesc.verdugo,nuria.pares,pedro.diez}@upc.edu

---

### Abstract

This article presents a space-time adaptive strategy for transient elastodynamics. The method aims at computing an optimal space-time discretization such that the computed solution has an error in the quantity of interest below a user-defined tolerance. The methodology is based on a goal-oriented error estimate that requires accounting for an auxiliary adjoint problem. The major novelty of this paper is using modal analysis to obtain a proper approximation of the adjoint solution. The idea of using a modal-based description was introduced in a previous work for error estimation purposes. Here this approach is used for the first time in the context of adaptivity. With respect to the standard direct time-integration methods, the modal solution of the adjoint problem is highly competitive in terms of computational effort and memory requirements. The performance of the proposed strategy is tested in two numerical examples. The two examples are selected to be representative of different wave propagation phenomena, one being a 2D bulky continuum and the second a 2D domain representing a structural frame.

**Keywords:** elastodynamics, adaptivity, goal-oriented error assessment, adjoint problem, quantity of interest, modal analysis.

---

## 1 Introduction

Computing high fidelity numerical approximations requires a fine discretization and leads to a large consumption of computational resources. Adaptivity aims at providing the optimal discretization (space mesh and time grid) guaranteeing some user-prescribed accuracy at a minimum computational cost. Many adaptive techniques have been developed with application to different problem types. These tools are particularly important in wave propagation problems, e.g. linear elastodynamics, because the features of the solution concentrate at the wave fronts and therefore a fine mesh is only required at specific regions of the domain.

Over the last three decades, a vast literature has been produced on adaptivity. Among the the pioneering works, references [1, 2] propose adaptive techniques for flow problems using curvature and gradient based error indicators. This type of heuristic error indicators are used to identify the parts of the solution requiring a finer mesh size. This approach is applicable to many problem types because error indicators do not rely on the problem properties, but in the geometrical features of the solution. This type of indicators detect properly the errors associated with inter-

polation but fail in capturing the error from other sources, e.g. pollution error.

A more reliable alternative to drive mesh adaptivity are a posteriori error estimators. They are used to efficiently control the accuracy of some output of the solution by means of refining the discretization only where is needed (in the zones where the error is emanating from). The available outputs for assessing the accuracy of the approximation are global norms, e.g. the energy or  $L^2$  norm [3, 4, 5], or *quantities of interest* [6, 7, 8, 9]. Error estimators considering quantities of interest are referred as *goal-oriented*.

Goal-oriented adaptivity is discussed in the literature for many problem types. For instance, for elliptic problems [6, 7, 10, 11, 12], for the convection-diffusion-reaction equation [13, 14], for non-linear structural problems [15, 16], for time-dependent parabolic problems [17, 18, 19] and for elastodynamics (or other 2nd order hyperbolic problems) [20, 21, 22, 23].

Goal-oriented adaptivity for elastodynamics is a very challenging topic and it is still ongoing research. The main difficulties are 1) solving the associated space-time adjoint solution accurately to estimate the error in the quantity of interest, 2) splitting the contributions of the space and time discretization errors and 3) transferring the solution

---

\*Manuscript under review

from one mesh to another without loss of accuracy.

References [20, 21, 23] are among the few discussing goal-oriented adaptivity in elastodynamics. The input of the adaptive procedure is a desired error tolerance in some quantity of interest. The adjoint solution is computed with the same time-integration method as the original solution. This approach might be memory demanding because at least the original or the adjoint solution has to be stored as a whole (at each mesh node and time point) prior to evaluate the error estimate.

The adaptive strategy presented in this article is an alternative to the previous approach. Here, the adjoint problem is approximated using modal analysis, as suggested in reference [24], to preclude the costly adjoint approximation and storage. The modal-based adjoint approximation is particularly efficient for some quantities of interest. This is because the adjoint solution is stored for a few vibration modes instead that for all time steps. Moreover, the time description of the adjoint solution is known analytically once the vibration frequencies and modes are available. This simplifies the algorithmic complexity of the adaptive procedure.

The remainder of this paper is organized as follows. Section 2 presents the equations of elastodynamics. Section 3 presents the weak and discrete versions of the problem using the double field time-continuous Galerkin method. The modal-based error assessment approach is presented in section 4. Section 5 presents the space-time adaptive procedure. Finally, the methodology is illustrated in section 6 with two numerical examples. The paper is concluded with some remarks.

## 2 Problem statement

### 2.1 Governing equations

A visco-elastic body occupies an open bounded domain  $\Omega \subset \mathbb{R}^d$ ,  $d \leq 3$ , with boundary  $\partial\Omega$ . The boundary is divided in two disjoint parts,  $\Gamma_N$  and  $\Gamma_D$  such that  $\partial\Omega = \bar{\Gamma}_N \cup \bar{\Gamma}_D$  and the considered time interval is  $I := (0, T]$ . Under the assumption of small perturbations, the evolution of displacements  $\mathbf{u}(\mathbf{x}, t)$  and stresses  $\boldsymbol{\sigma}(\mathbf{x}, t)$ ,  $\mathbf{x} \in \Omega$  and  $t \in I$ , is described by the visco-elastodynamic equations,

$$\rho(\ddot{\mathbf{u}} + a_1 \dot{\mathbf{u}}) - \nabla \cdot \boldsymbol{\sigma} = \mathbf{f} \quad \text{in } \Omega \times I, \quad (1a)$$

$$\mathbf{u} = \mathbf{0} \quad \text{on } \Gamma_D \times I, \quad (1b)$$

$$\boldsymbol{\sigma} \cdot \mathbf{n} = \mathbf{g} \quad \text{on } \Gamma_N \times I, \quad (1c)$$

$$\mathbf{u} = \mathbf{u}_0 \quad \text{at } \Omega \times \{0\}, \quad (1d)$$

$$\dot{\mathbf{u}} = \mathbf{v}_0 \quad \text{at } \Omega \times \{0\}, \quad (1e)$$

where an upper dot indicates derivation with respect to time, that is  $(\dot{\bullet}) := \frac{d}{dt}(\bullet)$ , and  $\mathbf{n}$  denotes the outward unit normal to  $\partial\Omega$ . The input data includes the mass density  $\rho = \rho(\mathbf{x}) > 0$ , the first Rayleigh coefficient  $a_1 \geq 0$ , the body force  $\mathbf{f} = \mathbf{f}(\mathbf{x}, t)$  and the traction  $\mathbf{g} = \mathbf{g}(\mathbf{x}, t)$  acting on the Neumann boundary  $\Gamma_N \times I$ . The initial conditions

for displacements and velocities are  $\mathbf{u}_0 = \mathbf{u}_0(\mathbf{x})$  and  $\mathbf{v}_0 = \mathbf{v}_0(\mathbf{x})$  respectively. For the sake of simplicity and without any loss of generality, Dirichlet conditions (1b) are taken as homogeneous.

The set of equations (1) is closed with the constitutive law,

$$\boldsymbol{\sigma} := \mathbf{C} : \boldsymbol{\varepsilon}(\mathbf{u} + a_2 \dot{\mathbf{u}}), \quad (2)$$

where the parameter  $a_2 \geq 0$  is the second Rayleigh coefficient, the tensor  $\mathbf{C}$  is the standard 4th-order elastic Hooke tensor. The strains are given by the kinematic relation corresponding to small perturbations, that is  $\boldsymbol{\varepsilon}(\mathbf{w}) := \frac{1}{2}(\nabla \mathbf{w} + \nabla^T \mathbf{w})$ .

### 2.2 Numerical approximation

In order to properly split the space and time error components, the adaptive strategy presented in this paper requires that the numerical solution under consideration fulfills the discrete version of a variational formulation. Thus, a weak residual (integrated both in space and time) associated with the numerical solution is readily introduced. The splitting procedure uses the fact that the residual vanishes for the functions in the test space, that is Galerkin orthogonality holds.

Among the possible space-time variational formulations available for transient elastodynamics, the double field *time-continuous Galerkin method* [25, 20] is the numerical solver selected. Note however that the rationale of this article can be easily extended to other space-time variational formulations, for instance, the one proposed by Johnson [26] or the one proposed by Hulbert and Hughes [27, 28].

The definition of the weak form of the problem requires introducing the following functional spaces: the standard Sobolev space associated with static displacement fields

$$\mathbf{V}_0 := \{\mathbf{w} \in [H^1(\Omega)]^d : \mathbf{w} = \mathbf{0} \text{ on } \Gamma_D\} \quad (3)$$

and the Bochner space  $L^2(I; \mathbf{V}_0)$  associated with  $\mathbf{V}_0$  of square-integrable functions from  $I$  into  $\mathbf{V}_0$ . With these notations, the trial space  $\mathbf{W}$  for the double field time-continuous Galerkin method is defined as

$$\mathbf{W} := \{\mathbf{w} \in L^2(I; \mathbf{V}_0) : \dot{\mathbf{w}} \in L^2(I; \mathbf{V}'_0)\}.$$

Note that,  $\mathbf{w} \in \mathbf{W}$  implies that  $\mathbf{w} \in C^0(\bar{I}; [L^2(\Omega)]^d)$  and therefore functions in  $\mathbf{W}$  are continuous both in space and time, but they do not necessarily have a continuous time derivative.

The test space is associated with a partition of the time interval  $I$  defined as  $\mathcal{T} := \{t_0, t_1, \dots, t_N\}$ , with  $0 = t_0 < t_1 < \dots < t_N = T$ . The time points in  $\mathcal{T}$  define the time intervals  $I_n := (t_{n-1}, t_n]$ ,  $n = 1, \dots, N$ . The time step length for each interval is  $\Delta t_n := t_n - t_{n-1}$ ,  $n = 1, \dots, N$  and the characteristic time step length for the partition  $\mathcal{T}$  is  $\Delta t := \max_{1 \leq n \leq N} (\Delta t_n)$ .

The test space is defined as

$$\widehat{\mathbf{W}} := \{\mathbf{w} \in L^2(I; \mathbf{V}_0) : \mathbf{w}|_{I_n} \in L^2(I_n; \mathbf{V}_0) \text{ and } \dot{\mathbf{w}}|_{I_n} \in L^2(I_n; \mathbf{V}'_0), n = 1, \dots, N\}.$$

Functions in  $\widehat{\mathcal{W}}$  when restricted to a time interval  $I_n$  have the same regularity as functions in  $\mathcal{W}$ . However, functions in  $\widehat{\mathcal{W}}$  are allowed to be discontinuous-in-time at the points in  $\mathcal{T}$ . This property is needed to define a time marching scheme, computing the solution successively in each time interval.

Using these notations, the space-time weak form of problem (1) reads: find  $\mathbf{U} = [\mathbf{u}_u, \mathbf{u}_v] \in \mathcal{W} \times \mathcal{W}$  such that

$$B(\mathbf{U}, \mathbf{W}) = L(\mathbf{W}) \quad \forall \mathbf{W} := [\mathbf{w}_u, \mathbf{w}_v] \in \widehat{\mathcal{W}} \times \widehat{\mathcal{W}}, \quad (4)$$

where the bilinear form  $B(\cdot, \cdot)$  and the linear functional  $L(\cdot)$  are defined as

$$\begin{aligned} B(\mathbf{U}, \mathbf{W}) &:= \int_I m(\dot{\mathbf{u}}_v + a_1 \mathbf{u}_v, \mathbf{w}_v) dt \\ &\quad + \int_I a(\mathbf{u}_u + a_2 \mathbf{u}_v, \mathbf{w}_v) dt + m(\mathbf{u}_v(0), \mathbf{w}_v(0)) \\ &\quad + \int_I a(\dot{\mathbf{u}}_u - \mathbf{u}_v, \mathbf{w}_u) dt + a(\mathbf{u}_u(0), \mathbf{w}_u(0)), \\ L(\mathbf{W}) &:= \int_I l(t; \mathbf{w}_v) dt \\ &\quad + a(\mathbf{u}_0, \mathbf{w}_u(0)) + m(\mathbf{v}_0, \mathbf{w}_v(0)), \end{aligned}$$

where

$$\begin{aligned} a(\mathbf{v}, \mathbf{w}) &:= \int_{\Omega} \boldsymbol{\varepsilon}(\mathbf{v}) : \boldsymbol{\mathcal{C}} : \boldsymbol{\varepsilon}(\mathbf{w}) d\Omega, \\ m(\mathbf{v}, \mathbf{w}) &:= \int_{\Omega} \rho \mathbf{v} \cdot \mathbf{w} d\Omega, \\ l(t; \mathbf{w}) &:= (\mathbf{f}(t), \mathbf{w}) + (\mathbf{g}(t), \mathbf{w})_{\Gamma_N}, \end{aligned}$$

and

$$(\mathbf{v}, \mathbf{w}) := \int_{\Omega} \mathbf{v} \cdot \mathbf{w} d\Omega, \quad (\mathbf{v}, \mathbf{w})_{\Gamma_N} := \int_{\Gamma_N} \mathbf{v} \cdot \mathbf{w} d\Gamma.$$

The weak problem (4) is a *double field* formulation, having two unknowns, displacements  $\mathbf{u}_u$  and velocities  $\mathbf{u}_v$ , which are a priori independent. That is, the velocity  $\mathbf{u}_v$  is not strongly enforced to coincide with  $\dot{\mathbf{u}}_u$ . However, the relation between displacements and velocities is weakly imposed by means of the term  $a(\dot{\mathbf{u}}_u - \mathbf{u}_v, \mathbf{w}_u)$ .

The initial conditions (1d) and (1e) are also weakly imposed introducing the terms  $a(\mathbf{u}_u(0) - \mathbf{u}_0, \mathbf{w}_u(0))$  and  $m(\mathbf{u}_v(0) - \mathbf{v}_0, \mathbf{w}_v(0))$  respectively. The weak problem (4) is consistent with the original strong problem (1) in the sense that the solution  $\mathbf{u}$  of problem (1) fulfills

$$B([\mathbf{u}, \dot{\mathbf{u}}], \mathbf{W}) = L(\mathbf{W}) \quad \forall \mathbf{W} \in \widehat{\mathcal{W}} \times \widehat{\mathcal{W}}.$$

The fully discrete version of problem (4) requires introducing a finite element partition of the domain  $\Omega$ , which in the framework of mesh adaptivity is allowed to be different at each time point in  $\mathcal{T}$ . The finite element mesh discretizing the spatial domain  $\Omega$  associated with time  $t_n \in \mathcal{T}$  is denoted in the following by  $\mathcal{P}_n$ . The associated finite element space of continuous, elementwise polynomials of degree  $p$  is referred as  $\mathcal{V}_0^H(\mathcal{P}_n) \subset \mathcal{V}_0$ . The notation emphasizing the dependence on  $\mathcal{P}_n$  highlights the fact that the finite

element space depends on the computational mesh. The upper-script  $H$  stands for the characteristic element size in the mesh and it is included in the notation to indicate the discrete character of the finite element space. In the case that different values of  $p$  have to be accounted for, the notation is completed adding  $p$  as upper-script, e.g. the spaces  $\mathcal{V}_0^{H,p}(\mathcal{P}_n)$  and  $\mathcal{V}_0^{H,p+1}(\mathcal{P}_n)$  are also used in the following.

The space meshes  $\mathcal{P}_n$  are built considering a hierarchical tree-based mesh refinement strategy [29, 30, 31]. In this framework, the computational meshes are obtained recursively splitting the elements of an initial background mesh denoted as  $\mathcal{P}_{\text{bg}}$  as shown in figure 1. Thus,  $\mathcal{V}_0^H(\mathcal{P}_{\text{bg}}) \subset \mathcal{V}_0^H(\mathcal{P}_n)$  for all the spatial meshes  $n = 0, \dots, N$ .

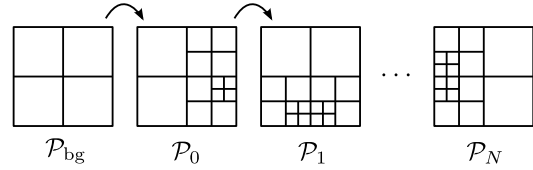


Figure 1: A hierarchical tree-based technique is used to build the space meshes  $\mathcal{P}_n$ ,  $n = 0, \dots, N$  from the background mesh  $\mathcal{P}_{\text{bg}}$ .

The tree-based structure enormously facilitates the mesh refinement and unrefinement operations as well as the data transfer between different meshes. However, this approach requires dealing with a conforming approximation on an irregular spatial meshes involving *hanging* or *irregular* nodes. A constrained finite element approximation is used to enforce the continuity of the finite element solution across the edges of the mesh containing hanging nodes (introducing constraints on the local basis functions). A detailed description is given in appendix A.

The fully discrete problem is obtained replacing in (4) the trial and test spaces  $\mathcal{W}$  and  $\widehat{\mathcal{W}}$  by their discrete counterparts. For the sake of simplicity and without loss of generality, the method is presented here for piecewise linear (in time) trial functions. Hence, the time dependence of the approximations for displacements and velocities corresponds to a linear interpolation inside the time intervals  $I_n$  (piecewise linear in  $I$ ). The space dependence is inherited from the spaces  $\mathcal{V}_0^H(\mathcal{P}_n)$ . The resulting discrete space-time functional spaces read

$$\begin{aligned} \mathcal{W}_u^{H,\Delta t} &:= \{\mathbf{w} \in \mathcal{W} : \mathbf{w}(0) = \mathbf{u}_0, \\ \mathbf{w}(t) &= \sum_{n=0}^N \theta_n(t) \mathbf{w}(t_n), \\ \mathbf{w}(t_n) &\in \mathcal{V}_0^H(\mathcal{P}_n), \quad n = 0, \dots, N\}, \end{aligned}$$

and

$$\begin{aligned}\mathcal{W}_v^{H,\Delta t} &:= \{\mathbf{w} \in \mathcal{W} : \mathbf{w}(0) = \mathbf{v}_0, \\ \mathbf{w}(t) &= \sum_{n=0}^N \theta_n(t) \mathbf{w}(t_n), \\ \mathbf{w}(t_n) &\in \mathcal{V}_0^H(\mathcal{P}_n), n = 0, \dots, N\},\end{aligned}$$

where  $\theta_n(t)$  are the linear shape functions associated with the time grid  $\mathcal{T}$ . Note that functions in  $\mathcal{W}_u^{H,\Delta t}$  and  $\mathcal{W}_v^{H,\Delta t}$  are continuous piecewise polynomials fulfilling the initial conditions for displacements and velocities respectively. Functions  $\mathbf{w} \in \mathcal{W}_u^{H,\Delta t}$  are such that at the points of the time grid,  $t_n \in \mathcal{T}$ , they belong to one of the standard Finite Element spaces, namely  $\mathbf{w}(t_n) \in \mathcal{V}_0^H(\mathcal{P}_n)$ . At an intermediate time  $t \in I_n$ ,  $t \neq t_n$ , function  $\mathbf{w}(t)$  belongs to  $\mathcal{V}_0^H(\mathcal{P}_{n-1}) + \mathcal{V}_0^H(\mathcal{P}_n)$ , that is the space generated by the superposition of the two meshes  $\mathcal{P}_n$  and  $\mathcal{P}_{n+1}$ , see figure 2. The same holds for functions in  $\mathcal{W}_v^{H,\Delta t}$ .

The fully discrete test space  $\widehat{\mathcal{W}}^{H,\Delta t}$  is defined as

$$\widehat{\mathcal{W}}^{H,\Delta t} := \{\mathbf{w} \in \widehat{\mathcal{W}} : \mathbf{w}|_{I_n} \in \mathbb{P}^0(I_n; \mathcal{V}_0^H(\mathcal{P}_n)), \\ n = 1, \dots, N\},$$

where  $\mathbb{P}^0(I_n; \mathcal{V}_0^H(\mathcal{P}_n))$  denotes the space of constant functions taking values in  $I_n$  and returning a value in  $\mathcal{V}_0^H(\mathcal{P}_n)$ . Functions in  $\widehat{\mathcal{W}}^{H,\Delta t}$  are continuous piecewise polynomials in space and piecewise constants in time. Function  $\mathbf{w} \in \widehat{\mathcal{W}}^{H,\Delta t}$  is such that, for a time  $t \in I_n$ ,  $\mathbf{w}(t) \in \mathcal{V}_0^H(\mathcal{P}_n)$ , see figure 2. The polynomial dependence in time of functions in  $\widehat{\mathcal{W}}^{H,\Delta t}$  is one degree lower (piecewise constants) than the polynomial dependence in time of the trial space  $\mathcal{W}_u^{H,\Delta t}$  (piecewise linear). In this case, the trial and test spaces have the same number of degrees of freedom.

Using the discrete trial and test spaces, the fully discrete problem reads: find  $\widetilde{\mathbf{U}} := [\widetilde{\mathbf{u}}_u, \widetilde{\mathbf{u}}_v] \in \mathcal{W}_u^{H,\Delta t} \times \mathcal{W}_v^{H,\Delta t}$  such that

$$B(\widetilde{\mathbf{U}}, \mathbf{W}) = L(\mathbf{W}) \quad \forall \mathbf{W} \in \widehat{\mathcal{W}}^{H,\Delta t} \times \widehat{\mathcal{W}}^{H,\Delta t}. \quad (5)$$

Problem (5) is integrated over the whole space-time domain  $\Omega \times I$ . However, having selected discontinuous test functions results in a time marching scheme that solves successively  $N$  problems in the time slabs  $\Omega \times I_n$ ,  $n = 1, \dots, N$ . Note that the step by step computational methodology resembles the classical time integration methods based on finite differences (i.e. Crank Nicholson, Newmark, etc.). In fact, if the mesh does not change, then the discrete displacements and velocities  $\widetilde{\mathbf{u}}_u$  and  $\widetilde{\mathbf{u}}_v$  at times  $t_n$ ,  $n = 1, \dots, N$ , coincide with the approximation given by the Newmark method with parameters  $\beta = 1/4$  and  $\gamma = 1/2$ , see [20] for a detailed proof. The actual resolution of problem (5) is detailed in appendix A.

### 2.3 Discretization error and error equation

The discretization error associated with  $\widetilde{\mathbf{U}}$  is defined as

$$\mathbf{E} := \mathbf{U} - \widetilde{\mathbf{U}} = [\mathbf{e}_u, \mathbf{e}_v] = [\mathbf{u} - \widetilde{\mathbf{u}}_u, \dot{\mathbf{u}} - \widetilde{\mathbf{u}}_v] \in \mathcal{W} \times \mathcal{W},$$

where  $\mathbf{e}_u$  and  $\mathbf{e}_v$  are the errors in displacements and velocities respectively. The error  $\mathbf{E}$  fulfills the following residual equation: find  $\mathbf{E} = [\mathbf{e}_u, \mathbf{e}_v] \in \mathcal{W} \times \mathcal{W}$  such that

$$B(\mathbf{E}, \mathbf{W}) = R(\mathbf{W}) := L(\mathbf{W}) - B(\widetilde{\mathbf{U}}, \mathbf{W}) \\ \forall \mathbf{W} \in \widehat{\mathcal{W}} \times \widehat{\mathcal{W}}, \quad (6)$$

which is derived replacing the exact solution  $\mathbf{U}$  by  $\widetilde{\mathbf{U}} + \mathbf{E}$  in (4) and using linearity of the forms  $B(\cdot, \cdot)$  and  $L(\cdot)$ .

The residual  $R(\cdot)$  fulfills the Galerkin orthogonality property

$$R(\mathbf{W}) = 0 \quad \text{for all } \mathbf{W} \in \widehat{\mathcal{W}}^{H,\Delta t} \times \widehat{\mathcal{W}}^{H,\Delta t}. \quad (7)$$

Although the Galerkin orthogonality property of the residual  $R(\cdot)$  is not necessary to derive an error estimate for the error in the quantity of interest, it is required in the space-time adaptive strategy in order to properly split the space and time error contributions.

## 3 Goal-oriented modal-based error assessment

### 3.1 Quantity of interest and adjoint problem

The proposed a posteriori error estimation adaptive strategy aims at assessing and controlling the discretization error  $\mathbf{E}$  measured using some specific quantity of interest. The quantity of interest is defined by means of a bounded linear functional  $L^\mathcal{O} : \mathcal{W} \times \mathcal{W} \rightarrow \mathbb{R}$  which extracts a single representative scalar value of the whole space-time solution, namely

$$L^\mathcal{O}(\mathbf{W}) := L_u^\mathcal{O}(\mathbf{w}_u) + L_v^\mathcal{O}(\mathbf{w}_v), \quad (8)$$

where  $L_u^\mathcal{O} : \mathcal{W} \rightarrow \mathbb{R}$  and  $L_v^\mathcal{O} : \mathcal{W} \rightarrow \mathbb{R}$  are linear functionals representing quantities of interest for displacements and velocities respectively.

The estimation of the value  $s^e := L^\mathcal{O}(\mathbf{E})$  requires introducing an auxiliary problem associated with the functional  $L^\mathcal{O}(\cdot)$ , usually denoted by *adjoint* or *dual* problem. The variational form of the adjoint problem reads: find  $\mathbf{U}^d := [\mathbf{u}_u^d, \mathbf{u}_v^d] \in \mathcal{W} \times \mathcal{W}$  such that

$$B(\mathbf{W}, \mathbf{U}^d) = L^\mathcal{O}(\mathbf{W}) \quad \forall \mathbf{W} \in \widehat{\mathcal{W}} \times \widehat{\mathcal{W}}. \quad (9)$$

The adjoint solution characterizes the quantity of interest  $L^\mathcal{O}(\cdot)$  in the sense that, if  $\mathbf{U}^d$  is available, then the functional  $L^\mathcal{O}(\cdot)$  coincides with  $B(\cdot, \mathbf{U}^d)$ , and in particular the computable quantity  $L(\mathbf{U}^d)$  is equal to the quantity of interest  $L^\mathcal{O}(\mathbf{U})$ .

In practice, the functional  $L^\mathcal{O}(\cdot)$  is selected with the same structure as  $L(\cdot)$ , namely

$$L_u^\mathcal{O}(\mathbf{w}_u) := a(\mathbf{u}^\mathcal{O}, \mathbf{w}_u(T)) \quad \text{and} \quad (10a)$$

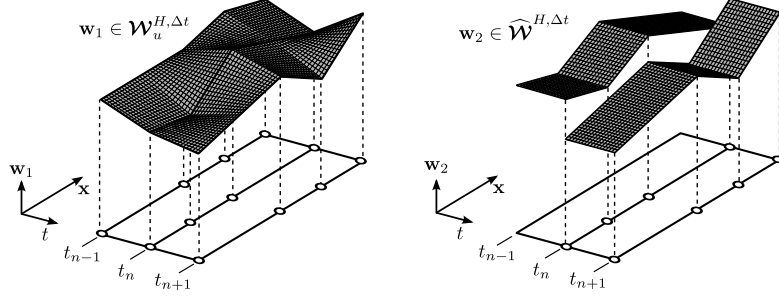


Figure 2: Illustration of two generic functions,  $\mathbf{w}_1 \in \mathcal{W}_u^{H,\Delta t}$  (left) and  $\mathbf{w}_2 \in \widehat{\mathcal{W}}^{H,\Delta t}$  (right), inside the time interval  $(t_{n-1}, t_{n+1}]$  when the time points  $t_{n-1}$ ,  $t_n$  and  $t_{n+1}$  have different computational meshes. The active nodes in meshes  $\mathcal{P}_{n-1}$ ,  $\mathcal{P}_n$  and  $\mathcal{P}_{n+1}$  are marked with circles ( $\circ$ ) on the  $x$ - $t$  plane.

$$L_v^{\mathcal{O}}(\mathbf{w}_v) := \int_0^T (\mathbf{f}^{\mathcal{O}}(t), \mathbf{w}_v(t)) dt + \int_0^T (\mathbf{g}^{\mathcal{O}}(t), \mathbf{w}_v(t))_{\Gamma_N} dt + m(\mathbf{v}^{\mathcal{O}}, \mathbf{w}_v(T)), \quad (10b)$$

where  $\mathbf{f}^{\mathcal{O}}$ ,  $\mathbf{g}^{\mathcal{O}}$ ,  $\mathbf{v}^{\mathcal{O}}$  and  $\mathbf{u}^{\mathcal{O}}$  are the data characterizing the quantity of interest. The functions  $\mathbf{f}^{\mathcal{O}}$  and  $\mathbf{g}^{\mathcal{O}}$  extract global or localized averages of velocities in  $\Omega$  and  $\Gamma_N$ , respectively, integrated over the whole time interval  $[0, T]$ . The fields  $\mathbf{v}^{\mathcal{O}}$  and  $\mathbf{u}^{\mathcal{O}}$  play the role of weighting functions to compute averages of velocities and strains at the final simulation time  $T$ .

For the description of  $L^{\mathcal{O}}(\cdot)$  given in (10), the weak adjoint problem (9) is equivalent to the following strong equation for the adjoint displacement  $\mathbf{u}^d$ ,

$$\rho(\ddot{\mathbf{u}}^d - a_1 \dot{\mathbf{u}}^d) - \nabla \cdot \boldsymbol{\sigma}^d(\mathbf{u}^d) = -\mathbf{f}^{\mathcal{O}} \quad \text{in } \Omega \times I, \quad (11a)$$

$$\mathbf{u}^d = \mathbf{0} \quad \text{on } \Gamma_D \times I, \quad (11b)$$

$$\boldsymbol{\sigma}^d(\mathbf{u}^d) \cdot \mathbf{n} = -\mathbf{g}^{\mathcal{O}} \quad \text{on } \Gamma_N \times I, \quad (11c)$$

$$\mathbf{u}^d = \mathbf{u}^{\mathcal{O}} \quad \text{at } \Omega \times \{T\}, \quad (11d)$$

$$\dot{\mathbf{u}}^d = \mathbf{v}^{\mathcal{O}} \quad \text{at } \Omega \times \{T\}, \quad (11e)$$

with the constitutive law

$$\boldsymbol{\sigma}^d(\mathbf{u}^d) := \mathcal{C} : \boldsymbol{\varepsilon}(\mathbf{u}^d - a_2 \dot{\mathbf{u}}^d). \quad (12)$$

The strong problem (11) has the same structure as the original one (1) except that the terms affected by  $a_1$  and  $a_2$  have opposite sign and the conditions (11d) and (11e) are stated for  $t = T$  instead that for  $t = 0$  (final conditions instead of initial). Thus, the adjoint problem is solvable and stable if integrated backwards in time. The change of sign in the time direction brings the adjoint problem back to the same features and properties as the direct one.

### 3.2 Error representation

The adjoint problem allows rewriting the error in the quantity of interest in terms of residuals, combining the original and adjoint problems. Indeed, taking  $\mathbf{W} = \mathbf{U}^d$  in

the error equation (6) and using the definition of the adjoint problem, the following representation for  $s^e$  is found

$$s^e := R(\mathbf{U}^d). \quad (13)$$

This error representation is useful because states that the error in the quantity of interest can be exactly computed if the adjoint solution  $\mathbf{U}^d$  is available. Moreover, in an error estimation setup where the exact adjoint solution is not known, replacing  $\mathbf{U}^d$  by a computable approximation  $\tilde{\mathbf{U}}^d$  in (13) gives an accurate approximation of the error in the quantity of interest

$$s^e \approx R(\tilde{\mathbf{U}}^d) =: \tilde{s}^e. \quad (14)$$

The scalar estimate  $\tilde{s}^e$  provides a single scalar quantity accounting both for the total error associated with the space and time discretizations and therefore, it does not directly provide enough information to adapt separately the space and time discretizations.

The error representation (13) is rewritten in such a way that the contributions of the space and time discretization errors are separated. This is achieved by introducing projection operators  $\Pi^H$  and  $\Pi^{\Delta t}$  associated with the space and time discretizations.

The spatial projection  $\Pi^H$  is defined for a function in  $\mathbf{W} \in \widehat{\mathcal{W}} \times \widehat{\mathcal{W}}$  and provides a function which is discrete in space. The spatial discretization (the mesh) varies along the time but it is constant in a time interval  $I_n$ . Thus, the operator  $\Pi^H$  is defined for  $t \in I_n$ ,  $n = 1, \dots, N$ , as

$$[\Pi^H \mathbf{W}](t) := [\pi_n^H \mathbf{w}_u(t), \pi_n^H \mathbf{w}_v(t)],$$

being  $\pi_n^H$  the standard interpolation operator from  $\mathcal{V}_0$  into  $\mathcal{V}_0^H(\mathcal{P}_n)$ . On the other hand, the projection in time operator  $\Pi^{\Delta t}$  maps the time-dependent function  $\mathbf{W} \in \widehat{\mathcal{W}} \times \widehat{\mathcal{W}}$  into a piecewise constant in time function. This projection is defined by taking the average of its displacement and velocity components inside each time interval  $I_n$

$$[\Pi^{\Delta t} \mathbf{W}]|_{I_n} := [\pi_n^{\Delta t} \mathbf{w}_u, \pi_n^{\Delta t} \mathbf{w}_v],$$

where

$$\pi_n^{\Delta t} \mathbf{w} := \frac{1}{\text{meas}(I_n)} \int_{I_n} \mathbf{w} dt.$$

**Remark 1.** Figure 3 illustrates the projection operators  $\Pi^H$  and  $\Pi^{\Delta t}$  using a generic function  $\mathbf{W} \in \widehat{\mathcal{W}} \times \widehat{\mathcal{W}}$ . Function  $\Pi^H \mathbf{W}$  belongs to the space  $\widehat{\mathcal{W}}^H \times \widehat{\mathcal{W}}^H$ , where

$$\widehat{\mathcal{W}}^H := \{\mathbf{w} \in \widehat{\mathcal{W}} : \mathbf{w}|_{I_n} \in L^2(I_n; \mathcal{V}_0^H(\mathcal{P}_n)), \text{ and } \dot{\mathbf{w}}|_{I_n} \in L^2(I_n; (\mathcal{V}_0^H(\mathcal{P}_n))') \ n = 1, \dots, N\}.$$

Note that  $\Pi^H \mathbf{W}$  is discrete in space: for each particular time  $t \in I$ , function  $[\Pi^H \mathbf{W}](t)$  belongs to one of the discrete finite elements spaces  $\mathcal{V}_0^H(\mathcal{P}_n) \times \mathcal{V}_0^H(\mathcal{P}_n)$ . However, the time description of  $\Pi^H \mathbf{W}$  is infinite dimensional: for a given  $\mathbf{x} \in \Omega$ ,  $\Pi^H \mathbf{W}(\mathbf{x}, \cdot) \in L^2(I) \times L^2(I)$ .

On the other hand, the function  $\Pi^{\Delta t} \mathbf{W}$  belong to  $\widehat{\mathcal{W}}^{\Delta t} \times \widehat{\mathcal{W}}^{\Delta t}$ , where

$$\widehat{\mathcal{W}}^{\Delta t} := \{\mathbf{w} \in \widehat{\mathcal{W}} : \mathbf{w}|_{I_n} \in \mathbb{P}^0(I_n; \mathcal{V}_0), \ n = 1, \dots, N\}.$$

Note that  $\Pi^{\Delta t} \mathbf{W}$  is piecewise constant in time, but its spatial description is infinite dimensional, namely  $\Pi^{\Delta t} \mathbf{W}(\cdot, t) \in \mathcal{V}_0 \times \mathcal{V}_0$ .

Once the space and time projections are introduced, the space and time errors are separated adding the value  $R(\Pi^H \mathbf{U}^d) - R(\Pi^H \mathbf{U}^d) + R(\Pi^H \Pi^{\Delta t} \mathbf{U}^d)$  in the right hand side of (13) (the latter term vanishes due to the Galerkin orthogonality property because  $\Pi^H \Pi^{\Delta t} \mathbf{U}^d \in \widehat{\mathcal{W}}^{H, \Delta t} \times \widehat{\mathcal{W}}^{H, \Delta t}$ ). That is,

$$s^e = \underbrace{R(\mathbf{U}^d - \Pi^H \mathbf{U}^d)}_{=: s_s^e} + \underbrace{R(\Pi^H (\mathbf{U}^d - \Pi^{\Delta t} \mathbf{U}^d))}_{=: s_t^e}. \quad (15)$$

The terms  $s_s^e$  and  $s_t^e$  are associated with the space and time discretization errors respectively. Note that  $s_s^e$  tends to zero as the space discretization is refined because  $\Pi^H \mathbf{U}^d$  tends to  $\mathbf{U}^d$ . Similarly,  $s_t^e$  tends to zero with  $\Delta t$  because  $\Pi^{\Delta t} \mathbf{U}^d$  tends to  $\mathbf{U}^d$ . The space and time error components  $s_s^e$  and  $s_t^e$  are used as refinement indicators because they can be reduced independently by respectively enriching the space and time discretizations.

The space and time splitting is straightforwardly transformed to the estimated version of the error  $\tilde{s}^e$ , replacing  $\mathbf{U}^d$  by the computable approximation  $\tilde{\mathbf{U}}^d$  in equation (15), namely

$$\tilde{s}^e = \tilde{s}_s^e + \tilde{s}_t^e, \quad (16)$$

where  $\tilde{s}_s^e := R(\tilde{\mathbf{U}}^d - \Pi^H \tilde{\mathbf{U}}^d)$  and  $\tilde{s}_t^e := R(\Pi^H \tilde{\mathbf{U}}^d - \Pi^H \Pi^{\Delta t} \tilde{\mathbf{U}}^d)$  are the computable space and time error contributions.

### 3.3 Modal-based adjoint approximation

The error estimate  $\tilde{s}^e$  is computable once the adjoint approximation  $\tilde{\mathbf{U}}^d$  is available. Typically, the adjoint approximation is computed using the same code used for the original problem (1), i.e. using direct time-integration methods, see reference [20]. An alternative approach proposed

in [24] considers modal analysis to compute the adjoint approximation. The modal-based strategy is particularly well suited for some particular quantities of interest and allows effectively computing and storing the adjoint problem. In that case, the adjoint solution is stored for each vibration mode instead of for each time step.

Modal analysis requires introducing the semidiscrete equation (discrete in space but exact in time) associated with the adjoint problem (11). Consequently, a discrete version of the functional space  $\mathcal{V}_0$  is required. The semidiscrete problem is defined using the finite element space  $\mathcal{V}_0^{H, p+1}(\mathcal{P}_{\text{bg}})$ , that stands for the finite element space associated with the mesh  $\mathcal{P}_{\text{bg}}$  of degree of interpolation  $p+1$  (a  $p$ -refined version of  $\mathcal{V}_0^H(\mathcal{P}_{\text{bg}})$ ). Having a  $p+1$  degree approximation of the adjoint solution,  $\tilde{\mathbf{U}}^d$ , precludes the Galerkin orthogonality effect and the corresponding underestimation of the error, see [24]. Recall that, along the adaptive process, the background mesh is used as the base to build up all the adapted meshes by local refinement. Thus, the representation of  $\tilde{\mathbf{U}}^d$  in the adapted mesh is simplified if  $\tilde{\mathbf{U}}^d$  is in  $\mathcal{V}_0^{H, p+1}(\mathcal{P}_{\text{bg}})$ .

With these definitions, the semidiscrete problem reads: find  $\mathbf{u}^{d, H, p+1}(t) \in \mathcal{V}_0^{H, p+1}(\mathcal{P}_{\text{bg}})$  verifying the final conditions  $\mathbf{u}^{d, H, p+1}(T) = \mathbf{u}^{\mathcal{O}}$  and  $\dot{\mathbf{u}}^{d, H, p+1}(T) = \mathbf{v}^{\mathcal{O}}$  and such that for all  $t \in I$

$$m(\ddot{\mathbf{u}}^{d, H, p+1}(t) - a_1 \dot{\mathbf{u}}^{d, H, p+1}(t) + a(\mathbf{u}^{d, H, p+1}(t) - a_2 \dot{\mathbf{u}}^{d, H, p+1}(t), \mathbf{w}) = -l^{\mathcal{O}}(t; \mathbf{w}) \quad \forall \mathbf{w} \in \mathcal{V}_0^{H, p+1}(\mathcal{P}_{\text{bg}}), \quad (17)$$

where  $l^{\mathcal{O}}(t; \mathbf{w}) := (\mathbf{f}^{\mathcal{O}}(t), \mathbf{w}) + (\mathbf{g}^{\mathcal{O}}(t), \mathbf{w})_{\Gamma_N}$ .

Equation (17) leads to an algebraic system of second order ordinary differential equations which is conveniently rewritten using the eigenvalues and eigenfunctions of the problem: find  $(\tilde{\omega}, \tilde{\mathbf{q}}) \in \mathbb{R} \times \mathcal{V}_0^{H, p+1}(\mathcal{P}_{\text{bg}})$  such that

$$a(\tilde{\mathbf{q}}, \mathbf{w}) = \tilde{\omega}^2 m(\tilde{\mathbf{q}}, \mathbf{w}) \quad \forall \mathbf{w} \in \mathcal{V}_0^{H, p+1}(\mathcal{P}_{\text{bg}}). \quad (18)$$

Note that the number of eigenpairs solution of this problem is the number of degrees of freedom in the finite element space  $\mathcal{V}_0^{H, p+1}(\mathcal{P}_{\text{bg}})$ , denoted by  $N_{\text{dof}}$ . The eigenpairs are sorted from low to high frequencies, namely  $\tilde{\omega}_1 \leq \tilde{\omega}_2 \leq \dots \leq \tilde{\omega}_{N_{\text{dof}}}$ , and the eigenfunctions are normalized to be orthonormal with respect the mass product, i.e.

$$m(\tilde{\mathbf{q}}_i, \tilde{\mathbf{q}}_j) = \delta_{ij}, \quad 1 \leq i, j \leq N_{\text{dof}}. \quad (19)$$

The semidiscrete approximation  $\mathbf{u}^{d, H, p+1}$  is expressed as a linear combination of the eigenfunctions  $\tilde{\mathbf{q}}_i$

$$\mathbf{u}^{d, H, p+1}(\mathbf{x}, t) = \sum_{i=1}^{N_{\text{dof}}} \tilde{\mathbf{q}}_i(\mathbf{x}) \tilde{y}_i(t). \quad (20)$$

Thus, the new unknowns of the problem are the time-dependent coefficients  $\tilde{y}_i(t)$ ,  $i = 1, \dots, N_{\text{dof}}$ . The representation in terms of the unknowns  $\tilde{y}_i(t)$  given in (20) allows uncoupling the system (17) into a set of ordinary

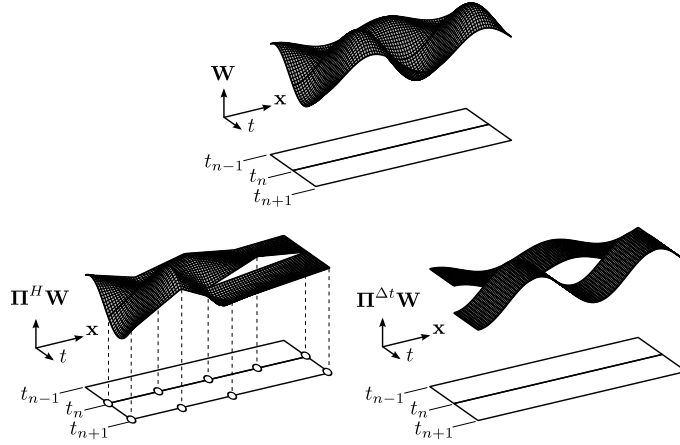


Figure 3: Illustration of the projection operators  $\Pi^H$  and  $\Pi^{\Delta t}$ . The figure displays (one field of) the original function  $\mathbf{W} \in \widehat{\mathcal{W}} \times \widehat{\mathcal{W}}$  inside the time intervals  $I_n = (t_{n-1}, t_n]$  and  $I_{n+1} = (t_n, t_{n+1}]$  (top) along with its projections in space and time  $\Pi^H \mathbf{W} \in \widehat{\mathcal{W}}^H \times \widehat{\mathcal{W}}^H$  (left) and  $\Pi^{\Delta t} \mathbf{W} \in \widehat{\mathcal{W}}^{\Delta t} \times \widehat{\mathcal{W}}^{\Delta t}$  (right).

differential equations, namely

$$\ddot{y}_i - [a_1 + a_2(\tilde{\omega}_i)^2]\dot{y}_i + (\tilde{\omega}_i)^2 y_i = \tilde{l}_i, \quad (21a)$$

$$y_i^H(T) = \tilde{u}_i, \quad (21b)$$

$$\dot{y}_i^H(T) = \tilde{v}_i, \quad (21c)$$

where the r.h.s. terms  $l_i$ ,  $u_i$  and  $v_i$  are computed using the data characterizing the quantity of interest (10) and the eigenfunction  $\tilde{\mathbf{q}}_i$

$$\begin{aligned} \tilde{l}_i(t) &:= (\mathbf{f}^\mathcal{O}(t), \tilde{\mathbf{q}}_i) + (\mathbf{g}^\mathcal{O}(t), \tilde{\mathbf{q}}_i)_{\Gamma_N}, \\ \tilde{u}_i &:= m(\mathbf{u}^\mathcal{O}, \tilde{\mathbf{q}}_i) \text{ and } \tilde{v}_i := m(\mathbf{v}^\mathcal{O}, \tilde{\mathbf{q}}_i). \end{aligned} \quad (22)$$

The time dependent coefficients  $\tilde{y}_i(t)$ ,  $i = 1, \dots, N_{\text{dof}}$ , may be computed analytically for many particular cases of the forcing data. The particular solution for constant-in-time data is given in [24]. Therefore the value of the adjoint solution  $\mathbf{u}^{\text{d},H,p+1}$  at any time  $t \in I$  is easily reconstructed from the computed eigenfunctions  $\tilde{\mathbf{q}}_i$  and the analytically computed time-dependent functions  $\tilde{y}_i(t)$  using expression (20).

In practice, it is not feasible to compute all the eigenpairs  $(\tilde{\omega}_i, \tilde{\mathbf{q}}_i)$ ,  $i = 1, \dots, N_{\text{dof}}$  and consequently the modal expansion (20) has to be truncated to the first  $M \ll N_{\text{dof}}$  terms, namely

$$\tilde{\mathbf{u}}^{\text{d}}(\mathbf{x}, t) := \sum_{i=1}^M \tilde{\mathbf{q}}_i(\mathbf{x}) \tilde{y}_i(t). \quad (23)$$

The number of required vibration modes  $M$  has to be selected such that the truncated high frequency modes (for  $i > M$ ) are negligible. That is,  $M$  is such that  $\tilde{\mathbf{u}}^{\text{d}}$  is a good approximation to  $\mathbf{u}^{\text{d},H,p+1}$ . This is equivalent to assume that for  $i > M$  the values of  $\tilde{l}_i$ ,  $\tilde{u}_i$  and  $\tilde{v}_i$ , as defined in (22), are close to zero, and consequently  $\tilde{y}_i(t) \approx 0$ . This is

guaranteed if the data  $\mathbf{f}^\mathcal{O}$ ,  $\mathbf{g}^\mathcal{O}$ ,  $\mathbf{u}^\mathcal{O}$  and  $\mathbf{v}^\mathcal{O}$  are well captured by the expansion of the first  $M$  eigenvectors. Consequently, a quantity of interest can be easily treated with the modal-based approach if its associated data  $\mathbf{f}^\mathcal{O}$ ,  $\mathbf{g}^\mathcal{O}$ ,  $\mathbf{u}^\mathcal{O}$  and  $\mathbf{v}^\mathcal{O}$  are well captured by the expansion of the first  $M$  eigenfunctions.

Once the computable adjoint approximation  $\tilde{\mathbf{u}}^{\text{d}}$  is available, the double field approximation  $\tilde{\mathbf{U}}^{\text{d}}$  used in the error estimate  $\tilde{s}^e$  given in (14) is readily defined as  $\tilde{\mathbf{U}}^{\text{d}} := [\tilde{\mathbf{u}}^{\text{d}}, \tilde{\mathbf{u}}^{\text{d}}]$ .

## 4 Space-time Adaptivity

### 4.1 Adaptivity framework

The space-time adaptive strategy aims at finding a time discretization  $\mathcal{T}$  and a space discretization  $\mathcal{P}_n$  at each time point  $t_n \in \mathcal{T}$  such that 1) they keep the error  $s^e$  below a user-prescribed tolerance  $s_{\text{tol}}^e$  and 2) they are optimal in the sense that they minimize the computational cost. In practice, the accuracy prescription is enforced for the estimated error and the property which is actually achieved is

$$|\tilde{s}^e| \leq s_{\text{tol}}^e. \quad (24)$$

Changing the space discretization at each time step  $t_n \in \mathcal{T}$  is not computationally affordable. This is because remeshing operations, matrix assembly and data transfer between different meshes are costly operations and cannot, in general, be performed at each time step. Here, an adaptive strategy organized in time-blocks, similar to the one proposed in reference [19], is adopted in order to reduce the number of mesh changes.

The blockwise adaptive strategy consist in splitting the time interval  $I$  into  $N^{\text{bk}}$  time intervals (or time blocks)

The time interval  $I$  is split into  $N^{\text{bk}}$  time intervals (or time blocks)

$$I_m^{\text{bk}} := \left( \frac{T}{N^{\text{bk}}}(m-1), \frac{T}{N^{\text{bk}}}m \right], \quad m = 1, \dots, N^{\text{bk}}.$$

The blockwise adaptive strategy consists taking the same space mesh inside each time interval  $I_m^{\text{bk}}$ , this mesh is denoted as  $\mathcal{P}_m^{\text{bk}}$  for  $m = 1, \dots, N^{\text{bk}}$ , see figure 4. Note that with this definition the computational meshes  $\mathcal{P}_n$  associated with the time points  $t_n \in I_m^{\text{bk}}$  are such that  $\mathcal{P}_n = \mathcal{P}_m^{\text{bk}}$ . A generic element of the mesh  $\mathcal{P}_m^{\text{bk}}$  is denoted by  $\Omega_k^m$ ,  $k = 1, \dots, N_m^{\text{el}}$ , where  $N_m^{\text{el}}$  is the number of elements in  $\mathcal{P}_m^{\text{bk}}$ .

Additionally, the time step length is assumed to be constant inside the intervals  $I_m^{\text{bk}}$  and denoted by  $\Delta t_m^{\text{bk}}$ . Consequently, the time step length  $\Delta t_n$  associated with times  $t_n \in I_m^{\text{bk}}$  are such that  $\Delta t_n = \Delta t_m^{\text{bk}}$ , see figure 4.

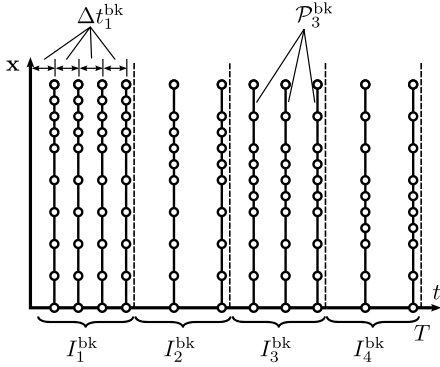


Figure 4: The space mesh is assumed to be constant inside the time intervals  $I_m^{\text{bk}}$ . Analogously, the time step length is taken constant inside each interval  $I_m^{\text{bk}}$ .

Following this approach and notation, the adaptive strategy is reformulated as computing the optimal space meshes  $\mathcal{P}_m^{\text{bk}}$  and time step lengths  $\Delta t_m^{\text{bk}}$ , for all the time intervals  $I_m^{\text{bk}}$ ,  $m = 1, \dots, N^{\text{bk}}$  such that the associated numerical solution fulfills (24).

Once the adjoint solution is computed and stored in the  $p+1$  version of the background mesh (keeping the same geometry and topology but increasing the degree of polynomials from  $p$  to  $p+1$ ), the main stages of the adaptive procedure are summarized as follows. The numerical solution is computed sequentially starting from the first time block  $I_1^{\text{bk}}$  until the last one  $I_{N^{\text{bk}}}^{\text{bk}}$ . In each time slab  $I_m^{\text{bk}}$ , the numerical solution is computed and the corresponding local error contributions are estimated. The computed solution in  $I_m^{\text{bk}}$  is *accepted* or *rejected* using the information given by the local error contributions. The specific acceptability criterion is detailed later. If the solution is accepted, the loop goes to the following time interval  $I_{m+1}^{\text{bk}}$ . Else, the space or time discretization (or both) associated with the interval  $I_m^{\text{bk}}$  are adapted using the local error information and the solution is re-computed in  $I_m^{\text{bk}}$ . The process of adapting the discretization and computing the numerical

solution is repeated in the interval  $I_m^{\text{bk}}$  until the solution is accepted.

The forthcoming subsections describe in detail 1) the local error contributions driving the adaptive process, 2) the criterion used to accept or reject the solution in each interval  $I_m^{\text{bk}}$  and 3) how to adapt the space and time discretizations when required.

## 4.2 Local error contributions

The space and time error estimates  $\tilde{s}_s^e$  and  $\tilde{s}_t^e$  are decomposed into contributions associated with the time blocks  $I_m^{\text{bk}}$ ,  $m = 1, \dots, N^{\text{bk}}$ , namely

$$\eta_m^s := R_{I_m^{\text{bk}}}(\tilde{\mathbf{U}}^d - \Pi^H \tilde{\mathbf{U}}^d), \quad \text{and}$$

$$\eta_m^t := R_{I_m^{\text{bk}}}(\Pi^H(\tilde{\mathbf{U}}^d - \Pi^{\Delta t} \tilde{\mathbf{U}}^d))$$

such that

$$\tilde{s}_s^e = \sum_{m=1}^{N^{\text{bk}}} \eta_m^s \quad \text{and} \quad \tilde{s}_t^e = \sum_{m=1}^{N^{\text{bk}}} \eta_m^t.$$

The local residual  $R_{I_m^{\text{bk}}}(\cdot)$  is the restriction of the residual  $R(\cdot)$  to the time interval  $I_m^{\text{bk}}$ ,

$$\begin{aligned} R_{I_m^{\text{bk}}}(\mathbf{W}) &:= \int_{I_m^{\text{bk}}} [(\mathbf{f}, \mathbf{w}_v) + (\mathbf{g}, \mathbf{w}_v)_{\Gamma_N}] \, dt \\ &\quad - \int_{I_m^{\text{bk}}} m(\dot{\tilde{\mathbf{u}}}_v + a_1 \tilde{\mathbf{u}}_v, \mathbf{w}_v) \, dt \\ &\quad + \int_{I_m^{\text{bk}}} a(\tilde{\mathbf{u}}_u + a_2 \tilde{\mathbf{u}}_v, \mathbf{w}_v) \, dt \\ &\quad - \int_{I_m^{\text{bk}}} a(\dot{\tilde{\mathbf{u}}}_u - \tilde{\mathbf{u}}_v, \mathbf{w}_u) \, dt. \end{aligned}$$

The indicator  $\eta_m^t$  is used to decide if the time discretization inside  $I_m^{\text{bk}}$  has to be modified. The criteria on whether the time grid has to be modified and how it has to be modified are presented in section 4.3.

The value of  $\eta_m^s$  is the indicator used to decide if the space mesh  $\mathcal{P}_m^{\text{bk}}$  in the time interval  $I_m^{\text{bk}}$  has to be further adapted. Again, the detailed criteria are introduced in section 4.3. In the case the mesh is to be adapted, the required local error indicators are obtained by restricting the space integrals involved in  $\eta_m^s$  to the elements  $\Omega_k^m$ . That is,

$$\eta_{m,k}^s := R_{\Omega_k^m \times I_m^{\text{bk}}}(\tilde{\mathbf{U}}^d - \Pi^H \tilde{\mathbf{U}}^d),$$

where

$$\begin{aligned} R_{\Omega_k^m \times I_m^{\text{bk}}}(\mathbf{W}) &:= \int_{I_m^{\text{bk}}} [(\mathbf{f}, \mathbf{w}_v)_{\Omega_k^m} + (\mathbf{g}, \mathbf{w}_v)_{\partial\Omega_k^m \cap \Gamma_N}] \, dt \\ &\quad - \int_{I_m^{\text{bk}}} m(\dot{\tilde{\mathbf{u}}}_v + a_1 \tilde{\mathbf{u}}_v, \mathbf{w}_v)_{\Omega_k^m} \, dt \\ &\quad + \int_{I_m^{\text{bk}}} a(\tilde{\mathbf{u}}_u + a_2 \tilde{\mathbf{u}}_v, \mathbf{w}_v)_{\Omega_k^m} \, dt \\ &\quad - \int_{I_m^{\text{bk}}} a(\dot{\tilde{\mathbf{u}}}_u - \tilde{\mathbf{u}}_v, \mathbf{w}_u)_{\Omega_k^m} \, dt. \end{aligned}$$

Note that the error estimate  $\bar{s}^e$  is expressed as the sum of the local error contributions defined above

$$\bar{s}^e = \sum_{m=1}^{N^{bk}} \left( \sum_{k=1}^{N_m^{el}} \eta_{m,k}^s \right) + \sum_{m=1}^{N^{bk}} \eta_m^t.$$

### 4.3 Acceptability and remeshing criteria

Following references [20, 19], the total target error  $s_{\text{tol}}^e$  is split into two error targets,  $\alpha_s s_{\text{tol}}^e$  and  $\alpha_t s_{\text{tol}}^e$ , associated with the space and time errors. The coefficients  $\alpha_s$  and  $\alpha_t$  are two user-defined positive values such that  $\alpha_s + \alpha_t = 1$  used to balance the space and time contributions to the total error. This leaves a free parameter to be tuned by the user, who must decide the amount of the total error  $s_{\text{tol}}^e$  assigned to the space and time discretizations. Discussing the optimal values for  $\alpha_s$  and  $\alpha_t$  is beyond the scope of this paper.

Thus, in order to achieve the accuracy prescription stated in (24), the adaptive strategy is designed aiming at finding a numerical solution such that

$$|\bar{s}_s^e| \leq \alpha_s s_{\text{tol}}^e \quad \text{and} \quad |\bar{s}_t^e| \leq \alpha_t s_{\text{tol}}^e. \quad (25)$$

Note that (25) guarantees that equation (24) holds, because

$$|\bar{s}^e| = |\bar{s}_s^e + \bar{s}_t^e| \leq |\bar{s}_s^e| + |\bar{s}_t^e| \leq \alpha_s s_{\text{tol}}^e + \alpha_t s_{\text{tol}}^e = s_{\text{tol}}^e.$$

The conditions (25) are more restrictive than (24). This is because in (24)  $\bar{s}_s^e$  and  $\bar{s}_t^e$  with different sign may cancel each other. The error compensation is not accounted for in (25) and therefore the resulting criterion is more demanding.

The error contributions are assumed to be uniformly distributed in time. That is, the space and time error tolerances,  $\alpha_s s_{\text{tol}}^e$  and  $\alpha_t s_{\text{tol}}^e$ , are divided into equal contributions associated with each time block  $I_m^{bk}$ . Thus, the solution is considered to be acceptable if

$$|\eta_m^s| \leq \frac{\alpha_s s_{\text{tol}}^e}{N^{bk}}, \quad (26a)$$

$$|\eta_m^t| \leq \frac{\alpha_t s_{\text{tol}}^e}{N^{bk}}. \quad (26b)$$

If the restrictions (26) hold, then the inequalities (25) are fulfilled, because

$$\begin{aligned} |\bar{s}_s^e| &= \left| \sum_{m=1}^{N^{bk}} \eta_m^s \right| \leq \sum_{m=1}^{N^{bk}} |\eta_m^s| \leq \alpha_s s_{\text{tol}}^e \quad \text{and} \\ |\bar{s}_t^e| &= \left| \sum_{m=1}^{N^{bk}} \eta_m^t \right| \leq \sum_{m=1}^{N^{bk}} |\eta_m^t| \leq \alpha_t s_{\text{tol}}^e. \end{aligned} \quad (27)$$

Similarly as when splitting the space and time contributions, criteria (26) are stronger than (25). This is more relevant for large values of  $N^{bk}$ , because the effect of the *triangular* inequalities in the equations (27) is more important. Thus, the adapted numerical solution might be very conservative if the number of blocks  $N^{bk}$  is large.

An additional condition is added to (26) in order to allow unrefinement (mesh coarsening). Note that the conditions (26) indicate only if the solution is acceptable and, if not, if the mesh has to be refined. They do not provide a criterion to unrefine the discretization when the error indicators  $\eta_m^s$  and  $\eta_m^t$  are small enough. Following reference [20], a lower bound based acceptability criterion is added to (26):

$$\beta_s \frac{\alpha_s s_{\text{tol}}^e}{N^{bk}} \leq |\eta_m^s|, \quad (28a)$$

$$\beta_t \frac{\alpha_t s_{\text{tol}}^e}{N^{bk}} \leq |\eta_m^t|, \quad (28b)$$

where the coefficients  $\beta_s$  and  $\beta_t$  are two user-defined values such that  $\beta_s, \beta_t \in [0, 1)$ . If the solution does not fulfill condition (28b), then the time discretization is modified (in this case unrefined). If (28a) is violated, then the space mesh is modified and it is expected to be globally coarsened. However, the space mesh adaption is performed locally and may result in refining some parts of the domain while others are unrefined. The space remeshing criterion is described below. The coarsening criterion (28) is only checked once for each time block. This is because the need of unrefining the space or the time grid is expected to be detected with the first discretization. Moreover, checking for unrefining at each adaptive step may result in an unstable scheme.

As previously said, conditions (26) and (28) are the criteria allowing to decide if the numerical solution is accepted or rejected inside the interval  $I_m^{bk}$ . If conditions (26) and (28) hold (or only (26) after the first adaptive iteration), then the solution is accepted. Otherwise, the space and/or time discretizations are modified.

The time adaptivity is carried out, depending on the value of  $\eta_m^t$ , by either refining the discretization by halving the time step  $\Delta t_m^{bk}$  (if (26b) is violated) or doubling it (if (28b) is violated). If both (26b) and (28b) hold, the time discretization is unchanged.

If either (26a) or (28a) are not fulfilled, the space mesh is to be modified. Then, local criterion is required to decide which elements have to be refined or unrefined, depending on the value of the local indicators  $\eta_{m,k}^s$ ,  $k = 1, \dots, N_m^{el}$  (for a given  $m = 1, \dots, N^{bk}$ ). Similarly as for the time discretization, the elements to be refined are subdivided (the element size divided by two) while the elements to be coarsened are collapsed with the neighboring elements, doubling the element size. In order to set up a space remeshing criterion, the optimal mesh is assumed to yield a uniform error distribution. Thus, the local versions (restricted to the contributions associated with element  $\Omega_k^m$ ) of the conditions (26a) and (28a) read

$$\gamma_m \beta_s \frac{\alpha_s s_{\text{tol}}^e}{N^{bk} N_m^{el}} \leq |\eta_{m,k}^s| \leq \gamma_m \frac{\alpha_s s_{\text{tol}}^e}{N^{bk} N_m^{el}}, \quad (29)$$

where

$$\gamma_m := \frac{\sum_{k=1}^{N_m^{el}} |\eta_{m,k}^s|}{\sum_{k=1}^{N_m^{el}} \eta_{m,k}^s} \geq 1.$$

The coefficient  $\gamma_m$  is introduced in order to mitigate the cancellation effect, see reference [32]. It is worth noting

that introducing the factor  $\gamma_m$  does not introduce a distortion in the criterion: if all the local element error contributions fulfill (29), then equation (28a) holds. This is shown by noting that

$$|\eta_m^s| = \left| \sum_{k=1}^{N_m^{\text{el}}} \eta_{m,k}^s \right| = \frac{1}{\gamma_m} \left( \sum_{k=1}^{N_m^{\text{el}}} |\eta_{m,k}^s| \right)$$

and therefore

$$\beta_s \frac{\alpha_s s_{\text{tol}}^e}{N^{\text{bk}}} = \frac{1}{\gamma_m} \left( \sum_{k=1}^{N_m^{\text{el}}} \gamma_m \beta_s \frac{\alpha_s s_{\text{tol}}^e}{N^{\text{bk}} N_m^{\text{el}}} \right) \leq \frac{1}{\gamma_m} \left( \sum_{k=1}^{N_m^{\text{el}}} |\eta_{m,k}^s| \right) = |\eta_m^s|$$

and

$$\frac{\alpha_s s_{\text{tol}}^e}{N^{\text{bk}}} = \frac{1}{\gamma_m} \left( \sum_{k=1}^{N_m^{\text{el}}} \gamma_m \frac{\alpha_s s_{\text{tol}}^e}{N^{\text{bk}} N_m^{\text{el}}} \right) \geq \frac{1}{\gamma_m} \left( \sum_{k=1}^{N_m^{\text{el}}} |\eta_{m,k}^s| \right) = |\eta_m^s|.$$

The complete space-time adaptive strategy is summarized in algorithm 1.

## 5 Numerical Examples

### 5.1 Example 1: perforated plate under impulse loading

This example illustrates the performance of the proposed space-time adaptive strategy in a 2D wave propagation problem. The computational domain  $\Omega$  is a perforated rectangular plate,  $\Omega := (-0.5, 0.5) \times (0, 0.5) \setminus \Omega_0$  m<sup>2</sup>, with  $\Omega_0 := \{(x, y) \in \mathbb{R}^2 : x^2 + (y - 0.25)^2 \leq 0.025^2\}$  m<sup>2</sup>, see figure 5. The plate is clamped at the bottom side and the horizontal displacement is blocked at both vertical sides. The plate is initially at rest,  $\mathbf{u}_0 = \mathbf{v}_0 = \mathbf{0}$ , and loaded with the time dependent traction

$$\mathbf{g}(t) = \begin{cases} -g(t)\mathbf{e}_2 & \text{on } \Gamma_g, \\ 0 & \text{elsewhere,} \end{cases} \quad (30)$$

where  $\Gamma_g := (-0.025, 0.025) \times \{0.5\}$  m,  $\mathbf{e}_2 := (0, 1)$  and  $g(t)$  is the impulsive time-dependent function defined in figure 5 with parameters  $g_{\text{max}} = 30$  Pa and  $t_g = 0.005$  s. No body force is acting in this example,  $\mathbf{f} = \mathbf{0}$ . The material properties of the plate are Young's modulus  $E = 8/3$  Pa, Poisson's ratio  $\nu = 1/3$ , the density  $\rho = 1$  kg/m<sup>3</sup> and the damping coefficients  $a_1 = 0$  s<sup>-1</sup>,  $a_2 = 10^{-4}$  s. The final simulation time is  $T = 0.25$  s.

The background mesh  $\mathcal{P}_{\text{bg}}$  for the quadtree remeshing strategy is plotted in figure 6. Note that only half of the domain is discretized due to the problem's symmetry by introducing proper symmetry boundary conditions. The finite element spaces  $\mathbf{V}_0^{H,1}(\mathcal{P}_n)$ ,  $n = 1, \dots, N$ , used for

#### Data:

*Problem statement:* Problem geometry  $(\Omega, \Gamma_N, \Gamma_D)$ , final time  $(T)$ , material data  $(E, \nu, \rho)$ , loads and initial conditions  $(\mathbf{f}, \mathbf{g}, \mathbf{u}_0, \mathbf{v}_0)$ .

*Problem discretization:* background computational mesh  $(\mathcal{P}_{\text{bg}})$ .

*Error control:* data defining the quantity of interest  $(\mathbf{f}^{\mathcal{O}}, \mathbf{g}^{\mathcal{O}}, \mathbf{u}^{\mathcal{O}}, \mathbf{v}^{\mathcal{O}})$  and number of vibration modes  $M$ .

*Adaptivity parameters:* Number of time blocks  $(N^{\text{bk}})$ , prescribed error  $(s_{\text{tol}}^e)$ , error splitting coefficients  $(\alpha_s, \alpha_t)$ , unrefinement parameters  $(\beta_s, \beta_t)$ .

**Result:** Numerical approximation  $\tilde{\mathbf{U}}$  and error estimate  $\tilde{s}^e$  fulfilling  $|\tilde{s}^e| \leq s_{\text{tol}}^e$ .

// Modal analysis

Generate higher order space  $\mathbf{V}_0^{H,p+1}(\mathcal{P}_{\text{bg}})$ ;

Compute the eigenpairs  $(\tilde{\omega}_i, \tilde{\mathbf{q}}_i)$ ,  $i = 1, \dots, M$  in the space  $\mathbf{V}_0^{H,p+1}(\mathcal{P}_{\text{bg}})$ ;

// Adjoint problem (modal solution)

Compute the values  $\tilde{l}_i, \tilde{u}_i, \tilde{v}_i$  (using  $\mathbf{f}^{\mathcal{O}}, \mathbf{g}^{\mathcal{O}}, \mathbf{u}^{\mathcal{O}}, \mathbf{v}^{\mathcal{O}}$  and  $\tilde{\mathbf{q}}_i$ ,  $i = 1, \dots, M$ );

Compute the time dependent functions  $\tilde{y}_i(t)$  (using  $\tilde{l}_i, \tilde{u}_i, \tilde{v}_i$  and  $\tilde{\omega}_i$ ,  $i = 1, \dots, M$ );

// Problem computation, error assessment and adaptivity

Initialize discretization:  $\mathcal{P}_1^{\text{bk}} = \mathcal{P}_{\text{bg}}$ ,  $\Delta t_1^{\text{bk}} = T/N^{\text{bk}}$ ;

for  $m = 1 \dots N^{\text{bk}}$  do

repeat

    // Compute solution and error

    estimate

    Compute solution  $\tilde{\mathbf{U}}$  in the time interval  $I_m^{\text{bk}}$  and the error indicators  $\eta_m^s, \eta_{m,k}^s$  and  $\eta_m^t$ ;

    // Mesh adaptivity

    if The acceptability criteria for  $\eta_m^s$  or  $\eta_m^t$  are not fulfilled then

        Refine/unrefine the spatial mesh  $\mathcal{P}_m^{\text{bk}}$  (using  $\eta_{m,k}^s$ ) and/or the time step  $\Delta t_m^{\text{bk}}$  (using  $\eta_m^t$ );

    end

until The acceptability criteria for  $\eta_m^s$  and  $\eta_m^t$  are fulfilled;

Set initial discretization for the next time

interval:  $\mathcal{P}_{m+1}^{\text{bk}} = \mathcal{P}_m^{\text{bk}}$ ,  $\Delta t_{m+1}^{\text{bk}} = \Delta t_m^{\text{bk}}$ ;

end

**Algorithm 1:** Algorithm for problem approximation with error control and space-time mesh adaptivity.

solving the direct problem are build using bilinear elements (quadrilaterals with 4 nodes, i.e.  $p = 1$ ) while the finite element space for the adjoint,  $\mathbf{V}_0^{H,2}(\mathcal{P}_n)$ , is build using serendipity elements (quadrilaterals with 8 nodes, i.e.  $p = 2$ ).

The quantity of interest considered in this example is a weighted average of the vertical velocities in the region

$$\Omega^{\mathcal{O}} := \{(x, y \in \mathbb{R}^2 : x^2 + (y - 0.1)^2 < 0.075^2)\} \text{ m}^2,$$

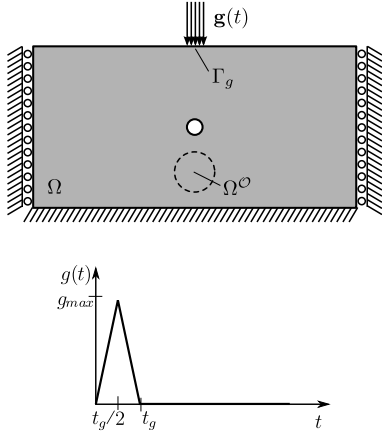


Figure 5: Example 1: Definition of the problem geometry (top) and time-dependence of the external load (bottom).

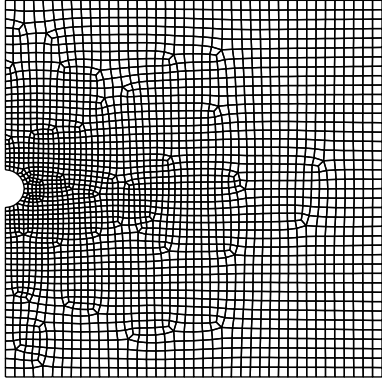


Figure 6: Example 1: Background mesh  $\mathcal{P}_{bg}$  with 2452 elements for the quadtree remeshing strategy and for the adjoint problem approximation. Only half of the domain is discretized due to the problem's symmetry.

see figure 5. Specifically, the quantity of interest is defined as

$$L^{\mathcal{O}}(\mathbf{W}) := m(\mathbf{v}^{\mathcal{O}}, \mathbf{w}_v(T)),$$

corresponding to  $\mathbf{f}^{\mathcal{O}} = \mathbf{g}^{\mathcal{O}} = \mathbf{u}^{\mathcal{O}} = \mathbf{0}$  in (8). The weighting function  $\mathbf{v}^{\mathcal{O}}$  with local support in  $\Omega^{\mathcal{O}}$  is  $\mathbf{v}^{\mathcal{O}} = [0, v_{aux}(\sqrt{x^2 + (y - 0.1)^2})]$  for

$$v_{aux}(r) = \begin{cases} \frac{10}{3\pi R^2 \rho} \left( 2 \left( \frac{r}{R} - 1 \right)^3 + 3 \left( \frac{r}{R} - 1 \right)^2 \right) & \text{for } 0 \leq r \leq R, \\ 0 & \text{for } R < r, \end{cases}$$

$R = 0.075$  being the radius of the region of interest. Note that since the  $x$ -component of  $\mathbf{v}^{\mathcal{O}}$  is zero, the quantity of interest gives an average of the vertical velocity in the region of interest  $\Omega^{\mathcal{O}}$  and at time  $t = T$ .

The adjoint problem associated to the quantity of interest is approximated using a truncated modal based approxi-

mation where only the first 60 vibration modes are kept. This corresponds to slightly modify the quantity of interest of the problem. In the following, the function  $\mathbf{v}^{\mathcal{O}}$  in the exact quantity of interest  $L^{\mathcal{O}}(\mathbf{W}) = m(\mathbf{v}^{\mathcal{O}}, \mathbf{w}_v(T))$  is replaced by its projection onto the first  $M = 60$  vibration modes  $\tilde{\mathbf{q}}_i$ ,  $i = 1, \dots, M$ , namely

$$\mathbf{v}^{\mathcal{O},M}(\mathbf{x}) := \sum_{i=1}^M v_i \tilde{\mathbf{q}}_i(\mathbf{x}), \quad \text{where } v_i := m(\mathbf{v}^{\mathcal{O}}, \tilde{\mathbf{q}}_i).$$

Figure 7 shows that the truncated discrete approximation  $\mathbf{v}^{\mathcal{O},M}$  provides a fairly good approximation of the exact weighting function  $\mathbf{v}^{\mathcal{O}}$ . It is worth noting that the quantity of interest is no longer strictly measuring only the vertical velocity of the solution and has no longer a local support. However, as can be seen, the influence of the horizontal velocity and the average outside  $\Omega^{\mathcal{O}}$  are small.

The exact solution  $\mathbf{U}$  (and therefore the exact quantity of interest  $s$ ) are unknown in this example. The exact solution is replaced here by an overkill approximation of the problem, namely  $\mathbf{U}^{ovk}$ , computed with a finite elements mesh with  $N^{el} = 627712$  elements and  $N = 1600$  time steps. The overkill discretization is finest discretization considered in this example. The exact value of the quantity of interest is approximated using the overkill approximation,  $s \approx s^{ovk} := L^{\mathcal{O}}(\mathbf{U}^{ovk}) = 2.4227 \cdot 10^{-2}$  m/s.

The behavior of the adaptive strategy is first analyzed for a prescribed target error  $s_{tol}^e = 5 \cdot 10^{-5}$  m/s. The user-prescribed parameters for the simulation are set to  $N^{bk} = 20$  for the number of space-time blocks,  $\alpha_s = 0.9$  and  $\alpha_t = 0.1$  for the coefficients used to split the total error budget into space and time and  $\beta_s = 0.5$  and  $\beta_t = 0.1$  for the lower bound factors.

Figure 8 shows several snapshots of an adapted numerical solution obtained with the proposed methodology. The quantity of interest associated with the numerical solution is  $\tilde{s} := L^{\mathcal{O}}(\tilde{\mathbf{U}}) = 2.4242 \cdot 10^{-2}$  m/s with an assessed error of  $\tilde{s}^e = -1.5756 \cdot 10^{-5}$  m/s. Thus the prescribed target error  $s_{tol}^e = 5 \cdot 10^{-5}$  m/s is fulfilled quite sharply, that is,  $|\tilde{s}^e| \leq s_{tol}^e$ , and  $|\tilde{s}^e|$  and  $s_{tol}^e$  are of the same order of magnitude. Moreover, the error with respect the overkill solution, namely  $s_{ovk}^e := s^{ovk} - \tilde{s} = -1.5125 \cdot 10^{-5}$  m/s, is also below (in absolute value) the user-defined value  $s_{tol}^e$ . Note that the assessed error is a good approximation of the overkill error. That is, the effectivity of the error estimate,  $\tilde{s}^e/s_{ovk}^e = 1.041$ , is fairly close to the unity.

Figure 9 shows the history of the number of elements and the time step length along the adapted computation. Note that the number of elements increases with time as the elastic waves spread along the plate and therefore a larger area has to be refined. The time step is refined only when the external load is acting at the beginning of the computation. Additionally, figure 9 also shows the number of iterations performed in each space-time block until reaching convergence. As can be seen, convergence is reached for the whole computation with at most four iterations per block.

The performance of the space-time adaptive strategy is also tested versus a uniform refinement. Three non-

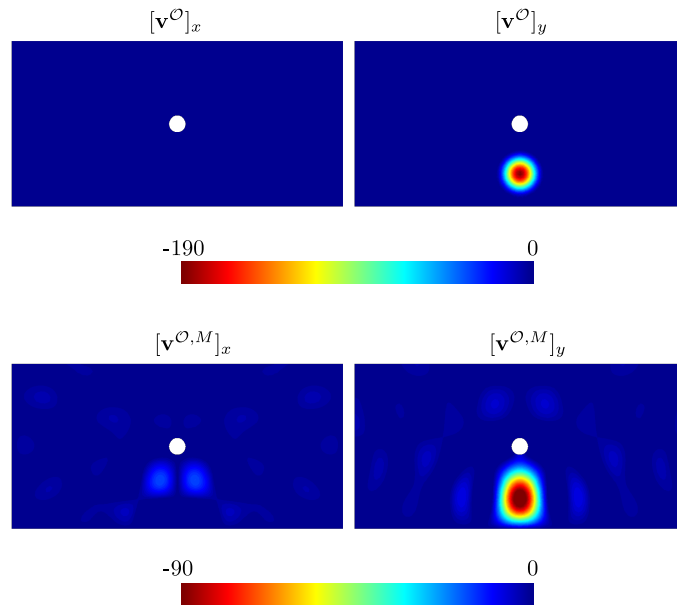


Figure 7: Example 1: Exact (top) and truncated (bottom) weighting functions  $\mathbf{v}^O$  defining the quantity of interest  $L^O(\cdot)$ .

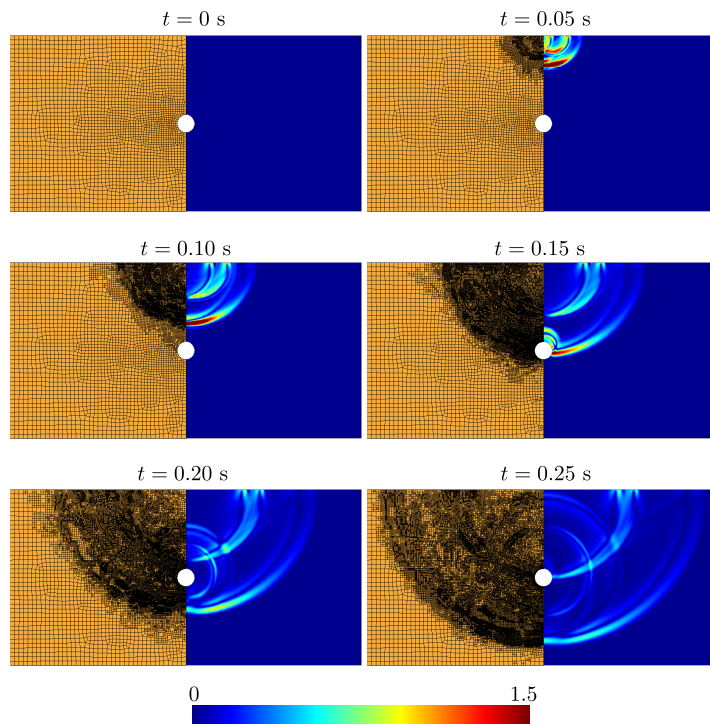


Figure 8: Example 1: Snapshots of the computed solution (magnitude of velocities in m/s) and the computational mesh at several time points for the adapted solution verifying the prescribed target error  $s_{\text{tol}}^e = 5 \cdot 10^{-5}$  m/s.

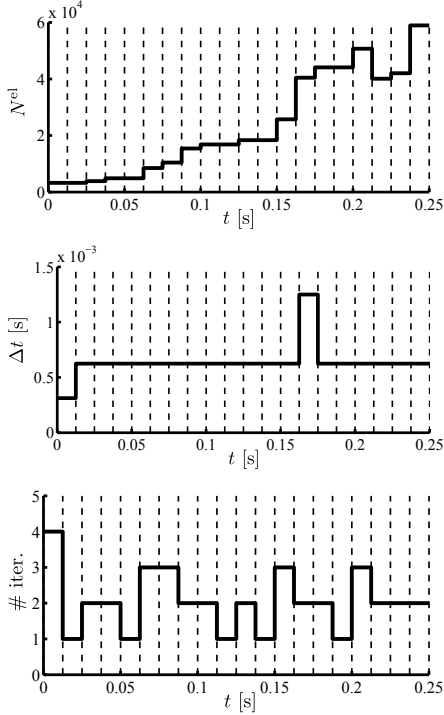


Figure 9: Example 1: History of the number of elements (top) and of the time step (middle). Number of iterations to achieve convergence in each block (bottom).

adapted (uniform) approximations are computed using three different space meshes and three different number of time steps  $N$ , see table 1. The initial space mesh corresponds to the background mesh showed in figure 6 which is recursively refined to obtain the other spatial meshes (each quadrilateral element is recursively subdivided into four new ones). The ratio  $H/\Delta t$ , or equivalently the ratio  $N/(N^{\text{el}})^{\frac{1}{2}}$ , is kept constant in the three uniform approximations. This is to ensure that the space and time errors are reduced at the same ratio taking into account that the space discretization error scales as  $H^2$  and the time discretization error as  $\Delta t^2$ , see [32] and [20].

Table 1: Example 1: Space and time discretizations for the three uniform solutions.

	$N^{\text{el}}$	# nodes	$N$
1	2452	2547	100
2	9808	9997	200
3	39232	39609	400

On the other hand, the space-time adaptive computations are performed prescribing similar total target errors as the errors obtained using uniform refinements. Specifically, four different simulations are performed setting  $s_{\text{tol}}^e = 1 \cdot 10^{-3}$ ,  $5 \cdot 10^{-4}$ ,  $1 \cdot 10^{-4}$  and  $5 \cdot 10^{-5}$  m/s combined with three different values for the number of blocks,  $N^{\text{bk}} =$

5, 10 and 20. The additional parameters of the adaptive procedure are  $\alpha_s = 0.9$ ,  $\beta_s = 0.5$  and  $\alpha_t = \beta_t = 0.1$ . The computational complexity of the simulations is measured here using the number of space-time elements (or cells), namely

$$N^{\text{cells}} := \sum_{m=1}^{N^{\text{bk}}} N_m^{\text{el}} \frac{T}{N^{\text{bk}} \Delta t_m^{\text{bk}}},$$

corresponding to sum up the number of space-time elements used inside each time interval  $I_m^{\text{bk}}$ ,  $m = 1, \dots, N^{\text{bk}}$ . Note that if a single space mesh is considered in the whole simulation time, then the number of space-time cells  $N^{\text{cells}}$  coincides with  $N^{\text{cells}} = N^{\text{el}} N$ .

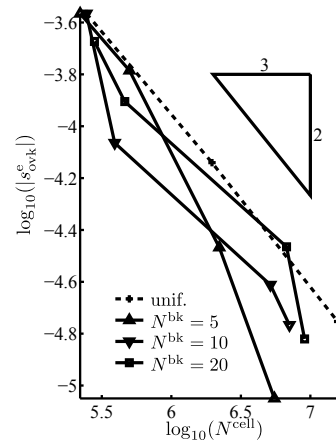


Figure 10: Example 1: Error convergence for the adapted and uniform computations. The adapted solutions are obtained using three different values of the number of time blocks  $N^{\text{bk}}$ .

Figure 10 shows the convergence of the estimates. The estimates obtained for the uniform refinement meet the expected a-priori convergence rate of  $-2/3$ . This expected convergence rate is obtained considering the a-priori estimates of the error  $s^e \propto H^2 + (\Delta t)^2$ , the relation  $N^{\text{cells}} \propto (H^2 \Delta t)^{-1}$  and noting that if the ratio  $H/\Delta t$  is constant, then  $H$  and  $\Delta t$  can be written as  $H = \kappa H^*$  and  $\Delta t = \kappa \Delta t^*$ , where  $H^*$  and  $\Delta t^*$  are the element and step length of the coarsest uniform discretization and  $\kappa$  is a refinement factor. It is then straightforward that,  $s^e \propto (N^{\text{cells}})^{-2/3}$  since  $(H^2 \Delta t)^{2/3} = C(H^2 + (\Delta t)^2) \propto s^e$  for  $C = ((H^*)^2 \Delta t^*)^{2/3} / ((H^*)^2 + (\Delta t^*)^2)$ . From figure 10 and table 2 it can be seen that besides converging at the correct convergence rate, the estimates are really accurate since their effectivities are very close to 1.

As expected, the use of an adaptive refinement strategy leads to better approximations for the quantity of interest with less computational cost. The adapted solutions have a lower error than the uniform approximations for the same number of space-time cells.

Table 2: Example 1: Performance of the estimate for both the uniform and adaptive strategies. The overkill value of the quantity of interest is  $s^{\text{ovk}} = 2.4227 \cdot 10^{-2}$  m/s obtained with  $N^{\text{cell}} = 1004339200$  space-time elements.

	$s_{\text{tol}}^e$ [m/s]	$N^{\text{cell}}$	$\bar{s}$ [m/s]	$\tilde{s}^e$ [m/s]	$s_{\text{ovk}}^e$ [m/s]	$\tilde{s}^e/s_{\text{ovk}}^e$
uniform	–	245200	$2.4498 \cdot 10^{-2}$	$-2.7186 \cdot 10^{-4}$	$-2.7180 \cdot 10^{-4}$	1.000
	–	1961600	$2.4299 \cdot 10^{-2}$	$-7.1606 \cdot 10^{-5}$	$-7.2345 \cdot 10^{-5}$	0.989
	–	15692800	$2.4244 \cdot 10^{-2}$	$-1.7813 \cdot 10^{-5}$	$-1.7659 \cdot 10^{-5}$	1.008
$N^{\text{bk}} = 5$	$1 \cdot 10^{-3}$	220680	$2.4498 \cdot 10^{-2}$	$-2.7186 \cdot 10^{-4}$	$-2.7180 \cdot 10^{-4}$	1.000
	$5 \cdot 10^{-4}$	499920	$2.4391 \cdot 10^{-2}$	$-1.6337 \cdot 10^{-4}$	$-1.6403 \cdot 10^{-4}$	0.996
	$1 \cdot 10^{-4}$	2211720	$2.4261 \cdot 10^{-2}$	$-3.3703 \cdot 10^{-5}$	$-3.4096 \cdot 10^{-5}$	0.988
	$5 \cdot 10^{-5}$	5511720	$2.4236 \cdot 10^{-2}$	$-1.0823 \cdot 10^{-5}$	$-8.9160 \cdot 10^{-6}$	1.213
$N^{\text{bk}} = 10$	$1 \cdot 10^{-3}$	245200	$2.4498 \cdot 10^{-2}$	$-2.7186 \cdot 10^{-4}$	$-2.7180 \cdot 10^{-4}$	1.000
	$5 \cdot 10^{-4}$	391280	$2.4313 \cdot 10^{-2}$	$-8.6724 \cdot 10^{-5}$	$-8.6226 \cdot 10^{-5}$	1.005
	$1 \cdot 10^{-4}$	5158120	$2.4251 \cdot 10^{-2}$	$-2.4351 \cdot 10^{-5}$	$-2.4455 \cdot 10^{-5}$	0.995
	$5 \cdot 10^{-5}$	7074440	$2.4244 \cdot 10^{-2}$	$-1.5773 \cdot 10^{-5}$	$-1.7111 \cdot 10^{-5}$	0.921
$N^{\text{bk}} = 20$	$1 \cdot 10^{-3}$	279900	$2.4439 \cdot 10^{-2}$	$-2.1096 \cdot 10^{-4}$	$-2.1219 \cdot 10^{-4}$	0.994
	$5 \cdot 10^{-4}$	462735	$2.4351 \cdot 10^{-2}$	$-1.2062 \cdot 10^{-4}$	$-1.2446 \cdot 10^{-4}$	0.969
	$1 \cdot 10^{-4}$	6732720	$2.4261 \cdot 10^{-2}$	$-3.6194 \cdot 10^{-5}$	$-3.4268 \cdot 10^{-5}$	1.056
	$5 \cdot 10^{-5}$	9080750	$2.4242 \cdot 10^{-2}$	$-1.5756 \cdot 10^{-5}$	$-1.5125 \cdot 10^{-5}$	1.041

### 5.2 Example 2: 2D structure

Consider the structure given in figure 11. The structure is initially at rest ( $\mathbf{u}_0 = \mathbf{v}_0 = \mathbf{0}$ ), clamped at the supports and subjected to the time-dependent traction

$$\mathbf{g} = \begin{cases} g(t)\mathbf{e}_1 & \text{on } \Gamma_g, \\ 0 & \text{elsewhere.} \end{cases}$$

The set  $\Gamma_g$  is the region of the Neumann boundary where the load is applied, vector  $\mathbf{e}_1 := (1, 0)$  is the first cartesian unit vector and function  $g(t)$  describes the time evolution of  $\mathbf{g}$  given in figure 11. The traction  $\mathbf{g}$  is the only external loading in this example (that is  $\mathbf{f} = \mathbf{0}$ ). Other material and geometric parameters univocally defining the problem are reported in table 3.

Table 3: Example 2: Problem parameterization

Geometry (data in m)	Physical properties
$P_1 := (0.55, 0.00)$	$E = 2 \cdot 10^{11}$ Pa
$P_2 := (0.45, 0.45)$	$\nu = 0.2$
$P_3 := (0.45, 0.55)$	$\rho = 8 \cdot 10^3$ kg/m <sup>3</sup>
$P_4 := (0.45, 1.45)$	$a_1 = 0$ s <sup>-1</sup>
$P_5 := (0.55, 1.55)$	$a_2 = 1 \cdot 10^{-5}$ s
$P_6 := (-0.55, 1.55)$	$T = 2 \cdot 10^{-3}$ s
$P_7 := (-0.45, 1.45)$	
$\Gamma_g := \{-0.55\} \times (1.45, 1.55)$	
External load	
$g_{\text{max}} = 10^8$ Pa	
$t_g = 2 \cdot 10^{-4}$ s	

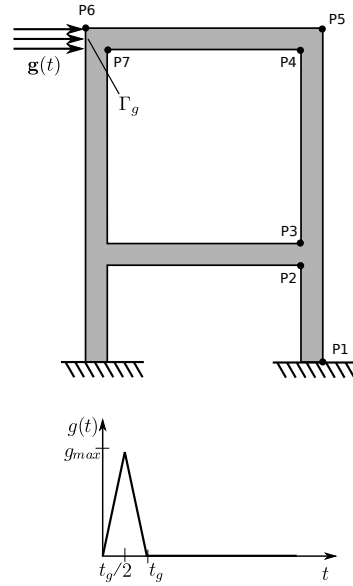


Figure 11: Example 2: Problem statement (top) and time dependent loading at  $\Gamma_g$  (bottom).

This example focusses in the quantity of interest

$$L^{\mathcal{O}}(\mathbf{W}) := \frac{1}{\text{meas}(\Gamma_g)} (\mathbf{e}_1, \mathbf{w}_u(T))_{\Gamma_g}, \quad (31)$$

which is the average of the final displacement in the boundary  $\Gamma_g$  where the external load is applied. Note that this quantity is not accounted in the generic quantity of interest given in equation (10). Consequently, quantity (31) is rewritten as

$$L^{\mathcal{O}}(\mathbf{W}) = a(\mathbf{u}^{\mathcal{O}}, \mathbf{w}_u(T)),$$

where  $\mathbf{u}^\mathcal{O}$  is the *exact* solution of the static linear elasticity problem: find  $\mathbf{u}^\mathcal{O} \in \mathcal{V}_0$  such that

$$a(\mathbf{u}^\mathcal{O}, \mathbf{w}) = \frac{1}{\text{meas}(\Gamma_g)} (\mathbf{e}_1, \mathbf{w})_{\Gamma_g}, \quad \forall \mathbf{w} \in \mathcal{V}_0. \quad (32)$$

After this reformulation, the quantity of interest is a particular case of the ones included in (10) and therefore the associated adjoint problem has the same structure as the original one. In particular, the function  $\mathbf{u}^\mathcal{O}$  is the final displacement condition for the adjoint problem. The other forcing data for the adjoint are zero in this case, namely  $\mathbf{v}^\mathcal{O} = \mathbf{f}^\mathcal{O} = \mathbf{g}^\mathcal{O} = \mathbf{0}$ . Note that function  $\mathbf{u}^\mathcal{O}$  is solution of an infinite dimensional problem and therefore it is unknown. In this example, the unknown function  $\mathbf{u}^\mathcal{O}$  is replaced by the computable one  $\tilde{\mathbf{u}}^\mathcal{O}$  obtained by solving problem (32) in the discrete space  $\mathcal{V}_0^{H,p+1}(\mathcal{P}_{\text{bg}})$  associated with the background mesh of the adaptive process. Three different background meshes are used in this example, see figure 12.

The quantity of interest (31) is well suited for the modal based approach because the weighting function  $\tilde{\mathbf{u}}^\mathcal{O}$  is well captured by the expansion of few eigenvectors. This ensures that the adjoint solution is also properly represented using few vibration modes. The projection of  $\tilde{\mathbf{u}}^\mathcal{O}$  into the expansion of the first  $M$  eigenvectors is defined as

$$\tilde{\mathbf{u}}^{\mathcal{O},M} := \sum_{i=1}^M \tilde{\mathbf{u}}_i \tilde{\mathbf{q}}_i,$$

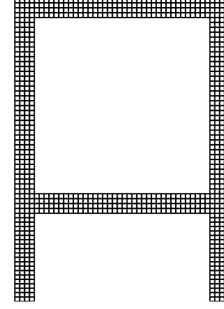
where  $\tilde{u}_i := m(\tilde{\mathbf{u}}^\mathcal{O}, \tilde{\mathbf{q}}_i)$ ,  $i = 1, \dots, M$ . Thus, the relative error in the projection is

$$\varepsilon^M := \frac{\|\tilde{\mathbf{u}}^\mathcal{O} - \tilde{\mathbf{u}}^{\mathcal{O},M}\|_m}{\|\tilde{\mathbf{u}}^\mathcal{O}\|_m},$$

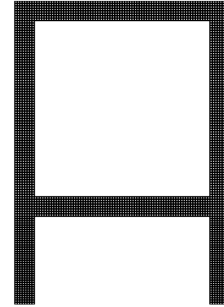
where  $\|\cdot\|_m := (m(\cdot, \cdot))^{1/2}$ . Figure 13 shows the error  $\varepsilon^M$  as a function of the number of eigenvectors  $M$ . Note that the error  $\varepsilon^M$  rapidly decreases as  $M$  increases. The number of eigenvectors considered in this example is  $M = 60$  and the associated projection error is  $\varepsilon^{60} = 5.94 \cdot 10^{-5}$ .

The exact value of the quantity of interest is unknown in this example. An overkill approximation of the quantity of interest,  $s^{\text{ovk}} := 1.2086 \cdot 10^{-3}$  m, is computed using a finite element mesh of  $N^{\text{el}} = 204800$  elements and  $N = 6400$  time steps. This discretization is the richest one considered in this example.

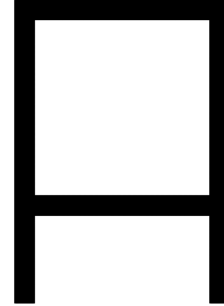
Figures 14 and 15 show snapshots of the computed solution and the computational mesh at several time points. This particular solution is obtained using the background mesh number 2, taking  $N^{\text{bk}} = 10$  time blocks and prescribing the error to the value  $s_{\text{tol}}^e = 5 \cdot 10^{-6}$  m. The coefficients used to split the total error budget into space and time are  $\alpha_s = 0.9$  and  $\alpha_t = 0.1$  and the unrefinement factors are taken as  $\beta_s = 0.5$  and  $\beta_t = 0.1$ . The computed quantity of interest is  $\tilde{s} = 1.2069 \cdot 10^{-3}$  m and the assessed error is  $\tilde{s}^e = 8.8942 \cdot 10^{-7}$  m. Note that the restriction  $|\tilde{s}^e| \leq s_{\text{user}}^e$  is also fulfilled in this example. Moreover, the error with respect the overkill solution,  $s_{\text{ovk}}^e = 1.7516 \cdot 10^{-6}$  m, is also below the user-defined value  $s_{\text{tol}}^e$ .



Background mesh 1



Background mesh 2



Background mesh 3

Figure 12: Example 2: Background meshes used in this example. The number of elements in each of them is 800, 3200 and 12800 respectively.

Figure 16 shows the history of number of elements in the computational mesh and the time step length for this particular computation. Note that the number of mesh elements increases in time because the stress waves spread in the structure. Note also that the time step length is smaller at the beginning of the computation due to the effect of the external load acting at the initial simulation time. Figure 16 also shows the number of iterations until achieve convergence in each time block. Note that the number of iterations is always equal or less than four.

The performance of the adaptive strategy is compared with respect to uniform mesh refinement. To this end, the uniform refined computations are obtained using the meshes plotted in figure 12 and three different number

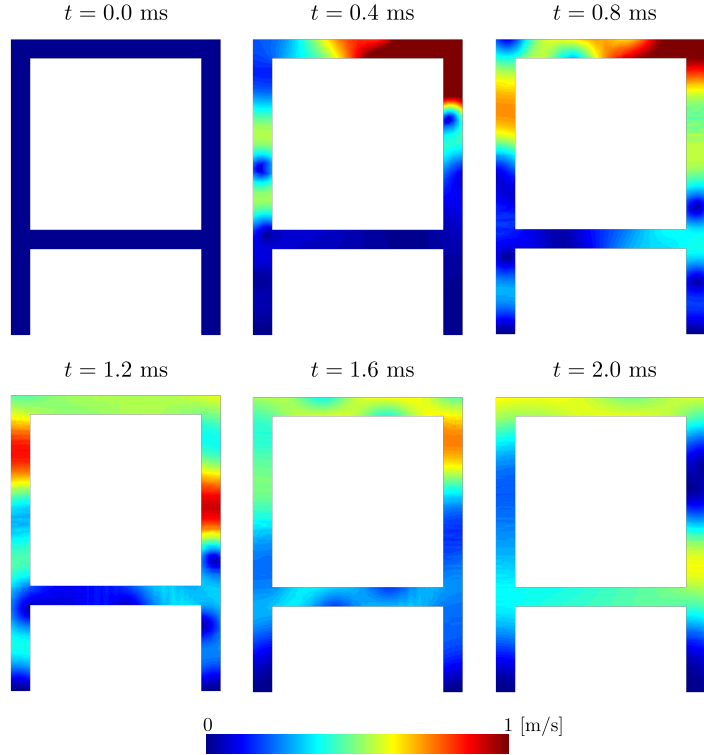


Figure 14: Example 2: Snapshots of the computed solution (magnitude of velocities in m/s) at several time points.

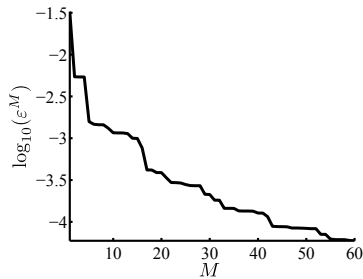


Figure 13: Example 2: Error in projecting the weighting function  $\tilde{\mathbf{u}}$  into the expansion of the first  $M$  eigenvectors  $\tilde{\mathbf{q}}_1, \dots, \tilde{\mathbf{q}}_M$ . The eigenvectors  $\tilde{\mathbf{q}}_i$  and the weighting function  $\tilde{\mathbf{u}}^{\mathcal{O}}$  are computed in the space  $\mathcal{V}_0^{H,p+1}(\mathcal{P}_{\text{bg}})$  associated with the background mesh number 2 plotted in figure 12.

of time steps  $N$ , see table 4. Note that the ratio  $H/\Delta t$  is also kept constant in this example to ensure that the space and time errors are reduced at the same rate. On the other hand, the adapted solutions are obtained using  $N^{\text{bk}} = 10$  and four different values of the prescriber error,  $s_{\text{tol}}^e = 5 \cdot 10^{-5}, 1 \cdot 10^{-5}, 5 \cdot 10^{-6}$  and  $1 \cdot 10^{-6}$  m. The dependence of the results on the chosen background mesh is studied by computing the adaptive solutions using the three background meshes plotted in figure 12. Twelve

adaptive solutions are computed all together (one for each value of the prescribed error and one for each background mesh).

Table 4: Example 2: Space and time discretizations for the three uniform solutions.

	$N^{\text{el}}$	# nodes	$N$
1	200	300	200
2	800	1000	400
3	3200	3600	800
4	12800	13600	1600

Table 5 and figure 17 and give the results for the adaptive and non-adaptive solutions. The convergence curves in figure 17 shows that the adapted solutions achieve a smaller error than the non-adapted solutions for the same number of space-time elements  $N^{\text{cells}}$ . The effectivity of the error estimate, namely  $\tilde{s}^e/s^e$ , is also shown in figure 17. Note that the computed effectivity (i.e. the quality of the error estimate) is better the finer is the background mesh. This is because the adjoint problem and the extractor  $\tilde{\mathbf{u}}^{\mathcal{O}}$  are computed using the background mesh. Thus, the finer the background mesh, the better the quality of the adjoint and, therefore, the better the quality of the error estimate. Note that the computed effectivities in this example are slightly worse than the ones obtained in the first numeri-

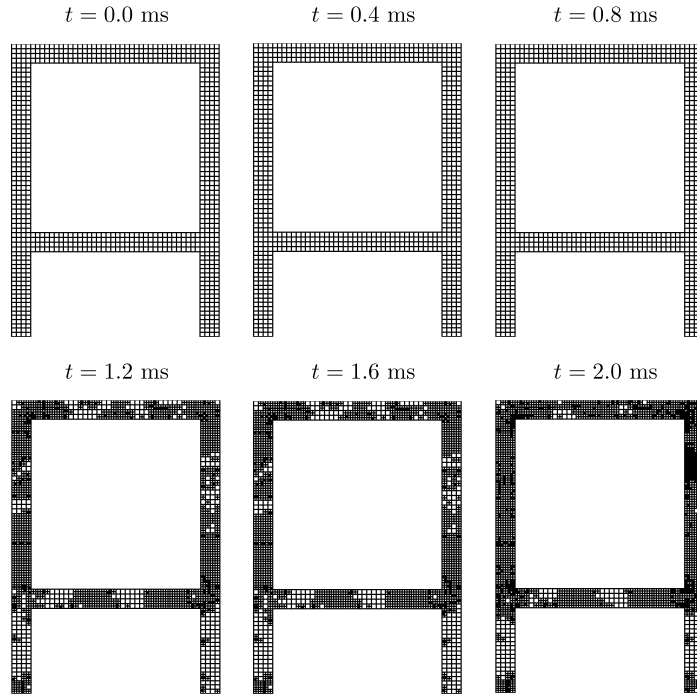


Figure 15: Example 2: Snapshots of the computational mesh at several time points.

cal example. Even though, the adaptive computations give more accurate results than the non-adapted solutions for the same number of space-time elements.

## 6 Closure

This article presents a goal-oriented space-time adaptive methodology for linear elastodynamics. The strategy aims at computing an optimal space-time discretization such that the numerical solution has an error in the quantity of interest below some user-defined tolerance. The space-time adaptation is driven by a goal-oriented error estimate that requires approximating an auxiliary adjoint problem.

The major novelty of this work is computing the adjoint solution with modal analysis instead of the standard direct time-integration methods. The modal-based approach is particularly efficient for some quantities of interest, because it allows to efficiently compute and store the adjoint solution.

The numerical examples show that the proposed strategy furnishes adapted solutions fulfilling the user-defined error tolerance. That is, both the assessed and computed errors are below the user-defined error value. Moreover, the discretizations obtained with the proposed adaptive strategy are more efficient than the ones obtained with a uniform refinement of all mesh elements and time steps.

The adaptive discretizations provide more accurate results than uniform remeshing, for the same number of space-time elements.

The proposed error estimate accounts for both the space and time discretization errors. The global error estimate is split into two contributions corresponding to the space and time errors using the Galerkin orthogonality property of the residual. This applies for space-time finite elements like time-continuous Galerkin methods. The extension of the approach to tackle other time-integration schemes, e.g. the ones based on finite differences and/or explicit methods with lumped mass matrix, requires further investigation.

## Acknowledgment

Partially supported by Ministerio de Educación y Ciencia, Grant DPI2011-27778-C02-02 and Universitat Poli-tècnica de Catalunya (UPC-BarcelonaTech), grant UPC-FPU.

## A Linear system to be solved at each time step

This appendix details how the time-continuous Galerkin approximation is computed when the space mesh changes

Table 5: Example 2: Performance of the estimate for both the uniform and adaptive strategies (for four different background meshes). The overkill value for the quantity of interest  $s^{\text{ovk}} = 1.2086 \cdot 10^{-3}$  m is obtained using a uniform spatial mesh of  $N^{\text{cell}} = 1310720000$  space-time elements.

	$s_{\text{tol}}^e$ [m]	$N^{\text{cell}}$	$\tilde{s}$ [m]	$\tilde{s}^e$ [m]	$s_{\text{ovk}}^e$ [m]	$\tilde{s}^e/s_{\text{ovk}}^e$
uniform	–	40000	$1.1914 \cdot 10^{-3}$	$1.4558 \cdot 10^{-5}$	$1.7262 \cdot 10^{-5}$	0.843
	–	320000	$1.2037 \cdot 10^{-3}$	$3.6897 \cdot 10^{-6}$	$4.8973 \cdot 10^{-6}$	0.753
	–	2560000	$1.2068 \cdot 10^{-3}$	$1.3679 \cdot 10^{-6}$	$1.8601 \cdot 10^{-6}$	0.735
	–	20480000	$1.2079 \cdot 10^{-3}$	$5.6641 \cdot 10^{-7}$	$7.0564 \cdot 10^{-7}$	0.802
bg. mesh 1	$5 \cdot 10^{-5}$	28696	$1.2048 \cdot 10^{-3}$	$1.4506 \cdot 10^{-6}$	$3.8845 \cdot 10^{-6}$	0.373
	$1 \cdot 10^{-5}$	86181	$1.2068 \cdot 10^{-3}$	$3.0110 \cdot 10^{-7}$	$1.8337 \cdot 10^{-6}$	0.164
	$5 \cdot 10^{-6}$	153536	$1.2067 \cdot 10^{-3}$	$4.2316 \cdot 10^{-7}$	$1.9152 \cdot 10^{-6}$	0.220
	$1 \cdot 10^{-6}$	239936	$1.2067 \cdot 10^{-3}$	$5.8772 \cdot 10^{-7}$	$1.9421 \cdot 10^{-6}$	0.302
bg. mesh 2	$5 \cdot 10^{-5}$	90400	$1.2025 \cdot 10^{-3}$	$4.9028 \cdot 10^{-6}$	$6.1079 \cdot 10^{-6}$	0.802
	$1 \cdot 10^{-5}$	113004	$1.2066 \cdot 10^{-3}$	$1.0330 \cdot 10^{-6}$	$2.0820 \cdot 10^{-6}$	0.496
	$5 \cdot 10^{-6}$	174672	$1.2069 \cdot 10^{-3}$	$8.8942 \cdot 10^{-7}$	$1.7516 \cdot 10^{-6}$	0.507
	$1 \cdot 10^{-6}$	1212673	$1.2079 \cdot 10^{-3}$	$1.5956 \cdot 10^{-7}$	$7.4439 \cdot 10^{-7}$	0.214
bg. mesh 3	$5 \cdot 10^{-5}$	368000	$1.2056 \cdot 10^{-3}$	$2.5760 \cdot 10^{-6}$	$3.0675 \cdot 10^{-6}$	0.839
	$1 \cdot 10^{-5}$	380800	$1.2063 \cdot 10^{-3}$	$1.8447 \cdot 10^{-6}$	$2.3364 \cdot 10^{-6}$	0.789
	$5 \cdot 10^{-6}$	435724	$1.2071 \cdot 10^{-3}$	$1.3130 \cdot 10^{-6}$	$1.5426 \cdot 10^{-6}$	0.851
	$1 \cdot 10^{-6}$	3024438	$1.2083 \cdot 10^{-3}$	$1.5152 \cdot 10^{-7}$	$3.7024 \cdot 10^{-7}$	0.409
bg. mesh 4	$5 \cdot 10^{-5}$	1472000	$1.2065 \cdot 10^{-3}$	$1.9816 \cdot 10^{-6}$	$2.1207 \cdot 10^{-6}$	0.934
	$1 \cdot 10^{-5}$	1523200	$1.2073 \cdot 10^{-3}$	$1.1698 \cdot 10^{-6}$	$1.3089 \cdot 10^{-6}$	0.893
	$5 \cdot 10^{-6}$	1676800	$1.2077 \cdot 10^{-3}$	$7.8304 \cdot 10^{-7}$	$9.2219 \cdot 10^{-7}$	0.849
	$1 \cdot 10^{-6}$	4461564	$1.2084 \cdot 10^{-3}$	$1.8781 \cdot 10^{-7}$	$2.2230 \cdot 10^{-7}$	0.844

between times slabs.

Recall that the numerical approximation  $\tilde{\mathbf{U}}$  solution of the discrete problem (5) is computed sequentially starting from the first time slab  $I_1$  until the last one  $I_N$ . Specifically, assuming that the solution at the time-slab  $I_{n-1}$  is known, the approximation  $\tilde{\mathbf{U}}$  restricted to the slab  $I_n$  is found solving the problem: find  $\tilde{\mathbf{U}}|_{I_n} \in \mathcal{W}_u^{H,\Delta t}|_{I_n} \times \mathcal{W}_v^{H,\Delta t}|_{I_n}$  such that

$$\int_{I_n} \left[ m(\dot{\tilde{\mathbf{u}}}_v + a_1 \tilde{\mathbf{u}}_v, \mathbf{w}_v) + a(\tilde{\mathbf{u}}_u + a_2 \tilde{\mathbf{u}}_v, \mathbf{w}_v) \right] dt = \int_{I_n} l(t; \mathbf{w}_v) dt, \quad \forall \mathbf{w}_v \in \mathcal{V}_0^H(\mathcal{P}_n), \quad (33a)$$

$$\int_{I_n} a(\dot{\tilde{\mathbf{u}}}_u - \dot{\tilde{\mathbf{u}}}_v, \mathbf{w}_u) dt = 0, \quad \forall \mathbf{w}_u \in \mathcal{V}_0^H(\mathcal{P}_n), \quad (33b)$$

$$\tilde{\mathbf{U}}(t_{n-1}^+) = \tilde{\mathbf{U}}(t_{n-1}), \quad (33c)$$

where, for  $n > 1$ ,  $\tilde{\mathbf{U}}(t_{n-1})$  is the solution at the end of the previous interval  $I_{n-1}$  and, for  $n = 1$ ,  $\tilde{\mathbf{U}}(t_{n-1} = t_0)$  is defined using the initial conditions,  $\tilde{\mathbf{U}}(t_0) = [\mathbf{u}_0, \mathbf{v}_0]$ .

From the definition of the discrete spaces  $\mathcal{W}_u^{H,\Delta t}$  and  $\mathcal{W}_v^{H,\Delta t}$ , the numerical displacements and velocities  $\tilde{\mathbf{u}}_u$  and  $\tilde{\mathbf{u}}_v$  inside the interval  $I_n$  are expressed as a combination of the values at times  $t_{n-1}$  and  $t_n$ , namely

$$\tilde{\mathbf{u}}_u|_{I_n} = \tilde{\mathbf{u}}_u(t_{n-1})\theta_{n-1}(t) + \tilde{\mathbf{u}}_u(t_n)\theta_n(t), \quad (34a)$$

$$\tilde{\mathbf{u}}_v|_{I_n} = \tilde{\mathbf{u}}_v(t_{n-1})\theta_{n-1}(t) + \tilde{\mathbf{u}}_v(t_n)\theta_n(t). \quad (34b)$$

Thus, using the initial conditions for the interval (33c), the values  $\tilde{\mathbf{u}}_u(t_{n-1})$  and  $\tilde{\mathbf{u}}_v(t_{n-1}) \in \mathcal{V}_0^H(\mathcal{P}_{n-1})$  are known and the only unknowns to be determined are  $\tilde{\mathbf{u}}_u(t_n)$  and  $\tilde{\mathbf{u}}_v(t_n) \in \mathcal{V}_0^H(\mathcal{P}_n)$ . These unknowns are found inserting the representation (34) in equation (33) and noting that the following properties of the time-shape functions hold,

$$\int_{I_n} \theta_{n-1}(t) dt = \int_{I_n} \theta_n(t) dt = \frac{\Delta t_n}{2} \quad \text{and}$$

$$-\int_{I_n} \dot{\theta}_{n-1}(t) dt = \int_{I_n} \dot{\theta}_n(t) dt = 1.$$

Specifically,  $[\tilde{\mathbf{u}}_u(t_n), \tilde{\mathbf{u}}_v(t_n)] \in \mathcal{V}_0^H(\mathcal{P}_n) \times \mathcal{V}_0^H(\mathcal{P}_n)$  is such that

$$m(\tilde{\mathbf{u}}_v(t_n), \mathbf{w}_v) + \frac{\Delta t_n}{2} c(\tilde{\mathbf{u}}_v(t_n), \mathbf{w}_v) + \frac{\Delta t_n}{2} a(\tilde{\mathbf{u}}_u(t_n), \mathbf{w}_v) = l_{v,n}(\mathbf{w}_v), \quad \forall \mathbf{w}_v \in \mathcal{V}_0^H(\mathcal{P}_n), \quad (35a)$$

and

$$a(\tilde{\mathbf{u}}_u(t_n), \mathbf{w}_u) - \frac{\Delta t_n}{2} a(\tilde{\mathbf{u}}_v(t_n), \mathbf{w}_u) = l_{u,n}(\mathbf{w}_u), \quad \forall \mathbf{w}_u \in \mathcal{V}_0^H(\mathcal{P}_n), \quad (35b)$$

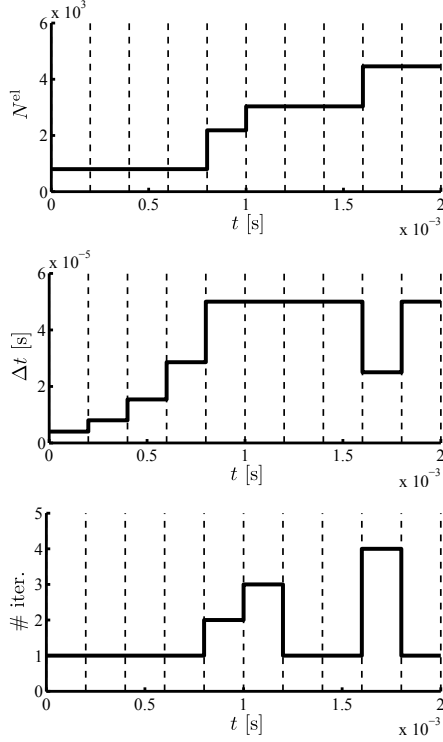


Figure 16: Example 2: Evolution along the adaptive process of the number of elements (top) and the time step (center). Number of remeshing iterations to achieve convergence in each block (bottom).

where

$$\begin{aligned}
 l_{v,n}(\mathbf{w}) &:= \int_{I_n} l(t; \mathbf{w}) \, dt + m(\tilde{\mathbf{u}}_v(t_{n-1}), \mathbf{w}) \\
 &\quad - \frac{\Delta t_n}{2} c(\tilde{\mathbf{u}}_v(t_{n-1}), \mathbf{w}) - \frac{\Delta t_n}{2} a(\tilde{\mathbf{u}}_u(t_{n-1}), \mathbf{w}), \\
 l_{u,n}(\mathbf{w}) &:= a(\tilde{\mathbf{u}}_u(t_{n-1}), \mathbf{w}) + \frac{\Delta t_n}{2} a(\tilde{\mathbf{u}}_v(t_{n-1}), \mathbf{w}), \\
 c(\mathbf{v}, \mathbf{w}) &:= m(a_1 \mathbf{v}, \mathbf{w}) + a(a_2 \mathbf{v}, \mathbf{w}).
 \end{aligned}$$

Note that since the values  $\tilde{\mathbf{u}}_u(t_{n-1})$  and  $\tilde{\mathbf{u}}_v(t_{n-1})$  are known, the terms associated with this values are placed in the right hand side of the equations.

The computation of the terms appearing in the left hand side of (35) entails no difficulty since all the spatial functions belong to  $\mathcal{V}_0^H(\mathcal{P}_n)$ . On the contrary, if different spatial computational meshes are used at times  $t_{n-1}$  and  $t_n$ , the computation of the nodal force vectors associated with  $l_{u,n}(\cdot)$  and  $l_{v,n}(\cdot)$  involves computing mass and energy products of functions defined in the mesh at time  $t_{n-1}$  and functions defined in the mesh at time  $t_n$ , e.g.  $m(\tilde{\mathbf{u}}_v(t_{n-1}), \mathbf{w}_v)$ .

The use of different spatial meshes is efficiently handled by solving the discrete problem (35) using the auxiliary *union* mesh  $\mathcal{P}_{n-1,n}$  containing in each zone of the domain

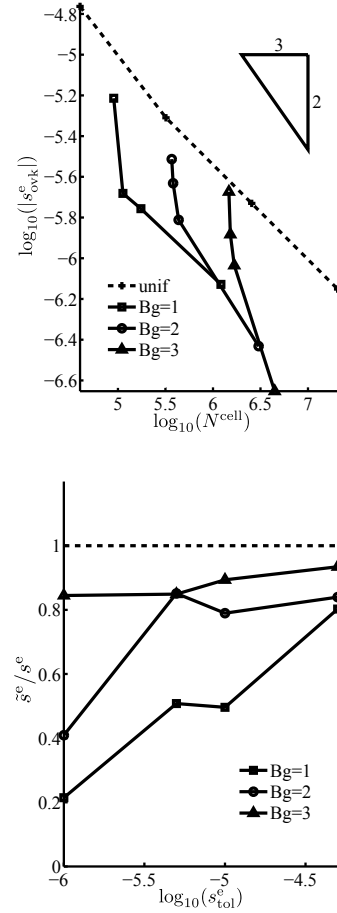


Figure 17: Example 2: Error convergence for the adapted and uniform computations (top) and computed effectivity of the error estimate (bottom). The adapted solutions are obtained using three background meshes.

the finer elements either in  $\mathcal{P}_{n-1}$  or  $\mathcal{P}_n$ , see figure 18, namely

$$\mathcal{P}_{n-1,n} := \{\omega = \Delta \cap \Delta' \text{ for } \Delta \in \mathcal{P}_{n-1}, \Delta' \in \mathcal{P}_n\}.$$

Note that, any function belonging either to  $\mathcal{V}_0^H(\mathcal{P}_{n-1})$  or  $\mathcal{V}_0^H(\mathcal{P}_n)$  can be represented in the finite element space associated to  $\mathcal{P}_{n-1,n}$ , namely  $\mathcal{V}_0^H(\mathcal{P}_{n-1,n})$ , without loss of information. Thus, the products involving functions in different meshes are efficiently computed after projecting the functions in the space  $\mathcal{V}_0^H(\mathcal{P}_{n-1,n})$ . However, discretizing problem (35) using the mesh  $\mathcal{P}_{n-1,n}$  requires introducing additional constraints to enforce that the computed fields  $\tilde{\mathbf{u}}_u(t_n)$  and  $\tilde{\mathbf{u}}_v(t_n)$  belong to  $\mathcal{V}_0^H(\mathcal{P}_n)$  and not to  $\mathcal{V}_0^H(\mathcal{P}_{n-1,n})$ . That is, problem (35) leads to the following system of equations when discretized in the auxiliary finite

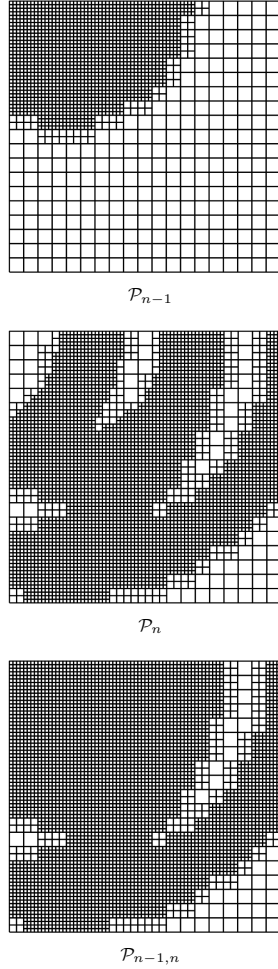


Figure 18: Illustration of the computational meshes  $\mathcal{P}_{n-1}$ ,  $\mathcal{P}_n$  and their *union*  $\mathcal{P}_{n-1,n}$ .

element mesh  $\mathcal{P}_{n-1,n}$ :

$$\begin{bmatrix} \mathbf{K}_n & -\frac{\Delta t_n}{2} \mathbf{K}_n & \mathbf{A}_n^T & \mathbf{0} \\ \frac{\Delta t_n}{2} \mathbf{K}_n & \mathbf{M}_n + \frac{\Delta t_n}{2} \mathbf{C}_n & \mathbf{0} & \mathbf{A}_n^T \\ \mathbf{A}_n & \mathbf{0} & \mathbf{0} & \mathbf{0} \\ \mathbf{0} & \mathbf{A}_n & \mathbf{0} & \mathbf{0} \end{bmatrix} \begin{bmatrix} \mathbf{U}_{u,n} \\ \mathbf{U}_{v,n} \\ \boldsymbol{\lambda}_{u,n} \\ \boldsymbol{\lambda}_{v,n} \end{bmatrix} = \begin{bmatrix} \mathbf{F}_{u,n} \\ \mathbf{F}_{v,n} \\ \mathbf{0} \\ \mathbf{0} \end{bmatrix} \quad (36)$$

where

$$\mathbf{F}_{u,n} := \mathbf{K}_n \mathbf{U}_{u,n-1} + \frac{\Delta t_n}{2} \mathbf{K}_n \mathbf{U}_{v,n-1},$$

$$\mathbf{F}_{v,n} := \left( \mathbf{M}_n - \frac{\Delta t_n}{2} \mathbf{C}_n \right) \mathbf{U}_{v,n-1} - \frac{\Delta t_n}{2} \mathbf{K}_n \mathbf{U}_{u,n-1} + \int_{I_n} \mathbf{F}(t) dt,$$

and  $\mathbf{C}_n := a_1 \mathbf{M}_n + a_2 \mathbf{K}_n$ . The matrices  $\mathbf{M}_n$  and  $\mathbf{K}_n$  and the vector  $\mathbf{F}(t)$  are the discrete counterparts of the bilinear forms  $m(\cdot, \cdot)$  and  $a(\cdot, \cdot)$  and the linear form  $l(t; \cdot)$  in the space  $\mathcal{V}_0^H(\mathcal{P}_{n-1,n})$  and the vectors  $\mathbf{U}_{u,n}$ ,  $\mathbf{U}_{v,n}$ ,  $\mathbf{U}_{u,n-1}$

and  $\mathbf{U}_{v,n-1}$  contain the degrees of freedom of functions  $\tilde{\mathbf{u}}_u(t_n)$ ,  $\tilde{\mathbf{u}}_v(t_n)$ ,  $\tilde{\mathbf{u}}_u(t_{n-1})$  and  $\tilde{\mathbf{u}}_v(t_{n-1})$  expressed in the discrete space  $\mathcal{V}_0^H(\mathcal{P}_{n-1,n})$ . Note that the linear constraints  $\mathbf{A}_n \mathbf{U}_{u,n} = \mathbf{0}$  and  $\mathbf{A}_n \mathbf{U}_{v,n} = \mathbf{0}$  are introduced in order to ensure that the computed fields  $\tilde{\mathbf{u}}_u(t_n)$  and  $\tilde{\mathbf{u}}_v(t_n)$  belong to  $\mathcal{V}_0^H(\mathcal{P}_n)$  and also to impose continuity of the solution at the hanging nodes, see figure 19. The vectors  $\boldsymbol{\lambda}_{u,n}$  and  $\boldsymbol{\lambda}_{v,n}$  are the associated Lagrange multipliers.

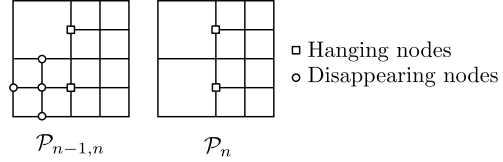


Figure 19: The numerical solution is constrained at the nodes of the mesh  $\mathcal{P}_{n-1,n}$  corresponding to hanging nodes in the mesh  $\mathcal{P}_n$  and also at the nodes of  $\mathcal{P}_{n-1,n}$  which disappear in mesh  $\mathcal{P}_n$ .

Note that system (36) is at the first sight of double size than the one associated with the Newmark method. However, system (36) can be rewritten in a more convenient way by subtracting to the second row of the matrix in (36) the first row multiplied by  $\frac{\Delta t_n}{2}$ . That is,

$$\begin{bmatrix} \mathbf{K}_n & -\frac{\Delta t_n}{2} \mathbf{K}_n & \mathbf{A}_n^T & \mathbf{0} \\ \mathbf{0} & \mathbf{M}_n + \frac{\Delta t_n}{2} \mathbf{C}_n + \frac{\Delta t_n^2}{4} \mathbf{K}_n & -\frac{\Delta t_n}{2} \mathbf{A}_n^T & \mathbf{A}_n^T \\ \mathbf{A}_n & \mathbf{0} & \mathbf{0} & \mathbf{0} \\ \mathbf{0} & \mathbf{A}_n & \mathbf{0} & \mathbf{0} \end{bmatrix} \begin{bmatrix} \mathbf{U}_{u,n} \\ \mathbf{U}_{v,n} \\ \boldsymbol{\lambda}_{u,n} \\ \boldsymbol{\lambda}_{v,n} \end{bmatrix} = \begin{bmatrix} \mathbf{F}_{u,n} \\ \mathbf{F}_{v,n} - \frac{\Delta t_n}{2} \mathbf{F}_{u,n} \\ \mathbf{0} \\ \mathbf{0} \end{bmatrix}.$$

This reformulation allows to compute the velocities separately from the displacements solving a system of the same size as the usual system arising in the Newmark method, namely,

$$\begin{bmatrix} \mathbf{M}_n + \frac{\Delta t_n}{2} \mathbf{C}_n + \frac{\Delta t_n^2}{4} \mathbf{K}_n & \mathbf{A}_n^T \\ \mathbf{A}_n & \mathbf{0} \end{bmatrix} \begin{bmatrix} \mathbf{U}_{v,n} \\ \boldsymbol{\lambda}_n^* \end{bmatrix} = \begin{bmatrix} \mathbf{F}_{v,n} - \frac{\Delta t_n}{2} \mathbf{F}_{u,n} \\ \mathbf{0} \end{bmatrix},$$

with  $\boldsymbol{\lambda}_n^* := \boldsymbol{\lambda}_{v,n} - \frac{\Delta t_n}{2} \boldsymbol{\lambda}_{u,n}$ . Once the velocities  $\mathbf{U}_{v,n}$  are known, the displacements are obtained solving the system

$$\begin{bmatrix} \mathbf{K}_n & \mathbf{A}_n^T \\ \mathbf{A}_n & \mathbf{0} \end{bmatrix} \begin{bmatrix} \mathbf{U}_{u,n} \\ \boldsymbol{\lambda}_{u,n} \end{bmatrix} = \begin{bmatrix} \mathbf{F}_{u,n} + \frac{\Delta t_n}{2} \mathbf{K}_n \mathbf{U}_{v,n} \\ \mathbf{0} \end{bmatrix}. \quad (37)$$

## References

- [1] J. Peraire, M. Vahdati, K. Morgan, and O. C. Zienkiewicz. Adaptive remeshing for flow computations. *J. Comp. Physics*, 72:449–466, 1987.

- [2] P. Nithiarasu and O. C. Zienkiewicz. Adaptive mesh generation for fluid mechanics problems. *Int. J. Numer. Meth. Engrg.*, 47:629–662, 2000.
- [3] I. Babuška and W. C. Rheinboldt. Error estimates for adaptive finite element computations. *SIAM J. Numer. Anal.*, 18:736–754, 1978.
- [4] P. Ladevèze and D. Leguillon. Error estimate procedure in the finite element method. *SIAM J. on Numerical Analysis*, 20:485–509, 1983.
- [5] O. C. Zienkiewicz and J. Z. Zhu. A simple error estimator and adaptative procedure for practical engineering analysis. *Int. J. Numer. Meth. Engrg.*, 24:337–357, 1987.
- [6] M. Paraschivoiu, J. Peraire, and A. T. Patera. A posteriori finite element bounds for linear-functional outputs of elliptic partial differential equations. *Comput. Methods Appl. Mech. Engrg.*, 150:289–321, 1997.
- [7] N. Parés, J. Bonet, A. Huerta, and J. Peraire. The computation of bounds for linear-functional outputs of weak solutions to the two-dimensional elasticity equations. *Comput. Methods Appl. Mech. Engrg.*, 195:406–429, 2006.
- [8] F. Cirak and E. Ramm. A posteriori error estimation and adaptivity for linear elasticity using the reciprocal theorem. *Comput. Methods Appl. Mech. Engrg.*, 156:351–362, 1998.
- [9] S. Prudhomme and J. T. Oden. On goal-oriented error estimation for elliptic problems: application to the control of pointwise errors. *Comput. Methods Appl. Mech. Engrg.*, 176:313–331, 1999.
- [10] N. Parés, P. Díez, and A. Huerta. A subdomain-based flux-free a posteriori error estimators. *Comput. Methods Appl. Mech. Engrg.*, 195:297–323, 2006.
- [11] R. Rannacher and F. T. Stutzmeier. A feed-back approach to error control in finite element methods: application to linear elasticity. *Comput. Mech.*, 19:434–446, 1997.
- [12] J. T. Oden and S. Prudhomme. Goal-oriented error estimation and adaptivity for the finite element method. *Computers and Math. with Appl.*, 41:735–765, 2001.
- [13] N. Parés, P. Díez, and A. Huerta. Exact bounds of the advection-diffusion-reaction equation using flux-free error estimates. *SIAM J. Sci. Comput.*, 31:3064–3089, 2009.
- [14] N. Parés, P. Díez, and A. Huerta. Computable exact bounds for linear outputs from stabilized solutions of the advection-diffusion-reaction equation. *Int. J. Numer. Meth. Engrg.*, 93:483–509, 2013.
- [15] F. Larsson, P. Hansbo, and K. Runesson. Strategies for computing goal-oriented a posteriori error measures in non-linear elasticity. *Int. J. Numer. Meth. Engrg.*, 55:879–894, 2002.
- [16] A. Meyer. Error estimators and the adaptive finite element method on large strain deformation problems. *Mathematical Methods in the Applied Sciences*, 32:2148–2159, 2009.
- [17] N. Parés, P. Díez, and A. Huerta. Bounds of functional outputs for parabolic problems. Part I: Exact bounds of the discontinuous galerkin time discretization. *Comput. Methods Appl. Mech. Engrg.*, 197:1641–1660, 2008.
- [18] N. Parés, P. Díez, and A. Huerta. Bounds of functional outputs for parabolic problems. Part II: Bounds of the exact solution. *Comput. Methods Appl. Mech. Engrg.*, 197:1661–1679, 2008.
- [19] V. Carey, D. Estep, A. Johansson, M. Larson, and S. Tavener. Blockwise adaptivity for time dependent problems based on coarse scale adjoint solutions. *SIAM J. Sci. Comput.*, 32:2121–2145, 2010.
- [20] W. Bangerth, M. Geiger, and R. Rannacher. Adaptive Galerkin finite element methods for the wave equation. *Computational Methods in Applied Mathematics*, 1:3–48, 2010.
- [21] W. Bangerth and R. Rannacher. Finite element approximation of the acoustic wave equation: error control and mesh adaptation. *East-West Journal of Numerical Mathematics*, 7:263–282, 1999.
- [22] W. Bangerth and R. Rannacher. Adaptive finite element techniques for the acoustic wave equation. *Journal of Computational Acoustics*, 9:575–591, 2001.
- [23] D. Fuentes, D. Littlefield, J. T. Oden, and S. Prudhomme. Extensions of goal-oriented error estimation methods to simulation of highly-nonlinear response of shock-loaded elastomer-reinforced structures. *Comput. Methods Appl. Mech. Engrg.*, 195:4659–4680, 2006.
- [24] F. Verdugo, N. Parés, and P. Díez. Modal based goal-oriented error assessment for timeline-dependent quantities in transient dynamics. *Int. J. Numer. Meth. Engrg.*, 95:685–720, 2013.
- [25] K. Eriksson, D. Estep, P. Hansbo, and C. Johnson. *Computational Differential Equations*. Studentlitteratur, 1996.
- [26] C. Johnson. Discontinuous galerkin finite element methods for second order hyperbolic problems. *Comput. Methods Appl. Mech. Engrg.*, 107:117–129, 1993.
- [27] T. J. R. Hughes and G. M. Hulbert. Space-time finite element methods for elastodynamics: Formulations and error estimates. *Comput. Methods Appl. Mech. Engrg.*, 66:339–363, 1988.
- [28] G. M. Hulbert and T. J. R. Hughes. Space-time finite element methods for second-order hyperbolic equations. *Comput. Methods Appl. Mech. Engrg.*, 84:327–348, 1990.

- [29] F. Casadei, P. Díez, and F. Verdugo. An algorithm for mesh refinement and un-refinement in fast transient dynamics. *International Journal of Computational Methods*, 10:1–31, 2013.
- [30] L. Demkowicz, J. T. Oden, W. Rachowicz, and O. Hardy. Toward a universal h-p adaptive finite element strategy, part 1. Constrained approximation and data structure. *Comput. Methods Appl. Mech. Engrg.*, 77:79–112, 1989.
- [31] M. A. Yerry and M. S. Shephard. A modified quadtree approach to finite element mesh generation. *IEEE Computer graphics and Applications*, 3:34–46, 1983.
- [32] P. Díez and G. Calderón. Remeshing criteria and proper error representations for goal oriented h-adaptivity. *Comput. Methods Appl. Mech. Engrg.*, 196:719–733, 2007.

Paper E

An algorithm for  
mesh refinement and  
un-refinement  
in fast transient dynamics

F. Casadei, P. Díez and F. Verdugo

---

*International Journal of Computational Methods*,  
Volume 10, Issue 04, Pages 1-31, 2013



AN ALGORITHM FOR MESH REFINEMENT AND  
UN-REFINEMENT IN FAST TRANSIENT DYNAMICS

FOLCO CASADEI

*Joint Research Center, Institute for the Protection and  
Security of the Citizen  
T.P. 480, I-21027 Ispira, Italy  
folco.casadei@jrc.ec.europa.eu  
<http://europlexus.jrc.ec.europa.eu>*

PEDRO DÍEZ\* and FRANCESC VERDUGO†

*Universitat Politècnica de Catalunya  
Barcelona, Spain  
\*vre.diez@upc.edu  
†francesc.verdugo@upc.edu*

Received 16 October 2011

Accepted 25 July 2012

Published 2 April 2013

A procedure to locally refine and un-refine an unstructured computational grid of four-node quadrilaterals (in 2D) or of eight-node hexahedra (in 3D) is presented. The chosen refinement strategy generates only elements of the same type as their parents, but also produces so-called hanging nodes along nonconforming element-to-element interfaces. Continuity of the solution across such interfaces is enforced strongly by Lagrange multipliers. The element split and un-split algorithm is entirely integer-based. It relies only upon element connectivity and makes no use of nodal coordinates or other real-number quantities. The chosen data structure and the continuous tracking of the nature of each node facilitate the treatment of natural and essential boundary conditions in adaptivity. A generalization of the concept of neighbor elements allows transport calculations in adaptive fluid calculations. The proposed procedure is tested in structure and fluid wave propagation problems in explicit transient dynamics.

*Keywords:* Mesh refinement; mesh un-refinement; adaptivity; 3D; explicit; transient dynamics.

## 1. Introduction

The numerical simulation of complex 3D fast transient dynamic phenomena, e.g., for the prediction of blast effects on critical infrastructures, requires long calculations even on today's computers, due to the large number of elements — typically in the order of millions or even more — needed to obtain the desired accuracy. One of

*F. Casadei, P. Díez & F. Verdugo*

the most promising techniques to save CPU time is mesh adaptivity, i.e., automatic mesh refinement and un-refinement in order to “put the small elements only where they are really needed”. Adaptive techniques based on error estimators/indicators are nowadays relatively common in statics, but their application in fast transient dynamic problems, characterized by wave propagation, is still challenging. In order to follow rapidly evolving phenomena, the chosen mesh adaptation techniques must be particularly simple, efficient and robust.

This paper presents a strategy to continuously refine and un-refine a computational mesh in explicit fast transient dynamics. The element shapes considered here are only the four-node quadrilateral (QUA4) in 2D and the eight-node hexahedron (CUB8) in 3D. However, the method can be applied with minor modifications also to other element shapes. One basic choice is that, when splitting an element in order to locally refine the mesh, only elements of the same shape as their “parent” (i.e., either QUA4 or CUB8) are generated. This simplifies the geometry- and connectivity-updating calculations and contributes to the robustness of the method, but also produces so-called “hanging” nodes along the nonconforming element-to-element interfaces, i.e., in the zones where element size varies.

Over the last three decades a vast literature has been produced on mesh refinement techniques related to adaptivity, and a review is out of scope here. As concerns the purely geometric aspects of element splitting and un-splitting and the tree-like data organization, the strategy chosen here resembles the one proposed for example in 2D by Yerry and Shephard already in 1983 and by Demkowicz *et al.* [1985, 1989]. Similar techniques are still used nowadays in complex 3D applications; see e.g., Meyer [2009] or Burstedde *et al.* [2009], where massive parallelization aspects are discussed.

Our final target is to use mesh adaptivity in safety studies to evaluate, in particular, the vulnerability of buildings or other critical infrastructure to blast loading. These applications require modeling of the fluid and of the structure (including failure and fragmentation), plus robust and efficient fluid–structure interaction (FSI) algorithms. Numerical models are huge in 3D, with millions of finite elements or finite volume cells, mainly in the fluid domain. Therefore, adaptivity can be exploited in a variety of manners. For example: to accurately track the shock fronts of blast waves, to improve the representation of material interfaces and of free surfaces (e.g., in blast loading of submerged structures), and to automatically refine the fluid mesh near structural walls for improved accuracy of embedded-type FSI algorithms. The first task requires suitable error indicators, see e.g., the pioneering work of Peraire *et al.* [1987], the comprehensive paper by Nithiarasu and Zienkiewicz [2000] and the article of Frey and Alauzet [2005], for fluid problems, or the recent paper by Erhart *et al.* [2006] on large deformation under impact, for solid problems.

The present work deals with only one ingredient of adaptive formulations, i.e., the geometrical and data-structure aspects related to continuous mesh refinement and un-refinement during a transient dynamic solution. The subject of

error estimators/indicators — or of any other criteria (e.g., structure proximity in FSI) needed to automatically drive mesh adaptation — is left for a subsequent contribution.

The class of problems of interest here, namely fast transient FSI phenomena related to blast loading of complex 3D structures up to failure and fragmentation, can partially justify the specific choice of elements shape (quadrilaterals/hexahedra instead of the simpler and more commonly used, in adaptivity, triangles/tetrahedra) and of refinement strategy (which produces nonconforming refined meshes due to hanging nodes). In this class of applications use is typically made of “embedded” FSI algorithms, see e.g., Casadei *et al.* [2011], whereby the structure mesh is immersed in a regular (even uniform sometimes) background fluid mesh. This explains the use of quadrilaterals/hexahedra, without need for complicated mesh generation tools that typically operate only on simplexes (triangles/tetrahedra). Although structure adaptivity is also considered below for full generality, we are thus mainly interested in adapting the fluid domain.

The interested reader may find it useful to compare the present mesh refinement strategy with the more widely used ones, based upon simplex elements, e.g., in the papers by Liu, Zhang and co-workers. The use of simplex shapes facilitates automatic meshing and re-meshing of arbitrarily complex domains, whenever this is needed: not only for the discretization of the computational domain in FE/FV solid mechanics [Zhang *et al.* (2008a, 2008b); Nguyen-Thoi *et al.* (2009); Li and Liu (2011)] and in fluids [Xu *et al.* (2010)], but also in those mesh-free formulations which still require a background mesh to perform numerical integration [Liu and Tu (2002); Liu *et al.* (2006); Kee *et al.* (2008); Tang *et al.* (2011)].

Mesh refinement in the cited references makes typically use of Delaunay triangulation and/or of its dual, the Voronoi diagram, in order to obtain optimal and conforming refined (arbitrary, unstructured) meshes. This may sometimes lead to badly-shaped (highly distorted) elements, thus requiring additional treatments such as redundant cells removal, diagonal swapping or grid smoothing. In the present approach refinement is conceptually straightforward, being based on simple bisection. This generates only descendent elements of the same shape and aspect as their parent (which is important, especially in 3D) and avoids any element distortion by construction. However, the price to be paid is the appearance of hanging nodes (nonconforming interfaces), which require a specific treatment, e.g., by Lagrange multipliers as proposed below. It is also clear that such a technique is especially useful when the base mesh is regular, although not necessarily structured (which is the case in the applications envisaged here). With geometrically complex domains to be discretized by conforming meshes, the use of simplexes is obviously superior. As concerns efficiency of the proposed procedure, no comparison with other methods (e.g., based on simplexes) was attempted. Despite its simplicity (bisection) the present procedure is relatively involved in 3D, due to hanging nodes. However, the resulting information on the nature of nodes and of neighboring elements greatly

*F. Casadei, P. Díez & F. Verdugo*

facilitates the treatment of boundary conditions (and of transport terms in fluids), thus recovering part of the effort devoted to geometrical calculations.

This paper is organized as follows. Section 2 presents the chosen mesh refinement strategy, the classification of nodes — in such a way to facilitate the treatment of boundary conditions and the enforcement of continuity constraints — and the neighborhood relations between elements, which are useful both for element adaptation and for the calculation of numerical fluxes in fluid problems. Then in Sec. 3 the element splitting and un-splitting algorithms are detailed. Section 4 shows how to impose constraints on the adaptive solution according to the nature of each node resulting from the algorithms of Sec. 3. The calculation of numerical fluxes in adaptive fluid meshes using a generalized notion of neighbors is also detailed. Numerical examples are presented in Sec. 5 and conclusions and perspectives for future developments are given in Sec. 6. Some auxiliary procedures are listed in appendix.

The proposed algorithms are implemented and tested in EUROPLEXUS [Casadei *et al.* (2012)], a computer program for fast transient analysis of fluid–structure systems under dynamic loading, which is jointly developed by the French Commissariat à l’Energie Atomique (CEA Saclay) and by the Joint Research Centre of the European Commission (JRC Ispra).

## 2. Mesh Refinement Strategy

The chosen mesh refinement strategy is illustrated in 2D for the QUA4 element (Fig. 1).

### 2.1. Base mesh

First, some terminology is introduced for the *base* mesh, i.e., the initial (coarse) mesh, assumed to be given in input (left drawing in Fig. 1). Let  $i$  be the generic *element*, of *vertices*  $V_I, I = 1, \dots, 4$  which coincide with the four *element nodes*  $I, J, K, L$ . Elements are numbered anti-clockwise, e.g.,  $IJKL$  for element  $i$  in the figure. Each element has four *faces*  $F_k, k = 1, \dots, 4$ , with two nodes each:  $IJ, JK, KL, LI$  in the example. The mesh information is completed by the list of neighbor

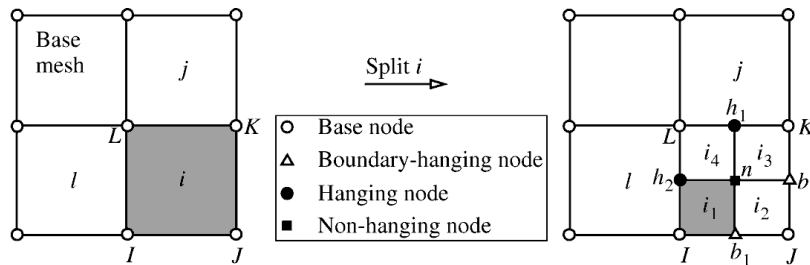


Fig. 1. Splitting a QUA4.

1350018-4

elements, or simply *neighbors*, across each face. This list is built up once by performing a search over the base mesh, after reading it as input data. Two elements are (reciprocally) neighbors across a given face if the face belongs to both elements (with opposite orientations). In Fig. 1 element  $i$  has no neighbor across faces 1 and 2 while it has neighbors  $j$  and  $l$  across faces 3 and 4, respectively. The presence of a neighbor indicates an *internal* face (within the domain), while its absence indicates an *external* face (on the domain boundary). The base mesh is assumed *conforming*, hence neighbors are reciprocal: if  $i$  has neighbor  $j$  across one of its faces  $F_k^{(i)}$ , then  $j$  has neighbor  $i$  across one of its faces  $F_l^{(j)}$ , and *vice versa*. Note also that the base mesh is assumed *unstructured* for full generality, although all numerical examples in Sec. 5 use structured element patches for simplicity.

### 2.2. Element splitting

A generic element  $i$  is split as shown in Fig. 1, right drawing. Four *descendent* elements  $i_1, i_2, i_3, i_4$  are created, all of which have element  $i$  as their parent element. In addition, one to five new descendent nodes are created. In the example,  $n$  is the *central node*, which is always created, while  $b_1, b_2, h_1, h_2$  are the *face nodes*. A new face node is created or not, depending upon the mesh state across the face itself. If there is a neighbor, and if this has been previously refined, then the face node exists already; otherwise, a new face node is created. In the example of Fig. 1 all four face nodes are created upon splitting of element  $i$ .

Element splitting is a recursive process, and can go on as shown in Fig. 2. Therefore, it seems convenient to store elements in a tree-like data structure [Yerry and Shephard (1983)], see Fig. 3 corresponding to the last mesh of Fig. 2. Each element occupies a certain *level* in the tree, with base elements (and only them) at level 1 by convention. Base elements have no parent. The notions of *right* and *left siblings* are also useful, to traverse the tree quickly in both directions. Elements with descendants are called *branches* while elements without descendants are called *leaves*. Note that only leaf elements take part in the computation. Branch elements are not computed, but are kept in memory (flagged as idle). This facilitates mesh un-refinement by simply re-activating a previously idle element.

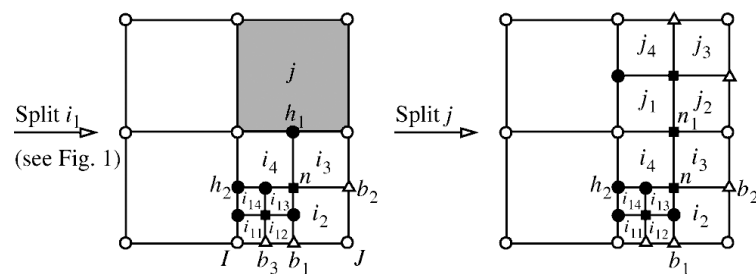


Fig. 2. Further splitting.

F. Casadei, P. Díez & F. Verdugo

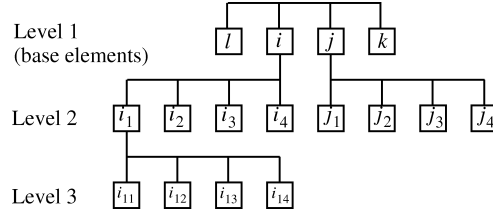


Fig. 3. Tree data structure for the elements.

In Fig. 2, the example of Fig. 1 is continued by showing further splitting of level-2 element  $i_1$ , which generates level-3 descendents  $i_{11}, i_{12}, i_{13}, i_{14}$  and five new nodes. Then, base element  $j$  is split into  $j_1, j_2, j_3, j_4$ , showing a case where one of the face nodes ( $h_1$ ) exists already and needs not be created. However, the nature of this node *changes* from hanging to nonhanging (see Sec. 2.3) and therefore it is renamed  $n_1$  for clarity.

### 2.3. Node types

With the chosen mesh refinement strategy there are up to *four* different types of nodes in a mesh, and the nature of each node is (continuously) tracked during the transient. Like for elements, a level is associated to each node. The nodes of the base mesh are called *base nodes* and are the only nodes at level 1. All other nodes are *descendent nodes*, of which there are three types: *hanging* nodes, *boundary-hanging* nodes and *nonhanging* nodes, see Table 1.

Hanging nodes, e.g.,  $h_1$  and  $h_2$  in Fig. 1, are a direct consequence of the chosen element splitting procedure. They occur at locally nonconforming element-to-element interfaces, i.e., wherever a “bigger” and a “smaller” element are contiguous but without sharing a common face. Suitable constraints have to be imposed at such nodes in order to ensure continuity of the numerical solution across the interface. For example, in a displacement-based FE formulation it is clear that the degrees of

Table 1. A classification of nodes.

Node type	Location	Classification	Interface
Base	Internal	—	—
	Boundary	—	—
Descendent	Internal	Nonhanging	Conforming
		Hanging	Nonconforming
	Boundary	Hanging (3D only)	Nonconforming (internally)
		B-hanging	—

Example of hanging nodes on 3D boundary

freedom of  $h_1$  in Fig. 1 are not free. They depend (“hang”) upon those of nodes  $L$  and  $K$  (i.e., the nodes of the face on which the hanging node is located), if continuity has to be ensured. These nodes are called the *masters* of the hanging node.

Boundary-hanging nodes (*b-hanging* for brevity in the following), e.g.,  $b_1$  and  $b_2$  in Fig. 1, are the descendent nodes, located on the boundary of the body (as the name implies), which lie on a conforming element-to-element interface. Note that in 2D a descendent node on the boundary is guaranteed to lie upon a conforming interface. Consequently, in 2D all descendent nodes on the boundary are b-hanging. However, in 3D the same property does *not* hold (see the inset in Table 1 and the discussion in Sec. 3), and therefore *both* conditions must be satisfied for a 3D node to be b-hanging. B-hanging nodes do not really “hang” upon any other nodes (and therefore the term is perhaps somewhat misleading), but their identification greatly facilitates the treatment of boundary conditions in an adaptive mesh. These nodes can be programmed so as to automatically “inherit” any boundary conditions that a user may have prescribed on the base mesh, i.e., on the nodes of the *base face* upon which the b-hanging node is located. Such nodes are called the *masters* of the b-hanging node. For example, in Fig. 2 nodes  $b_1$  and  $b_3$  inherit conditions from base nodes  $I$  and  $J$ . Note that the masters of a b-hanging node are always base (boundary) nodes, while the masters of a hanging node can be of any type. For the element shapes considered here, each hanging or b-hanging node has two masters in 2D, two or four masters (depending on whether it is on a corner or on a face) in 3D.

Nonhanging nodes are any other descendent nodes. They are necessarily located in the interior of the domain, at locally conforming element-to-element interfaces. The degrees of freedom associated with these nodes are completely free. In fact, the case of “boundary” conditions (constraints) imposed by a user on *internal* nodes is not considered in this paper.

#### 2.4. *Neighbors and pseudo-neighbors*

Another consequence of the chosen element splitting procedure is that the simple bi-univocal neighborhood relations valid for the (conforming) base mesh no longer hold for a locally refined mesh, see Fig. 4. Neighbors are connected by a double arrow

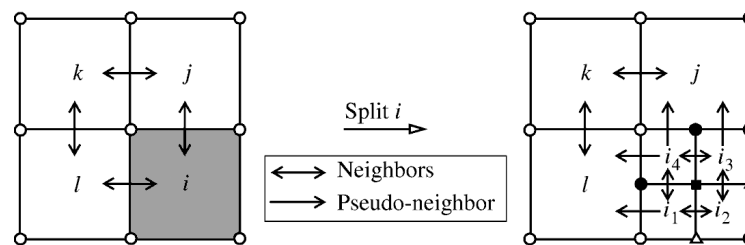


Fig. 4. Neighbors and pseudo-neighbors.

*F. Casadei, P. Díez & F. Verdugo*

as in  $i \leftrightarrow j$ . When element  $i$  is split into its descendants, there are *two* of these (smaller) elements  $i_3$  and  $i_4$  adjacent to element  $j$ . We identify this situation by saying that  $i_3$  and  $i_4$  have  $j$  as *pseudo-neighbor* (or simply *p-neighbor* for brevity), across their upper face in the example. Note that this relation is univocal: element  $j$  does *not* have  $i_3$  and  $i_4$  as p-neighbors across its bottom face in the example. In fact, it (still) has element  $i$  (their parent, now idle) as neighbor. P-neighbors are connected by a single arrow as in  $i_4 \rightarrow j$ . The following definitions of neighbor and of p-neighbor are adopted:

- The *neighbor* of an element across a face is the element of the same level, active (leaf) or idle (branch), adjacent to the face, or 0 if there is no such element.
- The *p-neighbor* of an element across a given face is the lower-level (i.e., larger) active (leaf) element adjacent to the face, or 0 if there is no such element.

Neighbor and p-neighbor are mutually exclusive at a given face. That is, an element can have either a neighbor, or a p-neighbor (or nothing) across a face, but it cannot have both. This choice simplifies the implementation and speeds up calculations because the table of neighbors and p-neighbors has a fixed, known length. The presence of a neighbor across a face indicates an internal, locally conforming element-to-element interface. The presence of a p-neighbor indicates an internal, locally nonconforming interface. In fact, on the concerned face (of the p-neighbor) there are always one or more hanging nodes; see the examples. The absence of a neighbor and p-neighbor indicates that the face is external. The p-neighbor relation is univocal according to the above definition. That is, if element  $i$  has  $j$  as p-neighbor, then  $j$  has  $i$  neither as p-neighbor, nor as neighbor. In fact, in this case  $j$  has an *ancestor* of  $i$  (more precisely, the one at the same level as  $j$ ) as neighbor.

Keeping track of neighbors and p-neighbors during mesh refinement and un-refinement serves two purposes: first, it is used in the mesh adapting algorithms themselves; second, it allows efficient computation of transport terms in fluid applications, see Sec. 4.3.

### 3. Element Splitting and Un-Splitting Algorithms

The element splitting and un-splitting algorithms are now presented, for generality in 3D for the CUB8 element shape, i.e., the 8-node hexahedron. The same algorithms are applied also in 2D to the QUA4 element shape, with the simplifications indicated in Sec. 3.7. Extensions to other 2D or 3D element shapes are also possible using the same strategy, with only minor modifications. Before detailing the algorithms, some further definitions are given and the data structure used in the implementation is shortly introduced.

#### 3.1. The CUB8 hexahedron

The CUB8 element is shown in Fig. 5. It has eight *vertices* (or nodes)  $V_I$ ,  $I = 1, \dots, 8$  enumerated (in the element connectivity table) in such a way that the first four are

*An Algorithm for Mesh Refinement and Un-Refinement in Fast Transient Dynamics*

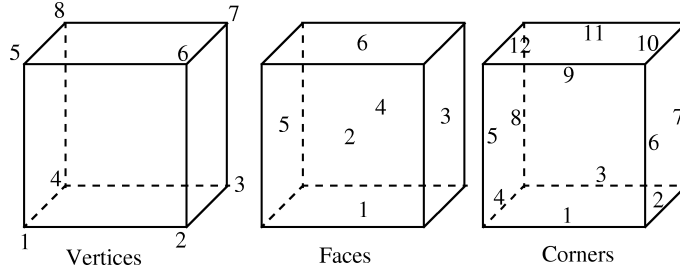


Fig. 5. CUB8 vertices, faces, corners.

located on the “bottom” element face, and so that the oriented normal to this face “enters” into the element. The last four vertices, located on the “upper” element face, are enumerated consistently (in this case the oriented normal “exits” from the element) so that  $V_5$  stays “above”  $V_1$ , etc.

The element has 6 *faces*  $F_k$ ,  $k = 1, \dots, 6$ , with four nodes each. Face numbering is such that the oriented normal always exits from the element. This convention is called *anti-clockwise* orientation. For example,  $F_1 = \{V_1, V_4, V_3, V_2\}$ , or  $F_1 = \{1, 4, 3, 2\}$  for brevity. Faces are shown in Fig. 5 and are listed (together with all other constant connectivity data) in Table 2.

3D elements also have *corners*, which do not exist in 2D. In the CUB8 there are twelve corners  $C_i$ ,  $i = 1, \dots, 12$ , with two nodes each, see Fig. 5. For example,  $C_1 = \{V_1, V_2\} = \{1, 2\}$ . Much of the complexity of 3D algorithms comes from the fact that in order to split or un-split an element one has to consider not only the elements adjacent to faces (i.e., neighbors and p-neighbors), but also “adjacent to corners”, see Sec. 3.3. This is not the case in 2D.

Each face of the CUB8 is bounded by four corners. This information is kept in a constant table  $F_C(c, f)$ ,  $c = 1, \dots, 4$ ,  $f = 1, \dots, 6$  where the first entry is the corner and the second entry is the face. For example, for the first face of the CUB8:  $F_C(c, 1) = \{C_4, C_3, C_2, C_1\} = \{4, 3, 2, 1\}$ . Note that the corners of a given face  $F_k$  are enumerated in the same order as face nodes: i.e., anti-clockwise starting from the first node of the face.

Table 2. Constant connectivity data used for the CUB8 element shape.

Data	Symbol	Values
Vertices	$V_{1\div 8}$	1-2-3-4-5-6-7-8.
Faces	$F_{1\div 4, 1\div 6}$	1-4-3-2; 1-2-6-5; 2-3-7-6; 3-4-8-7; 4-1-5-8; 5-6-7-8.
Corners	$C_{1\div 2, 1\div 12}$	1-2; 2-3; 3-4; 4-1; 1-5; 2-6; 3-7; 4-8; 5-6; 6-7; 7-8; 8-5.
Faces to corners	$F_{C, 1\div 4, 1\div 6}$	4-3-2-1; 1-6-9-5; 2-7-10-6; 3-8-11-7; 4-5-12-8; 9-10-11-12.
Corners to face	$C_{F, 1\div 2, 1\div 12}$	1-2; 1-3; 1-4; 1-5; 2-5; 3-2; 4-3; 5-4; 2-6; 3-6; 4-6; 5-6.
Corners to corner nodes	$C_{C, 1\div 2, 1\div 12}$	1-2; 2-3; 3-4; 4-1; 1-5; 2-6; 3-7; 4-8; 5-6; 6-7; 7-8; 8-5.
Faces to face nodes	$F_{F, 1\div 2, 1\div 6}$	1-3; 1-6; 2-7; 3-8; 4-5; 5-7.
Corners to descendants	$C_{D, 1\div 2, 1\div 12}$	1-2; 2-3; 3-4; 4-1; 1-5; 2-6; 3-7; 4-8; 5-6; 6-7; 7-8; 8-5.

F. Casadei, P. Díez & F. Verdugo

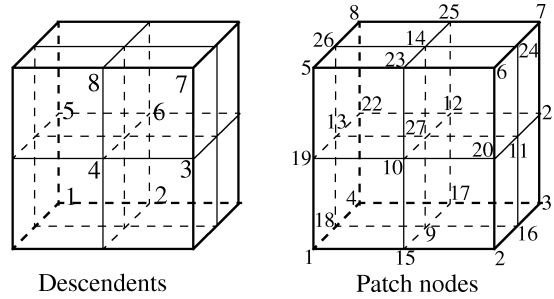


Fig. 6. Splitting/un-splitting a CUB8.

Each corner is adjacent to two faces of the element. This information is kept in a constant table  $C_F(f, c)$ ,  $f = 1, 2$ ,  $c = 1, \dots, 12$  where the first entry is the face and the second entry is the corner (this is somehow the “inverse” of  $F_C$ ). For example, for the first corner of the CUB8:  $C_F(f, 1) = \{F_1, F_2\} = \{1, 2\}$ .

The CUB8 element is split into a *patch* of eight CUB8 *descendents*  $d_j$ ,  $j = 1, \dots, 8$ , see Fig. 6. They are enumerated in such a way that the  $j$ th descendent  $d_j$  is adjacent to (contains) the  $j$ th vertex  $V_j$  of the parent. In the splitting/un-splitting process, the following nodes have to be considered in addition to the cube vertices: one node for each face, called the *face nodes*  $N_F$ ,  $F = 1, \dots, 6$ , one node for each corner, called the *corner nodes*  $N_C$ ,  $C = 1, \dots, 12$ , and one node at the element centre, called the *central node*  $N_M$ . Thus, by including also the vertices, there are  $8 + 6 + 12 + 1 = 27$  *patch nodes*, involved in the splitting or un-splitting of a CUB8. These are set in an array  $P_p$ ,  $p = 1, \dots, 27$  in the following order, see Fig. 6: first the eight vertices of the parent element ( $P_{1\div 8} = V_{1\div 8}$ ), then the six face nodes ( $P_{9\div 14} = N_{F,1\div 6}$ ), then the twelve corner nodes ( $P_{15\div 26} = N_{C,1\div 12}$ ), and finally the central node ( $P_{27} = N_M$ ). The notation  $A_{a\div b}$  is used as a shorthand to indicate all items from  $a$  to  $b$  in array  $A$ .

An important assumption in the algorithms to be presented below is that all descendent elements are *numbered consistently* with their parent. This means, for example, that if the first face of an element points (say) “downward”, then all its descendents’ first faces also point downward, etc. This choice is quite natural and greatly facilitates the splitting/un-splitting operations. However, this assumption can only be satisfied for elements which, in adaptivity, produce descendents of the same shape as — and which can be oriented in the same way as — their parent, like is the case here.

There are also other (constant) data useful in the element splitting/un-splitting process. Consider first the following problem: given a branch element  $i$ , identify the (corner) node  $N_c$  located in the middle of its  $c$ th corner, *without* having at disposal the patch nodes table  $N_p$  for  $i$  (the construction of this table is relatively expensive and is performed only for the current element  $i$  being split or un-split, *not* for its adjacent elements). Note that node  $N_c$  does *not* belong to element  $i$ , but

it belongs to at least one (more precisely, to two) of its descendents. A constant table  $C_C(m, c)$ ,  $m = 1, 2$ ,  $c = 1, \dots, 12$  solves the problem: the first entry  $C_C(1, c)$  is the index of the descendent, the second entry  $C_C(2, c)$  is the index of the node. Thus, for example, the corner node on corner 1 of a branch element is the second node ( $C_C(2, 1) = 2$ ) of its first descendent ( $C_C(1, 1) = 1$ ).

A similar constant table  $F_F(m, f)$ ,  $m = 1, 2$ ,  $f = 1, \dots, 6$  allows to find the face node on the  $f$ th face of a branch element  $i$ . The first entry  $F_F(1, f)$  is the index of the descendent; the second entry  $F_F(2, f)$  is the index of the node. Thus, for example, the face node on face 1 of a branch element is the third node ( $F_F(2, 1) = 3$ ) of its first descendent ( $F_F(1, 1) = 1$ ).

Finally, a constant table  $C_D(m, c)$ ,  $m = 1, 2$ ,  $c = 1, \dots, 12$  lists the two descendents adjacent to each corner  $c$  of a branch element, in the same order as corner nodes are listed in table  $C_i$ . For example, the descendents adjacent to the first corner of a parent are (in this order)  $d_1$  and  $d_2$  (thus  $C_D(1, 1) = 1$  and  $C_D(2, 1) = 2$ ). Note that, with the numbering conventions assumed here for the CUB8, it is  $C_i = C_C = C_D$  so only one of these three tables would suffice. However, the tables are kept distinct for generality in view of the application of these algorithms to other element shapes.

### 3.2. *Some auxiliary procedures*

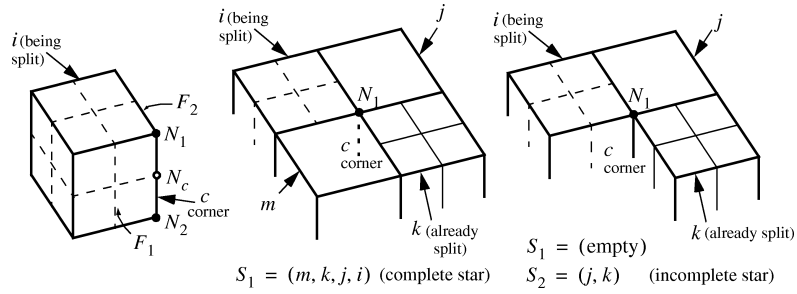
There are some auxiliary procedures which are useful in the splitting/un-splitting algorithms to be detailed below. The first one computes the *nature of a face*  $F_k$  of an element  $i$ , i.e., whether the face is internal to the computational domain or external, i.e., on the boundary of the domain, based upon the neighbor and the p-neighbor at the face. The procedure (Algorithm A.1) is listed in the appendix.

Another procedure (Algorithm A.2 in appendix) computes the *nature of an external corner*  $C_i$  of a descendent element  $d_j$ , i.e., whether this corner lies on a base corner  $C_B$  or on a base face  $F_B$ . A criterion to find whether a corner is internal or external will be presented in Sec. 3.3, based on the concept of corner star introduced there. Note that with the element splitting/un-splitting strategy used here an element corner — whatever the level of the element — is either (completely) internal to the domain or (completely) external, i.e., on the domain boundary. It is impossible to have partially internal, partially external corners.

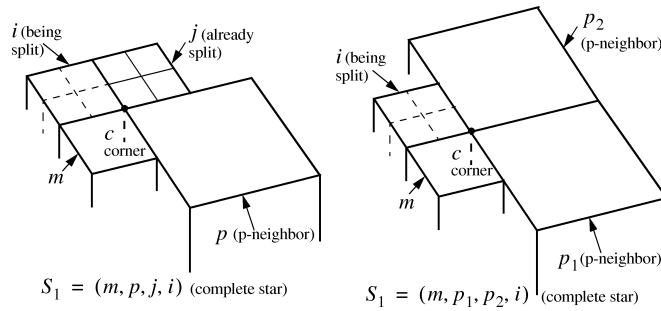
### 3.3. *Corner neighbors and corner star data structure*

The nature of a corner node (hanging, b-hanging, nonhanging) depends upon the whole set of elements “adjacent” (in a broad sense) to the corner. We call such elements *corner neighbors* and the list of these elements the *corner star* of element  $i$  with respect to (i.e., around) its corner  $c$ , see Fig. 7. The number of neighbors to a corner is potentially unlimited for an unstructured mesh, but in practice there are between one (element  $i$  itself) and slightly more than four elements in a corner

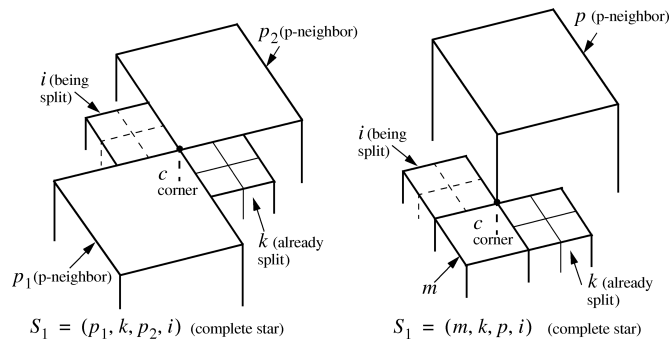
F. Casadei, P. Díez & F. Verdugo



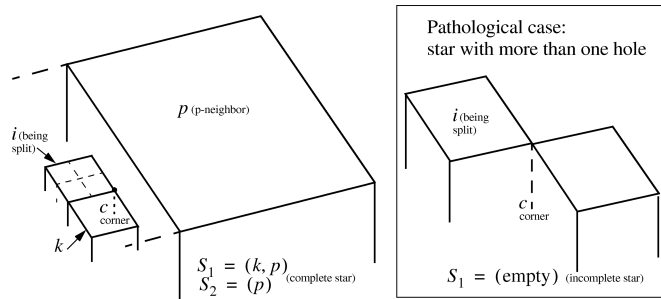
(a)



(b)



(c)



(d)

Fig. 7. Examples of corner stars (complete or incomplete).

1350018-12

star. Values much larger than four are unlikely because the elements would be badly shaped. For a *regular* mesh of CUB8 there are *exactly* between one and four elements in each corner star.

As shown in Fig. 7, it is useful to distinguish between a *complete* star and an *incomplete* star. A star is complete if the space around the corner is entirely filled by elements (without “holes”), else the star is incomplete. One sees then immediately that an element’s *corner* is *external* if and only if its corner star is incomplete, else the corner is *internal*. This distinction is useful because Algorithm A.2 needs to be applied only to external corners. Note incidentally that the nature of a corner *cannot* be computed based only upon the nature of its nodes: in fact a corner whose nodes are all external can be internal. The same holds for faces.

The procedure to determine whether or not a star is complete is listed in the appendix (see Algorithm A.3).

### 3.4. Computing a corner star

The calculation of the corner star of an element  $i$  around its corner  $c$  is the most CPU-expensive component of the present algorithms, because it must deal with a large variety of geometrical cases; see e.g., Fig. 7. Two different approaches have been tentatively considered.

The first one consists in performing a (fast) geometrical search in the vicinity of the corner under consideration, in order to locate all the potentially involved elements. To this end the extent of the concerned zone around the corner has to be chosen, and this is not simple in the presence of elements of very different sizes (p-neighbors), like is the case here. The zone must be large enough to ensure that no potential neighbor is overlooked, but using large zones increases the cost of the search. A second drawback is that the search uses real-number quantities, e.g., nodal coordinates. The associated tests are delicate and the robustness of the method can be affected. Finally, elements which lie within the zone are not guaranteed to be corner neighbors and the verification requires further complex calculations.

The second approach is based on the observation that star elements are (recursively) the neighbors or p-neighbors of  $i$  across its two faces  $F_1, F_2$  adjacent to  $c$ , see Fig. 7(a). So an algorithm can start from face  $F_1 = C_F(1, c)$  and recursively compute neighbor and p-neighbor elements (adjacent to this corner) until it either reaches (again) the current element  $i$ , or the search terminates. In the first case the star is complete, and this can be recognized by the presence of  $i$  as the last element in the list. In the second case, the same search process is repeated, but starting from face  $F_2 = C_F(2, c)$ . Thus a generic corner star is made of *two* element lists,  $S_1$  and  $S_2$ . Let  $n_{S_1}, n_{S_2}$  be the number of items in the lists. Note that element  $i$  is not inserted at the beginning of the lists, which start directly with  $i$ ’s neighbor or p-neighbor across the corresponding face. Element  $i$  can be present (as the last item) in  $S_1$ , and in this case the star is complete just by using the first list, so that  $n_{S_2} = 0$  and  $S_2$  is not built up at all. However, element  $i$  cannot appear in  $S_2$ .

*F. Casadei, P. Díez & F. Verdugo*

The advantage of the second method, which is the one chosen here, is that the search is entirely integer-based and therefore very robust. In fact, there are no tests on real-number quantities, subjected to a tolerance. Only element connectivity is used (nodal coordinates are never considered), and the knowledge of neighbors and p-neighbors resulting from the algorithms is fully exploited, resulting in a very efficient algorithm.

The method has only one limitation: since it is based on (recursively) using neighbors and p-neighbors, it can only deal with corner stars containing *at most one* “hole”. As shown in Fig. 7(d) (last drawing), a star with more than one hole would not be entirely detected by this procedure (although it would be correctly marked as incomplete). However, such a case can be considered pathological, and thus impossible in real applications, since it is not good practice in Finite Elements to connect different 3D continuum mesh zones just along a corner.

The procedure to build up a corner star is relatively involved (although not difficult) due to the variety of possibilities, especially in the presence of p-neighbors, see some examples in Fig. 7. It is not completely detailed here for brevity. The constant data structures listed in Table 2 are exploited to speed up the calculations.

### 3.5. *Element splitting algorithm*

With the definitions and the procedures given in the previous sections, the element splitting and un-splitting algorithms can now be detailed. The tasks of the element splitting algorithm are:

- To find the node numbers of the split element patch  $P_{1\div 27}$  defined in Sec. 3.1, by creating any face- or corner nodes as needed, or by locating and re-using them if they already exist.
- To define the hanging status (hanging, b-hanging or nonhanging) of newly created nodes; to check the hanging status of re-used nodes and to update it if necessary.

The algorithm consists of four parts:

- (A) Loop on the eight parent element nodes to find the cube vertices  $P_{1\div 8}$ . Their hanging status is not affected.
- (B) Loop on the six element faces to find the face nodes  $N_{9\div 14}$ .
- (C) Loop on the twelve element corners to find the corner nodes  $N_{15\div 26}$ .
- (D) Generate the element central node  $P_{27}$  and set it nonhanging.

Parts (A) and (D) of the algorithm are trivial and need no further comment. Parts (B) and (C) are detailed below. The updating of neighbors and p-neighbors just after an element is split is given in Sec. 3.8.

(B) — Loop on element faces

1. Loop on the six faces  $F$  of current element  $i$ . Let  $j$  be the neighbor, and  $p$  the p-neighbor, of  $i$  across face  $F$ .

*An Algorithm for Mesh Refinement and Un-Refinement in Fast Transient Dynamics*

2. If  $j = 0$ , i.e., there is no neighbor, then:
  - Create face node  $P_{8+F}$ .
  - If  $p = 0$  the face is external. Set  $P_{8+F}$  as b-hanging upon the four nodes of the corresponding *base face*  $F_B$ , i.e., face  $F$  of  $i$ 's *base element*.  $F_B$  must exist in this case, since  $i$  has neither a neighbor nor a p-neighbor across  $F$ .
  - Else  $p > 0$  and  $P_{8+F}$  is internal. Set it as hanging upon  $F$ 's four nodes.
  - Interpolate coordinates and nodal variables at  $P_{8+F}$ .
3. Else  $j > 0$  (so it must be  $p = 0$ ).
  - a. If  $j$  is a leaf, then:
    - Create face node  $P_{8+F}$ .
    - Set it as hanging upon  $F$ 's four nodes.
    - Interpolate coordinates and nodal variables at  $P_{8+F}$ .
  - b. Else  $j$  is a branch. Then:
    - Find old face node (which must exist already)  $P_{8+F}$ .
    - Check that it was hanging and set it as nonhanging.
4. Next face  $F$ .

(C) — Loop on element corners

1. Loop on the twelve corners  $C$  of current element  $i$ , of level  $L$ . Let  $F_1, F_2$  be the two faces of  $i$  adjacent to the present corner  $C$ , let  $N_1, N_2$  be the end-nodes of corner  $C$ , and let  $N_C$  indicate the corner node (either existing or to be created), see Fig. 7(a).
2. Determine whether faces  $F_1, F_2$  are internal or external by Algorithm A.1.
3. Build up the corner star of elements around  $C$ , see Sec. 3.4.
4. Find the corner node  $N_C$ , if it exists already, otherwise create it:
  - If the corner star is not empty and contains at least one element  $m$  (other than  $i$ ) of level  $L$  (i.e., if  $m$  has a corner  $C_m$  of extremes  $N_1, N_2$ ) and  $m$  is a branch, then  $N_C$  exists and is readily determined from  $m$ 's descendents. Check that  $N_C$  was hanging upon  $N_1$  and  $N_2$ . Set  $N_{14+C} = N_C$ .
  - Else  $N_C$  is created by interpolation between  $N_1$  and  $N_2$ . Set  $N_{14+C} = N_C$ .
5. Compute the (new) hanging status of  $N_C$ :
  - If the corner star is either empty or contains only elements of level  $L$  (i.e., if there are only neighbors and no p-neighbors) and if all such elements are branches, then:
    - If  $C$  is external (the star is incomplete), then  $N_C$  is b-hanging. More precisely:
      - If  $C$  is part of an (external) base corner  $C_B$  (see Algorithm A.2), then  $N_C$  b-hangs upon the two (base) nodes of  $C_B$ .

*F. Casadei, P. Díez & F. Verdugo*

- Else  $C$  is not part of a base corner, it just lies upon an (external) base face  $F_B^e$  (see Algorithm A.2), and  $N_C$  b-hangs upon the four (base) nodes of  $F_B^e$ .
  - Else  $C$  is internal (the star is complete) and  $N_C$  is nonhanging.
  - Else the corner star is not empty and either contains at least one element of level  $M < L$  (i.e., a p-neighbor), or it contains only elements of level  $L$ , but at least one of them is a leaf. Then,  $N_C$  is hanging upon  $N_1$  and  $N_2$ .
6. Next corner  $C$ .

### 3.6. *Element un-splitting algorithm*

The task of this algorithm is to un-split an element, i.e., to re-activate a previously split (idle) element, starting from its eight descendents (which must be all leaves). At the beginning of the algorithm  $P_{1\div 27} > 0$  and all corresponding nodes exist. Upon un-splitting some nodes are deleted, the others are kept but possibly their hanging status changes. The algorithm consists of four parts:

- (A) Fill  $P_{1\div 27}$  from the descendents of the element being un-split.
- (B) Loop on the six element faces to treat the face nodes  $P_{9\div 14}$ .
- (C) Loop on the twelve element corners to treat the corner nodes  $P_{15\div 26}$ .
- (D) Verify that the old central node  $P_{27}$  was nonhanging and destroy it.

Parts (A) and (D) of the algorithm are trivial and need no further comment. Parts (B) and (C) are detailed below. The updating of neighbors and p-neighbors after element un-splitting is given in Sec. 3.9.

#### (B) — Loop on element faces

1. Loop on six faces  $F$  of current element  $i$ . Let  $j$  be the neighbor to  $i$  across  $F$ .
2. If  $j = 0$ , i.e., if there is no neighbor, then:
  - Check that face node  $P_{8+F}$  was hanging or b-hanging, then destroy it.
3. Else  $j > 0$  i.e., there is a neighbor.
  - If  $j$  is a leaf: check that face node  $P_{8+F}$  was hanging, then destroy it.
  - Else  $j$  is a branch. Check that face node  $P_{8+F}$  was nonhanging, then set it hanging upon the four face nodes of  $F$ .
4. Next face  $F$ .

#### (C) — Loop on element corners

1. Loop on the twelve corners  $C$  of current element  $i$ , of level  $L$ . Let  $N_1, N_2$  be the end-nodes of corner  $C$ , and let  $N_C$  indicate the corner node, see Fig. 7(a).
2. Build up the corner star of elements around corner  $C$ , see Sec. 3.4.

3. If the corner star is not empty and contains at least one element  $m$  (other than  $i$ ) of level  $L$  (i.e.,  $m$  has a corner  $C_m$  of extreme nodes  $N_1, N_2$ ), and  $m$  is a branch, then  $N_C$  is kept, and its hanging status is checked and set as follows:
  - If  $C$  is external, i.e., if the star is incomplete, then check that  $N_C$  was either b-hanging (either on two or on four base nodes) or hanging upon  $N_1, N_2$ .
  - Else  $C$  is internal, i.e., the star is complete. Check that  $N_C$  was either non-hanging or hanging upon  $N_1, N_2$ .
  - Set  $N_C$  hanging upon  $N_1$  and  $N_2$ .
4. Else, destroy  $N_C$ .
5. Next corner  $C$ .

### 3.7. *The QUA4 quadrilateral*

The element splitting and un-splitting algorithms for the QUA4 quadrilateral in 2D follow exactly the same strategy as those for the CUB8 element in 3D, with obvious adjustments in the number of nodes, faces, neighbors, etc. The most notable simplification is the absence of corners, and therefore also of corner stars, so that part (C) of the algorithms of Secs. 3.5 and 3.6 do not exist in 2D.

### 3.8. *Treatment of p-neighbors upon element splitting*

When an element  $i$  of level  $L$  is split as shown in Sec. 3.5, it generates descendents of level  $L + 1$  and  $i$  is flagged as idle. Then:

- Any element  $p$  that was a p-neighbor of  $i$  across a certain face, remains its p-neighbor across that same face, see Fig. 8(a).
- Any element  $k$  which had  $i$  as a p-neighbor must be treated. Such elements are sought among *all* descendents (both leaves and branches) of  $i$ 's neighbors, at any level  $K > L$ . Note that  $i$ 's p-neighbors are not considered here because they are necessarily at a level  $M < L$  and by definition they have no descendents. Let  $K$  be the level of one such element  $k$ , which had  $i$  as p-neighbor. Then:
  - If  $K = L + 1$ , then one of the descendents of  $i$  (to be determined) becomes neighbor of  $k$  and reciprocally, see Fig. 8(b).
  - Else  $K > L + 1$ . Then one of the descendents of  $i$  (to be determined) becomes p-neighbor of  $k$ , see Fig. 8(c).

### 3.9. *Treatment of p-neighbors upon element un-splitting*

When an element  $i$  of level  $L$  is un-split as shown in Sec. 3.6, its descendents of level  $L + 1$  are destroyed and  $i$  (which was flagged as idle) becomes active again. Then:

- Any element  $p$  that was a p-neighbor of  $i$  across a certain face, remains its p-neighbor across that same face, see Fig. 8(d).

*F. Casadei, P. Díez & F. Verdugo*

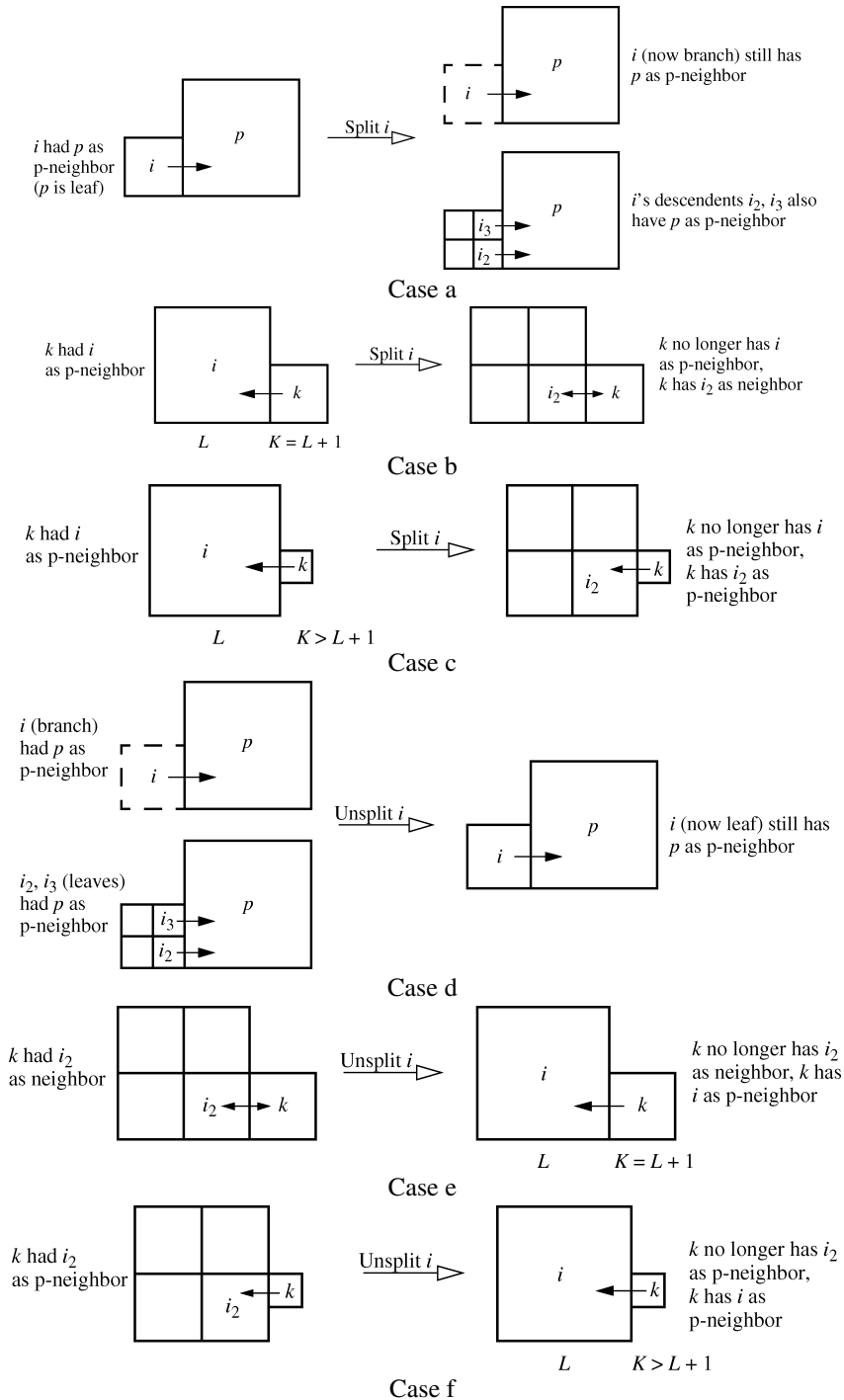


Fig. 8. Updating neighbors and p-neighbors.

1350018-18

- No elements could have  $i$  as p-neighbor because  $i$  was idle (branch). However, some elements  $k$  could have one of  $i$ 's descendents as neighbor or p-neighbor. Such elements must be sought among *all* descendents (both leaves and branches) of  $i$ 's neighbors, at any level  $K > L$ . Note that  $i$ 's p-neighbors are not considered here because they are necessarily at a level  $M < L$  and by definition they are leaves. Let  $K$  be the level of one of such elements  $k$ , having one of  $i$ 's descendents as neighbor or p-neighbor. Then:
  - If  $K = L + 1$ , then  $k$  and one of  $i$ 's descendents (to be determined) were neighbors. Element  $i$  becomes p-neighbor of  $k$ , see Fig. 8(e).
  - Else  $K > L + 1$ . Then  $k$  had one of  $i$ 's descendents (to be determined) as p-neighbor. Element  $i$  becomes p-neighbor of  $k$ , see Fig. 8(f).

#### 4. Exploiting the Adaptive Data Structure

The knowledge of hanging and b-hanging nodes resulting from the algorithms of Sec. 3 is exploited in order to impose suitable constraints ensuring consistency of the adaptive solution. First, continuity of the solution must be satisfied at nodes on locally nonconforming element-to-element interfaces (hanging nodes). Second, essential boundary conditions at b-hanging nodes must be inherited from the corresponding (base) master nodes. All such constraints are of course nonpermanent because nodes nature can change step by step during the transient.

Finally, the notion of neighbor and p-neighbor across an element's face allows to efficiently compute numerical fluxes (transport terms) in adaptive fluid calculations.

##### 4.1. Constraints on hanging nodes

As an example of hanging node consider node  $h_1$  in the right part of Fig. 1, which results from the splitting of element  $i$ . In the current mesh configuration this node hangs upon two master nodes,  $K$  and  $L$ . These happen to be *base* nodes in the present case, but this is not necessary in general, and is irrelevant as concerns the proposed treatment.

A displacement-based finite element formulation is used in the code. Time integration is done explicitly by the central difference scheme and the fundamental quantity is the velocity  $\mathbf{v}$ , discretized at nodes. Therefore, in order to ensure continuity of the solution around a generic hanging node  $H$  the constraint to be imposed is:

$$\mathbf{v}_H = \sum_{i=1}^m N_i \mathbf{v}_{M_i}, \quad (1)$$

where  $M_i$  are the  $m$  master nodes upon which node  $H$  is hanging, and  $N_i$  are suitable coefficients. In the example of Fig. 1,  $m = 2$  and Eq. (1) becomes  $\mathbf{v}_{h_1} = (\mathbf{v}_K + \mathbf{v}_L)/2$ .

Constraints (1) are written for each hanging node. Each constraint is split into  $d$  components, one for each global axis, where  $d$  is the space dimension (2 or 3). All such constraints, plus any essential boundary conditions imposed by the user,

*F. Casadei, P. Díez & F. Verdugo*

form a linear system of constraints on the (velocity) degrees of freedom (dofs) of the system. Note that this system contains *only the constrained dofs*, not all system dofs. To enforce such constraints a method of Lagrange multipliers is used. This requires the numerical solution, at each time step, of a linear system of equations and is the only implicit part of the transient solution strategy. Interested readers can find full details of the procedure in Casadei and Halleux [1995, 2009].

#### **4.2. Constraints on b-hanging nodes**

As an example of b-hanging node consider node  $b_1$  in the right part of Fig. 1, which results from the splitting of element  $i$ . In the current mesh configuration this node b-hangs upon two master nodes,  $I$  and  $J$ . Note that, in contrast with the case of hanging nodes of Sec. 4.1, the masters of a b-hanging node are always base nodes.

An important practical aspect of using adaptivity in real applications is the specification of essential boundary conditions. Here we assume that users only know the base mesh, which is provided in input to the code, and therefore *boundary conditions are specified only for the base nodes*. It is then desirable that such conditions be automatically propagated to any descendent nodes on the boundary that are (automatically, i.e., out of user's control) created during the mesh adaptation process.

To this end, we exploit the knowledge of b-hanging nodes resulting from the algorithms of Sec. 3. The  $m$  masters  $M_i$  of a generic b-hanging node are inspected. If *all* of them share the *same* type of boundary condition, then this condition is imposed on the b-hanging node as well, and is added to the system of constraints to be solved by the Lagrange multipliers method as described in Sec. 4.1. This explains why the masters of a b-hanging node are always base nodes: because boundary conditions are explicitly known only for base nodes, not for descendents.

For example, assume that in the case of Fig. 1 node  $I$  is blocked in the vertical direction, while node  $J$  is blocked in both directions. Then, b-hanging node  $b_1$  would also be blocked in the vertical direction. This strategy works well, at least for the simplest types of boundary conditions, as shown in the numerical examples of Sec. 5.

#### **4.3. Numerical fluxes in fluid calculations**

The knowledge of the neighbor or p-neighbor at each element face resulting from the algorithms of Sec. 3 allows a precise and efficient calculation of *numerical fluxes* across element-to-element interfaces, an essential ingredient in the solution of fluid equations. The procedure is briefly outlined for the case of fluid modeling by finite elements using a classical *fractional step* approach, but it can be extended along the same lines also to other schemes, e.g., to node-centered or cell-centered finite volume formulations.

In the chosen fractional step approach, transport terms (numerical fluxes) across neighboring elements — resulting from Euler equations for compressible inviscid fluids — are computed according to the so-called *lowest-index rule*.

Assuming for the moment a conforming mesh, if elements  $i$  and  $j$  are neighbors at a given face, then the flux of mass and energy across the face is evaluated (with the appropriate sign, depending on nodal velocities) while treating the element with the *minimum index*, i.e.,  $\min(i, j)$  in the general loop over all elements. This ensures two things: first, the transport across each face is evaluated only once (correctness); second, when an element is treated all fluxes across its faces have been evaluated so that the element state can be directly updated, without the need of an additional loop over elements (efficiency). This algorithm is generalized as follows to the case of nonconforming meshes (adaptivity):

1. Set total mass and energy fluxes to zero for all elements.
2. Loop over elements. Let  $i$  be the current element.
3. Loop over  $i$ 's faces. Let  $F$  be the current face,  $j$  the neighbor and  $p$  the  $p$ -neighbor of  $i$  across face  $F$ .
4. If  $j = 0$  then:
  - If  $p = 0$  or  $0 < p < i$  then skip flux calculations for face  $F$ .
  - Else  $p > i$ . Compute the (signed) mass and energy fluxes from  $i$  to  $p$  across  $F$ , subtract them from the total fluxes of  $i$  and add them to the total fluxes of  $p$ .
5. Else  $j > 0$ . Then:
  - If  $j$  is a leaf, then:
    - If  $j < i$  then skip flux calculations for face  $F$ .
    - Else  $j > i$ . Compute the (signed) mass and energy fluxes from  $i$  to  $j$  across  $F$ , subtract them from the total fluxes of  $i$  and add them to the total fluxes of  $j$ .
  - Else  $j$  is a branch. Then loop on all active (leaf) descendents  $d_j$  of  $j$  having  $i$  as  $p$ -neighbor across one of their faces  $f_j$ :
    - If  $d_j < i$  then skip flux calculations for face  $f_j$ .
    - Else  $d_j > i$ . Compute the (signed) mass/energy fluxes from  $i$  to  $d_j$  across  $f_j$ , subtract them from the total fluxes of  $i$  and add them to the total fluxes of  $d_j$ . Note that the geometry of (the smaller) face  $f_j$ , and not of (the larger) face  $F$ , is used in this case to compute the fluxes.
    - Next  $d_j$ .
6. Next face (GOTO 3).
7. All faces have been considered for the current element  $i$  and therefore its total mass and energy fluxes have been computed. Update the element's physical state and compute internal forces.
8. Next element (GOTO 2).

## 5. Numerical Examples

Three numerical examples are presented to illustrate the proposed mesh refinement and un-refinement algorithms in action. In all cases mesh adaptation is piloted by a

*F. Casadei, P. Díez & F. Verdugo*

special WAVE directive simulating the propagation of waves in a continuum. Two types of waves are considered in these tests: a plane wave and a spherical wave. The first type is characterized by a source point and by a direction of propagation, while the second only requires the source point. To each wave are assigned a constant imposed propagation speed  $v$  and a starting time  $t_0$ . Each wave front has two associated length parameters:  $h_1$  specifies the thickness of the wave front zone in which the mesh has to be refined up to an imposed maximum level  $L_{\max}$ ;  $h_2$  specifies the thickness of the whole wave. The mesh refinement level is varied linearly from  $L_{\max}$  (finest mesh) to 1 (base mesh) in the zone between  $h_1$  and  $h_2$ .

The values of all wave parameters are prescribed according to known analytical solutions for the simple academic problems chosen. The following tests cannot be considered real adaptive calculations, because in adaptivity mesh refinement should rather be (automatically) piloted by suitable error estimators/indicators. However, the tests are sufficient to check all geometric aspects of the proposed mesh refinement and un-refinement algorithms, and to verify their effects on explicit numerical solutions in fast transient dynamics.

### 5.1. *Spherical wave in a 3D slab*

The first test simulates propagation of a spherical wave in a square slab of  $10 \times 10$  units and of thickness 1. The wave originates in one corner of the slab at time 0. The base mesh consists of  $10 \times 10 = 100$  regular cubes and the chosen wave parameters are:  $L_{\max} = 3$ ,  $h_1 = 1.5$ ,  $h_2 = 5.0$ ,  $v = 5000$ . The material is linear elastic but material properties are irrelevant in this case because the wave is purely fictitious: no loading is applied and thus no stresses are generated.

The initial mesh is shown in Fig. 9(a). Note that some refinement occurs near the wave origin (marked by a dot) already at the initial time, so that the wave is then properly captured. Since a spherical wave is used rather than a cylindrical one, mesh refinement is not uniform across the slab thickness. This is done on purpose in order to submit the splitting and un-splitting algorithms to a larger variety of cases than with a cylindrical wave. Figures 9(b) and 9(c) show the advancing wave front at 1.5 ms on the surface and within the body, respectively. Note that with the chosen parameters mesh transition is quite sharp and some base elements ( $L = 1$ ) are adjacent to some maximum-refined elements ( $L = 3$ ). This is probably not a good choice in practical applications but again, it is used here just to show that the proposed algorithms are general and can deal with arbitrary level jumps between neighboring elements. An option in the code allows to automatically prescribe smooth mesh transitions, such that the level jump between any couple of neighboring elements is at most one. This is to say that *the index of irregularity* of the mesh is one, or that a *1-irregular mesh* is prescribed, following the terminology introduced by Demkowicz *et al.* [1989].

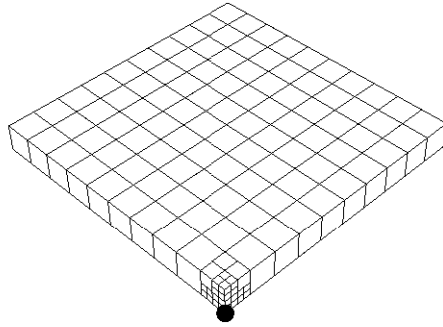
Figure 9(d) shows b-hanging nodes at 1.5 ms. These are all located on the slab surface, by definition. Finally, Figs. 9(e) and 9(f) show hanging nodes at 1.5 ms.

AN ALGORITHM FOR MESH REFINEMENT AND UN-REFINEMENT IN FAST  
TRANSIENT DYNAMICS

---

*An Algorithm for Mesh Refinement and Un-Refinement in Fast Transient Dynamics*

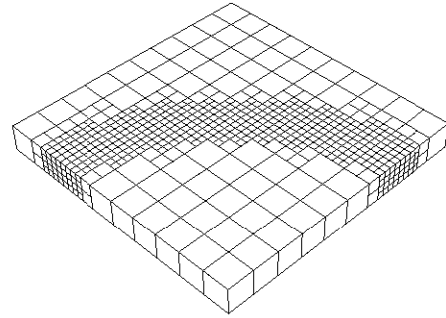
TEST01  
TIME: 0.00000E+00 STEP: 0



Source

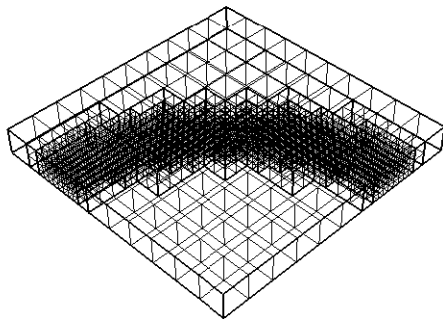
(a) Initial mesh (refined near the source)

TEST01  
TIME: 1.48956E-03 STEP: 43



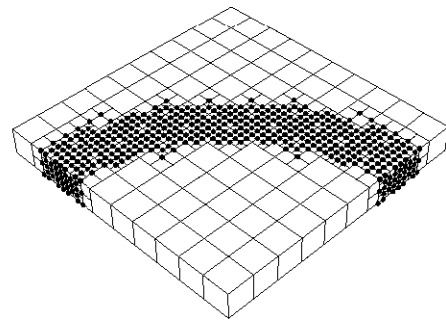
(b) Wave at 1.5 ms

TEST01  
TIME: 1.48956E-03 STEP: 43



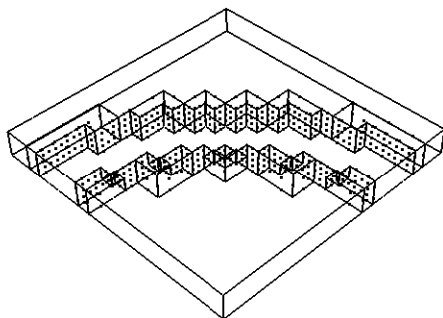
(c) Internal mesh view at 1.5 ms

TEST01  
TIME: 1.48956E-03 STEP: 43



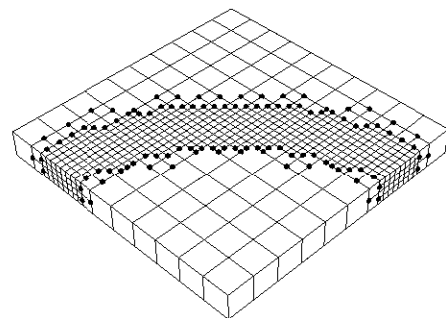
(d) B-hanging nodes at 1.5 ms

TEST01  
TIME: 1.48956E-03 STEP: 43



(e) Wave fronts and hanging nodes at 1.5 ms

TEST01  
TIME: 1.48956E-03 STEP: 43



(f) Hanging nodes on slab surface at 1.5 ms

Fig. 9. Spherical wave propagation in a 3D slab.

*F. Casadei, P. Díez & F. Verdugo*

These are located on the advancing wave fronts. In Fig. 9(e) the slab is made transparent to show all hanging nodes, most of which are in the body interior. Figure 9(f) shows only the hanging nodes on the body surface, a possibility which exists only in 3D cases as mentioned above.

The mesh adaptation algorithms behave as expected in this test. The maximum number of elements reached during the transient (including both branches and leaves) is 2460, of which 100 are base elements. The maximum number of nodes is 3183, of which 242 are base nodes.

### 5.2. Plane step wave in an elastic bar

The second test considers an elastic bar of length  $l = 1$  m, with a square cross-section of  $0.1 \times 0.1$  m subjected to a constant pressure  $p = 1.0 \times 10^8$  Pa at the left end, and blocked at the right end. The material is linear elastic with density  $\rho = 8000$  kg/m<sup>3</sup>, Young's modulus  $E = 2.0 \times 10^{11}$  Pa, Poisson's coefficient  $\nu = 0$  (so that the problem is physically 1D). With these values, sound speed is  $c = \sqrt{E/\rho} = 5000$  m/s. Adaptivity is piloted by *two* WAVE directives. The first one represents the incident wave produced by the pressure load, starting at the left end at  $t = 0$  and propagating to the right. The second one represents the reflected wave, starting at the (blocked) right end at  $t = l/c = 2 \times 10^{-4}$  s and moving to the left. Both waves have  $h_1 = 0.15$ ,  $h_2 = 0.5$  and  $L_{\max} = 4$ . The base mesh uses only 10 regular cubes.

This test is a first example of the treatment of boundary conditions with the present adaptivity strategy. The pressure (an example of *natural* condition) is applied by a special *boundary-condition* (b.c.) *element* attached to the left end of the bar. This element has the shape of a 4-node quadrilateral, whose nodes are merged with the nodes of the (base) cube face at the left end of the bar. The advantage of this technique is evident from the mesh at  $t = 0$ , shown in Fig. 10(a) (first picture): the first WAVE command refines the bar mesh (cube elements) at the left end at  $t = 0$ , in order to properly capture the incoming wave. Whenever a cube is refined or un-refined, the algorithm checks whether there is a b.c. element attached to any of its (external) faces, and if so then the b.c. element is automatically split or un-split as well. In this way, the applied load (pressure in this case) is transferred from the parent to the descendent b.c. elements and, ultimately, properly scaled loads result on the appropriate surface nodes of the descendent cubes, in a fully automatic and transparent way.

The imposed blockage of nodes at the right bar end is another example of boundary condition, in this case of the *essential* type. It seems natural that users impose constraints only on the *base* nodes, in this case the four nodes of the right-most cube face. The present adaptivity strategy makes it relatively simple to program automatic transfer of constraints to any descendent nodes created in the adaptive process (Sec. 4.2). In fact, all such nodes are *b-hanging nodes* whose masters are the blocked face nodes. Since all masters are subjected to the *same* constraint (horizontal blockage), this constraint can be easily and automatically propagated to

*An Algorithm for Mesh Refinement and Un-Refinement in Fast Transient Dynamics*

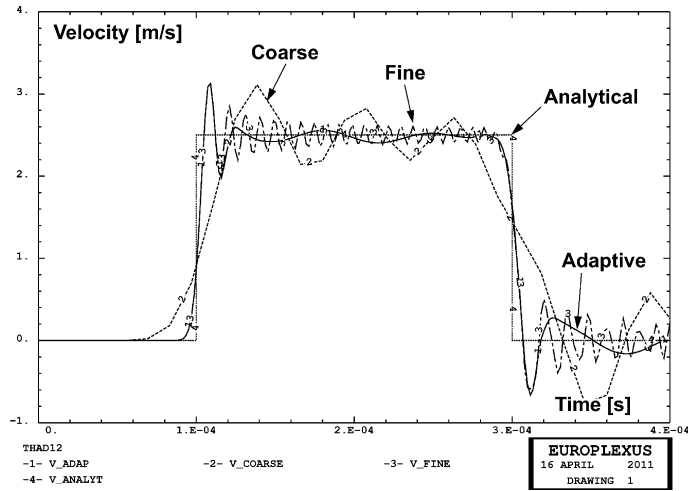
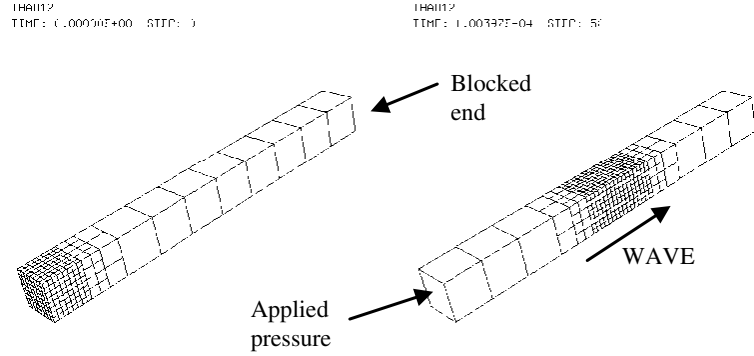


Fig. 10. Plane step wave in an elastic bar.

all the relevant descendent nodes. Figure 10(a) (second picture) shows the adapted mesh at a later time, when the incident wave is traversing the bar. Note that the mesh at the left bar extremity (including the b.c. elements) has been automatically un-refined and the base mesh is recovered.

Figure 10(b) compares solutions without and with adaptivity against the analytical solution of the bar problem. The curves represent the time history of velocity at the bar center. The analytical solution is the step function represented by the dotted curve. Numerical solutions present oscillations, due to the elastic nature of the material (no numerical damping). Two solutions with uniform cube meshes are shown (dashed lines): one with a coarse mesh (only 10 elements) and one with a fine mesh (80 elements), corresponding to the maximum mesh refinement in the adaptive solution (level 4). The adaptive solution, represented by the solid line, coincides exactly with the fine-mesh solution near the jumps at 0.1 and 0.3 ms (where the

*F. Casadei, P. Díez & F. Verdugo*

WAVE directive keeps the mesh fine), while far from them it has an oscillatory behavior. Oscillations have lower amplitude and lower frequency than both uniform mesh solutions, so the adaptive solution looks somewhat smoother. Probably some numerical damping is introduced by the mesh un-refinement process, whereby stresses in a parent element are computed by averaging the stresses in its children. The adaptive solution looks very good: it captures the shocks as precisely as the fine-mesh model, and presents less oscillations.

The maximum number of cube elements reached during the transient (including both branches and leaves) is 1,386, of which 10 are base elements. The maximum number of special b.c. elements (to impose the pressure) reached during the transient (including both branches and leaves) is 85, of which only 1 is a base element. The maximum number of nodes is 1,656, of which 44 are base nodes. The same bar problem has been solved also with 2D elements, QUA4 4-node quadrilaterals. Results (not shown for brevity) are nearly identical to the 3D case, both with uniform and with adaptive meshes.

### 5.3. Shock tube

The third and last test is the classical shock tube problem. A rigid tube of length  $l = 1$  m and  $0.01 \times 0.01$  m square cross section is filled by a perfect gas and is subdivided in two equal parts by an ideal wall. The left part is initially at higher pressure than the right part. At the initial time the separation between the two parts is removed and waves start to propagate along the tube: a *shock wave* and a *contact discontinuity* wave propagate towards the low-pressure zone, and a *rarefaction wave* propagates towards the high-pressure zone. A complete analytical solution of this problem is available.

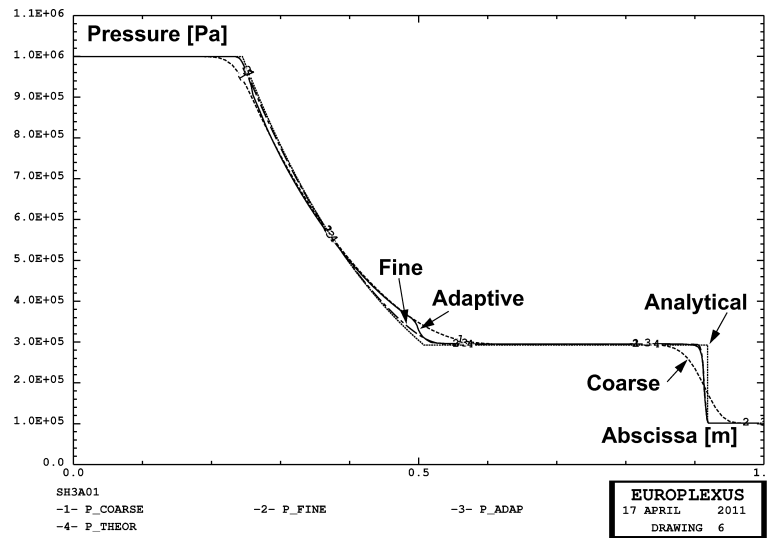
The assumed gas equation is  $p = (\gamma - 1)\rho i$  where  $p$  is the pressure,  $\gamma$  is the ratio of specific heats,  $\rho$  is the density and  $i$  is the specific internal energy. We take  $\gamma = 1.269$  and  $i = 3.046 \times 10^6$  J/kg in both zones. The left zone has  $\rho_1 = 1.22$  kg/m<sup>3</sup> and thus  $p_1 = 1 \times 10^6$  Pa, while the right zone has  $\rho_2 = 0.1237$  kg/m<sup>3</sup> and thus  $p_2 = 1.01 \times 10^5$  Pa.

Two uniform-mesh solutions are obtained, one with a coarse mesh of 100 cube fluid elements and the other with a fine mesh of 800 cubes. Then an adaptive solution is obtained using a base mesh of 100 cubes, and *four* WAVE directives, one for the shock wave, one for the contact discontinuity and two for the initial and final fronts of the rarefaction fan. All waves originate at the tube center at the initial time and propagate in the relevant direction with the analytically computed velocities: 1,672 m/s for the shock, 925.4 m/s for the contact discontinuity,  $-30.12$  m/s and  $-1,020$  m/s for the rarefaction wave. All waves use  $h_1 = 0.015$ ,  $h_2 = 0.05$  and  $L_{\max} = 4$ . The boundary conditions are as follows: all (base) nodes on the tube surface are blocked in the  $y$  and  $z$  directions; the four (base) nodes of the left tube face and the four (base) nodes of the right tube face are blocked also in the  $x$  direction. Like in the previous example, b-hanging (descendent) nodes automatically

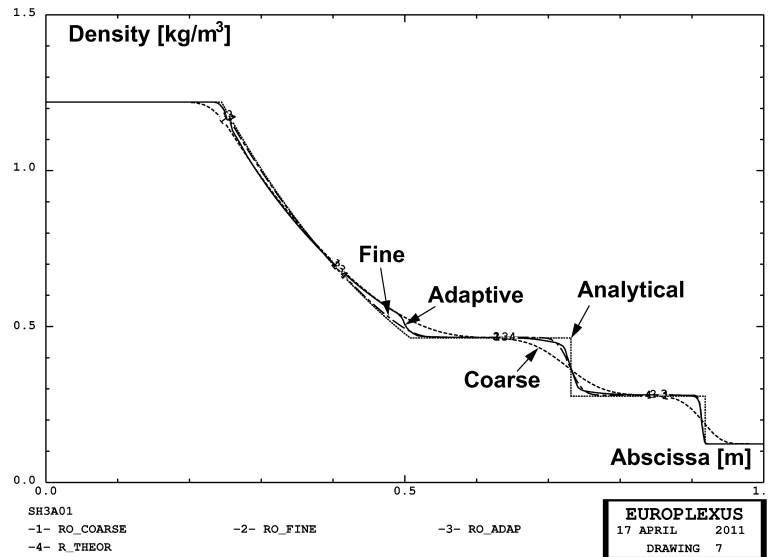
*An Algorithm for Mesh Refinement and Un-Refinement in Fast Transient Dynamics*

inherit such constraints from the corresponding master (base) nodes, thanks to the strategy proposed in Sec. 4.2. Numerical fluxes in the fluid are computed according to the technique described in Sec. 4.3.

Figures 11(a) and 11(b) show the distributions of fluid pressure and of fluid density along the tube, respectively, at 0.25 ms. The analytical solution is the step



(a) Pressure along the tube at 0.25 ms



(b) Density along the tube at 0.25 ms

Fig. 11. Shock tube.

*F. Casadei, P. Díez & F. Verdugo*

function represented by the dotted curve. The two solutions with uniform (coarse or fine) meshes are the dashed curves. The adaptive solution is the solid line. Both the shock and the contact discontinuity are captured by the adaptive solution with the same accuracy as the fine-mesh solution. In the rarefaction wave, only the two fronts are captured with great accuracy, while inside the fan the adaptive solution is similar to the coarse-mesh solution. This is normal since the chosen WAVE directives refine the mesh only at the fronts. All solutions are quite smooth and no oscillations are induced by mesh adaptation.

The maximum number of elements reached during the transient (including both branches and leaves) is 5,084, of which 100 are base elements. The maximum number of nodes is 6,290, of which 404 are base nodes. Identical uniform-mesh and adaptive solutions are obtained in 2D with quadrilateral elements, and are not presented here for brevity.

#### **5.4. Efficiency**

A rough estimate of the efficiency of the proposed mesh refinement and un-refinement algorithms can be obtained by comparing CPU times for uniform-mesh and adaptive solutions. Such times are too small for the elastic bar test of Sec. 5.2, but for the shock tube problem of Sec. 5.3 (3D version) we have the following results. The adaptive solution with 100 base elements, 4 WAVE directives and  $L_{\max} = 4$  needs 44s on a laptop computer. Since the present algorithms refine the mesh in all spatial directions, this should be compared against a uniform fine-mesh nonadaptive solution with  $8 \times 8 \times 800 = 51,200$  elements, which needs 229s. Therefore, a speed-up factor of 5.2 is obtained in this case (including the overhead needed to compute the WAVE fronts in the adaptive solution).

## **6. Conclusions and Perspectives**

The paper presents procedures to arbitrarily refine and un-refine a computational grid of QUA4 (in 2D) or CUB8 (in 3D) element shapes. The chosen strategy, based only upon element connectivity (integer data), is simple and robust and lends itself well to fast transient dynamic applications, dominated by wave propagation.

The numerical tests, performed using a simple wave propagation paradigm (WAVE directive) both in solid- and in fluid mechanics, show that mesh-adaptive solutions are as accurate as uniform fine-mesh solutions near the advancing wave fronts, without causing instability or loss of accuracy in zones where the solution is smooth.

Special attention is devoted to boundary conditions in adaptivity, an aspect of great importance in realistic applications. As concerns essential conditions, a technique exploiting the information resulting from the proposed mesh adaptation algorithms allows propagating the user-imposed constraints from the base nodes to the descendent (adaptive) nodes in an automatic and transparent way. Similarly,

for natural conditions (e.g., an imposed pressure) a technique, based on special boundary-condition elements also subjected to adaptivity (in a natural way), is proposed in the bar test of Sec. 5.2.

This is only a first step (covering mostly geometric aspects) towards implementation of full mesh adaptivity in fast dynamics. Ongoing work focuses on error indicators, which should ultimately be used to automatically pilot mesh adaptation especially in fast transient fluid–structure interaction problems, see Ref. [Casadei *et al.* (2011)], by the algorithms proposed in this paper. To this end, calculation of numerical fluxes in adaptive fluid meshes will have to be extended to finite volume formulations, along the lines already presented for finite elements in Sec. 4.3.

### Appendix A.

Here are the auxiliary procedures mentioned in Secs. 3.2 and 3.3.

Algorithm A.1 — Determination of internal and external faces.

Let  $j$  be the neighbor and  $p$  the  $p$ -neighbor of element  $i$  across its face  $F_k$ . Then:

- If  $j > 0$ , then  $F_k$  is internal and lies upon a locally conforming element-to-element interface.
- Else, if  $p > 0$  then  $F_k$  is internal and lies upon a locally nonconforming element-to-element interface.
- Else,  $F_k$  is external.

Algorithm A.2 — Determination of base corner or base face of an external corner.

Let  $c$  be an *external* corner of element  $i$  (see criterion in Sec. 3.3). Let  $F_1 = C_F(1, c)$  and  $F_2 = C_F(2, c)$  be the two faces of  $i$  adjacent to  $c$ , see Table 2. Then:

- If  $F_1$  and  $F_2$  are either both external or both internal (see Algorithm A.1), then corner  $c$  lies upon a base corner  $c_B$ . This is the  $c$ th corner of  $B_i$ , the base element from which element  $i$  descends (this element is called the *base ancestor* of  $i$ ). The base ancestor is readily determined by (recursively) computing  $i$ 's parent up to level 1 in the elements tree.
- Else,  $F_1$  and  $F_2$  are one external ( $F_e$ ) and one internal ( $F_i$ ). Let  $d_A, d_B$  be the two descendents of the generic CUB8 element adjacent to its  $c$ th corner:  $d_A = C_D(1, c)$  and  $d_B = C_D(2, c)$ , see Table 2. Then:
  - If  $i$  is either the  $d_A$ th or the  $d_B$ th descendent of its parent, and if this property holds recursively up to level 1 of the elements tree, then corner  $c$  lies upon a base corner  $c_B$ , namely the  $c$ th corner of  $B_i$ , the base ancestor of  $i$ .
  - Else, corner  $c$  lies upon a base face  $F_B$ , namely the  $F_e$ th face of  $B_i$ , the base ancestor of  $i$ .

*F. Casadei, P. Díez & F. Verdugo*

Algorithm A.3 — Determination of complete or incomplete corner star.

The corner star around corner  $c$  of element  $i$  (see Sec. 3.4), represented by element lists  $S_1$  and  $S_2$ , of length  $n_{S_1}$ ,  $n_{S_2}$  is complete if and only if:

- Either  $n_{S_1} > 0$  and  $S_1(n_{S_1}) = i$ . In this case it is  $n_{S_2} = 0$ .
- Or,  $n_{S_1} > 0$  and  $n_{S_2} > 0$  and  $S_1(n_{S_1}) = S_2(n_{S_2}) \neq i$ . This happens when there is a “big” p-neighbor without a corner superposed to corner  $c$  which “closes” the star, see e.g., Fig. 7(d). We denote such a p-neighbor a *face p-neighbor*, as opposed to a *corner p-neighbor*.

## References

- Burstedde, C. *et al.* [2009] “ALPS: A framework for parallel adaptive PDE solution,” *J. Phys.: Conference Series* 180, doi: 10.1088/1742-6596/180/1/012009.
- Casadei, F. and Halleux, J. P. [1995] “An algorithm for permanent fluid–structure interaction in explicit transient dynamics,” *Comput. Meth. Appl. Mech. Eng.* **128**(3–4), 231–289.
- Casadei, F. and Halleux, J. P. [2009] “Binary spatial partitioning of the central-difference time integration scheme for explicit fast transient dynamics,” *Int. J. Numer. Meth. Eng.* **78**, 1436–1473.
- Casadei, F., Larcher, M. and Leconte, N. [2011] “Strong and weak forms of fully non-conforming FSI algorithm in fast transient dynamics for blast loading of structures,” in *Proc. COMPDYN 2011 Conference*, eds. Papadrakakis, M., Fragiadakis, M. and Plevris, V., Corfu, Greece, 26–28 May 2011.
- Casadei, F. *et al.* [2012] EUROPLEXUS User’s Manual: see <http://europlexus.jrc.ec.europa.eu/>.
- Demkowicz, L., Devloo, Ph. and Oden, J. T. [1985] “On an h-type mesh-refinement strategy based on minimization of interpolation errors,” *Comput. Meth. Appl. Mech. Eng.* **53**, 67–89.
- Demkowicz, L. *et al.* [1989] “Towards a universal h-p adaptive finite element strategy, Part 1. Constrained approximation and data structure,” *Comput. Meth. Appl. Mech. Eng.* **77**, 79–112.
- Erhart, T., Wall, W. A. and Ramm, E. [2006] “Robust adaptive remeshing strategy for large deformation, transient impact simulations,” *Int. J. Numer. Meth. Eng.* **65**, 2139–2166.
- Frey, P. J. and Alauzet, F. [2005] “Anisotropic mesh adaptation for CFD computations,” *Comput. Meth. Appl. Mech. Eng.* **194**, 5068–5082.
- Kee, Bernard B. T., Liu, G. R. and Lu, C. [2008] “A least-square radial point collocation method for adaptive analysis in linear elasticity,” *Eng. Anal. Bound. Elem.* **32**, 440–460.
- Li, Y. and Liu, G. R. [2011] “An adaptive NS/ES-FEM approach for 2D contact problems using triangular elements,” *Finite Elem. Anal. Design* **47**, 256–275.
- Liu, G. R. and Tu, Z. H. [2002] “An adaptive procedure based on background cells for meshless methods,” *Comput. Meth. Appl. Mech. Eng.* **191**, 1923–1943.
- Liu, G. R., Kee, Bernard B. T. and Chun, L. [2006] “A stabilized least-squares radial point collocation method (LS-RPCM) for adaptive analysis,” *Comput. Meth. Appl. Mech. Eng.* **195**, 4843–4861.
- Meyer, A. [2009] “Error estimators and the adaptive finite element method on large strain deformation problems,” *Math. Meth. Appl. Sci.* **32**, 2148–2159.

- Nguyen-Thoi, T., Liu, G. R. *et al.* [2009] “Adaptive analysis using the node-based smoothed finite element method,” *Commun. Numer. Meth. Eng.* DOI: 10.1002/cnm.1291.
- Nithiarasu, P. and Zienkiewicz, O. C. [2000] “Adaptive mesh generation for fluid mechanics problems,” *Int. J. Numer. Meth. Eng.* **47**, 629–662.
- Peraire, J. *et al.* [1987] “Adaptive remeshing for compressible flow computations,” *J. Comput. Phys.* **72**, 449–466.
- Tang, Q., Zhang, G. Y., Liu, G. R. *et al.* [2011] “A three-dimensional adaptive analysis using the meshfree node-based smoothed point interpolation method (NS-PIM),” *Eng. Anal. Bound. Elem.* **35**, 1123–1135.
- Xu, George X., Liu, G. R. and Tani, A. [2010] “An adaptive gradient smoothing method (GSM) for fluid dynamics problems,” *Int. J. Numer. Meth. Fluids* **62**, 499–529.
- Yerry, M. A. and Shephard, M. S. [1983] “A modified quad-tree approach to finite element mesh generation,” *IEEE Comput. Graphics Appl.* **3**(1), 34–46.
- Zhang, G. Y., Liu, G. R. and Li, Y. [2008a] “An efficient adaptive analysis procedure for certified solutions with exact bounds of strain energy for elasticity problems,” *Finite Elem. Anal. Design* **44**, 831–841.
- Zhang, J., Liu, G. R. *et al.* [2008b] “A gradient smoothing method (GSM) based on strong form governing equation for adaptive analysis of solid mechanics problems,” *Finite Elem. Anal. Design* **44**, 889–909.

